Faculdade de Engenharia da Universidade do Porto

Experimental Characterisation of Induced Partial Saturation for Liquefaction Mitigation

Ahmed Mansour Ali Ali Elbarbary

A research thesis submitted to the Faculty of Engineering of the University of Porto for obtaining the degree of Doctor in Civil Engineering

Supervisor: Dr. Cristiana Maria Fonseca Ferreira

January 2026

Acknowledgements

I am grateful to the many kind people who supported me throughout my PhD journey, and I would like to express my appreciation through these acknowledgements.

I would like to express my sincere gratitude to my supervisor, Dr. Cristiana Ferreira, for her guidance, patience, and continuous support throughout this research. Her professionalism, understanding, and open-door approach created an environment in which I could learn, develop confidence, and progress steadily. I am especially grateful for the opportunity she provided me to conduct the dynamic centrifuge experiments at the Schofield Centre, University of Cambridge, through my participation in the GEOLAB project.

I also wish to thank Professor Giulia Viggiani (Head of Division, Civil Engineering, University of Cambridge) and Director of the GEOLAB project, for facilitating and supporting the dynamic centrifuge work carried out at the Schofield Centre.

At FEUP, I am grateful to Professor Viana da Fonseca, Director of LabGeo, for facilitating my work in the laboratory and supporting the completion of the experimental program. I am equally grateful to Professor Topa Gomes, Sara Rios, and all staff of the Geotechnical Department for their teaching, support, and constructive input during my studies.

I also thank Daniela Coelho, and Cláudia Pinto; the laboratory technicians for their valuable guidance and for dedicating time to explain experimental procedures and train me in experimental laboratory testing.

In addition, I would like to thank my colleagues and friends; Nelson, Isabela, Toninho, Neya, Rashid, Isabela, Celso, Ali, Asmaa, and Leonardo—who shared this journey with me. Their collaboration, discussions, and encouragement contributed greatly to the overall experience.

I acknowledge Fundação para a Ciência e a Tecnologia (FCT) for the financial support provided through grant UI/BD/150978/2021; without this funding, completing this work would have been significantly more difficult.

Finally, my family.

My beautiful Mom Azza, I'm truly lucky to have you in my life. Most of the best parts of me come from you. Love u.

My Father Mansour, thank you for teaching me resilience and strength. That mindset helped me finish this work and face difficult situations. You always encouraged me to pursue a good education. Love u.

My Sister Shaymaa, the kindest heart, and my best friend. Love you and Ali, and lots of love to your little angels, Malak and Liela.

My Brother Abdo, thank you for always encouraging me, supporting me, and standing by me. Love u.

My Brother Youssef, thank you for always having my back and keeping me strong. Love u.

To Noha, you have a special place in my heart that will always remain yours, whatever happens. Love u.

Imagine all the people living life in peace

You may say I'm a dreamer, but I am not the only one!

On the other side, I see

trees of green

Red roses too

I see them bloom

For me and you

And I think to myself

What a wonderful world!

Abstract

High-intensity earthquakes have left profound impacts on communities and landscapes worldwide. These seismic events have caused widespread devastation, resulting in loss of life, population displacement, and economic disruption. Infrastructure such as buildings, roads, and bridges has collapsed, making recovery efforts even more challenging. Earthquake-induced soil liquefaction is a complex phenomenon in which soil progressively loses its shear strength and begins to behave like a fluid, potentially leading to catastrophic damage to buildings and infrastructure. To reduce and mitigate the risks associated with this phenomenon, several liquefaction mitigation techniques have been developed. These approaches include a broad set of methods, namely physical, chemical, and biological techniques, as well as Induced Partial Saturation (IPS). IPS has received increasing attention because a small reduction in the degree of saturation can increase the compressibility of the pore-fluid mixture, limit excess pore-water pressure build-up, and improve cyclic resistance.

In the literature review of this work, a comprehensive analysis of different soil liquefaction mitigation methods is presented, with particular emphasis on the IPS technique, which constitutes the main idea of this research. Through an extensive program of geotechnical laboratory testing, the liquefaction resistance of a Portuguese sand collected in the North Benavente (NB) area, Lisbon, Portugal, was investigated under fully and partially saturated conditions. NB sand is highly susceptible to liquefaction, with historical occurrences of liquefaction.

For this purpose, the physical and geo-mechanical properties of NB-sand were characterized and its critical state parameters were determined. Subsequently, an extensive program of cyclic triaxial tests was carried out to evaluate the liquefaction resistance of NB sand under fully and partially saturated conditions across different degrees of saturation (Sr). The influence of key parameters, including relative density and cyclic stress ratio (CSR), on the cyclic resistance of the soil was also examined. Seismic wave velocities were systematically measured using bender elements during the different testing phases, providing a direct indicator of the soil state throughout the experimental stages. These measurements were also used to evaluate the stress dependency of the small-strain shear modulus. Secant stiffness and hysteretic damping were assessed through the analysis of stress–strain hysteresis loops obtained from cyclic triaxial tests on fully and partially saturated specimens. This analysis enabled evaluating the effect of occluded air bubbles within the pore fluid on altering the soil's damping and stiffness, independently of matric suction. Complementarily, liquefaction resistance was also investigated for a reference sand, Hostun sand HN31, under fully and partially saturated conditions.

Additionally, a series of geotechnical centrifuge tests was performed at the Schofield Centre, University of Cambridge (UCAM), using Hostun sand HN31, with the objective of providing a robust assessment of air injection as a liquefaction mitigation technique under representative loading conditions. The results showed that a slight reduction in the degree of saturation significantly reduced pore water pressure build-up and increased the cyclic resistance of sands. It was also verified that occluded air bubbles influence both stiffness development and the energy dissipation mechanisms associated with cyclic loading.

Finally, a methodology was proposed to integrate cyclic triaxial testing and centrifuge modelling for Hostun sand HN31. The centrifuge response was interpreted through equivalent CSR–N_L points derived from the measured dynamic response up to liquefaction triggering, enabling direct comparison with liquefaction resistance curve obtained from

cyclic triaxial tests. The resulting comparison showed excellent agreement between the two experimental scales, indicating that the centrifuge tests captured liquefaction triggering trends consistent with those obtained from element testing.

The main contribution of this research is the combined assessment of induced partial saturation from complementary experimental approaches, linking changes in degree of saturation to pore pressure generation, liquefaction resistance, wave velocities, small-strain stiffness, secant stiffness, damping, and energy dissipation mechanisms.

Keywords: Liquefaction; Induced partial saturation (IPS); Cyclic triaxial testing; Centrifuge modelling.

Resumo

Os sismos de maior intensidade têm deixado impactos profundos nas comunidades e nas paisagens em todo o mundo. Estes eventos sísmicos causam devastação generalizada, resultando em perda de vidas humanas, deslocação de populações e perturbações económicas. Infraestruturas como edifícios, estradas e pontes colapsaram, tornando os esforços de recuperação ainda mais difíceis.

A liquefação dos solos induzida por sismos é um fenómeno complexo, no qual o solo perde progressivamente a sua resistência ao corte e passa a comportar-se como um fluido, podendo originar danos catastróficos em edifícios e infraestruturas.

Para reduzir e mitigar os riscos associados a este fenómeno, foram desenvolvidas várias técnicas de mitigação da liquefação. Estas abordagens incluem um conjunto alargado de métodos, nomeadamente intervenções físicas, químicas e biológicas, bem como a saturação parcial induzida (Induced Partial Saturation, IPS). A IPS destaca-se como uma das técnicas mais promissoras para a mitigação da liquefação. Esta abordagem inovadora tem demonstrado resultados relevantes no aumento da resistência do solo à liquefação.

Na revisão bibliográfica deste trabalho é apresentada uma análise abrangente de diferentes métodos de mitigação da liquefação dos solos, com especial enfoque na técnica de saturação parcial induzida (IPS), que constitui o principal objeto de estudo desta investigação.

Através de um programa extenso de ensaios laboratoriais geotécnicos, foi analisada a resistência à liquefação de uma areia portuguesa, recolhida na zona Norte de Benavente (NB), Lisboa, Portugal, em condições totalmente e parcialmente saturadas. A areia NB é um solo com elevada suscetibilidade à liquefação, com ocorrência histórica de liquefação.

Para esse efeito, foram caracterizadas as propriedades físicas e geomecânicas da areia NB e determinados os seus parâmetros no estado crítico. De seguida, foi realizado um programa abrangente de ensaios triaxiais cíclicos para avaliar a resistência à liquefação da areia NB em condições totalmente e parcialmente saturadas, para diferentes graus de saturação (Sr). Foi igualmente estudada a influência de parâmetros fundamentais, incluindo a densidade relativa e a razão de tensão cíclica (CSR), na resistência cíclica do solo. As velocidades de propagação de ondas sísmicas foram medidas de forma sistemática com bender elements durante as diferentes fases dos ensaios, constituindo um indicador direto do estado do solo ao longo das várias etapas experimentais. Estas medições foram ainda utilizadas para avaliar a dependência do módulo de distorção de pequenas deformações com o nível de tensão.

A rigidez secante e o amortecimento histerético foram avaliados através da análise dos ciclos de histerese tensão–deformação obtidos nos ensaios triaxiais cíclicos em provetes totalmente e parcialmente saturados. Esta análise permitiu quantificar de que forma as bolhas de ar ocluídas modificam a evolução da rigidez e do amortecimento, evitando simultaneamente a influência de sucção, que pode aumentar a rigidez aparente. Complementarmente, foi também investigada a resistência à liquefação para uma areia de referência, a areia Hostun HN31, em condições totalmente e parcialmente saturadas, como forma de validar os resultados e estabelecer uma metodologia universal.

Adicionalmente, foi realizada uma série de ensaios em centrifugadora geotécnica no Schofield Centre, University of Cambridge (UCAM), utilizando a areia Hostun HN31, com o objetivo de fornecer uma avaliação realista da injeção de ar como técnica de mitigação da

liquefação, sob condições fronteira e de carregamento representativas. Os resultados mostraram que uma ligeira redução do grau de saturação diminuiu significativamente a acumulação de pressão de água nos poros e aumentou a resistência cíclica das areias. Verificou-se, adicionalmente, que as bolhas de ar ocluídas influenciam tanto o desenvolvimento da rigidez como os mecanismos de dissipação de energia associados ao carregamento cíclico.

Por fim, foi proposta uma metodologia para integrar ensaios triaxiais cíclicos e modelação em centrifugadora para a areia Hostun HN31. A resposta observada nos ensaios em centrifugadora foi interpretada através de pontos equivalentes CSR–N_L, derivados da resposta dinâmica medida até à ocorrência de liquefação, permitindo uma comparação direta com a curva de resistência à liquefação obtida a partir dos ensaios triaxiais cíclicos. A comparação obtida revelou uma excelente concordância entre as duas abordagens experimentais, indicando que os ensaios em centrifugadora captaram tendências de desencadeamento da liquefação consistentes com as obtidas nos ensaios triaxiais.

O principal contributo desta investigação reside na avaliação integrada da saturação parcial induzida através de abordagens experimentais complementares, estabelecendo a ligação entre a variação do grau de saturação e a geração de pressão intersticial, a resistência à liquefação, as velocidades de propagação das ondas, a rigidez a pequenas deformações, a rigidez secante, o amortecimento e os mecanismos de dissipação de energia.

Palavras chave: Liquefação; Saturação parcial induzida (IPS); Ensaios triaxiais cíclicos; Modelação em centrifugadora.

Table of contents

Acknowledgements i
Abstract v
Resumo vii
Table of contents ix
List of figures xiii
List of tables xxv
List of acronyms and symbols xxvii
List of acronyms xxvii
List of symbols xxviii
1. Introduction 1
1.1. Motivation 1
1.2. Objectives 1
1.3. Structure of the thesis 2
2. Literature review 3
2.1. Introduction 3
2.2. Liquefaction assessment, triggering, and hazards 3
2.2.1. Liquefaction susceptibility 4
2.2.2. Liquefaction triggering 4
2.2.3. Types of liquefaction 12
2.3. Liquefaction mitigation methods and classification 17
2.3.1. Historical background on liquefaction mitigation methods 17
2.3.2. Recent physical mitigation methods 17
2.3.3. Recent chemical mitigation Methods 19
2.3.4. Recent biological mitigation methods 29
2.3.5. Desaturation 34
2.4. Summary and main research gaps 56
3. Materials, methods and testing program 59
3.1. Tested materials 59
3.1.1. NB sand 59
3.1.2. Hostun sand 61
3.2. Physical characterization 61

3.2.1. NB sand 61
3.2.2. Hostun sand 69
3.3. Seismic wave measurements using bender elements 71
3.4. Monotonic Triaxial Tests 73
3.4.1. Introduction 73
3.4.2. Brief description of the conventional triaxial apparatus and procedures 74
3.4.3. Monotonic triaxial testing procedures 75
3.5. Double-wall triaxial chamber tests 77
3.5.1. Brief description 77
3.5.2. Double wall triaxial apparatus setup 78
3.6. Cyclic triaxial tests 83
3.6.1. Brief description 83
3.6.2. Cyclic triaxial apparatus setup 84
3.7. Physical modelling (centrifuge modelling) 90
3.7.1. Main concept and objective 90
3.7.2. Centrifuge testing and setup 90
3.8. Remarks 101
4. Monotonic triaxial tests: results and analyses 103
4.1. Geomechanical properties of NB sand (Tx) 103
4.1.1. Stress-strain results 103
4.1.2. Critical state line (CSL) 105
4.2. Monotonic behavior of fully and partially saturated NB sand (UTx) 108
4.2.1. Stress-strain results 108
4.2.2. Volumetric change of fully and partially saturated NB sand 109
4.2.3. Critical State line (CSL) 112
4.2.4. Shear resistance based on the volumetric water content Theta θ ... 113
4.3. Main findings 115
5. Cyclic triaxial tests (CTx): results and analyses 117
5.1. Cyclic behavior of NB sand 117
5.1.1. Assessment of the degree of Saturation 117
5.1.2. Void ratio and small strain stiffness assessment 121
5.1.3. Stress dependency and small-strain behavior 125
5.1.4. Liquefaction resistance of fully saturated tests 133
5.1.5. Liquefaction resistance of partially saturated tests 136

5.1.6. Liquefaction resistance analysis using volumetric water content, θ . 138
5.2. Hysteresis stress-strain behavior of NB sand 145
5.2.1. Analysis of stress-strain cyclic loops under fully and partially saturated conditions 145
5.2.2. Secant shear stiffness 152
5.2.3. Influence of cyclic stress ratio CSR on secant stiffness 153
5.2.4. Evolution of secant stiffness with shear strain amplitude 153
5.2.5. Secant stiffness and excess pore water pressure 155
5.2.6. Damping ratio evolution for fully and partially saturated conditions 157
5.2.7. Cyclic stress-path for fully and partially saturated conditions 159
5.3. Undrained dynamic soil properties of fully and partially saturated NB sand 161
5.4. Cyclic behavior of Hostun sand 168
5.4.1. Stress dependency and small-strain behavior 168
5.4.2. Liquefaction resistance of fully and partially saturated 171
5.5. Main findings 174
6. Centrifuge modelling tests on Hostun sand: results and analyses 177
6.1. Experimental Program details 177
6.2. Seismic wave measurement system 180
6.2.1. Bender Elements setup 180
6.2.2. Calibration of BE tests 181
6.2.3. BE testing results 182
6.3. Experimental results 189
6.3.1. Accelerations 189
6.3.2. Arias Intensity 195
6.3.3. Excess pore pressure ratio r_u 202
6.3.4. Excess pore pressure ratio, r_u (Isochrones) 208
6.3.5. Maximum excess pore pressure ratio r_u 212
6.3.6. Soil surface settlement 213
6.3.7. Air injection 215
6.4. Discussion on shear stresses and strains 216
6.5. IPS influence on shear stiffness G_{sec} and dissipated energy ΔW 220
6.5.1. Concept 220
6.5.2. Comparative analysis per depth 221
6.5.3. Global analysis of the soil profile response 232

6.6. Main findings 234
7. Linking centrifuge modelling with cyclic triaxial testing 237
7.1. Introduction 237
7.1.1. Cyclic stress ratio time history CSR(t) 237
7.1.2. The Palmgren-Miner Cumulative Damage Hypothesis 240
8. Conclusions 249
8.1. Key findings 249
8.2. Future work 253
References 255

List of figures

Figure 2-1 MSF suggested by several authors (Youd et al., 2001)..... 6
Figure 2-2 Stress reduction ratio (r_d) for, different soil profiles (Seed & Idriss, 1971) 8
Figure 2-3 Equivalent number of cycles for different earthquake magnitudes (Seed et al., 1975) 9
Figure 2-4 Identification of liquefaction zone using cyclic strain approach (Kramer, 1996b) 9
Figure 2-5 Hysteresis shear stress-strain loop (Green, 2001)..... 10
Figure 2-6 Liquefaction chart proposed by (J. B. Berrill & Davis, 1985)..... 11
Figure 2-7 Graphical calculation of cumulative absolute strain (Millen et al., 2020) 12
Figure 2-8 Flow slide along the shore of Lake Merced in San Francisco 1957 (Kramer, 1996b) 13
Figure 2-9 Lateral spreading of flat ground toward the Motagua River following the 1976 Guatemala earthquake. Note: the orientation of ground surface cracks is parallel to the riverbank (Kramer, 1996b) 13
Figure 2-10 Fourth Avenue slide in Anchorage, Alaska following 1964 Good Friday earthquake. (Photo by U.S. Army, courtesy of USGS.), (Kramer, 1996b)..... 14
Figure 2-11 Critical state representation a) Stress-strain; b) stress-void ratio curves for loose and dense sands at the same effective confining pressure sheared under drained conditions (Kramer, 1996) 15
Figure 2-12 CVR line separating loose (contractive state) and dense (dilative state) (Kramer, 1996) 15
Figure 2-13 Behavior of initially loose and dense specimens in drained and undrained conditions: a) arithmetic; b) logarithmic effective confining pressure (Kramer, 1996)..... 16
Figure 2-14 State parameter of soil (Kramer, 1996) 16
Figure 2-15 Formation of siloxane bonds as a colloidal silica particle gel (Conlee et al., 2012)..... 20
Figure 2-16 Typical colloidal silica gel time curves for 5 % by weight solutions at different pH values (Gallagher & Lin, 2005) 21
Figure 2-17 Percent colloidal silica versus strain during cyclic loading at CSR=0.4 (Patricia & James ,2002) 22
Figure 2-18 Normalized mean excess pore pressure vs. normalized number of cycles to liquefaction – dash line represents a range of values from the literature (El Mohtar et al., 2014)..... 23
Figure 2-19 Cyclic resistance of clean sand and sand-Laponite specimens with Dr=15-25% (Ochoa-Cornejo et al., 2014) 25
Figure 2-20 Cyclic resistance of clean sand and sand-bentonite specimens with Drsk=30-40% (Ochoa-Cornejo et al., 2014)..... 25

Figure 2-21 Injection of gas bubbles in saturated sand for the prevention of liquefaction (Chu, 2013)..... 30

Figure 2-22 Pore water pressure ratios measured from model tests on bacteria-desaturated sand (He, 2013)..... 31

Figure 2-23 Pore water pressure ratio versus degree of saturation (Consolidated undrained compression, CUC, and extension tests, CUE. The pore water pressure ratio is expressed as the ratio of the maximum pore water pressure during shear to the initial effective confining stress $r_{u,max} = u_{max}/ p'_o$) He & Chu (2014)..... 33

Figure 2-24 Undrained shear strength ratio versus degree of saturation (The undrained shear strength ratio is defined as the ratio of undrained shear strength obtained from an undrained test to the initial effective confining stress: s_u/p'_o) He & Chu (2014) 34

Figure 2-25 Degree of saturation Vs. Matric suction for a hypothetical porous medium, modified after (Vanapalli et al., 1996)..... 36

Figure 2-26 Probable variation of water/air area in different stages of a SWCC, after (Vanapalli et al., 1996)..... 36

Figure 2-27 Fully, partially, and unsaturated soil zones (Tsukamoto et al., 2014) 37

Figure 2-28 Relationship between a) P-wave velocity and B-value; b) Degree of saturation and B-value, for Toyoura sand, Dr=60%, Kb=165.8Mpa, G=76.5Mpa (Yang, 2002)..... 40

Figure 2-29 Effect of a) solubility of air bubble; b) air bubble size; c) S-wave velocity; d) porosity; e) P-wave velocity of soil skeleton on the B-Vp and, f) air bubble size on the Sr-Vp relationships (Tamura et al., 2002)..... 41

Figure 2-30 Relationship between a) B-value and VP; b) Sr and VP for different Dr (Molina-Gómez, 2023) 42

Figure 2-31 Building's response in fully and partially saturated soils, after (Bayat et al., 2009) 43

Figure 2-32 Relationship between liquefaction resistance ratio and volumetric strain (He et al., 2014) 44

Figure 2-33 Liquefaction resistance ratio Vs. Pore pressure coefficient B (He et al., 2014)..... 45

Figure 2-34 Centrifuge model layout in performed experiments (Zeybek & Madabhushi, 2017b) 46

Figure 2-35 Comparison between the excess pore pressure ratio time histories in treated and untreated areas at 1.5 m. (Flora et al., 2021) 50

Figure 2-36 Effect of degree of saturation on liquefaction resistance of partially saturated specimen, after (Zeybek, 2022) 51

Figure 2-37 Liquefaction resistance curves of TP-Lisbon sand (Dr = 50% and p' = 50 kPa) (Molina-Gómez et al., 2025) 52

Figure 2-38 Dependence of shear modulus at 10th cycle on degree of saturation for: a) Babolsar sand; and b) Toyoura sand (Jafarzadeh & Sadeghi, 2012) 52

Figure 2-39 Effect of saturation ratio on damping of: a) Babolsar sand; b) Toyoura sand at 10th cycle (Jafarzadeh & Sadeghi, 2012)..... 53
Figure 2-40 Variations in damping ratio with the number of cycles for saturated: a) Babolsar sand ;b) Toyoura sand under undrained condition (Jafarzadeh & Sadeghi, 2012)..... 53
Figure 2-41 Effect of Degree of saturation on: a) G; b) D, after Khan et al. (2021) 54
Figure 2-42 Effect of Matric Suction on: a) Shear Modulus; b) Damping ratio; Effects of degree of saturation on: c) Shear Modulus; d) Damping ratio (Le & Ghayoomi, 2016)..... 54
Figure 2-43 Variation of the damping ratio with Sr for fine sand at different relative densities for $\sigma'3$: a) 100 kPa; b) 300 kPa (Madhusudhan & Kumar, 2013)..... 55
Figure 2-44 Variation of the damping ratio with Sr for Medium sand at different relative densities for $\sigma'3$: a) 100 kPa; b) 300 kPa (Madhusudhan & Kumar, 2013) 55
Figure 2-45 Variation of the damping ratio with Sr for coarse sand at different relative densities for $\sigma'3$: a) 100 kPa; b) 300 kPa (Madhusudhan & Kumar, 2013) 55
Figure 2-46 Variation of energy response with respect to number of cycles (Okur & Umu, 2013) 56
Figure 3-1 Intensity data points and tentative isoseismal map of the 1909 Benavente earthquake (Teves-Costa & Batlló, 2011)..... 59
Figure 3-2 - Google Maps picture showing North Benavente area (NB soil location) 60
Figure 3-3 - Electrical sieves shaker used in the Geotechnical laboratory, LabGeo, FEUP 62
Figure 3-4 Grain size distribution curve of NB Soil..... 62
Figure 3-5 - Grain size distribution of NB soil, compared against liquefaction boundaries by (Tsuchida, 1970) 63
Figure 3-6 Grain size distribution curve NB soil comparison with results by Ramos (2021)..... 63
Figure 3-7 Different angularity zones set by (Altuhafi et al., 2013) showing NB soil classification, after (Ramos, 2021) 64
Figure 3-8 Tools used for the determination of e_{min} and e_{max} 65
Figure 3-9 Collective picture showing the tools used in the filter paper test, showing the filter paper, wet soil, thermal isolating film, high-precision digital balance and the thermal box for storing samples 67
Figure 3-10 Soil-water characteristic curves SWCC for NB sand: a) Matric suction Vs. Volumetric water content; b) Matric suction Vs. degree of saturation..... 68
Figure 3-11 Particle size distribution for the HN31 sand (Zeybek & Hall, 2017) .. 69
Figure 3-12 Grain size distribution (NB and Hostun sands), comparison against liquefaction boundaries by (Tsuchida, 1970)..... 70
Figure 3-13 SWRC and suction stress for a loose Hostun sand deposit (Zeybek & Hall, 2017)..... 71

Figure 3-14 Schematic setup of the bender elements testing 72
Figure 3-15 Setup of the waves measurement system during measuring S-wave in the Laboratory. 72
Figure 3-16 P-wave propagation captured from the oscilloscope 73
Figure 3-17 Schematic diagram for conventional triaxial testing apparatus..... 74
Figure 3-18 a) Lubricated end platens for triaxial tests; b) Conventional monotonic triaxial apparatus in LabGeo, FEUP..... 75
Figure 3-19 Double wall triaxial chamber: a) schematic; b) actual photograph of the developed system..... 78
Figure 3-20 Double wall triaxial chamber accessories and parts: a) Pneumatic actuator; b) and c) Step motors with different capacities..... 79
Figure 3-21 picture and schematic drawing of the Cell pressure/ Back pressure tank 79
Figure 3-22 Presentation of the SoilTest software graphical interface..... 80
Figure 3-23 General scheme of the equipment's operation mode (Costa, 2009) .. 80
Figure 3-24 Porous stone base cap, equipped with T-shaped BE..... 81
Figure 3-25 The mechanical connections of the pneumatic actuator 82
Figure 3-26 Cyclic triaxial apparatus in LabGeo, FEUP 84
Figure 3-27 Rubber V-ring utilized in the top cap..... 85
Figure 3-28 a) Bender elements attached to the top and bottom loading caps; b) The axial and radial HE glued and well fixed on the specimen membrane..... 85
Figure 3-29 a) Automatic volume change gauge; b) Linear Variable Differential Transformer LVDT and; c) Pressure/Volume Controller..... 86
Figure 3-30 schematic of the Turner beam centrifuge at the University of Cambridge. 91
Figure 3-31 Turner beam centrifuge at the University of Cambridge. 92
Figure 3-32 Servo-hydraulic earthquake shaker system used for dynamic centrifuge testing at the Schofield Centre. 92
Figure 3-33 The model box after preparation and instrumentation placement ... 93
Figure 3-34 The LVDTs including the floating (middle) LVDT..... 94
Figure 3-35 BE measuring components a) The function generator; b) The PicoScope 95
Figure 3-36 BE installed in the acrylic frame 95
Figure 3-37 The automatic sand pourer during pluviation 96
Figure 3-38 a) The arrangement of the instrumentation inside the soil box; b) Rubber air curtain hose..... 97
Figure 3-39 Saturation process of the model box 98
Figure 3-40 Weighting the model for the balance calculations 99
Figure 3-41 An elevation view of the centrifuge model#1 and its instrumentation (Prototype Scale) 99

Figure 3-42 A view and sketch of the air injection control system adopted from (Zeybek & Hall, 2017) *101*

Figure 4-1 Typical monotonic triaxial test plots of NB-sand: a) stress-strain behavior; b) stress path with CSL in the q: p´ space; c) pore-pressure change; d) CS points in the e: p´ space. *103*

Figure 4-2, Variations of a) void ratio a) and; b) corresponding relative densities, during testing phases *105*

Figure 4-3 Critical state line of NB sand CSL: a) Linear; b) Non-linear regression *106*

Figure 4-4 comparison between CSL of current study and CSL of NB sand obtained by (Ramos, 2021): a) Linear; b) Non-linear *107*

Figure 4-5 Normalized deviatoric stress (q/p´) with the axial strain (ε_a%) *107*

Figure 4-6 typical shear characteristics plots of the three saturated specimens a) stress-strain behavior; b) Stress path with CSL in the q: p` space; c) pore-pressure change; d) e: p´ space *108*

Figure 4-7 Typical shear characteristics plots of the three unsaturated specimens a) stress-strain behavior; b) Stress path with CSL in the q: p` space; c) pore-pressure change; d) e: p´ space *109*

Figure 4-8 Comparing UTx1 and UTx5: a) ΔU against ε_v; b)r_u against ε_a *110*

Figure 4-9 Comparing UTx3 and UTx7: a) ΔU against ε_v; b)r_u against ε_a *110*

Figure 4-10 Comparing UTx3 and UTx7: a) ΔU against ε_v; b)r_u against ε_a..... *111*

Figure 4-11 the existence of occluded air bubbles in the partially saturated specimens *112*

Figure 4-12 CSL of fully and partially saturated set of tests for NB sand *112*

Figure 4-13 Non-linear CSL of Tx and UTx sets of tests *113*

Figure 4-14 Relationship between theta values and pore pressure build-up of saturated and partially saturated specimens *114*

Figure 4-15 Relationship between degrees of saturation and pore pressure build-up of saturated and partially saturated specimens *114*

Figure 4-16 Relationship between void ratio and pore pressure build-up of saturated and partially saturated specimens *114*

Figure 5-1 P-wave analysis in the time domain from CTx1, indicating the first arrival time using various frequencies *119*

Figure 5-2 P-wave analysis in the time domain for various CTx tests with various Sr% *119*

Figure 5-3 Correlation between V_p (m/s) and B-value by the end of consolidation of all performed tests, p'=100kPa *121*

Figure 5-4 Correlation between V_p (m/s) and Sr (%) by the end of consolidation of all performed tests, p´=100kPa *121*

Figure 5-5 Void ratio evolution during testing stages *122*

Figure 5-6 Evolution of relative density during testing stages *122*

Figure 5-7 S-wave analysis in the time domain from CTx1, indicating the first arrival time using various frequencies 123

Figure 5-8 Evolution of shear wave velocity S-wave during testing stages of (CTx) 123

Figure 5-9 Evolution of maximum shear modulus G_{max} during the different testing stages of (CTx) 125

Figure 5-10 Seismic wave velocities Vp and Vs evolution at various confining stress for NB sand 126

Figure 5-11 Seismic wave velocity Vp and Vs evolution at various confining stress for NB sand compared with (Ferreira et al., 2021) 127

Figure 5-12 Stress dependency a) Vs and; b) Gmax stress dependency at different p´ of NB sand..... 128

Figure 5-13 G_{max} Normalized to the different adopted void ratio functions in dry and fully saturated states of NB sand 129

Figure 5-14 Poisson's ratio stress dependency on different p′ in dry and fully saturated conditions 131

Figure 5-15 Poisson's ratio stress dependency on different p' in dry and fully saturated conditions plotted against Ferreira et al. (2021) 132

Figure 5-16 Poisson's ratio ν for CTx tests, under different saturation and mean effective stress conditions 133

Figure 5-17 Typical undrained cyclic shear characteristic plots for Test (CTx1); a) stress-strain behavior; b) Stress path q: p′ space; c) excess pore water pressure Δu against axial strain ε_a; d) Excess pore water pressure build-up ratio r_u with the number of cycles N_L 134

Figure 5-18 liquefaction resistance curve of fully saturated NB-soil..... 135

Figure 5-19 Comparative analysis between the Liquefaction resistance curve LRC of fully saturated NB sand generated from the current study and the LRCs produced by (Ramos, 2021) 135

Figure 5-20 Liquefaction resistance of fully saturated NB sand compared with other soils 136

Figure 5-21 Typical cyclic shear characteristics for tests (CTx9 and, 25); a) stress-strain behavior; b) Stress path q: p` space; c) excess pore water pressure; d) Excess pore pressure ratio with the number of cycles 137

Figure 5-22 r_u and p'_o evolution with the number of cycles N_L cycles for CTx9 and CTx25 138

Figure 5-23 The Liquefaction Resistance Curves LRCs curves for the four testing groups arranged based on the values of (θ). 140

Figure 5-24 LRCs of the four testing groups along with other LRCs from different authors 141

Figure 5-25 liquefaction resistance ratio LRR Vs theta values θ, for the three partially saturated groups of tests 143

Figure 5-26 liquefaction resistance ratio LRR Vs theta values θ/ $\theta_{sat.}$, for the three partially saturated groups of tests 143
Figure 5-27 liquefaction resistance ratio LRR with the degree of saturation Sr for the three partially saturated groups of tests 144
Figure 5-28 liquefaction resistance ratio LRR with the compressional wave velocities V_P measurements for the three partially saturated groups of tests..... 144
Figure 5-29 LRR obtained from the current study compared with other data from the literature 145
Figure 5-30 Typical hysteresis stress-strain loop for the estimation of secant shear modulus and estimation of material damping D 147
Figure 5-31 Shear stress and shear strain cyclic loops: a) Sr=100%; b) Sr=86%, excluding the loops where liquefaction occurred 148
Figure 5-32 Shear stress and shear strain cyclic loops number 2, 5, and 18; a) CTx6, Sr=100% b) CTx41, Sr=86% 149
Figure 5-33 Shear stress and shear strain cyclic loops a) Sr=100%; b) Sr=86% including the loops where liquefaction occurred..... 151
Figure 5-34 Cycle by cycle evolution of secant shear modulus a) Sr=100%; b) Sr=86% 152
Figure 5-35 Shear modulus evolution along the number of cycles for partially and fully saturated specimens (Jafarzadeh & Sadeghi, 2012) 153
Figure 5-36 High strain stiffness degradation a) Secant shear modulus Gsec with the strain amplitude obtained from each hysteresis stress-strain cyclic loop; b) Gsec/Gsec,max with the shear strain amplitude, both a& b for Sr=100 and 86% 154
Figure 5-37 Complete stiffness degradation curve for NB sand a) shear modulus G with the strain amplitude b) G/Go with the shear strain amplitude 155
Figure 5-38 Secant shear modulus G_{max} and coincident r_u evolution cycle per cycle: a) Sr=100%; b) Sr=86% 156
Figure 5-39 Cycle by cycle material damping based on the stress-strain hysteresis loops: a) Sr=100%; b) Sr=86%..... 157
Figure 5-40 Scattered behavior of damping D with number of cycles under constant-volume conditions (Undrained), for fully saturated conditions (Jafarzadeh & Sadeghi, 2009) 157
Figure 5-41 Material damping with the shear strain amplitude estimated from the stress-strain hysteresis loops a) Sr=100%; b) Sr=86% 158
Figure 5-42 Cyclic stress paths (q-p'); a) Sr=100%; b) Sr=86% 160
Figure 5-43 stress path results (q-p') for: a) Sr=100%, q_{ampl} = 20kPa; b) Sr=86%, q_{ampl} = 20kPa (Knittel & Lieske, 2025) 161
Figure 5-44 Applied load against the number of cycles for each load increment of the two specimens CTx43 and CTx44. 162
Figure 5-45 Cyclic shear response of the two specimens under undrained stress-controlled cyclic shearing 163

Figure 5-46 Resulting shear stress–shear strain loops for CTx43 and CTx44 (cycle no. 10) from each loading step..... 165

Figure 5-47 Evolution of the cyclic stress-strain loops for both tests CTx43 and CTx44 up to liquefaction 165

Figure 5-48 Resulting trends of CTx43 and CTx44 where; a) maximum r_u-cummulative dissipated energy; b) maximum r_u-CSR; c) maximum r_u-shear strain amplitude; d) maximum stored strain energy-CSR; e) Cumulative dissipated energy – minimum mean effective stress p'_{min}; f) Maximum r_u-Damping ratio; g) Damping ratio-shear strain amplitude; h) Secant stiffness- shear strain amplitude; i) secant stiffness – damping ratio. 167

Figure 5-49 Seismic wave velocity (V_p/V_s) evolution at various confining stress for HN31 sand..... 168

Figure 5-50 stress dependency at different p′ of HN31 sand a) Shear wave velocity stress dependency; b) Gmax stress dependency 169

Figure 5-51 G_{max} normalized to the different adopted void ratio functions in dry and fully saturated states of HN31 sand 170

Figure 5-52 undrained cyclic shear characteristic plots for saturated Hostun sand HN31: a) stress-strain behavior; b) Stress path q: p` space; c) excess pore water pressure Δu against axial strain ε_a; d) Excess pore water pressure build-up ratio r_u with the number of cycles N_L..... 172

Figure 5-53 undrained cyclic shear characteristic plots for partially saturated Hostun sand HN31: a) stress-strain behavior; b) Stress path q: p` space; c) excess pore water pressure Δu against axial strain ε_a; d) Excess pore water pressure build-up ratio r_u with the number of cycles N_L 172

Figure 5-54 LRC of Hostun sand HN31, Sr=100 and 86%, Dr=50 to55% 173

Figure 5-55 Liquefaction resistance ratio LRR_{15} for Hostun sand plotted against a) Sr(%); b) Vp(m/s) 173

Figure 5-56 Liquefaction resistance ratio as a function of VP..... 174

Figure 6-1 Centrifuge model layout for M1 179

Figure 6-2 Centrifuge model layout for M2 179

Figure 6-3 Centrifuge model layout for M3 179

Figure 6-4 Idealization of the BE fixed to the frame within the model box 180

Figure 6-5 Configuration of the transmitted and received signals 180

Figure 6-6 P-wave propagation time..... 181

Figure 6-7 Interpretation of P-wave in the time domain where signals were sent from: a) top; b) middle; c) bottom BE 183

Figure 6-8 Interpretation of S-wave in the time domain where signals were sent from: a) top; b) middle; c) bottom BE 184

Figure 6-9 travel time calculation of Vp using first arrival method..... 186

Figure 6-10 First arrival propagation time of Vp at different depths under various centrifuge accelerations..... 187

Figure 6-11 First arrival propagation time of Vs at different depths under various centrifuge accelerations..... 187
Figure 6-12 Evolution of Vp at different effective stress 188
Figure 6-13 Evolution of Vs at different effective stress p'..... 188
Figure 6-14 First arrival propagation time of Vs at different depths for the three shakes of M1..... 189
Figure 6-15 Acceleration time histories for M1 at various depths..... 191
Figure 6-16 Acceleration time history-M2 at various depths (note that acceleration time history is not included in this plot at level 15.9m, due to malfunctioning accelerometer)..... 193
Figure 6-17 Acceleration time history-M3 at various depths 195
Figure 6-18 Normalized Arias Intensity Ia time history-M1 at various depths 197
Figure 6-19 Normalized Arias Intensity I_a time history-M2 at various depths..... 199
Figure 6-20 Normalized Arias Intensity I_a time history-M3 at various depths..... 201
Figure 6-21 Excess pore pressure ratio r_u time history for the three shakes of M1 at various depths..... 203
Figure 6-22 Excess pore pressure ratio r_u time history for the three shakes of M2 at various depths..... 206
Figure 6-23 Excess pore pressure ratio ru time history for the three shakes of M3 at various depths..... 207
Figure 6-24 a) Excess pore pressure Du and; b) excess pore pressure ratio ru at various time instants (Isochrones) for the three shakes of M1 209
Figure 6-25 a) Excess pore pressure Δu and; b) excess pore pressure ratio r_u at various time instants (Isochrones) for the two shakes of M2 210
Figure 6-26 a) Excess pore pressure Δu and; b) excess pore pressure ratio r_u at various time instants (Isochrones) for the three shakes of M3 211
Figure 6-27 Escaped air bubbles shown at the model box surface after air injection for Model M3 212
Figure 6-28 Maximum excess pore pressure ratio $r_{u,max}$ with depths for the three models; a) M1, b) M2, and c) M3 213
Figure 6-29 Time history soil surface settlement during shakes and air injections, followed by dissipation-M1..... 213
Figure 6-30 Time history of soil surface settlement during shakes and air injections, followed by dissipation-M2..... 214
Figure 6-31 Time history soil surface settlement during shakes and air injections, followed by dissipation-M3..... 214
Figure 6-32 Time history of the water level and soil surface variations during the air injection process performed before applying EQ1.2 of M1 215
Figure 6-33 Air injection pressure time history applied before starting EQ1.2 of M1 216

Figure 6-34 a) Shear stress time histories at various depths for the three shakes of M1 along the full shake durations; b) Shear strain time histories; and c) Stress-strain hysteresis loops from 7 to 15 seconds of the shake durations..... 218
Figure 6-35 Shear stress time history at depth 19.2m: a) EQ1.1; b) EQ1.2 and; c) EQ1.3 222
Figure 6-36 Shear strain time history at depth 19.2m: a) EQ1.1; b) EQ1.2 and; c) EQ1.3 222
Figure 6-37 Stress-strain hysteresis loops for all three shakes at 19.2m: a) full data; b) representative loops from 7 to 15s..... 222
Figure 6-38 Shear stress time history at depth 16.5m: a) EQ1.1; b) EQ1.2 and; c) EQ1.3 223
Figure 6-39 Shear strain time history at depth 16.5m: a) EQ1.1; b) EQ1.2 and; c) EQ1.3 223
Figure 6-40 Stress-strain hysteresis loops for all three shakes at16.5m: a) full data; b) representative loops from 7 to 15s..... 224
Figure 6-41 Shear stress time history at depth 13.8m: a) EQ1.1; b) EQ1.2 and; c) EQ1.3 224
Figure 6-42 Shear strain time history at depth 13.8m: a) EQ1.1; b) EQ1.2 and; c) EQ1.3 224
Figure 6-43 Stress-strain hysteresis loops for all three shakes at13.8m: a) full data; b) representative loops from 7 to 15s..... 225
Figure 6-44 Shear stress time history at depth 10.8m: a) EQ1.1; b) EQ1.2 and; c) EQ1.3 225
Figure 6-45 Shear strain time history at depth 10.8m: a) EQ1.1; b) EQ1.2 and; c) EQ1.3 226
Figure 6-46 Stress-strain hysteresis loops for all three shakes at 10.8m: a) full data; b) representative loops from 7 to 15s..... 226
Figure 6-47 Shear stress time history at depth 7.8m: a) EQ1.1; b) EQ1.2 and; c) EQ1.3 227
Figure 6-48 Shear strain time history at depth 7.8m: a) EQ1.1; b) EQ1.2 and; c) EQ1.3 227
Figure 6-49 Stress-strain hysteresis loops for all three shakes at 7.8m: a) full data; b) representative loops from 7 to 15s..... 227
Figure 6-50 Stress-strain hysteresis loops for the first 7 cycles for the three shakes at 7.8m depth: a) EQ1.1; b) EQ1.2 and; c) EQ1.3 227
Figure 6-51 Shear stress time history at depth 4.5m: a) EQ1.1; b) EQ1.2 and; c) EQ1.3 228
Figure 6-52 Shear strain time history at depth 4.5m: a) EQ1.1; b) EQ1.2 and; c) EQ1.3 228
Figure 6-53 Stress-strain hysteresis loops for all three shakes at 4.5m: a) full data; b) representative loops from 7 to 15s..... 228

Figure 6-54 Stress-strain hysteresis loops for the first 7 cycles for the three shakes at 4.5m: a) EQ1.1; b) EQ1.2 and; c) EQ1.3 229

Figure 6-55 Shear stress time history at depth 1.2m: a) EQ1.1; b) EQ1.2 and; c) EQ1.3 229

Figure 6-56 Shear strain time history at depth 1.2m: a) EQ1.1; b) EQ1.2 and; c) EQ1.3 229

Figure 6-57 Stress-strain hysteresis loops for all three shakes at 1.2m: a) full data; b) representative loops from 7 to 15s..... 230

Figure 6-58 Stress-strain hysteresis loops for the first 7 cycles for the three shakes at 1.2m: a) EQ1.1; b) EQ1.2 and; c) EQ1.3 230

Figure 6-59 Shear stress time history at depth 0.6m: a) EQ1.1; b) EQ1.2 and; c) EQ1.3 230

Figure 6-60 Shear strain time history at depth 0.6m: a) EQ1.1; b) EQ1.2 and; c) EQ1.3 231

Figure 6-61 Stress-strain hysteresis loops for all three shakes at 0.6m: a) EQ1.1; b) EQ1.2 and; c) EQ1.3: a) full data; b) representative loops from 7 to 15s 231

Figure 6-62 Stress-strain hysteresis loops for the first 7 cycles for the three shakes at 0.6m: a) EQ1.1; b) EQ1.2 and; c) EQ1.3 231

Figure 6-63 Secant shear stiffness (G_{sec}), dissipated energy (ΔW), evaluated during Cycle #10 for depths: (19.2 to 10.8m) and cycle#2 for depths: (7.8 to 0.6m) across the three shaking events (data are calculated at the sensors locations, based on the sensors records. The figure also presents the (r_{umax}) distribution and illustrative, unscaled shapes of the resulting hysteresis loops. 232

Figure 6-64 (a) Secant shear stiffness (G_{sec}) and (b) dissipated energy (ΔW) evaluated during Cycle #10 for depths: (19.2 to 10.8m) and cycle#2 for depths: (7.8 to 0.6m) across the three shaking events (data are calculated at the sensors locations and midpoints) 233

Figure 6-65 a) Variation of (a) secant shear stiffness (Gsec); and b) dissipated energy (DW) with maximum induced shear strain γmax..... 233

Figure 6-66 Illustrative figure showing the dynamic behavior evolution for fully, partially, and unsaturated soil states..... 235

Figure 7-1 CSR(t) at depth 1.2m for shake EQ1.1-Centrifuge test M1 238

Figure 7-2 CSR(t) at depth 1.2m for shake EQ1.2-Centrifuge test M1 238

Figure 7-3 CSR(t) at depth 1.2m for shake EQ1.3-Centrifuge test M1 239

Figure 7-4 Liquefaction resistance curves (LRC) for fully saturated Hostun sand (HN31) before and after the loading type and overburden pressure correction in addition to N_{eq} at CSR_{ref} of the three points computed for the three centrifuge shaking events..... 246

Figure 7-5 Liquefaction resistance curve (LRC) for fully saturated Hostun sand (HN31) after the loading type and overburden pressure correction in addition to N_{eq} at CSR_{ref} of the three points computed for the three centrifuge shaking events 247

Figure 8-1 illustrative summary of the dynamic behaviour of partially saturated sands under undrained conditions as observed in the present study. 252

List of tables

Table 2-1 Advantages and disadvantages of the above-reported liquefaction mitigation methods 57

Table 3-1 Primary physical characteristics of NB soil..... 64

Table 3-2 Mineralogy evaluation of the studied NB soil, after (Ramos, 2021)..... 64

Table 3-3 e_{max}, e_{min} and Gs for the tested samples..... 65

Table 3-4 Fitting parameters adjusting the theoretical model soil water characteristic curve of NB sand 68

Table 3-5 Physical properties of HN31 sand (Zeybek & Hall, 2017)..... 70

Table 3-6 Details of the performed monotonic triaxial tests 76

Table 3-7 Characteristics of the tested specimens in this apparatus (UTx)..... 83

Table 3-8 Characteristics of conducted cyclic triaxial tests for Hostun sand HN3188

Table 3-9 Characteristics of conducted cyclic triaxial tests for NB sand 89

Table 3-10 Scaling laws of main parameters in centrifuge modelling (Zeybek & Hall, 2017)..... 91

Table 4-1 Critical state parameters of NB soil..... 107

Table 4-2 Critical state parameters for fully and partially saturated specimens 112

Table 5-1 Stress dependency fitting parameters of NB-sand 126

Table 5-2 Void ratio function F(e) and resulting fitting parameters for normalized Gmax of NB sand..... 128

Table 5-3 Characteristics of grouped CTx of NB sand..... 139

Table 5-4 Parameters of the CTx tests used for the stress-strain analysis of NB sand 146

Table 5-5 Details of performed CTx43 and CTx44..... 161

Table 5-6 Fitting parameters of Vs and Vp of Hostun sand HN31 169

Table 5-7 Fitting parameters from the G_{max} normalized to various F(e) of Hostun sand HN31..... 170

Table 6-1 Main parameters of the performed centrifuge models..... 178

Table 6-2 Compressional wave velocity measured by the three levels of BE 182

Table 6-3 Compressional wave velocity measured by the three levels of BE for M1 after 60g centrifugal acceleration..... 186

Table 6-4 Secant shear stiffness (G_{sec}) and dissipated energy (ΔW) calculated for Cyclic loop #10 across the three shaking events at a prototype depth of 19.2 m 223

Table 6-5 Secant shear stiffness (G_{sec}) and dissipated energy (ΔW) calculated for Cyclic loop #10 across the three shaking events at a prototype depth of 16.5 m 224

Table 6-6 Secant shear stiffness (G_{sec}) and dissipated energy (ΔW) calculated for Cyclic loop #10 across the three shaking events at a prototype depth of 13.8 m 225

Table 6-7 Secant shear stiffness (G_{sec}) and dissipated energy (ΔW) calculated for Cyclic loop #10 across the three shaking events at a prototype depth of 10.8 m 226

Table 6-8 Secant shear stiffness (G_{sec}) calculated for cyclic loop #10 and dissipated energy (ΔW) evaluated for Cyclic loop #2 across the three shaking events at a prototype depth of 7.8m. 228

Table 6-9 Secant shear stiffness (G_{sec}) calculated for cyclic loop #10 and dissipated energy (ΔW) calculated for Cyclic loop #2 across the three shaking events at a prototype depth of 4.5m 229

Table 6-10 Secant shear stiffness (G_{sec}) calculated for cyclic loop#10 and dissipated energy (ΔW) calculated for Cyclic loop #2 across the three shaking events at a prototype depth of 4.5m 230

Table 6-11 Secant shear stiffness (G_{sec}) calculated for cycle # 10 and dissipated energy (ΔW) calculated for Cyclic loop #2 across the three shaking events at a prototype depth of 0.6m 231

Table 7-1 Correction factors (C_r and K_σ) for converting cyclic stress ratios from triaxial (CSR_{CTX}) to direct simple shear (CSR_{DSS}) conditions. 244

Table 7-2 CSRi, CSRref, and resulting ∑Neq for the three shakes EQ1.1, EQ1.2, and EQ1.3 245

List of acronyms and symbols

List of acronyms

ASTM	American Society for Testing and Materials
B-value	Pore-pressure coefficient B
BP	Back pressure
BE	Bender elements
CP	Cell pressure
CONSTRUCT	Institute of Research and Development in Structures and Construction
CS	Critical state
CSL	critical state line
CSR	cyclic stress ratio
CSR_{15}	cyclic stress ratio at 15 cycles
$CSR_{15,sat}$	cyclic stress ratio of fully saturated sand at 15 cycles
CTx	Cyclic triaxial tests
DA	Double strain amplitude
FCT	Fundação para a Ciência e a Tecnologia
GDS	Grain size distribution
HN31	Hostun sand
IPS	Induced partial saturation
LabGeo	Geotechnical Laboratory of Faculty of Engineering of University of Porto
LRC	Liquefaction resistance curve
LRR	Liquefaction resistance ratio
CRR	Cyclic resistance ratio
FS_{liq}	Factor of safety against liquefaction
LRR_{15}	Liquefaction resistance ratio at 15 cycles
LSN	Liquefaction severity number
LVDT	Linear vertical displacement transducer
NB	North Benavente sand

P-wave	Compressional wave/ primary wave
PPA	Pressure plate apparatus
AP	Air pluviation
S-wave	Shear wave/ Secondary wave
SWCC	Soil-water characteristic curve
Tx	Monotonic triaxial tests
r_d	Stress reduction factor at particular depth
MSF	Magnitude scaling factor

List of symbols

a_g	Design ground acceleration (m/s^2)
a_{max}	Peak horizontal acceleration on the ground surface (m/s^2)
Cu	Coefficient of uniformity
Cc	Coefficient of curvature
Dr	Relative density (%)
D	Sample diameter (mm)
D_{50}	Mean diameter particle size (mm)
e	Void ratio
e_{max}	Maximum void ratio
e_{min}	Minimum void ratio
EQ1.1	Centrifuge Model#1 shake#1
F	Frequency (Hz)
F(e)	Void ratio function
Fc	Fines content (%)
g	Gravitational acceleration (m/s^2)
G	Shear modulus (MPa)
G_{sec}	Secant shear modulus (MPa)
G_{max}	Maximum shear modulus (MPa)
h	Specimen height (mm)
K_a	Bulk modulus of air (kPa)

K_{CO2}	Bulk modulus of carbon dioxide (kPa)
Kf	Bulk modulus of pore fluid (kPa)
K_g	Bulk modulus of grain (kPa)
K_{sk}	Bulk modulus of soil skeleton (kPa)
K_{soil}	Bulk modulus of the soil (kPa)
K_{sus}	Bulk modulus of fluid and solid particle (kPa)
K_w	Bulk modulus of water (kPa)
M_w	Earthquake magnitude (Richter)
n	Soil porosity
N_L	Number of cycles to trigger liquefaction
P′	mean effective stress (kPa)
P'_o	Initial mean effective stress (kPa)
P_a	Atmospheric pressure
r_u	Excess pore pressure ratio (%)
r_{umax}	Maximum excess pore pressure ratio (%)
S_r	Degree of saturation (%)
t	Time (s)
t_i	Wave propagation time
t_d	Direct (horizontal) Wave propagation time
t_{i1}	Indirect 1 (inclined) Wave propagation time
t_{i2}	Indirect 2 (inclined) Wave propagation time
u_a	Pore air pressure
VP	P-wave velocity (m/s)
VS	S-wave velocity (m/s)
ΔW	Total dissipated energy per unit volume (J/m^3)
Γ	Void ratio defined at p′ = 1 kPa
γ	Shear strain
ε_a	Axial strain
ε_v	volumetric strain
θw	Volumetric water content
λ	Slope of CSL line
v	Poisson’s ratio
v_{sk}	Poisson’s ratio of soil skeleton

ξ	Damping ratio of RC system (%)
ρ_{dry}	Mass density of dry soil (kg/cm^3)
ρ_f	Mass density of fluid (kg/cm^3)
ρ_{soil}	Mass density of soil grains (kg/cm^3)
ρ_{sus}	Mass density of fluid and soil (kg/cm^3)
ρ_w	Mass density of water (kg/cm^3)
ρa	Mass density of the air (kg/cm^3)
σ	Confining pressure (kPa)
$\sigma'v$	Vertical effective stress (kPa)
σ'_{v0}	Initial vertical effective stress (kPa)
σ_{v0}	Initial Vertical stress (kPa)
τ	Shear stress (kPa)
K_σ	Overburden pressure correction factor
N_{eq}	Equivalent number of cycles at a uniform reference stress

1. Introduction

1.1. Motivation

Earthquake-induced liquefaction has been documented globally, causing significant damage and loss of life. Liquefaction occurs when the effective stress of saturated soil is substantially reduced, or approaches zero, due to the rapid accumulation of excess pore water pressure during dynamic loading.

Humanity has suffered from many destructive earthquakes such as the 1964 Niigata earthquake in Japan, the 1964 Alaska earthquake, and the 1985 Mexico City earthquake. More recently, the 2010 Canterbury earthquake in New Zealand, and the 2011 Tohoku earthquake and tsunami in Japan highlighted the destructive potential of earthquake-induced liquefaction.

Those earthquakes caused catastrophic liquefaction-induced damage such as slope failures, bridge and building failures and floatation of buried infrastructures. Since then, liquefaction became one of the most common research topics in geotechnical earthquake engineering.

These incidents and others have stimulated research efforts focused on developing strategies to mitigate liquefaction and enhancing assessments of seismic hazards.

Soil liquefaction mitigation techniques aim to reduce the risk of soil losing its strength during seismic events. Common methods include Soil densification, such as vibro-compaction or dynamic compaction, which increases soil density and stiffness, making it less prone to liquefaction. Drainage techniques, like installing gravel drains or sand drains, help dissipate pore water pressure that builds up during an earthquake. Another approach is ground improvement using cement or chemical grouting to stabilize the soil. Structural solutions, such as deep foundations or soil reinforcement with geosynthetics, can also be employed to mitigate the effects of liquefaction on buildings and infrastructure.

Among these approaches, induced partial saturation (IPS) has received increasing attention as a desaturation-based liquefaction mitigation technique. By slightly reducing the degree of saturation, IPS increases the compressibility of the pore-fluid mixture, thereby limiting excess pore-water pressure build-up during cyclic loading and improving liquefaction resistance.

1.2. Objectives

Many research studies have extensively examined the response of granular soils to seismic loading under fully saturated conditions, leading to significant understanding of the liquefaction mechanisms. However, the importance of partial saturation, where soil contains both water and air, has been relatively underexplored in the context of liquefaction studies.

The primary objective of this research is to investigate how the presence of air in the pore spaces of sandy soils improves its liquefaction resistance during seismic events and how this can be employed and optimized for liquefaction mitigation. Therefore, this study focuses on induced partial saturation (IPS) as a technique for mitigating soil liquefaction. To achieve that, a comprehensive research program has been designed, including numerous and various

geotechnical laboratory experiments. In addition, the opportunity to access the geotechnical facilities at Cambridge University was an invaluable chance to enhance the work by conducting dynamic centrifuge tests for assessing the air injection influence on the soil liquefaction resistance.

The investigation will encompass various aspects in evaluating the liquefaction resistance of partially saturated sand, such as the different degrees of saturation, relative density, volumetric water content, pore water pressure, shear stresses and strains, in addition to damping and stiffness.

Secant stiffness and energy dissipated resulted from the hysteresis stress-strain loops were computed from the cyclic triaxial tests and the dynamic centrifuge modelling to investigate their dependency on the degree of saturation.

It is anticipated that the results of this study will clarify the sophisticated relationship between soil saturation, and soil stiffness and damping characteristics.

To achieve these outcomes, the document is structured as detailed in the section below.

1.3. Structure of the thesis

This document is structured into eight chapters as follows:

Chapter 2 presents a comprehensive and up-to-date review of the liquefaction phenomenon, including its definition, triggering factors, and consequences. It also discusses recent advances in soil liquefaction mitigation methods, with particular emphasis on desaturation-based techniques. These methods are critically reviewed in terms of their effectiveness and practical applicability, supported by relevant scientific literature.

Chapter 3 details the materials and methodologies adopted, describing the soil's characteristics, the laboratory work conducted, and the equipment and procedures employed for the tests and physical models carried out in this investigation.

Chapter 4 presents results and interpretations of the performed monotonic triaxial tests including the critical state parameters and a comparison between the fully and partially saturated NB sand under monotonic loading conditions.

Chapter 5 presents the results of cyclic triaxial tests performed on reconstituted specimens under different saturation levels, to assesses the effect of several factors on the soil cyclic liquefaction resistance, including degree of saturation, void ratio, confining pressure, various applied stress levels (CSR) in addition to damping and stiffness time history evolution during undrained cyclic loading.

Chapter 6 shows the results and analysis of Centrifuge modelling, comparing the Arias intensities, surface settlement, pore pressure build-up, stiffness and energy dissipation of fully and partially saturated sands.

Chapter 7 compares the liquefaction resistance of Hostun HN31 sand using results from dynamic centrifuge tests at different degrees of saturation, together with results from cyclic triaxial (CTx) tests.

Chapter 8 summarizes the main conclusions and proposed future work.

2. Literature review

2.1. Introduction

Soil liquefaction is one of the main problems in geotechnical seismic engineering as it might cause catastrophic damage to buildings and structures, resulting in life-threatening, human injuries, and significant economic losses. Soil liquefaction is a phenomenon that may occur in loose, saturated soils subjected to dynamic loading, such as earthquakes. During liquefaction, soil loses its shear strength and behaves like fluid because of the excess pore water pressure generated. Consequently, several soil liquefaction mitigation techniques have been developed.

This chapter is a detailed and up-to-date literature review on the solutions and methods recently developed for the mitigation of soil liquefaction. It includes an extensive analysis of their effectiveness and applicability using numerous scientific references and citations, focusing specifically on desaturation mitigation measures. These are considered one of the most promising techniques for liquefaction mitigation, which is also adopted in the current research work.

2.2. Liquefaction assessment, triggering, and hazards

Earthquake-induced soil liquefaction is a complex phenomenon where soil gradually loses its shear strength and behaves like a liquid, resulting in catastrophic damage to buildings and infrastructure.

After the Good Friday earthquake (Mw = 9.2) in Alaska and the Niigata earthquake (Mw = 7.5) in Japan in 1964, geotechnical engineers' attention has been drawn to the liquefaction phenomenon because of its destructive consequences. Both earthquakes caused catastrophic liquefaction-induced damage such as slope failures, bridge and building failures, and floatation of buried structures. Since then, liquefaction has become one of the most common research topics in geotechnical engineering.

Liquefaction is more likely to occur in loose, saturated soil when exposed to undrained monotonic or cyclic loading, where the effective pressure decreases and tends to zero due to the accumulation of pore pressure build-up.

Kramer (1996a) mentioned that to undertake a full analysis of the possible liquefaction risk, three critical questions must be formulated and addressed as follows:

1. Is the soil susceptible to liquefaction?
2. If the soil is susceptible, will liquefaction be triggered?
3. If liquefaction is triggered, will damage occur and what damage may occur?

Simply put, if the response to all three questions was yes, it means that there will be a major issue and the site needs to be remediated or improved utilizing one or more liquefaction mitigation techniques. If the response were not "yes", different outcomes would be anticipated. The following section will provide explanations for the three questions and their several scenarios.

2.2.1. Liquefaction susceptibility

This first question is the cornerstone of the entire evaluation because liquefaction hazards will not exist, and evaluation will not be necessary if the soil is not susceptible to liquefaction.

The liquefaction susceptibility of soils would be assessed through different criteria, namely historical, geological, compositional, and state criteria.

Historical criterion

When soil and groundwater conditions of previously liquified soil stay unchanged, liquefaction might occur again at the exact locations; thus, liquefaction case histories could be used to recognize the susceptibility of particular locations to liquefaction in the future.

Geologic criterion

The depositional formation, hydrological conditions, and soil deposit age all contribute to assessing liquefaction susceptibility based on the geologic criterion. Geological processes that sort soils into uniform grain size distributions in a loose state would lead to highly susceptible soils to liquefaction. Furthermore, saturated soils are susceptible to liquefaction therefore, the effects of liquefaction are commonly observed at locations where groundwater is within a few meters of the ground surface. Finally, the susceptibility of newer soil deposits to liquefaction is higher than that of older deposits.

Compositional criterion

Soil compositional properties such as particle shape, size, and gradation associated with high volume change potential, would likely be susceptible to liquefaction. Also, rounded-shaped soil particles are more likely to have liquefaction susceptibility than sharp edges particles because rounded particles are known to densify more easily. In addition, poorly graded soils are more susceptible to liquefaction than well-graded soils because well-graded soils usually have fewer voids than poorly graded soils, resulting in lower volume change potential in drained conditions and, consequently, lower excess pore pressure under undrained conditions.

State criterion

Even though soil may meet the aforementioned liquefaction susceptibility criteria, liquefaction susceptibility may still strongly depend on the initial state of the soil (i.e., initial stress and relative density) prior being exposed to the loading, because the initial soil state has a significant influence on the soil´s potential to develop excess pore pressure or volume change. e.g., when soils are monotonically sheared, initially loose sands tend to decrease in volume (contract), while initially dense sands tend to contract at first but then dilate (increase in volume).

2.2.2. Liquefaction triggering

The fact that a soil deposit is susceptible to liquefaction does not guarantee that liquefaction will necessarily occur in the given earthquake. That is why the second question (liquefaction triggering) must be addressed and answered. There are many common approaches to assessing the liquefaction triggering of soils, such as stress-based, strain-

based, and energy-based approaches. Applying two or more approaches to evaluate liquefaction initiation is not uncommon.

Cyclic stress approach

The central concept behind the cyclic stress approach is to compare earthquake-induced loading with soil resistance to liquefaction. Both are expressed in terms of cyclic shear stresses. Liquefaction triggering assessment was initially developed based on the simplified procedure proposed by Seed & Idriss (1971). This generally computes a factor of safety against liquefaction [FS_{liq}] by defining the relationship between the cyclic resistance ratio CRR, which represents the resistance of the soil against liquefaction, and the cyclic stress ratio CSR, which expresses the seismic demand placed on the soil, as shown in equation (2-1).

$$FS_{liq} = \frac{CRR}{CSR} \tag{2-1}$$

Even though numerous adjustments and modifications have been proposed over the years, the basic idea remains the same. It continues to be the most commonly used stress-based approach to evaluate liquefaction triggering.

Cyclic stress ratio (CSR)

The cyclic stress ratio CSR represents earthquake-induced seismic loading. Seismic loading could be estimated by performing ground response analysis or using a simplified method. Ground response analysis can estimate time histories of shear stress at various depths within a soil profile. Such analysis produces time histories with the transient and irregular characteristics of actual earthquake motions, which then converge to equivalent uniform stress cycles to be compared with the uniform amplitudes of cyclic shear stresses obtained from laboratory tests. Another approach for computing the earthquake-induced loading is a simplified method proposed by Seed & Idriss (1971) to correlate the average cyclic shear stress to the initial effective vertical stress as shown in equation (2-2), Where:

$$CSR = \frac{\tau_{av}}{\sigma'_{v0}} = 0.65 \left(\frac{a_{max}}{g}\right)\left(\frac{\sigma_{v0}}{\sigma'_{v0}}\right) rd \tag{2-2}$$

Where:

- τ_{av}: Average cyclic shear stress.
- σ'_{v0}: Initial effective vertical stress.
- a_{max}: Peak ground surface acceleration.
- g: Gravitational acceleration.
- σ_{v0}: Initial total vertical stress.
- r_d: Stress reduction factor at a particular depth.

Cyclic resistance ratio (CRR)

The cyclic resistance ratio CRR reflects the capacity of the soil to resist liquefaction triggering. Laboratory testing was primarily used in the early development of the cyclic stress approach to characterize liquefaction resistance.

Over the years, various laboratory tests have been adjusted and modified for better understanding the cyclic behavior of soils and the factors affecting this behavior. However, the two most typical tests were the cyclic triaxial test and the cyclic simple shear test.

On the other hand, several field tests, such as the Standard Penetration Test SPT, the Cone Penetration Test CPT, the Flat Dilatometer Test DMT, and measurements of shear wave velocity Vs, have been used to assess CRR based on the in-situ resistance parameters.

The simplified procedure proposed by Seed & Idriss (1971) was utilized for a standard earthquake magnitude Mw of 7.5, 1 atm of vertical effective stress and leveled ground therefore, various adjustment factors were computed to generalize the CRR calculations for various earthquake magnitudes.

The Magnitude Scaling Factor MSF is a factor used to adjust the CRR for different earthquake magnitudes. This adjustment is fundamental because the potential for soil liquefaction is influenced by both the amplitude of the seismic shaking and the duration of shaking, which is correlated with earthquake magnitude.

The MSF is used to normalize the CRR to a reference magnitude, typically magnitude 7.5, because liquefaction resistance curves are often developed based on case histories of this magnitude. The MSF is typically derived from empirical relationships based on historical earthquake data and laboratory test results. Figure 2-1 shows the relationships between the earthquake magnitude and the MSF proposed by different authors in addition, a common formula used to calculate the MSF is shown in equation (2-3).

$$MSF = \left(\frac{M_w}{7.5}\right)^{-2.56} \quad \text{(Youd et al., 2001)} \tag{2-3}$$

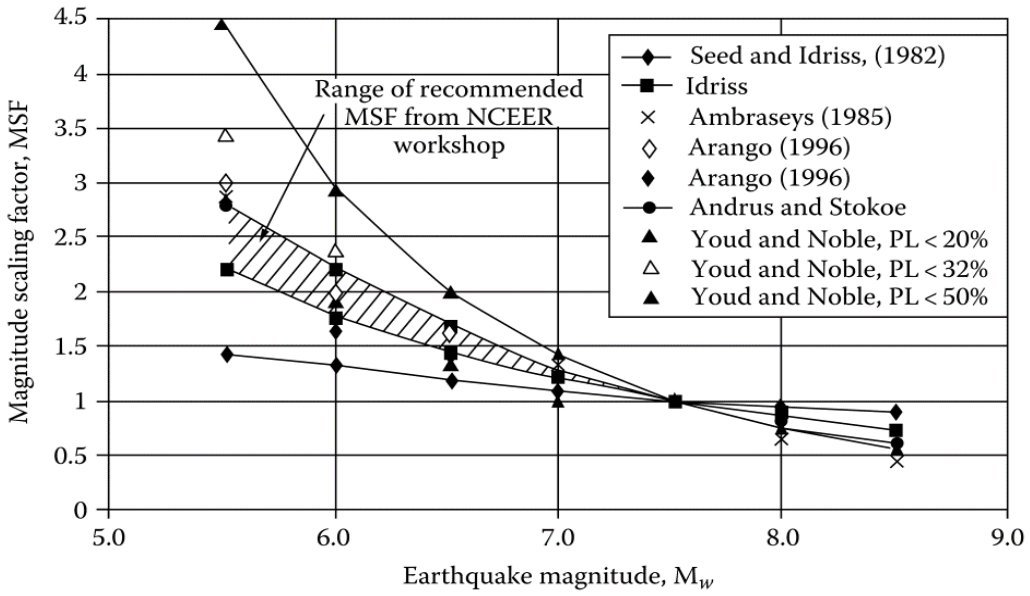

Figure 2-1 MSF suggested by several authors (Youd et al., 2001)

In addition to the MSF, another correction factor K_σ, equation (2-4) was also developed to account for the effects of overburden stress on the soil's resistance to liquefaction, it adjusts the CRR to reflect the influence of effective vertical stress on the soil's ability to resist cyclic loading through defining the ratio between the CRR at any effective vertical stress to the CRR at 1 atm effective vertical stress.

$$K_\sigma = \left(\frac{\sigma'_{v0}}{P_a}\right)^{n-1} \quad \text{(Youd et al., 2001)} \tag{2-4}$$

Where: σ'_{v0} is the effective vertical stress; P_a is the atmospheric pressure (typically 100 kPa) and, n is an empirical exponent. As reported by (Youd et al., 2001), n = 0.7–0.8 for relative densities between 40% and 60% and n = 0.6–0.7 for relative densities between 60% and 80%.

A shear stress adjustment factor K_α was also introduced, this factor is particularly relevant in situations where soils are subject to both cyclic loading (due to earthquake shaking) and static shear stresses. K_α adjusts the CRR to reflect the influence of static shear stresses on the soil's cyclic resistance, ensuring that liquefaction assessments are accurate for conditions where these stresses are significant.

K_α represents the ratio between CRR at a certain value of α and the CRR at α = 0 as represented in equations (2-5) and (2-6). The parameter α is introduced as the ratio between the initial static shear stress to the normal effective stress on the horizontal plane and can be obtained from simple shear or triaxial shear tests.

$$K_a = \frac{CRR_a}{CRR_{a=0}} \quad \text{(Seed et al., 1983)} \tag{2-5}$$

$$\alpha = \frac{\tau_{st}}{\sigma'_{vc}} \text{ (Seed et al., 1983)} \tag{2-6}$$

Where, τ_{st} is the static shear stress, σ'_{vc} is the effective vertical stress. K_α is often used in conjunction with other adjustment factors such as the Magnitude Scaling Factor (MSF) and the overburden correction factor K_σ to ensure a comprehensive evaluation of liquefaction potential under varying conditions of static shear stress, overburden stress, and earthquake shaking. According to Seed et al., (1983), CRR is adjusted using the above-mentioned correction factors as revealed in equation (2-7).

$$CRR = CRR_{7.5} * MSF * K_\sigma * K_\alpha \tag{2-7}$$

CRR depends on the duration and intensity of the cyclic loading, represented by the number of equivalent cycles. Equivalent cycles refer to the cumulative effect of cyclic stresses over time, and the CRR is often defined for a specific number of these cycles. For example, a CRR value may be given for 15 equivalent cycles, which typically corresponds to the effects of a magnitude 7.5 earthquake. As the number of cycles increases, the CRR decreases, indicating a reduced resistance to liquefaction. This relationship is crucial in earthquake engineering because it informs the design and assessment of foundations and structures to ensure stability and safety during seismic events. Understanding the threshold number of equivalent cycles and its impact on CRR is essential for accurately predicting soil behavior and mitigating liquefaction risks (Seed et al., 1985).

Cyclic strain approach

Laboratory investigation of liquefaction resistance using the cyclic stress approach can be sometimes challenging due to the numerous variables affecting the cyclic stresses needed to trigger liquefaction.

Dobry & Ladd (1980) and Dobry et al. (1982) demonstrated a different approach that assesses earthquake-induced loading and liquefaction resistance using cyclic strains instead of cyclic stresses. The existence of a volumetric shear strain threshold below which excess pore pressures do not arise, in addition to the unique relationship between excess pore pressures and cyclic shear strain, makes compelling arguments for adopting a strain-based approach for evaluating liquefaction potential rather than the stress-based approach by Seed & Idriss (1971).

To estimate the earthquake-induced loading, the time history of cyclic strain for an actual earthquake resulting from ground response analysis, which is transient and irregular, must be converted to an equivalent series of uniform strain cycles to be comparable with laboratory-measured liquefaction resistance. Hence, a simple method has been suggested by Dobry et al. (1982) to compute the uniform cyclic strain amplitude from the cyclic stress amplitude, as in equation (2-8).

$$\gamma_{cyc} = 0.65 \frac{a_{max}}{g} \frac{\sigma_v r_d}{G\,(\gamma_{cyc})} \tag{2-8}$$

Where a_{max} is the peak ground surface acceleration; g is the gravitational acceleration; σ_v is the total vertical stress at a particular depth; r_d is the stress reduction factor at a particular depth, (see Figure 2-2); $G\,(\gamma_{cyc})$is the soil shear modulus at $\gamma = \gamma_{cyc}$. G is calculated from iterations using the modulus reduction curves and; N_{eq} is the equivalent number of strain cycles, could be estimated from Figure 2-3.

Liquefaction may trigger if $\gamma_{cyc} > \gamma_t$ (the threshold shear strain), in that case, soil liquefaction resistance must be evaluated.

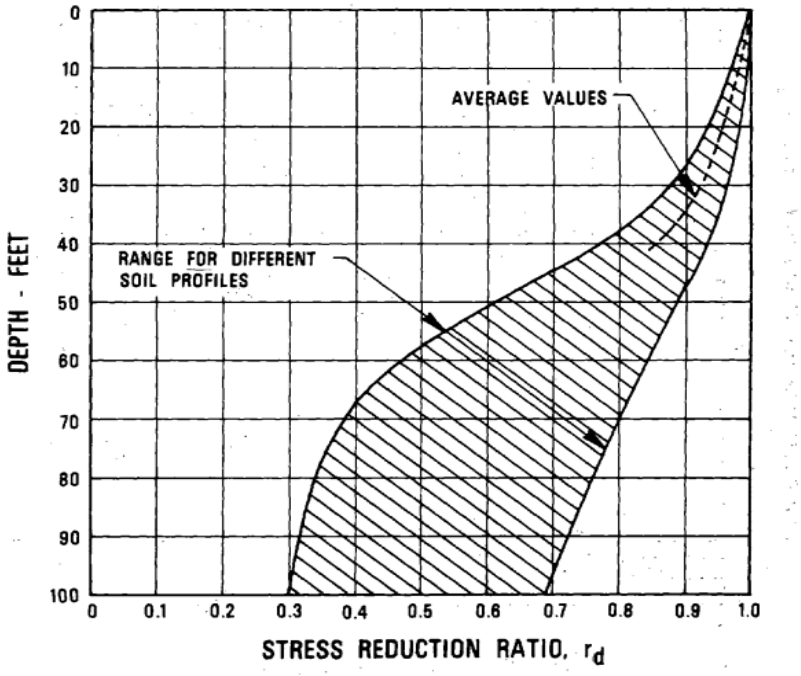

Figure 2-2 Stress reduction ratio (r_d) for, different soil profiles (Seed & Idriss, 1971)

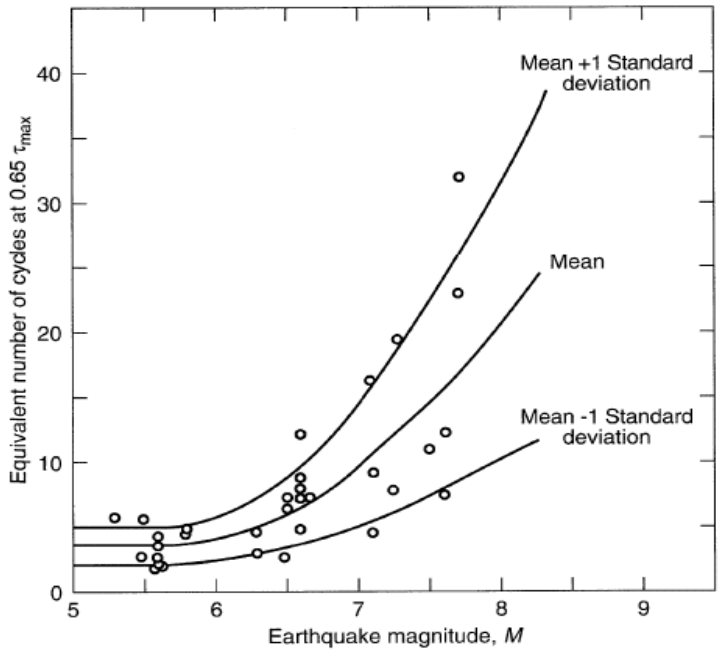

Figure 2-3 Equivalent number of cycles for different earthquake magnitudes (Seed et al., 1975)

To characterize soil liquefaction resistance in the laboratory based on the cyclic strain approach, several laboratory tests have been conducted to study the factors that influence the triggering of liquefaction, such as relative density and initial soil state.

The assessment of liquefaction potential using the cyclic strain approach could be applied where the cyclic loading imposed by the earthquake and characterized by the amplitude of a series of uniform strain cycles is compared to the liquefaction resistance, which is expressed in terms of the cyclic strain amplitude required to trigger liquefaction in the same number of cycles.

As clear in Figure 2-4, liquefaction would be expected at depths where the cyclic loading exceeds the liquefaction resistance. Unlike the cyclic stress approach, the cyclic strain approach does not adopt a safety factor against liquefaction.

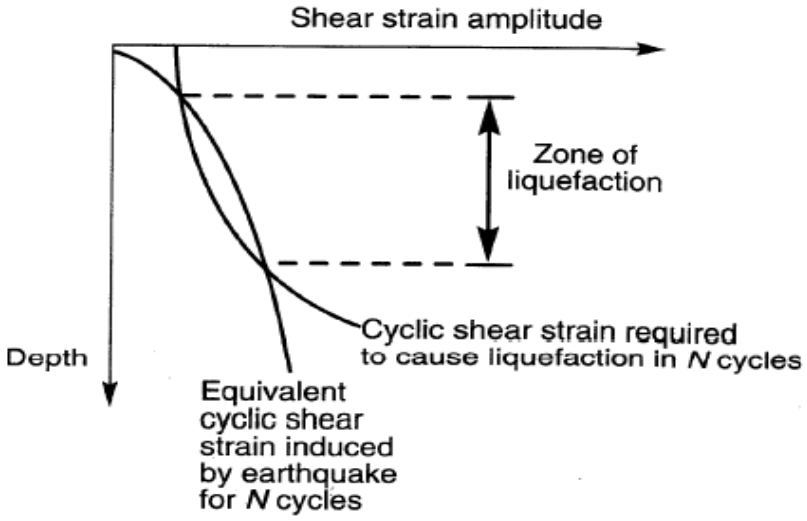

Figure 2-4 Identification of liquefaction zone using cyclic strain approach (Kramer, 1996b)

Energy-based approach

The energy-based approach uses dissipated energy measurements and their correlation with pore water pressure for the liquefaction assessment. As a result, the energy-based approach can potentially incorporate both stress and strain-based methodologies' advantages e.g., dry soils tend to densify under cyclic shear strains, requiring energy to re-arrange the grains. In addition, the energy needed for particle rearrangement increases with soil density. On the other hand, when undrained saturated soil tends to densify, pore pressure increases and the contact forces between the grains decrease; consequently, the energy needed to rearrange soil particles decreases (Ramos, 2021).

Green (2001) proposed a correlation between the total dissipated energy ΔW when the soil was exposed to cyclic shearing and the stress-strain hysteresis loop (shown in Figure 2-5). This correlation could be practically applied in laboratory procedures throughout cyclic triaxial testing using equation (2-9).

$$\Delta W = \frac{1}{2}\sum_{i=1}^{n-1}(\sigma_{d,i+1} + \sigma_{d,i})(\varepsilon_{a,i+1} - \varepsilon_{a,i}) \quad (2\text{-}9)$$

Where:

- ΔW: Total dissipated energy.
- n: Number of increments (Load increments).
- $\sigma_{d,i}$: Increments of deviatoric stress.
- $\varepsilon_{a,i}$: Increments of axial strain.

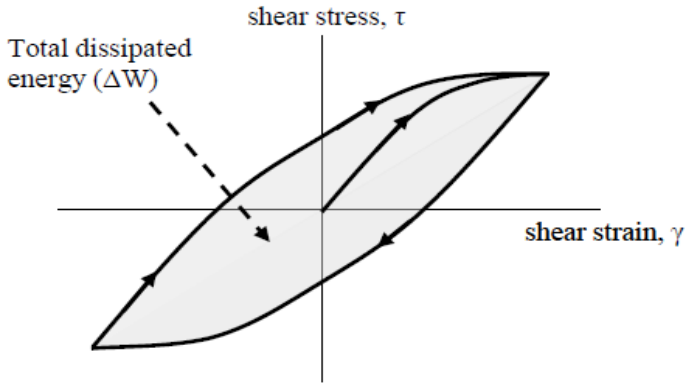

Figure 2-5 Hysteresis shear stress-strain loop (Green, 2001)

One of the most common energy-based methods for estimating the induced seismic loading is performed by combining an estimate of the energy content of seismic waves at a distance (r) from an earthquake of magnitude (M) with a simple energy dissipation function calibrated by experimental and field tests. e.g., the correlation between the seismic demand and the normalized number of blow counts from SPT databases, proposed by (J. B. Berrill & Davis, 1985), is presented in Figure 2-6.

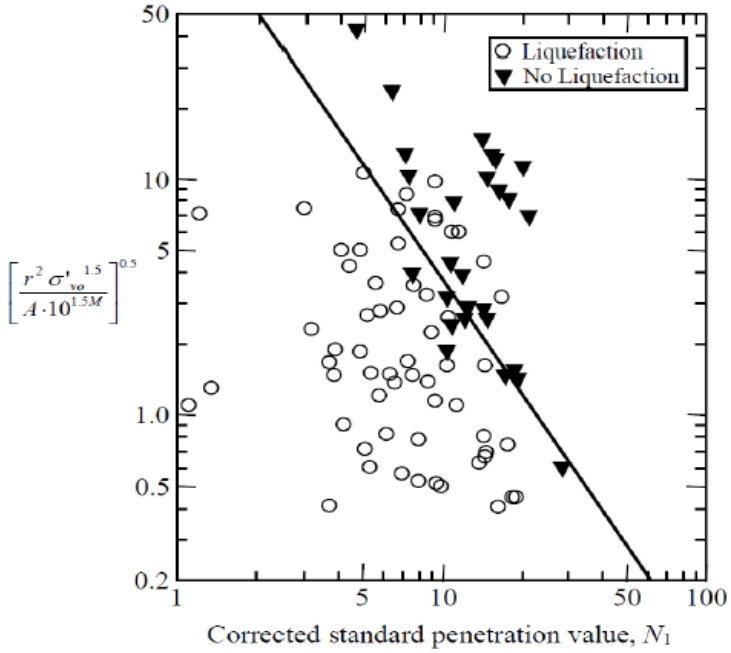

Figure 2-6 Liquefaction chart proposed by (J. B. Berrill & Davis, 1985)

Several laboratory tests have been conducted to study the soil resistance to liquefaction based on the energy approach. For instance, Baziar et al. (2011) presented a model to predict the strain energy density amount that is required for the liquefaction triggering of sand-silt mixtures based on the soil physical characteristics.

Another strain energy-based approach was proposed by Millen et al. (2020). The normalized cumulative absolute (change in) strain energy (NCASE), which is computed through dividing the cumulative change in absolute peak strain energy by the starting vertical effective stress at rest equation (2-10). In addition, NCASE would be represented graphically as the sum of the absolute change in strain energy between the strain energy peaks in the response as shown in Figure 2-7 (Millen et al., 2020; Viana da Fonseca et al., 2023).

Using equation (2-11), the average absolute stress between peaks can be computed which then would be multiplied by the change in strain between the peak points divided by the vertical effective stress to compute the NCASE, equation (2-10).

The peak strain energy points j which includes both local maximum and minimum, can be identified graphically or by determining the points where the derivative of shear strain intersects, as described by equation (2-12). In this context, (i) refers to the incremental step of each parameter measurement, and $\Delta\gamma_i$ represents the variation in shear strain between the current i(th) measurement and the previous one. To avoid flat peaks, any points where the derivatives are equal to zero should be excluded from the time series.

$$NCASE = \frac{1}{\sigma'_{v0}} \sum_{j=0}^{n_{peaks}} |\tau_{av.j}| . \left| \gamma_{j+1} - \gamma_j \right| \tag{2-10}$$

$$|\tau_{av.j}| = \begin{cases} \frac{|\tau_{j+1} + \tau_j|}{2} & \tau_{j+1} . \tau_j \geq 0 \\ \frac{|\tau_{j+1}^2 + \tau_j^2|}{2 . |\tau_{j+1} - \tau_j|} & \tau_{j+1} . \tau_j < 0 \end{cases} \tag{2-11}$$

$$Peak_j = \Delta\gamma_i . \Delta\gamma_i + 1 < 0 \tag{2-12}$$

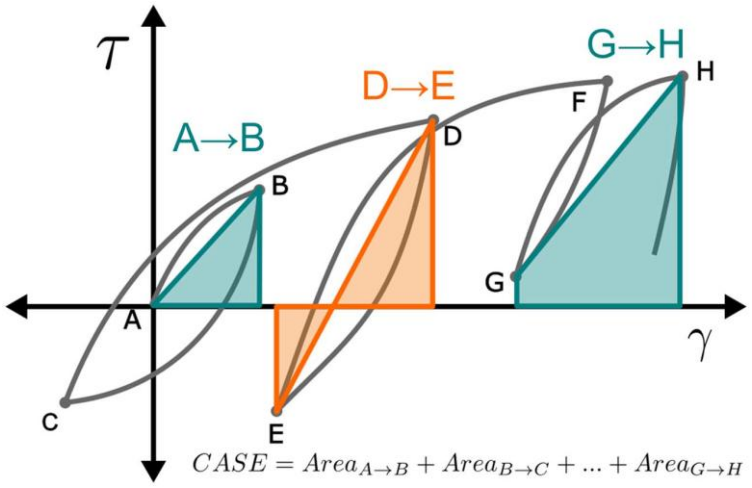

Figure 2-7 Graphical calculation of cumulative absolute strain (Millen et al., 2020)

2.2.3. Types of liquefaction

According to Kramer (1996b), Earthquake-induced liquefaction failures are fundamentally categorized into flow liquefaction and cyclic liquefaction, also introduced another term (Cyclic softening) and reported that these three phenomena are related soil softening/ weakening during earthquakes.

Flow Liquefaction

In general, flow liquefaction is a strain softening response that might cause the most destructive consequences among the three types of liquefaction failure. It occurs under undrained conditions, being triggered by monotonic or cyclic loading when the equilibrium static shear stress exceeds residual strength at liquefaction where, large deformation is driven by static shear stress, stiffness will drop due to the dynamic load induced instability and flow failure will occur.

However, and additionally, it can also occur in drained conditions if the mean effective stress decreases steadily; for instance, when the pore-pressure increases under constant deviatoric stresses or when extrusion occurs (removal of lateral confinement of a slope as an example).

Once this occurs, the flow liquefaction-induced large deformations are driven by static shear forces. The cyclic stresses might put the soil in an unstable state where the strength drops sufficiently to allow the static stresses to produce the flow.

The sudden nature of the failure, the speed, and the considerable distance over which the liquefied materials move could be enough to recognize flow liquefaction failures and damages. Figure 2-8 shows the fluid nature of liquefied soil as a consequence of the San Francisco earthquake in 1957.

Figure 2-8 Flow slide along the shore of Lake Merced in San Francisco 1957 (Kramer, 1996b)

Cyclic liquefaction

Cyclic liquefaction is another catastrophic soil failure, triggers when the static shear stress is less than the shear strength of the liquefied soil where, soil shows rapid pore pressure build-up, leading to the decrease in soil stiffness during cyclic loading. During the dynamic loading, deformations (which are produced by both static and cyclic shear stresses in this case) increased gradually and diminish by the shake end. These deformations may cause lateral spreading in areas with very mild slopes or even in flat ground near rivers, lakes, or the sea, as shown in Figure 2-9.

Figure 2-9 Lateral spreading of flat ground toward the Motagua River following the 1976 Guatemala earthquake. Note: the orientation of ground surface cracks is parallel to the riverbank (Kramer, 1996b)

Cyclic softening

Cyclic softening might occur when fine-grained soils with significant plasticity are exposed to dynamic loading which will develop large deformations and decrease soil stiffness. An

example of cyclic softening is the Fourth Avenue Slide in the 1964 Alaska earthquake, which caused displacements of up to 5m, as shown in Figure 2-10.

Figure 2-10 Fourth Avenue slide in Anchorage, Alaska following 1964 Good Friday earthquake. (Photo by U.S. Army, courtesy of USGS.), (Kramer, 1996b)

As the current study focuses on the soil behavior under monotonic and cyclic loading, the Critical state soil mechanics theory will be briefly explained in the following section, where it generally explains the mechanical behavior of soils.

Critical state soil mechanics

The Critical State Soil Mechanics (CSSM) framework is an approach within geotechnical engineering that provides a comprehensive understanding of the mechanical behavior of soils under various stress and strain conditions. The critical state (the core of the CSSM), is defined as the state at which the soil continues to deform at constant void ratio and effective stress (Roscoe et al., 2015). This criterion is selected to be the shear failure criterion adopted in the performed set of experimental monotonic triaxial tests.

The critical state can be thoroughly understood through the explanation of its fundamental parameters, namely the critical void ratio and the state parameter.

Critical void ratio

Casagrande (1936) performed a set of drained strain controlled triaxial tests on initially dense and initially loose sand samples. The results as shown in Figure 2-11 revealed that at the same effective confining pressure, all tested specimens approached the same density when shearing to large strains.

Initially loose samples contracted or densified during shearing. On the other side, initially dense specimens first contracted but then very quickly started to dilate. However, at large strains, all specimens approached the same density and continued to shear with constant shear resistance. The void ratio corresponding to this constant density termed the Critical void ratio e_{cs}. Then, a set of tests has been performed at various effective confining pressures and concluded that the critical void ratio is uniquely related to the effective confining pressure and described that locus as the critical void ratio CVR line as shown in Figure 2-12.

So, by identifying the state of the soil in terms of void ratio and effective confining pressure, the CVR line might be used to distinguish the boundary between loose and dense or contractive and dilative states respectively.

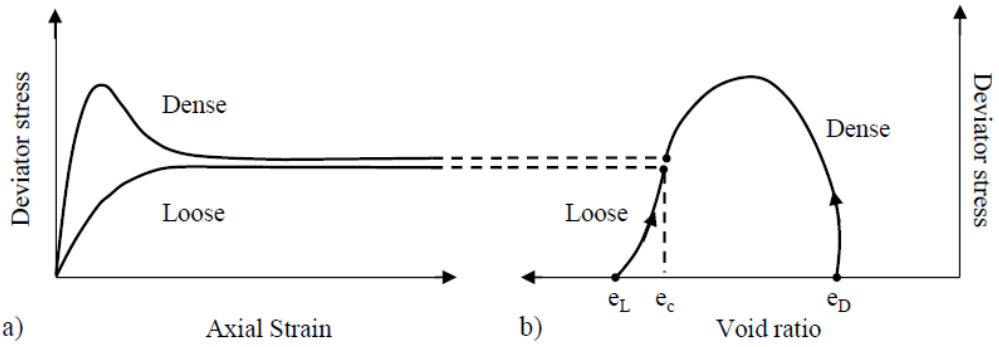

Figure 2-11 Critical state representation a) Stress-strain; b) stress-void ratio curves for loose and dense sands at the same effective confining pressure sheared under drained conditions (Kramer, 1996)

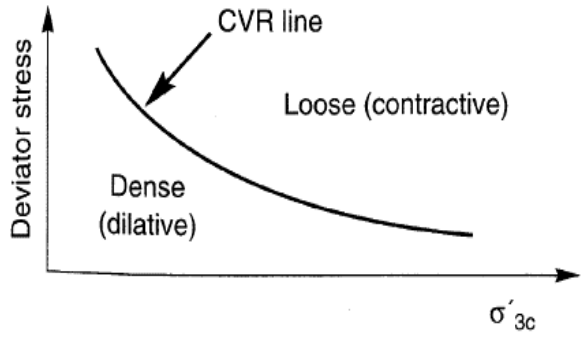

Figure 2-12 CVR line separating loose (contractive state) and dense (dilative state) (Kramer, 1996)

The CSL position can be represented in the void ratio *versus* mean stress plot, following equation (2-13), where:

$$e_{cs} = \Gamma - \lambda \log p'_{cs} \tag{2-13}$$

Where e_{cs} is the critical state void ratio; p'_{cs} is the mean effective stress at critical state; $e_{o,cs}$ is the critical state for p` = 0 kPa and; $\Gamma$ and $\lambda$ are intrinsic properties of the soil, $\Gamma$ is the void ratio intercept (void ratio at P` = 1 kPa) on the logarithmic scale while, λ: is the gradient (slop) of the CSL.

The critical state line which is defined as the Mohr-Coulomb failure line in the stress-path plot could be represented by critical shear stress ratio M_{cs} and critical friction angle ϕ_{cs} as shown in equation (2-14).

$$M_{cs} = \frac{6 \sin \phi'_{cs}}{3 - \sin \phi'_{cs}} \tag{2-14}$$

It is worth mentioning that, for undrained tests, the critical state can be represented through the pore pressure change since the volume is not allowed to change. Dense specimens develop negative excess pore pressure, as they tend to dilate, while loose specimens develop positive excess pore pressure, as they tend to contract.

The critical state line defines the ultimate state of any soil specimen at high strains, regardless of initial state or drainage conditions. Moreover, the uniqueness of the CSL is

accepted by many authors whereas, for drained tests, the volume change during shearing might be used to identify contraction behavior of loose samples by volume decrease and dilation behavior of dense samples by volume increase. Figure 2-13 identifies the general behavior of loose and dense sands under drained and undrained conditions in the (e-p´) and, (e-log p´) area (Atkinson, 2017).

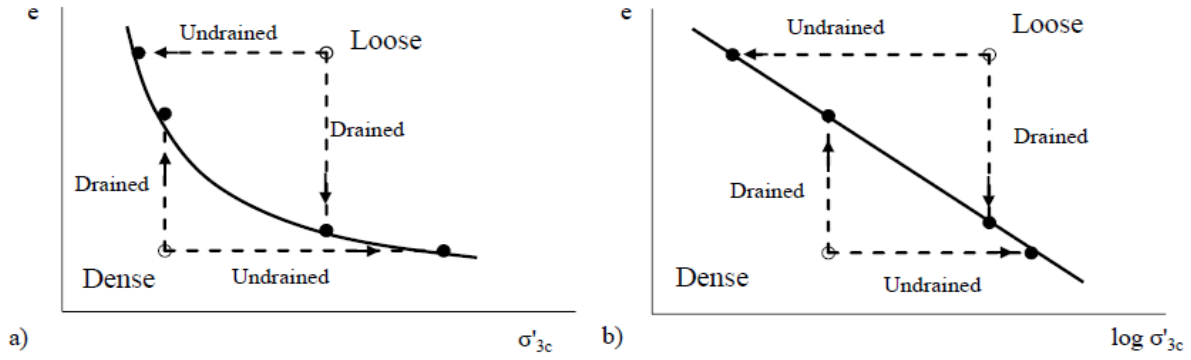

Figure 2-13 Behavior of initially loose and dense specimens in drained and undrained conditions: a) arithmetic; b) logarithmic effective confining pressure (Kramer, 1996)

2.2.3.1. State parameter

State parameter ψ, as shown in

Figure 2-14 defines the soil void ratio compared to the critical state void ratio. In other words, samples in states located at the same distance from the critical state line should exhibit similar behavior. State parameter would be computed using equation (2-15).

$$\psi = e - e_{cs} \tag{2-15}$$

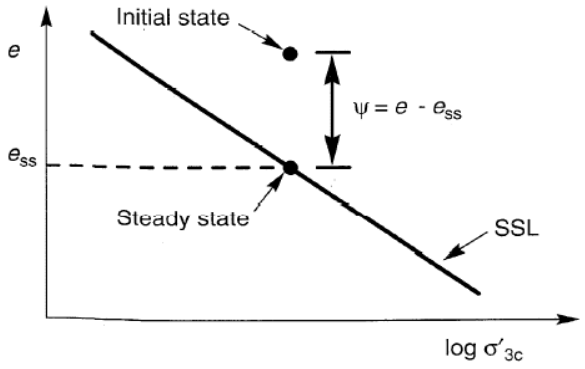

Figure 2-14 State parameter of soil (Kramer, 1996)

2.3. Liquefaction mitigation methods and classification

2.3.1. Historical background on liquefaction mitigation methods

As the soil liquefaction phenomenon usually triggers in loose saturated soils, most of the earlier liquefaction mitigation methods relied on compaction or groundwater table lowering, such as soil replacement, sand compaction piles, vibration compaction, dynamic compaction, blast compaction, grouting, deep mixing pile method, gravel pile method, dissipation using screen pipes, and lowering the groundwater table (Huang & Wen, 2015).

Even though these earlier methods for increasing soil resistance to liquefaction have been adjusted and updated over time, they still have significant complexities, such as high construction cost, high-energy consumption, and impact on surrounding infrastructures and adjacent structures. Moreover, their applicability is restricted by site conditions. Generally, it cannot be applied under structures sensitive to deformation or vibration at developed sites (Gallagher et al., 2007) e.g., despite the wide use of traditional cement and chemical grouting, it may pollute the surrounding environment and waterways and risk damaging adjacent buildings when mishandled. Also, soil densification through dynamic compaction is energy intensive and dramatically impacts the surrounding infrastructure, and the compaction depth is limited (Huang & Wen, 2015).

Researchers have continued to explore new liquefaction countermeasures that might be lower in cost, have less effect on existing and surrounding structures, and be environmentally friendly, durable, and pollution-free.

Therefore, liquefaction mitigation methods have been constantly emerging due to the rapid development of science, technology, and multidisciplinary engineering approaches. New concepts like passive site remediation, microbial geo-technology, biological treatment, and recycled materials have been suggested. Lately, induced partial saturation IPS has been proposed as a promising technique for liquefaction mitigation because numerous studies have revealed that soil resistance to liquefaction increases significantly as the degree of saturation decreases (Bao et al., 2019).

Flora et al. (2021) have classified the liquefaction mitigation techniques into direct technologies that act on the pore pressure changes causing liquefaction (e.g., drainage or desaturation) and indirect technologies that aim to increase soil capacity to resist liquefaction (e.g., soil reinforcement).

In the next sections, a variety of liquefaction mitigation techniques will be discussed based on previous literature.

2.3.2. Recent physical mitigation methods

The environment faces a serious threat from too much disposal of waste materials such as tires, plastics, metals, glass, and others. Therefore, scientists and researchers are always trying to use these waste materials at their best. The following section shows the efficiency of using some of these materials to improve soil behavior.

2.3.2.1. Tire chips

Hazarika et al. (2010) mentioned that the scrapped tire-derived materials, such as tire chips and tire shreds, can be categorized as three-dimensional geosynthetics. Moreover, a model shaking table test on a caisson-type quay wall has been conducted for the same purpose. The results demonstrated that sand tire chip mixtures can prevent liquefaction if the optimum mixture percentage is used.

Hazarika et al. (2010) stated that as backfill material, tire chips mixed with sand exert less lateral earth pressure than sand due to their relatively low density.

For evaluating the seismic response characteristics of tire chips and tire chip-sand mixtures, Kaneko et al. (2013) performed online pseudo-dynamic response tests on a model consisting of either tire chip-mixed sand or layers of sand and tire chips. The study results clarified that when tire chips were mixed with sand or placed as layers, higher damping and seismic isolation effects were noticed due to increasing damping characteristics.

Using a series of shaking table model tests, Bahadori & Manafi (2015) investigated the impact of adding various tire chip quantities on saturated sand. The findings demonstrated that as the quantity of tire-chip increases, the damping ratio increase, and pore-water pressure generation decreases.

Cost-effective and environmentally friendly shredded waste tires were used by Nikitas & Bhattacharya (2023). Triaxial tests (monotonic and cyclic) and dynamic 1g shaking-table tests have been conducted. Based on the collected data, displacements and tilts were reduced by the inclusion of tire chips beneath the foundation; moreover, the tire chips prevented the liquefaction phenomenon from occurring by influencing excess pore pressure generation. Additionally, it was observed that the inclusion of a tire sub-base decreased the natural frequency of the foundation (by analyzing acceleration data). This demonstrates that the suggested approach could help in seismically protecting a structure from inputs of greater frequency.

Amanta & Dasaka (2023) Performed series of strain controlled triaxial tests and found that the particle size of tire derivative has a significant effect on the dynamic properties and liquefaction behavior of sand-tire derivative mixes.

Bernal-Sanchez et al. (2025) conducted resonant column and cyclic triaxial tests and reported that that soil-rubber mixtures containing bigger or more elongated rubber particles tend to lose stiffness more quickly, but they also provide greater damping. Adding 10% to 20% shredded rubber by mass notably improved internal stability, limits stiffness loss at strains up to 1%, and reduces pore water pressure build-up, which in turn increases liquefaction resistance.

2.3.2.2. Recycled / waste materials

To protect “lifelines” from liquefaction hazards in sandy backfills, Otsubo et al. (2016) evaluated the seismic response of underground lifelines. The study aimed to develop new backfilling methods using recycled or waste materials to mitigate the liquefaction-induced floating of embedded lifelines. The waste materials used in this study were crushed glass, crushed concrete, and a mixture of tire chips and sand. Thus, a series of shaking model tests were conducted to investigate the performance of the recycled backfill materials.

The results showed that using recycled materials in backfilling significantly prevents the pipes from floating. Crushed glass and crushed concrete are the most promising materials used for backfilling to prevent pipeline damage caused by liquefaction. Moreover, liquefaction mitigation using tire chips was recommended due to their effectiveness in reducing pore water pressure development, ease of compaction, and decreasing displacement due to their relatively low unit weight.

Akbas et al. (2023) did a numerical study to investigate the behavior of pavements made of 100% recycled concrete aggregates RCA and natural aggregates NA waste materials, constructed on highly liquefiable sand soil. Three model scenarios were created: Model 1 includes a layer of sand with high liquefaction potential over the bedrock (without pavement), while Models 2 and 3 include pavement constructed with 100% RCA and NA, respectively, over the soil profile in Model 1. Dynamic analyses were carried out by the PM4Sand model. The findings related to that study were that, when compared to the other two models, the liquefaction-induced settlement in the model without pavement was found to be significantly larger. This could be attributed to the RCA and NA abilities to limit the drainage.

The thickness of the liquefied soil layer beneath a pavement constructed using NA or RCA was considerably lower than that with no pavement. This study provides an alternative technique through using RCA waste materials instead of NA in pavements. This alternative would be more environmentally friendly and economical, since it is a waste material.

Zachariah & Jakka (2025) performed a set of cyclic triaxial tests to explore the efficacy of partially replacing the soil with sugarcane bagasse -available agricultural waste- The results showed that bagasse can replace a substantial portion of the soil, roughly between 19% and 41%, without reducing the initial cyclic strength of the natural soil. The best performance was observed at about 30% bagasse, where the mixture showed greater resistance to excess pore water pressure build-up and, therefore, better liquefaction resistance.

2.3.3. Recent chemical mitigation Methods

Nanomaterials e.g., colloidal silica, bentonite, and laponite, have been widely used in soil improvement due to their nano-scale particle size, which could penetrate finer soils without high-pressure infusion.

A nanoparticle is a small particle with at least one spatial dimension of fewer than 100 nm, has a unique structure, a huge specific surface area, and strong activity on the surface (Moug et al., 2022; Siddique et al., 2023b). In addition, this improvement method has a less disruptive effect on surrounding environments than other traditional materials.

2.3.3.1. Nano colloidal silica

Colloidal silica CS is an aqueous dispersion of spherical silica nanoparticles (2 to 100 nm) produced from saturated solutions of silica acid. During manufacturing, alkali solutions are used to stabilize the CS solution against gelation. Alkaline solutions ionize the nanoparticles therefore, they repel each other.

Gelation is induced by decreasing these repulsive forces through a coherent network of siloxane (Si-O-Si) bonds as shown in Figure 2-15, that restrain the pore fluid by binding the soil particles together (Hamderi & Gallagher, 2015; Conlee et al., 2012).

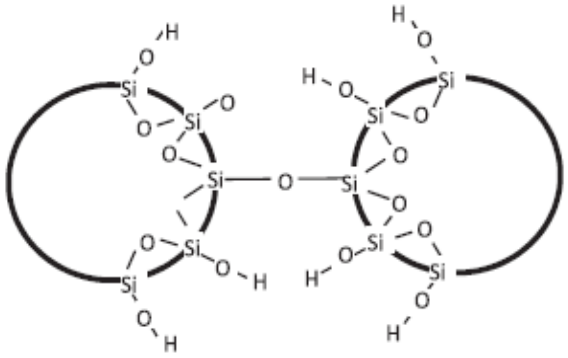

Figure 2-15 Formation of siloxane bonds as a colloidal silica particle gel (Conlee et al., 2012)

The mechanism of stabilizing liquefiable soil using the colloidal silica grouting is summarized by Patricia & James (2002), where the diluted colloidal silica with low viscosity is injected from a particular site boundary to be transported to the desired location through natural groundwater flow, and then the fluid gradually restores its viscosity due to transforming into the colloidal state, thus strengthening the bonding of the soil grains.

The main function of such mitigation technique is to use colloidal silica for bonding individual sand grains. Moreover, the viscosity of pore fluid may be a significant factor to reduce the excess pore water pressure by reducing the hydraulic conductivity (Gallagher et al., 2007). Colloidal silica would be injected into the proper location before it gels, as the gelling time of colloidal silica can be adjusted by changing the pH and the ionic strength of the solution (Gallagher et al., 2007).

Experiments carried out by Persoff et al. (1999) concluded that the treated sand-bearing capacity is directly proportional to the colloidal silica particle concentration. Moreover, as the gelling time increases, the soil shear strength increases. In addition, the unconfined compressive strength of the sand is increasing by increasing the concentration of CS particles up to a maximum of 400 kPa. On the other hand, increasing the CS concentration will decrease the CS-treated soil permeability, resulting in non-uniform distribution of the CS, especially in large areas.

Gallagher & Lin (2005) performed column tests and found that CS could effectively penetrate and uniformly distribute on liquefiable sand when the CS content was 5% by weight with a pH value between 7.5 and 8.7, as shown in Figure 2-16.

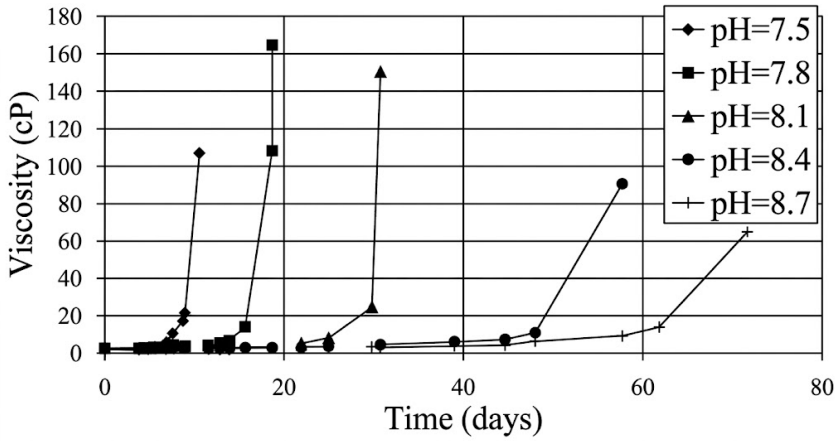

Figure 2-16 Typical colloidal silica gel time curves for 5 % by weight solutions at different pH values (Gallagher & Lin, 2005)

Hamderi & Gallagher (2015) developed a 10m^3 pilot-scale box model accompanied by 3D fluid simulations to investigate the ability of injecting dilute CS (injecting rates ranging from 65 to 9000 ml/min/well). The study concluded that in low concentrations of about 1% by weight, CS could significantly reduce the risk of liquefaction in loose sand by cementing individual particles together. Moreover, due to its low initial viscosity and reasonable control of gelling time, it can be injected and spread over longer distances than other grouting materials. Colloidal silica density is slightly higher than that of water; therefore, it tends to sink due to gravity before reaching the target location. Based on that, it is strongly recommended to use an appropriate injection method such that the horizontal travel component exceeds the vertical travel component. Furthermore, the gelling time must be adequately optimized to ensure that the viscosity remains low until the colloidal silica is delivered to the desired location and then increased to avoid gravitational settling.

Conlee et al. (2012) performed two centrifuge tests to investigate the response of loose sand treated with 4, 5, and 9% colloidal silica by weight. The study concluded that by increasing the CS concentration, soil deformation decreased continuously. In addition, CS treatment could drastically reduce the lateral spreading of slopes resting on liquefiable soil layers. Furthermore, cone tip resistance and shear wave velocity increase in sands treated with CS. Finally, the improved soil experienced lower cyclic shear strains and higher cyclic resistance ratios.

A set of cyclic triaxial tests was conducted by Patricia & James (2002) on samples stabilized with colloidal silica at concentrations between 5 and 20%, to investigate how colloidal silica grout affects the deformation characteristics and liquefaction resistance of loose sand. The study showed that before the liquefaction occurrence, untreated soils showed small axial strain values. However, once the liquefaction was triggered, large strains developed rapidly, and the samples collapsed within a few additional loading cycles. On the other hand, the soil treated with CS at concentrations of either 5, 10, 15, or 20% could bear more cycles with very little strain during cyclic loading, and none of the treated samples collapsed, as shown in Figure 2-17.

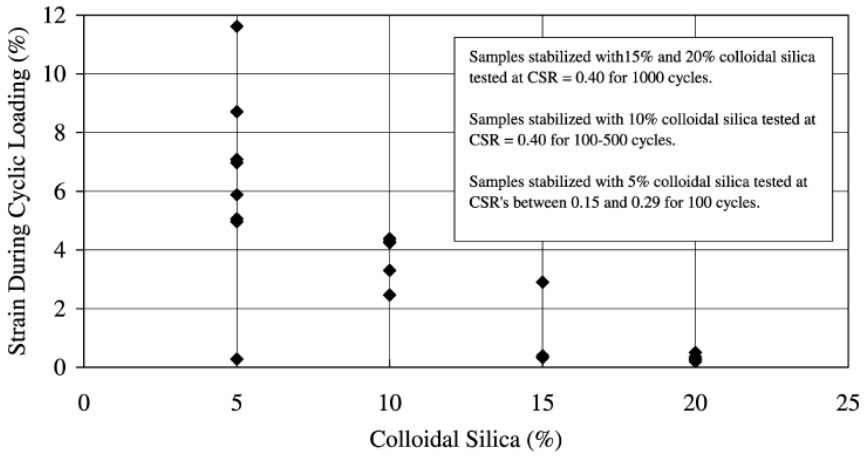

Figure 2-17 Percent colloidal silica versus strain during cyclic loading at CSR=0.4 (Patricia & James ,2002)

Furthermore, the study showed that the effect of a 20% CS concentration on the cyclic strength of loose sands was approximately equivalent to dense sands' cyclic strength with a relative density of 80%.

Salvatore et al. (2020) performed a set of drained monotonic and undrained cyclic triaxial tests to investigate the effect of injecting low-pressure of aqueous nano-silica suspensions on the soil resistance to liquefaction.

The suspension of nano-silica particles in water was kept in a colloidal state by adding sodium ions Na+, which resulted in a pH of approximately 10, creating conditions suitable for the formation of isometric nanoparticles ranging from 2 to 100 nm. The viscosity of the suspension in this state was 10 times the viscosity of water which makes it ideal for injection into low-permeability sands. The author used the salt (10% sodium chloride water solution, pH ≈ 7), as an activator of the nano-silica to form the gel. Scanning electron microscope SEM, was utilized on samples prepared with variable dosages enabled analysis of the microstructure of the original material and grouted sand. SEM showed that the silica gel created a matrix of microscopic bubbles with radii ranging up to 10 μm which successfully enveloped the sand particles and filled the intergranular pores.

The study concluded that the gelling strength increased progressively over time, which in turn increased the shear resistance of the treated soil. In addition, the performed study allowed for quantifying the impact of grout composition, particularly the amount of activator salt NaCl, on both the gelling time and the decay of soil grout permeability.

Furthermore, the used triaxial apparatus was equipped with bender elements thus, shear wave velocities of grouted soil were measured and found to be fast in the beginning (0–9) days but continued for longer periods (up to 24 days in the present analysis) consistently with the development of strength in the nano-silica gel.

Therefore, it can be concluded from previous studies that CS has the advantages of relatively low cost, low initial viscosity, controllable gel times, good long-term mechanical stability, and minimal disruption to infrastructure due to the small particle size and surface charge of the silica particles. In addition, CS is colorless, non-toxic, has stable biological and chemical properties, has excellent durability characteristics, and is environmentally friendly.

2.3.3.2. Nano bentonite

Bentonite is a low-cost, environmentally friendly material; it is an absorbent aluminum phyllosilicate clay consisting mainly of montmorillonite. Bentonite suspension is injected into the soil and then becomes bentonite gel (Siddique et al., 2023b).

The bentonite dispersion characteristics depend on several factors, such as pH, soil type, and clay concentration. Bentonite can significantly increase the soil resistance to liquefaction by forming a bentonite gel inside the pore space, which hinders the development of pore water pressure during seismic actions (Bao et al., 2019).

The dispersion homogeneity of bentonite is significantly impacted, especially in wide areas, by its high initial viscosity and therefore quick gelation duration (Huang & Wen, 2015).

For this purpose, Rugg et al. (2011) conducted rheological tests to examine the suspensions' penetrability and thixotropic strength recovery. The study showed that adding 2% sodium pyrophosphate SPP to 10% bentonite suspensions effectively reduced the bentonite suspension's initial viscosity and yield stress so that the bentonite suspension can permeate the soil faster. Meanwhile, due to the thixotropic nature of the bentonite suspensions, yield stress and viscosity gradually increased again. In the same study, consolidated undrained triaxial tests were performed to evaluate the shearing response. loose Ottawa sand specimens were treated with bentonite suspension. Results reported that clean sand has the same internal frictional angle as sand treated with bentonite suspension, which indicates that the bentonite suspension permeation pressure does not affect the soil fabric.

Resonant column tests, static triaxial tests, and cyclic triaxial tests have been conducted by El Mohtar et al. (2014) on specimens prepared by dry-mixing Ottawa sand and bentonite. This study investigated the effect of adding small percentages of bentonite (3% and 5% by dry mass of the sand) and the ageing period preceding shear (1 to 10 days) on pore pressure generation and hence seismic resistance, Figure 2-18.

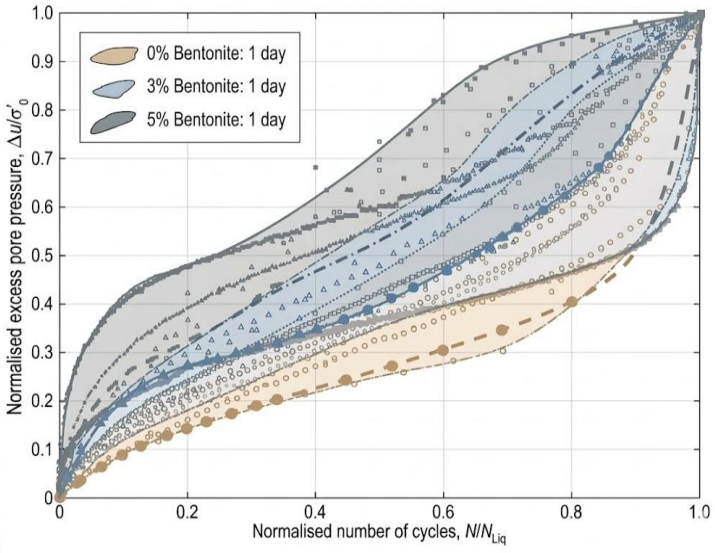

Figure 2-18 Normalized mean excess pore pressure vs. normalized number of cycles to liquefaction – dash line represents a range of values from the literature (El Mohtar et al., 2014)

In resonant column tests, bentonite increased the shear strain required to generate excess pore pressure build-up. In contrast, during cyclic tests, the mean pore pressure developed

per loading cycle has been reduced, allowing the soil to lose some of its effective stress prior to liquefaction initiation. Furthermore, in static tests, it is noted that extending the ageing time significantly affects the soil behavior stability. These effects have a significant influence on increasing the resistance to liquefaction.

These results are compatible with cyclic tests done by El Mohtar et al. (2013) on bentonite-treated sands that showed a significant increase in the number of cycles required to trigger liquefaction compared to clean sand with the same relative density and cyclic stress ratio.

Sadiq (2023) used a 1g shaking table apparatus to mitigate soil liquefaction using cement kiln dust and bentonite clay. For loose saturated sand samples, liquefaction was reported at 60 s, 25 s, and 10 s for 0.5 Hz, 0.75 Hz, and 1 Hz, respectively. After the mitigation, the soil liquefaction did not occur until 100 s, 60 s, and 30 s for the same frequencies.

2.3.3.3. Nano laponite

Laponite is a synthetic nano-clay with a particle diameter of 25 nm and a thickness of 1 nm. Laponite materials are commonly used to stabilize soils because they are environmentally friendly, nontoxic, have high plasticity, and are small in particle size. Several factors affect the dispersion characteristics of laponite-treated soil, such as the concentration and PH value.

Huang & Wang (2016) performed dynamic triaxial tests, rheology tests, and SEM imaging to examine the mechanism, efficiency, and cyclic behavior of using laponite for liquefaction mitigation. The study reported that the formation of the laponite suspension in the pore space shows solid-like properties as time passes. In other words, laponite material could bond with the sand particles and fill the pores as a fluid. Based on that, Laponite materials can significantly increase soil liquefaction resistance by solidifying pore fluid, cementing soil grains, and delaying pore pressure development. Moreover, the liquefaction resistance of the laponite–silty sand samples improves when the laponite concentration or curing time increases, where the effect of laponite concentration is more significant in the first few cycles and the effect of curing time is more significant as the number of cycles increases.

To study the effect of adding small percentages of laponite (1 to 5%) by dry mass of the sand on the cyclic response of liquefiable sand, Ochoa-Cornejo et al. (2016) conducted a set of cyclic triaxial tests. The cyclic resistance was found to be increasing during the first loading cycle. In addition, more resistance is gained by extending shear ageing or increasing the laponite concentration (3 to 5%). The author attributed that behavior to the resulting contact bonding between the charged laponite fines and the sand grains in addition to the formation of a pore fluid with solid-like properties.

Ochoa-Cornejo et al. (2014) carried out an experimental program where the main objective of these tests is to examine the effect of adding 1% laponite on the undrained cyclic triaxial response of the sand. Compared to the clean sand tested under the same conditions, adding 1% laponite dramatically increases the number of cycles to liquefaction.

The results were compared with findings obtained using bentonite and it was discovered that adding 1% laponite was equivalent to samples containing 3% bentonite, as shown in Figure 2-19 and Figure 2-20. The author attributed the increase in cyclic resistance to the gel resulting from the laponite hydration in the pore spaces and the semi-solid behavior that hindered the sand particles mobility. Through cementations, nano-clay laponite could significantly hinder pore pressure development and thus efficiently mitigate liquefaction.

According to the triaxial test results, performed by Siddique et al., (2023a), laponite percent (0.5% by dry mass of sand) decreased the pore-water pressure generation by 17 kPa compared to that of pure sand with the same condition. The study also revealed that, for an identical amount of strain, the required stress of the sand-laponite specimens is almost four times higher than that of the pure sand. Furthermore, the results indicated that temperature has a significant impact on how the sand-laponite mixture behaves. Even in studies with less laponite, the higher temperature accelerated the gelation process, while the lower temperature significantly slowed it down.

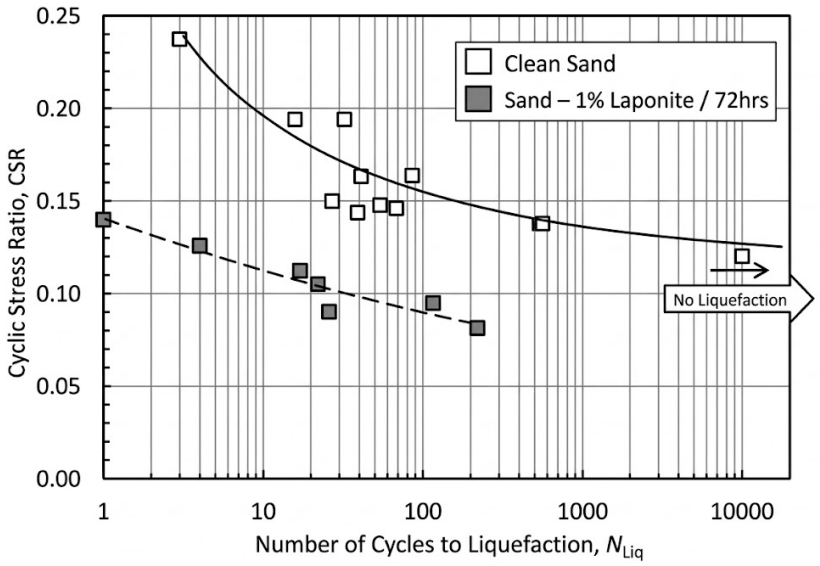

Figure 2-19 Cyclic resistance of clean sand and sand-Laponite specimens with Dr=15-25% (Ochoa-Cornejo et al., 2014)

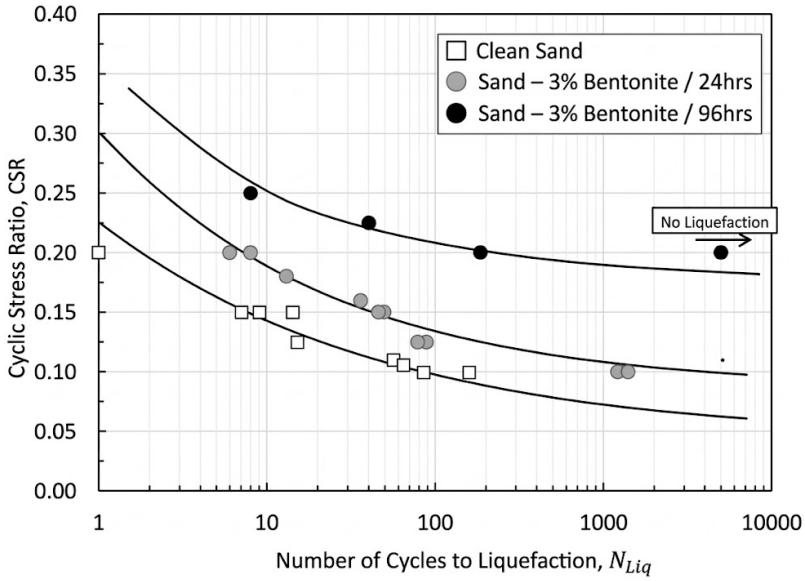

Figure 2-20 Cyclic resistance of clean sand and sand-bentonite specimens with Drsk=30-40% (Ochoa-Cornejo et al., 2014)

Generally, it could be concluded from the observed consistency of the results that using nanomaterials, particularly the three mentioned materials, can significantly increase

liquefaction resistance by increasing soil strength, cementing the soil grains, and effectively delaying pore pressure generation. Moreover, they considered relatively economical and environmentally friendly materials compared to chemical grouting techniques because adding the minimum quantity of nanomaterials can be as effective as adding large quantities of other materials scales.

2.3.3.4. Chemical grouting

Chemical grouting can significantly improve the liquefaction resistance of sand under various loading conditions. Cement, lime stabilization, fly ash, gypsum, and other materials significantly enhance soil behavior characteristics and consequently increase resistance to liquefaction.

Zeghal & El Shamy (2008) performed A coupled continuum-discrete hydromechanical model accompanied by some numerical simulations to investigate the dynamic response of saturated granular soils in loose and cemented deposits during the complex phenomenon of liquefaction. The results reported that the inter-particle cementation generated by grouted cement has a significant effect on resisting earthquakes.

The grouting process can be implemented either to form rigid inclusions, such as treated columns that do not overlap when the final treatment radius R_{max} less than the column spacing s or to provide cementation to the entire liquefiable soil, which involves partially overlapping treated columns when R_{max} is greater than or equal to s. In both scenarios, the advantageous outcome of the treatment is a reduction in the Cyclic Stress Ratio CSR, (Flora et al., 2023).

Resonant column and cyclic triaxial tests were conducted by Maher et al. (1994) to discover the effect of chemical grouting on soil dynamic properties, namely shear modulus and damping ratio. The materials used in this set of tests were sodium silicate, acrylate polymer AC-400, and polyurethane CG5610. The findings reported that the shear modulus has increased, and the damping ratio has decreased relatively using sodium silicate grouts, which produce stiff gels. CG5610 grouts have slightly increased the shear modulus and damping ratio, while AC-400 grouts have significantly increased the damping ratio and have no effect on the shear modulus. In addition, it has been noticed that the damping ratio increased, and the shear modulus decreased very fast in grouted sand with increasing shearing strain amplitude for the strain range of 10^{-4} to 1%. Moreover, curing time does not affect shear modulus or damping after a particular curing time. Despite having a negligible effect on the damping ratio, increasing the confining pressure in the tested stress range from 50 to 200 kPa has increased the shear modulus.

The long-term durability of silica-based grout has been tested in a number of indoor tests by Saito et al. (2012), with a focus on the curing conditions, which simulates the impact of groundwater inflow on actual sites by periodically replacing the curing liquid. A grouted soil evaluated in a static liquid bath is seen to suitably retain long-term durability throughout a curing time of 360 days without showing any decline in unconfined compressive strength. On the other hand, a degradation in the unconfined compressive strength has been recorded when the grout liquid is periodically replenished to accelerate the leaching of silica after a period between 56 and 91 days from the curing initiation. So, this investigation has verified that even under extreme conditions, the silica sol-based grout material and the activated silica-based grout material can have sufficient durability to maintain strength.

Re-liquefaction due to repeated earthquakes threatens structures and infrastructure; therefore, Porcino et al. (2015) have performed a set of (two phases of cyclic loading) triaxial tests and cyclic simple shear tests to examine the effect of previously triggered liquefaction on the subsequent cyclic behavior of chemically grouted sandy soil using (Silacsol) grouting material. The evaluated parameters in this study were strength, deformability, and pore pressure characteristics. Findings observed an increase in liquefaction resistance, particularly at low initial void ratios and low vertical practical stress values. In addition, grouted sand samples were found to be stiffer in the second cyclic loading and more resistant to liquefaction. Moreover, pore pressure build-up for treated samples after pre-shearing followed a different trend (significantly slower) than for virgin samples. The study reported that chemical grouting is a very effective method for liquefaction mitigation for the first seismic loading and subsequent shakings.

The effectiveness of chemical grouting as a preventative measure against the liquefaction of sand, with existing oil tanks on the surface was examined by Imamura et al. (2022), through a series of dynamic centrifuge model experiments. Active silica was used as the chemical grouting material in these tests. The grouting depth ratio to the depth of the liquefiable layer is the principal test parameter. The tests showed that the maximum and differential settlements dropped roughly linearly as the improvement depth increased. Pore water pressure was found to be noticeably different between non-improved and improved soil. e.g., at one of the centrifuge tests points, the maximum ratio of the excess pore water pressure of non-improved soil was about 0.4 during shaking, while for all tests with improvement, the maximum ratios of excess pore water pressure were about 0.3.

2.3.3.5. Water Electrolysis Method

The water electrolysis method is an alternative desaturation method used to introduce quantities of gas into liquefaction-susceptible soils.

Water electrolysis, as defined by Yegian et al. (2007), is the ionization of hydrogen and oxygen gases when a current is sent to electrodes in water, generating oxygen and hydrogen gases at the anode and cathode as shown in equations (2-16) and (2-17):

At the Cathode $4H_2O + 4e^- \rightarrow 4OH^- + 2H_2$ (2-16)

At the Anode $2H_2O - 4e^- \rightarrow 4H^+ + O_2$ (2-17)

A flexible liquefaction box was designed and fabricated by Yegian et al. (2007) to allow the application of cyclic shear strains in large loose sand specimens using a shaking table.

Cross-well radar was used to detect the various saturation degrees, for examining the soil desaturation impact on the pore water pressure generation for partially saturated sand soils using two different techniques, "water electrolysis method, and drainage- recharge method". In addition, the stability of the gas amount in soil voids was investigated in a prepared deep sand column.

The anode and cathode were made of titanium mesh, and a current was passed through the system, generating oxygen and hydrogen bubbles. The study results showed that, in fully saturated sand, cyclic shear strains yielded an excess pore pressure ratio of about 1, resulting in liquefaction triggering before two shear strain cycles of 4 HZ frequency and 0.2%

amplitude. On the other hand, partially saturated sand by the water electrolysis method with a degree of saturation of 96.3% yielded excess pore pressure ratios significantly smaller than fully saturated (liquefaction is unlikely to occur), matching the visual experimental observation. The alternative desaturation method used in this study was the drainage-recharge method, in which the reduction of saturation degree was achieved by slowly draining water from the sample and then slowly re-pouring the drained water onto the sample from its top. The degree of saturation achieved using the drainage-recharge method was 86%, resulting in excess pore pressure ratios significantly smaller than those of fully saturated soil, confirming the visual results where the soil did not liquefy. In addition, cross-well radar was found to be a promising and efficient technique for detecting the experimental and in-situ soil degrees of saturation.

Finally, the drainage-recharge method was used to prepare a 151 cm desaturated sand column to investigate the stability of the trapped bubbles in the soil. It has been concluded that the degree of saturation has increased from 82.9 to 83.9% after 442 days, showing a little tendency for the trapped bubbles to escape.

It has also been reported that electrolysis technique may change the pore fluid pH value; however, this pH value does not significantly affect saturation, pore pressure development, or liquefaction.

Chen et al. (2021) have studied the resistivity of soil at different depths under various currents. Field tests were conducted using the electrolysis desaturation method. The experiments employed a novel variety of electro-kinetic geosynthetics EKG for the electrode materials, which are extensively utilized in electro-osmosis. According to the results, the saturation levels of the treated foundation were 87%, 83%, and 80% for constant currents of 1 A (ampere, the unit of direct current), 2 A, and 3 A. In addition, the study concluded that the dispersion and stability of the gas were improved by increasing the electrode spacing. It revealed also that this mitigation method is very economical for repeated anti-liquefaction treatment of foundations, e.g., with 3 A of constant current and 3 m of electrode spacing, the maximum consumption of electricity for 12 h of electrolysis was found to be 8.98 kW·h.

2.3.3.6. Chemical method

Chemical desaturation generates air/gas bubbles through chemical reactions made by adding particular materials to the liquefiable soil. Eseller-Bayat et al. (2013) have conducted a set of experimental tests by manufacturing a cyclic simple shear liquefaction box on a shaking table. The box was provided with pore pressure and displacement transducers, bender elements, and bending disks to examine the cyclic response of chemically partially saturated soils. A high-resolution digital camera measured the bubble's size and distribution inside the samples. Finally, the trapped air sustainability was examined using a partially saturated long column subjected to hydrostatic and upward flow conditions and horizontal cyclic base excitation, simulating the potential effect of seismic ground motions.

The wet pluviation method was used to prepare the loose saturated Ottawa sand, the chemical reaction was achieved by combining the soil with a powder of sodium perborate monohydrate to generate ting oxygen bubbles.

The study concluded the following:

- Using S-waves generated by bender elements is an efficient way to confirm the sample density uniformity.
- Although the bender element wave measurements (P-waves) cannot estimate the degree of saturation, they can confirm the partial saturation presence.
- High resolution digital cameras can efficiently screen the gas bubbles' distribution into the soil.
- Regardless of the amplitude and number of cycles, chemically partially saturated specimens with a degree of saturation less than 90% did not trigger initial liquefaction ($r_{u,max}$ <1.0) compared to fully saturated samples.
- The partially saturated long column experienced a long-term sustainability of bubbles while subjected to an upward flow gradient and base excitation.

2.3.4. Recent biological mitigation methods

2.3.4.1. Bio-cementation

Biological materials soil treatment, also called bio-cementation, is the process of injecting nutrients, microorganisms, and microbially induced calcite precipitation MICP with urea and a dissolved calcium source into the soil. With time, microorganisms perform some biological reactions, forming a gel so that the sand particles bond together, increasing the shear strength of the soil. Biological materials are considered a practical, pollution-free, and environmentally friendly soil improvement technique.

DeJong et al. (2006) have used Bacillus pasteurii, an aerobic bacteria found in natural soil deposits, to achieve microbially induced calcite precipitation MICP. According to the study, MICP-treated specimens exhibited increased axial capacity under undrained monotonic shearing conditions. The (q/p') response of the specimens indicated a non-collapse behavior. They exhibited increased initial shear stiffness and higher elastic capacity than untreated loose specimens, according to a set of isotopically consolidated undrained compression triaxial tests. In addition, the production of a cemented sand matrix with a concentration of precipitated calcite forming bonds at particle-particle interactions was confirmed using SEM imaging. The presence of calcite-cement linkages was confirmed by X-ray compositional mapping.

Zamani et al. (2021) performed centrifuge modeling to study the effectiveness of loose sand treated with microbial-induced calcium carbonate precipitation MICP to increase liquefaction resistance and alleviate the total and differential settling of shallow foundations. According to the results, the total settlement and maximum angular distortion of the foundation systems were decreased by up to 57% and 75%, respectively, depending on the depth of the MICP improvement and the soil layering. Overall, the findings demonstrate that MICP improvement can be successful in lowering earthquake-induced building damage.

Xiao et al. (2018) conducted undrained cyclic triaxial tests to investigate microbial-induced calcite precipitation's effect on the liquefaction mitigation of calcareous sand. Different specimens were tested, including sand treated with 0.2 L, 0.4 L, and 0.6 L of (cementation solution) CS and untreated clean sand. The results showed that the liquefaction resistance, strength, and stiffness of the sand treated by the microorganism were increased under cyclic loading. At the same time, the generation of pore water pressure and the settlement of the foundation were reduced.

Alternatively, Simatupang & Okamura (2017) proposed a new biological treatment method, namely, enzymatically induced calcite precipitation EICP, used for liquefaction mitigation where, urease enzyme is used instead of bacteria as a promoter for the hydrolysis of urea. Utilizing the urease enzyme, which causes Ca^{2+} and CO_3^{2-} and precipitate CaCO3 crystals in the void spaces and surface of grains, is more straightforward than using bacteria. In this study, a series of undrained cyclic triaxial tests have been conducted to examine the effect of the degree of saturation on the EICP-treated sand during the precipitation of calcite. Microscopic observations by scanning electron microscopy SEM showed that, at low saturation levels, EICP could precipitate more calcites concentrated at particle contacts than was the case in fully saturated sand, resulting in more soil resistance to liquefaction. It was confirmed that only 1% of calcite precipitation at a lower degree of saturation (30%) can double the liquefaction resistance.

2.3.4.2. Microbial methods (Biogas)

Initially, generating gas bubbles in soils and ensuring their stability over time was very complicated because the gases tend to dissolve in water or escape from the soil (Chu, 2013). Earlier gas pumping has been widely used, as shown in Figure 2-21.

Gas pumping proved to have some disadvantages, such as the stability of the gas bubbles inside the soil, and the gas uneven diffusion in soils; therefore, it was crucial to discover a different, more efficient way to produce gas bubbles such as the microorganisms.

Compared to gas injection, biogas has several advantages:

- The process does not need too much energy to deliver the gas bubbles into the targeted soil zone because of the low viscosity of bacteria and the nutrient fluid.
- The gas produced by microorganisms can be diffused and distributed evenly compared to other injection methods.
- The size of the generated gas bubbles induced by bacteria is small enough to be trapped in the soil.
- Valid and efficient for existing structures without causing any disruption to the surroundings.

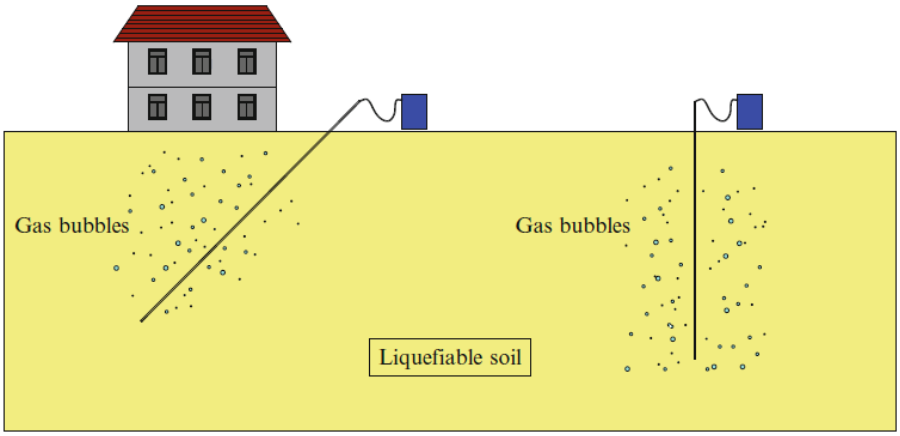

Figure 2-21 Injection of gas bubbles in saturated sand for the prevention of liquefaction (Chu, 2013)

Consequently, triaxial experiments were carried out by He (2013) to investigate the mechanical behavior and liquefaction potential of sand. A laminar box and shaking table

testing equipment were used to verify the effectiveness of the biogas approach for limiting sand liquefaction under cyclic stress. The morphology and stability of gases in sand are also investigated experimentally. Microbial denitrification process is used for the production of N_2 gas bubbles in sand. From this research, the following conclusions have been drawn:

- In the undrained triaxial tests performed on loose sand, the undrained shear strength increased as the degree of saturation decreased. The undrained shear strength increased 2.1 times in compression tests and 1.7 times in extension tests when the pore water pressure coefficient B-value was reduced from around 0.95 (saturated state) to 0.3. Furthermore, as the degree of saturation was reduced, the stress-strain response changed from complete strain-softening to strain-hardening behavior.
- The data resulting from the laminar box and shaking table testing equipment revealed that, for saturated samples, medium-dense sand liquefied at $a_{max.}$ = 1.5 $m/s^{2,}$ whereas loose sands liquefied at $a_{max.}$ =0.5 m/s^2. On the other hand, for biogas desaturated samples with saturation levels between 80% and 95%, liquefaction did not occur under the same conditions. Furthermore, the relative density of saturated samples must be as high as about 90% to produce a non-liquefaction response under a_{max} = 1.5 m/s^2.
- Figure 2-22 shows some results by plotting the pore water pressure ratio against the relative density for the various studied degrees of saturation, the pore water pressure ratio is the maximum excess pore water pressure ratio to the initial effective overburden stress. From the plot, it may be concluded that a slight decrease in the degree of saturation can effectively reduce the pore water pressure ratio, which decreases the probability of liquefaction triggering. In addition, it can be noted that the pore pressure ratio is inversely proportional to the relative density, which is why increasing the relative density of sand is one of the effective liquefaction mitigation techniques, which can be achieved by energy-intensive and high-cost methods such as dynamic compaction. Meanwhile, lowering the degree of saturation slightly has a significant effect on increasing the relative density with less energy and cost.

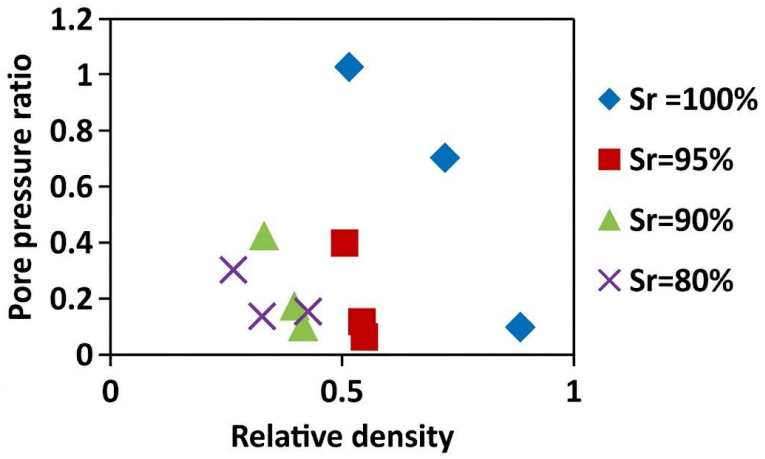

Figure 2-22 Pore water pressure ratios measured from model tests on bacteria-desaturated sand (He, 2013)

He et al. (2016) adopted the microbially induced soil desaturation method as a cost-effective method for mitigating soil liquefaction. The desaturation treatment of soils is made simply by generating microbially tiny nitrogen gas bubbles from the denitrification

process, and introducing the desaturation solution into soil pores by mixing, flushing, or injection. The authors carried out a detailed experimental study to investigate the efficacy of the microbially induced soil desaturation process, gas bubble shape and distribution, the dynamic response of desaturated soil, and gas bubble stability in soil. Then, computer tomography CT technology was used to make a suitable screening of the gas bubbles inside the soil; the main findings of the study were:

- The microbial technique can efficiently reduce the saturation degree of sand. The initial nitrate concentration employed in the desaturation solution is related to the ultimate saturation degree; e.g., the higher the nitrate concentration, the lower the saturation degree that could be achieved.
- On the CT scan, the soil´s gas phase was seen as small gas pockets, and those pockets were found to have a larger size than sand particles.
- In shaking table experiments, microbially induced desaturation effectively increased soil liquefaction resistance by limiting pore pressure generation, decreasing volumetric strain, and diminishing structure settlement in desaturated soil compared to saturated soil.
- In the undrained triaxial tests, loose desaturated sand exhibits an increase in strength, a shift in the stress-strain response from strain softening to strain hardening, and a declining trend in pore pressure generation as the saturation degree decreases.
- In the hydrostatic condition, the gas phase in microbially desaturated soil was found to be stable; however, it becomes unstable in steady flow conditions.

Huang & Wen (2015) stated that researchers tried to generate gas bubbles in soils in different ways to decrease the soil's degree of saturation; several studies adopted producing gases microbially based on the idea of microbial wastewater treatment; they concluded that nitrogen gas is more efficient than other gases due to the following reasons: it is an inert gas, has the highest gas percentage in the atmosphere (high availability), is very difficult to dissolve in water, and its density is similar to air density.

Peng & Zhang (2017) have adopted the microbial denitrification method to generate nitrogen gas bubbles from *Pseudomonas stutzeri* bacteria. The author mentioned that this bacterium offers several advantages compared to the other biogas treatment methods, including a faster average rate of gas generation and a shorter initial standstill period.

For this purpose, shaking table tests have been performed on saturated and microbially-desaturated samples under various acceleration amplitudes, the study revealed the following:

- During the suggested denitrification, Pseudomonas stutzeri showed outstanding denitrification capability when the culture time was 21 hours and the nitrate removal rate was 100% with a little residual concentrated amount of nitrite (0.82 mmol/L).
- The biogas was generated at temperatures between 4 and 30°C. The biogas generation rate was found to be directly proportional to the temperature.
- Generating nitrogen gas from bacteria has a more uniform diffusion and a faster gas generation rate than injecting gas into soil.
- Moreover, the microbial desaturation method has limited the development of excess pore water pressure compared to saturated samples; the final settlement of the de-saturated sample with a degree of saturation of 85.2% was almost one-third that of the fully saturated sample at an acceleration amplitude of $1 m/s^2$.

He & Chu (2014) have reported that the microbial denitrification process used for the desaturation of sand has various pros, such as:

- Nitrogen gas is not likely to be dissolved in water (Durability aspect).
- Nitrogen gas does not chemically react as it is an inert gas (stability aspect).
- The diffusion is more homogenous as it is generated in-situ (distribution aspect).
- The generated gas bubbles are so tiny. Therefore, it is unlikely to escape from the soil.

Therefore, the author has applied the microbial denitrification process by isolating the denitrifying bacteria from an anaerobic digester in a wastewater treatment plant. The ethanol has been used as an electron donor. Thus, a particular chemical reaction occurred, resulting in the following chemical form, equation (2-18):

$$5C_2H_5OH+12KNO_3 \rightarrow 10CO_2+6N_2\uparrow+9H_2O+12KOH \quad (2\text{-}18)$$

According to the equation, CO_2 will dissolve since nitrogen is less soluble in water than carbon dioxide. In that case, nitrogen is a free gas.

Then, undrained compression and extension triaxial tests were conducted under monotonic loading to analyze the cyclic shear strength of desaturated soil using nitrogen gas bubbles. Figure 2-23 and Figure 2-24 revealed that the undrained shear strength ratio increased by a factor of 2.1 for the compression triaxial tests by slightly lowering the degree of saturation to 95% and by 1.7 for the extension triaxial tests at the degree of saturation of 88 % compared to fully saturated samples. Delaying the pore pressure generation was the cornerstone of that mitigation. It is also reported that the undrained stress-strain behavior of loose sand can change from strain-softening to strain-hardening, hence “unlikely to liquefy”.

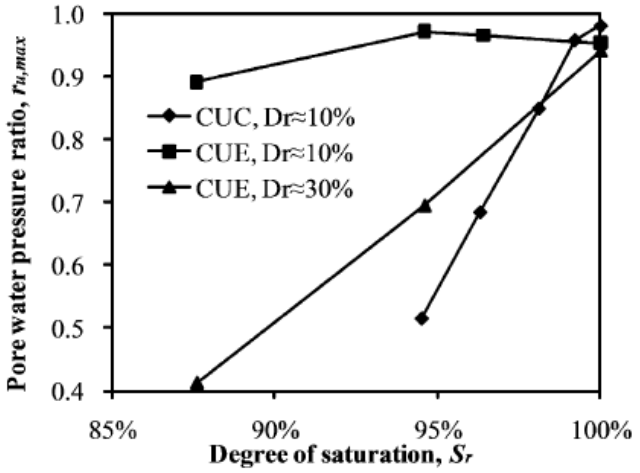

Figure 2-23 Pore water pressure ratio versus degree of saturation (Consolidated undrained compression, CUC, and extension tests, CUE. The pore water pressure ratio is expressed as the ratio of the maximum pore water pressure during shear to the initial effective confining stress $r_{u,max} = u_{max}/ p'_o$) He & Chu (2014)

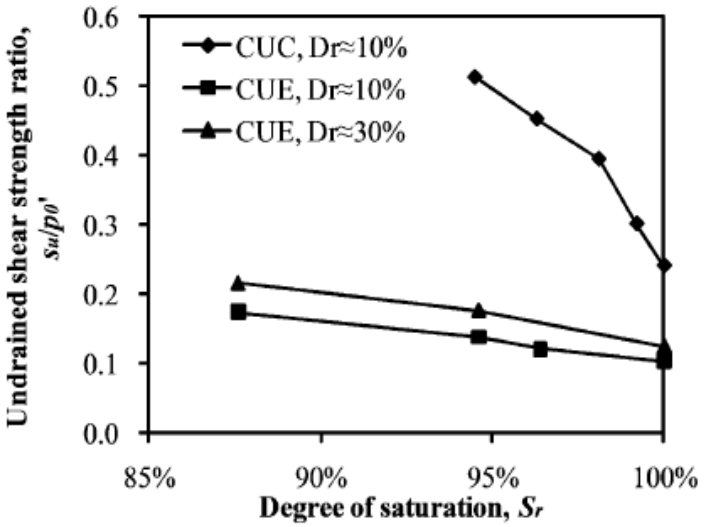

Figure 2-24 Undrained shear strength ratio versus degree of saturation (The undrained shear strength ratio is defined as the ratio of undrained shear strength obtained from an undrained test to the initial effective confining stress: s_u/p'_o) He & Chu (2014)

Rebata-Landa & Santamarina (2012) have adopted the same procedure used by He & Chu (2014) to generate gas bubbles in their studies. An experimental study has been performed to deeply understand the biogenic nitrogen gas generation in soils using Paracoccus denitrificans. Then, poroelastic models were used to examine its effect on P-wave velocity and Skempton´s B parameter, the results revealed the following:

- A few nitrogen gas bubbles can effectively increase the liquefaction resistance by reducing the fluid bulk stiffness, P-wave velocity, and Skempton's B parameter.
- Nitrogen gas has many pros, as it is environmentally friendly, not combustible, and less soluble in water.
- The generation of biogenic gas bubbles depends on the temperature.
- Unlike the injection method, biogenic gas generates submicron-size bubbles, which are more uniform and can be diffused homogeneously in soils.
- Soil fines content dramatically affects the gas bubbles' stability in soil, and sands with fewer fines may fail to trap the gas bubbles resulting in a transient decay in P-wave velocity and then a partial recovery to the final stable state. On the other hand, much higher fines content helps diminish the transient period; thus, a fast and stable p-wave velocity can be achieved.

2.3.5. Desaturation

2.3.5.1. Concept

Since most of the previously described liquefaction mitigation technologies are relatively expensive, have implementation restrictions, or environmental effects, the researcher´s attention has been drawn to a new technique of soil liquefaction mitigation namely, the desaturation method which refers to decreasing the degree of saturation of the soil. This method has gained increasing interest in recent years as it may become more cost-effective than many other methods. Additionally, it is considered a practical solution even for closely constructed buildings (Shi et al., 2019).

The terminologies fully saturated, unsaturated, and partially saturated can sometimes be confusing in the geotechnical engineering context.

Fully saturated refers to soil layers below the groundwater table, where all soil pores are filled with water. However, unsaturated soil could be found above the groundwater table, where pores are filled with both air and meniscus water, resulting in negative pore water pressure due to capillary suction (Most common soils). Partially saturated soil could describe soil below the groundwater table but with some trapped (occluded) air bubbles where the matric suction could be negligible.

The various soil saturation states could be also identified using the soil water characteristics curve SWCC or retention curve where volumetric content which is the ratio of volume of water to the total volume of soil and hence degree of saturation can be plotted against soil matric suction.

Soil suction comprises two fundamental components: matric and osmotic suction (Krahn & Fredlund, 1972). Matric suction represents the capillary forces that draw water into the unsaturated soil matrix, in other words, it's the suction associated with the pressure difference between pore air and pore water, can be expressed as $\psi_m=u_a-u_w$. Osmotic suction, conversely, results from variations in dissolved salt concentrations within the pore water. Total suction is the sum of these two components and is physically quantified by the relative humidity directly above the pore water surface (Eyo et al., 2022). By generating SWCC, different saturation stages can be identified (White et al., 1970).

Vanapalli et al., (1996) classified these states into three saturation stages (Figure 2-25): the boundary effect stage, the transition stage (Primary and secondary); and residual stage of unsaturation, Figure 2-26 describes the saturation status of each zone. Within the boundary effect stage Figure 2-26a, pores are filled with water (the water menisci is continuous). The air entry value (AEV), see Figure 2-25 (or bubbling pressure) represents the suction value at which air begins to enter the soil's largest voids (Fredlund & Xing, 1994), where the soil starts to desaturates only in the transition stage. In this phase, water content significantly decreased by increasing suction. Figure 2-25b and c where the water menisci isn't continues anymore. Finally, Figure 2-26d shows the residual zone of unsaturation where the suction is high in this phase and water menisci is small. Figure 2-27 reveals these various saturation phases (Tsukamoto et al., 2014; Zeybek & Hall, 2017).

The concept of suction stress σ_s has been adopted by authors, which is a representation of the matric suction u_a-u_w and a representation of the degree of saturation Sr (Chowdepalli et al., 2025). This stress parameter effectively captures the compound effect of the hydraulic state and mechanical stiffness. Under cyclic loading, the total effective stress σ' can be expressed as follows, (Bishop, 1959):

$$\sigma' = (\sigma - u_a) + x\,(u_a - u_w) \tag{2-19}$$

Where σ' is the effective stress; σ is the total stress; u_a is the pore air pressure; u_w is the pore water pressure, and u_a-u_w represent the matric suction pressure, s.

In addition, x is the Bishop's effective stress parameter and related to the degree of saturation, where:

- For fully saturated soil: x = 1 where the σ' formula simplifies to Terzaghi's classic effective stress equation $\sigma'=\sigma - u_w$.
- Dry soil: x = 0 where, suction has zero effect on the effective stress.

- Unsaturated soil: 0 <x < 1, in this case *x* depends on the soil type, size and distribution of the soil pores and hydraulic hysteresis (Wetting/Drying) (Khalili & Khabbaz, 2002).

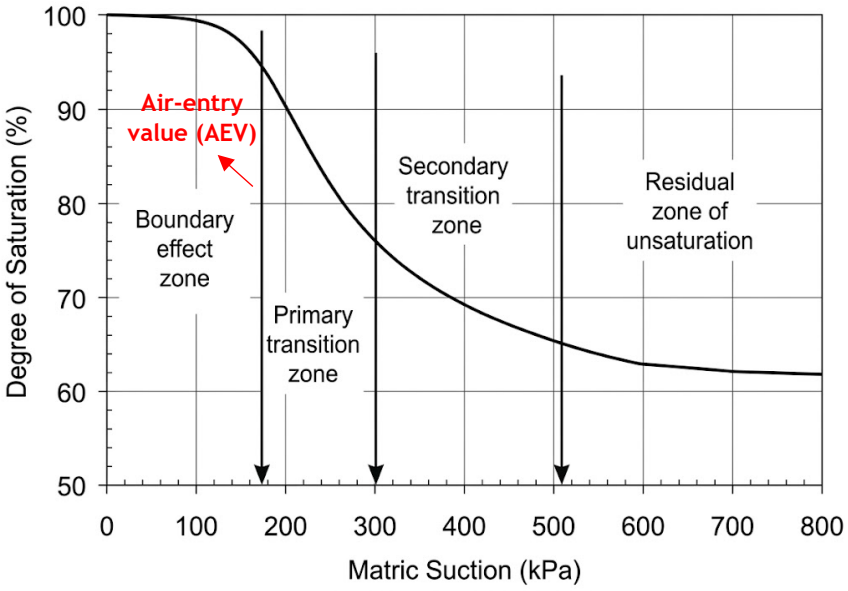

Figure 2-25 Degree of saturation Vs. Matric suction for a hypothetical porous medium, modified after (Vanapalli et al., 1996)

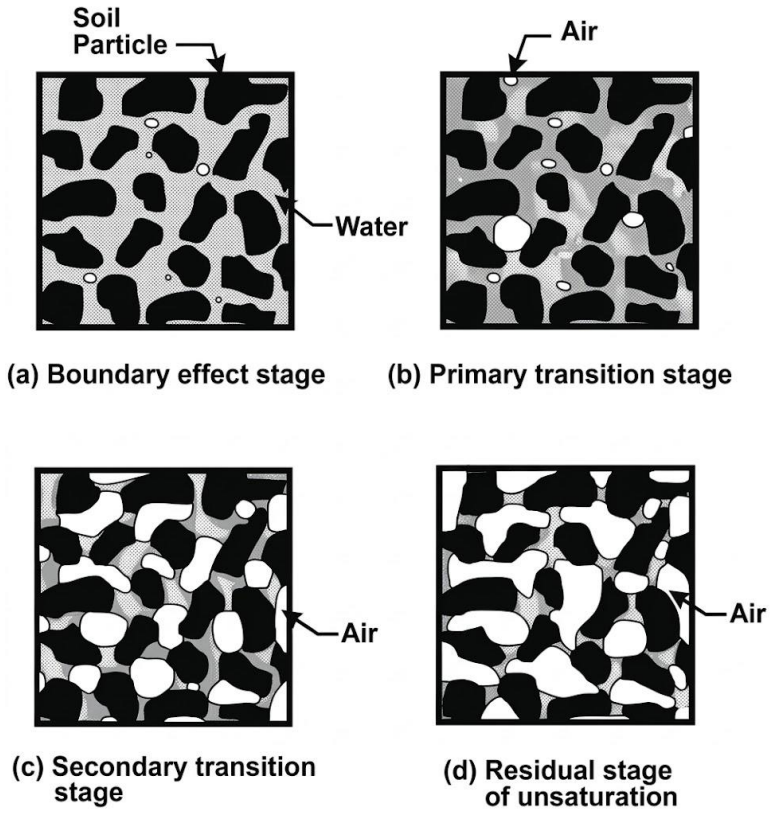

Figure 2-26 Probable variation of water/air area in different stages of a SWCC, after (Vanapalli et al., 1996)

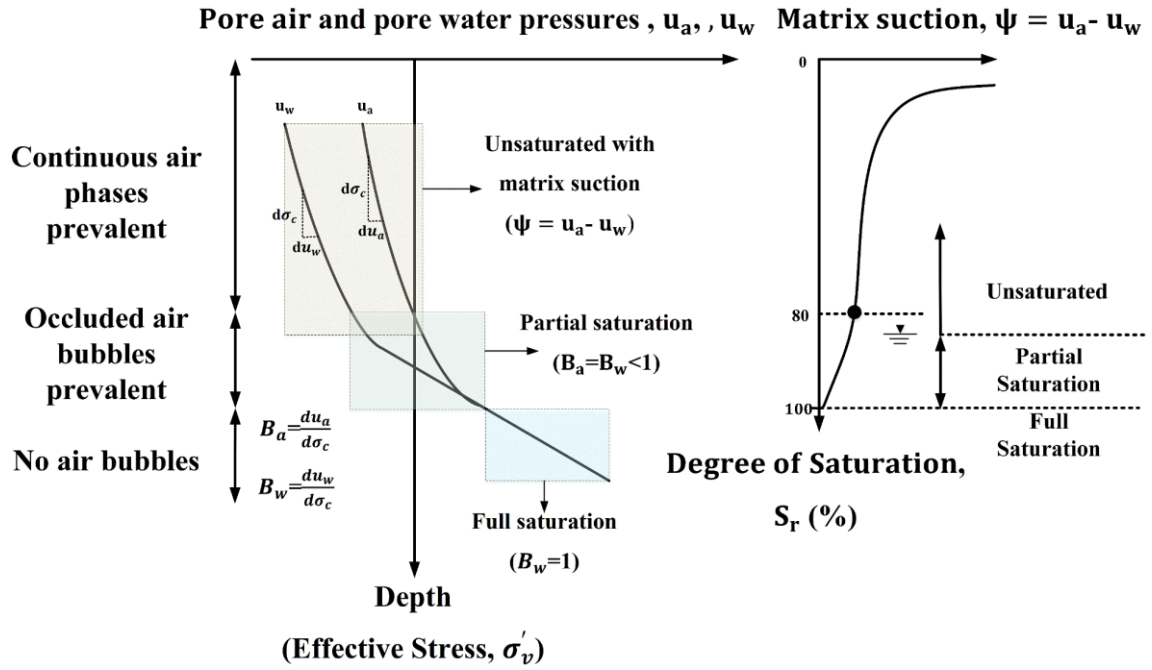

Figure 2-27 Fully, partially, and unsaturated soil zones (Tsukamoto et al., 2014)

It is worth noting that some studies regarding unsaturated soil behavior often use the term (partially saturated) to describe the soil condition above the groundwater table, as the difference between them is believed to be intangible and due to semantics (Zeybek & Hall, 2017). However, the liquefaction resistance enhancement mechanism resulting from unsaturated soil behavior is different from that resulting from partially saturated soil.

Unsaturated sands gain liquefaction resistance mainly from matric suction. Matric suction increases effective stress and stiffness and reduces tendency for zero effective confining pressure during cyclic loading, so mitigation is related to the induced suction in addition to the increased bulk modulus of the pores (Banerjee et al., 2022).

Kocaman et al. (2025) studied the effect of matric suction on the monotonic and cyclic behavior of silty sand, and concluded that however, both saturation scenarios had the same preparation void ratio, increasing matric suction led to increased soil strength (dilative behavior) and reduced pore pressure build-up under monotonic loading compared to fully saturated baseline specimens which showed contractive behavior followed by failure. Cyclic triaxial tests conducted at a constant cyclic stress ratio CSR demonstrated that increasing Sr from 45 to just 50% sufficiently reduced the matric suction to induce failure, resulting in axial deformations exceeding 5%. This highlights the significant influence of matric suction on the soil cyclic behavior.

On the other hand, partially saturated sands gain liquefaction resistance mainly from the existence of occluded air bubble which, increases bulk compressibility of the pore fluid, lowering pore-pressure build-up and so mitigating liquefaction triggering even when suction is negligible, (Mele et al., 2022; Molina-Gómez, 2023).

2.3.5.2. Measurement and verification of the degree of saturation

Skempton's Pore Pressure Coefficient (B-value)

Skempton's number (B-value) is a standard laboratory parameter used to assess saturation in element testing. Under an undrained isotropic increment of confining pressure, it is defined as the ratio of the induced pore pressure increment to the applied confining pressure increment, B=Δu/Δσ (Skempton, 1954). This parameter can also be expressed theoretically in terms of the compressibility of the soil skeleton and the pore fluid. For incompressible solid grains it is expressed as shown in equation (2-20), (Yang, 2002).

$$B = \left(1 + n.\frac{K_{sk}}{K_f}\right)^{-1} \quad (2\text{-}20)$$

where n represents soil's porosity, K_{sk} is the bulk modulus of the soil skeleton, and K_f is the bulk modulus of the pore fluid mixture. When the pore fluid is treated as a water–gas mixture, K_f would be computed as a function of the respective compressibility of the water and gas phases, equation (2-21):

$$K_f = \left(\frac{S_r}{K_w} + \frac{1 - S_r}{K_a}\right)^{-1} \quad (2\text{-}21)$$

Substituting this fluid compressibility K_f back into the original framework, yields the final theoretical definition for the B-value equation (2-22), (Yang, 2002):

$$B = \left[1 + n.K_{sk}\left(\frac{S_r}{K_w} + \frac{1 - S_r}{K_a}\right)\right]^{-1} \quad (2\text{-}22)$$

where Sr is the degree of saturation, and K_w and K_a are the bulk moduli of water and gas, respectively.

Compressional Wave Velocity (Vp)

Due to the inherent difficulties in measuring the B-value under certain experimental conditions, such as in centrifuge testing, on shaking tables, or in the field, compressional wave velocity Vp has emerged as a highly efficient, non-invasive alternative for estimating Sr.

Extensive literature has documented the sensitivity of Vp propagation to variations in saturation. Tsukamoto et al. (2002) concluded that P-wave velocity could be used to identify the degree of saturation of near-saturated samples, furthermore, the study demonstrated that the velocity of P-wave propagation increased from about 500 m/sec to about 1800 m/sec when the B-value rose from 0 to 0.95 corresponding, respectively to the saturation ratio Sr of about 90 and 100%. Emerson & Foray (2006); J. Kim et al. (2021) ;and Molina-Gómez (2023) also documented the sensitivity of Vp to variations of the saturation levels.

In addition, Santamarina et al. (2001) reported Vp of higher than 1482 m/s for fully saturated soil where the compressional wave propagation is mainly controlled by the water pores. The Biot-Gassmann theory, Biot (1956) is a cornerstone for the theoretical modeling of elastic wave propagation in fluid-saturated porous media. The relationship for estimating Vp is expressed in equation (2-23):

$$V_p = \sqrt{\frac{K_{soil} + \frac{4}{3} G_{soil}}{\rho_{soil}}} \quad (2\text{-}23)$$

Where ρ_{soil} represents the mass density of the soil; K_{soil} is the soil's bulk modulus and, G_{soil} is the soil's shear modulus $G_{soil}=\rho. V_s^2$.

Assuming soil particles are incompressible, Foti et al. (2002) demonstrated that this expression simplifies to equation (2-24):

$$V_p = \sqrt{\frac{\left(K_{sk} + \frac{4}{3} G_{soil}\right) + \frac{K_f}{n}}{(1-n)\,\rho_{soil} + n\,.\rho_f}} \quad (2\text{-}24)$$

Furthermore, (Yang, 2002) proposed a theoretical prediction model to estimate Vp directly as a function of the B-value, equation (2-25):

$$V_p = \sqrt{\frac{\frac{4}{3}\ G_{soil} + \frac{K_{sk}}{1+B}}{(1-n)\,\rho_{soil} + n\,\rho_f}} \quad (2\text{-}25)$$

For applying this theoretical model, the constitutive parameters are defined as follows:

K_{sk} is the bulk modulus of the soil skeleton, can be computed using equation (2-26):

$$K_{sk} = \frac{2\,G_{soil}\,(1+\nu_{sk})}{3(1-2\nu_{sk})} \quad (2\text{-}26)$$

Where ν_{sk} is the Poisson's ratio of the soil skeleton, computed via measuring the seismic wave velocities: shear wave velocity Vs, and compressional wave velocity Vp, in dry stat, equation (2-27):

$$\nu_{sk} = \frac{\left(V_p/V_s\right)^2 - 2}{2\left[\left(V_p/V_s\right)^2 - 1\right]} \quad (2\text{-}27)$$

ρ_{soil} is the total mass density of the soil, computed by equation (2-28):

$$\rho_{soil} = (1-n)\ \rho_g + n\rho_f \quad (2\text{-}28)$$

Where ρ_g is the mass density of soil grains and, ρ_f is the fluid mass density, computed using equation (2-29):

$$\rho_f = (1-n)\,\rho_a + S_r\,\rho_w \quad (2\text{-}29)$$

Where ρ_a and ρ_w are the mass density of air and water respectively.

By utilizing these relationships, the model serves as a robust predictive framework for Vp and B as a function of Sr.

Parametric Influence and Literature Validation

Yang (2002) applied the theoretical model and reported that, both B-value and P-wave velocity are sensitive to Sr variation, also indicated that at full saturation, B approaches 1 and Vp exceeds 1500m/s, in addition, Sr of 90% may lead to a B-value of 0.01 with Vp of about 370m/s, as shown in Figure 2-28.

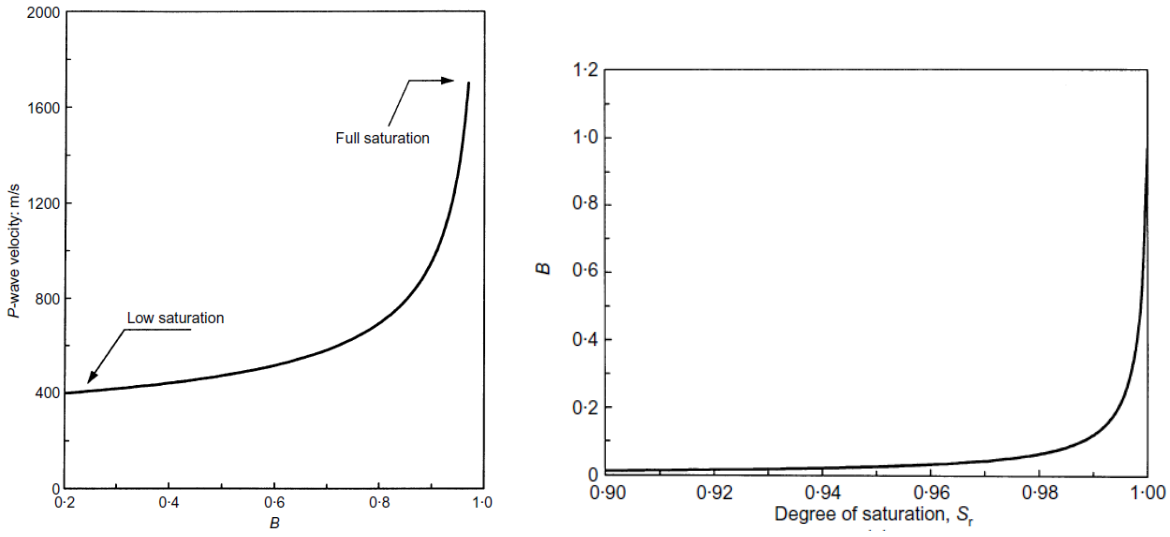

a) b)

Figure 2-28 Relationship between a) P-wave velocity and B-value; b) Degree of saturation and B-value, for Toyoura sand, Dr=60%, Kb=165.8Mpa, G=76.5Mpa (Yang, 2002)

Tamura et al. (2002) investigated the effects of the size and solubility of an air bubble on the B-value and P-wave velocity of a partly saturated sand. The relations between B-value and P-wave velocity were determined for large triaxial specimens with Dr= 64% and 84%. The theoretical formulas have been derived for determining the P-wave velocity of a partly saturated sand containing air bubbles. The study concluded that the air bubble solubility and size have significant influence on the B-Vp relationship.

Their results detailed in Figure 2-29 present the influence of solubility of air bubble, shear wave velocity, porosity, air bubble size on the B- Vp and Sr-Vp relationship.

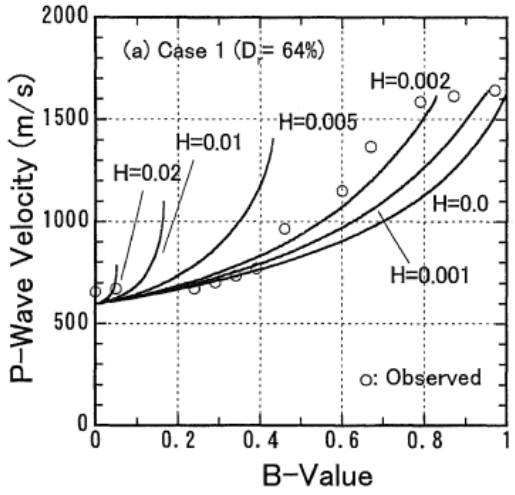

a) Effect of solubility of air bubble for d_0 =0.1 mm

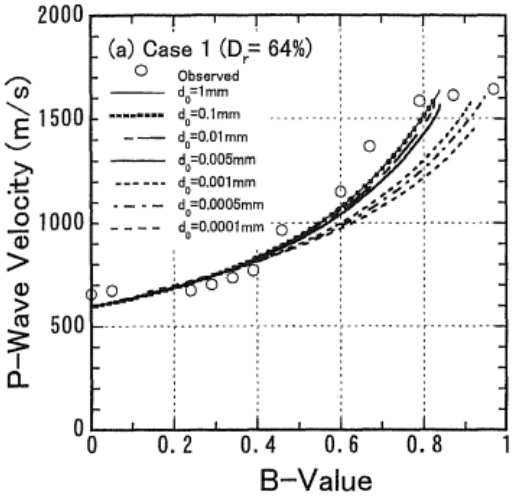

b) Effects of air bubble size for H = 0.002

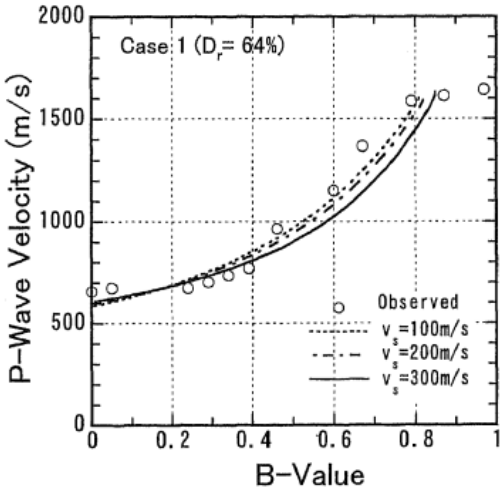

c) Effects of S-wave velocity for d_0=0.1 mm and H=0.002

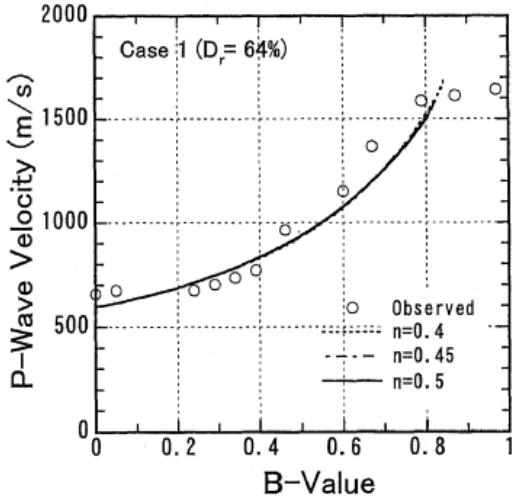

d) Effects of porosity for d_0 =0.1 mm and H=0.002

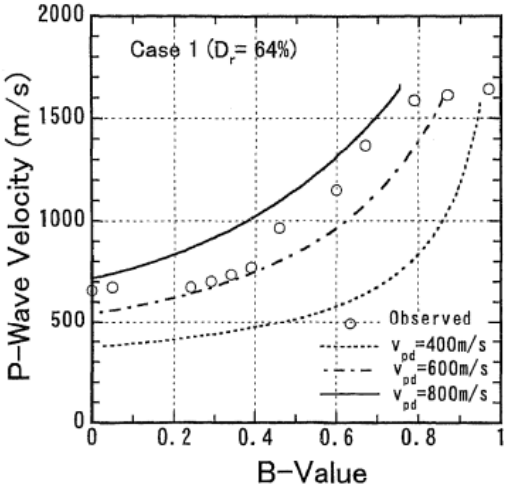

e) Effects of P-wave velocity of soil skeleton for d_0 = 0.1 mm and H=0.002

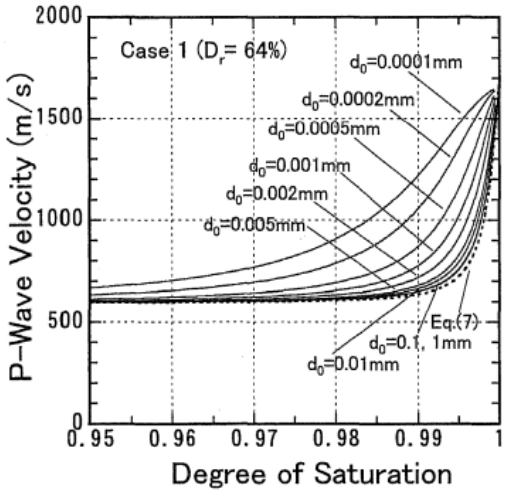

f) Relation between degree of saturation and P-wave velocity for H=0.002

Figure 2-29 Effect of a) solubility of air bubble; b) air bubble size; c) S-wave velocity; d) porosity; e) P-wave velocity of soil skeleton on the B-Vp and, f) air bubble size on the Sr-Vp relationships (Tamura et al., 2002)

Molina-Gómez (2023) conducted a set of cyclic triaxial tests for different Sr at various Dr levels, seismic wave velocities were measured using Bender element BE in addition to the B-value measurements, the experimental results were interpreted and compared with the wave propagation theory in fluid-saturated media (Biot, 1956).

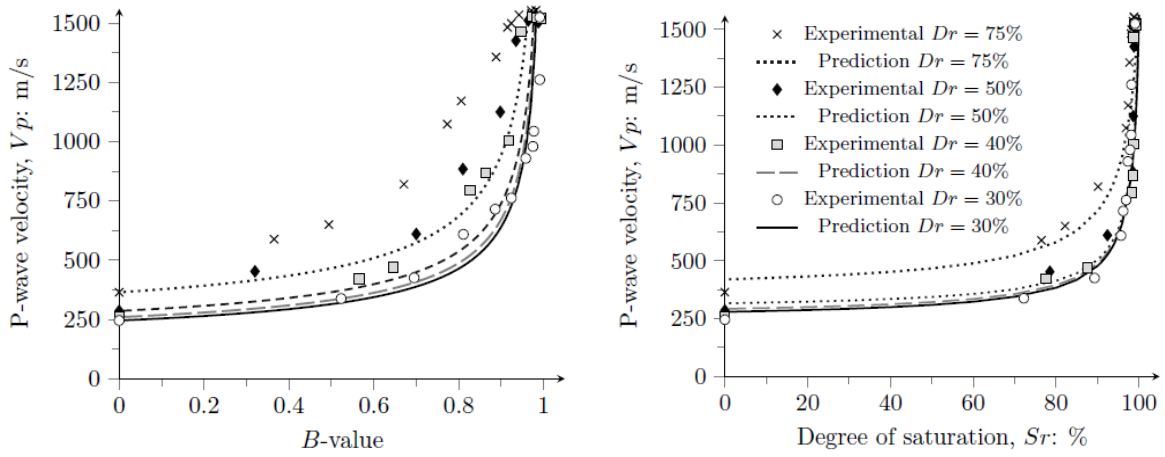

a) b)

Figure 2-30 Relationship between a) B-value and VP; b) Sr and VP for different Dr (Molina-Gómez, 2023)

Experimental data showed excellent agreement with theoretical predictions for the Sr-Vp relationship as revealed in Figure 2-30b. On the other side, Experimental data did not match the theoretical predictions for B-Vp relationship Figure 2-30a, and attributed this behavior to the volumetric strains ε_v induced during the B-value measuring.

He et al. (2014) have stated that the desaturation liquefaction mitigation technique is less expensive and more applicable than other mitigation methods, and Bayat et al. (2009) have reported in his study that entrapping air/gas bubbles into the soil pores is a significant liquefaction mitigation technique.

Partially saturated sand has proven to have higher liquefaction resistance than saturated sand. The basic idea behind that is that, because pore water is incompressible during seismic loading actions, the presence of air/gas bubbles can quickly increase the pores' compressibility. As a result, the generation of excess pore pressure can be delayed and mitigated because of the volume decrease of air/gas bubbles therefore, the effective stress won't drop significantly and rapidly, and liquefaction is unlikely to happen. Figure 2-31 is a simple schematic diagram showing the desaturation efficiency in soil liquefaction mitigation (Bayat et al., 2009).

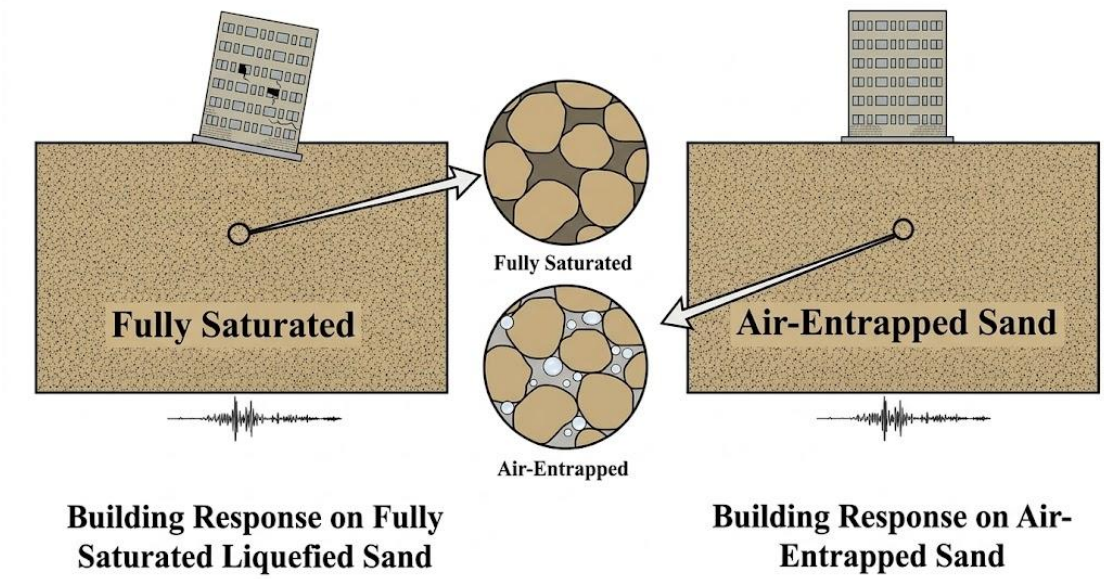

Figure 2-31 Building's response in fully and partially saturated soils, after (Bayat et al., 2009)

Chu (2013) showed that inserting gas bubbles to achieve a degree of saturation between 85 and 95 % would significantly reduce the excess pore water pressure generated in soil.

Dewatering, air injection, biogas created by bacteria in the soil, electrolysis, sand compaction piles, and chemical ways to produce tiny gas bubbles from nutrients are the most common utilized desaturation methods. Even though induced partial saturation IPS is considered one of the most promising and innovative mitigation approaches, several uncertainties still exist regarding its applications on the field, such as injection mechanism of air or gas, usage of bacteria, and durability, which are still being researched (Xu et al., 2019).

Rupam (2014) stated that there are two different methods to introduce air or gas into the soil; one is through the generation of hydrogen and oxygen gases in the sand through electrolysis, and the other is through air entrapment in the voids by draining and reintroducing water into the fully saturated sand.

The main principle of the desaturation method is to reduce the degree of saturation of saturated soil by injecting insoluble bubbles, resulting in higher liquefaction strength. Shi et al. (2019) stated that the desaturation process must meet three requirements: -

The degree of saturation must be accurately controlled, injected bubbles should be distributed homogeneously. In addition, bubbles with low solubility in water that are chemically inert are recommended as they can be maintained in soil for long periods of time.

A set of cyclic torsional shear tests has been done by Yoshimi et al. (1989) to evaluate the degree of saturation impact on the undrained cyclic behavior of sands. The study concluded that the liquefaction resistance of 70% degree of saturation samples was found to be three times higher than that in fully saturated conditions. Additionally, the cyclic shear strength was three times higher than fully saturated specimens.

Okamura & Soga (2006ª) presented an equation (2-30), correlating the liquefaction resistance and degree of saturation through quantifying the resulting volumetric strain based on dynamic triaxial tests as:

$$LRR = \log\left(6500\ \varepsilon_v^* + 10\right) \tag{2-30}$$

Where LRR is the liquefaction resistance ratio, defined as the strength of unsaturated sand normalized to that of fully saturated sand; ε_v* is the volumetric strain and can be obtained from equation (2-31).

$$\varepsilon_{v^*} = \frac{\sigma'_c}{p_o + \sigma'_c}\,(1 - S_r)\,\frac{e}{1+e} \tag{2-31}$$

Where p_o is the absolute pressure of the pore fluid; σ_c' is the initial confining pressure; S_r is the degree of saturation; e is the initial void ratio.

The logarithmic form used in the aforementioned equation indicates that the increase in liquefaction resistance is more pronounced for small reductions in Sr near full saturation, while the incremental benefit becomes smaller at lower degrees of saturation.

Then, He et al. (2014) carried out multiple compression and extension triaxial tests to verify the established correlations between the undrained behavior of soil and degree of saturation. The detailed experimental results suggested that the correlation proposed by Okamura & Soga (2006b) can be modified to the form shown in equation (2-32) :

$$LRR = \log(\alpha\,.\,\varepsilon_v^* + 10) \tag{2-32}$$

Where, the experimental results have been used to calibrate the parameter α by plotting the correlation between the liquefaction resistance ratio LRR and the volumetric strains ε_v^* as shown in Figure 2-32.

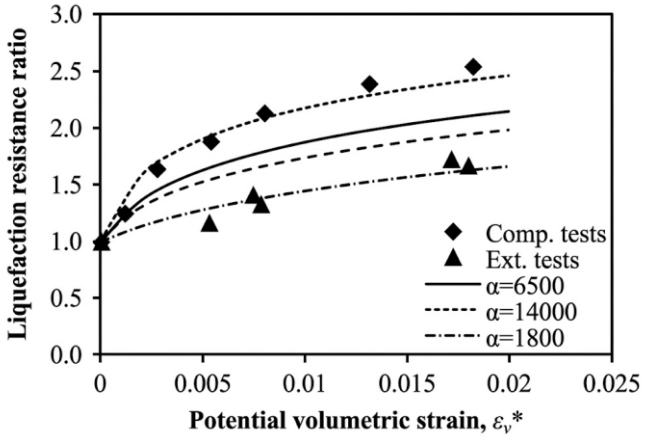

Figure 2-32 Relationship between liquefaction resistance ratio and volumetric strain (He et al., 2014)

From the shown plot, compression and extension tests showed perfect agreement with the proposed equation for α = 14000, and 1800, respectively. Additionally, the curve for the original equation proposed by Okamura & Soga (2006ª) with α = 6500 is projected between the compression and extension curves.

Based on some laboratory tests Yang et al. (2004) obtained another relationship between cyclic strength ratio CSR and pore pressure coefficient B as shown in equation (2-33):

$$CSR_{part} = CSR_{sat}\, e^{[\alpha\,(1-B)]} \quad (2\text{-}33)$$

Where CSR_{part} denotes the cyclic stress ratio required to cause liquefaction at 20 cycles under partially saturated conditions; CSR_{sat} denotes the corresponding cyclic stress ratio under fully saturated conditions; B is the pore pressure coefficient; and **α** is a parameter to be calibrated from the test results, may be related to some factors such as the number of cycles used for defining the liquefaction strength. The author suggested **α** of 0.71 to fit the cyclic test results.

Then, LRR data obtained from this study has been plotted against B by He et al. (2014); as shown in Figure 2-33 it can be revealed that the LRR data for compression and extension tests follow equation (2-33) with **α** = 1.15 and 0.65, respectively. The **α** parameter value suggested by Yang et al. (2004) to be 0.71 falls between the compression and extension tests results.

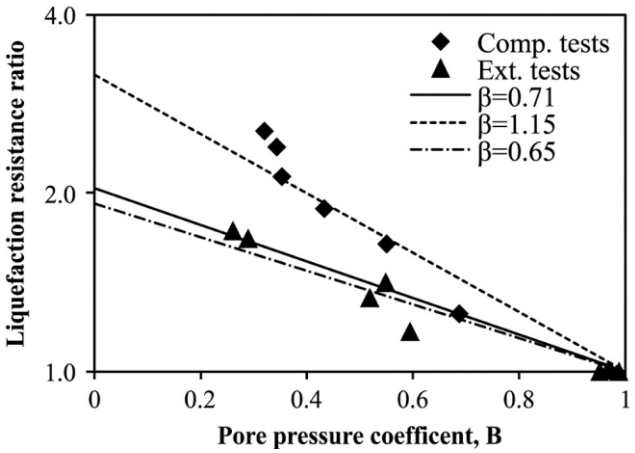

Figure 2-33 Liquefaction resistance ratio Vs. Pore pressure coefficient B (He et al., 2014)

From these relationships, it can be concluded that a slight decrease in the saturation degree significantly affects soil cyclic strength.

Grozic et al. (1999) mentioned in their study that loose sand behavior has been altered from strain-softening to strain-hardening under undrained compression testing when decreasing the degree of saturation to less than 90 %.

2.3.5.3. Air injection

Air injection is a geotechnical mitigation method that introduces trapped air into fully saturated soils to create an induced partial saturation (IPS) state. It works through the injection of pressurized air or gas into the subsurface soil or groundwater to achieve various goals, depending on the specific application.

Zeybek & Madabhushi (2017b) conducted a series of centrifuge experiments to assess the efficacy of the air injection desaturation approach in soil liquefaction mitigation. Experiments were carried out on shallow foundations under varied bearing pressures.

The degree of saturation was determined based on the conventional mass and volume method. A rubber air curtain hose with multiple tiny apertures of around 0.5mm diameter and 5mm spacing was used at the bottom of sand beds to inject air bubbles into the saturated soil. Figure 2-34 depicts the configuration of the employed centrifuge.

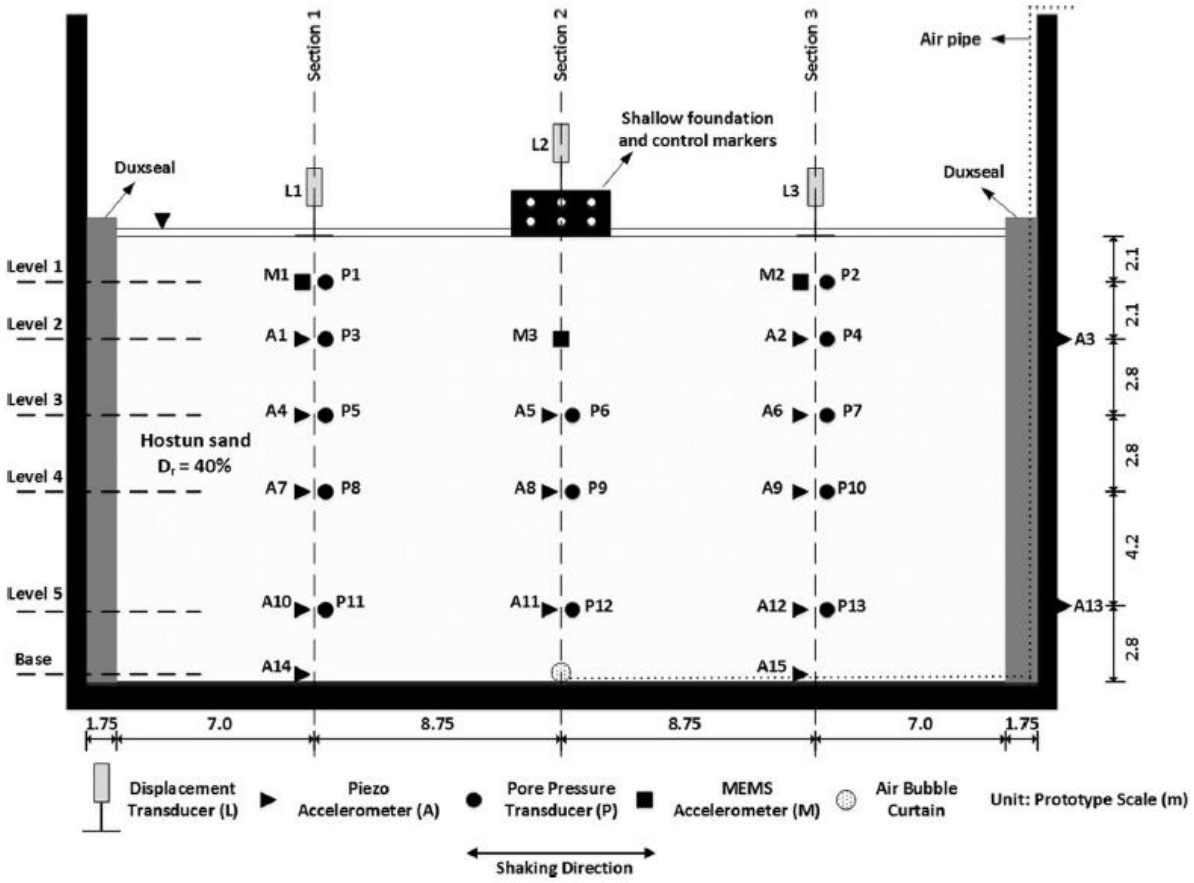

Figure 2-34 Centrifuge model layout in performed experiments (Zeybek & Madabhushi, 2017b)

The results reported that reducing the degree of saturation to a range between 80 and 99 % has a significant effect on limiting the developing excess pore pressure and the consequent post-seismic shallow foundation settlement, enhancing the post shaking bearing capacity, decreasing the liquefied soil layer depth, and increasing the soil resistance to liquefaction. Moreover, reducing the saturation degree was found to be more influential in limiting pore pressure generation when applying high confining pressures to the soil; consequently, the efficiency of the air injection desaturation technique was found to be dependent on the stress level applied.

Four dynamic centrifuge tests were conducted by Marasini & Okamura (2015) to investigate the air injection desaturation liquefaction countermeasure for a liquefiable foundation soil under relatively lightweight structures. The models were prepared in a rigid container, and the soil used for the foundation soil layer was Toyoura sand. Air injections were performed using a two-dimensional air injector with 1mm-wide orifices on both sides placed on the

dense sand layer on the container's base. After that, numerical simulations were performed, attempting to simulate the desaturated sand with an approximately 85% degree of saturation by reducing the bulk modulus of the pore fluid. The numerical study confirmed that the seismic behavior of desaturated soil can be efficiently simulated by reducing the bulk modulus of pore fluid. The whole study concluded that soil desaturation is a significant technique for mitigating the settlement of relatively light structures, such as one or two-story residential buildings.

Okamura et al. (2011) implemented an in-situ air injection desaturation test to examine the validity and efficiency of air injection as a common desaturation liquefaction mitigation technique; the injected air source was an air injector deployed in a 6m depth saturated sand layer. A 3D electric resistivity tomography technique has been used to screen the change in resistivity "induced degree of saturation" before and after injecting the air. It has been reported that the air injection pressure and airflow rate are directly proportional, and the de-saturated zone was generated within 4 m from the injection point. After the air injection procedure stopped, soil freezing was performed, and in-situ undisturbed soil samples were taken to the laboratory to determine the in-situ degree of saturation. The saturation degree was between 68 and 98 %, which was low enough to practically double the soil liquefaction resistance. Numerical simulations using gas-liquid two-phase flow calculations were performed using a commercial simulator of TOUGH2 to verify the in-situ test results; the numerical results were found to match those of the in-situ results. Moreover, the recovered frozen soil samples were examined to evaluate the actual liquefaction resistance by conducting triaxial tests under cyclic shear conditions. Finally, it has been concluded that the liquefaction resistance of desaturated sand was almost doubled compared to fully saturated sand.

Although it is commonly understood that soil resistance to liquefaction increases as the saturation degree of the soil reduces, lowering the saturation degree of the ground uniformly and homogeneously has proven to be complicated. Therefore, Nagao (2007) performed a series of column tests on saturated sand injected with micro-scale air bubbles to examine the diffusion efficiency resulting from injecting micro-scale air bubbles into sandy soils, and the results revealed that the optimum air-bubble diameter has to be in the range of 10 to 100 μm (micro-bubbles). For further investigations regarding the rates and magnitudes of soil desaturation driven by air injection along with the distributions of the desaturated zones.

Yasuhara et al. (2008) conducted simplified model tests simulating the injected air into saturated soils using air-injection probes within two different sizes of soil containers. The smaller container investigations are meant to investigate the nominal rates and magnitudes of soil desaturation driven by air injection. In contrast, the bigger one is designed to investigate rates, magnitudes, and the distributions of desaturated zones within the soil. In the small-container tests, at air pressures of 8, 10, and 13 kPa, the degrees of saturation monotonically decreased to 88, 67, and 60% respectively, within a relatively short time, followed by a steady state. After stopping the airflow process, the degrees of saturation recover to the maximum liquid degree of saturation for imbibition (e.g., approximately 85%) and never reach a fully saturated degree due to air trapped within pore voids. Time Domain Reflectometry TDR probes are used in the large-container tests to measure the local degrees of saturation, which revealed that even after a sharp decrease down to about 60% at three locations, those degrees of saturation remained constant even if the airflow rates rose as the air pressure rose. The degrees of saturation suddenly rose to 80% when the airflow was stopped, which is consistent with the findings of the small-container studies. These findings

clearly demonstrate the significance of the injected air pressure's impact on desaturation efficiency.

Then, a numerical study was performed using a multiphase flow simulator to evaluate its ability to predict the desaturation evolution and distribution. Excellent agreement was observed in the small-size container tests, whereas it showed overestimated measurements for the bigger container tests.

Zeybek & Madabhushi (2017a) performed a series of 1g vertical sand column and high-g centrifuge tests to examine the durability of injected air bubbles using the air-injection technique. Tests done under various simulated field circumstances (hydrostatic conditions at low and high fluid pressure, upward and downward vertical flow, varying pore fluid pressure, and lateral excitation) which may cause dissolution, diffusion, compression and escape of air bubbles. In addition, the dynamic response of shallow foundations resting on partially saturated soil exposed to a combination of field conditions was studied. A small amount of partially saturated soil's entrapped air bubbles lost their function, increasing the specimens' saturation degree. Therefore, the study reported that air bubbles could sustain their function for most simulated field conditions and restrain the excess water pore pressure generation for a sufficient time. The seismic settlement of the shallow foundations, investigated under a combination of simulated field conditions, has been significantly reduced using the air injection desaturation technique. However, a large settlement was noticed when decreasing the gravitational acceleration g-level, so the equilibrium between the entrapped air and surrounding pore fluid found to be very significant.

It is unclear how air injection impacts the deformation mechanisms below shallow foundations (Zeybek & Madabhushi, 2017c). For this purpose, a series of dynamic centrifuge tests have been performed. Displacement contours are used to identify the dominant deformation mechanisms in a novel approach. Deviatoric and volumetric soil strains were observed in saturated soil, although the deviatoric strains appeared to dominate the settlement of shallow foundations. This was clear from the strong tendency of horizontal soil movements within the saturated soil layer and the formation of an extended failure mechanism. The soil beneath and around the foundation edges lost its lateral support as it was already liquified and had accumulated vertical settlement. Conversely, air bubbles in partially saturated soils significantly reduced the deviatoric deformations under static and dynamic stresses. The liquefaction depth was also significantly decreased, and no complete bearing failure mechanism formed beneath the shallow base. The results concluded that the air injection technique could significantly reduce developing excess pore pressure, diminish deformations, and minimize the liquefaction-induced shallow foundations and ground settlement thus, increasing soil liquefaction resistance.

Amanta & Dasaka (2021) conducted strain-controlled cyclic triaxial tests to study the impact of the air injection method on the liquefaction of saturated granular soil under various confining pressures. The used triaxial apparatus was adapted and equipped with the capability to use the air injection technique. To ensure that the air can penetrate the sample's pores effectively, the author maintained the air injection pressure higher than the summation of the hydrostatic pressure and capillary pressure at any air injection point. The key conclusions of the study showed that decreasing the degree of saturation can significantly increase the soil resistance to liquefaction. In addition, confining pressure levels does not affect too much the required saturation level. Furthermore, within a given air injection pressure, there is a limit on the minimum degree of saturation that could be attained, and the saturation level will barely vary after reaching that lowest level if the desaturation process is continued. Finally, although some air bubbles could escape with

time, the remaining air amount was enough to ensure the desaturation even after 30 days of observation.

Chavan et al. (2022) performed a set of undrained cyclic triaxial experiments performed on desaturated sandy soil by adopting the air injection mitigation technique. The cyclic strength of desaturated sand, with a degree of saturation of 80%, was observed to be double that of saturated sand, under a relative density of 40%.

The number of cycles needed for initial liquefaction N_L showed an exponential increase with decreasing degree of saturation, regardless of the initial effective pressure, relative density and CSR.

The Induced Partial Saturation IPS is regarded as a highly promising and innovative solution for preventing liquefaction. It is eco-friendly, cost-effective, and ideal for use beneath existing structures without causing damage. IPS works by modifying the compressibility of the pore fluid, which prevents the build-up of excess pore water pressure that can lead to soil liquefaction and hence, increases the cyclic resistance ratio. In addition, seasonal fluctuations in groundwater table depth can increase the risk of gas or air bubbles in soils losing their effectiveness. The study also mentioned that over a time period of 442 days under hydrostatic conditions, there was minimal change in the degree of saturation, shifting only slightly from 82.1% to 83.9% (Flora et al., 2023).

Flora et al. (2021) investigated the effectiveness of two liquefaction mitigation techniques: horizontal drains and induced partial saturation IPS, in a field trial located in Emilia Romagna Region, Italy. Large-scale field shaking tests were conducted at an instrumented site equipped with pore pressure transducers and geophones. Horizontal drains were intended to accelerate the dissipation of excess pore pressure, whereas IPS relied on the introduction of gas within the pore fluid to increase its compressibility and thus reduce excess pore pressure build-up during shaking.

The results showed that both techniques succeeded to prevent liquefaction triggering compared to untreated areas. However, many challenges and uncertainties were raised including the geometrical setup of the horizontal drains in addition to the accuracy of assessing the Sr achieved by IPS. Also, the study reported the significant enhancement achieved by IPS through reducing pore water pressure ratio to be $r_{u(max)} \approx 0.1$, highlighting the capability of Ips to mitigate liquefaction problems in highly urbanized areas.

The resulting comparison of pore pressure increments between the untreated and treated areas is shown in Figure 2-35. It reveals the significant gain of liquefaction resistance of treated soil area.

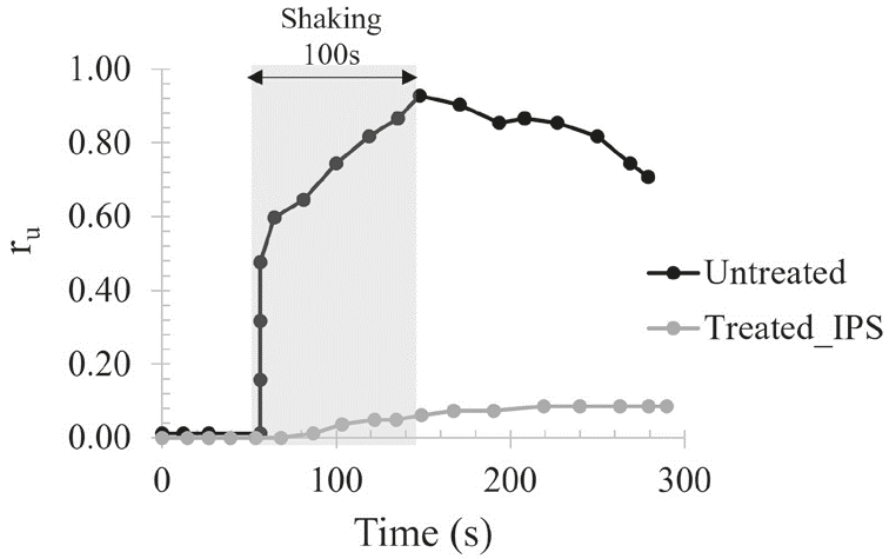

Figure 2-35 Comparison between the excess pore pressure ratio time histories in treated and untreated areas at 1.5 m. (Flora et al., 2021)

Mele et al. (2019) proposed an energy-based framework in which the total energy required to trigger liquefaction is composed of volumetric and deviatoric contributions, Equation (2-34).

$$E_{total} = E_{v,liq} + E_{s,liq} \quad (2\text{-}34)$$

The study showed that, desaturation increases liquefaction resistance because the presence of gas lowers the pore-fluid volumetric stiffness, allowing compressive volumetric strains to develop during undrained cyclic loading and thereby reducing pore pressure build-up. The volumetric energy component $E_{v,liq}$ increases as the degree of saturation decreases and acts as a state variable governing the upward shift of the cyclic resistance curve, while the deviatoric energy component is related to the cyclic stress level and the number of cycles to liquefaction. The study also revealed that unsaturated sands require higher specific energy to reach liquefaction compared to saturated sands. Two practical approaches were then proposed as design tools for induced partial saturation: a simpler approach based on the increase in cyclic resistance, and a more general approach based on total specific energy, with the latter providing better predictions of unsaturated cyclic resistance. The authors also note that these approaches were calibrated mainly for loose fine sands under relatively low confining stresses, so further validation is still needed for broader soil types and stress conditions.

Zeybek (2022) conducted undrained cyclic triaxial tests on fully and partially saturated specimens. The study demonstrated that reducing Sr increased the soil liquefaction resistance (Figure 2-36). In addition, proposed an empirical formulas which showed good agreement with experimental data, for evaluating the liquefaction resistance of partially saturated sands as a function of pore-fluid bulk modulus, maximum volumetric strains, and normalized excess pore-pressure ratios, as shown in equations (2-35); (2-36); (2-37), respectively.

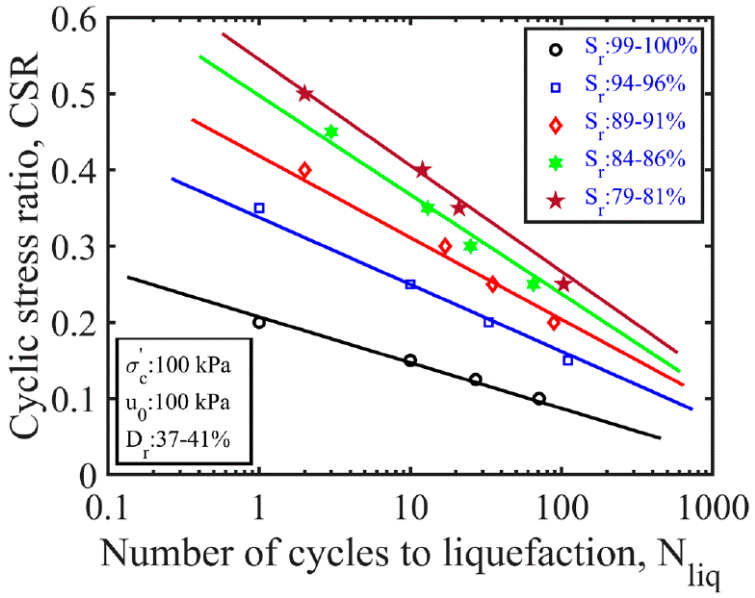

Figure 2-36 Effect of degree of saturation on liquefaction resistance of partially saturated specimen, after (Zeybek, 2022)

$$LRR = 0.0017 \cdot \left(\frac{K_{f(part)}}{K_{f(sat)}}\right)^{-0.9} + 0.9983 \quad (2\text{-}35)$$

$$LRR = 0.9 \cdot (\varepsilon_v^*)^{0.45} + 1 \quad (2\text{-}36)$$

$$\frac{1}{LRR} = \frac{r_{u(part)}}{r_{u(sat)}} \quad (2\text{-}37)$$

Based on undrained cyclic triaxial tests on TP-Lisbon sand (Local historically liquefied Portuguese sand) soil having different Sr levels, Molina-Gómez et al. (2025) concluded that, the undrained resistance increases as Sr decreases, but at the same time the study didn't exclude the possibility of liquefaction occurrence in partially saturated state. In addition, they found that the liquefaction onset is primarily triggered by the pore water pressure ratio r_u than by the accumulated strain criterion. Finally, they highlighted the efficiency of Vp in estimating Sr.

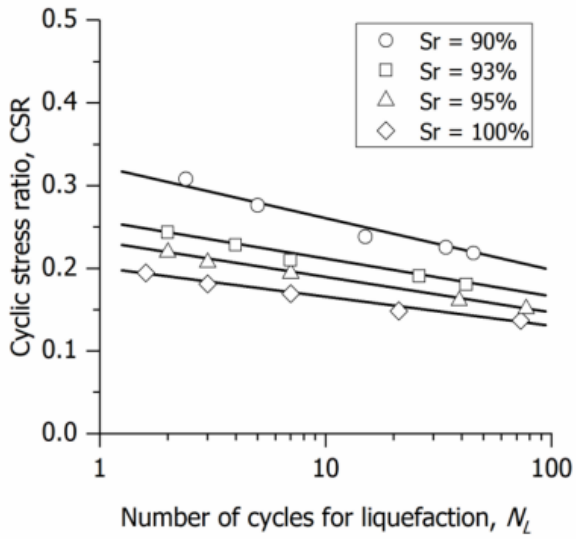

Figure 2-37 Liquefaction resistance curves of TP-Lisbon sand (Dr = 50% and p' = 50 kPa) (Molina-Gómez et al., 2025)

Experimental results showed that even a small reduction in the degree of saturation can markedly increase the resistance of sands to earthquake-induced liquefaction (Molina-Gómez et al., 2024).

Influence of Sr on soil damping and stiffness

Jafarzadeh & Sadeghi (2012) studied the influence of Sr on the soil shear modulus and damping through carrying out cyclic simple shear tests on two different soils. Soil stiffness and damping characteristics found to be not influenced by Sr at the Sr range between 25 to 75%. However, approaching the full saturation, shear modulus decreased and damping increased (Figure 2-38 and Figure 2-39). They also highlighted the significant influence of vertical consolidation stress, relative density and, shear strain amplitude on the soil stiffness and damping.

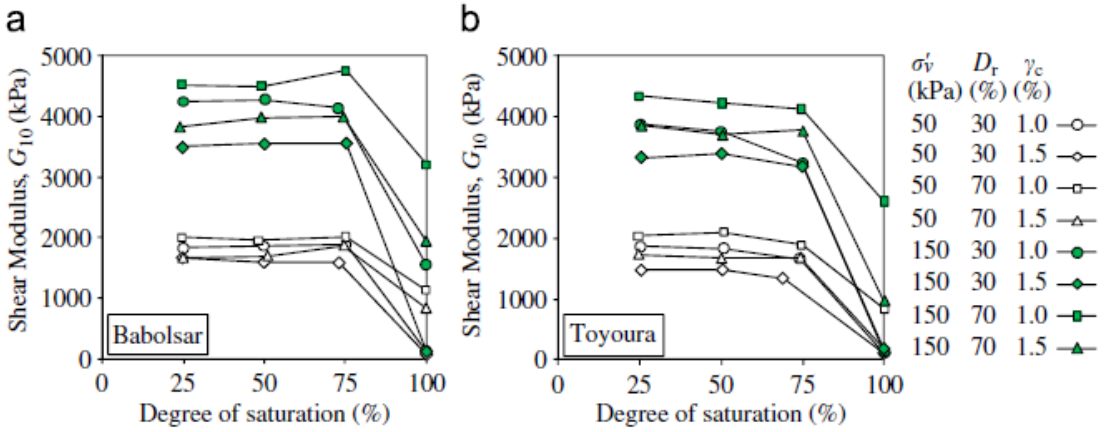

Figure 2-38 Dependence of shear modulus at 10th cycle on degree of saturation for: a) Babolsar sand; and b) Toyoura sand (Jafarzadeh & Sadeghi, 2012)

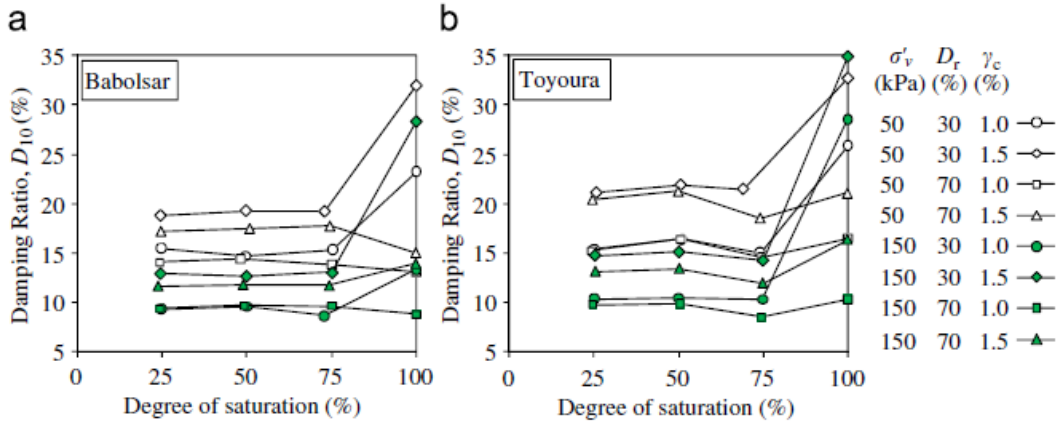

Figure 2-39 Effect of saturation ratio on damping of: a) Babolsar sand; b) Toyoura sand at 10th cycle (Jafarzadeh & Sadeghi, 2012)

Also, Jafarzadeh & Sadeghi (2012) plotted the damping evolution with the number of dynamic cycles N_L of fully saturated sand under undrained conditions, as shown in Figure 2-40.

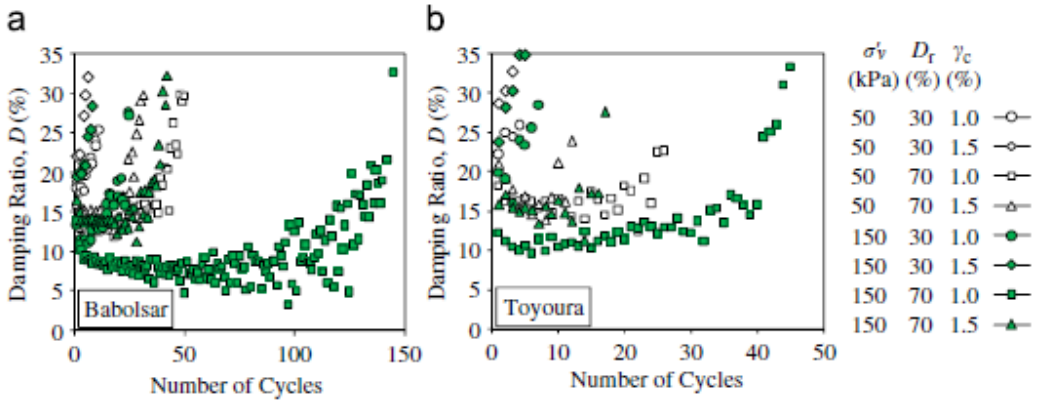

Figure 2-40 Variations in damping ratio with the number of cycles for saturated: a) Babolsar sand ;b) Toyoura sand under undrained condition (Jafarzadeh & Sadeghi, 2012)

Jafarzadeh et al. (2021) reported that the initial matric suction ψ and degree of saturation Sr significantly controls the stiffness G and damping D evolution against number of dynamic cycles N_L.

Khan et al. (2021) conducted a set of Resonant Column experiments to find the dynamic soil properties in low strain range for different degrees of saturation, the range of Sr utilized was (0, 25, 50, 75 and 100%). The study demonstrated that at the small strain range, decreasing the degree of saturation effectively increased the small strain stiffness for the three different confining pressures due to the induced suction and consequently increased effective stress, while higher confining pressure still gives higher stiffness throughout the full saturation range, Figure 2-41(a).

In addition, as presented in Figure 2-41(b), damping ratio increased approximately linearly with increasing saturation for the different applied confining pressures.

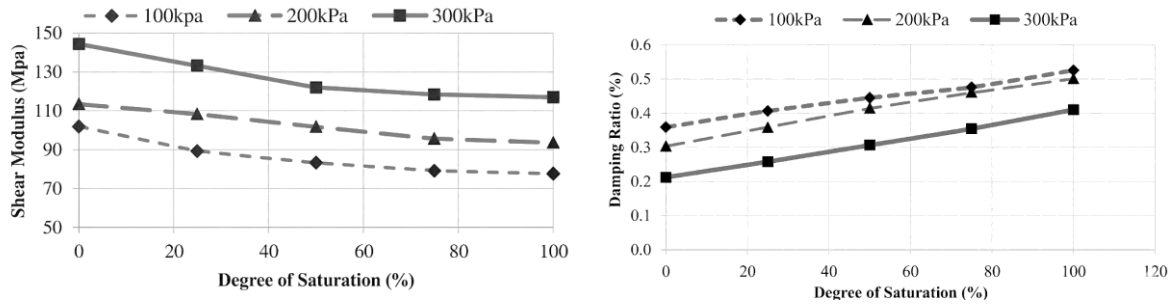

a) b)

Figure 2-41 Effect of Degree of saturation on: a) G; b) D, after Khan et al. (2021)

Le & Ghayoomi (2016) performed constant suction cyclic simple shear test and the study revealed that Suction in unsaturated soil increased the shear modulus and decreased the damping ratio comparing with those in dry and saturated conditions, the relationships are presented in Figure 2-42.

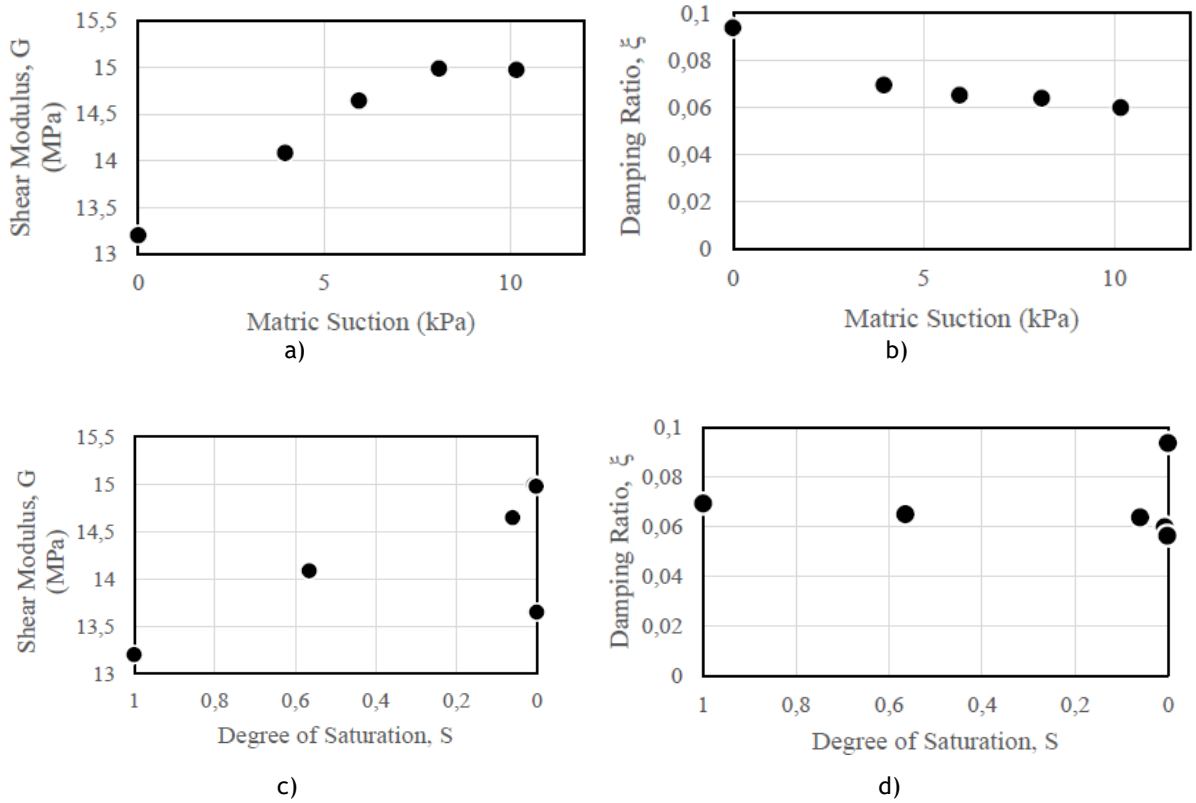

a) b)

c) d)

Figure 2-42 Effect of Matric Suction on: a) Shear Modulus; b) Damping ratio; Effects of degree of saturation on: c) Shear Modulus; d) Damping ratio (Le & Ghayoomi, 2016)

Le & Ghayoomi (2017a) has clearly realized that soils subjected to larger matric suctions (unsaturated specimens) were stiffer with higher shear modulus G and lower damping D. The damping ratio of nearly dry up to fully saturated tests were studied by Madhusudhan & Kumar (2013) through conducting resonant column tests performed in the torsional mode of vibration, for different initial confining pressures and different types of sands (fine, medium, and coarse). The variation of the damping ratio based on the changes in degree of saturation for different values of relative density and confining pressure for all three sands,

are presented in Figure 2-43, Figure 2-44, and Figure 2-45. These authors reported that as Sr decrease from fully saturation state, matric suction increases, and a continuous increase in effective stress and hence stiffness was realized, accompanied by decrease in damping. Also, the terminology optimum Sr for fine sand was defined, where damping ratio is minimum, and beyond this Sr level damping ratio increased continuously.

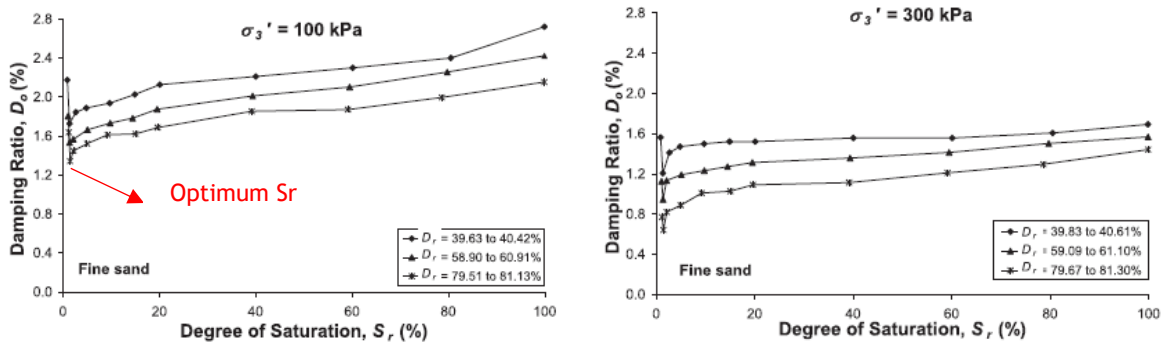

a) b)

Figure 2-43 Variation of the damping ratio with Sr for fine sand at different relative densities for σ'3: a) 100 kPa; b) 300 kPa (Madhusudhan & Kumar, 2013)

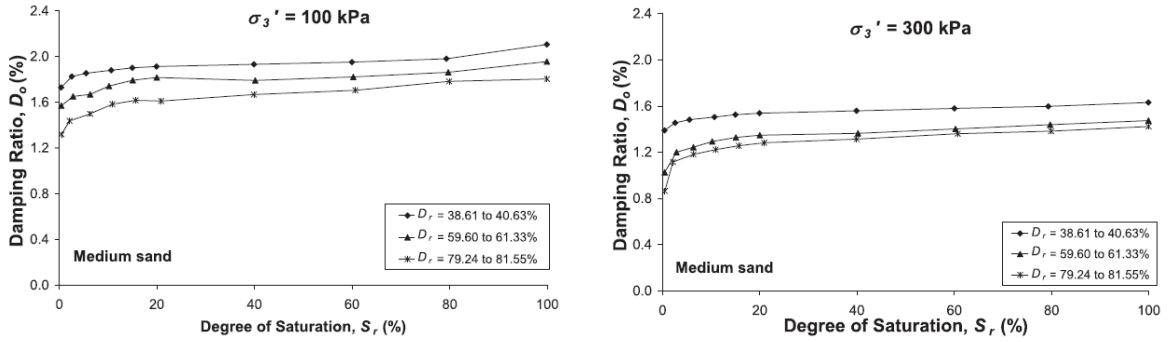

a) b)

Figure 2-44 Variation of the damping ratio with Sr for Medium sand at different relative densities for σ'3: a) 100 kPa; b) 300 kPa (Madhusudhan & Kumar, 2013)

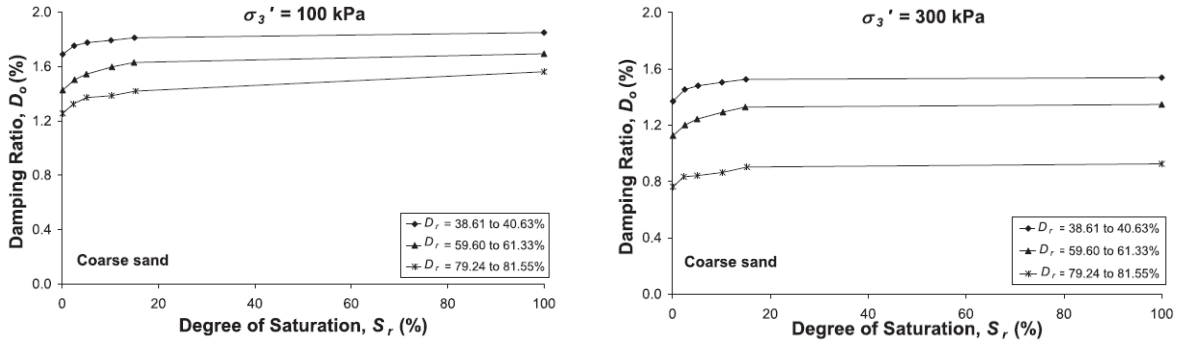

a) b)

Figure 2-45 Variation of the damping ratio with Sr for coarse sand at different relative densities for σ'3: a) 100 kPa; b) 300 kPa (Madhusudhan & Kumar, 2013)

Biglari et al. (2011) Concluded in their study that Modulus of elasticity E, shear modulus G increased while damping D decreased by inducing suction, at the same strain level and number of cycles.

Dissipated Energy

It was common evaluating the liquefaction resistance by means of stresses or strains concepts, as elaborated earlier, however, energy approaches are also of high importance as they converge the stresses and strains in the same analysis (Berrill & Davrs, 1985). Liquefaction evaluation can be performed using the amount of energy dissipated in soil during the propagation of seismic waves through soil deposits, rather than the induced cyclic shear stress or strain, The dissipated energy per unit volume is represented by the area of the hysteretic stress-strain loop and can be determined experimentally (Okur & Umu, 2013). A relationship between the dissipated energy and generated pore pressure has been reported by (Nemat-Nasser & Shokooh, 1979).

Okur & Umu (2013) reported that measuring the hysteresis loop area expresses the energy loss in the system particles in a two-dimensional stress space, in terms of stress and strain, the bounded area quantifies the accumulated energy dissipated per unit volume W and hence, considered a common procedure of energy dissipation evaluation.

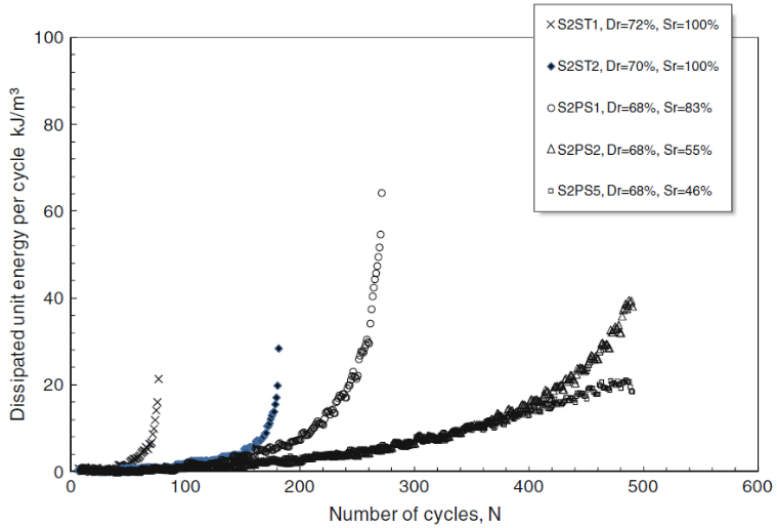

Figure 2-46 Variation of energy response with respect to number of cycles (Okur & Umu, 2013)

Furthermore, the author performed a study to evaluate the influence of degree of saturation on the energy dissipated through conducting a series of resonant column and cyclic torsional tests were conducted on loose to medium-dense sand specimens prepared at different degrees of saturation and then tested under constant effective confining pressure. Figure 2-46 shows that reducing the degree of saturation increased the cyclic resistance of the sand, as reflected by the slower build-up of dissipated unit energy per cycle and the greater number of cycles sustained before failure. This improvement became more pronounced as Sr decreased, whereas the fully saturated specimens and those with Sr>80% exhibited a sharp rise in dissipated unit energy near failure, indicating abrupt softening. By contrast, the lower Sr specimens followed smoother upward concave trends, and the authors indicated that samples with Sr > 60% were safe against cyclic shear because of the induced suction. Finally, for partially saturated specimens, reaching the same deformation state required about three to four times more unit energy than for fully saturated specimens.

2.4. Summary and main research gaps

Based on the previously detailed liquefaction mitigation methods, Table 2-1 has been generated summarizing the advantages and disadvantages of the listed mitigation methods.

Table 2-1 indicates that the advantages of applying IPS outweigh its drawbacks, making it a promising liquefaction mitigation option among the other techniques. Based on the up-to-date literature review, further research is still needed on its implementation, long-term durability, air-bubble distribution and size, assessment of the degree of saturation, and long-term monitoring.

It may also be concluded that desaturation, as a general concept involving a reduction in degree of saturation, has been studied extensively at relatively low values of Sr, that is, below the air-entry value AEV, where suction is induced and governs soil behavior. In contrast, the behavior of partially or nearly saturated soils at degrees of saturation above the AEV, where suction is negligible and occluded air bubbles are the main mechanism behind the increase in liquefaction resistance, has received limited attention and still requires further investigation, constituting an important research gap.

Table 2-1 Advantages and disadvantages of the above-reported liquefaction mitigation methods

Mitigation method	Advantages	Disadvantages	Concept
Physical	Cost-effective; eco-friendly	Inadequate in the presence of existing structures	Soil mixing /replacement; compaction
Chemical	Durability	High cost; environmentally unfriendly; concerns of inhabitants and neighbors	Cementation/Bind particles; fill voids
Biological	Efficient for existing structures	High cost; concerns of inhabitants and neighbors; durability	Gelling; Densification
Desaturation	Environmentally friendly; cost effective; Efficient for existing structures	Lack of knowledge regarding implementation and durability; complex monitoring	Introduce a gas phase/occluded air bubbles to hinder Pore pressure build-up

With regard to stiffness and damping, previous studies have generally reported an increase in stiffness and a reduction in damping in unsaturated soils, due to the effect of induced matric suction. However, no studies have yet reported the effect of partial saturation on dynamic soil properties parameters.

Therefore, the present study also focuses on assessing the increase in liquefaction resistance provided by IPS at degrees of saturation higher than the AEV, in order to exclude suction

effects, through cyclic undrained triaxial testing and centrifuge modelling. To further address the existing research gap, the influence of Sr on the cycle-by-cycle dissipated energy, damping, and stiffness properties independently of suction effects.

The novelty of the present study lies in its examination of the change in dynamic soil properties effects stemming from the introduction of air bubbles into soil pores. This enables understanding of how such damping mechanisms influence soil behavior under liquefaction conditions.

This framework encompasses the analysis of two different granular soils. By doing so, the research aims to provide a holistic perspective on the efficacy and potential challenges associated with IPS technique.

3. Materials, methods and testing program

3.1. Tested materials

The current study focuses on investigating and characterizing two types of soil: North Benavente (NB) and Hostun (HN31) sands.

3.1.1. NB sand

The sand used for the first part of the ongoing research is from the Lower Tagus Valley region, namely in the North Benavente (NB sand), near Lisbon, Portugal. This region has been recognized as a region of particular interest due to its designation as a pre-liquefied experimental site and its classification as a seismic risk zone in Portugal under Eurocodes 7 and 8. The Lower Tagus River Valley has experienced significant seismic activity, including both distant events such as the earthquake of 1755, and local earthquakes, such as those occurring in the years 1344, 1531, and 1909. One of the most catastrophic seismic events to strike the southwestern coast of Portugal was the 1909 Benavente earthquake. On April 23rd, 1909, the Benavente earthquake struck in close proximity to Benavente, NE of Lisbon, Portugal, boasting a moment magnitude of 6.0. It stands out as one of the most significant crustal earthquakes in the 20th century.

This disaster resulted in significant human casualties and extensive damage to various engineering structures near the Tagus River Valley. Figure 3-1 shows the isoseismal map and intensity data points associated with this seismic occurrence (Teves-Costa & Batlló, 2011).

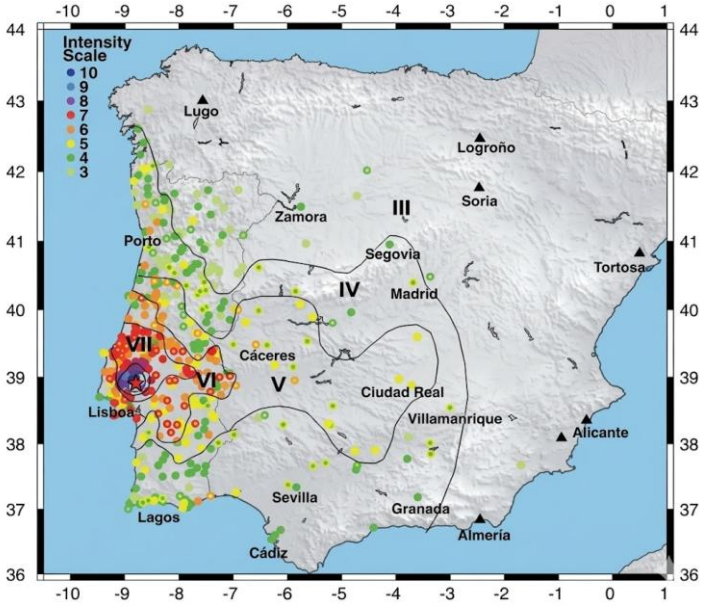

Figure 3-1 Intensity data points and tentative isoseismal map of the 1909 Benavente earthquake (Teves-Costa & Batlló, 2011)

The experimental site consists of two primary areas located near the municipalities of Vila Franca de Xira and Benavente, where the Benavente earthquake occurred on April 23rd, 1909. The selected area is part of the Lower Tagus River Valley (LTV) and is situated within Lezíria Grande de Vila Franca de Xira, a property managed by the Associação dos Beneficiários da Lezíria Grande de Vila Franca de Xira (Ramos, 2021).

In the alluvial plain of the Tagus and Sorraia rivers, instances of liquefaction-induced damage have been documented, such as sand boils, soil cracks, and ejected sand (Teves-Costa & Batlló, 2011). This phenomenon is likely attributed to the interaction of regional geology and local site conditions, rendering this area highly susceptible to liquefaction.

The physical and mechanical properties of North Benavente NB sand will be investigated, followed by assessing the liquefaction resistance under various degrees of saturation. Also, the influence of IPS on the dynamic soil properties will be discussed.

More details regarding the in-situ geotechnical tests, collecting disturbed and undisturbed soil samples and soil packing of NB-soil is explained in Ramos (2021). The geotechnical campaigns were carried out as part of two research projects at the CONSTRUCT-GEO research center of FEUP: the national project "Liquefaction Assessment Protocols to Protect Critical Infrastructures against Earthquake Damage: LIQ2PROEARTH," supported by the Portuguese Foundation for Science and Technology (FCT), and the European project "LIQUEFACT" (Assessment and mitigation of liquefaction potential across Europe: a holistic approach to protect structures/infrastructures for improved resilience to earthquake-induced liquefaction disasters), funded by the European Union's Horizon 2020 research and innovation program. Figure 3-2 shows the NB-site area near Lisbon, in the South of Portugal obtained by Google maps.

Figure 3-2 - Google Maps picture showing North Benavente area (NB soil location)

3.1.2. Hostun sand

The well-know Hostun sand HN31 (Flavigny et al., 1990) has been used for the second part of this study.

The primary objective of the ongoing research is attempting to establish a comprehensive framework for evaluating the liquefaction resistance of sands under conditions of partial saturation. To achieve this goal, besides cyclic triaxial tests, centrifuge modeling was conducted to assess the liquefaction resistance of fully and partially saturated Hostun sand HN31 sand. The centrifuge modelling part in this thesis was facilitated through the Transnational Access (TA) granted within the GeoLAB project (https://project-geolab.eu), for utilizing the dynamic centrifuge at Cambridge University's Schofield Centre. The initial centrifugal models were executed as part of the CENLIMIT1 proposal, focusing on the physical modeling of desaturation for soil liquefaction mitigation. Subsequently, another proposal for conducting centrifuge testing, CENLIMIT2, has been recently accomplished - July 2024, aiming for deepening the investigation under the same topic. Hostun HN31 sand serves as a crucial reference material in geotechnical engineering, sourced from SIKA plants located in Hostun (Drôme), near the western flank of the Vercors mountains, approximately two kilometers away from the town, France. For further insights into the screening, collection, and packaging of Hostun sand, additional details can be found in the work of Flavigny et al. (1990).

This study will include the physical properties of Hostun HN31 sand, followed by the presentation of Geo-mechanical properties and liquefaction resistance characterization for various degrees of saturation followed by the centrifuge testing and analysis.

3.2. Physical characterization

This section outlines the physical properties of both types of soils in addition to the equipment and experimental procedures adopted during the laboratory testing program. All tests were conducted at the Geotechnical Laboratory (LabGEO) of FEUP, University of Porto, Portugal. While the centrifuge modeling was performed in the Schofield center, university of Cambridge, UK.

3.2.1. NB sand

A large quantity (around 250 kg) of disturbed NB soil was collected at the pilot site and transported in bags to LabGEO, FEUP. Subsequently, the soil was spread on the floor of the laboratory, homogenized, and quartered to obtain representative specimens for systematic testing, comprising physical properties assessment and grain size distribution analyses, and numerous mechanical laboratory tests in reconstituted conditions.

Using the Standard Test Method for Particle Size Analysis of Soils ASTM D422, particle size analyses were carried out using the electrical sieves shaker shown in Figure 3-3 for the selected soil samples.

The grain size distribution curve GSD of this soil is shown in Figure 3-4. The analysis revealed a poorly graded soil SP based on the Unified Soil Classification system USCS. Also, the low values of C_u and C_c confirm the low gradation of the soil particles.

Subsequently, the resulting grain size curve has been compared with the liquefaction boundaries set by Tsuchida (1970) for evaluating the susceptibility of liquefaction based on soil compositional criterion. The analysis revealed that the grain size distribution curve of NB sand falls within the designated limits indicating that the soil is susceptible to liquefaction, as illustrated in Figure 3-5. Ramos (2021) conducted an extensive study to characterize the behavior of NB soil, therefore, grain size curve of the current study was plotted and compared against that GSD curves obtained by Ramos (2021), as shown in Figure 3-6. The comparison revealed a close match between the curves, except for the fines content, Fc%, which could be attributed to the variations that may occur during soil packing. The main physical grain size properties of NB soil are presented in Table 3-1.

Figure 3-3 - Electrical sieves shaker used in the Geotechnical laboratory, LabGeo, FEUP

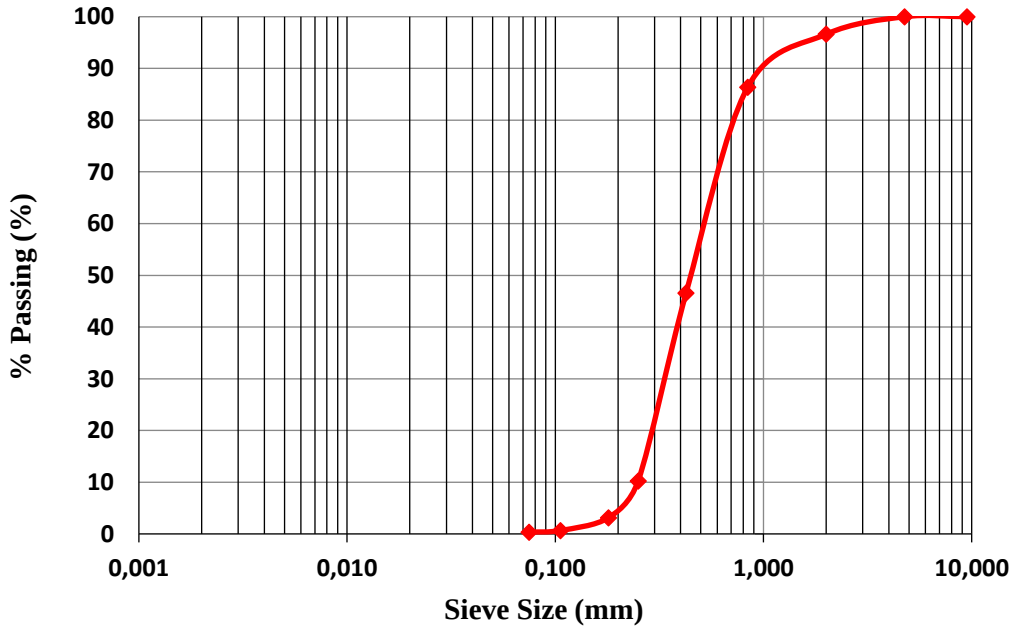

Figure 3-4 Grain size distribution curve of NB Soil

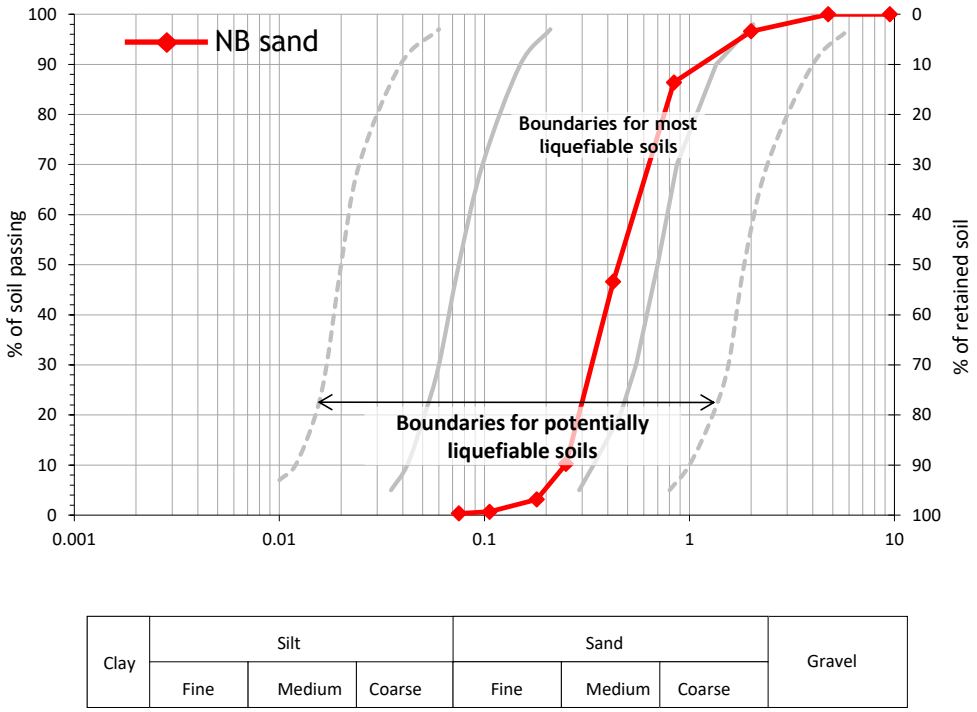

Figure 3-5 - Grain size distribution of NB soil, compared against liquefaction boundaries by (Tsuchida, 1970)

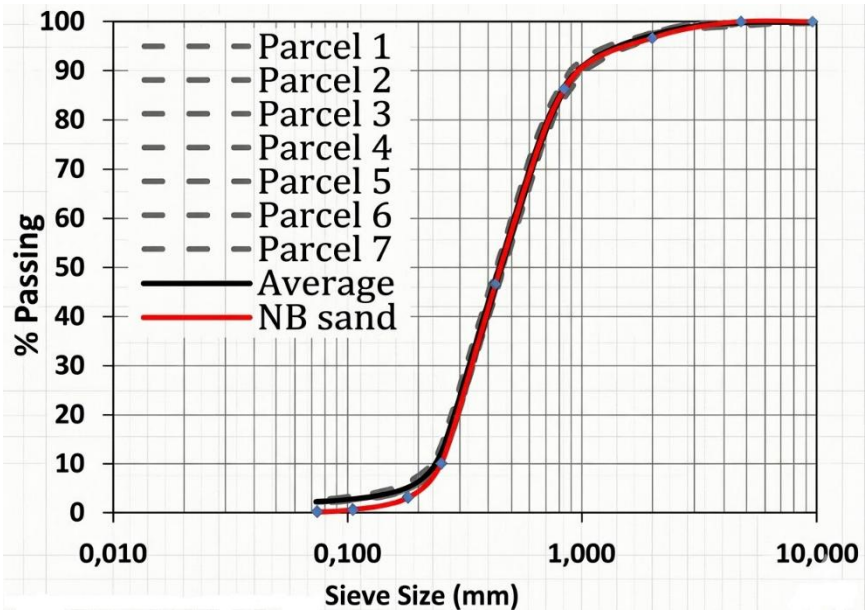

Figure 3-6 Grain size distribution curve NB soil comparison with results by Ramos (2021)

Table 3-1 Primary physical characteristics of NB soil

D_{50} (mm)	Cc	Cu	F_C (%)
0.45	0.84	2.16	0.67

Using X-ray diffraction, Ramos (2021) has assessed the mineral composition of NB soil. This study revealed that the soil predominantly consists of quartz, with additional presence of orthoclase, albite, and muscovite. The results of the mineralogy analysis are listed in Table 3-2.

Table 3-2 Mineralogy evaluation of the studied NB soil, after (Ramos, 2021)

Mineral	NB soil
Quartz	65
Orthoclase	6
Albite	9
Muscovite	20

In addition to mineralogy analysis, Ramos (2021) conducted particle shape analysis at University College London (UCL) using the Morphologi G3 apparatus. The results were plotted in the various angularity zones map, established by Altuhafi et al. (2013).The findings depicted in Figure 3-7 indicated that the NB soil exhibits subangular-shaped particles.

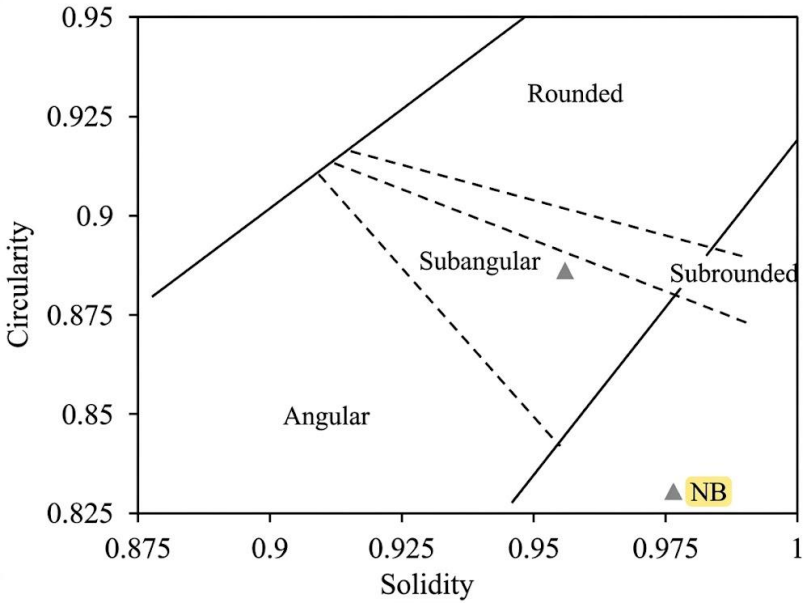

Figure 3-7 Different angularity zones set by (Altuhafi et al., 2013) showing NB soil classification, after (Ramos, 2021)

Minimum and maximum void ratios e_{min}& e_{max} and Specific Gravity Gs

Assigning the minimum and maximum void ratios e_{min} and e_{max} is highly essential as it enables computing the relative densities of the soil for any experimental test.

The maximum and minimum densities and corresponding void ratios were determined following the Japanese Geotechnical Society standard (JGS-0161). The tools used in this test are shown in Figure 3-8. In addition, laboratory tests were also performed to obtain the specific gravity Gs of NB soil. Two tests were performed for repeatability check.

Resulting e_{max}., e_{min} and, Gs values are provided in Table 3-3, in addition to results obtained by Ramos (2021). Both analyses revealed slightly different e_{min}, e_{max} and, Gs. These variations could be linked to differences in fines content between the two tested specimens, as mentioned before.

Table 3-3 e_{max}, e_{min} and Gs for the tested samples

	e_{max}	e_{min}	Gs
Current study	0.870	0.540	2.633
Ramos (2021)	0.846	0.590	2.640

Figure 3-8 Tools used for the determination of e_{min} and e_{max}

Soil water characteristics curve (SWCC)

The quantification of soil suction is a fundamental requirement in unsaturated soil mechanics, serving as a primary stress state variable for predicting hydraulic conductivity, shear strength, and volume change behavior. Reducing the soil´s saturation degree Sr enhances the resistance to liquefaction in unsaturated and partially saturated soils as reported in the literature review, primarily due to the influence of matric suction (Ψ) in addition to the compressibility of existing air bubbles.

Based on Cappellaro (2019) , the increase in liquefaction resistance observed in specimens with lower water content is attributed to suction, which facilitates the formation of more stable fabric structures. Matric suction, commonly known as capillary pressure, is a measure of the difference between the pore-air pressure U_a and the pore-water pressure U_w within the soil.

The soil-water characteristic curve SWCC of a soil defines the correlation between the soil's volumetric water content and matric suction, as outlined by Fredlund & Xing (1994).

In the current study, SWCC was identified and hence, the range of Sr% adopted for the IPS liquefaction mitigation method was selected (below AEV) based on the SWCC to have a minimum (neglected) suction effect.

Different authors have adopted varying methods and procedures for the determination of SWCC such as Tensiometric plates, Osmotic membrane, Vapor equilibrium, Pressure plate and, Filter paper (Eyo et al., 2022).

Among the various techniques available for computing suction and producing SWCC, the filter paper method FPM was selected in the current study due to its availability, perceived simplicity, low cost, and remarkably wide measurement range (Leong et al., 2016). It's worth mentioning that, the Pressure Plate Apparatus PPA test have been conducted according to ASTM recommendation in the standard D6836-16 ASTM International (206), but due to the inaccuracies particularly in very low range of applied suction pressures, controlling and maintaining those low pressures during the recommend days (Equilibrium period), was not an easy and accurate job.

Therefore, filter paper method has been adopted as the author was having the full control on the applied water content and then computing the corresponding suction as will be detailed. The American Society for Testing and Materials ASTM provided a standardized protocol for the filter paper method in ASTM D5298-16.

The filter paper method operates on the principle of local hydraulic equilibrium. When a dry filter paper is placed in direct contact with a soil specimen, moisture transfers from the soil to the paper until the suction in both media is equal (Bicalho et al., 2007) . The filter paper in this case acts as a miniature pressure plate or a calibrated sponge.

In this condition, the paper and the soil will have the same suction, but different gravimetric water content. The relationship between its gravimetric water content w_f and the suction s is used to infer the soil suction value.

Within the filter paper testing, the distinction between contact and non-contact methods is critical for sandy soils. If the flow occurs in the form of vapor (by avoiding direct contact between the paper and the soil), the suction measured will be total (matric plus osmotic) on the other side, If the flow occurs only by capillarity, the suction measured will be the matric suction. This is achieved through direct contact between the paper and the soil.

In the current study, the filter paper used is Whatman No. 42, it is a commonly used filter paper for this test because of its high purity and consistency (Kim et al., 2016).

The filter paper was put in a perfect contact with the soil for an equilibrium period. While ASTM D5298-10 recommended a minimum of 15 days, earlier literature often suggested 7 days (Chandler & Gutierrez, 1986; Houston et al., 1994).

Test specimens were meticulously prepared by mixing the soil to the target water content and compacting it into (well pre-defined dimensions) stainless-steel rings via controlled tamping.

The surface of each specimen was leveled using a straight metal edge to ensure a flat, uniform boundary. The rings were weighed and, three supplementary soil samples were extracted from the remaining material to accurately verify the initial water content. The relative density Dr of the tamped soil was about 35.5%

Two filter papers (one on each side of the specimen) were placed in direct contact with the soil. The whole set (paper plus specimen) was then wrapped in several layers of PVC film to prevent the transfer (loss or gain of moisture) of water with the medium, and stored in a thermal box (Styrofoam box) throughout a the 7-day equilibration period.

Following the equilibration phase, the wet filter papers were transferred to a high-precision digital balance (200g capacity, 0.0001g sensitivity). As emphasized by (Chandler & Gutierrez, 1986), the transfer time must be minimized to prevent evaporative moisture loss from the wetted paper. In this study, the wet paper transfer was executed within a rapid 5 to 10-second window. The papers were subsequently oven-dried at 105°C for 24 hours. To prevent the dry paper from absorbing ambient atmospheric moisture from the laboratory air before the final weighing, it was transported directly from the oven to the scale inside a silica gel desiccator. Even accounting for this transport, the total exposure time for weighing the dry paper remained strictly under the 30-second maximum recommended in the literature.

Finally, the measured filter paper water contents were converted into matric suction values. While numerous calibration curves exist for Whatman No. 42 filter paper, this analysis utilized the widely validated calibration equations developed by Chandler et al. (1992) These specific calibration relationships are summarized in equations (3-1) and (3-2).

By definition, this procedure produces a wetting curve, where test began with a dry soil specimen, small controlled amounts of water were added, sealed to equilibrium, and finally suction was measured for each water content. Figure 3-9 shows the testing procedure and used tools used for the filter paper tests.

Figure 3-9 Collective picture showing the tools used in the filter paper test, showing the filter paper, wet soil, thermal isolating film, high-precision digital balance and the thermal box for storing samples

Reference	w_f (%) of paper	Formula of suction (kPa)	
Chandler et al. (1992)	w_f <47	$\log_{10} s = 4.842 - 0.0622 w_f$	(3-1)
	w_f >47	$\log_{10} s = 6.05 - 2.48 \log_{10} w_f$	(3-2)

The resulting experimental SWCC data were presented in Figure 3-10, plotted alongside the theoretical prediction model proposed by Fredlund & Xing (1994), defined by (3-3).

Specifically, Figure 3-10a illustrates the relationship between matric suction and volumetric water content θ_w, while Figure 3-10b depicts the corresponding relationship between matric suction and the degree of saturation Sr.

$$\theta_w = \frac{\theta_s}{\left\{ ln\left[\exp(1) + \left(\frac{\Psi}{a}\right)^b \right] \right\}^c} \tag{3-3}$$

Where θ_w is the volumetric water content; θ_s is saturated water content, exp is the Euler's number ≈ 2.71828; Ψ is the soil suction and, a, b and c are fitting parameters.

Table 3-4 summarizes the specific fitting parameters defining the theoretical model of the SWCC for NB sand.

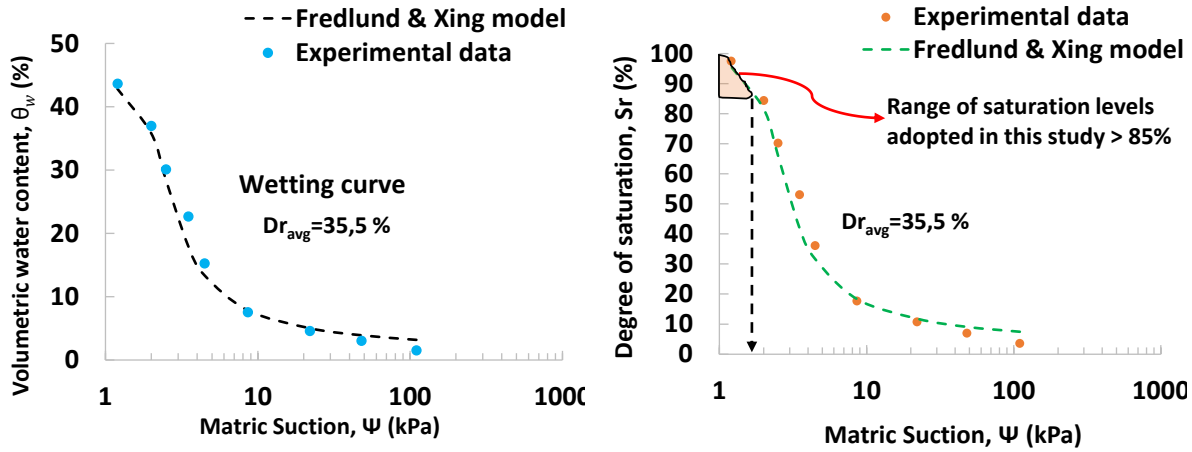

Figure 3-10 Soil-water characteristic curves SWCC for NB sand: a) Matric suction Vs. Volumetric water content; b) Matric suction Vs. degree of saturation

Table 3-4 Fitting parameters adjusting the theoretical model soil water characteristic curve of NB sand

Fitting parameter	Value
θ_s (%)	43.64
a	2.1
b	5
c	0.88

The SWCC for NB sand yields an air entry value AEV of approximately 1.8 kPa, corresponding to a degree of saturation S_r of roughly 82%. Above this threshold, matric suction would be considered negligible, and the soil acts as a two-phase system (solid and liquid). So, selecting Sr range for the IPS before AEV would just consider introducing occluded air bubbles within the pore fluid not creating a third phase of air pores. And hence, any enhancement due to IPS with Sr> 82%, would be attributed to the high pore fluid compressibility due to introducing occluded air bubbles.

The shaded region in Figure 3-10b visually confirms this minimal suction within the specific high-saturation threshold targeted in this Induced Partial Saturation IPS study.

3.2.2. Hostun sand

Hostun sand HN31, a well-established reference soil within the geotechnical community, has had its physical properties extensively studied and documented in numerous scientific publications. Hostun sand HN31 was used for the centrifuge modelling tests and also undrained cyclic triaxial tests.

Figure 3-11 shows the particle size distribution curve drawn by Zeybek & Hall (2017), which was obtained using the Single Particle Optical Sizing technique (D. J. White, 2002). Hostun sand HN31 sand is a fine-grained siliceous sand with high liquefaction susceptibility (Zeybek & Hall, 2017).

The grain size distribution curve for Hostun sand along with NB soil was evaluated against the liquefaction boundaries defined by Tsuchida (1970) which assess liquefaction susceptibility based on soil composition. The analysis revealed that the grain size curve of both types of sand falls within these specified liquefaction limits, confirming the soil's vulnerability to liquefaction, as depicted in Figure 3-12.

Figure 3-11 Particle size distribution for the HN31 sand (Zeybek & Hall, 2017)

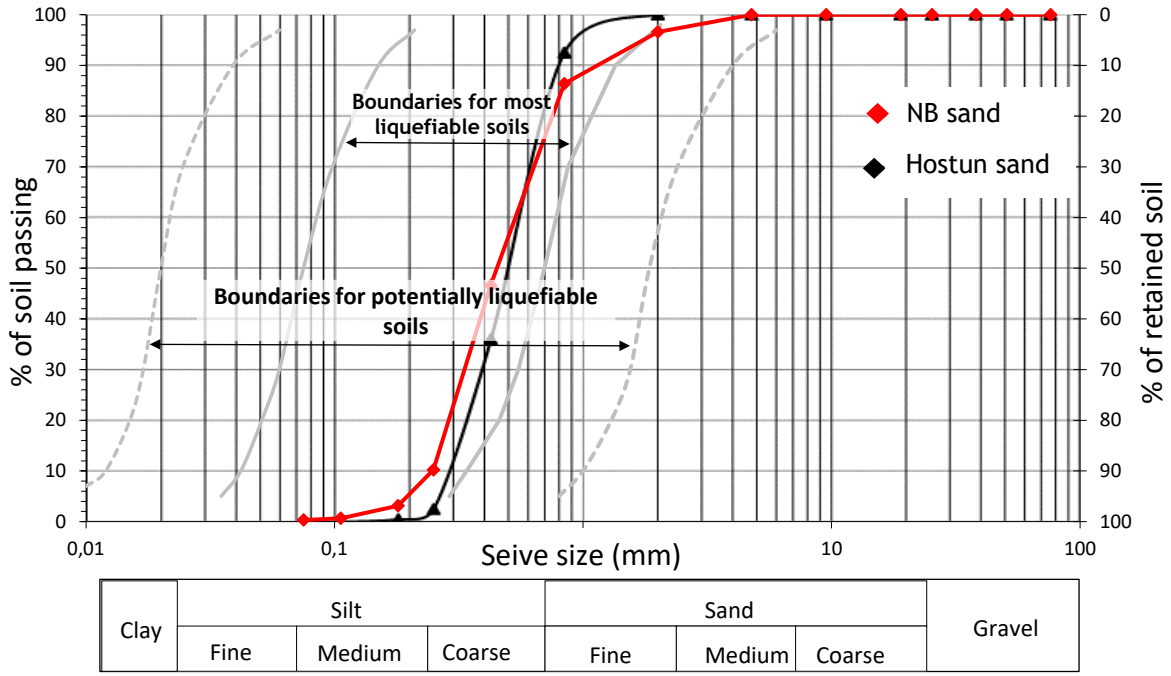

Figure 3-12 Grain size distribution (NB and Hostun sands), comparison against liquefaction boundaries by (Tsuchida, 1970)

The essential physical properties of Hostun sand are listed in Table 3-5, as reported by Zeybek & Hall (2017).

Table 3-5 Physical properties of HN31 sand (Zeybek & Hall, 2017)

Property	Value	Unit
Uniformity coefficient, C_u	1.67	-
Specific gravity, $\boldsymbol{Gs}$	2.638	-
Minimum void ratio, $\boldsymbol{e_{min}}$	0.63	-
Maximum void ratio, $\boldsymbol{e_{max}}$	1.01	-
Minimum density, $\boldsymbol{\rho_{min}}$	1318	kg/m^3
Maximum density, $\boldsymbol{\rho_{max}}$	1620	kg/m^3
Average particle size, $\boldsymbol{D_{50}}$	0.480	mm

Moreover, Lins et al. (2009) have studied the soil-water retention curve SWRC of Hostun sand HN31 as reported by Zeybek & Hall (2017) through conducting a series of steady state and transient state tests. Using the published test data, Zeybek & Hall (2017) replotted the variation of the matric suction with degree of saturation for a loose Hostun sand (Figure 3-13), Subsequently, Zeybek & Hall (2017) used the van Genuchten SWRC fitting parameters for fitting.

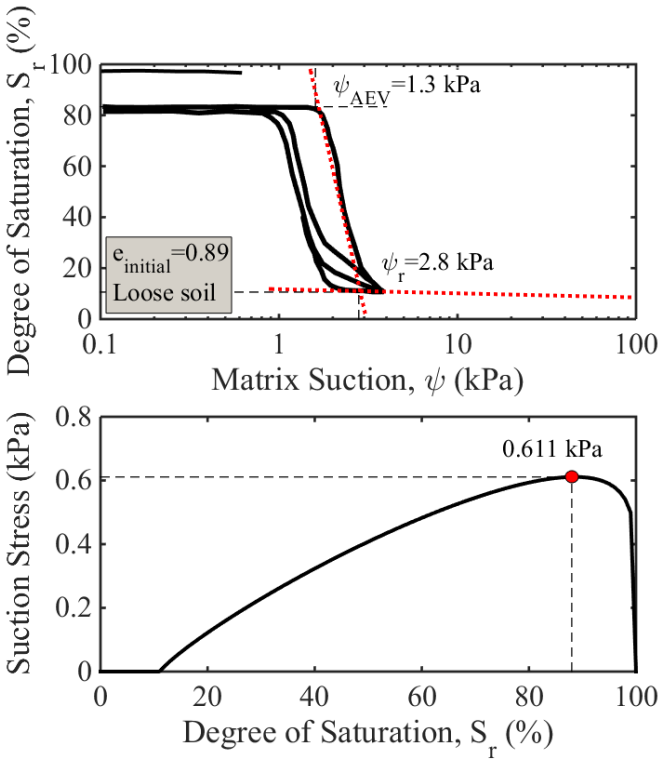

Figure 3-13 SWRC and suction stress for a loose Hostun sand deposit (Zeybek & Hall, 2017)

The study revealed that the suction stress increases as the degree of saturation Sr decreases, reaching its peak value at Sr of 88% at a suction stress of 0.611 kPa, and reported that the influence of such small suction on effective stress could be neglected.

3.3. Seismic wave measurements using bender elements

Bender elements are non-destructive testing tool that could be attached to many geotechnical apparatuses to measure the compressional and shear wave velocities during testing and assess soil stiffness (Ferreira et al., 2021). In the current study, BE are used in three apparatus namely; Double wall triaxial apparatus, Cyclic triaxial apparatus and the physical modelling performed in the dynamic centrifuge.

Bender elements (BE) consists of two piezoceramic transducers thin plates firmly attached to a central metallic sheet, with electrodes located on the outer surfaces of these plates.

Measuring seismic wave velocities using BE requires a whole compatible system of electronic equipment, which was already setup and calibrated at LabGEO. This compatible system consists of a function generator (TTi TG1010) which generates the electrical signal that excites the transmitter BE. In the current research, sine pulses at varying frequencies were used as input signals. In addition to an amplifier to magnify the signal received by the receiver BE, an oscilloscope (Tektronix TDS 220) and a computer with WaveStar software were also used to acquire the wave signals.

Figure 3-14 is schematic sketch of the bender elements with the electronic equipment set up. BE are installed in the top and base loading caps (the two ends of the specimen), they act and vibrate as fixed-free cantilever beams. The transmitter BE generates a mechanical

excitation, the pulse travels through the specimen's body until it is detected by the receiver BE, where it is then converted into a voltage signal (Rio, 2006).

Figure 3-15 shows the real setup of the wave measurement system while measuring S-wave velocity in the current study.

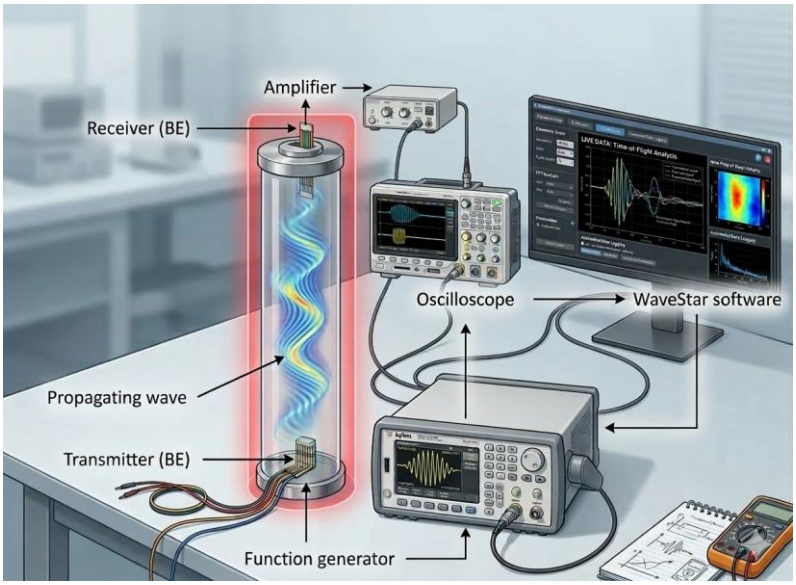

Figure 3-14 Schematic setup of the bender elements testing

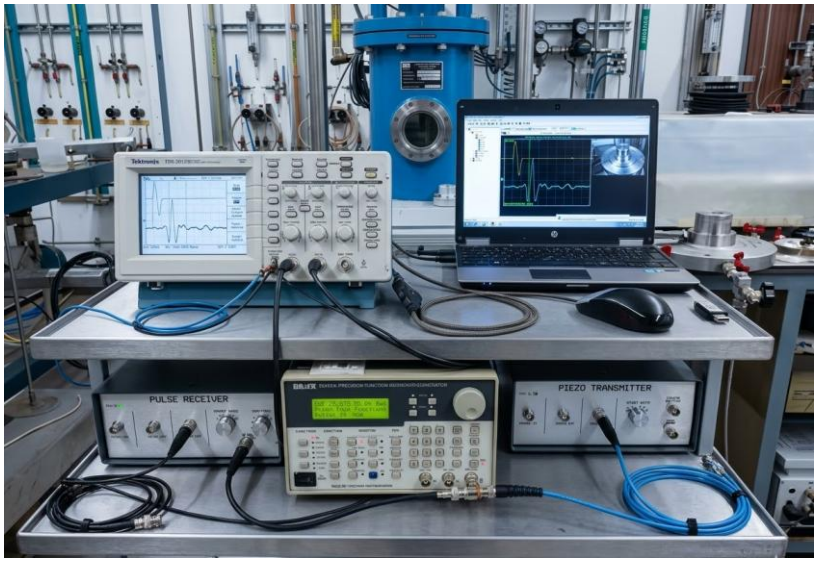

Figure 3-15 Setup of the waves measurement system during measuring S-wave in the Laboratory.

Seismic wave velocities could be used to obtain many soil parameters. In the current study, shear wave velocities were measured for the assessment and monitoring of soil stiffness, however compressional wave velocities were measured to confirm the achieved saturation levels of the soil specimens.

Ferreira et al. (2021) reported that measuring P and S-wave velocities can be done by a single pair of BE, through changing the frequencies of the transmitted signal. In general, the arrival of P-waves can be detected by applying higher input frequencies.

It is worth reporting that, for each single test, at least three to four input frequencies were applied as the input signals which ranged from 1 to 10 kHz for shear wave velocities and from 10 to 70 kHz in compressional wave velocities following Viana da Fonseca et al. (2009), Ferreira et al. (2021) and Molina-Gómez (2023), this approach aimed to enhance the accuracy of measuring wave propagation time.

P and S-wave arrival time was identified using the first arrival time method (Santamarina & Fam, 1997). The seismic wave velocities were calculated as the ratio between tip-to-tip bender element distance, divided by the wave propagation time.

Figure 3-16 shows a picture captured from the oscilloscope for a P-wave propagation signal.

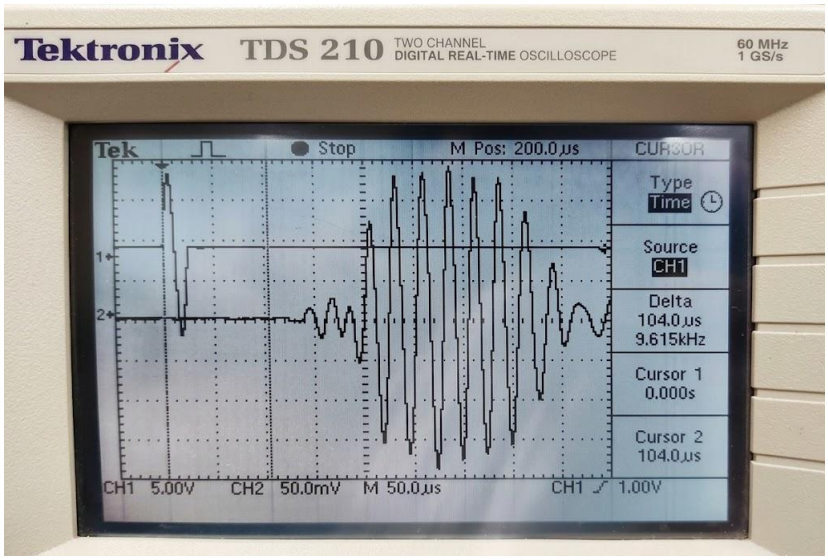

Figure 3-16 P-wave propagation captured from the oscilloscope

Seismic wave measurements were performed in every testing apparatus, from triaxial to centrifuge tests, except for a few monotonic triaxial tests for CSL characterization.

3.4. Monotonic Triaxial Tests

3.4.1. Introduction

In geotechnical laboratories, Monotonic triaxial testing is commonly used to assess the soil mechanical behavior and the critical state locus, in addition to many other soil properties depend on the purpose. Triaxial testing is one of the most commonly and efficient methods of assessing soil strength and exploring soil behavior (Viana da Fonseca et al., 2021).

Triaxial apparatus considers a many-sided testing equipment, users can model and solve many geotechnical problems by controlling the horizontal and vertical stresses, drainage and, measuring pore water pressure. Moreover, triaxial testing can be used for accurately measuring consolidation and permeability parameters of soils. Simple schematic diagram for conventional triaxial testing equipment is shown in Figure 3-17.

Commonly, triaxial testing could be performed under three different consolidation and drainage conditions:

- CID, Consolidated isotropic drained tests.
- CIU, Consolidated isotropic undrained tests.
- UU, Unconsolidated undrained tests.

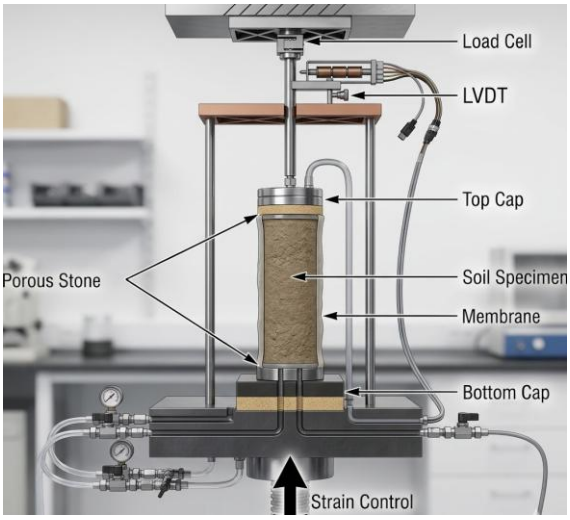

Figure 3-17 Schematic diagram for conventional triaxial testing apparatus

3.4.2. Brief description of the conventional triaxial apparatus and procedures

The monotonic triaxial chamber used in this study is a cylindrical transparent acrylic plastic, reinforced with fiber glass confinement. The apparatus includes data acquisition box with various channels, LabVIEW® software to control the tests and the used channels, hydraulic piston with flow control valves to ensure a constant rate of applied axial displacement. Furthermore, a displacement transducer LVDT is installed above the triaxial chamber, to measure the axial displacement.

The applied pressures are regulated by three pressure transducers equipped with controlling valves situated at the base of the chamber, to measure, and control the pressures applied to the chamber cell to control and measure the cell pressure and to the sample through the top and base caps which enables measuring pore water pressure. Moreover, a volume gauge is included to measure the water variations during testing, specifically during consolidation as shearing will be performed under undrained conditions.

Figure 3-18a, shows the oversized lubricated end platens used as the top and the base caps of the specimens to ensure a high uniformity of stresses and strains. In addition, it reflects reliable readings and measurements through reducing the stress concentration due to the friction between the soil specimen and the platen restraint to negligible amounts.

The lubricated end platens are provided with two typical triaxial latex membrane discs and an extremely smooth and firm platen. Additionally, it has two thin silicone grease layers sandwiched between the surface platen and the two latex discs. Applying silicone grease carefully is necessary to prevent interference with sample drainage.

In addition to an embedded connection piston into the top cap to avoid specimen tilting (Viana da Fonseca et al., 2021). The specimens were encapsulated by a thin latex rubber membrane. The axial load was measured using a conventional load cell, and pore pressure was measured using a pressure transducer. Tests were performed based on Strain-control approach therefore, an axial displacement was applied at a constant rate, and the resulting axial force and change in pore pressure (effective stress) were measured. The conventional triaxial test apparatus used in this study is shown in Figure 3-18b.

The diameter of all triaxial test specimens was about 70 mm, the height of the specimens tested with an oversized lubricated end platens was 145 mm hence, the ratio of length to diameter L/D was approximately 2.1.

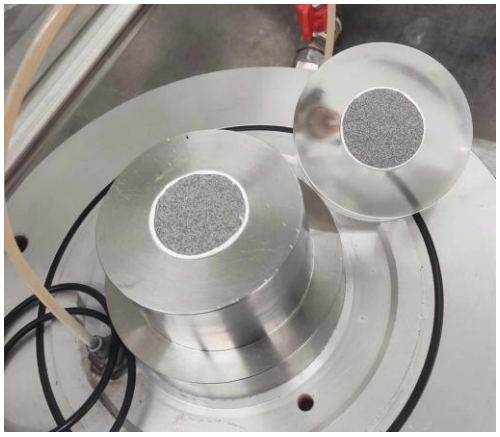

a)

b)

Figure 3-18 a) Lubricated end platens for triaxial tests; b) Conventional monotonic triaxial apparatus in LabGeo, FEUP

3.4.3. Monotonic triaxial testing procedures

To characterize the stress-strain behavior and critical state parameters of NB sand, seven undrained saturated isotropic monotonic triaxial compression tests were conducted. Reconstituted samples were prepared using the moist tamping preparation technique to produce loose to medium dense sands.

Before consolidating samples, the degree of saturation Sr was measured to ensure full saturation through manually computing Skempton's B-value (Skempton, 1954). B is a key parameter used to evaluate the degree of saturation achieved in soil samples based on the relationship between the increment of confining pressure and the undrained pore pressure increment during testing. When Skempton's B approaches unity, it indicates that the soil is fully saturated; in other words, the increase in cell pressure closely matches the increase in undrained pore pressure.

The standard testing procedures followed in this series of monotonic triaxial tests are outlined as follows:

- **Preparation of Specimens**: Soil specimens were carefully prepared according to standard procedures, ensuring uniformity and consistency, using Moist tamping preparation method with initial water content of 5%.
- **Saturation**: The prepared specimens were saturated with water to ensure full saturation conditions. Saturation begins by introducing low-pressure CO_2 to replace air bubbles, which are forced through the top cap into a tube and collected in an inverted water-filled bottle until it is fully displaced.
- **Water flushing**: Flushing water from the sample bottom drainage line until it gets out from the top drainage line, finally increasing the back pressure inside the soil specimen until 300 kPa while maintaining 10 kPa effective pressure.
- **Isotropic Consolidation**: Isotopic consolidation was carried out to apply different levels of initial mean effective stress P_o' to the specimens.
- **Shearing**: The saturated, consolidated specimens were then sheared up to an axial strain of about 30% at controlled loading rates ranging from 0.025 to 0.03mm/min, in an attempt to reach the critical state.
- **Frozen Preservation**: Following the completion of each test, specimens were frozen to maintain the water content within the samples. The weight of the specimens before and after freezing was measured to determine the final water content and void ratio.
- **Interpretation**: The results of the triaxial tests were interpreted to understand the soil's response to loading and to determine its critical state parameters.

Table 3-6 summarizes the details of the performed undrained monotonic triaxial tests for NB sand, where: test# refers to the test number, e_o is the initial void ratio (after preparation), p'_o is the initial mean confining stress, while e_f is the final void ratios, (before shearing).

Table 3-6 Details of the performed monotonic triaxial tests

Test #	e_o	p'_o(kPa)	e_f
Tx1	0.745	500	0.687
Tx2	0.700	200	0.662
Tx3	0.788	100	0.742
Tx4	0.801	100	0.752
Tx5	0.804	50	0.749
Tx6	0.813	20	0.764
Tx7	0.801	100	0.733

3.5. Double-wall triaxial chamber tests

3.5.1. Brief description

Performing partially saturated triaxial tests under monotonic loading is fundamental to the current study. Accordingly, a double-wall triaxial chamber was employed to perform both saturated and partially saturated monotonic triaxial set of tests.

The double-wall triaxial chamber is designed to conduct triaxial tests under both fully and partially saturated conditions as it is designed to maintain uniform pressure inside and outside the chamber wall, thereby enabling control over volumetric change.

The characteristics of the developed equipment have already been in details presented in (Costa, 2009; Gomes, 2008).

The main components of the apparatus include a double-walled triaxial chamber in addition to a data acquisition unit (Datascan) that enables the simultaneous acquisition of up to 16 channels, and the control unit is housed in a computer where all the necessary software has been installed.

In addition to a set of stepper motors, MPP (Mechanical Power Producer) to ensure control over various variables, including pressure inside the chamber and between the internal and external chamber walls, pressure inside specimens, external axial displacement, and volume change. Figure 3-19 displays a schematic picture and real setup of the triaxial chamber, indicating the testing tools utilized in the equipment.

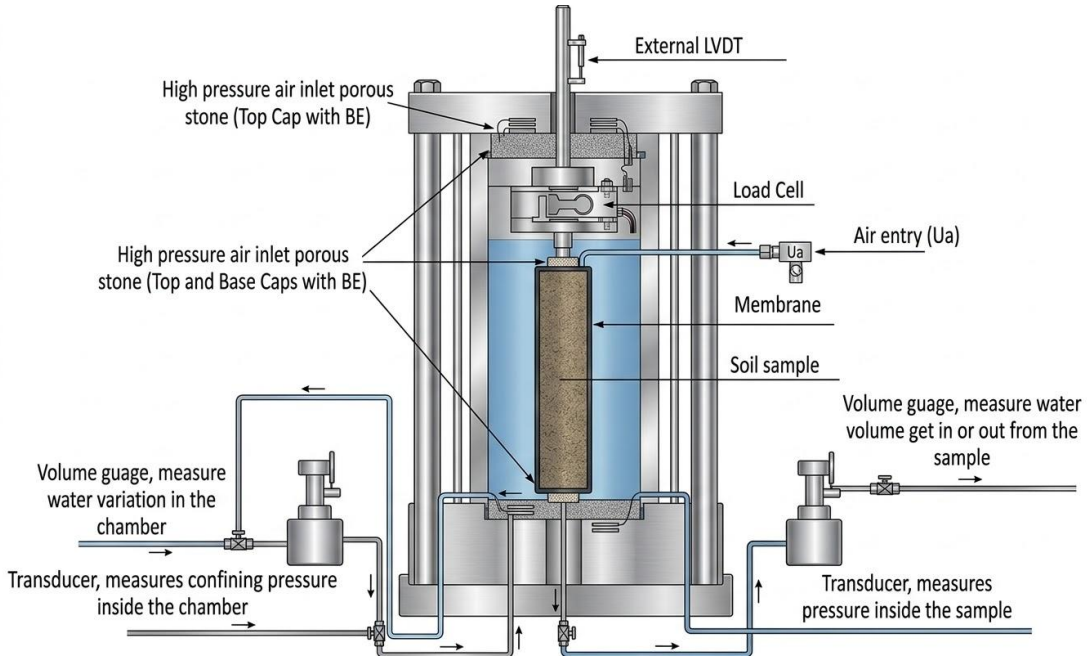

a)

b)

Figure 3-19 Double wall triaxial chamber: a) schematic; b) actual photograph of the developed system

3.5.2. Double wall triaxial apparatus setup

The main operational equipment parts are detailed as follows:

Actuators

The apparatus comprises actuators with varying capacities. For instance, the actuator that regulates pressures within the chamber has a stroke of 460 mm and a diameter of 96 mm.

Actuators consist of a piston, a cylinder and a spindle, controlled by a stepper motor MPP. The spindle is mechanically linked to an MPP, and with each impulse, the MPP induces a rotation that increases the pressure of the water within the actuator. In addition to a pneumatic actuator which is employed to apply vertical load to the load cell, which in turn transfers the load to the sample during shearing.

The pneumatic actuator that controls the axial load transferred to the soil specimen through the load cell is shown in Figure 3-20a, in addition to two Stepper motors MPP that control pressures inside the chamber and the sample are shown in Figure 3-20b and c.

a) b) c)

Figure 3-20 Double wall triaxial chamber accessories and parts: a) Pneumatic actuator; b) and c) Step motors with different capacities

The LABGEO compressors shown in Figure 3-21 were considered as an alternative system for applying pressure to the chamber and sample. This is achieved by manually introducing pressurized air into cylinders filled with water where, these cylinders are equipped with a pressure regulator to ensure the maintenance of the required pressure level. Subsequently, a tube is connected from the cylinder to the triaxial cell or back pressures (to the chamber or the sample), facilitating the transmission of the regulated pressure to the desired location.

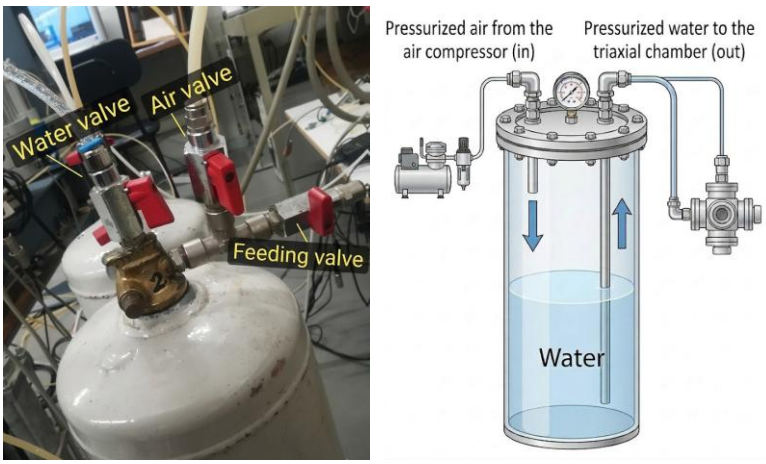

Figure 3-21 picture and schematic drawing of the Cell pressure/ Back pressure tank

Data acquisition unit which allows the acquisition of 16 channels and the control unit. Data acquisition is performed automatically, using a multichannel acquisition box. The software developed for this equipment is called SoilTest. Figure 3-22, shows the user interface of the SoilTest software, which was developed in the Labview environment.

Figure 3-23 shows schematic diagram by Costa (2009), explaining the apparatus main operational parts in addition to the connection between the data scan, labview application, the various motors and their connections with the chamber.

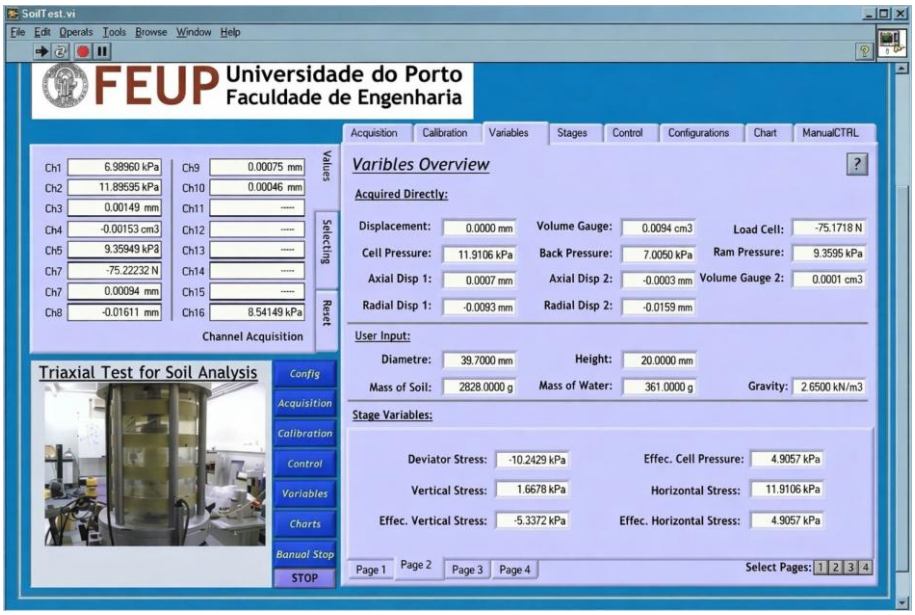

Figure 3-22 Presentation of the SoilTest software graphical interface

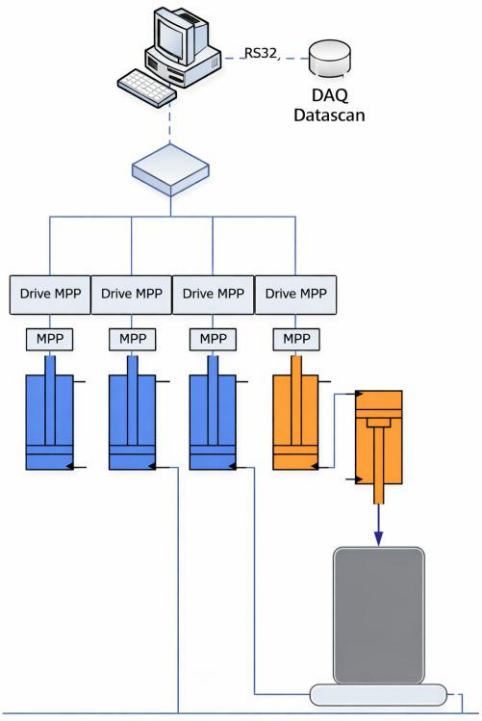

Figure 3-23 General scheme of the equipment's operation mode (Costa, 2009)

The base of the triaxial apparatus is a typical conventional triaxial chamber base. However, it includes an extra pressure transducer, which introduces and regulates pressures between the inner and outer chamber walls.

The equipment comprises two volume transducers, one controls and measures the changes in water volume within the inner chamber which supposed to be equivalent to the volumetric variation of the specimen in saturated conditions, while the other volume gauge measures the variation in water volume within the specimen itself. Both volume transducers are limited to water quantity of 100 cm^3. Furthermore, a 50mm length LVDT installed at the chamber top to measure the axial deformation during loading. Two high pressure air inlets porous stones (top and base caps) were fixed at the two ends of the specimens to enable pressurized air/ Water, equipped with T-shape Piezoelectric transducers bender elements BE, in the middle of the two porous stones for the seismic wave measurements as shown in Figure 3-24.

Figure 3-24 Porous stone base cap, equipped with T-shaped BE

The hydraulic movements of the Pneumatic actuator which transfer the load to the Load cell, were done through pressurizing a calibrated viscous oil to ensure smooth and controlled actuator movements as shown in Figure 3-25.

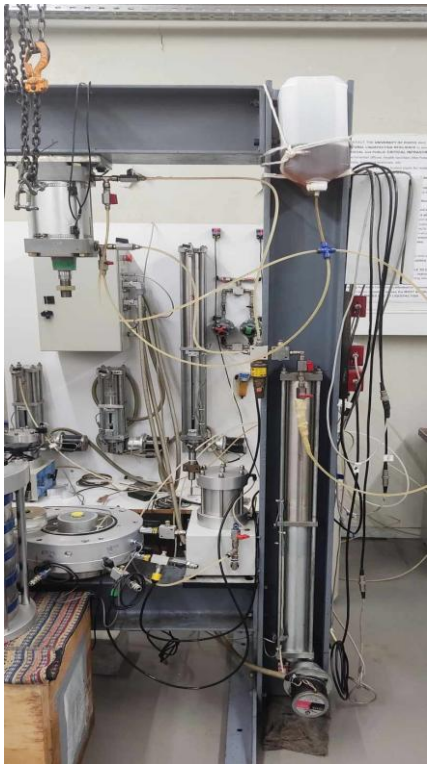

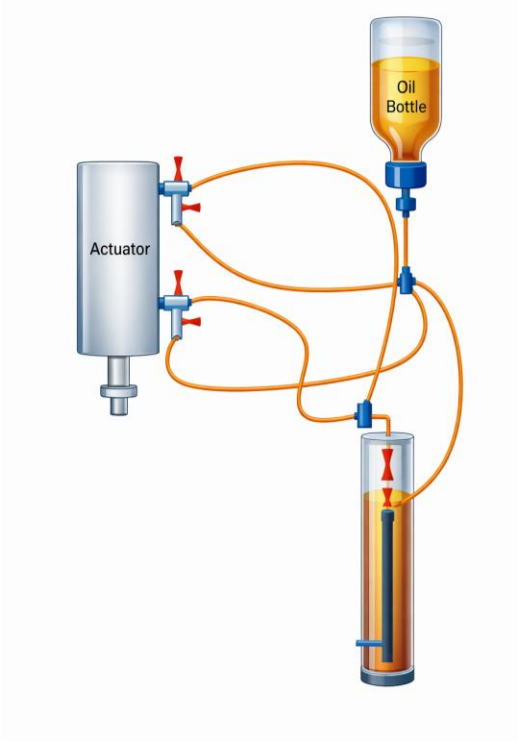

Figure 3-25 The mechanical connections of the pneumatic actuator

The chamber allows testing samples with a diameter of up to 100 mm and heights of 200mm. Seven undrained monotonic triaxial tests were prepared in loose to medium dense conditions using the dry air pluviation preparation method. Following preparation, samples were saturated then, isotopically consolidated and finally sheared at constant shearing rate of about 0.03 mm/min. The saturation, consolidation and shearing were done following same procedures used in the Tx series of tests with only few exceptions illustrated as follows;

The two volume gauges facilitates precise measurement of water quantity variations within the specimen during processes such as water flushing, as well as during the increase of the saturation degree by elevating back pressure values and during consolidation as well.

Furthermore, the degree of saturation was verified by calculating the Skempton's B-value, alongside measuring the compressional wave velocity using the BE method.

Also, BE enabled measuring shear wave velocity and assessing small strain stiffness of studied specimens. Finally, the additional volume gauge facilitated the prediction of the volume of occluded air bubbles during the shearing of partially saturated specimens.

These tests were done for assessing the shear strength resistance, particularly in terms of pore pressure build-up of the studied sands in both fully and partially saturated conditions.

The first four tests namely; UTx1,2,3 and 4 were done under fully saturated conditions. Full saturation was achieved by introducing CO_2 gas then increasing the Back pressure until 300 kPa while maintaining an effective stress of 10 kPa.

However, the last three tests were conducted under conditions of partial saturation, aiming to achieve uniform degrees of saturation across the three tests through not applying CO_2 gas and raising the back pressure up to only 100 kPa.

All saturated and partially saturated tests were consolidated under various mean confining pressures; 50, 100, and 200 kPa. Degree of saturation was assessed before consolidation by manually computing B value and measuring compressional wave velocity Vp using bender elements. In addition, to the conventional mass and weight calculations.

The properties of the tested specimens of NB sand are detailed in Table 3-7.

Table 3-7 Characteristics of the tested specimens in this apparatus (UTx)

Test #	CO_2	BP (kPa)	e_o	p'_o (kPa)	e_f (after test)	Sr (%)
UTx1	✓	300	0.738	50	0.722	100.0
UTx2	✓	300	0.772	200	0.717	100.0
UTx3	✓	300	0.755	100	0.732	100.0
UTx4	✓	300	0.775	100	0.757	100.0
UTx5	x	100	0.795	50	0.703	93.2
UTx6	x	100	0.780	200	0.692	93.5
UTx7	x	100	0.795	100	0.698	94.1

3.6. Cyclic triaxial tests

3.6.1. Brief description

This section outlines the methodology for evaluating the cyclic response and liquefaction resistance of NB and Huston sand soil through performing stress controlled cyclic triaxial tests on fully and partially saturated specimens. Various parameters were thoroughly investigated, including the number of cycles needed to trigger liquefaction, the relative density and pore pressure build-up. In addition, the influence of degree of saturation, confining stress, amplitude of the earthquake CSR on the seismic response of saturated and partially saturated soils will be discovered.

Cyclic response and liquefaction resistance will be explored using the cyclic triaxial test apparatus, which basically consists of a conventional triaxial cell, loading system and, measuring tools. Figure 3-26 shows the cyclic triaxial apparatus with the testing tools used in LabGeo, FEUP.

Figure 3-26 Cyclic triaxial apparatus in LabGeo, FEUP

3.6.2. Cyclic triaxial apparatus setup

Cyclic Loading

The cyclic loading was applied by a servo-actuator composed of a hydraulic piston with displacement and load transducers, which allows varying the loading frequency between 0.001 and 2 Hz. The cyclic loading frequency adopted in the current set of tests was 0.1Hz. This hydraulic system is powered by an oil pump, which allows applying a maximum load of 10 kN.

Cell body and frame

The main frame is made of anti-corrosive metal, while the cell body is a cylindrical acrylic to allow monitoring and capturing photos of the samples during testing stages. In addition, the cell is reinforced with diagonal fiberglass to resist high radial stresses.

The cell base has three main pressure transducers equipped with valves for applying and regulating pressure and drainage inside the chamber and the sample.

The load is transferred from the loading piston to the sample through the top loading cap. To ensure a robust contact between the piston and the sample's top cap during loading, a rubber V-ring is attached to the top loading cap as shown in Figure 3-27.

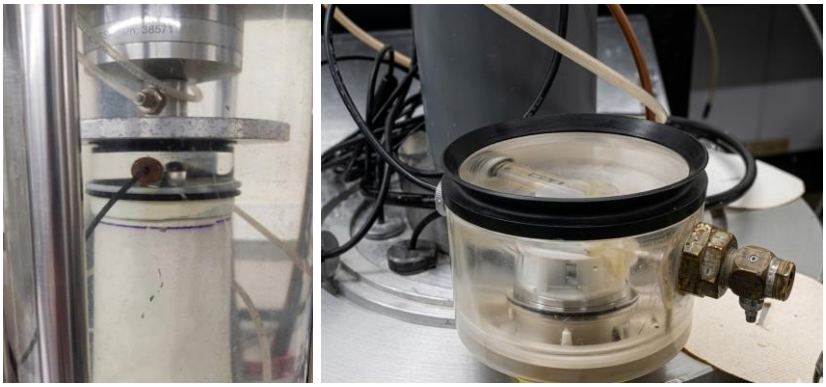

Figure 3-27 Rubber V-ring utilized in the top cap

Measuring tools and instrumentations

Piezoelectric transducers BEs were installed on both top and base loading caps to measure compressional and shear wave velocities during testing, Figure 3-28a.

In addition, four Hall-Effect transducers were used to measure axial and radial strains during testing phases. They were carefully glued on the sample's membrane to accurately monitor the volumetric strain change during the test phases. Each of them, whether axial or radial, comprises two primary magnetic metallic plates sliding against each other. These plates are glued to the soil specimen membrane to measure strain by converting the measured magnetic flux. This method enables precise measurement of the evolution of volumetric strain. Figure 3-28b shows the axial and radial HE glued on the specimen's membrane.

a) b)

Figure 3-28 a) Bender elements attached to the top and bottom loading caps; b) The axial and radial HE glued and well fixed on the specimen membrane

Cell pressure CP gauge for measuring pressure inside the cell. Back pressure and Pore pressure gauges for measuring pressure (inside specimens) at the top and bottom drainage lines of specimens. Figure 3-29a shows the volume gauge used to measure the volume change of the specimens during the testing phases by measuring the quantity of water that flows in and out of specimens.

A 10 kN capacity load cell is utilized for measuring the vertical (deviator) load. A Linear Variable Differential Transformer LVDT shown in Figure 3-29b is attached externally to the load piston to measure the piston movement and consequently the specimen axial strain during shearing. The maximum range of the LVDT is 50 mm, which is enough to cover the targeted axial strain.

Finally, a pressure controller was used to introduce and control pressures (Cell and back pressures), Figure 3-29c. The software used for test control and data acquisition was DynaTester V2.0 for cyclic triaxial tests.

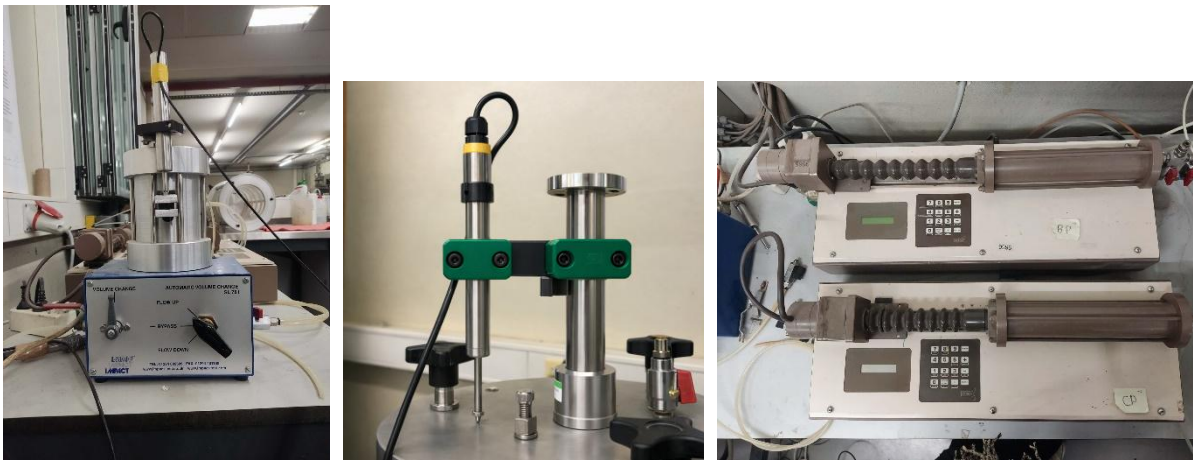

a) b) c)

Figure 3-29 a) Automatic volume change gauge; b) Linear Variable Differential Transformer LVDT and; c) Pressure/Volume Controller

Saturation process

During cyclic triaxial tests, full saturation condition has been achieved by applying carbon dioxide gas CO_2 from the specimen's bottom drainage line (back pressure inlet) to replace the air voids as CO_2 is known to be less compressible than air, forcing the soil specimen's entrapped air bubbles to flow upward and get out through a tube connected to the top cap (pore pressure valve) then, to a 1.5 l bottle full of water inverted into a bucket. Hence, air bubbles started to get out from the sample and bubbling in the inverted bottle to replace the water. This process was done under low and controllable CO_2 pressure around 2 to 3 kPa.

After that, water flushing process started through introducing water from the base cap (back pressure valve), forcing the CO_2 gas to leave the top cap drainage to a tube ending in an empty measuring cup to account for the quantity of water get out of the sample.

During water flushing, the cell pressure CP was set to 20 kPa, and the back pressure BP to 10 kPa, while the pore pressure PP was maintained at atmospheric pressure. This resulted in an effective confining pressure of 10 kPa, which facilitated water flow. Water flushing, would be stopped whenever the quantity of water in the cup reaches twice the sample voids volume.

To ensure dissolving occluded air and CO_2 bubbles, BP have been increased gradually to 300 kPa, while keeping a mean effective stress of 10 kPa.

Assessing the saturation degree precisely before consolidating and shearing the specimen is very fundamental because incorrectly assessing the degree of saturation could result in inaccurate soil resistance. Therefore, three techniques have been adopted in cyclic triaxial

tests to confirm the saturation level. These techniques involve measuring compressional wave velocity Vp using bender elements BE and manually calculating Skempton's number B. Once the targeted degree of saturation is confirmed, isotropic consolidation followed by cyclic loading can be applied. Furthermore, Sr was precisely computed by the end of each test using the volumetric strains and hence void ratio obtained from the Hall-Effect transducers HE using the basic equation (3-4).

Where; S_f is the degree of saturation before shearing, w_f is the water content by the end of the test. Usually, samples were carefully disassembled and dried to compute precisely the amount of water inside the sample, e_f is the final void ratio which was calculated using the volumetric strains obtained by the HE.

$$S_f = W_f * G_s / e_f \quad (3\text{-}4)$$

Full saturation was confirmed whenever the compressional wave velocity Vp reaches approximately about 1500 m/s, typical for fluid-saturated granular media. Further confirmation was achieved when Skempton's parameter B approached unity, indicating that increases in cell pressure closely matched increases in undrained pore pressure.

Partially saturation with varying degrees of saturation were achieved through a trial-and-error approach, which involved managing CO_2 gas application in addition to adjusting the elevated back pressure during the saturation process.

Therefore, numerous preliminary trials were conducted to evaluate the effect of decreasing the back pressure BP to different values with and without CO_2 gas, in order to confirm the resulting degrees of saturation before performing the actual shearing.

By the end of fully and partially saturated tests, specimens were carefully weighted then over dried in the oven. The weight of specimens before and after drying was calculated to assess the final water content and void ratio.

Cyclic Triaxial testing plan

In the present study, a systematic experimental investigation has been carried out to understand liquefaction resistance of fully and partially saturated sands. The range of degrees of saturation adopted in the present study varies from about 86% up to full saturation, as this range represents the range of partial saturation where matric suction can be neglected based on the SWCC of both soils.

A total of 41 undrained cyclic triaxial tests have been conducted on reconstituted NB soil specimens, in addition to 6 tests for Hostun sand using the dry air pluviation preparation method.

Loose to medium dense sand specimens have been prepared and isotopically consolidated at the same effective confining pressures of 100 kPa. Then, samples were subjected to cyclic loading (compression and extension) at various cyclic shear stress ratio CSR to evaluate of the liquefaction resistance. The stress controlled undrained cyclic triaxial tests have been conducted with a sinusoidal loading in addition at a low loading frequency of 0.1 Hz.

$$CSR_{cTx} = \frac{q}{2P_0'} \quad (3\text{-}5)$$

The diameter of all triaxial test specimens was about 70 mm while, the height of the tested specimens was around 140 mm. The characteristics of all conducted tests are summarized in Table 3-9. Where, Test # is the test identification, CO_2 indicates whether CO_2 gas was used or not, BP is the applied back pressure value during the saturation process, e_0 and Dr_o, are the void ratio and relative density of specimens after the preparation, respectively whereas, Dr_f and Sr_f% the relative density and degree of saturation before shearing, respectively. CSR is the cyclic stress ratio, N_{liq} represents the number of cycles required to reach r_u = 1.0. In some tests, this condition coincided with the development of 5% double-amplitude axial strain.

Cyclic triaxial tests for Hostun sand were also performed for fully and partially saturated conditions. The details are presented in Table 3-8.

Table 3-8 Characteristics of conducted cyclic triaxial tests for Hostun sand HN31

Test#	CO_2	BP (kPa)	e_o	Dr_o(%)	p'_0 (kPa)	Dr_f(%)	Sr_f(%)	CSR	N_L
Hn-CTx1	✓	300	0.811	52.38	100	55	100	0.26	2
Hn-CTx2	✓	300	0.818	51	100	52.6	100	0.177	8
Hn-CTx3	✓	300	0.827	48.01	100	50.1	100	0.11	150
Hn-CTx4	x	100	0.825	48.83	100	50.5	86	0.312	1
Hn-CTx5	x	100	0.812	52.17	100	53.7	86	0.24	34
Hn-CTx6	x	100	0.819	50.17	100	51.05	86	0.232	98

Table 3-9 Characteristics of conducted cyclic triaxial tests for NB sand

Test #	CO_2	BP (kPa)	e_o	Dr_o(%)	p'_0 (kPa)	Dr_f(%)	Sr_f(%)	CSR	N_L
CTx1	✓	300	0.795	22.857	100	41.73	100.00	0.130	11.00
CTx2	✓	300	0.791	23.917	100	46.73	100.00	0.122	39.00
CTx3	✓	300	0.811	17.916	100	38.43	100.00	0.132	10.98
CTx4	✓	300	0.797	22.185	100	44.28	100.00	0.139	8.98
CTx5	✓	300	0.772	29.556	100	44.37	100.00	0.140	12.08
CTx6	✓	300	0.795	22.829	100	39.48	100.00	0.108	22.10
CTx7	✓	300	0.789	24.54	100	43.31	100.00	0.102	63.46
CTx8	✓	100	0.794	23.14	100	28.48	96.00	0.126	16.00
CTx9	✓	300	0.804	20.06	100	37.36	100.00	0.142	4,00
CTx10	✓	300	0.795	22.76	100	41.19	100.00	0.116	21.00
CTx11	✓	300	0.809	18.50	100	34.75	100.00	0.099	40.70
CTx12	✓	300	0.793	23.36	100	38.54	100.00	0.127	9.00
CTx13	✓	300	0.788	24.89	100	38.47	100.00	0.082	188.00
CTx14	✓	100	0.801	20.85	100	28.9	97.04	0.122	40.00
CTx15	✓	100	0.784	26.21	100	31.52	97.58	0.111	25.98
CTx16	✓	100	0.816	16.30	100	23.75	93.86	0.120	29.98
CTx17	✓	100	0.806	19.44	100	26.67	95.13	0.094	65.76
CTx18	✓	150	0.801	20.96	100	26.9	93.32	0.137	12.00
CTx19	✓	120	0.814	16.93	100	25.44	95.79	0.130	15.00
CTx20	✓	120	0.791	23.87	100	27.73	95.52	0.131	7.00
CTx21	✓	100	0.806	19.42	100	27.52	96.36	0.123	13.10
CTx22	x	100	0.790	24.23	100	30.05	89.92	0.137	125.00(Noliq)
CTx23	x	200	0.786	25.41	100	33.39	94.20	0.147	14.00
CTx24	✓	50	0.783	26.28	100	33.84	95.47	0.145	10.00
CTx25	✓	100	0.779	27.58	100	34.95	94.60	0.138	10.00
CTx26	✓	100	0.782	26.58	100	34.72	97.67	0.129	7.00
CTx27	x	100	0.813	17.39	100	25.85	90.18	0.133	127.00
CTx28	x	100	0.809	18.47	100	25.76	88.44	0.137	107.00
CTx29	x	150	0.813	17.61	100	27.5	92.93	0.139	32.60
CTx30	x	300	0.823	15.00	100	24.3	94.95	0.147	20.00
CTx31	x	100	0.777	28.47	100	36.3	89.11	0.145	114.00
CTx32	x	100	0.760	33.26	100	41.76	90.10	0.171	55.00
CTx33	✓	300	0.783	26.41	100	37.98	100.00	0.095	99.10
CTx34	x	100	0.797	22.23	100	30.8	90.02	0.175	12.00
CTx35	x	100	0.767	31.23	100	38.1	89.55	0.195	8.00
CTx36	x	100	0.782	26.67	100	34.85	90.50	0.122	315.00
CTx37	x	50	0.785	26.49	100	32.79	86.98	0.280	1.00
CTx38	x	50	0.767	31.27	100	34.13	85.44	0.180	170.00
CTx39	x	50	0.778	27.90	100	35.86	85.64	0.221	12.00
CTx40	x	50	0.786	25.5	100	34.60	85.70	0.216	19.00
CTx41	x	50	0.760	33.33	100	37.91	86.65	0.215	21.00
CTx42	x	50	0.781	28.69	100	34.58	86.26	0.158	300(Noliq)

3.7. Physical modelling (centrifuge modelling)

3.7.1. Main concept and objective

In this section, centrifuge modelling procedures and equipment will be presented. The physical model in centrifuge testing aims to evaluate the effectiveness of induced partial saturation IPS through air injection as a liquefaction mitigation method. The studied soil is Hostun sand HN31.

Three different models of centrifuge testing have been carried out. The main objective of this physical modelling is to assess the efficacy of air injection in preventing liquefaction-induced damage, with an emphasis on the excess pore pressure generation, and dissipation, settlement and shaking accelerations. Moreover, dissipated energy and stiffness characteristics of fully and partially saturated soils will be explained in detail in the subsequent sections.

3.7.2. Centrifuge testing and setup

3.7.2.1. Introduction

Conducting full-scale prototypes is both costly and time-consuming in addition, small-scale 1-g physical modelling techniques behavior is expected to be the same as the response of its prototype only for linear systems furthermore, the stress-strain characteristics of real soils are highly non-linear. That made a big dilemma to the geotechnical community.

The principle of centrifuge modelling is to expose scaled-down models to an increased gravitational field and accomplish the stress and strain similarities at homologous points in the soil between model and prototype, which is the simplified version of the full-scale system (Zeybek & Hall, 2017).

The centrifuge is a large rotating drum that can spin at high speeds. The model is installed on the centrifuge arm, and as the centrifuge rotates, it generates increased gravitational forces on the model, simulating higher gravitational acceleration therefore, the model will be subjected to “N” times of the gravitational earth N*g.

3.7.2.2. Scaling factors

Centrifuge modelling adopts scaling laws to ensure that the model response is representative of the corresponding full-scale prototype behavior. Different quantities, including dimensions, stresses, accelerations, time, and seepage-related parameters, are scaled according to the applied centrifugal acceleration. Table 3-10 summarizes the main scaling factors for a model tested at an acceleration level of Ng. In the present study, a viscous pore fluid was used, with viscosity selected to satisfy the seepage scaling requirements. Therefore, the seepage/consolidation time scale of 1/N is applicable.

Table 3-10 Scaling laws of main parameters in centrifuge modelling (Zeybek & Hall, 2017)

Parameter	Scale factor: Model/Prototype
Acceleration	N
Linear dimension	1/N
Mass	$1/N^3$
Stress	1
Strain	1
Force	$1/N^2$
Velocity (seepage)	1*
Velocity (dynamic)	1
Time (seepage)	1/N*
Time (dynamic)	1/N
Frequency	N

*Valid for models using a viscous pore fluid with viscosity approximately N times that of the prototype fluid.

3.7.2.3. Centrifuge equipment main parts

The Turner Beam Centrifuge

The Turner beam centrifuge at Cambridge University's Schofield Centre was used for the dynamic centrifuge tests performed in this study. The centrifuge capacity is 1000 kg with a spinning of 150 g acceleration.

Figure 3-30 and Figure 3-31 show a schematic and real photo of the Turner beam centrifuge at the Scofield center, University of Cambridge.

The centrifuge has a 10 meters arm, where the counterweight mass is loaded on the red end, and the model is positioned on the blue end.

The top surface of the swinging platforms has a radius of 4.125 meters when it is swung up. The centrifuge's central spindle is equipped with electrical and hydraulic slip rings, facilitating the transmission of electric power, fiber optics, water, and air lines to the model package. These slip rings also allow for data connections between the control room, computers on the beam, and the model package. Additional information on the Turner beam centrifuge can be found in Madabhushi (2017).

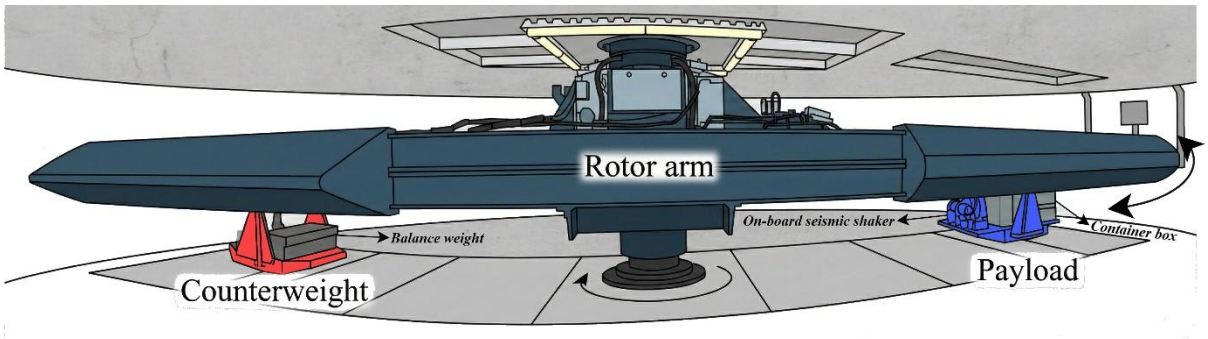

Figure 3-30 schematic of the Turner beam centrifuge at the University of Cambridge.

Figure 3-31 Turner beam centrifuge at the University of Cambridge.

The servo-hydraulic earthquake shaker

In this study, dynamic centrifuge tests were performed using the servo-hydraulic earthquake shaker system at the Schofield Centre, University of Cambridge as shown in Figure 3-32. The actuator imposed controlled base shaking on the model package. For the present tests, sinusoidal input motions with prescribed frequency, amplitude, and duration were applied. The actual input motion was recorded by the base accelerometer and used as the reference motion in the subsequent dynamic response analysis.

Figure 3-32 Servo-hydraulic earthquake shaker system used for dynamic centrifuge testing at the Schofield Centre.

Model Containers

A stiff container, shown in Figure 3-33, with three metal sides and a transparent Perspex window was used as a model container. The transparent window allowed visual inspection of the model during preparation and testing, including checking the soil surface, water level, and general deformation pattern during shaking. Due to the high stiffness of this type of model container, boundary effects may occur due to its rigid end walls and affect the model response, particularly when liquefaction is reached (Zeybek & Hall, 2017). However, in the present study, for free-field conditions and centerline analysis, this effect may be considered negligible.

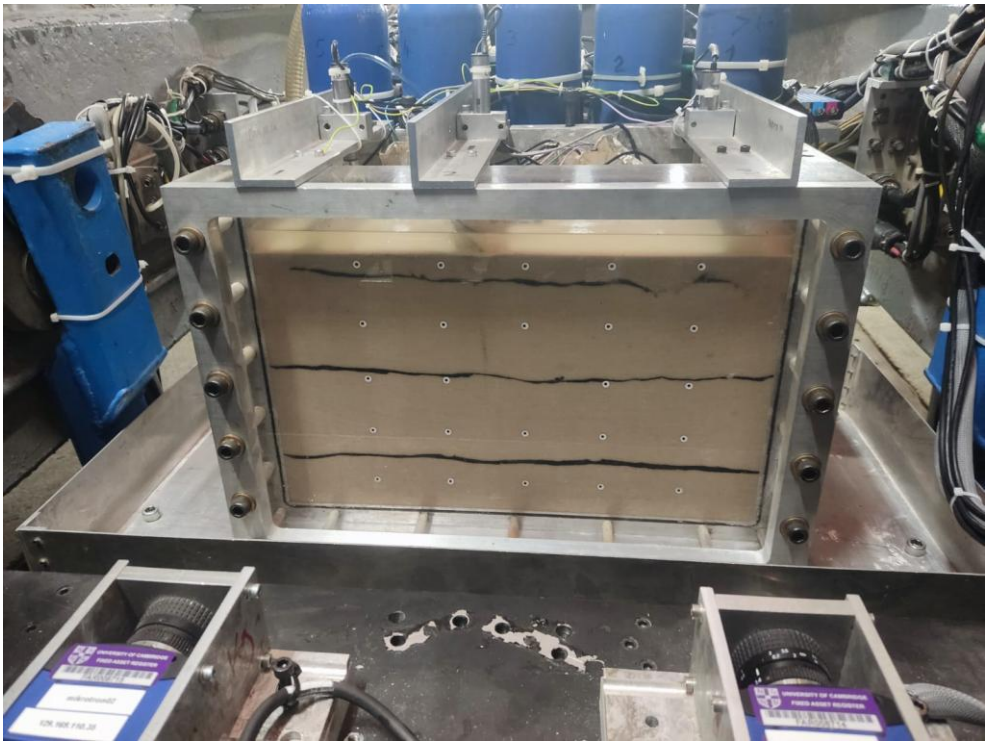

Figure 3-33 The model box after preparation and instrumentation placement

Based on the testing objectives, numerous and diverse instruments have been selected to monitor and control the soil model behavior and parameters during the centrifuge testing.

Pore Pressure Transducers (PPTs)

Pore Pressure Transducers, or PPTs, were used to measure pore fluid pressures, from which hydrostatic and excess pore pressures can be derived. Their dimensions were 11.4 mm in length and 6.4 mm in diameter, and these were isolated from direct contact with soil by covering the tip with sintered bronze porous stone. PPTs were calibrated before testing and placed at specific locations in the model, perpendicular to the shaking direction.

Piezoelectric Accelerometers

Pre-calibrated piezoelectric accelerometers were used to record the seismic acceleration at different locations in the soil model. The accelerometers were placed with the same orientation inside the model, parallel to the shaking direction

Linear Variable Displacement Transducers (LVDTs)

Linear Variable Displacement Transducers LVDTs were used to record the cumulative settlement at the top surface. LVDTs were calibrated and installed at different locations on the soil surface used. In order to accurately measure the fluid level variation, which is a fundamental aspect for monitoring saturation and air injection, one of the LVDTs (the middle one) was sitting on a Styrofoam disc to remain floating throughout the tests. Figure 3-34 shows the LVDTs including the floating LVDT.

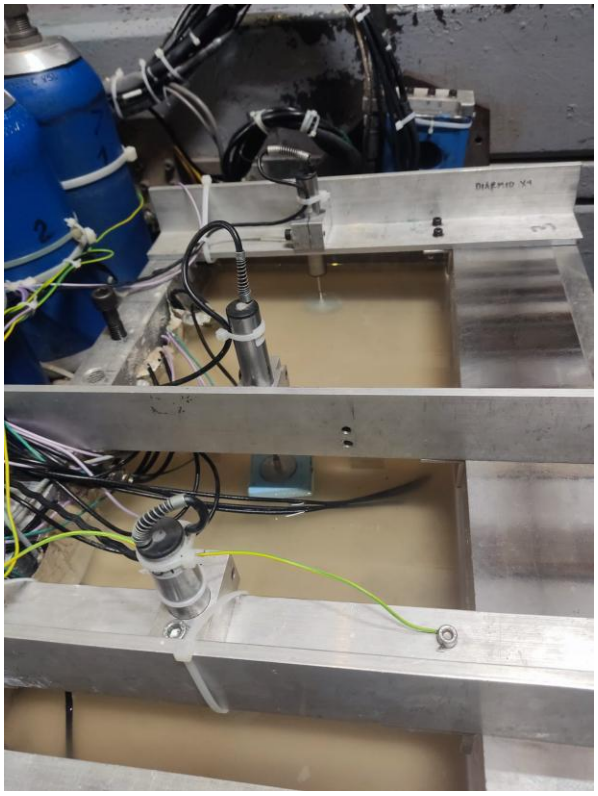

Figure 3-34 The LVDTs including the floating (middle) LVDT

Bender elements (BE)

Three pairs of BE, originally manufactured at LabGEO-FEUP, were installed and fixed to an acrylic frame, and embedded within the soil model, as shown in Figure 3-36. These allow measuring the compressional and shear wave velocities during testing, from which soil parameters including stiffness and degree of saturation can be assessed.

A holistic system of compatible devices has been acquired and well connected for precisely measuring seismic wave velocities, consisting of a function generator (TTi TGF4042) which generates the electrical signal that excites the transmitter BE, in addition to a oscilloscope (PicoScope 4000 series) and a computer with PicoScope software, for signal acquisition.

Figure 3-35(a) and (b) show the function generator and Picoscope utilized in the centrifuge modelling tests. Different frequencies were applied as the input signals which ranged from 1 to 100 kHz to alternate between shear and compressional wave velocities

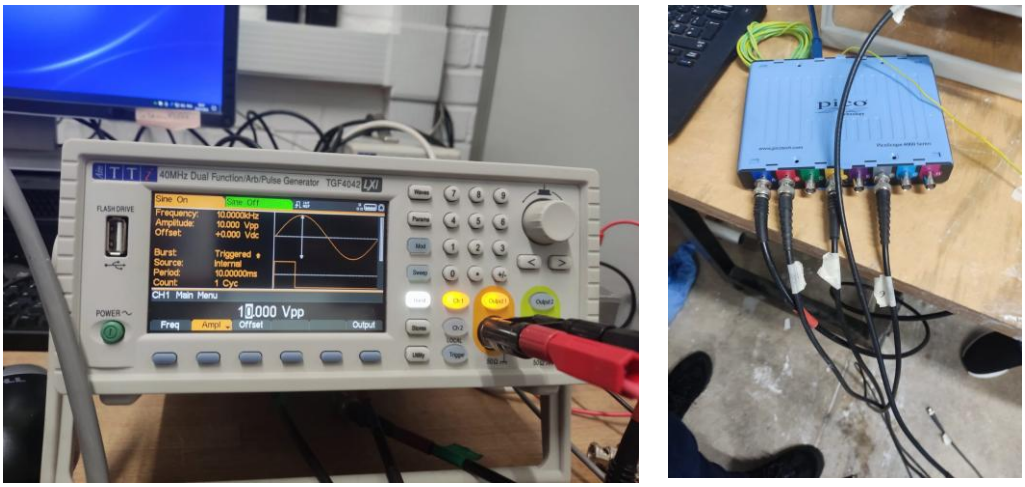

a) b)

Figure 3-35 BE measuring components a) The function generator; b) The PicoScope

Figure 3-36 BE installed in the acrylic frame

One of the difficulties in bender element testing, particularly in the centrifuge testing, refers to electrical noise, so special attention and care was given to properly insulating and grounding the BE cables.

Particle image velocimetry, PIV

Particle Image Velocimetry (PIV) was used as a complementary visual tool to capture images before and after air injection and earthquake shaking. The images were used to observe the general deformation pattern and surface settlement near the transparent Perspex wall. Since the observations were made at the model boundary, possible wall effects cannot be fully excluded; therefore, PIV results were used mainly for qualitative interpretation, while quantitative settlement assessment was based on the LVDT measurements.

Data Acquisition

The centrifuge system includes a data acquisition box for several channels which enables recording data channels accurately and simultaneously, which runs on DASYLab software.

Testing stages

The setup of the centrifuge model began with sand pluviation into the model container, installation of the required instrumentation, and overnight saturation under vacuum. After sample preparation, the model was weighed for balance calculations. The counterweight was then attached to one end of the centrifuge rotor arm, while the servo-hydraulic earthquake shaker system and saturated soil model were installed at the opposite end.

The testing stages were as follows:

- Sample preparation (sand pouring, instrumentation, saturation)
- Balance calculation
- Installation in the centrifuge
- Swing up
- Achieving 60g acceleration
- EQ shaking
- Air injection

These stages will be briefly described as follows.

3.7.2.4. Sample preparation (sand pouring, instrumentation, saturation)

The centrifuge model testing begins with meticulously pouring and distributing the soil into the model to ensure even compaction and homogenous layering. To achieve the required relative density, samples were prepared using the air-pluviation method through controlling flow rate and the fall height of the automatic sand pourer, as shown in the two pictures revealed in Figure 3-37. The targeted preparation relative densities were about 45%.

Figure 3-37 The automatic sand pourer during pluviation

Sand pouring was done alternatively with placing the instrumentations in the pre-defined depths and locations. Figure 3-38(a) shows the installation and positioning a layer of the

instrumentations inside the soil box during the sand pouring, while Figure 3-38(b) shows the positioning of the air injector on the model base.

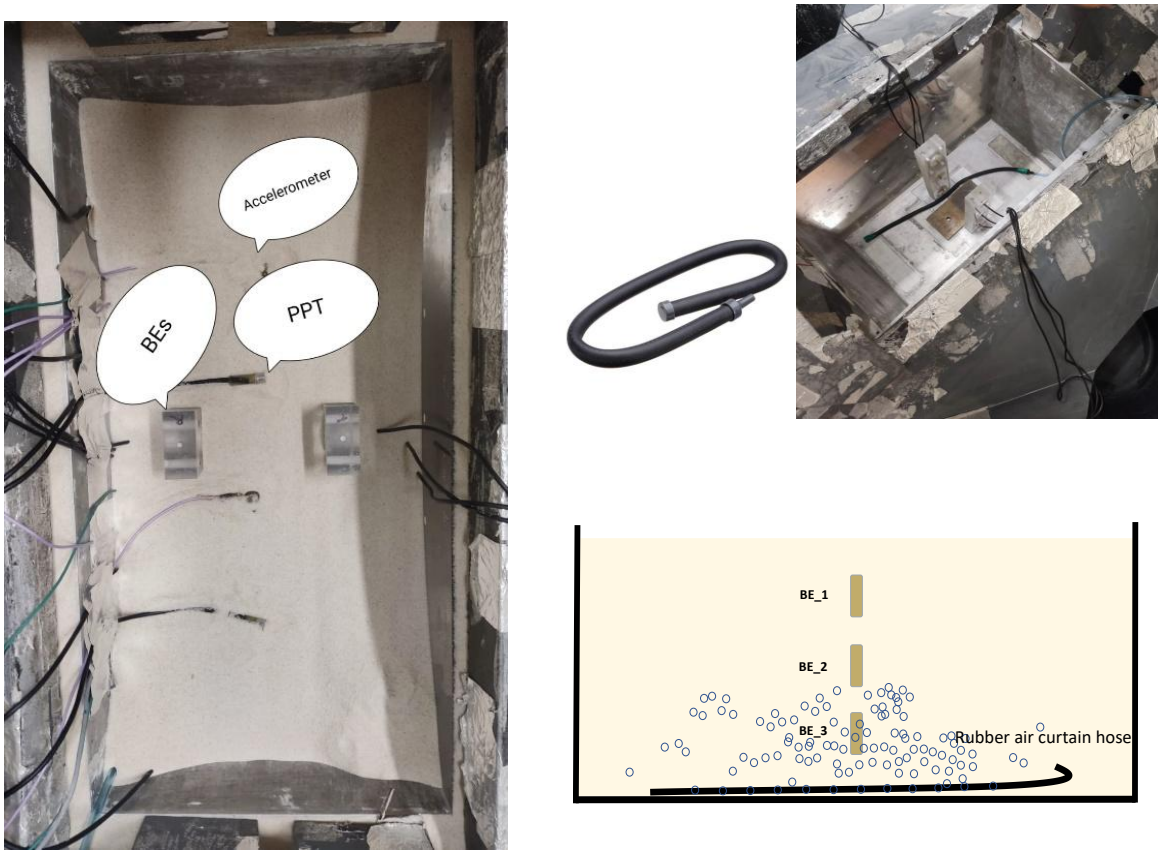

a) b)

Figure 3-38 a) The arrangement of the instrumentation inside the soil box; b) Rubber air curtain hose

After the soil was poured and the necessary instrumentation installed, the model box was subjected to the saturation process. Full saturation condition has been achieved by applying -90 kPa vacuum pressure then carbon dioxide CO_2 was introduced to replace air pores. After that, soil was saturated through percolating viscous fluid from the base. Hydroxy-Propyl Methyl Cellulose HPMC was selected as the viscous pore fluid for the centrifuge tests' saturation process with a viscosity of N (g-level) times that of water. This viscosity was selected to satisfy the centrifuge seepage scaling requirement; by increasing the pore-fluid viscosity by a factor of N, the seepage time scale becomes compatible with the dynamic time scale of 1/N.

To provide the required solution, boiling water was added to dry METHOCEL F50 Food Grade HPMC to minimize the dissolving time.

Stewart et al. (1998) employed an empirical equation (3-6), which is also utilized in this study, to ascertain the quantity of HPMC powder required to achieve the desired viscosities (Zeybek & Hall, 2017).

This formula allows determining the concentration of solution where C is the mass percentage of the total solution given a kinematic viscosity at a temperature of 20° C (υ_{20}).

$$\upsilon_{20} = 6.92 * C^{2.54} \quad (3\text{-}6)$$

Required viscosity has been confirmed through checking the attained fluid viscosity in a viscosimeter, so decision for further mixing time or move to the next step would be made based on the achieved viscosity.

The common method of assessing saturation levels using mass and volume measurements can have inherent inaccuracies. Therefore, in addition to this method, compressional wave velocity measurements via bender elements BE have been employed as a complementary approach, offering a more accurate evaluation of the soil's degree of saturation. Figure 3-39 shows the saturation process of the model box.

Figure 3-39 Saturation process of the model box

3.7.2.5. Balance calculations

The cameras and LVDTs were then installed, the junction boxes and the PicoScope were positioned to accurately assess the total weight of the model (Figure 3-40). Subsequently, calculations were performed to determine the necessary counterweight, ensuring the correct moment of inertia and the safe operation of the model during the centrifuge flight.

Figure 3-41 shows a schematic elevation view of the centrifuge model #1 and its instrumentation (Prototype Scale).

Figure 3-40 Weighting the model for the balance calculations

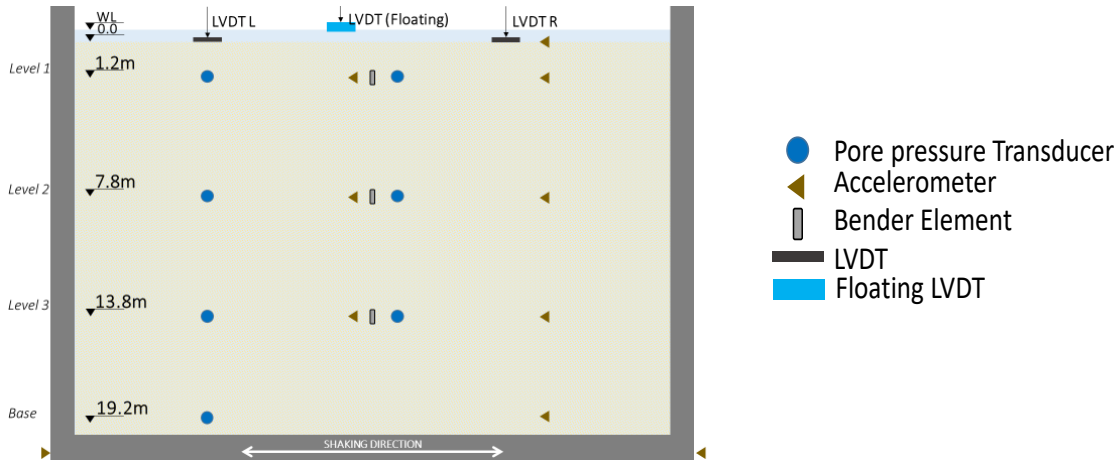

Figure 3-41 An elevation view of the centrifuge model#1 and its instrumentation (Prototype Scale)

3.7.2.6. Model installation in the centrifuge

The model was then installed and positioned on the blue end of the centrifuge arm, while the pre-calculated counterweight was placed on the red end.

Swing up to the 60g acceleration

After that, checking if the instrumentations are powered and connected to the data acquisition system including the air injection system and cameras. Then, the model was swing up to firstly a centrifugal acceleration of 10 g then,20,40 and 60g before applying the shaking excitation. PPTs, LVDTs, shear and compressional wave velocities and images were recorded during the swing up.

EQ shaking

At 60g, earthquake shaking and air injection were introduced according to specific pre-planned procedures adopted for each centrifuge model and its objectives. Minor adjustments were made between models, including variations in earthquake load (excitation shake) amplitudes and the timing of air injection. These adjustments enable more comprehensive and robust analysis by accommodating different test conditions and enhancing the versatility of the experimental setup. The specifics of these variations and their impact on the analysis will be explained and discussed in detail in the final thesis.

For example, in Model M1, the fully saturated soil was first subjected to shaking event EQ1.1, with a model frequency of 60 Hz, corresponding to 1 Hz in prototype scale at N=60. The input motion consisted of 15 cycles with an amplitude of 1.5 V and was applied parallel to the long side of the model using the SAM earthquake actuator. Air was then injected to induce partial saturation before the second shaking event, EQ1.2, which had the same frequency, amplitude, and number of cycles as EQ1.1. A further air injection was applied before the third shaking event, EQ1.3, which had the same frequency and amplitude but was extended to 30 cycles. Images and BE measurements were taken before and after the shaking events. The full testing sequences are presented in Chapter 6.

3.7.2.7. Air injection

Induced partial saturation using air injection is a technique used to decrease the degree of saturation through introducing air bubbles to the saturated soil, the presence of those bubbles increases the compressibility of the pore fluid that fills the pores between soil and hence increase the soil resistance to liquefaction.

Air injection was applied through introducing highly compressed air into the soil model using an air diffuser (Rubber air curtain hose) placed diagonally on the center-bottom of the model containers, which in turn reduces the saturation degree. Rubber air curtain hose with many tiny openings of about 0.5 mm diameter and 5 mm spacing, found to be optimal for this function (Zeybek & Hall, 2017). Many experiments were conducted in Perspex box before starting the centrifuge modelling, just to check the optimal air injection pressure and the to avoid bubbles coalescence and non-homogeneity. The pressure of the injected air was controlled through a pressure controller.

As revealed in Zeybek & Hall (2017), the injected air originates from the main source in the laboratory and then passes through a sequence of components. It begins with the flow sensor, followed by the adjustable air flow regulator, the pressure transducer, and the solenoid valves. From there, it moves to the air diffuser which is located at the bottom of the soil beds, spanning the full diagonal of the model boxes to inject air into the saturated soils (Figure 3-42). Images and BE measurements were captured before and after the applied air injection. The floating LVDT was used to monitor (start/stop) the air injection process, as it recorded negative settlements (upward movement) during the injection process.

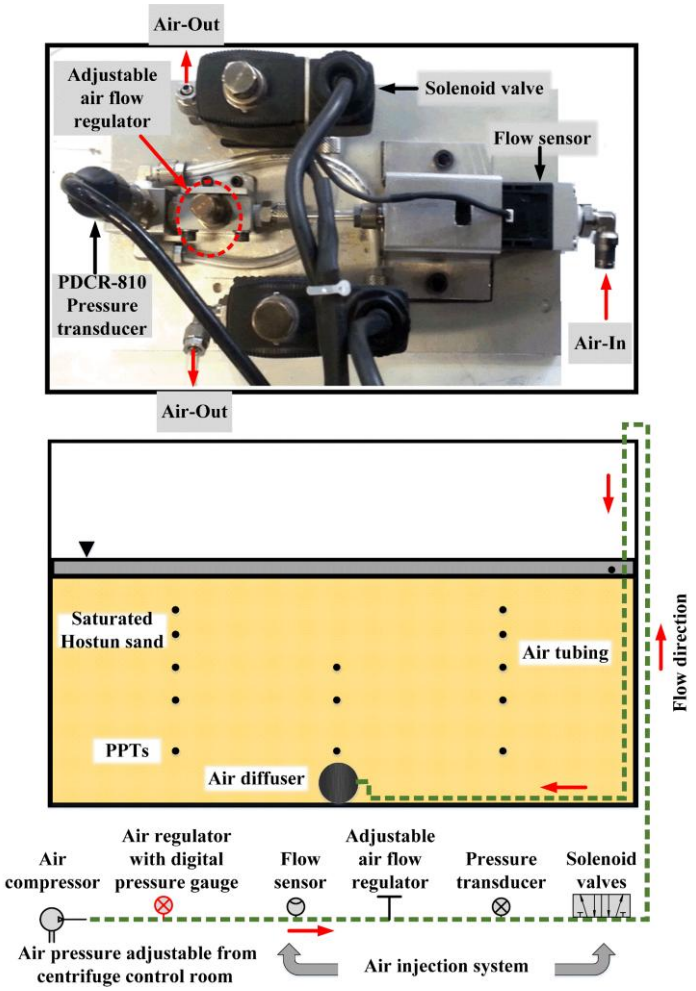

Figure 3-42 A view and sketch of the air injection control system adopted from (Zeybek & Hall, 2017)

Swing down

By the end of each test, centrifuge was then swung down gradually in 10g increments until it stops besides recording the final values of all the instrumentation. Python software was used to process the electrical voltage values resulting from the data acquisition system to clean the data, do the necessary calculations such as calibrations, scaling, analysis and produce the plots.

3.8. Remarks

In this chapter, the physical properties, material description and experimental methods adopted in this study are presented in detail. The soils used in the subsequent chapters are described, together with the rationale for their selection: NB sand, a local Portuguese sand with historical evidence of liquefaction and a potentially high susceptibility to future liquefaction, and Hostun sand HN31, a well-established reference material widely investigated within the geotechnical engineering community. The physical characterization of both sands is reported, including the procedures used to determine the key index properties. These properties are fundamental for the remainder of the thesis, such as the determination of the maximum and minimum void ratios, which underpin the calculation of

relative density for all advanced testing programs presented in later chapters. The experimental procedures for monotonic and cyclic triaxial testing are then described, including specimen preparation, saturation and partial saturation procedures, measurement and control of the main testing parameters, and the adopted instrumentation; representative photographs are provided to support the description. Finally, the centrifuge modelling program and testing procedures are outlined. Overall, this chapter establishes the methodological framework and documents the quality-control measures implemented to ensure accuracy, consistency, and repeatability across the different experimental campaigns reported in the thesis.

4. Monotonic triaxial tests: results and analyses

4.1. Geomechanical properties of NB sand (Tx)

4.1.1. Stress-strain results

This set of tests namely Tx aims to characterize the stress-strain behavior and critical state parameters of NB sand.

The plots illustrated in Figure 4-1, describe the shear characteristics resulting plots, as obtained through the analysis of the conducted undrained monotonic triaxial tests Tx where; (a) represents stress-strain path q-ε_a, (b) illustrates shear stress path q-p`, Critical state line and, phase transformation points. (c) depicts pore water pressure build-up with the axial strain Δu-ε_a and finally, (d) shows void ratio variation with the confining stress e- p´, defining the critical state CS points.

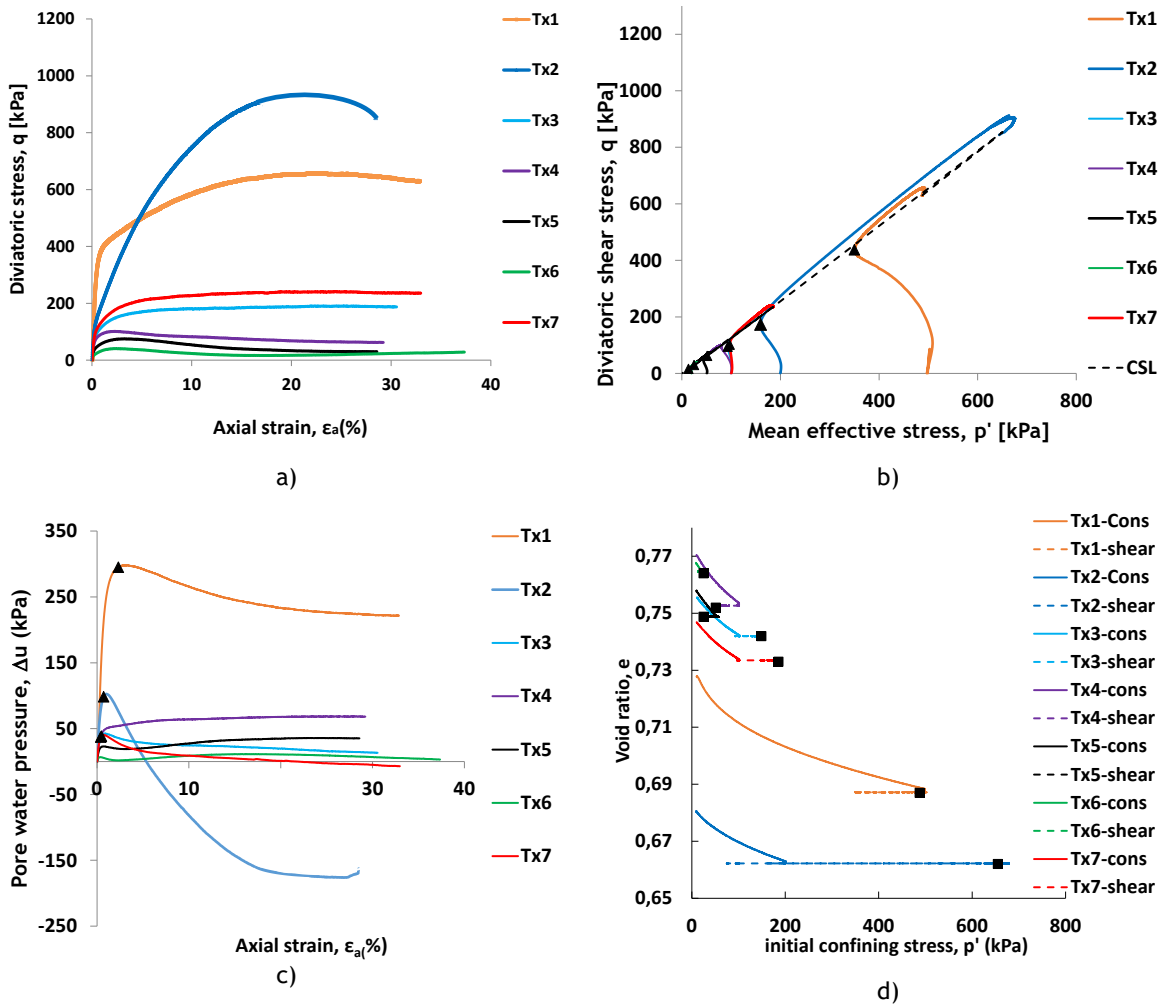

Figure 4-1 Typical monotonic triaxial test plots of NB-sand: a) stress-strain behavior; b) stress path with CSL in the q: p´ space; c) pore-pressure change; d) CS points in the e: p´ space.

The analysis of this set of tests was done according to the undrained monotonic response of sands. The critical state is determined through defining the critical state of each test while, the pre-critical state behavior is identified by locating the phase transformation points.

Phase transformation is an undrained sand response prior to reaching the critical state. it was explained by as the change in sand response from contractive to dilative behavior in undrained conditions. Phase transformation is associated with a local minimum in the mean effective stress. Phase transformation is followed by deviatoric stress increase and subsequently pore pressure decrease.

The seven tests were performed with varying preparation relative densities, leading to different final relative densities before loading. As a result, the specimens exhibited diverse behaviors. However, samples showed dilative and contractive behavior-depend on the initial void ratio-they formed a clear and defined critical state line.

Black squares represent the CS points which was recognized by the end of tests at high strain values. Whereas, the black triangles indicate the phase transformation points of tests.

Evolution of void ratio in addition to relative densities during the testing stages were recorded to explain the dilative and contractive behavior of specimens as seen in Figure 4-2 (a and b) respectively. The plots revealed that the relative densities of tests Tx1, Tx2, Tx3 and, Tx7 (before loading) was ranging between 38.8 and 63 % indicating medium to dense samples. In contrast, relative densities of tests Tx4,5 and 6 ranged from 32 to 36.7 % which is typically loose to medium sands.

Furthermore, Tx1, Tx2, Tx3 and, Tx7 showed phase transformation within the first 3% axial strain, followed by higher deviatoric stress and pore pressure decrease, as shown in Figure 4-1(c).

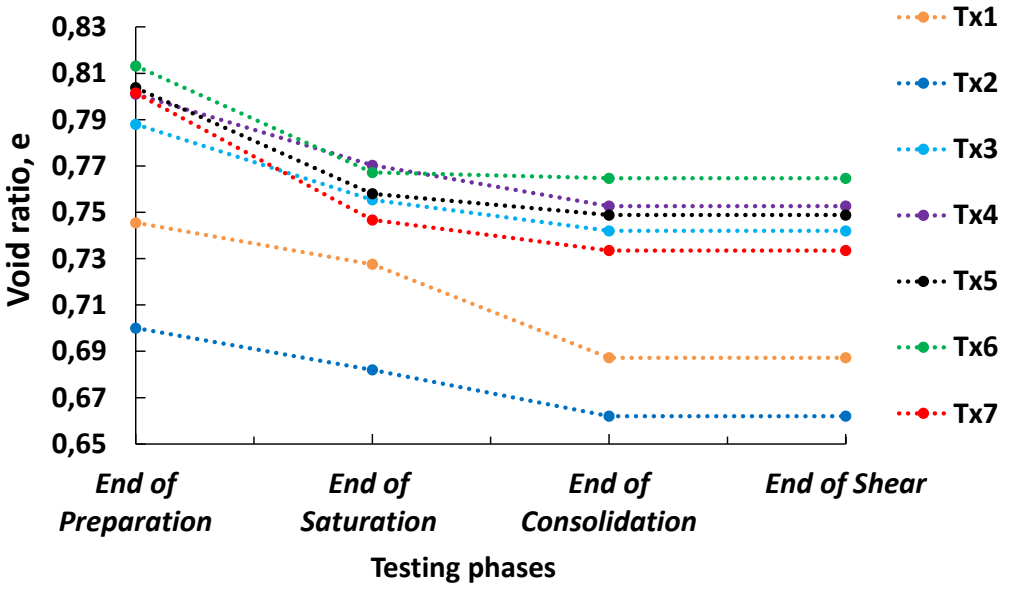

a)

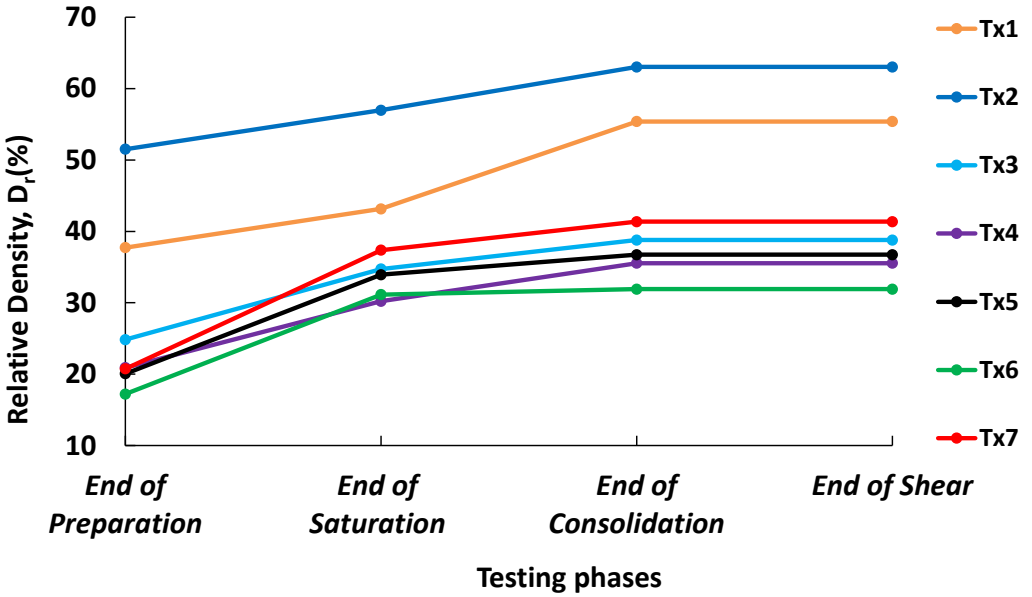

b)

Figure 4-2, Variations of a) void ratio a) and; b) corresponding relative densities, during testing phases

Figure 4-2 validates the considerable densification occurred to specimens during the saturation process due to applying CO_2 gas, flushing water, in addition to the skills and consistency of the operator. Furthermore, predicting the final relative density (post-saturation) proves challenging, as it is influenced by a combination of these factors. Additionally, the tests confirmed the significant influence of the saturation and isotropic consolidation phase on increasing soil´s relative density during the tests.

4.1.2. Critical state line (CSL)

In all tests, at higher strain rates, ranging from 25 to 30%, the deviatoric stress tended to stabilize however, pore pressure remained constant. This observation provides strong evidence that the soil has reached the critical state. The critical state for these tests was determined by considering the final state of these tests.

As clear in the q-p´-space in Figure 4-1b, the unique critical state line CSL is a straight line defined by the endpoints of all tests. Critical state of all tests was used to assess the critical state parameters. Moreover, there was no indication of liquefaction occurrence.

Figure 4-1d indicates the relationship between the void ratio e and mean effective stress p´ during consolidation and undrained shearing. The angle of shearing resistance at high strains (critical state friction angle Φ_{cs}) was found to be 32.4° corresponding to a critical friction ratio M_{cs} of 1.306.

Figure 4-3a and b show the best fitting of Linear and non-linear critical state lines respectively in the e-logp´ space of NB sand.

Then, a comparison between the resulting linear and nonlinear CSL and the CSLs obtained by Ramos (2021) for the same sand type was drawn in Figure 4-3, a, and b, respectively. Noting that Ramos (2021) has divided the CSL into two portions with two different slopes

and attributed that to the grains crushing that probably occurred at higher confining stresses.

The comparison unveiled parallel Critical State CS lines, indicating the same slope. However, the Critical State Line CSL obtained in the current study exhibited slightly lower void ratio values (lower vertical position) at equivalent confining pressures, particularly noticeable at lower confining pressures.

This difference can be attributed to variations in the fines content of the specimens utilized in the two studies, as explained in the grain size distribution analysis detailed in Chapter 3. Based on Poulos et al. (1985) , the grain size characteristics notably impact the vertical position of the Critical State Line CSL.

Critical state parameters were computed based on equation (4-1) which was adopted to define the linear CSL. where, e_{cs} is the critical state void ratio, Γ is the reference void ratio at p′ = 1 kPa and λ represents the slope of the CSL in the e-log p′ space. CS points allowed defining a unique CSL with a correlation coefficient R^2 =0.87.

$$e_{cs} = \Gamma - \lambda \log p' \quad (4\text{-}1)$$

In addition to the drawn linear Critical State Line CSL with an R^2 of 0.87, a curved CSL was introduced with the aim of achieving a higher R^2 value. Figure 4-4, Plot a presents the curved CSL, which was then compared with the curved CSL obtained by Ramos (2021) in Plot b of the same figure. The resulting R^2 was found to be 0.9957. The two nonlinear CSLs were nearly identical within the range of mean confining pressure between 300 to 600 kPa. However, for lower confining stresses, the curved CSL exhibited a lower vertical position compared to the linear CSL.

The plotted CSLs shown in Figure 4-3 and Figure 4-4 excluded only one point (one test) as it might be considered outlier. Table 4-1 provides the resulting critical state parameters, including those obtained by Ramos (2021).

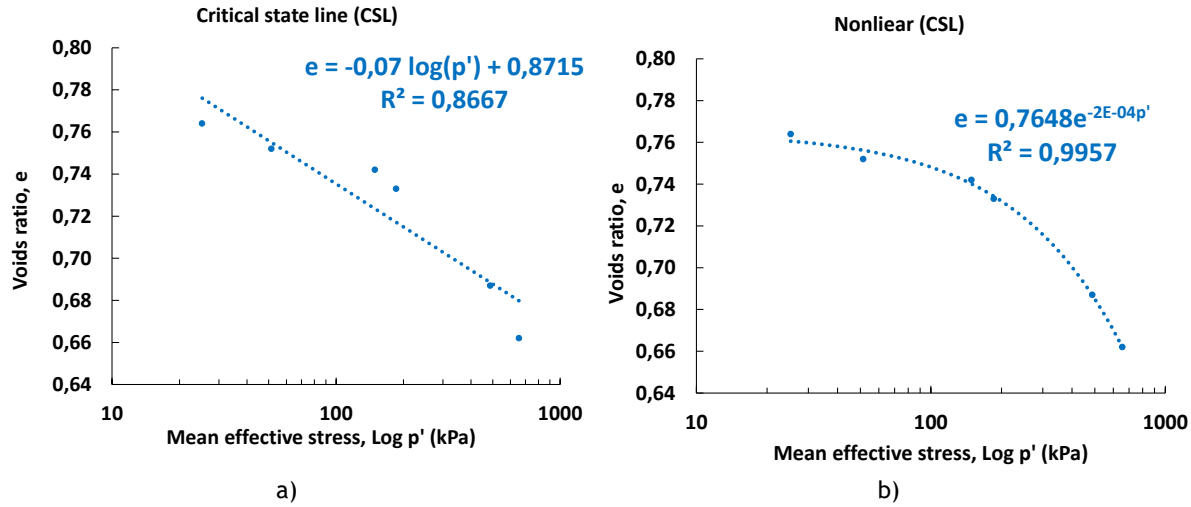

Figure 4-3 Critical state line of NB sand CSL: a) Linear; b) Non-linear regression

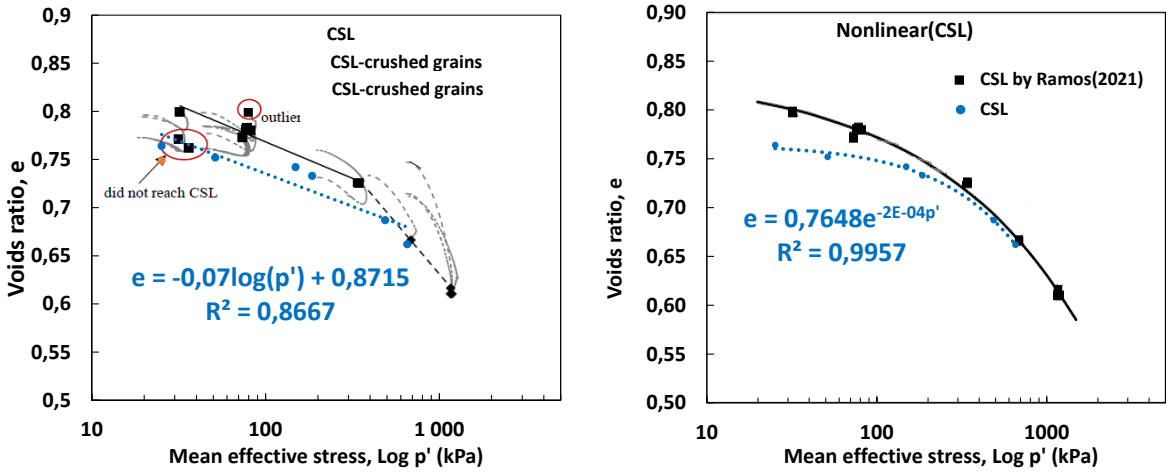

Figure 4-4 comparison between CSL of current study and CSL of NB sand obtained by (Ramos, 2021): a) Linear; b) Non-linear

Table 4-1 Critical state parameters of NB soil

	Γ	λ	M_{cs}	Φ_{cs}
Current study	0.872	0.07	1.306	32.4
Ramos (2021)	0.919	0.076	1.31	32.6

Figure 4-5 eliminates the effect of the mean effective stress through plotting normalized deviatoric stress by the mean effective stress q/p´ along with the axial strains ε_a%.

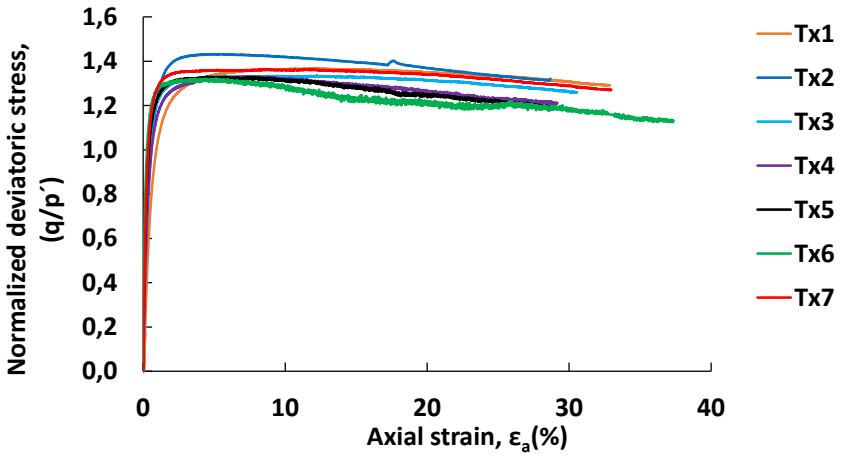

Figure 4-5 Normalized deviatoric stress (q/p´) with the axial strain (ε_a%)

All tests exhibited similar behavior which reflects the significant influence of the mean effective stress on altering the mechanical behavior of sands.

4.2. Monotonic behavior of fully and partially saturated NB sand (UTx)

4.2.1. Stress-strain results

Seven monotonic undrained triaxial tests UTx were conducted in the double-wall triaxial chamber under both fully and partially saturated conditions. These tests aimed not only to investigate shear characteristics but also to evaluate how the degree of saturation affects the soil mechanical properties and monotonic shear strength. Figure 4-6 and Figure 4-7, depicts typical shear characteristics plots derived from the double-wall monotonic triaxial tests for both fully and partially saturated sets of tests, respectively. Where; (a) represents stress-strain path q-ε_a while, (b) illustrates shear stress path q-p`, Critical state line and, phase transformation, (c) depicts pore water pressure build-up with the axial strain Δu-ε_a, and finally (d) shows void ratio variation with the confining stress e- p´, defining the critical state locus CSL.

It is worth mentioning that test UTx4 was having same mean effective stress of UTx3 therefore, data from test UTx4 were only used in identifying the CSL as elaborated in following parts.

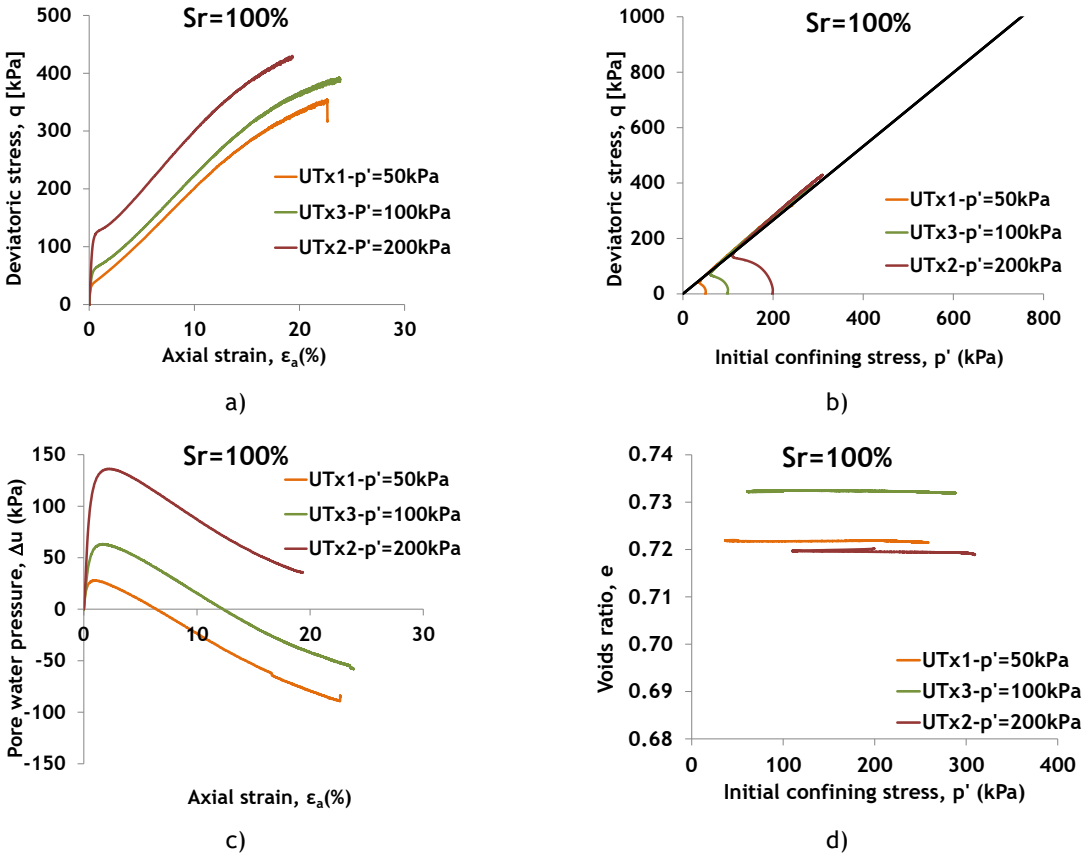

Figure 4-6 typical shear characteristics plots of the three saturated specimens a) stress-strain behavior; b) Stress path with CSL in the q: p` space; c) pore-pressure change; d) e: p´ space

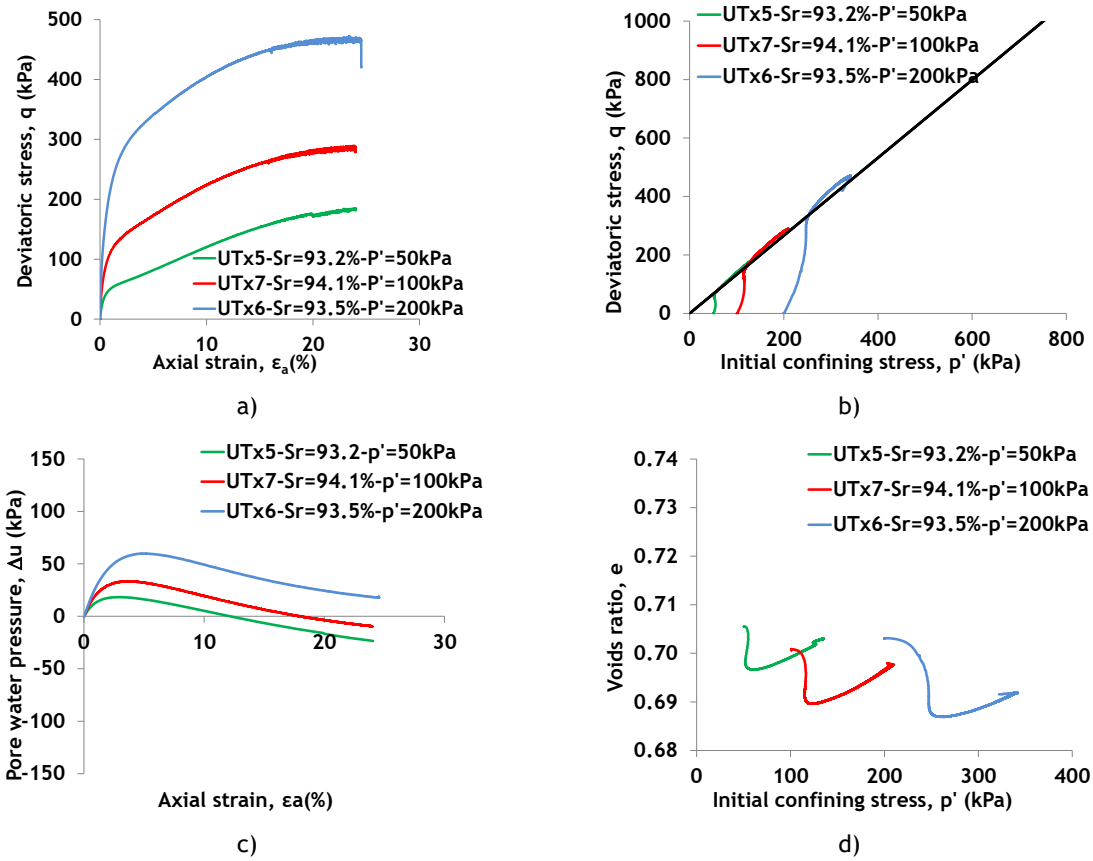

Figure 4-7 Typical shear characteristics plots of the three unsaturated specimens a) stress-strain behavior; b) Stress path with CSL in the q: p` space; c) pore-pressure change; d) e: p´ space

All conducted tests exhibited dilative behavior; however, dilative behavior was more pronounced in partially saturated specimens. This dilative behavior in partially saturated specimens can be attributed to their denser initial state before shearing compared to fully saturated specimens.

4.2.2. Volumetric change of fully and partially saturated NB sand

During the undrained monotonic shearing, the volume gauge transducer connected to the internal chamber allowed precise measurement of the water entering or exiting the triaxial chamber while the sample was monotonically sheared. At the end of each test, the volume of the piston that entered the chamber during shearing was preciously calculated and subtracted from the volume of water expelled from the cell due to the compression.

A very important observation was recorded; in saturated tests, the volume of water that got out from the sample closely matched the volume of the piston's portion that entered the chamber during shearing, with the exception of test UTx2, which exhibited a minor difference between the two volumes. This disparity could be attributed to the presence of small air bubbles that may have become trapped within the chamber ceiling, adhered to the chamber wall, or surrounded the piston. Also, this minor volume difference might be attributed to the soil particles crushing that may occurred.

Conversely, in partially saturated specimens, a notable difference between the two volumes was always reported, confirming the presence of compressed air bubbles within the soil pores.

To provide graphical clarification on the previous observation, comparative plots have been generated to illustrate the evolution of volumetric change (compressed air bubbles) measured by the volume gauge attached to the triaxial cell during shearing.

Figure 4-8(a and b) compares fully and partially saturated tests (UTx1 and UTx5) conducted under identical initial isotropic confining stress by correlating pore water pressure ΔU and volumetric strain ε_v, in addition to pore pressure ratio r_u with axial strain ε_a, respectively.

Figure 4-9 and Figure 4-10 show the same relationships for tests (UTx3 and UTx7), and (UTx2 and UTx6), respectively. It should be noted that the computation of ε_v involves deducting the volume of the portion of the piston that entered the cell from the volume of water exited the sample during shearing.

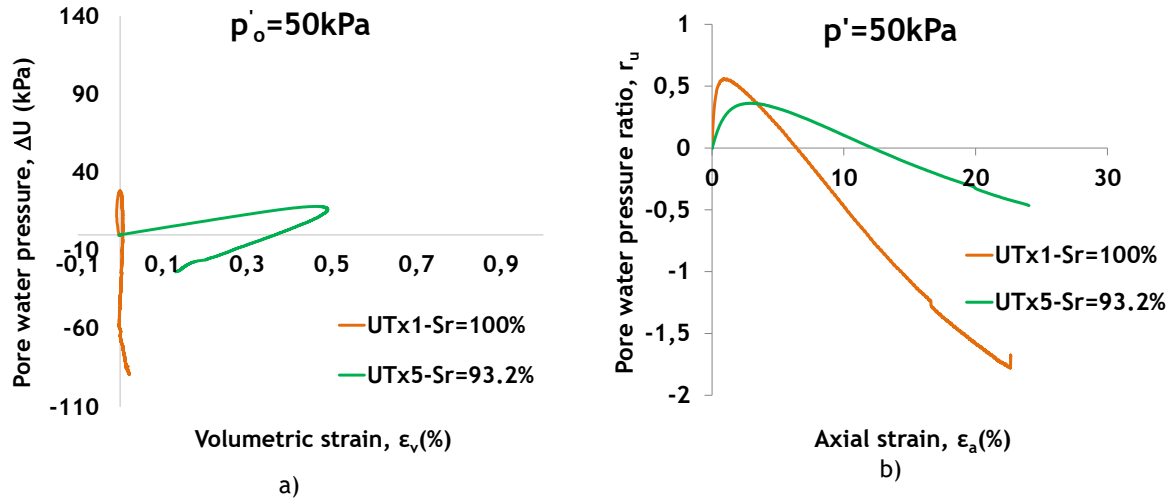

Figure 4-8 Comparing UTx1 and UTx5: a) ΔU against ε_v; b)r_u against ε_a

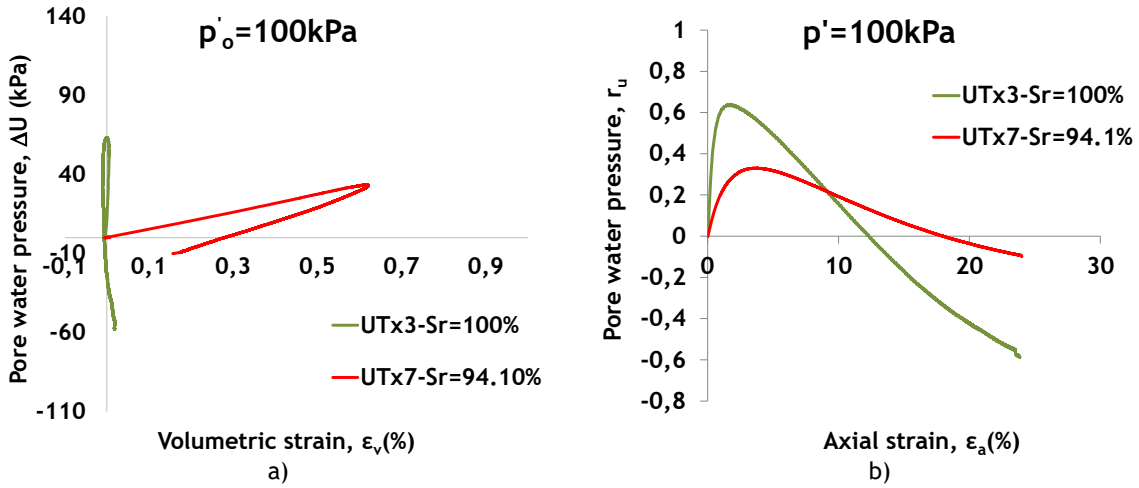

Figure 4-9 Comparing UTx3 and UTx7: a) ΔU against ε_v; b)r_u against ε_a

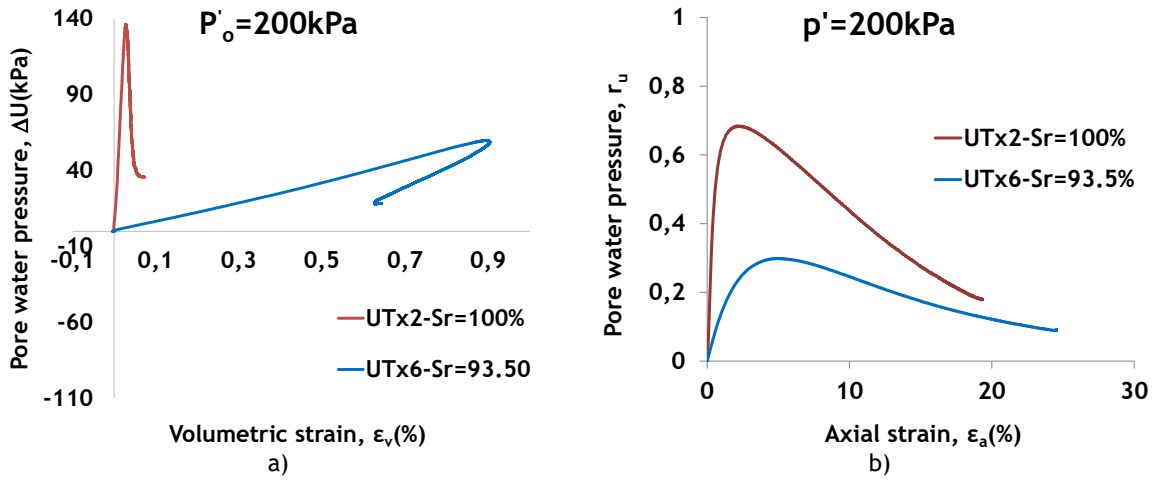

Figure 4-10 Comparing UTx3 and UTx7: a) ΔU against ε_v; b)r_u against ε_a

From the analysis of the three plots, it can be observed that the volumetric strain ε_v increases with higher initial confining stress. Specifically, the maximum volumetric strain was exhibited by UTx6, where the initial confining stress p´ was 200 kPa. This was found to be higher than the volumetric strain observed in UTx7, where P' was 100 kPa, which in turn was higher than UTx5, where p´ was 50 kPa. This trend suggests a direct correlation between initial confining stress and volumetric strain, with higher confining stresses resulting in greater volumetric deformations during shearing.

It is important to note that the observation of volumetric changes recorded in this set of partially saturated tests could not be performed during the cyclic triaxial testing, which will be discussed later. During cyclic loading, the application of both compression and tension loads makes it difficult to obtain meaningful data on volumetric strains using the means of Hall effects transducers HE. As the cyclic loading causes the volumetric strains to fluctuate, increasing and decreasing until the sample potentially liquefies, the nature of this loading process makes it challenging to collect and analyze volumetric strain data during the loading phase. The r_u- ε_v, reveals the gained strength in terms of the pore water pressure ratio r_u, where $r_u = \Delta u/p'_o$. All partially saturated specimens showed less pore pressure ratio build up compared to fully saturated ones.

The resulting gain in shear resistance is not solely attributed to the decrease in the degree of saturation; it may also be influenced by changes in void ratio.

Small trapped air bubbles were always observed during the disassembly of partially saturated tests, as shown in Figure 4-11. This visual evidence confirms the partial saturation of specimens.

Figure 4-11 the existence of occluded air bubbles in the partially saturated specimens

4.2.3. Critical State line (CSL)

By recognizing these differences, the characterization and understanding of soil behavior must consider the distinct responses of fully and partially saturated specimens. Critical State Lines CSL for each saturation condition showed different slopes and positions as shown in Figure 4-12. The two different Linear CSLs were drawn following equation (4-1) where critical state parameters were computed and listed in Table 4-2.

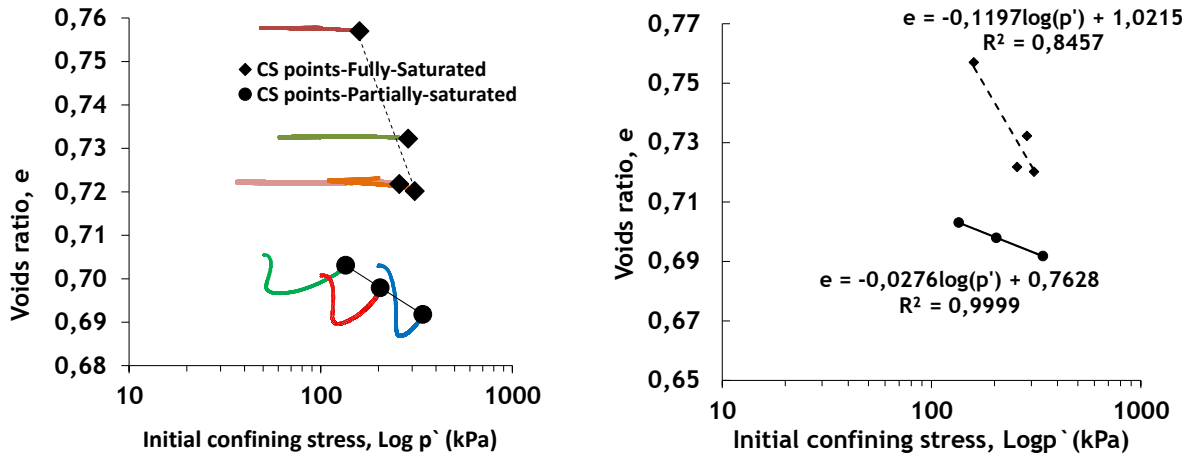

Figure 4-12 CSL of fully and partially saturated set of tests for NB sand

Table 4-2 Critical state parameters for fully and partially saturated specimens

	Γ	λ	M_{cs}	Φ_{cs}
Fully saturated	1.0215	0.1197	1.33	33
Partially saturated	0.7628	0.0276	1.33	33

The CS points of saturated UTx tests in addition to CS points obtained from the Tx set of tests were plotted together, resulting Curved CSL was drawn as shown in Figure 4-13.

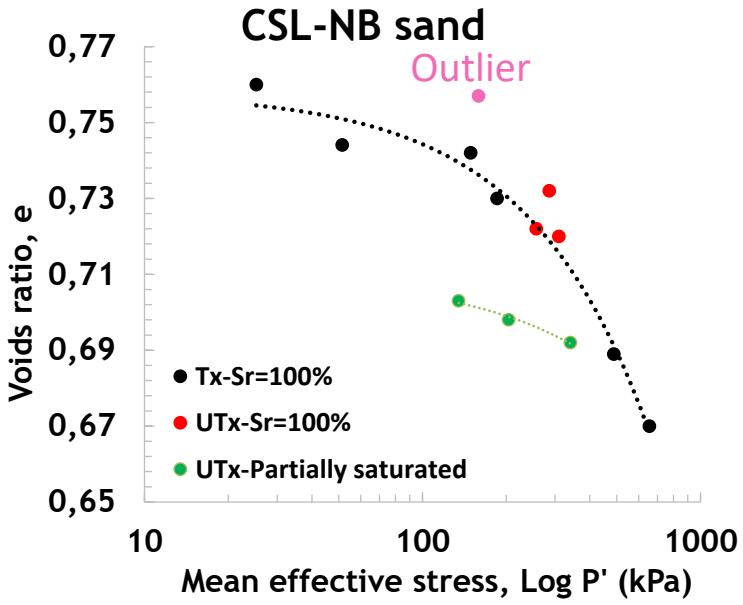

Figure 4-13 Non-linear CSL of Tx and UTx sets of tests

The fully saturated critical state points lie above the partially saturated points in the present e-log p′ representation (Figure 4-13). This trend is consistent with the larger bulk volume changes measured in the partially saturated specimens during undrained shearing. In the double-cell triaxial system, volume change is inferred from the inner cell water variation, and under undrained conditions partially saturated specimens are still contractive because of the compressibility of the air voids, whereas fully saturated specimens remain approximately constant in volume. The observed separation should therefore be interpreted as a response influenced by pore fluid compressibility and the experimental volume measurement method, rather than directly as a pure shift of the soil skeleton critical state line. Based on that, this CSL resulting from the partially saturated tests can be considered an apparent CSL.

4.2.4. Shear resistance based on the volumetric water content Theta θ

An additional analysis was conducted using the volumetric water content, Theta (θ or θ_w). Theta θ is a holistic approach, where it combines impact of both saturation degree and void ratio on soil behavior. In general, the parameter theta θ is utilized to characterize the water content retained within a porous material. It is defined as the ratio of the volume of water V_W to the total volume V_T of the material. Alternatively, theta θ can also be represented by correlating the final degree of saturation S_r % with the void ratio e. This correlation provides a relationship between the amount of water present in the material and its void ratio. Mathematically, theta θ can be expressed by equation (4-2) (Woessner & Poeter, 2020).

$$\theta = \frac{v_w}{v_T} = S_r * \frac{e_f}{1 + e_f} \quad (4\text{-}2)$$

Degree of saturation was calculated using the conventional mass and weight method. The two-volume gauge helped to accurately measure the amount of water entering or exiting specimens during the testing phases hence degree of saturation was precisely calculated. Then, theta θ was computed for all tests using the above provided equation. Subsequently, maximum pore pressure build-up r_{umax} was plotted against theta θ for both fully and partially

saturated tests, as depicted in Figure 4-14 . Following this, r_{umax} values were plotted against the degree of saturation Sr % and the void ratio e, separately(Figure 4-15 and Figure 4-16) respectively, to evaluate the influence of each parameter on pore pressure build-up. These plots illustrated the respective impacts of saturation degree and void ratio on the observed pore pressure ratio build-up.

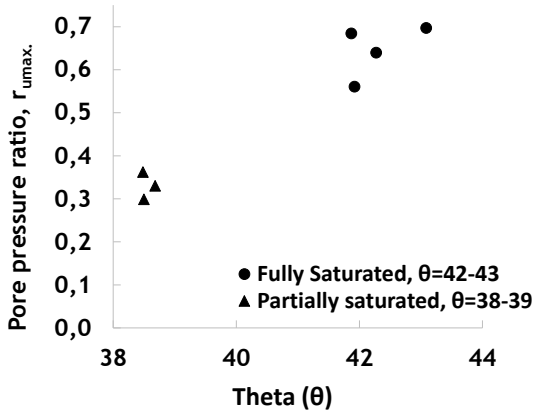

Figure 4-14 Relationship between theta values and pore pressure build-up of saturated and partially saturated specimens

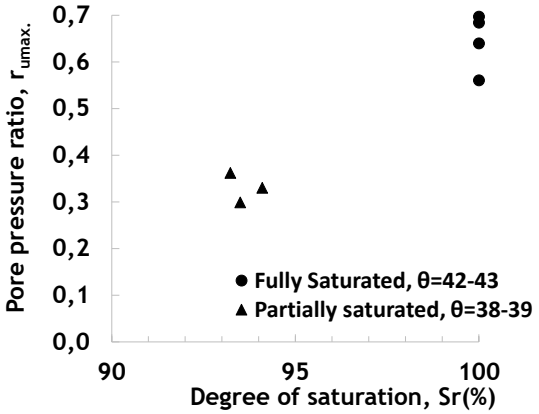

Figure 4-15 Relationship between degrees of saturation and pore pressure build-up of saturated and partially saturated specimens

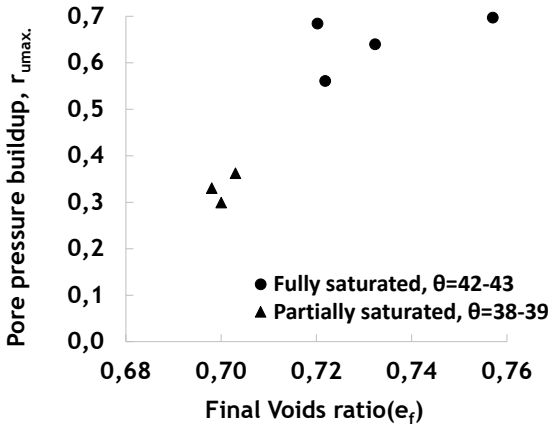

Figure 4-16 Relationship between void ratio and pore pressure build-up of saturated and partially saturated specimens

It can be concluded that the shear strength variation was less pronounced among the partially saturated tests due to their close values of degrees of saturation. However, it was notable that partially saturated specimens exhibited a significant increase in shear resistance compared to fully saturated tests. This gain in shear resistance was evidenced by the lower pore pressure build-up observed in partially saturated tests. Figure 4-14 reported that as theta θ values increased, pore pressure build-up increased, resulting in a shear resistance decay. This relationship can be attributed to the fact that θ is influenced by both void ratio and degree of saturation. Figure 4-16 showed that the void ratio influenced pore pressure build-up. As the void ratio increases (indicative of a looser material), pore pressure build-up increases hence, shear resistance decreases, and vice versa.

4.3. Main findings

This chapter presents the results of the undrained monotonic triaxial tests performed in this study for NB sand. Two experimental series were conducted under both fully saturated and partially saturated conditions. The first series was carried out using a conventional monotonic triaxial apparatus. The second series was performed using a double-wall (double-cell) triaxial apparatus, in which equal pressures are applied inside and outside the inner chamber wall to minimize cell-wall deformation and enable improved control and/or measurement of specimen volumetric change during undrained conditions.

Based on the monotonic test results, the critical state parameters of NB sand were determined and compared with values reported in the literature. The critical state parameters were also evaluated for different saturation conditions. In addition, volumetric strain responses during compression loading were analyzed for the various degrees of saturation.

A direct comparison of pore water pressure build-up under monotonic undrained loading was performed between fully and partially saturated specimens. The results showed that partial saturation significantly reduced pore pressure build-up relative to the fully saturated condition. Consistent with this behavior, the effective stress paths indicated a clear difference between saturation states: fully saturated specimens exhibited a marked reduction in mean effective stress, p′ followed by an increase of p′, whereas partially saturated specimens showed an elevated of p′, during loading.

5. Cyclic triaxial tests (CTx): results and analyses

This chapter summarizes the results and interpretation of the cyclic triaxial tests carried out on NB sand and Hostun sand under fully saturated and partially saturated conditions. Cyclic triaxial tests CTx were performed on fully and partially saturated NB and Hostun sands to assess the efficiency of induced partial saturation IPS as a liquefaction mitigation method.

For NB sand, the relationship between compressional-wave velocity Vp and degree of saturation Sr will be presented, and then evaluating the relationship between Vp and Skempton's B-value as a practical indicator of saturation state. The chapter then evaluates the evolution of void ratio and small-strain stiffness during specimen preparation, consolidation, and cyclic loading. followed by the role of effective stress (stress dependency). Next, it analyses liquefaction resistance across the tested saturation levels. Moreover, it discusses the evolution of soil stiffness and viscous damping during cyclic loading, evaluating the stiffness and damping evolution of fully saturated and partially saturated specimens until liquefaction.

Finally, the stress dependency of seismic wave propagation of Hostun sand will be studied followed by the liquefaction resistance at various Sr degrees.

Liquefaction failure could be distinguished by two common forms; flow liquefaction and cyclic mobility. In numerous instances of documented liquefaction sites, cyclic mobility has been observed to occur more frequently than flow liquefaction, yet its impact is typically less severe.

In the conducted tests, the observed failure was identified as cyclic mobility. Flow liquefaction involves a total loss of strength, characterized by a sudden reduction to zero in both deviatoric and mean effective stresses, accompanied by significant deformations while, cyclic mobility in medium dense sands is characterized as a state of strength softening resulting from a pore pressure build up to 100% corresponding to $r_u = 1$ and usually, with consequent development of about double strain amplitude criterion (Ishihara, 1993) following the strain-based criterion.

5.1. Cyclic behavior of NB sand

5.1.1. Assessment of the degree of Saturation

Achieving different degrees of saturation required controlling three main factors during the saturation phase: the use of CO_2 flushing, the applied back-pressure level, and the volume of flushing water introduced into the specimen. For instance, in CTx20, to reach a saturation level of 95.5%, CO_2 gas was introduced in addition, water flushing was performed, while a controlled back pressure was increased up to only 120 kPa instead of achieving 300 kPa as in the saturated samples.

The choice of whether to introduce CO_2 gas or not and the application of varying levels of back pressure BP have been demonstrated to have a notable impact on the final void ratio and degree of saturation.

Extending the test duration beyond the usual timeframe tended to increase both degree of saturation and relative density, mainly because additional time under confinement allows continued water redistribution, probable further dissolution of entrapped air (when back

pressure is applied), and ongoing consolidation that slightly change the void ratio. In practice, fully saturated tests typically required more time than partially saturated tests because the saturation stage involved additional operations: CO_2 introduction, and a controlled increase in back pressure (commonly up to 300 kPa with a particular pressure rate) until the full saturation level is verified via Skempton's B-value and Vp. When saturation is difficult to achieve, an additional flushing round may be needed, further extending the overall test duration.

To verify the attainment of the targeted degree of saturation Sr, assessments were conducted by measuring Vp using BEs and computing B-value.

A calibration of the BEs was conducted before starting the set of tests, where the cyclic triaxial chamber was filled with de-aired and distilled water (same water used to fill the chamber during the experimental program), the height difference between the two BE was maintained about 140mm which equal to the samples height, furthermore, the pressure of the water was elevated to 300 kPa to mimic the back pressure applied to samples during saturation, the resulting Vp was found to be around 1485 m/s, which is consistent with the velocity of sound in water.

While performing the experimental program and by the end of every test, confirmation of the degree of saturation achieved before cyclic loading was conducted. Hall effects HE was utilized to analyze both axial and radial strains. Following this, the evolution of volumetric strains was calculated, which enabled the determination of the final void ratio and water content.

Compressional wave velocities Vp were measured through BEs using the first arrival time, to improve confidence in the first arrival pick and therefore in Vp, several sine wave pulse frequencies were applied. This provides a simple check that the measured travel time is not being influenced by frequency dependent effects or by the particular shape of a single input signal (Viana da Fonseca et al., 2009).

As an example, by the end of the saturation phase of test CTx1, the P wave propagation travel time was measured by applying frequencies of 30, 40, and 50 kHz (Figure 5-1). The recorded signals showed excellent agreement in the first arrival time across all three frequencies, hence a stable travel time estimate and a reliable calculation of the signal travel time. Consequently, Vp was determined by dividing the travel distance (BE tip to tip distance) by the measured signal travel time (Viggiani & Atkinson, 1995). Figure 5-2 shows the relationship between Sr and Vp for various tests under various degrees of saturation. The plot shows an inverse correlation between compressional wave propagation time and degree of saturation, which indicates that Vp propagates faster in fully saturated media.

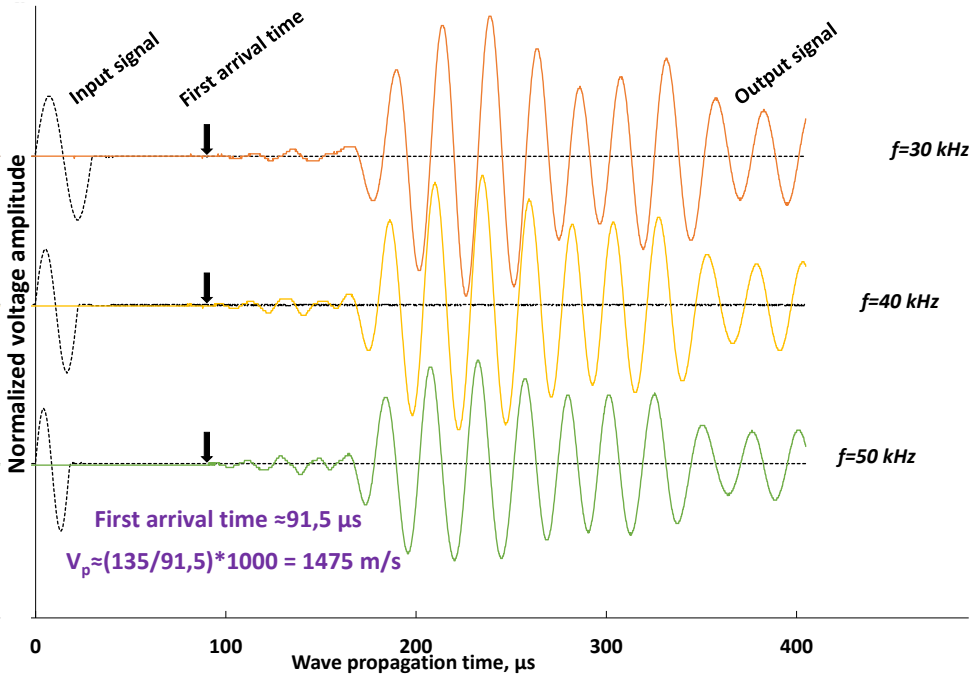

Figure 5-1 P-wave analysis in the time domain from CTx1, indicating the first arrival time using various frequencies

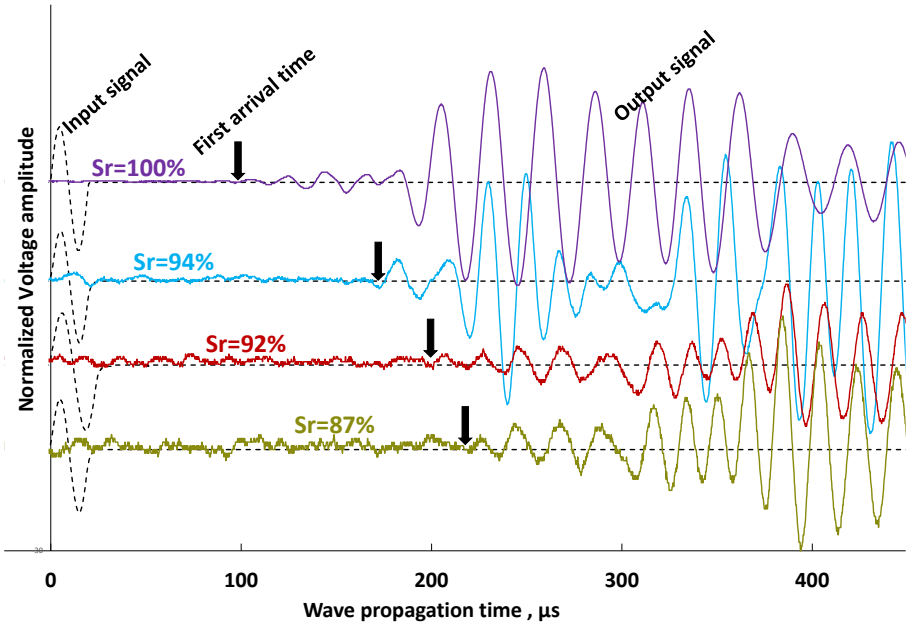

Figure 5-2 P-wave analysis in the time domain for various CTx tests with various Sr%

Due to the reasons outlined above, it was not possible to achieve identical relative density values across all specimens prior to cyclic loading. Therefore, the datasets presented in Figure 5-3 and Figure 5-4 which reveal the correlation between Vp with both B and Sr of the fully and partially saturated NB soil specimens, respectively, include only the tests with relative densities in the 25–35% range, which were selected to ensure a consistent basis for comparison. The plots show a defined trend but with some scattering nature because of the various relative density, however they all were loose to medium dense samples.

Figure 5-3 presents a comparison between experimental data and theoretical model developed by Yang (2002). This comparison reveals a notable divergence between the experimental results and the theoretical predictions within the Skempton's pore pressure coefficient B range of 0 to 0.9. This lack of agreement is documented phenomenon in the literature. For instance, Molina-Gómez (2023) reported similar discrepancies for B values between 0 and 0.75. Astuto et al. (2023) stated that for relatively low values of B-value of about 0.70, the Vp measurements was equal to Vp in fully saturated soils (1400–1500 m/s) which isn't reliable.

At near-saturation (B-values between 0.9 and 1.0), the experimental data closely matched the theoretical model. The disagreement occurred at lower saturation levels would be primarily attributed to the volumetric strain that physically occurs while measuring the B-value itself. As originally defined by Skempton (1954), reliable B value equations assume an idealized state of zero volumetric strain. In partially saturated soils, the presence of air bubbles makes the pore fluid highly compressible. When confining pressure is applied during testing, these bubbles compress. This generates volumetric strain and physically reduces the expected pore pressure build-up, which, violates the theoretical zero-strain assumption. Furthermore, the varying relative densities Dr used in this study likely introduced additional divergence, further widening the gap between the physical data and the prediction model.

Figure 5-4 compares the experimental Vp-Sr data against the theoretical model derived from Biot's theory, (Biot, 1956).

For the theoretical model, the equivalent fluid bulk modulus K_f was derived from the respective bulk modulus of water K_w = 2.2 GPa, and carbon dioxide gas K_a = 0.05 GPa. Skeleton Poisson's ratio ν_{sk} and shear wave velocity Vs were computed as detailed in Figure 5-14. A porosity of 0.435 was applied, corresponding to a relative density Dr of 30%, which effectively averages the 25% to 35% Dr range of the tested specimens.

This comparison yielded a significantly stronger agreement than the B value analysis (Figure 5-3) While minor deviations remain due to the varying Dr of the experimental samples, the overall alignment is distinctly clear.

Experimental data demonstrated a gradual increase in Vp until Sr reached about 86%. Afterwards, Vp sharply increased until reaching about 1500 m/s (full saturation). Beyond this threshold, the soil entered a nearly saturated state where air exists as occluded bubbles within the fluid and Vp is controlled by the fluid showing the significant increase in in Vp.

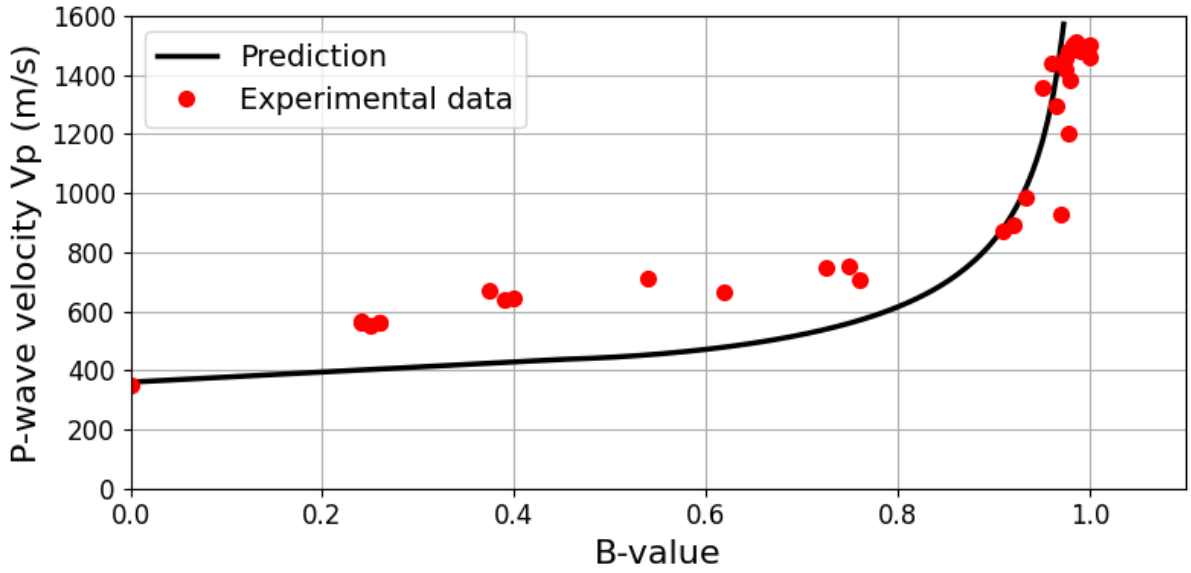

Figure 5-3 Correlation between V_p (m/s) and B-value by the end of consolidation of all performed tests, p'=100kPa

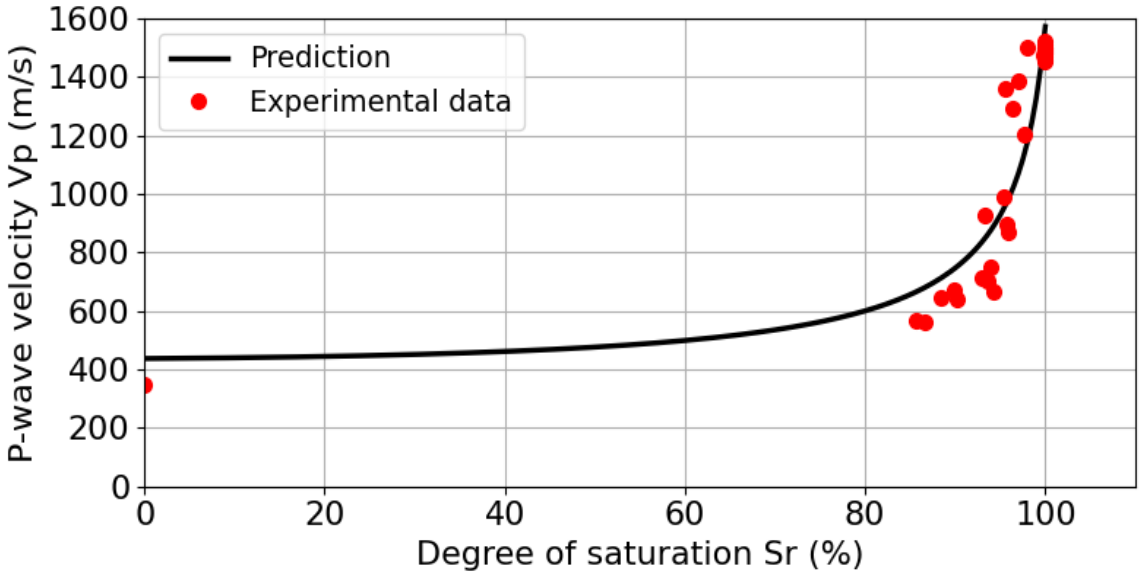

Figure 5-4 Correlation between V_p (m/s) and Sr (%) by the end of consolidation of all performed tests, p´=100kPa

Ultimately, this analysis proves the high sensitivity of Vp to changes in Sr, demonstrating it to be a far more reliable technique for confirming saturation levels than the B-value. However, the B-value remains a robust verification tool strictly for full saturation conditions, where induced volumetric gas strain is no longer an interfering factor.

5.1.2. Void ratio and small strain stiffness assessment

Figure 5-5 and Figure 5-6 , illustrate the fluctuations of void ratio and relative density, respectively throughout the different testing phases (soil preparation, saturation, consolidation, and cyclic shearing) for the performed cyclic triaxial tests of NB sand.

Volumetric strain during the cyclic loading stage was not evaluated in this study. The cyclic phase was performed under undrained conditions with the drainage valves closed, so specimen volume change could not be inferred from water exchange measured by the back-pressure/volume controller. Although local strain instrumentation HE was available, the volumetric response became difficult to interpret near liquefaction due to the large deformation and localization effects.

It's worth reminding that the specimens tested exhibited different relative densities. This variations in density can be attributed to the introduction of CO_2, which has been reported to increase specimen density. Additionally, the fully saturated tests took nearly twice as long to complete as the partially saturated tests, further contributing to the observed differences in density.

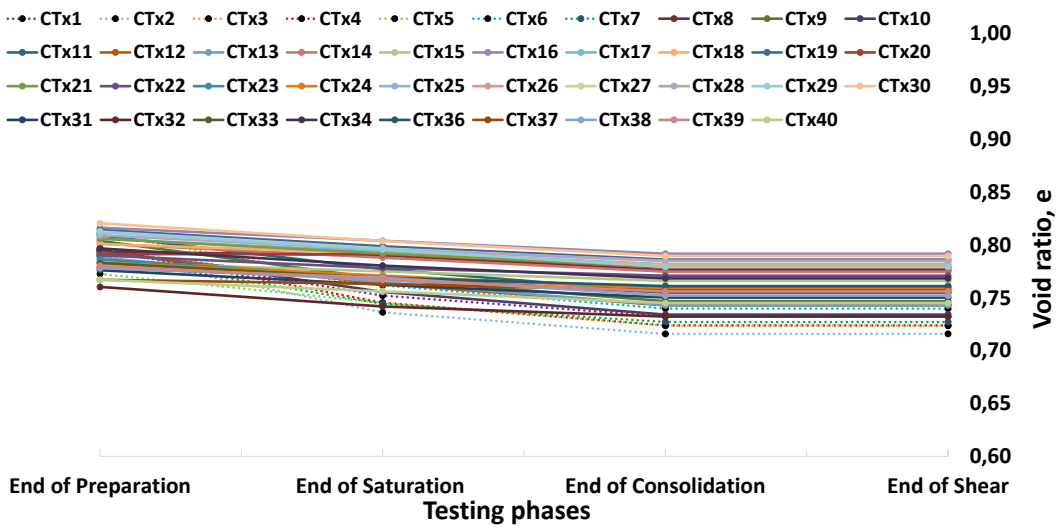

Figure 5-5 Void ratio evolution during testing stages

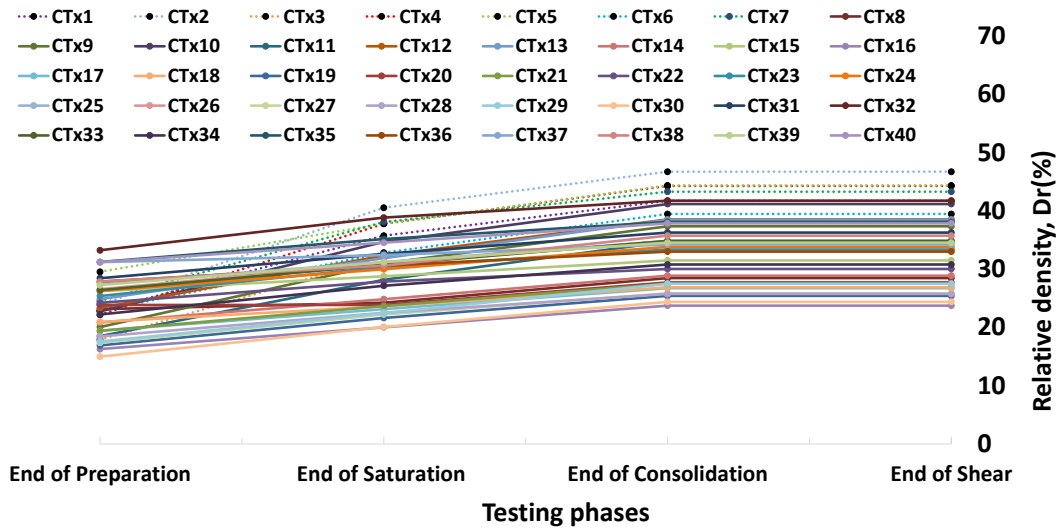

Figure 5-6 Evolution of relative density during testing stages

It should also be noted that the reduction in void ratio associated with the saturation process (particularly water flushing phase) is broadly comparable to the reduction driven by consolidation phase. This effect should therefore be accounted for in the analysis and interpretation of the results.

Bender elements BEs were used to measure shear wave velocity Vs as an indicator of small strain shear stiffness during the testing procedures. To verify the reliability of the first arrival time interpretation, a frequency sweep was performed (1 to 8 kHz). By the end of the saturation phase of test CTx1, frequencies of 1, 2, 4, 6 and, 8 kHz were applied, as shown in Figure 5-7. as clear they all yielded a consistent first arrival time, providing confidence in the selected arrival pick and the resulting Vs estimates. Figure 5-8 reveals the s-wave evolution during the various testing phases.

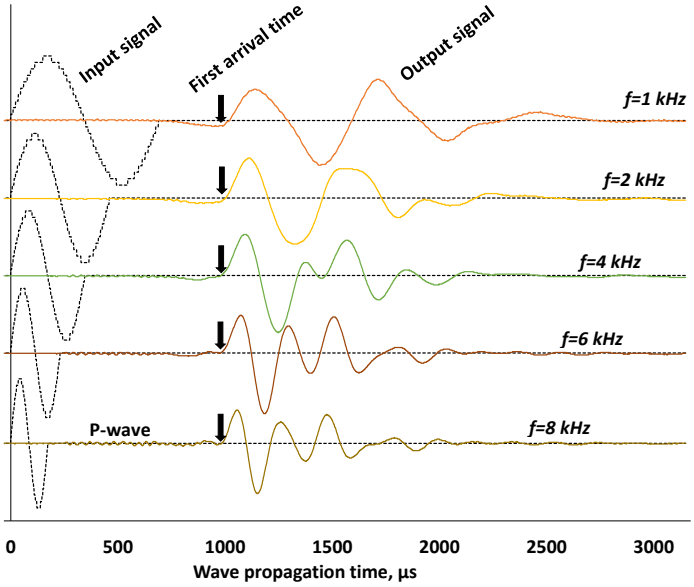

Figure 5-7 S-wave analysis in the time domain from CTx1, indicating the first arrival time using various frequencies

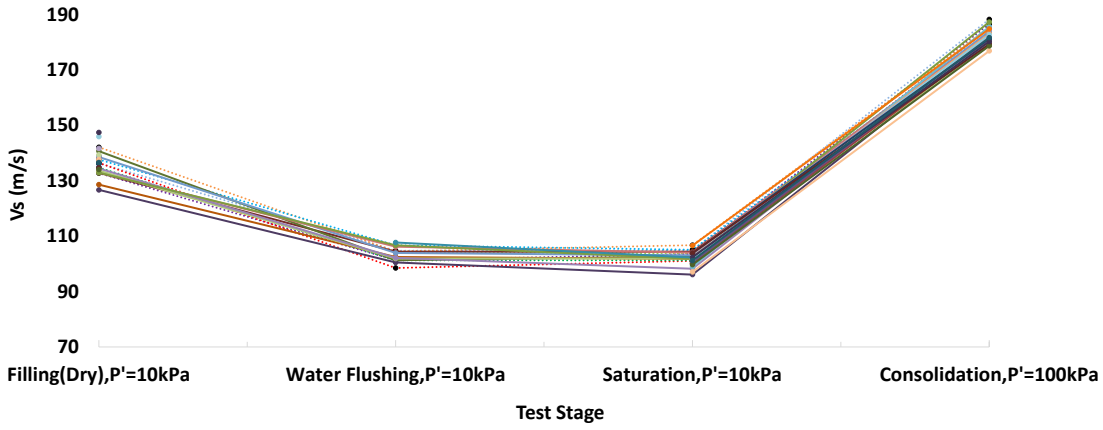

Figure 5-8 Evolution of shear wave velocity S-wave during testing stages of (CTx)

It was observed that the shear wave velocity of soils post water flushing was lower than that in dry conditions at the same confining pressure of 10 kPa. This behavior is unexpected because the introduction of water typically leads to particles rearrangement and settlement, which would typically densify samples and, consequently, increase shear wave velocity. To further investigate that behavior, maximum elastic shear modulus G_{max} was computed using the measured s-wave velocities through equation (5-1) and plotted in Figure 5-9, across the testing stages. Shear modulus G_{max}, plays a critical role in soil dynamics due to its influence on the soil's response to dynamic loading conditions where it represent the maximum shear stiffness of the soil at very small strains.

A higher G_{max} indicates greater small strain shear stiffness of the soil skeleton. At very small strains, stiffness is governed primarily by state variables (e.g., void ratio and current effective stress) and contact level mechanics, including interparticle contact stiffness associated with mineralogy, angularity, and surface roughness.

Small strain wave-based stiffness can be used as a measure of the soil state at the current stress condition. At such a small strain range, stiffness is determined at essentially constant fabric during the wave measurement and reflects contact level deformation.

Cho et al. (2007) explicitly noted that fabric changes occur when soil experiences strains beyond that elastic threshold.

$$G_{max} = \rho * Vs^2 \quad (5\text{-}1)$$

The plot reported a decay in G_{max} from dry to wet state (post water flushing) was but considerably less pronounced than the decay observed in the shear wave velocity between the two soil saturation states, in other words, G_{max} has relatively closer values in both dry and wet conditions.

The smaller apparent change in G_{max} compared to V_s is also consistent with the formula $G_{max} = \rho.Vs^2$ where, wetting increased the bulk density ρ as water fills some pores, partially offsetting the decrease in Vs^2 and yielding closer inferred G_{max} values between the dry and partially saturated conditions.

Gu et al. (2015) reported that, despite having the same void ratio and effective confining pressure, the small strain shear modulus G_o of saturated Toyoura sand was approximately 7-10% lower than that of dry sand. They noted that saturation is commonly assumed to have negligible influence on G_o because water has no shear resistance; however, they attributed the observed reduction to wetting-induced changes at grain contacts. In particular, they suggested that weak layers formed on particle surfaces under saturated conditions reduce interparticle contact stiffness, leading to a small but systematic decrease in G_o and Vs.

During the saturation process and post water flushing, back pressure was increased to 300 kPa for full saturation or other less values for partial saturation while keeping the mean effective stress at 10 kPa. Another degradation of V_s and consequently G_{max} between the end of flushing and end of the whole saturation process was reported but less than the decrease that occurred during water flushing.

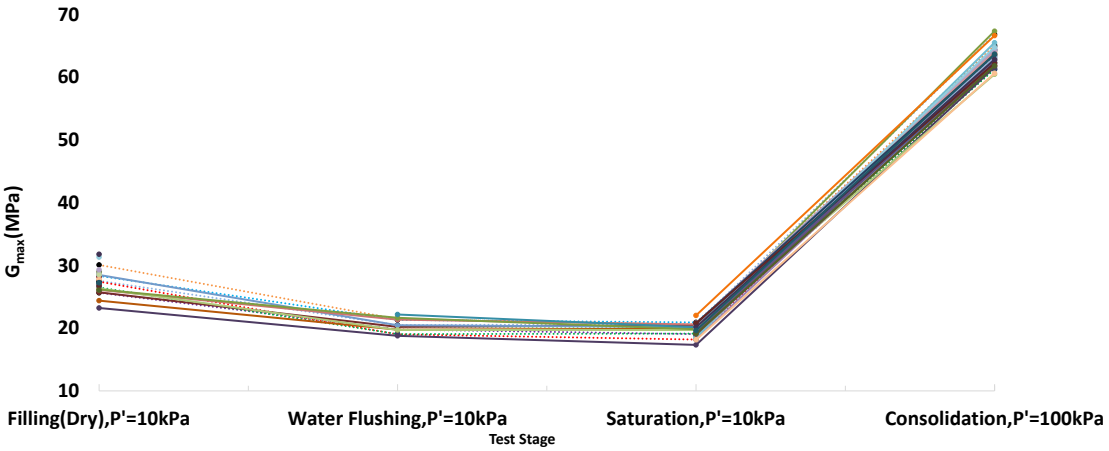

Figure 5-9 Evolution of maximum shear modulus G_{max} during the different testing stages of (CTx)

Upon consolidating the samples to an isotropic mean effective stress of 100 kPa, a significant increase in Vs and consequently G_{max} due to the higher particle to particle contact resulting from increased effective stress, leading to a denser soil state.

5.1.3. Stress dependency and small-strain behavior

5.1.3.1. Stress dependency based on seismic wave measurements

Small strain behavior was studied to investigate the stress dependency of NB sand. The small strain shear modulus G_{max} is a fundamental soil parameter for many geotechnical applications including soil liquefaction analysis.

For this purpose, a particular undrained cyclic triaxial test was performed where, specimen was prepared by dry air pluviation and seismic wave velocities (p and S waves) were measured using bender elements installed in the triaxial chambers.

After soil preparation, confining effective stress was then applied in the dry state in stages from 10 to 500 kPa, followed by staged (incremental) unloading back to 10 kPa. The specimen was then saturated, and the same loading–unloading sequence was repeated in the saturated state (10 to 500 kPa, then 500 to 10 kPa). Shear and compressional wave velocities Vs and Vp, along with Skempton's B-value, were recorded after each loading and unloading step.

Figure 5-10 presents the measured Vs and Vp as functions of the effective confining stress p′, for both dry and fully saturated conditions. The evolution of Vs and Vp with p′ is shown for each state, together with the corresponding regression. The fitting parameters were obtained using the power-law relationships given in equation (5-2), (Cho et al., 2007).

$$Vs \text{ or } Vp = \alpha\,(p')^{\beta} \tag{5-2}$$

Where α is the shear or compressional wave velocity Vs or Vp at p'=1 kPa. ß serves as the exponent of the stress-state dependency law of wave propagation velocities where, it represents the degree to which the seismic wave velocity Vs or Vp is influenced by changes in effective confining pressure p', providing insight into how changes in stress affect the propagation of seismic waves through the soil medium. Fitting parameters α and ß for shear wave velocities were found to be 74.15 and 0.239 in the dry state, and 61.17 and 0.244 in the saturated state. These reports that the stress dependency exponents ß for dry and saturated conditions fell within the typical values for natural sands reported by (Ferreira et al., 2021; Cho et al., 2007).

The fitted curves indicated that Vs in the dry condition is consistently, though only slightly, higher than in the fully saturated condition over the tested stress range. This difference is primarily reflected in the coefficient α; the larger α for the dry trend produced an upward shift (an offset) relative to the saturated trend. In contrast, the exponents ß are nearly identical, indicating a very similar stress sensitivity (similar slope), with the two trends differing mainly by a systematic offset rather than by their rate of increase with confining stress.

In addition, Figure 5-10 presents the evolution of the compressional-wave velocity, Vp, under dry and fully saturated conditions. In the dry state, Vp showed a stress-dependent increase similar to the Vs trend, and the best-fit power law parameters were α=199.32 and ß=0.195. However, after saturation Vp trend was approximately constant and forms a plateau at around 1500 m/s with α=1530 and ß=-0.001. This behavior reflects the fact that, once the pores are fully water filled, compressional wave propagation is dominated by the bulk modulus of the pore fluid. Fitting parameters for the different scenario trends are listed in Table 5-1.

Table 5-1 Stress dependency fitting parameters of NB-sand

Seismic wave	α (m/s)	β
Vp(dry)	199.32	0.195
Vp(saturated)	1530	-0.001
Vs(dry)	74.15	0.239
Vs(saturated)	61.17	0.244

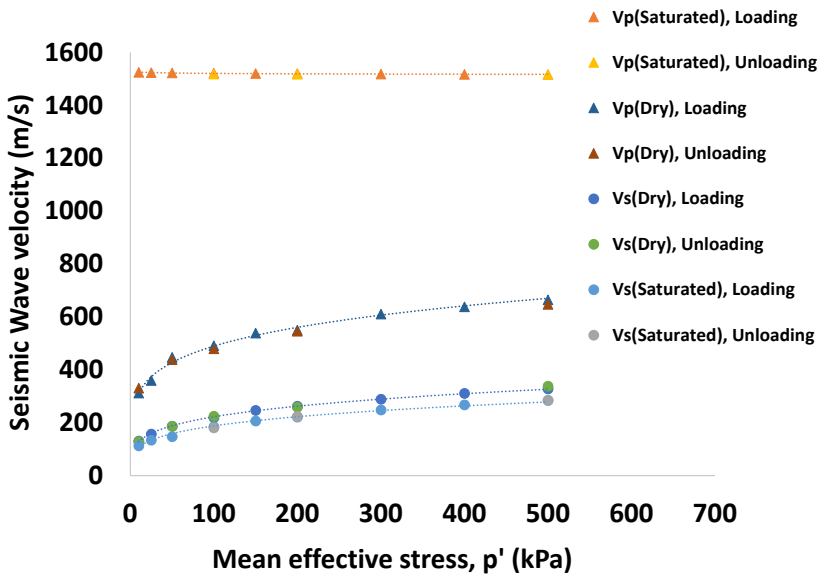

Figure 5-10 Seismic wave velocities Vp and Vs evolution at various confining stress for NB sand

Figure 5-11 compares the stress dependency trends obtained in this study with those reported by (Ferreira et al., 2021) which was performed on the same sand NB soil. The shear wave velocity Vs results matched closely across the tested saturation states (dry and fully saturated), indicating a strong agreement between the two datasets. In contrast, the present work yielded systematically higher compressional wave velocity Vp values in both dry and saturated conditions.

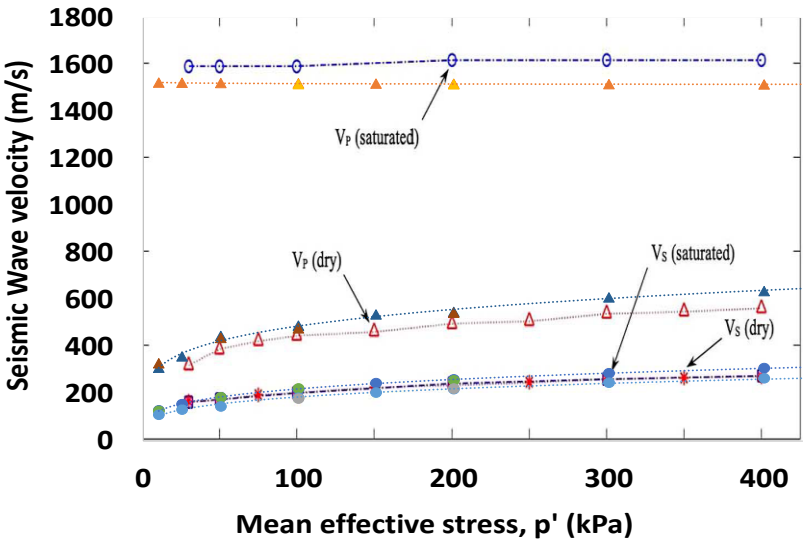

Figure 5-11 Seismic wave velocity Vp and Vs evolution at various confining stress for NB sand compared with (Ferreira et al., 2021)

The evolution of the small strain shear modulus G_{max}, was then computed for both dry and fully saturated conditions using shear wave velocities, equation (5-1) and plotted against the mean effective stress p′. G_{max} formula accounts for the change in specimen density ρ associated with the addition of water during saturation. As a result, the separation between the dry and saturated G_{max} trends is smaller than the separation observed in the corresponding Vs trends.

Figure 5-12 illustrates this clearly, showing that the two trends became closer when the results are expressed in terms of G_{max} rather than Vs.

The fitted exponents revealed the expected scaling between V_S and G_{max}. Since the small-strain shear modulus is computed from shear wave velocity, a power law of the form $Vs \propto (p')^{\beta}$ implies $G_{max} \propto (p')^{2\beta}$.

In the present dataset, β for Vs was 0.2386 (dry) and 0.2439 (saturated), while β for G_{max} was 0.4833 (dry) and 0.4897 (saturated). Accordingly, 2β equals 0.4772 (dry) and 0.4878 (saturated), which closely matches the corresponding β_G_{max} values. The small differences are within what would be expected from the density changes between the dry and saturated states.

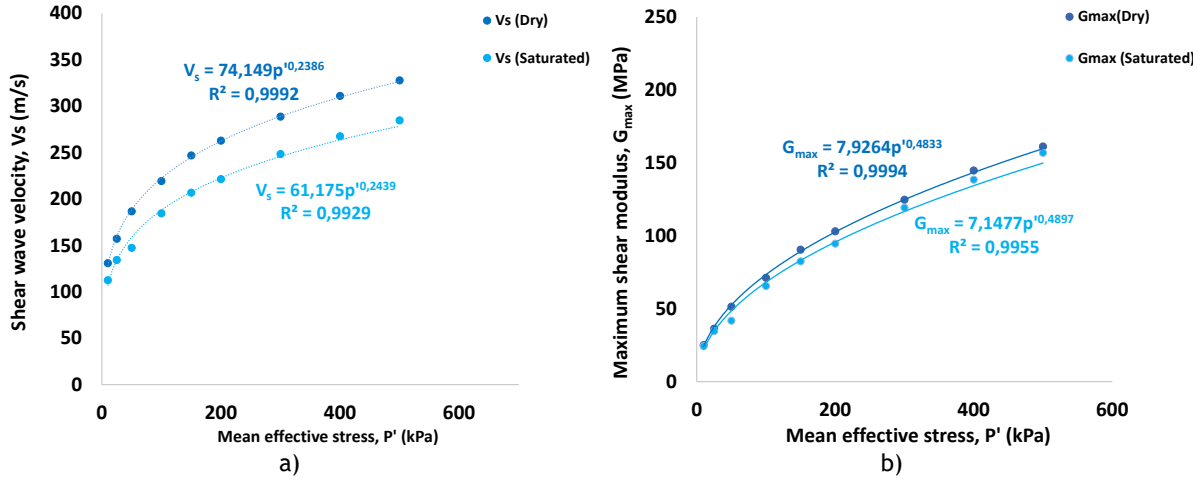

Figure 5-12 Stress dependency a) Vs and; b) Gmax stress dependency at different p´ of NB sand

Shear wave velocity Vs is strongly dependent on both void ratio and mean effective stress hence, to eliminate the void ratio influence from the stress dependency behavior, G_{max} was normalized by void ratio function. Different void ratio functions were proposed by various authors, three different functions were adopted in the current study as depicted in Table 5-2 and shown in Figure 5-13.

Table 5-2 Void ratio function F(e) and resulting fitting parameters for normalized Gmax of NB sand

#	Void ratio Function	Author	S_r	α (MPa)	β
F(e) 1	$\frac{(2.17-e)^2}{1+e}$	(Hardin & Richart Jr, 1963; Iwasaki et al., 1978)	Dry	67.50	0.4624
			Sat.	60.82	0.4758
F(e) 2	$\frac{1}{0.3+0.7e^2}$	(Hardin, 1978; Chung et al., 1984)	Dry	53.29	0.4676
			Sat.	48.37	0.4791
F(e) 3	e^{-x}, with x=1.3	Jamiolkowski et al. (1995)	Dry	53.106	0.4658
			Sat.	48.073	0.4777

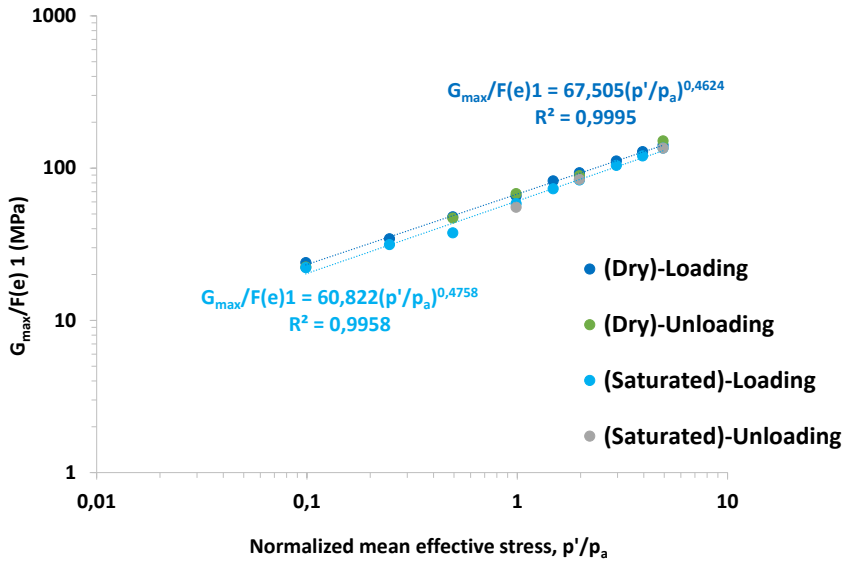

a)

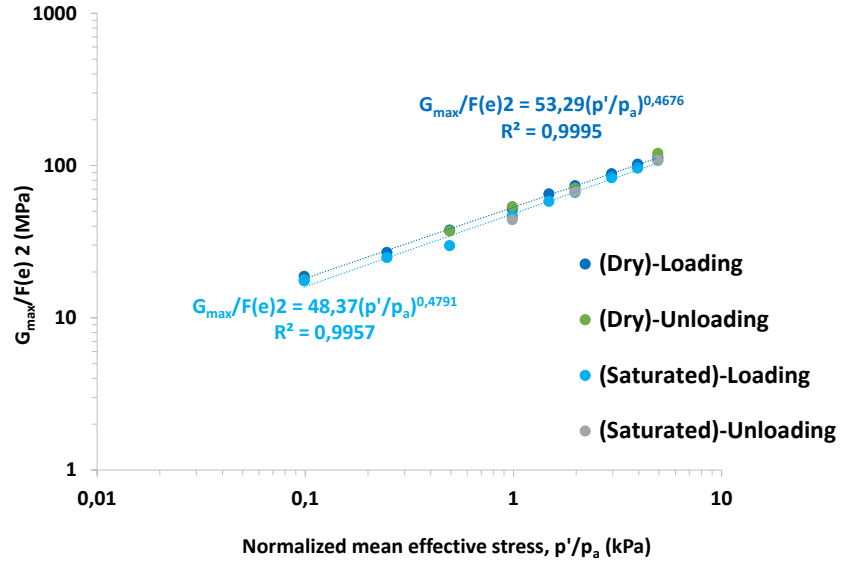

b)

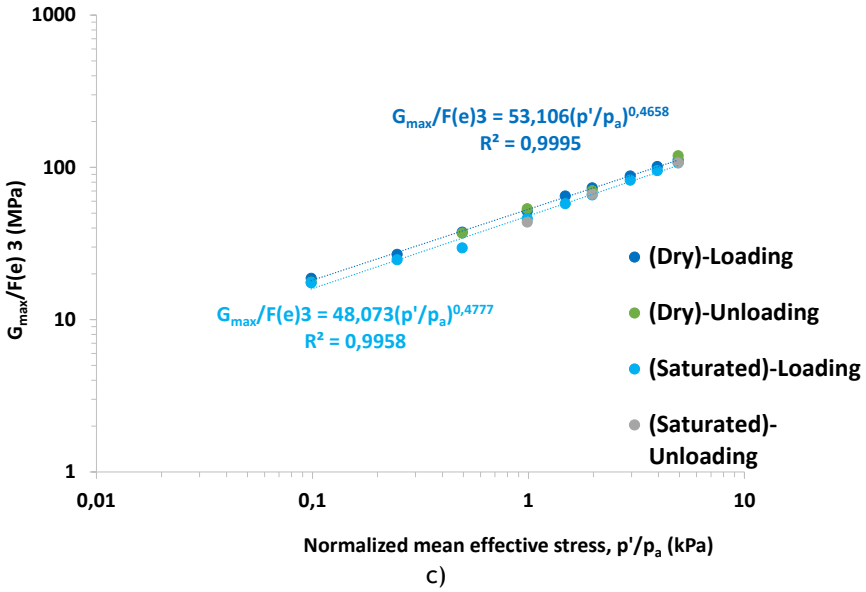

c)

Figure 5-13 G_{max} Normalized to the different adopted void ratio functions in dry and fully saturated states of NB sand

The normalized shear modulus G/F(e) was plotted against the mean effective stress normalized by the atmospheric pressure p'/p_a. The stress dependency was fitted using equation (5-3), in which normalized G_{max} is expressed as a power law function of p'/p_a. The best fit trends were obtained by regression of the experimental data.

$$\frac{G_{max}}{F(e)} = \alpha \left(\frac{p'}{p_a}\right)^{\beta} \quad (5\text{-}3)$$

Where, at $p' = p_a$, then $\frac{G_{max}}{F(e)} = \alpha$, consequently α is the void ratio normalized shear modulus at atmospheric pressure.

The fitting parameter resulting from F(e) 1 were;

- Dry: α = 67.505 MPa, β = 0.4624
- Saturated: α = 60.822 MPa, β = 0.4758

So, at the same p′, the ratio between the two trends will be:

$$\frac{G_{max}/F(e)_{sat.}}{G_{max}/F(e)_{dry}} = \frac{60.822}{67.505}\left(\frac{p'}{p_a}\right)^{(0.4758-0.4624)} = 0.901\left(\frac{p'}{p_a}\right)^{0.0134}$$

So, the saturated trendline is lower than the dry by roughly:

- at p'/p_a= 1, about 9.9%.
- at p'/p_a=0.1, about 12.5%.
- at p'/p_a= 5, about 8%.

Therefore, it can be concluded that fully saturated conditions trend exhibited a 9.9% lower soil small strain stiffness than dry conditions trend at the same p′ (when $p'=p_a$) and same void ratio based on BE measurements.

Repeating the same comparison using the alternative void ratio functions $F(e)2$ and $F(e)3$ gives reductions of 9.2% and 9.5%, respectively, for the fully saturated condition relative to the dry condition at p'/p_a.

These observations align with the findings of (Gu et al., 2015), who reported that, at the same void ratio and confining pressure, the small strain shear modulus G_{max} of saturated sand is typically about 7–10% lower than that of dry sand.

5.1.3.2. Poisson's ratio

The evolution of Poisson's ratio ν, in dry and fully saturated states is presented in Figure 5-14 as a function of mean effective stress p′, covering the full range of stresses tested.

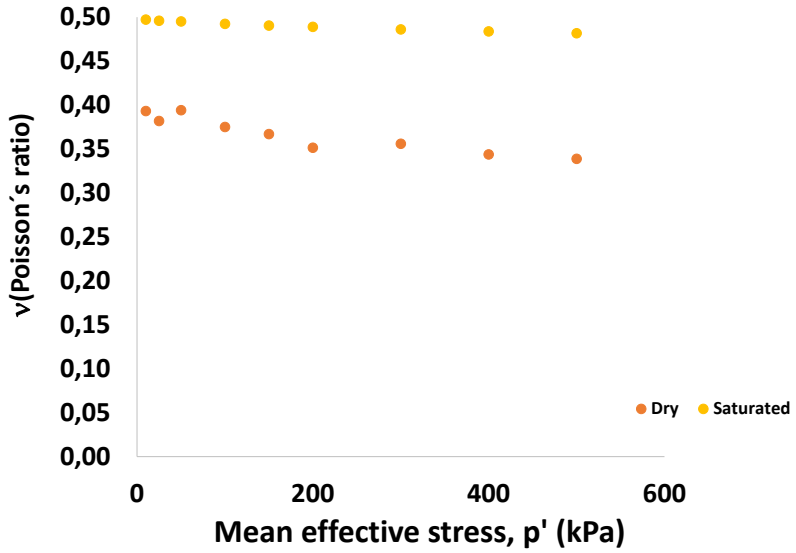

Figure 5-14 Poisson's ratio stress dependency on different p′ in dry and fully saturated conditions

Poisson's ratio, ν is a dimensionless elastic parameter that quantifies the coupling between axial and lateral strain under small strain loading. In the context of wave-based characterization, Poisson's ratio can be derived assuming an isotropic, linear elastic continuum (homogenous) from the measured compressional and shear wave velocities Vp and Vs, poison's ratio was estimated using equation (5-4).

$$\nu = \frac{\left(\frac{\mathrm{Vp}}{Vs}\right)^2 - 2}{2\left(\frac{\mathrm{Vp}}{Vs}\right)^2 - 2} \tag{5-4}$$

For granular soils, ν is strongly influenced by the bulk compressibility (and therefore Vp), because saturation substantially increases the constrained (bulk) stiffness through the pore fluid bulk modulus, whereas the shear stiffness (and Vs) is comparatively less sensitive. This effect is captured directly through the elastic relationship between ν and the velocity ratio Vp/Vs.

In the present study, the average of estimated ν ranged from 0.35 to 0.4 in dry conditions which is higher than typical values for unsaturated soils (about 0.15± 0.05) however values about 0.25 to 0.3 were proposed for sands by (Kumar & Madhusudhan, 2010 ; Ferreira et al., 2021).

Under fully saturated conditions, the average ν increased to approximately 0.49 to 0.50. This significant increase is driven mainly by the strong change of Vp after saturation. Therefore, this value should not be interpreted as the Poisson's ratio of the sand but rather as an apparent response of the saturated sand-pore water system.

Figure 5-15 compares the evolution of Poisson's ratio, ν, with mean effective stress range p′ obtained in this study against the data from (Ferreira et al., 2021), for the same type of sand. The two datasets agree well in terms of ν across the tested stress range in dry and saturated conditions.

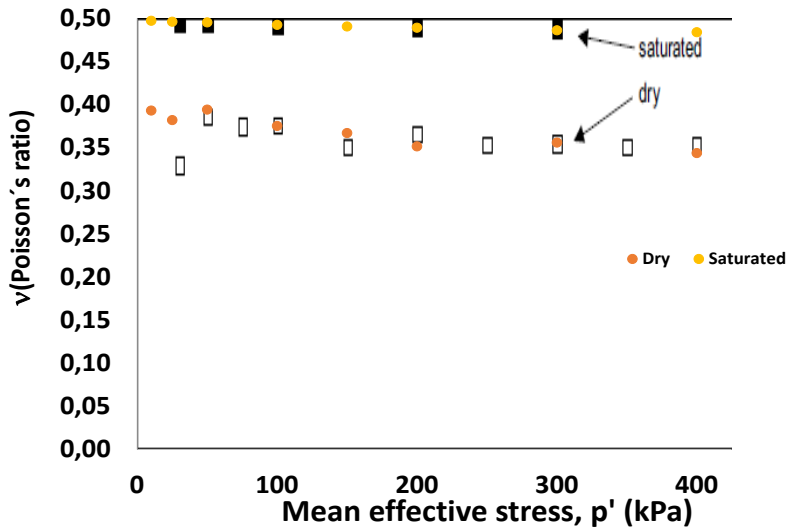

Figure 5-15 Poisson's ratio stress dependency on different p' in dry and fully saturated conditions plotted against Ferreira et al. (2021)

Poisson's ratio ν for the cyclic triaxial CTx specimens was estimated prior to cyclic loading from the measured seismic wave velocities, assuming linear isotropic elasticity.

Figure 5-16 compiled the values obtained for representative tests. All specimens exhibited the same overall trend, while some scatter was observed, which is attributed to differences in the initial soil state, and degree of saturation. The initial ν values after specimen preparation varied between approximately 0.30 and 0.38.

During saturation, ν increased markedly because Vp is highly sensitive to the compressibility of the pore fluid. As saturation progressed (water flushing followed by back pressure elevation), the pore fluid bulk modulus increased substantially leading to a sharp rise in Vp. whereas even small gas contents can reduce Vp dramatically. In contrast, Vs is governed primarily by the shear stiffness of the soil skeleton and is therefore much less sensitive to saturation than Vp. The net effect is an increase in Vp/Vs, which drives ν toward higher values of about 0.49.

With subsequent consolidation (increasing p′), the small strain stiffness of the skeleton increased, and Vs increased. Once the specimen was fully saturated, Vp was already high and typically shows a weaker sensitivity to further increases in p′ than Vs. Consequently, Vp/Vs decreased and the back calculated ν reduced slightly, from values close to 0.49 toward ~0.46 to 0.48).

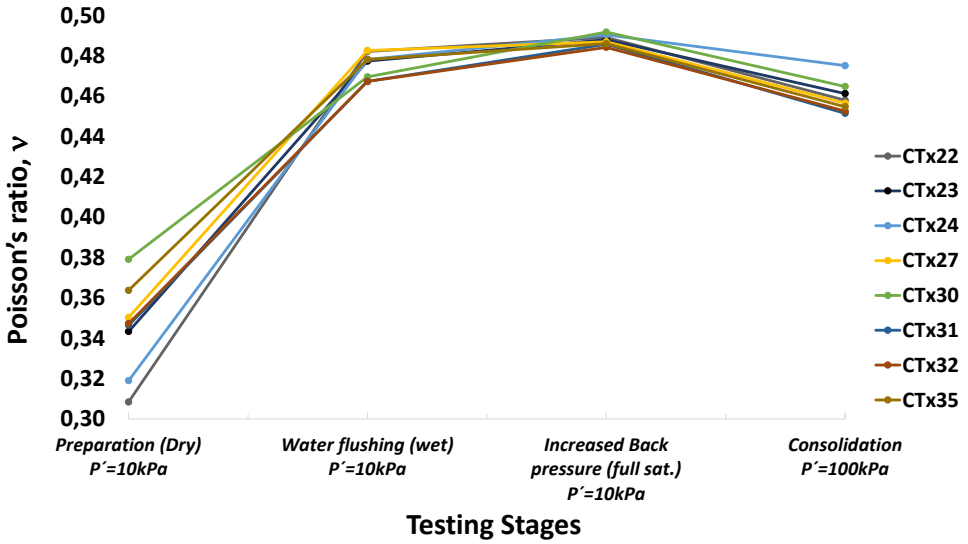

Figure 5-16 Poisson's ratio ν for CTx tests, under different saturation and mean effective stress conditions

Limitations while using BE

Although P-waves can propagate in solids, liquids, and gases, their detectability in bender element BE testing is strongly influenced by (i) the effective bulk stiffness of the pore-fluid phase and (ii) signal-to-noise effects intrinsic to the BE system. In saturated soils, the pore fluid has a high bulk modulus (no compressibility), which increases the undrained bulk stiffness of the porous medium and typically leads to higher P-wave velocities and clearer received waveforms. In contrast, in dry or partially saturated conditions the presence of air dramatically increases the compressibility of the pore fluid, reducing the P-wave velocity and often increasing attenuation and waveform distortion. As a result, it was observed many times that, the received P-wave may have a lower amplitude and a less distinct onset, making the first-arrival pick less straightforward than under saturated conditions.

furthermore, in some cases, electromagnetic crosstalk was also reported while measuring seismic waves due to the electromagnetic coupling between the transmitter and receiver circuitry. This EM is not a wave propagating through the specimen rather, it is a direct electrical coupling through cables, grounding, and the surrounding test setup, and it usually appear at the receiver before the arrival of the true wave.

The presence of this crosstalk can mask the initial portion of the received response and complicate arrival-time interpretation unless appropriate action is done (e.g., shielding, careful grounding, and wiring/layout practices).

5.1.4. Liquefaction resistance of fully saturated tests

The typical resulting plots of test number CTx1 as an example, were shown in Figure 5-17 where, a) shows the relationship between the deviatoric shear stress q and the axial strain ε_a while, b) represents the soil stress path; the relationship between the deviatoric shear stress (q) and mean effective confining pressure p′, c) indicate the excess pore water

pressure evolution with the axial strain, finally d) reveals the number of cycles required to trigger liquefaction N_L with the corresponding excess pore water pressure ratio build-up $r_u = \Delta u/p'_o$.

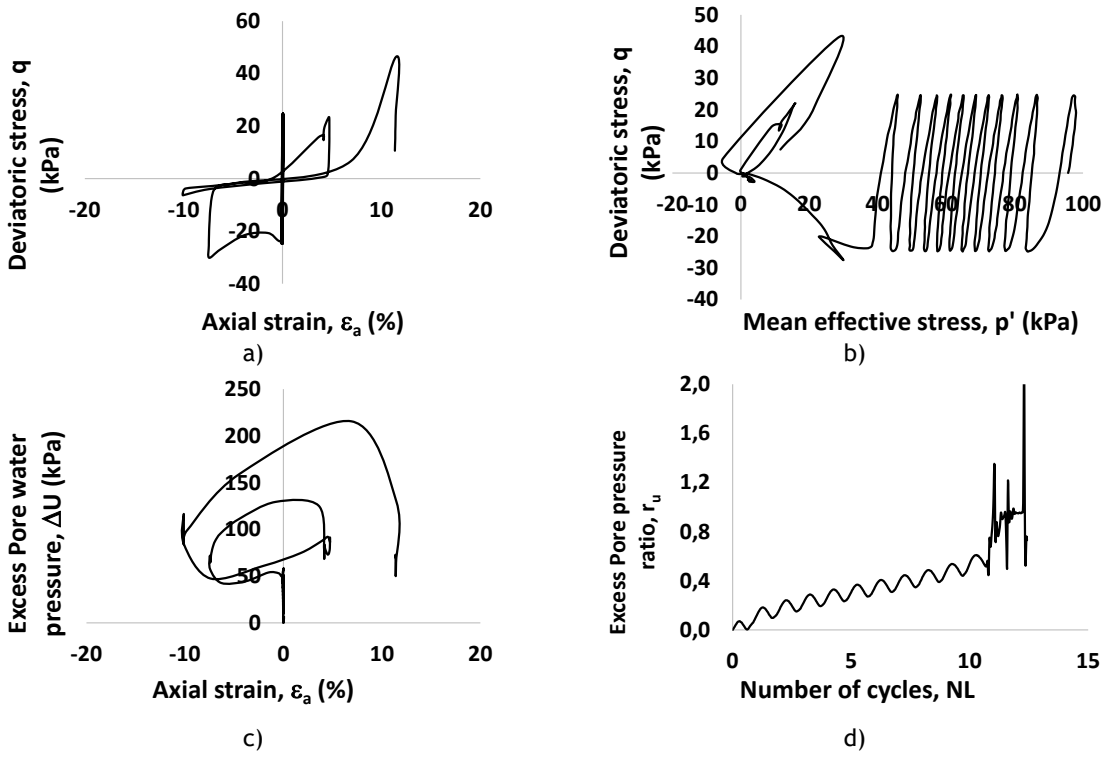

Figure 5-17 Typical undrained cyclic shear characteristic plots for Test (CTx1); a) stress-strain behavior; b) Stress path q: p′ space; c) excess pore water pressure ∆u against axial strain ε_a; d) Excess pore water pressure build-up ratio r_u with the number of cycles N_L

The liquefaction resistance curve LRC for fully saturated NB sand samples was generated by plotting the cyclic stress ratio CSR calculated by equation (5-5) against the number of cycles required to trigger liquefaction N_L as shown in Figure 5-18. Tests were performed under the same mean effective confining pressure p'_o =100 kPa, while applying various CSR values.

$$CSR = {}^{q}/_{2p'_o} \tag{5-5}$$

The plot demonstrates that liquefaction resistance decreased (defined by lower number of cycles required to trigger liquefaction) as cyclic stress ratios increase.

A best fitting regression was performed based on the formula (5-6) where a and b are the equation fitting parameters.

$$CSR = a\, N_L{}^{-b} \tag{5-6}$$

Several CTx tests were performed. However, because the testing program was conducted in typical phases (Preparation, Saturation, consolidation, cyclic shearing) and the final relative density Dr was not fully consistent across specimens, only tests with comparable final states were chosen for this particular analysis. The selected specimens had final Dr values between 37% and 44%, corresponding to void ratios e = 0.747–0.724, even-though this void ratio range

is narrow (Δe = 0.023), it produced a noticeable difference in Dr because this sand has a small void ratio span (e_{min} = 0.54, e_{max} = 0.87) so, a minor change in e, becomes amplified and lead to a relatively large change in Dr for otherwise similar specimens.

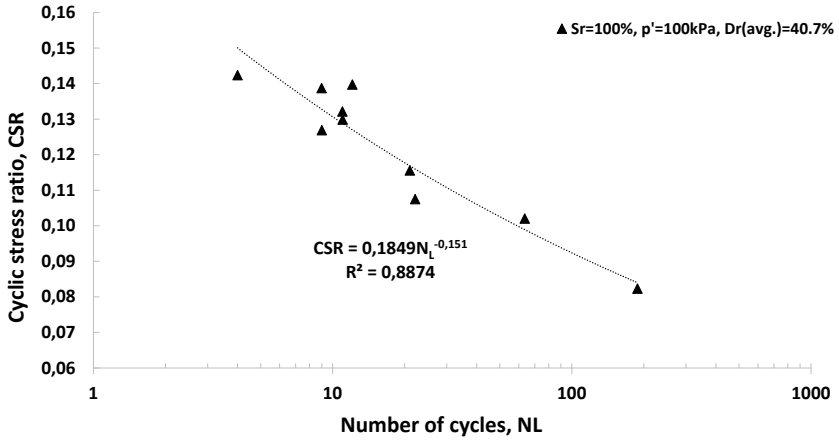

Figure 5-18 liquefaction resistance curve of fully saturated NB-soil.

To validate the findings and enable comparison with other references, Figure 5-19 provides a comparative analysis between the LRC generated in the current study and the LRCs produced by Ramos (2021) for fully saturated NB soil specimens as well. They developed multiple LRC_s considering various void ratios and mean effective stresses. The blue triangles symbols represent the tests conducted in the current study.

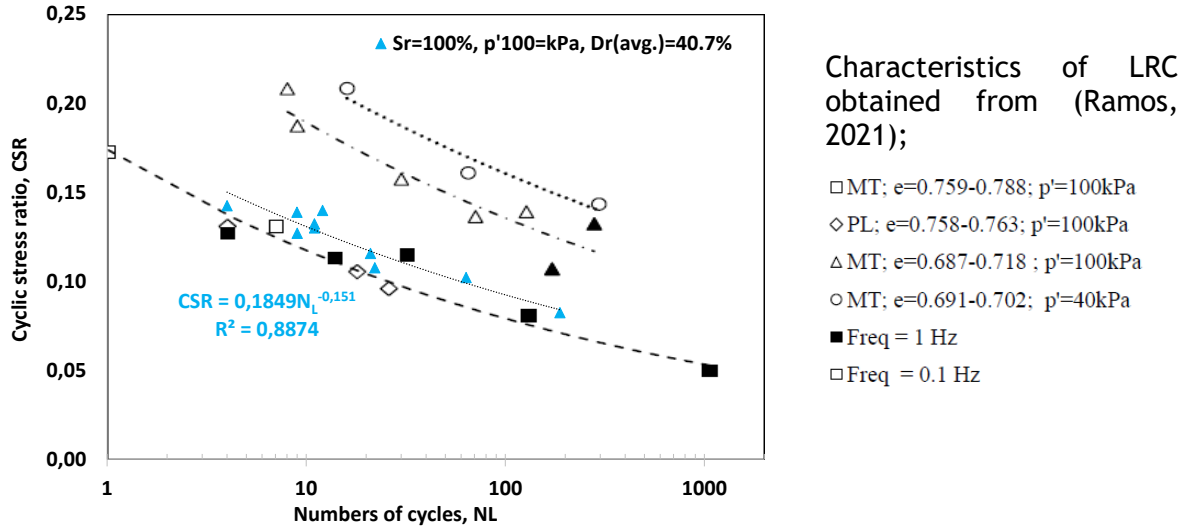

Figure 5-19 Comparative analysis between the Liquefaction resistance curve LRC of fully saturated NB sand generated from the current study and the LRCs produced by (Ramos, 2021)

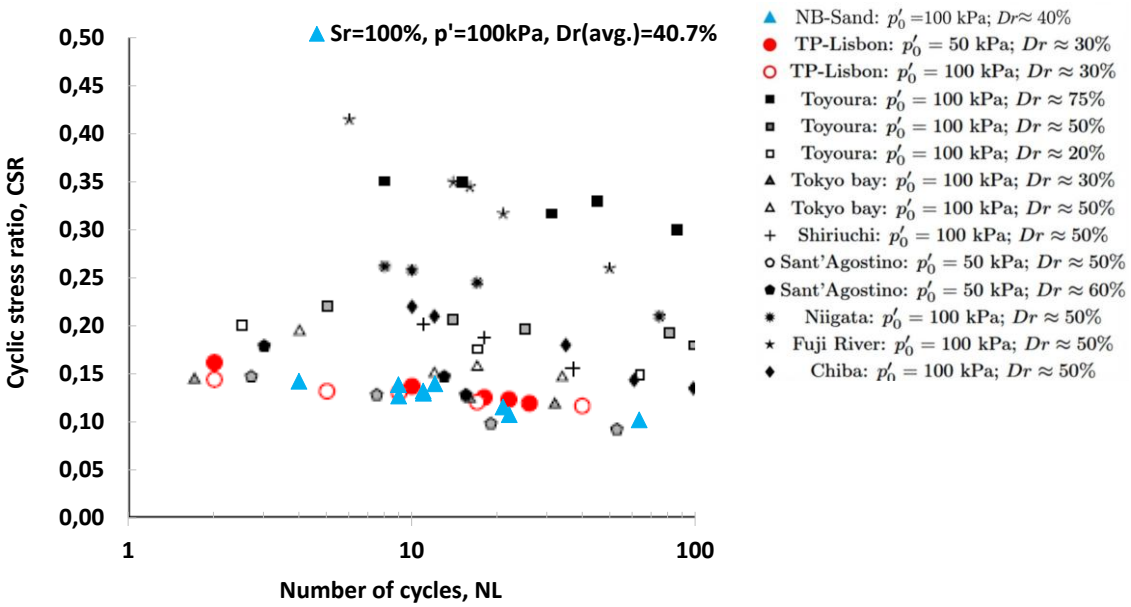

Figure 5-20 Liquefaction resistance of fully saturated NB sand compared with other soils

The comparison between these results revealed that the LRC aligned parallel to the LRCs presented by Ramos (2021), indicating a consistent trend in liquefaction resistance behavior. Furthermore, Figure 5-20 shows a comparison between LRC of the current analysis with LRC of other types of soils reported by under various p'$_o$ and Dr.

5.1.5. Liquefaction resistance of partially saturated tests

Undrained cyclic triaxial tests were performed on partially saturated NB sand specimens under identical preparation methods, and the same initial confining stresses, as pre-reported. However, it was noted that the relative densities prior to cyclic shearing were not always consistently similar. These fluctuations could be attributed to the expected minor differences during samples preparation the variations in volumetric change occurred during the testing phases in addition to the different Back pressure BP values achieved by the end of saturation. The tests were performed under various degrees of saturation and cyclic stress ratio levels CSR to assess their influence on the liquefaction resistance of partially saturated NB sand. The Initial effective confining pressure used in the study was 100 kPa. Typical cyclic shear characteristic plots for fully saturated test CTx9 and partially saturated test CTx25 were plotted together in Figure 5-21.

A direct comparison between CTx9 and CTx25 was performed because the two tests were conducted under nearly identical loading conditions, with only small differences in initial state. Before cyclic loading, the Dr of CTx9 and CTx25 was 37.4 and 34.9% respectively. The applied cyclic stress ratio was also very similar, with CSR = 0.142 for CTx9 while CSR = 0.138 for CTx25. The key difference was the saturation level, CTx9 was fully saturated, while CTx25 had Sr=94.6%. Under these conditions, the small differences in relative density and CSR had opposite directions influence on the liquefaction resistance, CTx9 is slightly denser (which would increase liquefaction resistance), but it was also loaded at a slightly higher CSR (which would reduce it). Given how close both differences are, neither provides a convincing explanation on its own. The most meaningful distinction between the two tests

is the degree of saturation, so any clear change in liquefaction resistance is best attributed to the reduction of Sr in CTx25.

Figure 5-21 (a) showed that the fully saturated specimen CTx9 accumulated substantially larger compressive axial strains (up to approximately 16–18%) than the partially saturated specimen CTx25 (approximately 11–12%) at comparable deviator stress levels. In extension, CTx9 reached slightly larger negative strains (approximately −10%) than CTx25 (approximately −8%). Figure 5-21(b) indicated progressive reduction of mean effective stress p′ during cycling for both specimens, with eventual migration toward low p′ as pore pressure accumulated.

In the pre-collapse segment shown, the mean effective stress for CTx9 exhibited a higher p′ level (approximately 60 kPa) however, CTx25 (approximately 40 kPa). Moreover, CTx25 exhibited comparatively narrower p′-oscillations, referring to smaller cyclic pore pressure increments. These narrower oscillations of p' shown in CTx25 would be attributed to the effect of partial saturation, whereby increased pore fluid compressibility reduces pore pressure generation and delays the approaching very low effective stress. Plot (c) showed higher excess pore pressure build-up Δu and larger strain accumulation in CTx9 compared with CTx25. Finally, plot (d) quantifies the gain in liquefaction resistance where, r_u accumulated more rapidly in CTx9 than in CTx25, and the number of cycles to reach the liquefaction criterion (defined here by $r_u \approx 1$) increased from approximately 4–5 cycles to approximately 10–11 cycles when Sr was reduced to 94.6%.

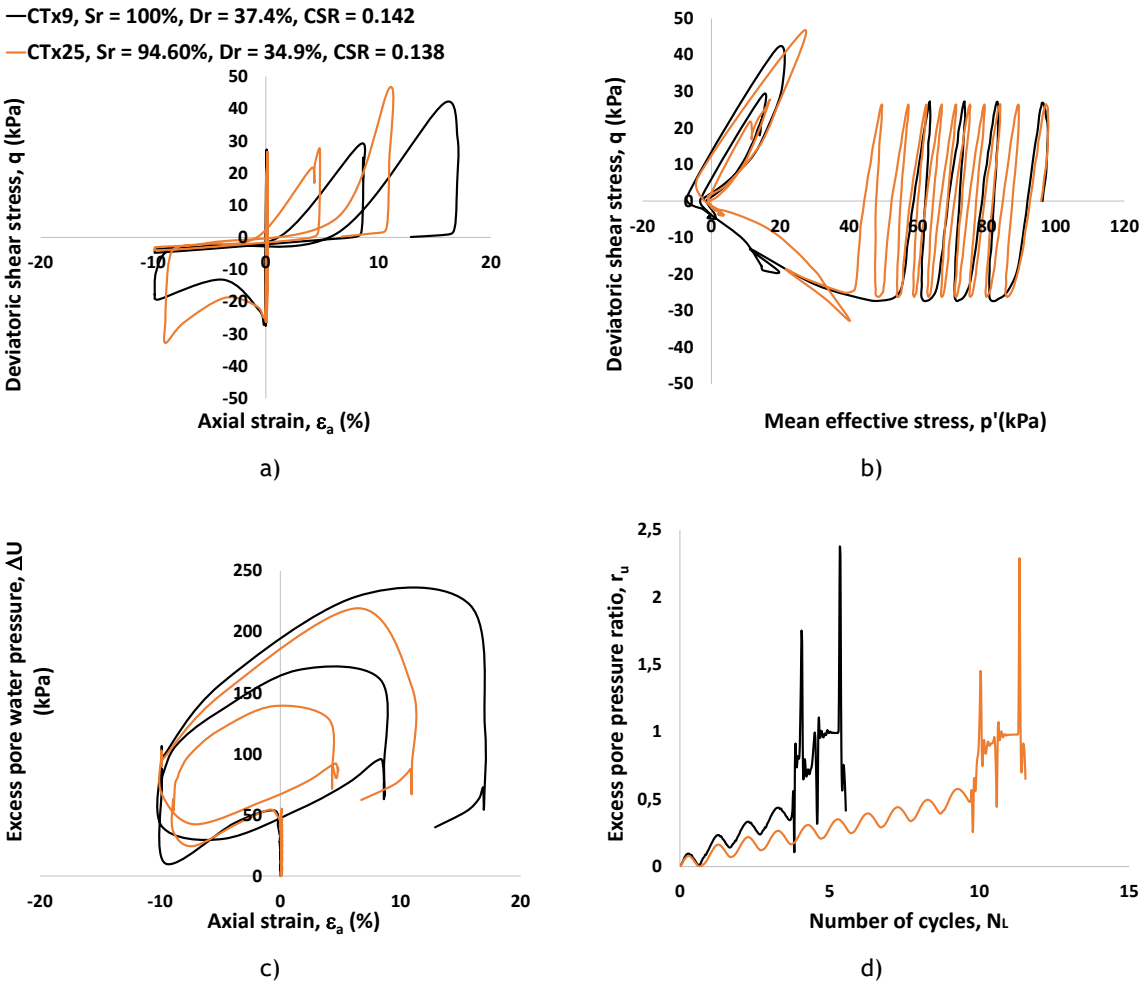

Figure 5-21 Typical cyclic shear characteristics for tests (CTx9 and, 25); a) stress-strain behavior; b) Stress path q: p` space; c) excess pore water pressure; d) Excess pore pressure ratio with the number of cycles

Figure 5-22 presents the instantaneous excess pore pressure ratio, r_u (primary y-axis) and the evolution of mean effective stress, p′ (secondary axis) with number of cycles for CTx9 and CTx25.

Both tests began from the same initial mean effective confining stress, p'_o=100 kPa. The fully saturated specimen (CTx9) showed a more rapid increase in r_u and a faster reduction in p′ from the first cycles, whereas the partially saturated specimen CTx25 exhibited the same trends at reduced rates compared with CTx9. Over the overlapping early cycles between the two tests, (N=1 to 4), the divergence between the two responses increased with cycle number, such that progressively larger differences in instantaneous r_u and p′ were observed at cycle 3 than at cycles 1 and 2.

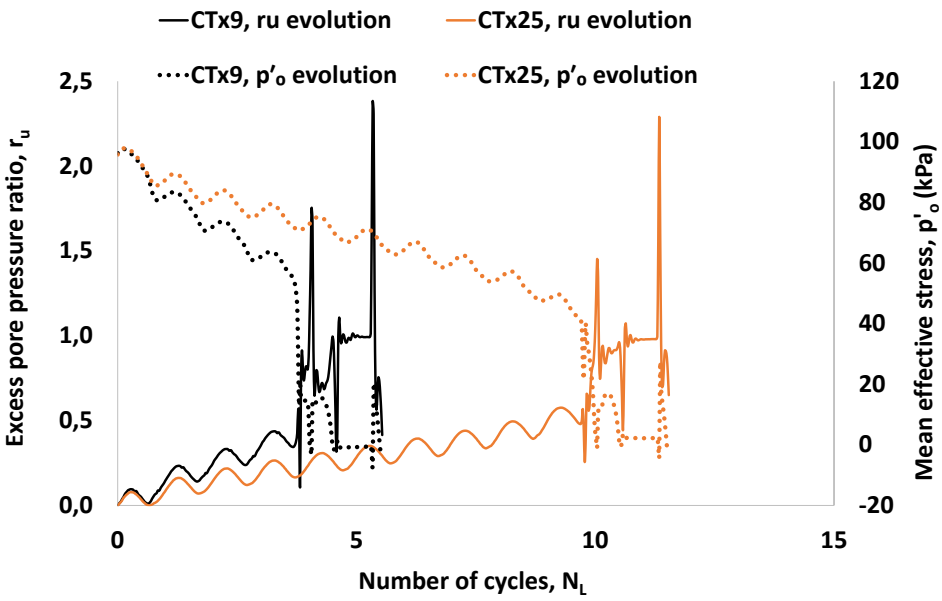

Figure 5-22 r_u and p'_o evolution with the number of cycles N_L cycles for CTx9 and CTx25

5.1.6. Liquefaction resistance analysis using volumetric water content, θ

The variation in void ratio before shearing necessitated the use of the volumetric water content parameter Theta θ, to assess the soil liquefaction resistance. As this approach incorporates the two key factors; the degree of saturation Sr and the final void ratio e_f, as detailed earlier.

Hence, the volumetric moisture content, theta θ, was employed to establish the liquefaction resistance curve LRC for partially and fully saturated tests. Tests were categorized into four groups based on their values of θ, which enables comparing the LRCs for various Sr and void ratio, as listed in Table 5-3.

Figure 5-23 displays LRC curve trendlines accompanied by R-squared values and fitting equations for the four groups where G_1 is represented in the plot by the small blue triangle symbols, G_2 represented by the green circle symbols and G_3 represented by the red circles and finally G_4 is plotted in the black circles. CSR is the cyclic stress ratio while N_L refers to the number of loading cycles required to trigger liquefaction.

Table 5-3 Characteristics of grouped CTx of NB sand

Testing group	Dr%	$Dr_{(avg.)}$%	Sr%	$Sr_{(avg.)}$%	Theta	$Theta_{(avg.)}$
G_1	44,37 44,28 43,31 41,73 41,19 39,48 38,54 38,47 38,43 37,36	40.71	100	100	43-42	42.38
G_2	26.90 23.75 25.78 28.37 27.52 26.76 28.90	26.96	93.32 93.86 95.79 95.84 96.36 96.60 97.03	95.54	42-41	41.9
G_3	36.30 38.11 30.81 41.76 34.85	36.36	89.11 89.55 90.02 90.09 90.5	89.86	39-38	38.51
G_4	32.79 34.13 35.86 34.60 37.91	35.06	86.98 85.44 85.64 85.69 86.65	86.08	37	37.01

Tests of group G_1 had higher relative densitiy due to the introduction of CO_2 gas during the saturation process, which significantly increased the relative densities of this group of testing. In addition, fully saturated testing time was longer than partially saturated tests which in turn densified the sample more. The relative density Dr for G_2 ranged between 24% and 29% before shearing, with corresponding saturation degrees Sr% ranging from 93% to 97%. In contrast, G_1 exhibited Dr ranging from 37% to 44% before shearing.

Group G_2 showed a volumetric water content θ of 41–42%, while the fully saturated group G_1 had θ values of 42–43%. Despite the near overlapping trendlines, G_2 consistently exhibited slightly higher liquefaction resistance as clear in the Figure 5-23.

The trendline of G_1&$_2$ reported that, eventhough speciemens of G_2 were substantially looser than those in G_1, the benefit associated with reduced saturation outweighed the adverse effect of lower relative density, resulting in a modest enhancement in liquefaction resistance.

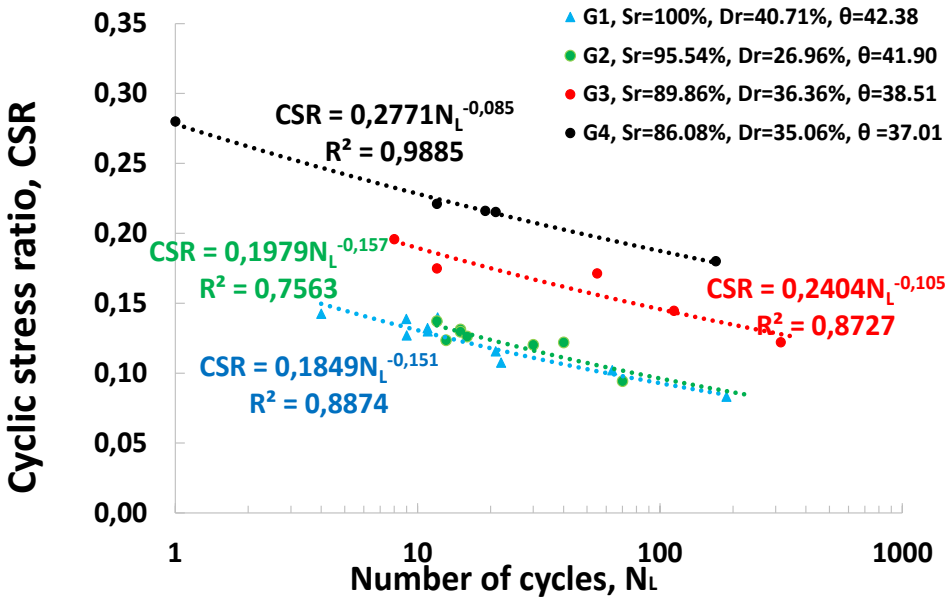

Figure 5-23 The Liquefaction Resistance Curves LRCs curves for the four testing groups arranged based on the values of (θ).

For this reason, θ is as a key state variable in the interpretation where even a small reduction in θ within this narrow band corresponded to a measurable gain in liquefaction resistance.

To quantify the increase in cyclic resistance, the experimental CSR-N_L data of the four testing groups were fitted using a power law regression of the form: $CSR = a\,{N_L}^{-b}$, where, a and b are best-fit regression parameters

Group G_3 showed a clear improvement in liquefaction resistance despite having a lower relative density than G_1 (by approximately 4%). Reducing the average degree of saturation to about 90% was sufficient to change the cyclic response. At N_L=15, the cyclic resistance of G_3 increased by approximately 47.3% relative to the fully saturated group G_1.

Group G_4 exhibited the highest liquefaction resistance of the four groups. Although its average relative density was only about 35% (about 5% looser than G_1) and its average degree of saturation was about 86%, the lower saturation substantially altered the cyclic behavior. At N_L=15, G_4 showed an increase of approximately 79% in cyclic resistance compared with G_1.

In the fitting regression, the exponent b controls the slope of the CRR-N_L relationship (i.e., how fast resistance decreases as the number of cycles increases). A smaller (less negative) exponent means the curve is flatter, so the resistance degrades more slowly with increasing N_L.

Beyond exhibiting higher cyclic resistance than G_1, G_3 and G_4 also showed an increasing cyclic resistance at higher N_L, because their fitted exponents are smaller (less negative) than the G_1 regression exponent (they decay more slowly with cycle count) that creates an additional enhancement at larger cycle counts. For instance, comparing the regression equation of G_4 with G_1, equation (5-7):

$$\frac{CSR_{G_4}}{CSR_{G_1}} = \frac{0.2771}{0.1849}\,{N_L}^{(0.151-0.085)} = 1.498\,{N_L}^{-0.066} \qquad (5\text{-}7)$$

This formulation explains why the improvement increased with cycle count; at N_L=15 the ratio is approximately 1.79 (about 79% higher), while at N_L=100 it increases to about 2.03 (about 103% higher).

comparing G_3 and G_4, which have similar relative density, the reduction in saturation from around 90% to 86% produced a marked additional increase in liquefaction resistance.

Moreover, Parameter theta θ, combines the effects of saturation and void's structure so it reflects changes in both e and Sr in a single parameter. θ was approximately 38–39% for G_3, about 37% for G4, and 42–43% for G_1. Even with some variability in void ratio, these θ ranges provide a coherent basis for interpretation.

Figure 5-24 compares the liquefaction resistance curve LRC trends obtained in this study for the four testing groups with those reported by Molina-Gómez (2023) for the local Portuguese TP-Lisbon sand reconstituted at Dr≈30%. The LRCs derived herein are in good agreement with the trends, exhibiting comparable curve shapes and similar fitted slopes.

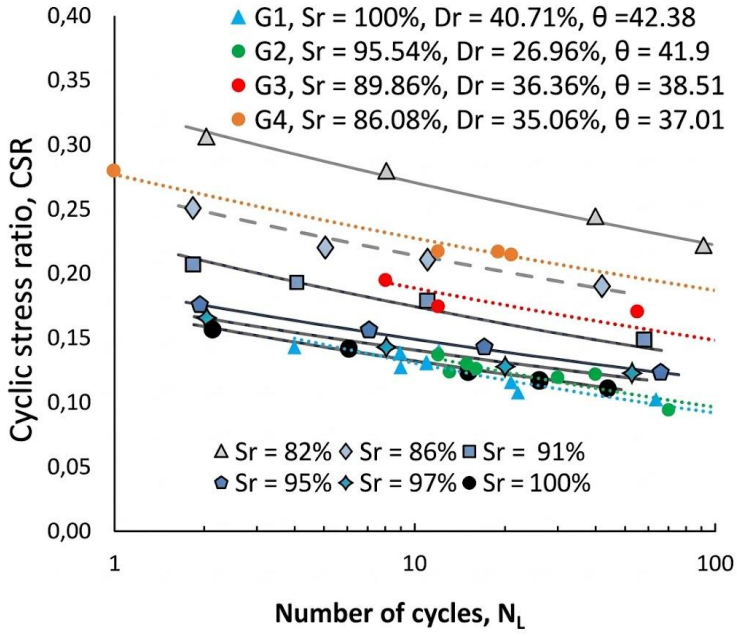

Figure 5-24 LRCs of the four testing groups along with other LRCs from different authors

Additionally, Figure 5-25 and Figure 5-26 illustrate the relationships between liquefaction resistance ratio LRR with theta θ and normalized theta θ/ $\theta_{sat.}$ respectively. While, Figure 5-27 and Figure 5-28 illustrate the relationships between liquefaction resistance ratio LRR along with theta values θ, degree of saturation Sr, and compressional wave velocities Vp measurements, respectively. The analysis was done for the four groups (G_1, G_2, G_3, G_4). The average values of Theta, Sr, and Vp was calculated for each group of tests.

The LRR for each testing group, was estimated by normalizing the average CSR of each group to the average CSR of fully saturated group at 15 number of cycles as shown in the formula (5-8).

$$LRR_{15} = \frac{CSR_{15}}{CSR_{15,sat}} \quad (5\text{-}8)$$

Where $CSR_{15,sat} = (CSR_{15})_{G1}$.

Figure 5-25 indicated an inverse relationship between volumetric water content, θ, and liquefaction resistance ratio across the testing groups, with LRR increasing as θ decreases.

Across the four groups, the degree of saturation decreased in relatively small, stepwise increments (approximately 4–6% between consecutive groups: 100%, 95.5%, 89.9%, and 86% for G_1 to G_4), yet the corresponding increases in liquefaction resistance LRR varied differently because LRR increment cannot be interpreted as a function of Sr alone, factors such as pore air/wetting distribution and the nonlinear cyclic response of sands may influence the rate of pore pressure accumulation and stiffness degradation. In the present dataset, density is a principal contributor to the variability in LRR increments. Between G_1 and G_2, G_1 was much denser than G_2 prior to cyclic loading (average Dr = 40.7% for G_1 versus 27% for G_2). Under this condition, the normalized liquefaction resistance at N_L=15 cycles increased only marginally from $(LRR_{15})_{G1}$ =1.0 (defined as $(CSR_{15})_{G1}/(CSR_{15})_{G1}$ to $(LRR_{15})_{G2}$ = 1.05 (defined as $(CSR_{15})_{G2}/(CSR_{15})_{G1}$.

Although G_2 is looser (which tends to reduce liquefaction resistance), it is also less saturated than G_1 (which tends to increase liquefaction resistance). Therefore, the compound parameter θ that accounts for those opposing influences of saturation level and density state changed only slightly over the same comparison (average θ =42.4 for G_1 to θ =41.9 for G_2), indicating that the reduction in Sr in G_2 was largely offset by its higher porosity (looser state). This near equivalence in θ aligned with the limited separation in (LRR_{15}) between G_1 and G_2.

Between G_2 and G_3, the average Sr decreased from 95.5% to 89.9% while the average relative density Dr increased from 27.0% to 36.4%. These concurrent changes act in the same direction; reducing pore pressure generation through partial desaturation and increasing cyclic resistance through densification thereby produced a pronounced decrease in average θ, from 41.9 to 38.5. The combined shift in Sr and density is reflected in the marked increase in liquefaction resistance at N=15 cycles, with $(LRR_{15})_{G3}$=1.47 compared with $(LRR_{15})_{G2}$=1.05.

Finally, when comparing G_4 to G_3, the two groups exhibited similar average relative density (36.4 and 35.1% for G_3 and G_4, respectively). While density effectively controlled, the observed change in response can be attributed primarily to the further reduction in degree of saturation, from Sr≈89.9% (G_3) to Sr≈86% (G_4). This is reflected by the decrease in volumetric water content from θ =38.5 to 37.

In this specific transition (G3→G4), the near-constant Dr means the decrease in θ is mainly driven by the decrease in Sr, and this coincides with a clear increase in liquefaction resistance at N=15 cycles: $(LRR_{15})_{G4}$=1.79 compared with $(LRR_{15})_{G3}$=1.47. The magnitude of this increment is larger than that observed between G_1 and G_2 (where a reduction in Sr was offset by a looser state), but smaller than the increment between G_2 and G_3 (where the reduction in Sr occurred alongside densification, producing a larger change in θ).

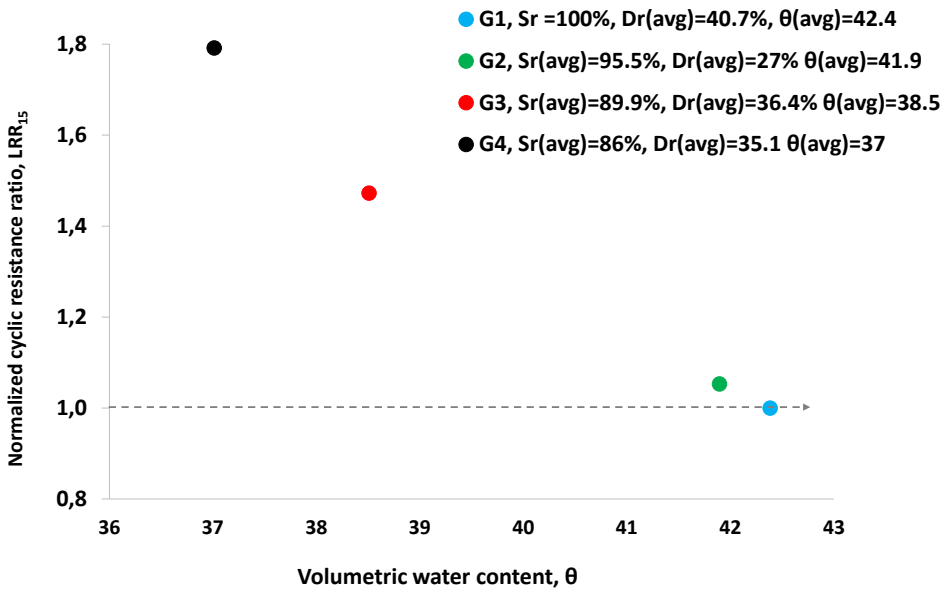

Figure 5-25 liquefaction resistance ratio LRR Vs theta values θ, for the three partially saturated groups of tests

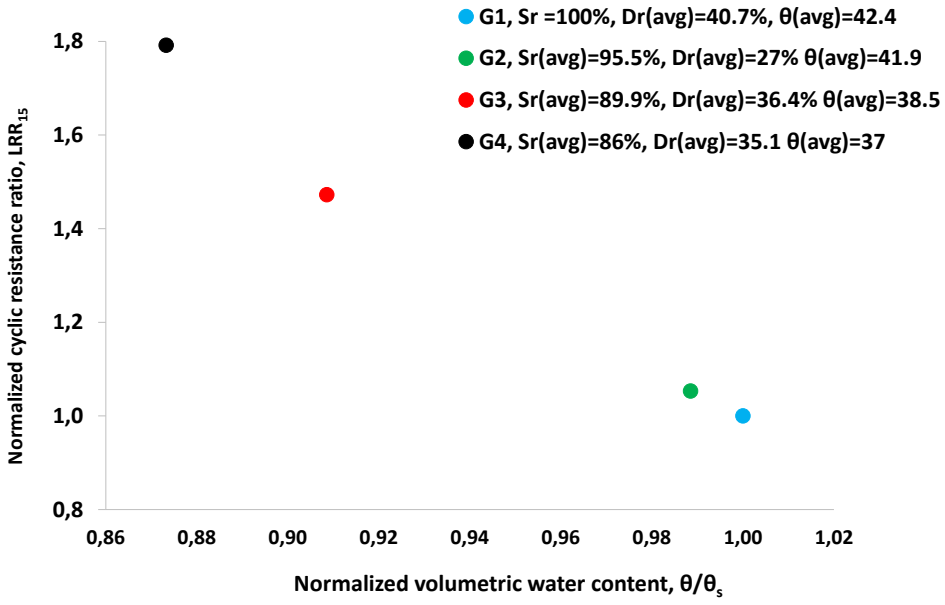

Figure 5-26 liquefaction resistance ratio LRR Vs theta values θ/ $\theta_{sat.}$, for the three partially saturated groups of tests

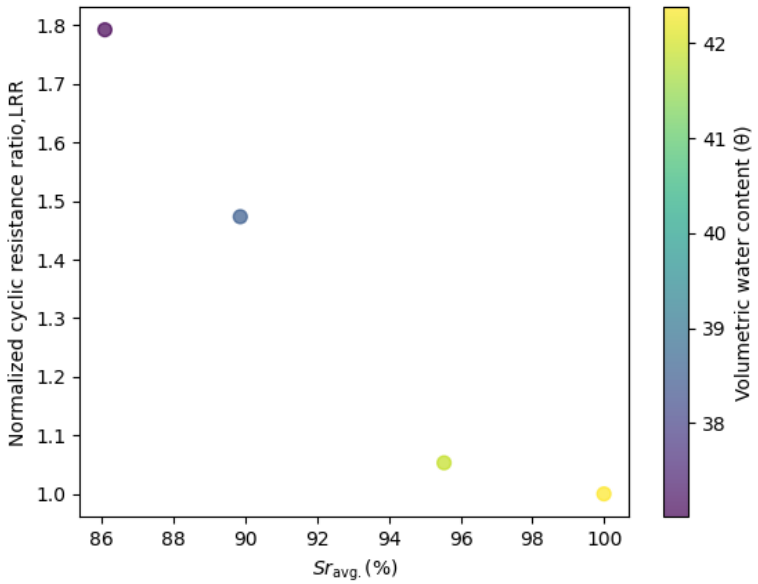

Figure 5-27 liquefaction resistance ratio LRR with the degree of saturation Sr for the three partially saturated groups of tests

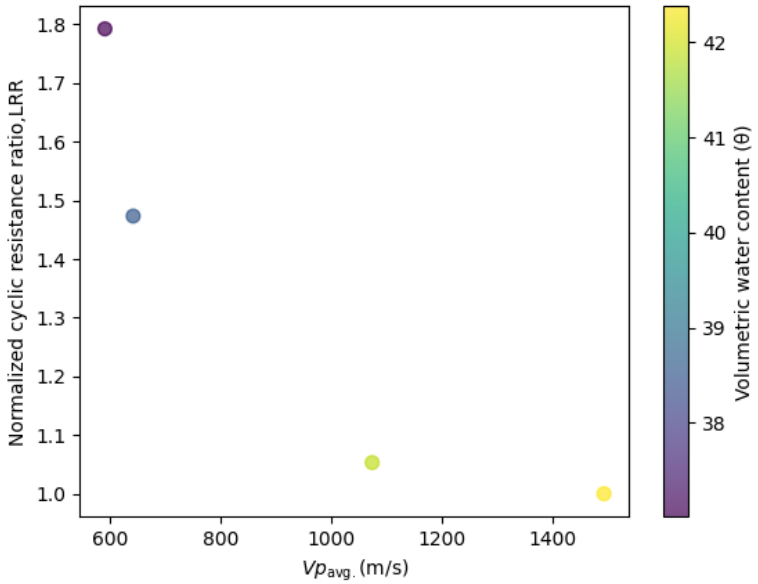

Figure 5-28 liquefaction resistance ratio LRR with the compressional wave velocities V_P measurements for the three partially saturated groups of tests

Figure 5-27 depicts LRR_{15} as a function of the average degree of saturation, $Sr_{,avg}$ %. The results demonstrated that the testing groups with lower average water content θ_{avg} exhibited lower $Sr_{,avg}$ and higher LRR_{15}. Figure 5-28 correlates LRR_{15} to the group-average compressional-wave velocity, $Vp_{,avg}$, together with θ_{avg} it showed that, a decrease in θ_{avg} is associated with lower $Vp_{,avg}$ and higher LRR_{15}.

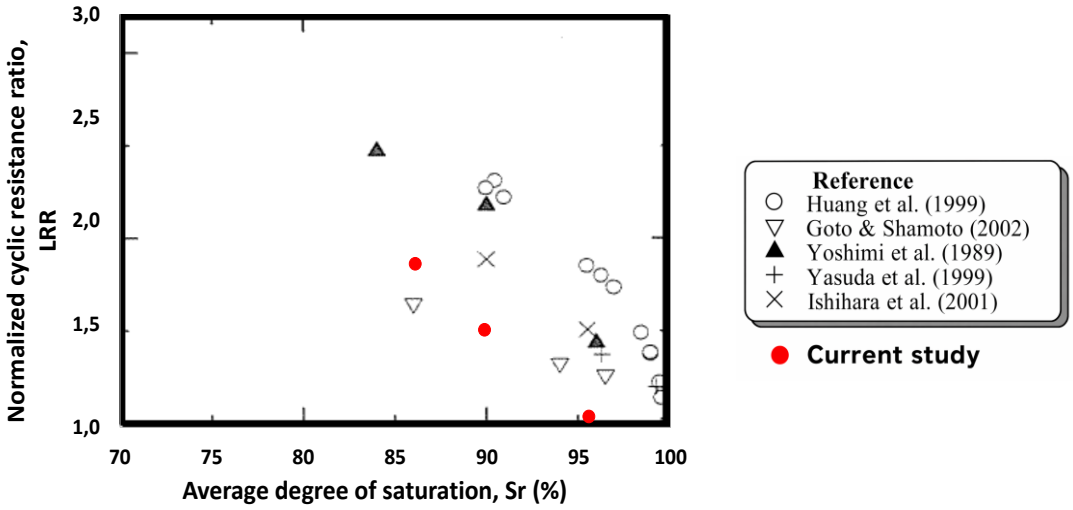

Figure 5-29 LRR obtained from the current study compared with other data from the literature

Figure 5-29 incorporate the LRR_{15} of the partially saturated groups of tests obtained from the current study, shown in red symbols into the plot obtained from (Okamura & Soga, 2006b) Where, it depicts some different results from different authors in the literature in the form of a relationship between Sr and liquefaction resistance of partially saturated soil normalized by fully saturated sand.

5.2. Hysteresis stress-strain behavior of NB sand

5.2.1. Analysis of stress-strain cyclic loops under fully and partially saturated conditions

This section investigates the undrained shear stiffness and damping evolution of NB sand in fully and partially saturated conditions. From the performed set of cyclic triaxial tests, five fully saturated and four partially saturated were used to analyze this behavior. These tests were selected as they share very close void ratio, same mean effective confining pressure of 100kPa and different Sr and various CSR too, all tests were done under undrained conditions as shown in Table 5-4.

Table 5-4 Parameters of the CTx tests used for the stress-strain analysis of NB sand

Test#	CO2	BP(kPa)	Sr_f (%)	e_f	CSR	N_L
CTx3	✓	300	100	0.743	0.132	11
CTx6	✓	300	100	0.740	0.108	22
CTx9	✓	300	100	0.747	0.142	4
CTx13	✓	300	100	0.743	0.082	188
CTx33	✓	300	100	0.755	0.095	99
CTx38	X	50	86	0.757	0.180	170
CTx39	X	50	86	0.752	0.221	12
CTx40	X	50	86	0.756	0.216	19
CTx41	x	50	86	0.745	0.215	21

For this purpose, the hysteresis shear stress-strain cyclic loops were studied. Shear stress τ was plotted against shear strain γ, forming stress-strain hysteresis loops for cyclic loading. Shear stress and shear strain were computed from the cyclic triaxial test results using equations (5-9) and (5-10).

$$\tau = q/2 \tag{5-9}$$

$$\gamma = (1 + \nu)\,\varepsilon_a \tag{5-10}$$

Where, τ is the shear stress, q is the deviatoric shear stress, ν is the soil's Poisson's ratio, γ is the shear strain and ε_a is the axial strains obtained using the axial Hall-Effect HE transducers. The resulting strains are defined as large strain range as it's resulting from cyclic triaxial testing.

For each plotted hysteresis cyclic loop, the equivalent secant shear modulus G_{sec} In addition to the corresponding material (hysteretic) damping ratio D were computed.

Each loop was centered around the plot origin (0,0). Damping ratio was obtained through computing the area of the hysteresis loop (energy dissipated per cycle, ΔW) relative to the maximum stored strain energy W, as depicted in equation (5-11).

$$D = \frac{\Delta W}{4\pi * W} \tag{5-11}$$

where ΔW is the area of the resulting hysteresis loop, and w is the area of a triangle formed by the secant stiffness to the peak point (the stored maximum elastic strain energy) (Figure 5-30), computed using the formula (5-12).

$$W = \frac{1}{2}\ \tau_a\,\gamma_a \tag{5-12}$$

where $\tau_a = \frac{\tau_{max} - \tau_{min}}{2}$ and $\gamma_a = \frac{\gamma_{max} - \gamma_{min}}{2}$

On the other hand, secant shear modulus (Figure 5-30) is defined as the slope of the line connecting the origin to the extreme points of the loop (stress amplitude divided by strain amplitude for that cycle), equation (5-13).

$$G_{sec} = \frac{\tau_{max} - \tau_{min}}{\gamma_{max} - \gamma_{min}} \quad (5\text{-}13)$$

Having various CSR for both sets of tests (Fully and partially saturated) was fundamental because lowering degree of saturation increases the soil cyclic strength and requires higher CSR to attain liquefaction triggering which in turn induces various strain levels between the two sets of tests which makes the comparison on the same strain level very challenging therefore, some normalization was adopted for sake of valid comparison. This section is not indeed a comparison, it's more into exploring the stiffness and damping evolution during cyclic loading at various saturation states. The objective was to assess how IPS affects the damping and stiffness behavior evolution during cyclic loading, in other words without inducing suction pressure as the Sr was above the threshold of saturation that may induce suction, how occluded air bubbles would affect the stiffness and damping characteristics of the soil during cyclic loading.

The tests were analyzed by evaluating the cycle-by-cycle evolution of stiffness and damping up to the onset of liquefaction. Specifically, the change of shear stiffness (secant modulus) and the corresponding evolution in hysteretic damping were tracked from the stress–strain loops as loading progressed. It is worth reporting that, shear strains were estimated from axial strains as shown in based on that assumption that ν is constant of about 0.5. This assumes an isotropic, small-strain elastic (constant ν), while real cyclic soil response is nonlinear and ν may not be constant across cycles/high strain level.

The corresponding shear stress and strain measurements were then processed in Python software, where a code was generated to estimate stress–strain hysteresis loops and to compute the key parameters; damping ratio and secant shear modulus. Figure 5-30 shows a typical stress strain hysteresis loop indicating the energy dissipated per cycle, ΔW and maximum stored strain energy, W).

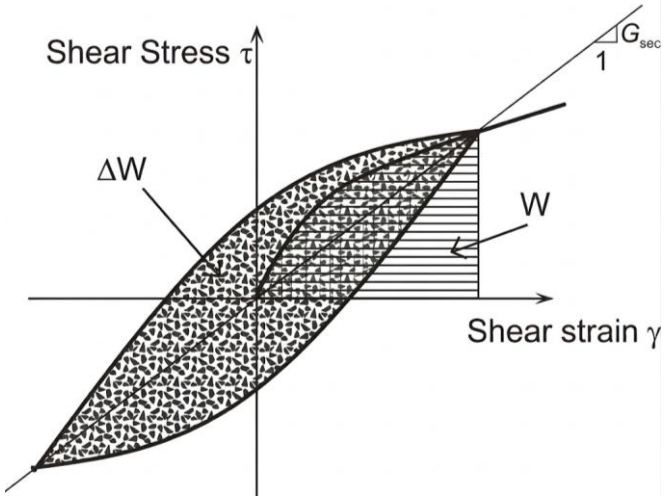

Figure 5-30 Typical hysteresis stress-strain loop for the estimation of secant shear modulus and estimation of material damping D

Figure 5-31a presents the successive shear stress–strain hysteresis loops recorded during the cyclic loading for tests CTx3, 6, 9 and, 13, respectively (fully saturated samples) while Figure 5-31b represents the resulting loops of tests CTx38, CTx39, 40, and 41 (partially saturated samples). These plots reveal all cycles resulting from cyclic loading excluding the irregular loops during liquefaction (last cycle (s), this was done intentionally because

liquefaction induced very large strains making it very difficult to recognize, evaluate and compare the cyclic loops near liquefaction.

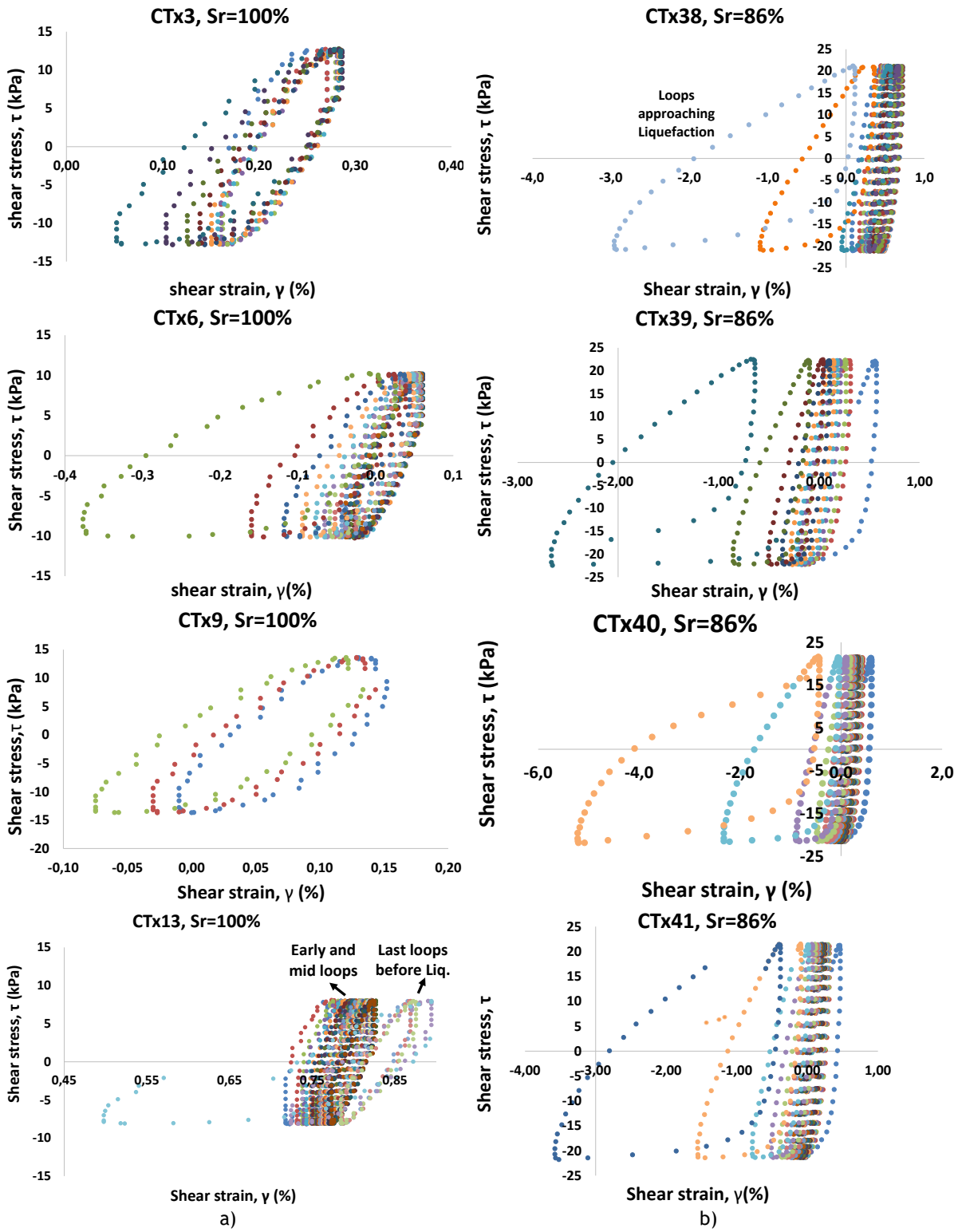

Figure 5-31 Shear stress and shear strain cyclic loops: a) Sr=100%; b) Sr=86%, excluding the loops where liquefaction occurred

As clear in Figure 5-31, the level of shear stress and generated strains are different for fully and partially saturated tests because they were carried out under various CSR values, but at the level of comparing the shapes and evolution of hysteresis stress-strain loops during cyclic loading, there are clear visual differences.

In fully saturated specimens, the progressive reduction in the slope of successive hysteresis loops was visually evident as liquefaction was approached, indicating rapid degradation of secant stiffness during cyclic loading. In contrast, the partially saturated specimens showed a more gradual reduction in loops slope, reflecting slower stiffness degradation.

The fully saturated specimens, particularly CTx3, 6 and, 9 exhibited directionally biased loops, with the response becoming anchored on one side while strains accumulated predominantly in the opposite direction, indicating the development of cyclic instability. By contrast, the partially saturated specimens showed a smaller overall drift of the loops, corresponding to the accumulation of mean plastic strain while mean effective stress, p′, was largely maintained.

Evaluating damping ratio from these plots (visually) would be misleading because visually stress strain hysteresis loops might appear bigger (higher dissipated energy) in some cases but when normalizing to the elastic strain energy it may end up with lowered damping ratio.

For clearer analysis, Figure 5-32 includes stress-strain hysteresis loops from selected representative cycles only (cycles N=2, 5, and 18) for tests CTx6 and CTx41, these two tests were selected for comparison because they reached liquefaction at more or less the same number of cycles; N_L=22 and 21, respectively. These plots confirm the visual observations of the stiffness evolution during cyclic loading for both tests.

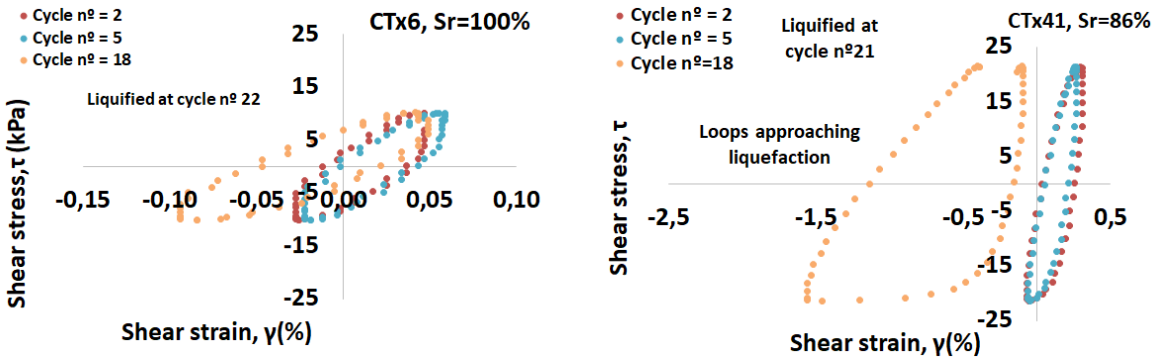

Figure 5-32 Shear stress and shear strain cyclic loops number 2, 5, and 18; a) CTx6, Sr=100% b) CTx41, Sr=86%

Figure 5-32a shows that CTx6 softened between loading Cycles 2 and 5, as indicated by the reduced loop slope. In contrast, Figure 5-32b reports that CTx41 exhibited a slight increase in stiffness over the same cycle interval, with the loop becoming slightly steeper from cycle 2 to cycle 5.

Figure 5-33a illustrates the hysterisis loops (shear stress-strain plots) of fully saturated spicemens while plot (b) illustrates the same for partially satuarted tests. This plotting shows the evoution of cyclic loops until the end of tests including last cycles where liquefaction occured.

Figure 5-33 shows that the partially saturated specimens tended to accumulate irrecoverable, or plastic, shear strain progressively with each loading cycle, resulting in larger cumulative shear strains up to liquefaction. This response was reflected by a gradual drift of the mean position of the hysteresis loops, rather than an immediate collapse. In contrast, the fully saturated specimens initially developed smaller shear strains, followed by a sudden and substantial increase in shear strain when liquefaction occurred.

This would be attributed to the presence of gas bubbles which increased the bulk compressibility of the pore fluid, so when shear induced volume contraction tendencies occur under undrained cyclic loading, a portion of the volume change is accommodated by compressing the gas bubbles rather than instantly elevating pore water pressure therefore soil deformed incrementally rather than collapsing suddenly. In contrast, the fully saturated specimens showed limited developed shear strains which is may be attributed to the lower applied CSR, followed by a sudden dramatic widening of the hysteresis loops and developed much higher strains once liquefaction was approached, at that point, stiffness dropped sharply and large shear strains occurred within a cycle or two, indicating the onset of instability and liquefaction.

In summary, induced partial saturation led to a more gradual hysteretic drift, with strains accumulating progressively during cyclic loading while delaying the abrupt strain development associated with liquefaction. Conversely, full saturation promoted a more sudden liquefaction-type response once excess pore pressure had built up sufficiently.

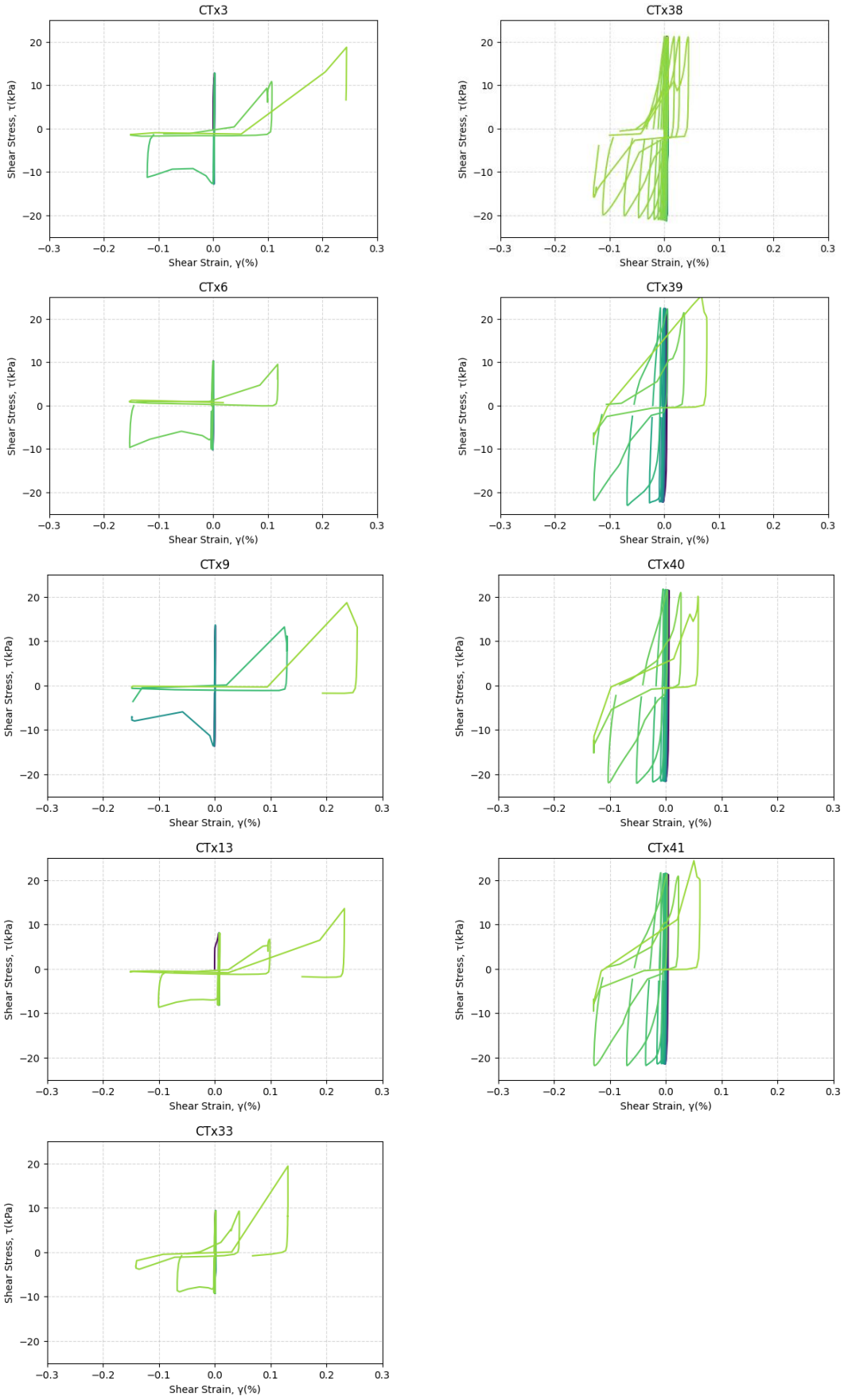

a) b)

Figure 5-33 Shear stress and shear strain cyclic loops a) Sr=100%; b) Sr=86% including the loops where liquefaction occurred

5.2.2. Secant shear stiffness

Beyond the visual observations, secant shear stiffness G_{sec} was estimated for each stress-strain cyclic loop and plotted against corresponding number of cycles for both sets of tests. As mentioned earlier, stiffness response of the first cycle may be misleading, so it was excluded from the analysis.

Figure 5-34 (a) shows the secant shear stiffness evolution with the number of cycles of fully saturated tests, while (b) presents the same for partially saturated ones.

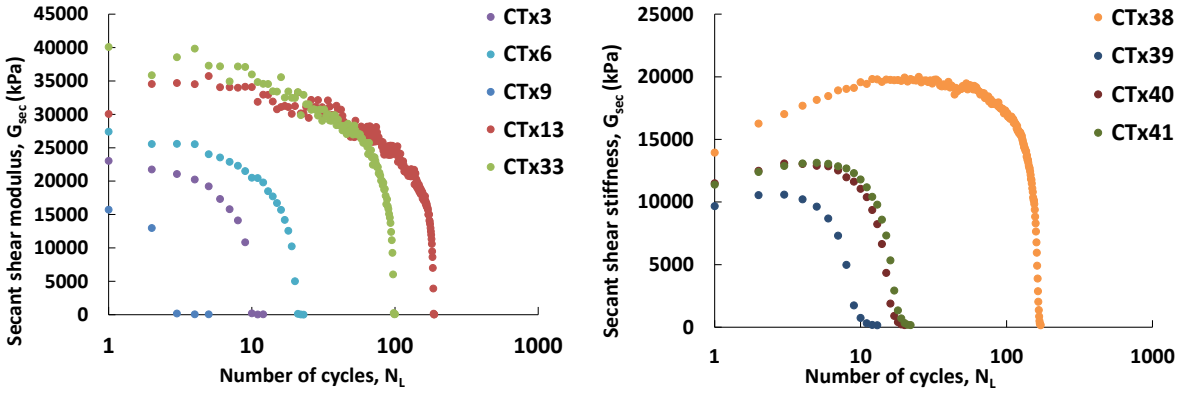

Figure 5-34 Cycle by cycle evolution of secant shear modulus a) Sr=100%; b) Sr=86%

From Figure 5-34, it can be concluded that the fully saturated specimens initially exhibited substantially higher secant stiffness than the partially saturated specimens. However, their stiffness degraded more rapidly during cyclic loading. In contrast, the partially saturated specimens showed lower initial stiffness followed by a temporary stiffness increase after the early cycles, followed by a more gradual degradation as loading progressed. But it's important to note that the applied CSRs for partially saturated tests were notably higher than that applied for fully saturated and was intentionally selected higher, to induce liquefaction and enable evaluating and comparing the behavior of fully and partially saturated soils under cyclic loading until liquefaction occurrence.

Moreover, at an equivalent number of loading cycles, stiffness degraded more rapidly in the fully saturated specimens than in the partially saturated ones. i.e., comparing the shear modulus evolution of CTx13 and CTx38 where, they needed 188 and 170 cycles respectively to liquefy. The shear modulus of CTx13 dropped from 34000 kPa to 24000 kPa between cycles 10 and 100, so the sample lost about 29.4% from its stiffness within these cycles. Whereas, the shear modulus of CTx38 dropped from 19400 to 16700kPa during the same interval of cycles so the sample only lost about 13.9% of its stiffness within these cycles.

The stiffness evolution of the fully saturated specimens is a typical response of contractive saturated sand under undrained cyclic loading, where excess pore-pressure build-up leads to progressive stiffness degradation. The more complex stiffness response of the partially saturated specimens can be interpreted in terms of pore-fluid compressibility. During the early loading cycles, the presence of occluded air bubbles increased the compressibility of the pore-fluid mixture, allowing part of the soil's contractive tendency to be accommodated through gas compression. This resulted in larger shear strains and lower initial secant stiffness. During the intermediate cycles, the rate of additional gas compression became

less pronounced, and a temporary increase in stiffness was observed. However, as excess pore pressure continued to accumulate gradually with cyclic loading, stiffness degradation eventually developed as liquefaction was approached.

Jafarzadeh & Sadeghi (2012) performed damping and stiffness analysis through doing strain controlled cyclic simple shear tests and, plotted the shear modulus G_{sec} against $N_{L,}$ for 25, 50, 75 and 100% Sr, resulting relationships are presented in Figure 5-35. Fully saturated tests were done under undrained conditions while unsaturated ones were performed under drained conditions. The unsaturated specimens showed increasing stiffness, however fully saturated samples showed stiffness degradation until failure.

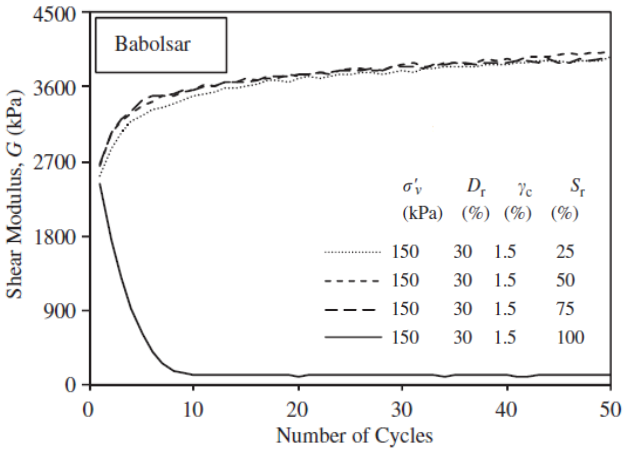

Figure 5-35 Shear modulus evolution along the number of cycles for partially and fully saturated specimens (Jafarzadeh & Sadeghi, 2012)

5.2.3. Influence of cyclic stress ratio CSR on secant stiffness

All tests had various applied CSR, but the group of partially saturated tests had higher CSR than fully saturated specimens. Based on that, the lower initial G_{ses} observed in partially saturated samples might be attributed to the higher applied CSR which induced higher cyclic shear strains from the first cycle leading to a lower secant modulus when calculated from the stress strain loop, while fully saturated set of tests were exposed to lower CSR which induced smaller shear strain amplitudes per cycle so their initial secant stiffness appeared higher.

5.2.4. Evolution of secant stiffness with shear strain amplitude

Figure 5-36a presents the secant shear modulus plotted against shear strain amplitude γ_c for each single loading cycle for all tests. shear strain amplitude γ_c was computed for each loading cycle using the formula (5-14).

$$\gamma_c = \frac{\gamma_{max} - \gamma_{min}}{2} \tag{5-14}$$

Figure 5-36b shows the corresponding normalized response, expressed as the ratio of secant shear modulus of each cycle to the maximum secant shear modulus of all cycles for the same test $G_{sec}/G_{sec,max}$, plotted against shear strain amplitude γ_c.

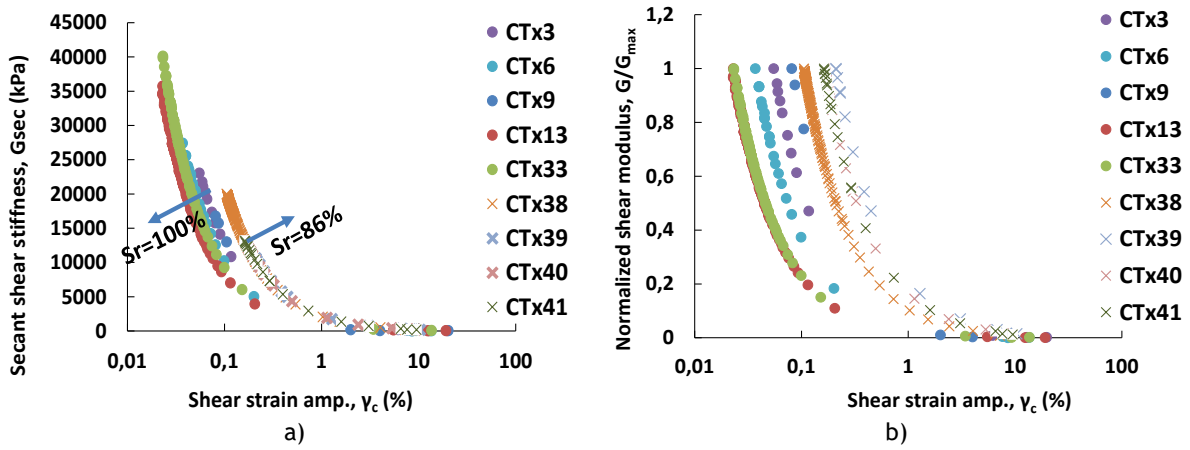

Figure 5-36 High strain stiffness degradation a) Secant shear modulus Gsec with the strain amplitude obtained from each hysteresis stress-strain cyclic loop; b) Gsec/Gsec,max with the shear strain amplitude, both a& b for Sr=100 and 86%

Figure 5-36a showed that the shear modulus decreased consistently by increasing the induced shear strain, also clearly showed that for a given shear strain amplitude γ_c, partially saturated specimens tended to maintain a higher secant shear modulus compared to fully saturated specimens. In other words, even when subjected to higher cyclic stress ratios (and consequently larger strains), partially saturated sand samples showed higher absolute secant shear modulus at equivalent strain levels than saturated samples.

When secant shear modulus was normalized by the maximum value for each specimen as shown in Figure 5-36b, the curves for partially saturated specimens lied above those for fully saturated specimens indicating that the partially saturated samples retained a higher fraction of their initial stiffness at a given shear strain amplitude, referring that partially saturated specimens showed slower stiffness decay with increasing cyclic shear strain.

Figure 5-37a presents the stiffness degradation curves for NB sand where it shows the relationship between the small-strain shear modulus, G_o, obtained from bender element measurements at a mean effective stress of p′=100 kPa (see Figure 5-12b), represented by the red symbol. The same plot also includes the secant shear modulus, G_{sec}, obtained from cyclic triaxial tests under fully and partially saturated conditions. To provide a continuous visual representation of the stiffness degradation trend between the small-strain BE measurement and the cyclic triaxial data, an interpolated curve is shown by the black line. This curve is used only for visualization and does not represent additional experimental measurements. On the other hand, Figure 3-39b presents the same data after normalization by the small-strain shear modulus, G_o, obtained from the BE test. The BE point was assigned a nominal very-small-strain level of $\gamma=10^{-6}$, equivalent to 10^{-4}%, which is within the strain range typically associated with small-strain stiffness measurements, (Jovcic, 2015).

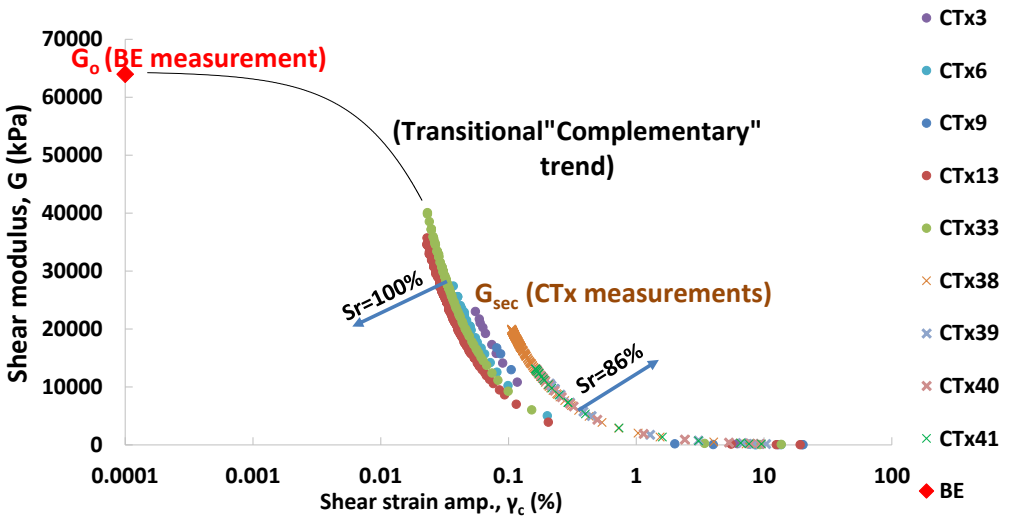

a)

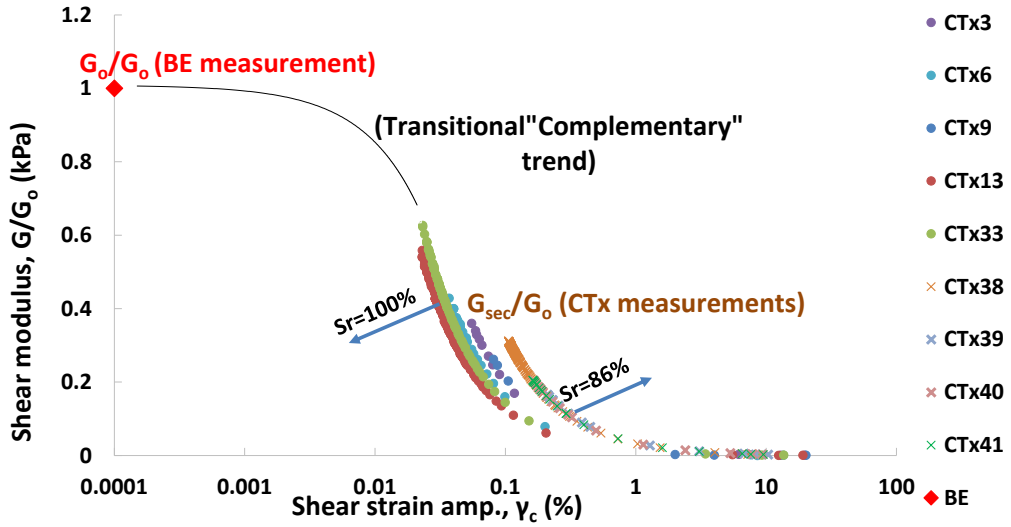

b)

Figure 5-37 Complete stiffness degradation curve for NB sand a) shear modulus G with the strain amplitude b) G/Go with the shear strain amplitude

The BE measurement represents the very-small-strain stiffness, G_0, and provides the upper-bound reference for the degradation curve. As the cyclic shear strain amplitude increases, the secant shear modulus decreases markedly, showing the expected nonlinear degradation of soil stiffness with strain evolution.

5.2.5. Secant stiffness and excess pore water pressure

Secant shear modulus G_{max} and coincident r_u evolution cycle per cycle for the two testing groups are illustrated in Figure 5-38.

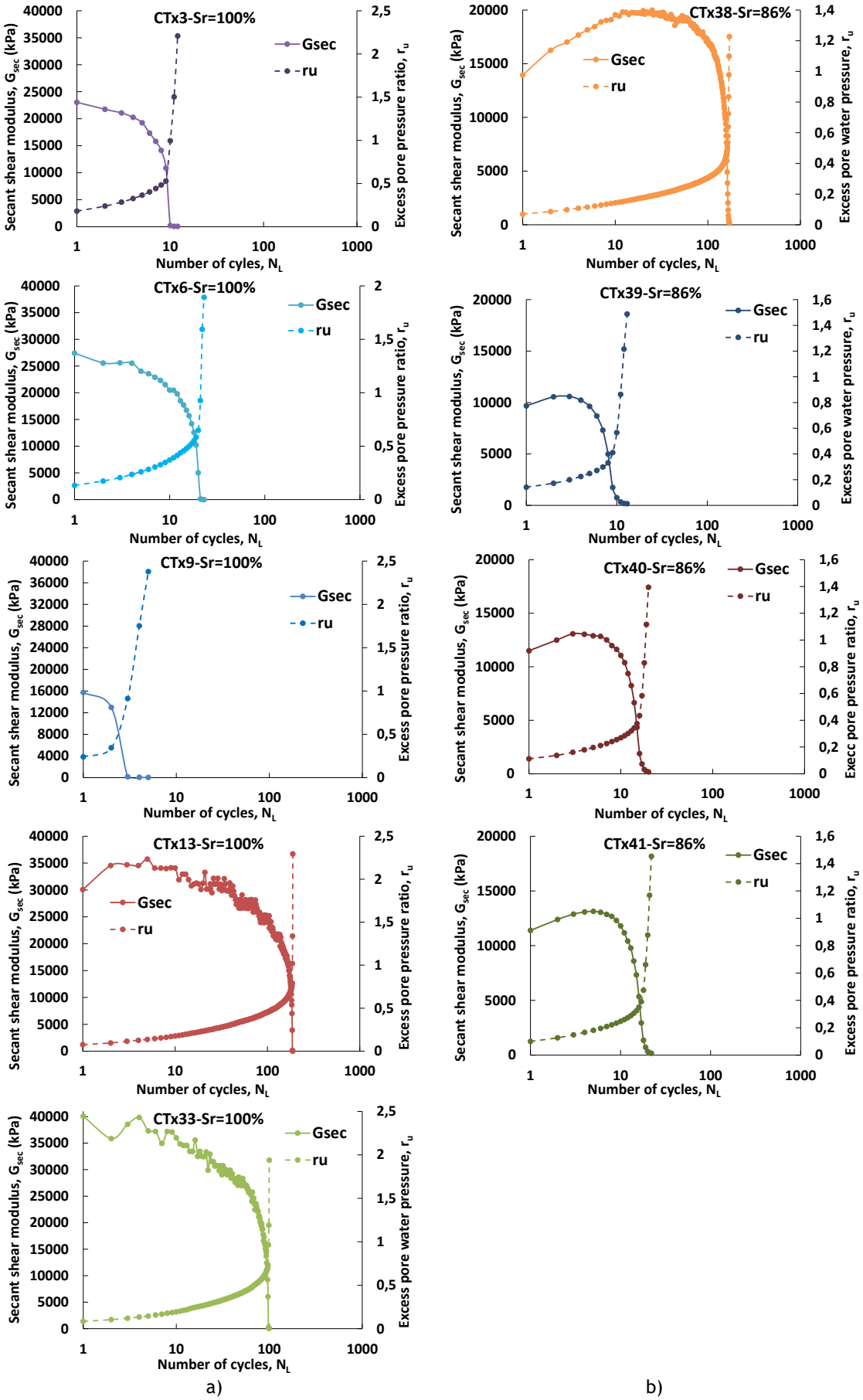

Figure 5-38 Secant shear modulus G_{max} and coincident r_u evolution cycle per cycle: a) Sr=100%; b) Sr=86%

In the partially saturated specimens, excess pore pressure developed during the early loading cycles; however, the response showed an initial increase in stiffness up to a threshold, followed by a pronounced stiffness reduction as pore pressure continued to accumulate and effective stress decreased. In the fully saturated specimens, stiffness decreased progressively as excess pore pressure built up throughout cyclic loading.

5.2.6. Damping ratio evolution for fully and partially saturated conditions

Damping ratio was estimated for each loading cycle of all tests. Figure 5-39 Reveals the relationship between the damping ratio and the corresponding number of cycles for fully and partially saturated samples, respectively.

The plots exclude the damping ratio of the first cycle for all tests as they may be misleading due to the particle rearrangement and last cycle(s) too where liquefaction occurred and hysteresis loops were very irregular and difficult to estimate damping.

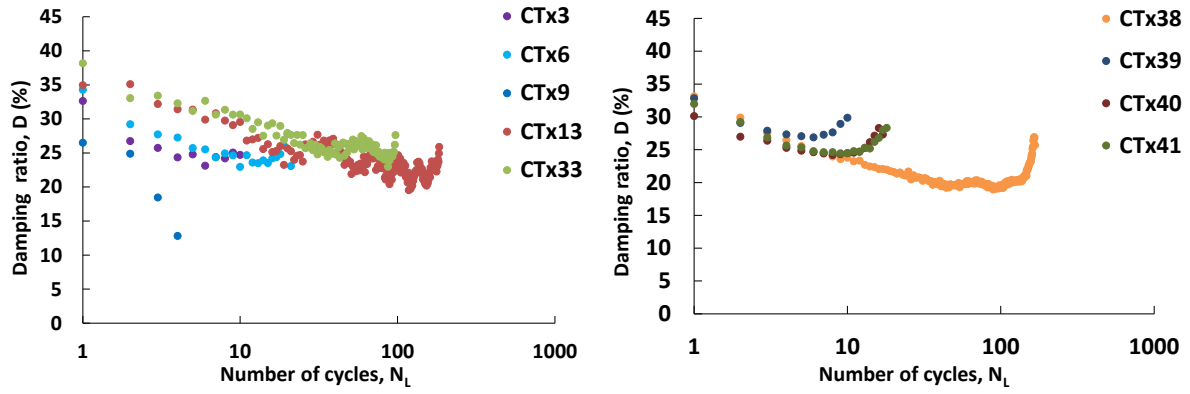

Figure 5-39 Cycle by cycle material damping based on the stress-strain hysteresis loops: a) Sr=100%; b) Sr=86%

A similar behavior for undrained fully saturated conditions was reported by Jafarzadeh & Sadeghi (2009), as shown in Figure 5-40.

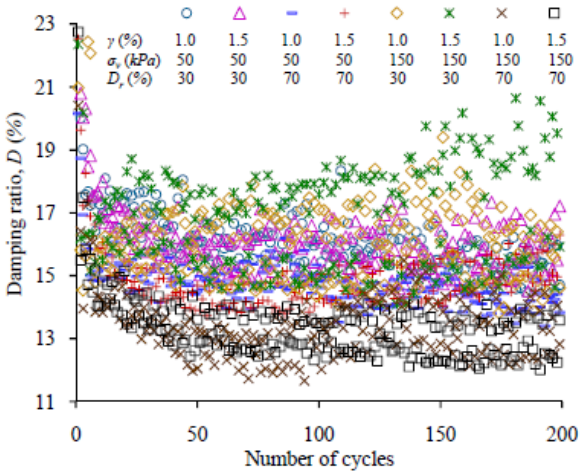

Figure 5-40 Scattered behavior of damping D with number of cycles under constant-volume conditions (Undrained), for fully saturated conditions (Jafarzadeh & Sadeghi, 2009)

Figure 5-39 revealed that in fully saturated sands, progressive cyclic loading tended to reduce the damping ratio as pore pressure builds and effective stress drops because the soil skeleton loses stiffness and frictional resistance under undrained loading which led to decreased damping ratios. For partially saturated sands, the cycle by cycle damping behavior was more complex, where the initial cycles showed a similar trend of damping reduction (likely due to initial fabric compaction and moderate pore pressure rise), but as failure was approached, they experienced damping ratio rebound (increase) in the final cycles before liquefaction. In Figure 5-32 , the last few cycles (e.g., cycle 18), the partially saturated test CTx41 exhibited a larger stress strain hysteresis loop than the fully saturated test CTx6, confirming higher cyclic energy dissipation.

This increased (rebounded) damping in partially saturated tests would be attributed to the occluded air bubbles which probably added additional damping characteristics. The presence of gas increased the compressibility of the pore fluid, so a portion of the cyclic work was absorbed by reversible compression/expansion of the gas rather than being immediately transferred to pore water pressure rise. By increasing pore-fluid compressibility, the air water mixture provided a cushioning effect under cyclic loading through volumetric compression. Furthermore, the partially saturated samples withstood higher cyclic stress ratios CSR as a result, just before failure they were enduring larger shear strain amplitudes before reaching liquefaction as shown in Figure 5-31Figure 5-31. These large strains, combined with some remaining effective stress (before 100% pore pressure ratio), likely produced pronounced frictional sliding and even micro cracking in the soil structure, consequently an increase in energy dissipation per cycle.

Figure 5-41 shows the damping ratio against shear strain amplitudes for fully and partially saturated tests respectively. The plotting excluded the first cycle and last cycle(s) where liquefaction occurred.

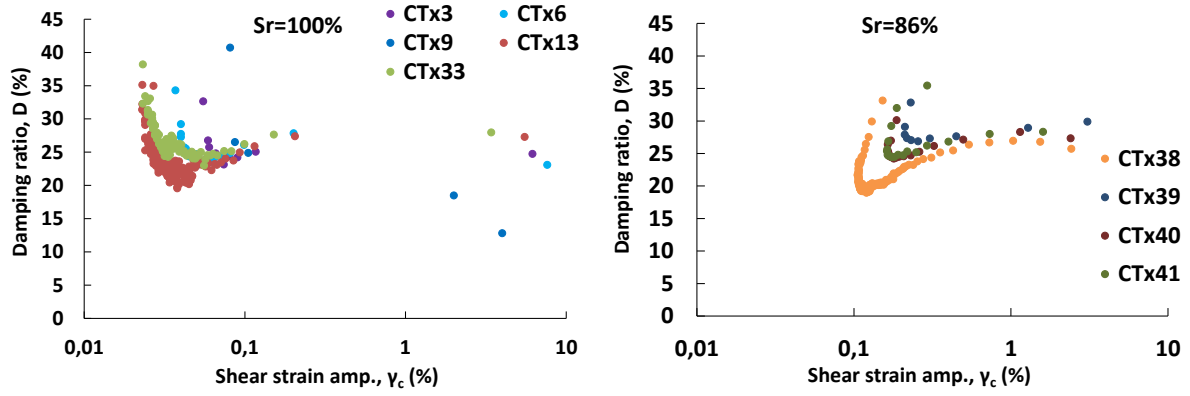

Figure 5-41 Material damping with the shear strain amplitude estimated from the stress-strain hysteresis loops a) Sr=100%; b) Sr=86%

Fully saturated sand specimens typically exhibited low damping ratios at small shear strains amplitudes and then increases to a moderate plateau value as strain amplitude increases and would probably decrease again when near failure or liquefaction. This relationship between damping ratio and shear strain amplitude usually plotted for various tests at a predefined cycle number and would produce this classical described S shape of damping. Hence, that is not the case in the current analysis, where the performed undrained stress-controlled tests, force the strain amplitude to evolve cycle by cycle as excess pore pressure

accumulates and stiffness degrades, and also due to the narrow strain range, so plotting damping against cycle number is not expected to produce similar trend and naturally might produce scatter and non-well-defined trends even for repeatable specimens.

As clear in the shown plots, damping varied within limited shear strain range, i.e., in fully saturated samples it ranged between about 0.025 to 0.08 before instability and liquefaction, the variation of damping along the shear strain amplitude showed high scattering values and the trend was not very clear to have assertive judgement and solid conclusion likely due to the narrow strain range and abrupt liquefaction.

In the current analysis as shown in Figure 5-41 , the damping ratio was observed to decrease within the low strain range with high scattering values at <0.1% and then stabilize, or even rise modestly, as higher shear strain amplitudes developed.

Notably, as the shear strain amplitudes approached levels associated with initial liquefaction, the damping ratio plateaued around a relatively constant value, at shear strain amplitude of about 0.1%.

But what is indeed curious is the damping capacity of partially saturated samples compared to fully saturated tests, as they showed scattered decreasing trend in damping in the early loops followed by increased damping at the range of shear strain of 0.1 to 0.7 while fully saturated specimens liquified before attaining such higher strain range.

5.2.7. Cyclic stress-path for fully and partially saturated conditions

Figure 5-42 illustrates a comparison between the cyclic stress path (q-p′) of fully and partially saturated tests. The effective stress paths of the fully saturated specimens showed typical response of undrained cyclic triaxial loading, with progressive excess pore pressure generation leading to a reduction in mean effective stress p′ during cycling. In contrast, the partially saturated specimens, despite being tested under undrained conditions as well, resulted in stress paths that are closer to drained or partially drained behavior. This is evidenced by inclination slope of the p′-q with 1:3. Although the undrained testing conditions, partially saturated behaves Like drained or partially drained unlike fully saturation. In fully saturated undrained loading, pore water is nearly incompressible. The contractive tendency of loose-to-medium sand cannot develop volume change, so excess pore pressure builds up rapidly and (p') decreases. In partially saturated specimens, occluded air bubbles compress during loading, allowing part of the contractive tendency to be accommodated without a large increase in excess pore pressure. As a result, (p') is better maintained, and the stress path becomes more inclined, closer to a drained response.

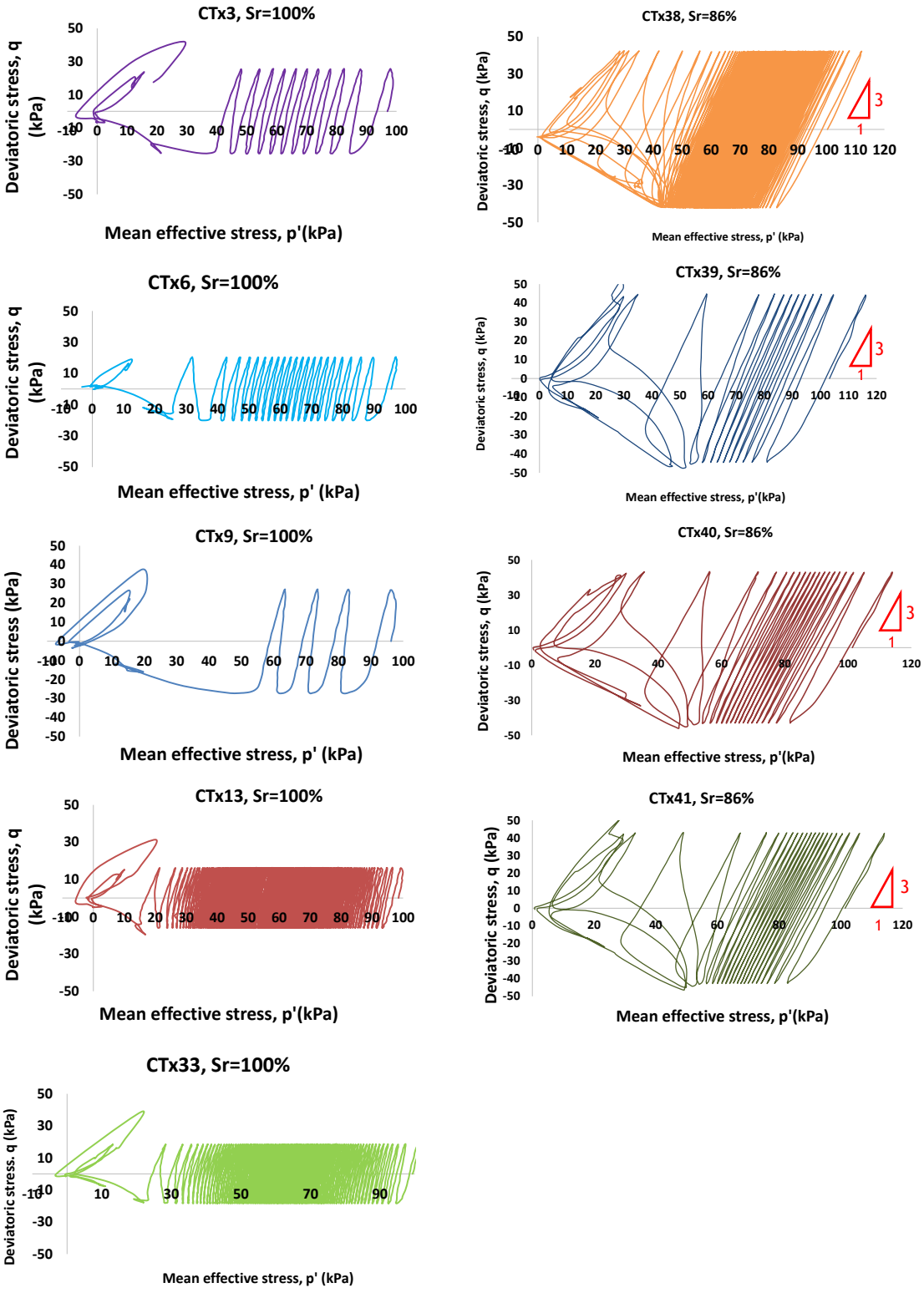

a) b)

Figure 5-42 Cyclic stress paths (q-p'); a) Sr=100%; b) Sr=86%

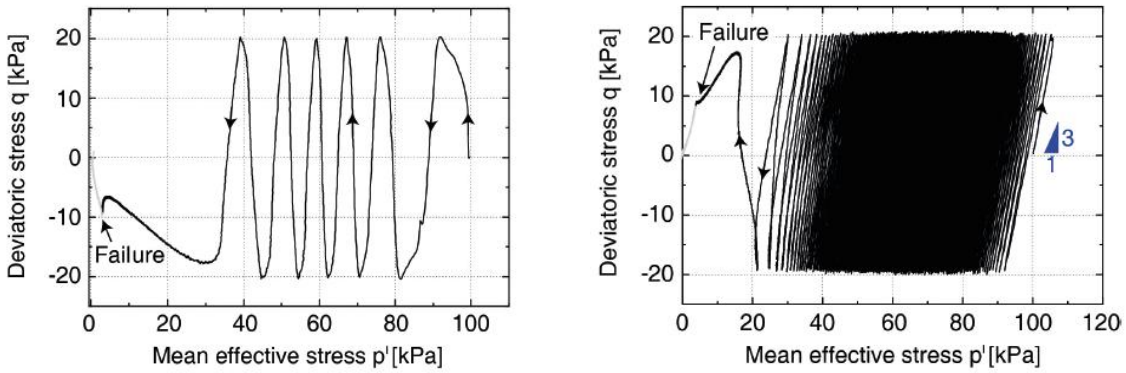

a) b)

Figure 5-43 stress path results (q-p′) for: a) Sr=100%, q_{ampl} = 20kPa; b) Sr=86%, q_{ampl} = 20kPa (Knittel & Lieske, 2025)

Similar behavior was also reported by (Knittel & Lieske, 2025), based on their experimental study, they reported that the entrapped air bubbles of the partially saturated samples act like a damping mechanism, which are reflected in the stress paths of the deviator stress q over the mean pressure p′ with an inclination of 1:3, as clear in Figure 5-43.

5.3. Undrained dynamic soil properties of fully and partially saturated NB sand

The previous section (section 5.2) assessed the evolution of the dynamic soil properties for two sets of cyclic triaxial tests performed at different degrees of saturation. However, this analysis could not be used for a direct comparison between fully and partially saturated conditions because the applied CSR levels were not identical. For this reason, an additional pair of tests was performed under nearly identical initial conditions, with the same preparation method and same void ratio. These tests were CTx43, tested under fully saturated conditions, and CTx44, tested at a degree of saturation of approximately 86%.

Both specimens were tested under identical undrained stress-controlled cyclic loading conditions. The cyclic loading started at 20 N and was increased in increments of 5 N. Each load increment was maintained for 10 cycles, and the loading was continued until liquefaction occurred. The fully saturated specimen, CTx43, liquefied at the first cycle of the 85 N load increment, whereas the partially saturated specimen, CTx44, liquefied later, at the fifth cycle of the 135 N load increment. This response is shown in Figure 5-44 ,where the applied load is plotted against the number of cycles for each load increment. The main details of both tests are summarized in Table 5-5.

Table 5-5 Details of performed CTx43 and CTx44

Test#	CO_2	p'_0 (kPa)	Sr_f (%)	e_o
CTx43	✓	100	100	0,766
CTx44	X	100	86	0,769

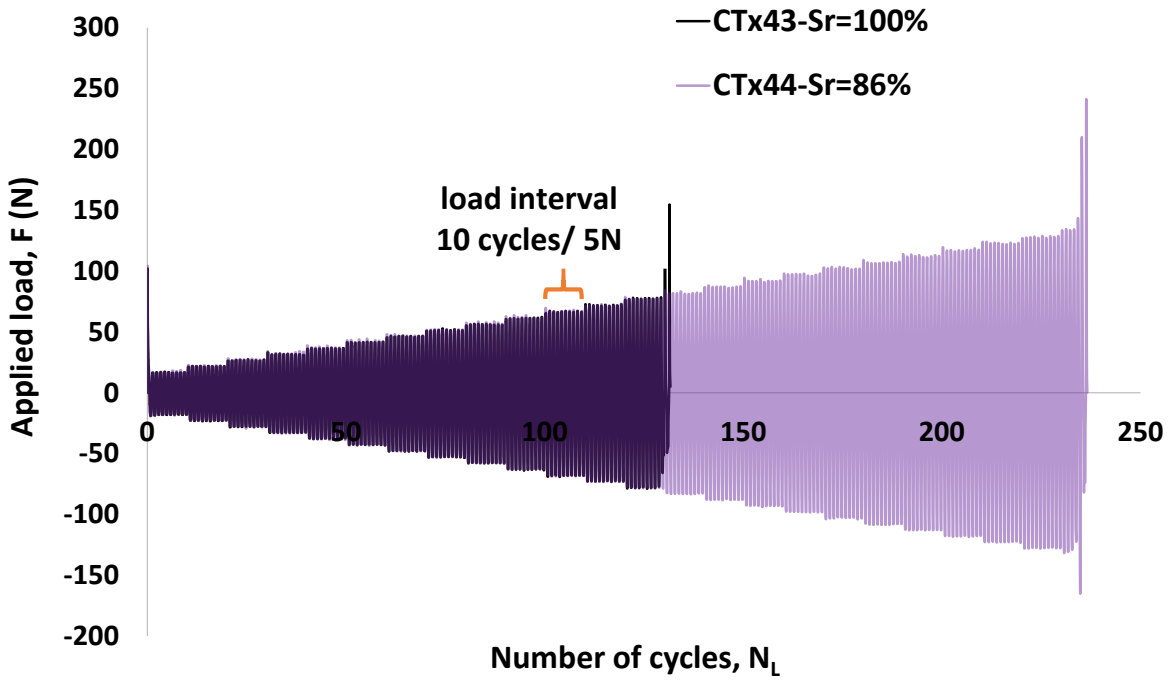

Figure 5-44 Applied load against the number of cycles for each load increment of the two specimens CTx43 and CTx44.

Figure 5-45 presents the cyclic shear response of the two specimens, CTx43 and 44 under undrained stress-controlled cyclic shearing where a) shows the relationship between the deviatoric shear stress q and the axial strain ε_a while, b) represents the soil stress path, c) presents the correlation between q and corresponding number of cycles required to trigger liquefaction N_L. Plot d) reveals N_L with the corresponding excess pore water pressure ratio build-up $r_u = \Delta u/p'_o$, e) illustrates the r_u-CSR relationship, f) demonstrates the correlation between the developing r_u and decreasing mean effective stress p´, finally g) reports the Δu- ε_a relationship.

For the comparative analysis, cycle no. 10 from each load increment was selected. The shear stress and shear strain were calculated for this cycle at each loading step for both tests, up to the liquefaction of the fully saturated specimen CTx43. Since CTx43 liquefied much earlier, the direct comparison was limited to the common loading range, from 20 N to 75 N.

The resulting shear stress-shear strain loops for CTx43 and CTx44, for cycle no. 10, for each loading step are shown in Figure 5-46.

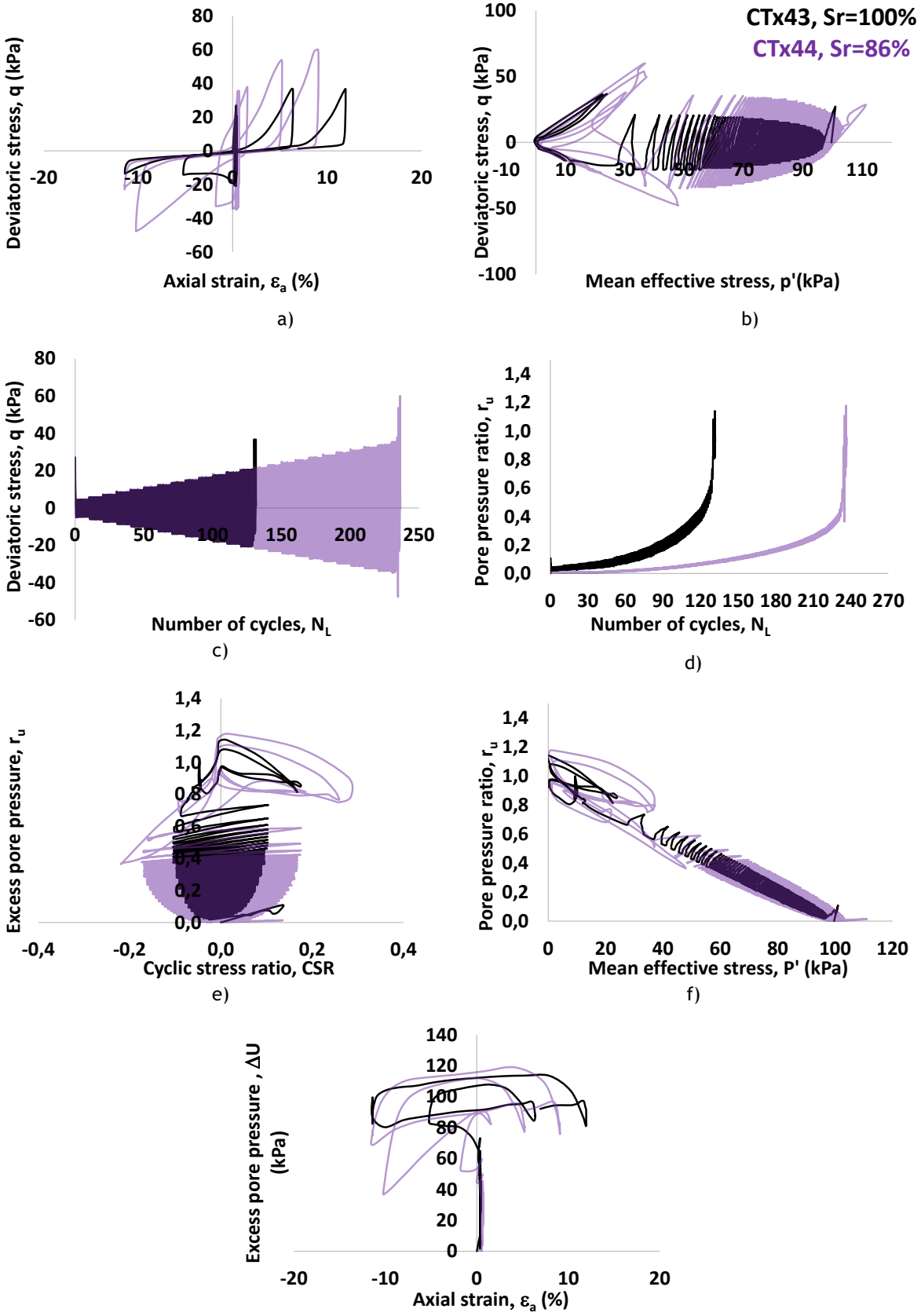

Figure 5-45 Cyclic shear response of the two specimens under undrained stress-controlled cyclic shearing

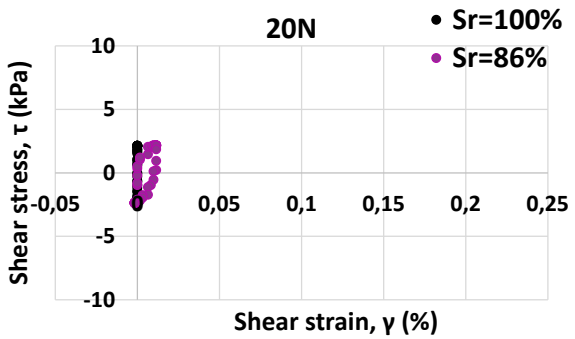
20N
Sr=100%
Sr=86%
Shear stress, τ (kPa)
Shear strain, γ (%)

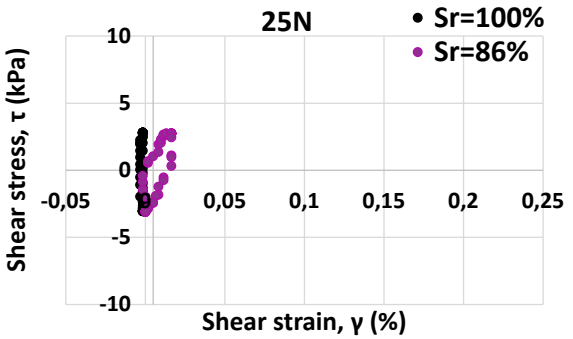
25N
Sr=100%
Sr=86%
Shear stress, τ (kPa)
Shear strain, γ (%)

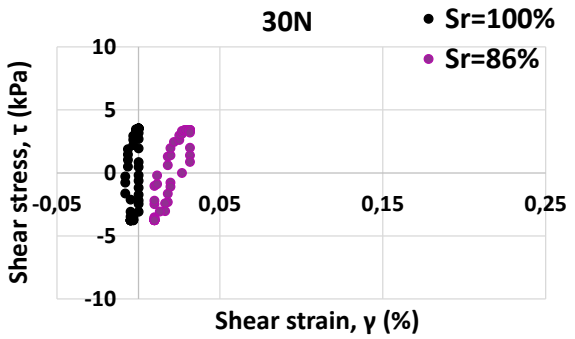
30N
Sr=100%
Sr=86%
Shear stress, τ (kPa)
Shear strain, γ (%)

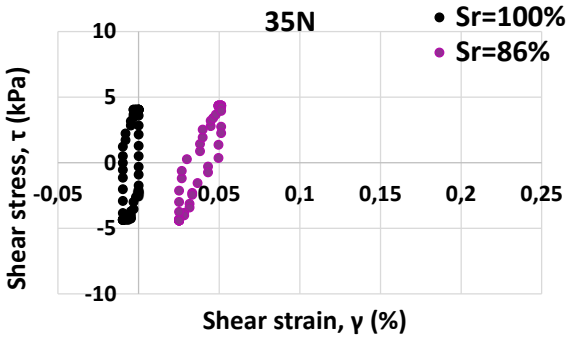
35N
Sr=100%
Sr=86%
Shear stress, τ (kPa)
Shear strain, γ (%)

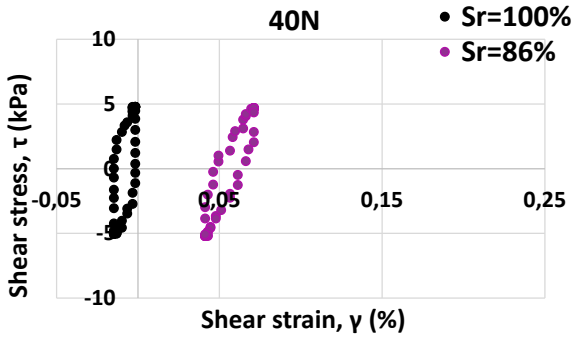
40N
Sr=100%
Sr=86%
Shear stress, τ (kPa)
Shear strain, γ (%)

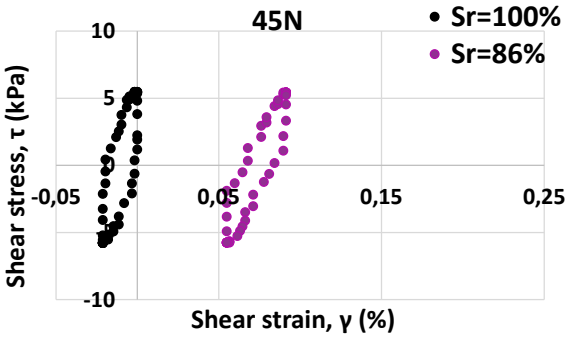
45N
Sr=100%
Sr=86%
Shear stress, τ (kPa)
Shear strain, γ (%)

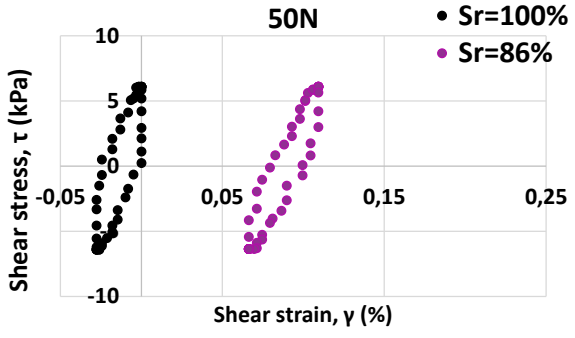
50N
Sr=100%
Sr=86%
Shear stress, τ (kPa)
Shear strain, γ (%)

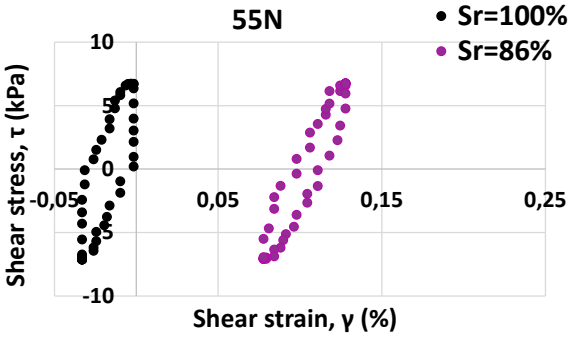
55N
Sr=100%
Sr=86%
Shear stress, τ (kPa)
Shear strain, γ (%)

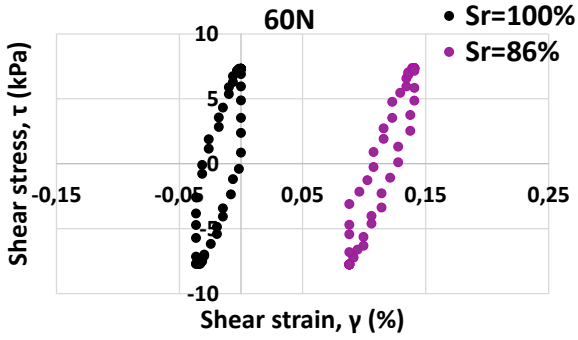
60N
Sr=100%
Sr=86%
Shear stress, τ (kPa)
Shear strain, γ (%)

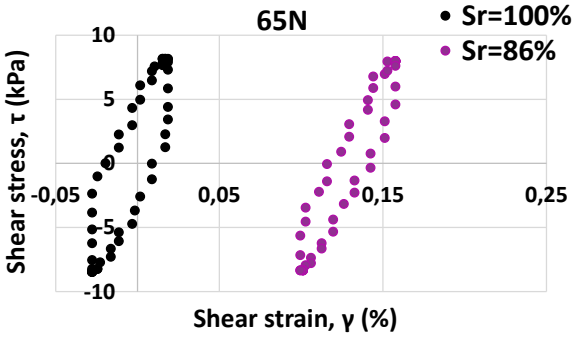
65N
Sr=100%
Sr=86%
Shear stress, τ (kPa)
Shear strain, γ (%)

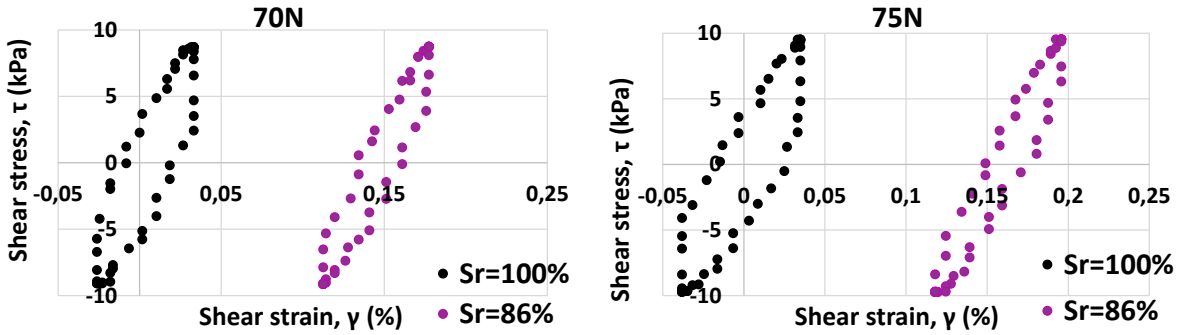

Figure 5-46 Resulting shear stress-shear strain loops for CTx43 and CTx44 (cycle no. 10) from each loading step

These loops show that the partially saturated specimen, CTx44, exhibited a softer response and developed noticeably larger shear strains at the same applied load increments. In the early and intermediate loading stages, up to approximately 45 N, CTx44 also showed visibly wider stress–strain loops than CTx43. As CTx43 approached liquefaction, however, its loops became larger and more distorted, reflecting the rapid degradation of the fully saturated specimen close to instability.

Figure 5-47 shows the full evolution of the cyclic stress–strain loops for both tests up to liquefaction. A clear difference can be observed between the two responses. In CTx43, the loops remained within a relatively narrow strain range for most of the test, before expanding rapidly near liquefaction. By contrast, CTx44 developed a much wider strain range throughout the loading history before reaching liquefaction. The loop evolution in CTx43 was also directionally biased, with the loops becoming anchored on one side and accumulating larger strains mainly in the extension direction. This behaviour suggests progressive instability. In CTx44, the loops showed a smaller overall drift, indicating the accumulation of mean plastic strain while the specimen was still able to sustain effective stress. To move beyond visual observations, the dissipated energy, cumulative dissipated energy, maximum stored strain energy, hysteretic damping ratio, and secant stiffness were calculated from cycle no. 10 at each load increment for both tests. The resulting trends are presented in Figure 5-48.

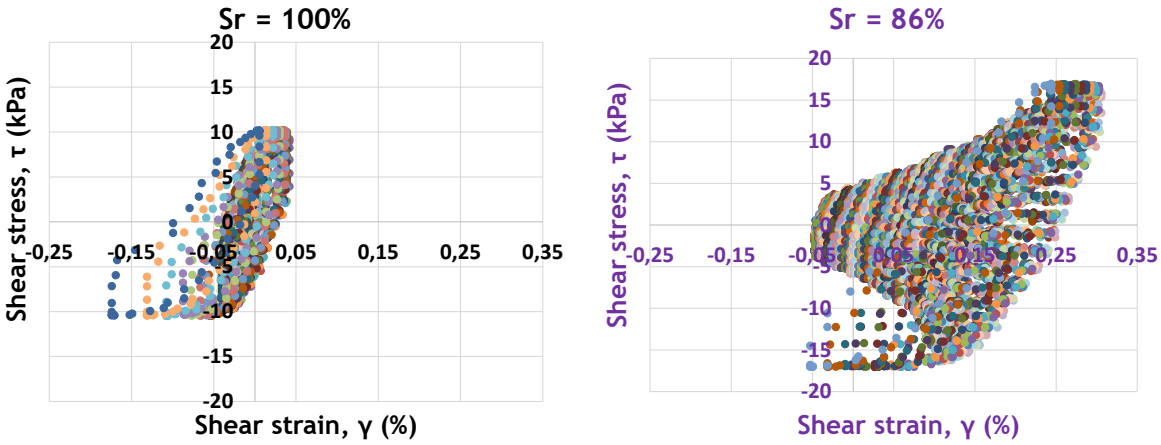

Figure 5-47 Evolution of the cyclic stress-strain loops for both tests CTx43 and CTx44 up to liquefaction

Cycle #10 for each load interval

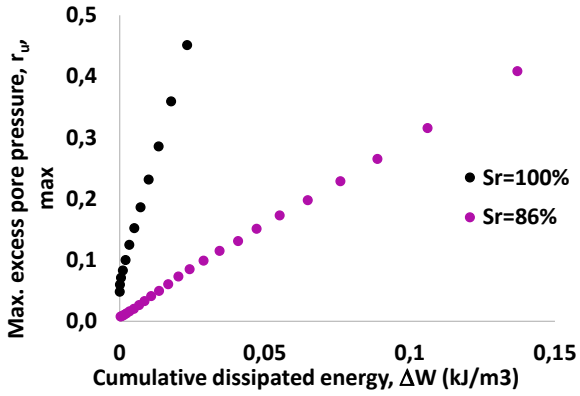

a)

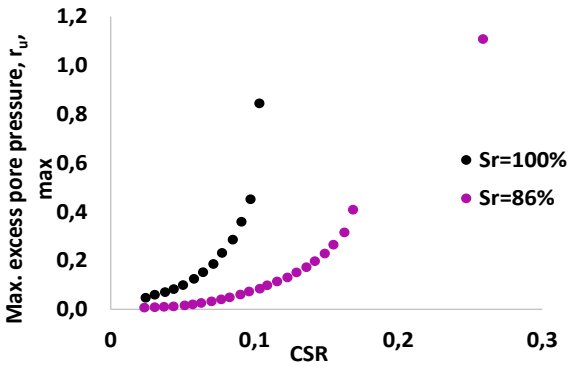

b)

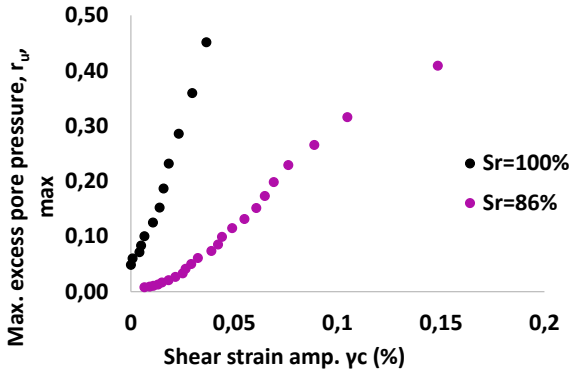

c)

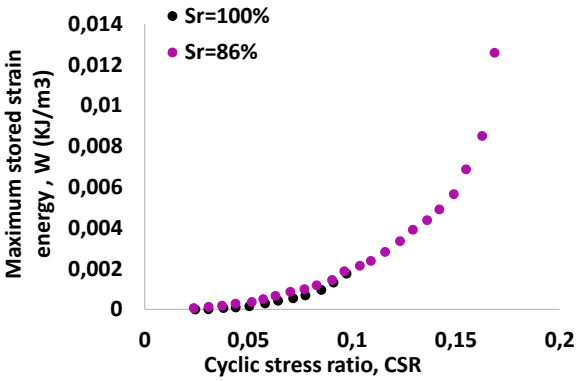

d)

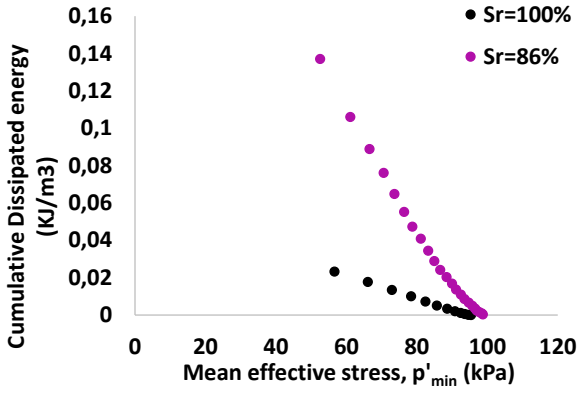

e)

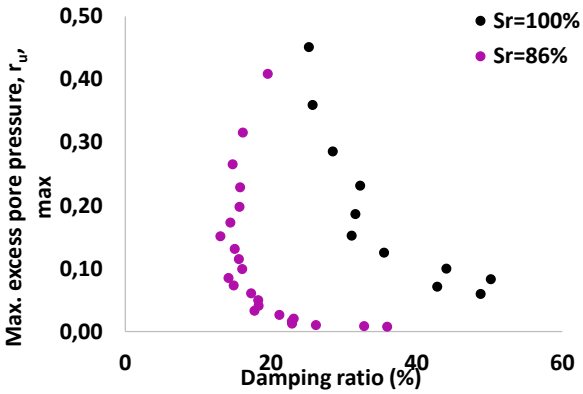

f)

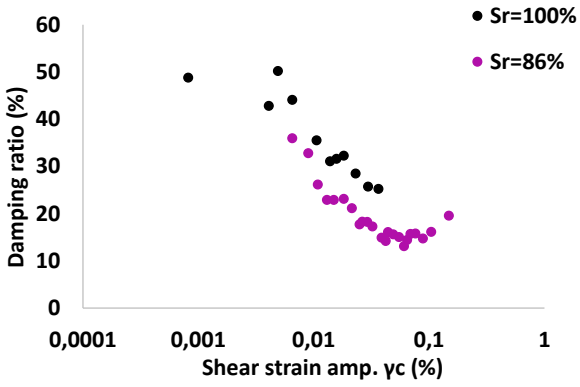

g)

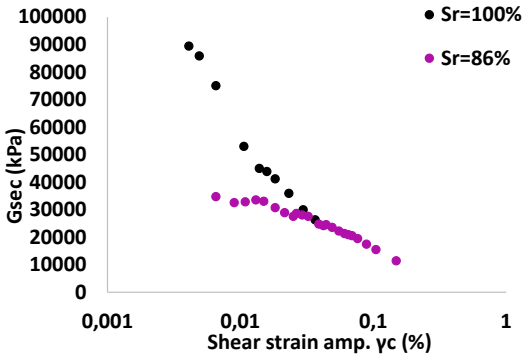

h)

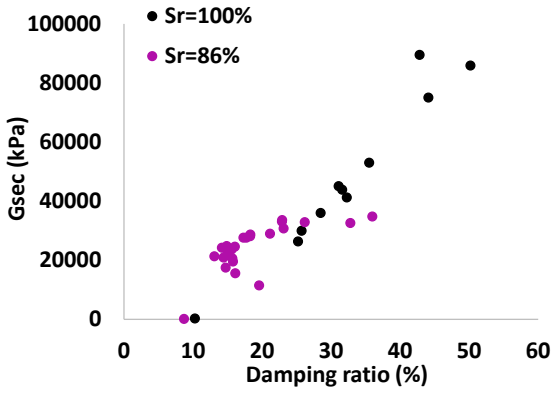

i)

Figure 5-48 Resulting trends of CTx43 and CTx44 where; a) maximum r_u-cummulative dissipated energy; b) maximum r_u-CSR; c) maximum r_u-shear strain amplitude; d) maximum stored strain energy-CSR; e) Cumulative dissipated energy – minimum mean effective stress p'_{min}; f) Maximum r_u-Damping ratio; g) Damping ratio-shear strain amplitude; h) Secant stiffness- shear strain amplitude; i) secant stiffness – damping ratio.

Figure 5-48a shows that, for the same excess pore-pressure ratio r_u, partially saturated specimen CTx44 accumulated a much higher cumulative dissipated energy than fully saturated specimen CTx43. Figure 5-48b shows the same trend from another perspective: for a given excess pore-pressure ratio, CTx44 required a higher CSR than CTx43. This confirms the improved resistance of the partially saturated specimen against pore-pressure accumulation and liquefaction.

Figure 5-48c shows that CTx44 developed significantly larger shear strains than CTx43 under the same loading conditions. Consistently, Figure 5-48d shows a higher maximum stored strain energy for CTx44, mainly due to its larger strain range. Figure 5-48e further shows that, for the same mean effective stress, CTx44 accumulated higher cumulative dissipated energy than CTx43. This suggests that partial saturation allowed the specimen to dissipate more energy while maintaining a higher effective stress state. The damping response is shown in Figure 5-48f and Figure 5-48g. In general, CTx43 exhibited higher damping ratios than CTx44. This is also observed when the damping ratio is plotted against shear strain amplitude. Although CTx44 dissipated more cumulative energy overall, its larger strain amplitudes and lower stiffness resulted in lower hysteretic damping ratios. Therefore, the damping ratio alone does not fully describe the energy response of the partially saturated specimen. The stiffness degradation trends are shown in Figure 5-48 h. CTx43 started with a much higher secant stiffness, but its stiffness degraded rapidly as loading progressed. In contrast, CTx44 started with a lower stiffness, but the degradation was more gradual. Figure 5-48i summarizes this behaviour by showing that CTx44 generally had both lower secant stiffness and lower damping ratio than CTx43 over the analysed loading range.

Overall, the direct comparison between CTx43 and CTx44 shows that partial saturation changed the cyclic response in two main ways. First, it delayed pore-pressure build-up and liquefaction, allowing the specimen to sustain much higher loading before failure. Second, it produced a softer response, with larger shear strains, higher stored strain energy, and greater cumulative dissipated energy. This behaviour is consistent with the increased compressibility of the pore-fluid mixture caused by occluded air bubbles. The partially saturated specimen was therefore able to accommodate part of the contractive tendency through compression of the pore fluid, rather than through rapid excess pore-pressure generation.

5.4. Cyclic behavior of Hostun sand

5.4.1. Stress dependency and small-strain behavior

As performed previously on NB sand, an undrained cyclic triaxial test was carried out for the purpose of investigating the stress dependency of seismic wave propagation for Hostun sand HN31. sample was prepared using dry air pluviation and seismic wave velocities were measured using bender elements installed in the triaxial apparatus. After preparation, the sample was exposed to different effective confining pressure in steps from 10 to 500kpa in dry conditions and then back in steps too, to 10 kpa. Then the sample was fully saturated. After that, p′ increased again in steps to 500 kpa under fully saturation conditions and back again to 10 kpa. After each p′ increasing increment, Vp, Vs and B-skempton's number was recorded.

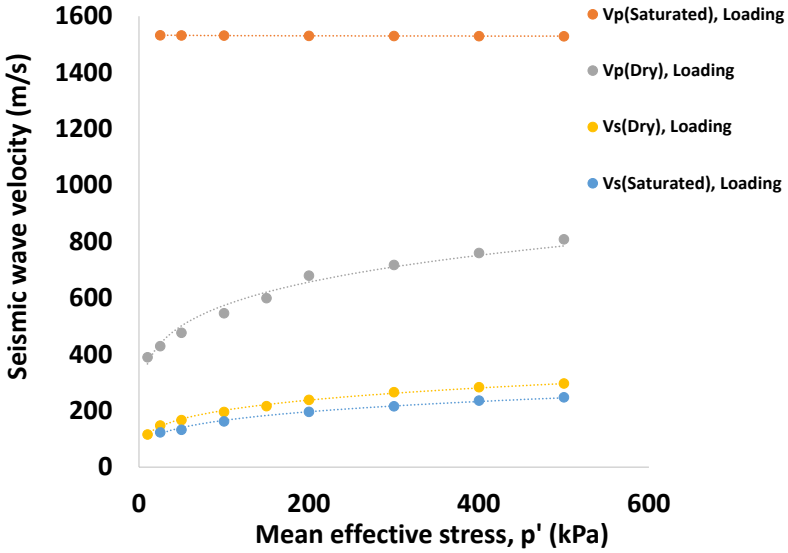

Figure 5-49 Seismic wave velocity (V_p/V_s) evolution at various confining stress for HN31 sand

The evolution of Vp and Vs under dry and fully saturated conditions were plotted in Figure 5-49 against p′, the power law regression (equation (5-2)) for Vp and Vs trends was adopted and the resulting fitting parameters are listed in Table 5-6 where, stress dependency exponents ß for Vs in dry and saturated conditions found to be 0.24 and 0.245 respectively, which fell within the typical natural sands values. Despite the very similar exponents ß, the values of α was found to be 66.56 and 53.61 for $Vs_{,dry}$ and $Vs_{,sat}$, this confirms that the sample in dry conditions showed higher resistance than in fully saturated conditions. The stress dependent $Vp_{,dry}$ reported power law regression with fitting parameters of α=233.82 and ß=0.1948. while in fully saturation conditions showed constant α=1536.8 and ß=-0.0008.

G_{max} evolution with p′ was then plotted for both dry and fully saturated conditions from the Vs values using equation (5-1). Figure 5-50 illustrates the stress dependency of Vs and G_{max} for HN31. The offset between the trend of $G_{max,dry}$ and $G_{max,sat}$ decreased relative to $Vs_{,dry}$ with $Vs_{,sat}$ due to the reasons discussed earlier. Furthermore, the exponent of G_{max} were found to be two times (2β) the the exponent of Vs (β) in both dry and saturated conditions.

Table 5-6 Fitting parameters of Vs and Vp of Hostun sand HN31

Seismic wave	α (m/s)	β
$Vp_{(dry)}$	233.82	0.1948
$Vp_{(saturated)}$	1536.8	-0.0008
$Vs_{(dry)}$	66.563	0.2402
$Vs_{(saturated)}$	53.609	0.245

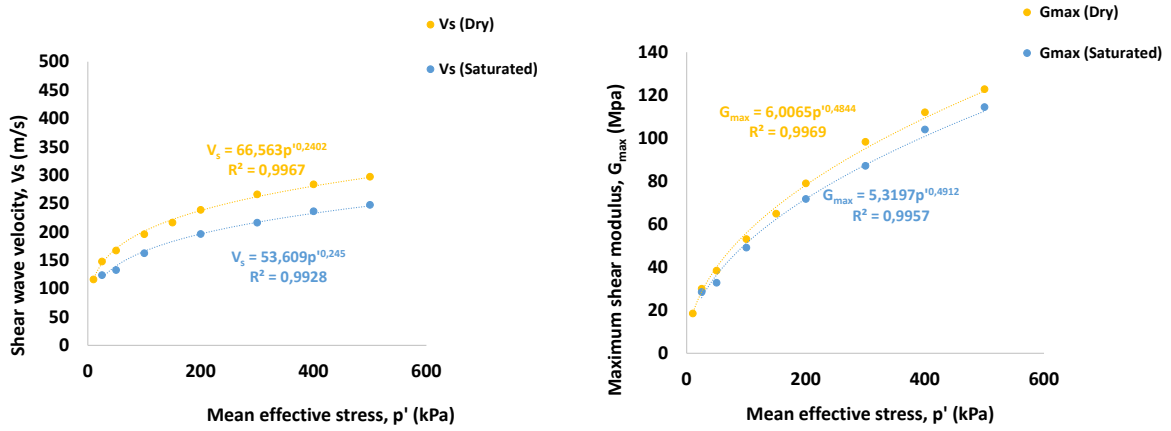

a) b)

Figure 5-50 stress dependency at different p′ of HN31 sand a) Shear wave velocity stress dependency; b) Gmax stress dependency

For diminishing the Effect of void ratio and investigate exclusively the effect of stress on the soil small strain stiffness, G_{max} was normalized by the three different functions ratio adopted in

Table 5-2. Normalized G_{max} was then plotted with the normalized p'/p_a. Table 5-7 summarizes the resulting fitting parameters. Figure 5-51 Show the $G_{max}/F(e)1,2$ and, 3 evolutions with p'/p_a respectively.

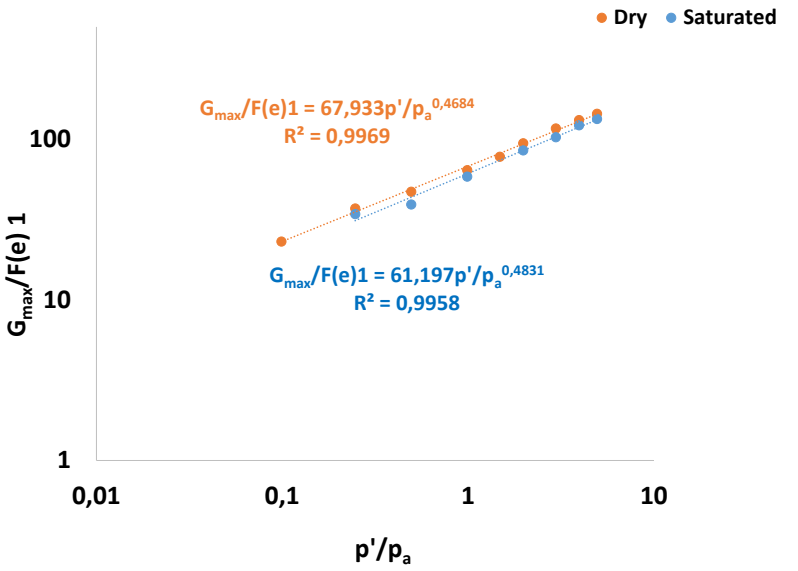

a)

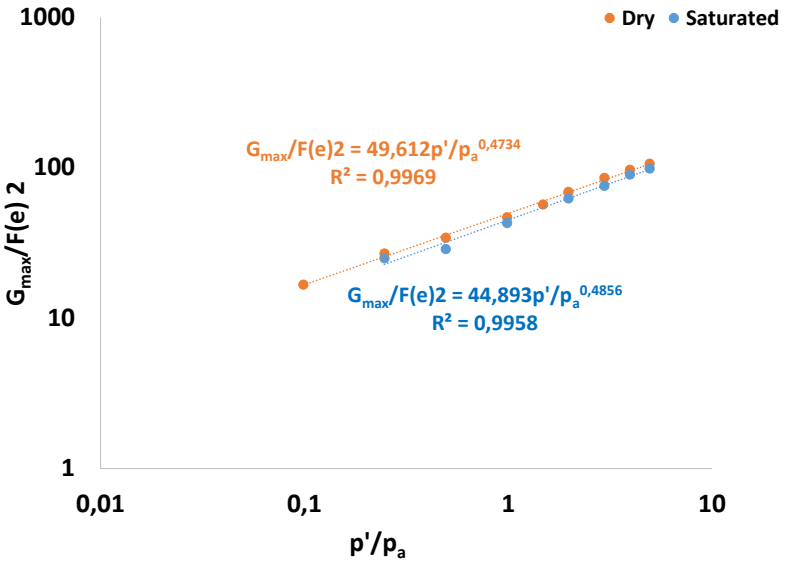

b)

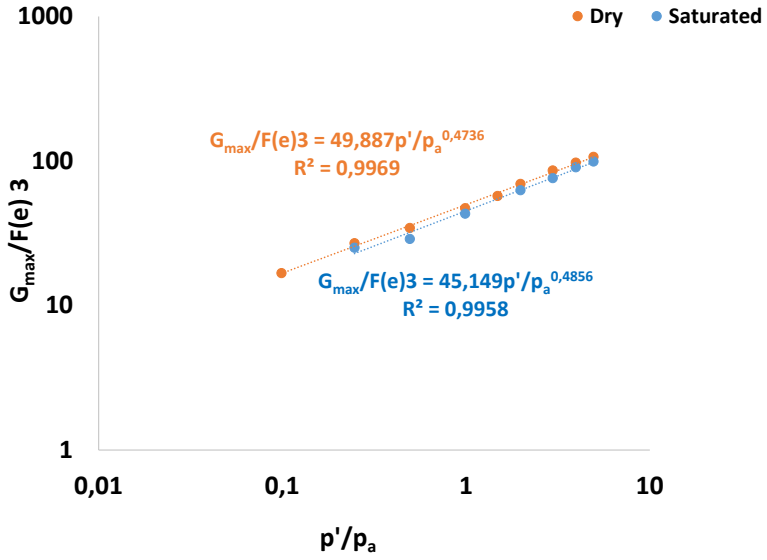

c)

Figure 5-51 G_{max} normalized to the different adopted void ratio functions in dry and fully saturated states of HN31 sand

Table 5-7 Fitting parameters from the G_{max} normalized to various F(e) of Hostun sand HN31

#	Sr	α(Mpa)	β
F(e)1	Dry	67.933	0.4684
	Sat.	61.197	0.4831
F(e)2	Dry	49.612	0.4734
	Sat.	44.893	0.4856
F(e)3	Dry	49.887	0.4736
	Sat.	45.149	0.4856

F(e) adopted by Resulted in higher α, showing higher soil small stiffness compared to the other two void ratio functions F(e)2&3.

G_{max} normalized by F(e) is expressed as a of p'/p_a using equation (5-15)

The fitting parameter resulting from the void ratio function, F(e)1 were;

- Dry: α = 67.933 MPa, β = 0.4684
- Saturated: α = 61.197 MPa, β = 0.4831

Therefore, the ratio between the saturated and dry normalized G_{max} trends at the same p′ will be equal to:

$$\frac{G_{max}/F(e)_{sat.}}{G_{max}/F(e)_{dry}} = 0.9\left(\frac{p'}{p_a}\right)^{0.0147} \quad (5\text{-}15)$$

- p′=pa, the normalized G_{max} in saturated conditions is 9% less than in dry conditions.
- At p′/pa =0.1, 12.9% lower
- At p′/pa =5, 7.8% lower

5.4.2. Liquefaction resistance of fully and partially saturated

Hostun Sand is the sand that is used in the dynamic centrifuge testing elaborated in the next chapter. Therefore, it was a complementary action to investigate the cyclic behavior of HN31 using cyclic triaxial testing.

Two sets of undrained cyclic triaxial tests namely (Hn-CTx) were carried out on Hostun sand HN31. One set was performed under full saturation conditions and the other set has around 86% degree of saturation. Tests were performed under identical conditions, in terms of the soil preparation method (dry-air pluviation) targeted relative density and initial mean effective stress. Minor differences are attributed to the volumetric changes occur during soil preparation and testing phases.

Dr before shearing was ranged between 50 and 55% for all samples. Compared to NB sand, HN31 was easier to target relative density as it's e_{min} and e_{max} were 0.63 and 1.01 respectively So, having longer span where small change in void ratio due to all may occurred pre reported reasons doesn't necessarily result in larger Dr. Before undrained cyclic shearing, samples were isotopically consolidated at 100kPa mean effective stress

Figure 5-52 and Figure 5-53 show the cyclic shear response resulting plots of the fully and partially saturated sand tests of HN31 sand, respectively.

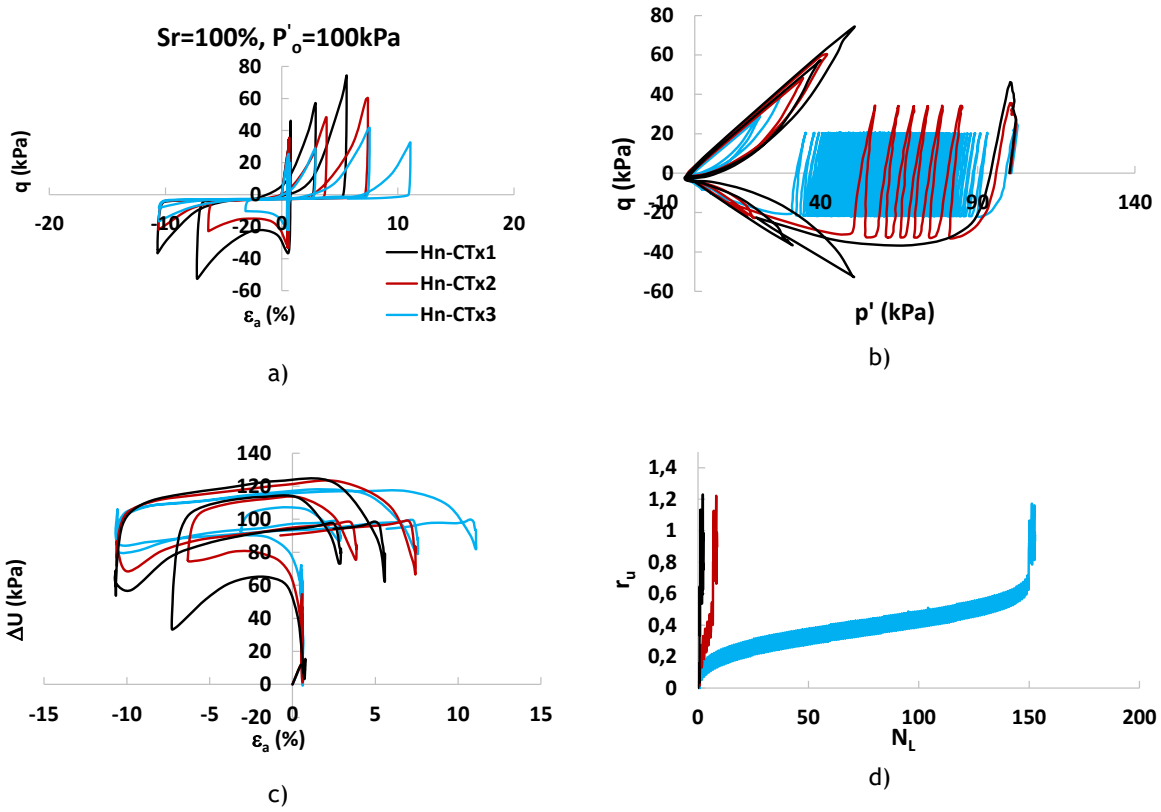

Figure 5-52 undrained cyclic shear characteristic plots for saturated Hostun sand HN31: a) stress-strain behavior; b) Stress path q: p` space; c) excess pore water pressure Δu against axial strain ε_a; d) Excess pore water pressure build-up ratio r_u with the number of cycles N_L

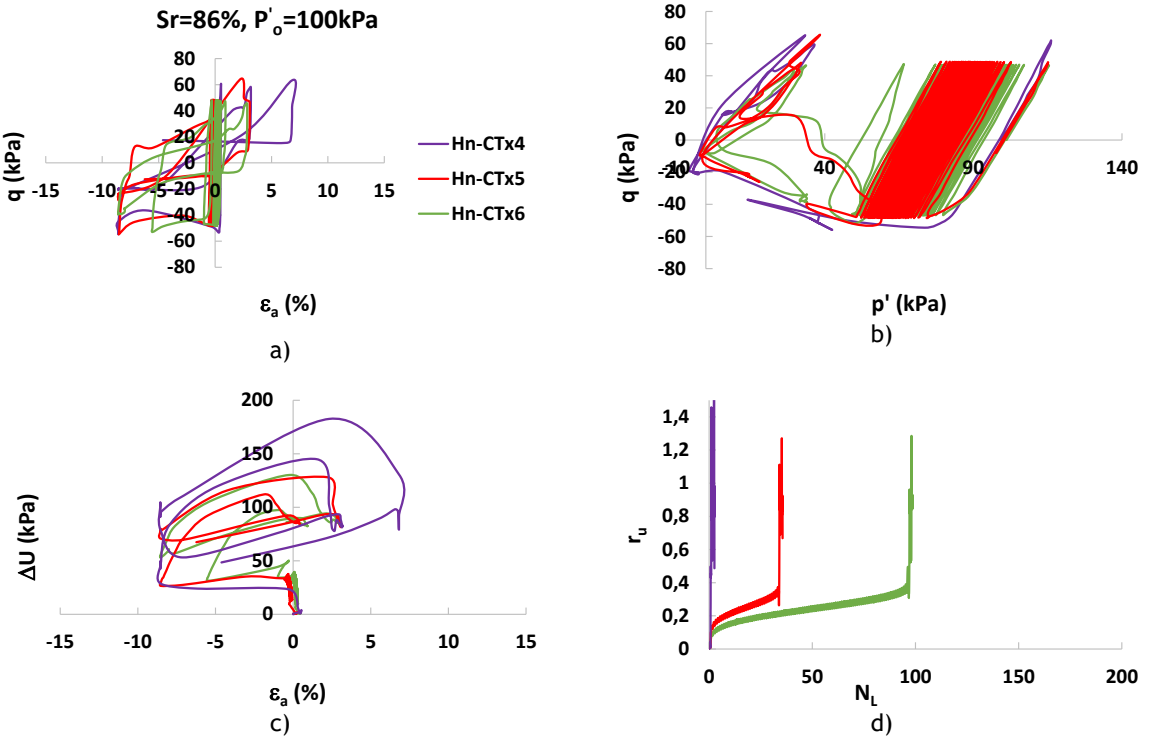

Figure 5-53 undrained cyclic shear characteristic plots for partially saturated Hostun sand HN31: a) stress-strain behavior; b) Stress path q: p` space; c) excess pore water pressure Δu against axial strain ε_a; d) Excess pore water pressure build-up ratio r_u with the number of cycles N_L

Figure 5-53b, exhibited the same trend observed for the partially saturated NB sand. In the q-p′ stress path, the relationship between deviator stress and mean effective stress follows an inclination of approximately 1:3, in contrast to the stress path obtained for the saturated specimens shown in Figure 5-52b.

Figure 5-54 shows the resulting liquefaction resistance curve for HN31 sand at various Sr% levels. The liquefaction resistance ratio (LRR) was calculated by normalising the CSR_{15} values of the two testing sets by the corresponding CSR_{15} value of the fully saturated test set. The resulting LRR_{15} values were then plotted against Sr and Vp, as shown Figure 5-55a& b respectively.

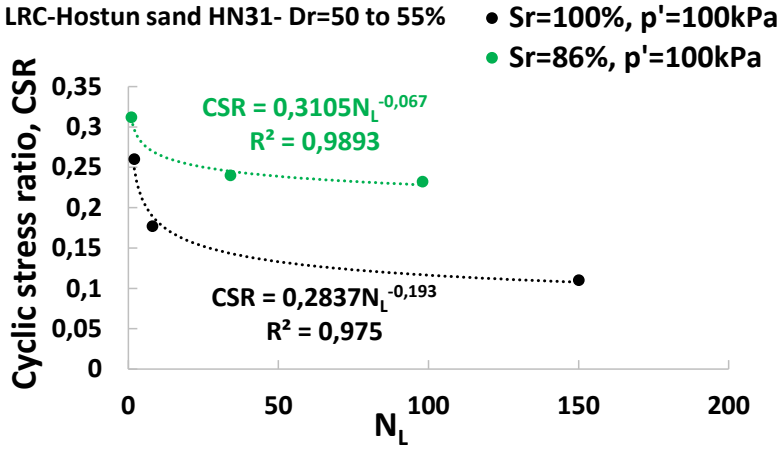

Figure 5-54 LRC of Hostun sand HN31, Sr=100 and 86%, Dr=50 to55%

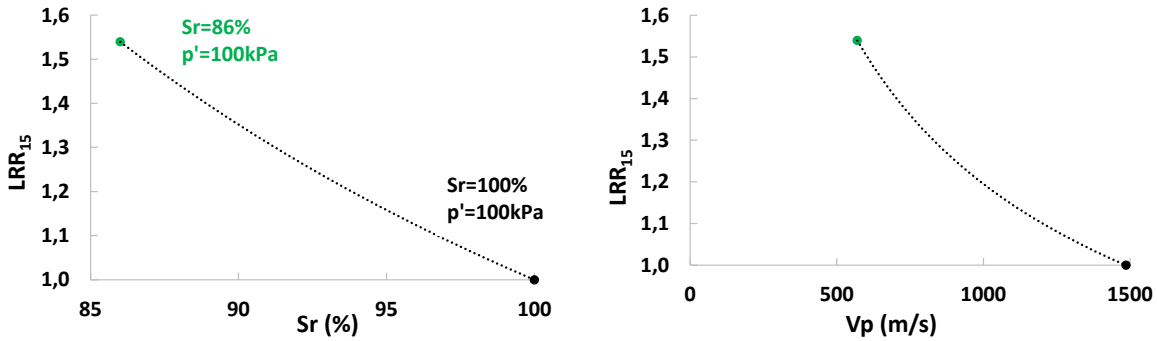

a) b)

Figure 5-55 Liquefaction resistance ratio LRR_{15} for Hostun sand plotted against a) Sr(%); b) Vp(m/s)

For comparison, the liquefaction resistance ratios at N_L=20 for both tested sands, NB and Hostun, under fully and partially saturated conditions were analyzed as a function of P-wave velocity. The results were compared with those reported for other sands by (Gómez, 2023) as shown in Figure 5-56.

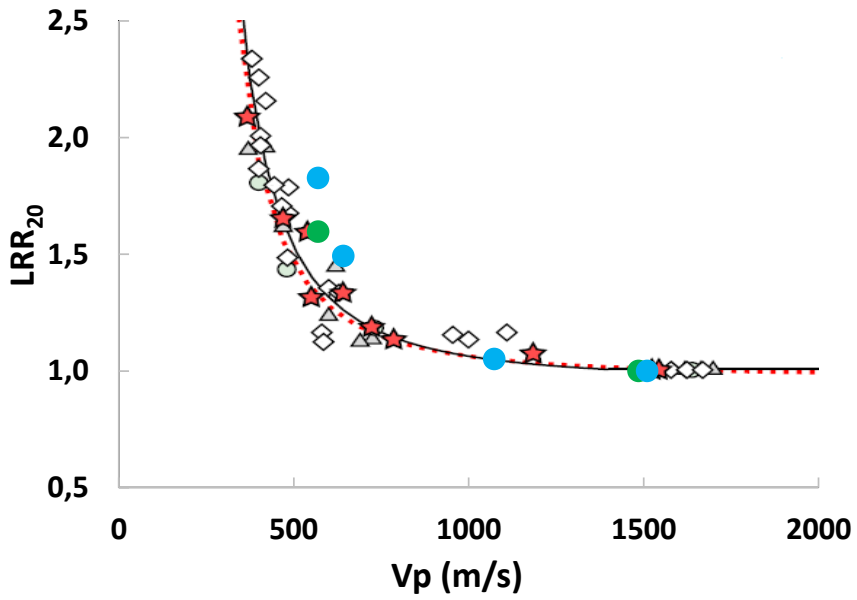

Figure 5-56 Liquefaction resistance ratio as a function of VP

A good agreement with other sands can be observed, evidenced an almost universal relationship between LRR and Vp.

5.5. Main findings

The performed partially saturated specimens exhibited degrees of saturation ranging from 86 to 99%, where the pore fluid is continuous while small air bubbles are present in a non-continuous, occluded state. In such composition, the suction effect is disregarded. Even slight reductions in Sr significantly affected the cyclic response of the soil by reducing and slowing excess pore-pressure build-up, altering material damping and stiffness, and modifying the undrained stress-path behaviour, as discussed below: -

- For an undrained, partially saturated specimen containing occluded air bubbles, the pore water and pore air may be treated as experiencing approximately the same excess pore-pressure increment, Δu, when suction effects are negligible. However, this remains an approximation, since the absolute air and water pressures are not strictly identical, and the difference may become more relevant as bubble size decreases, with possible effects on air dissolution amount and rate, particularly at low loading frequencies. Within this approximation, the associated volumetric strains of each constituent may be expressed in bulk-modulus form, $\varepsilon w = \Delta p / Kw$ and $\varepsilon a = \Delta p / Ka$, where, Kw is the bulk modulus of water and Ka is the air bulk modulus. Because Kw is very large (commonly taken as $Kw \approx 2.2 \times 106$ kPa), so even a small amount of occluded air bubbles dominates the compressibility of the pore-fluid mixture and causes the effective pore-fluid bulk modulus Kf to drop sharply below the fully saturated limit ($Kf \approx Kw$). This higher pore-fluid compressibility allows part of the cyclic volumetric tendency to be accommodated by gas compression, reducing the rate of excess pore-pressure accumulation and delaying effective stress collapse during cyclic loading. Furthermore, void ratio plays a vital role in altering soil liquefaction resistance. Therefore, in this chapter it was found that, induced partial saturation, IPS increased pore fluid compressibility due to the high compressibility

of the occluded gas, hence reduces pore pressure generation and delays the approaching very low effective stress.

- It was also reported that IPS, has not just increased number of cycles required to trigger liquefaction at the same CSR but also increased resistance as the number of cycles increases, tendency to have kind of more dilative behavior.

- The stress–strain loops highlighted a clear difference between the fully and partially saturated responses. For the fully saturated specimens, the loops progressively became asymmetric, with strain accumulation concentrated in one loading direction, reflecting the onset of cyclic instability. For the partially saturated specimens, the loops exhibited a more gradual shift of their mean position, indicating progressive plastic strain accumulation while mean effective stress, p′, was still largely preserved.

- Unlike fully saturated specimen, partially saturated sand developed higher shear strains under the same loading conditions, which resulted in lower cycle-by-cycle secant stiffness. Furthermore, the cycle-by-cycle material damping of partially saturated specimen was reported to be less than damping ratios of fully saturated specimen under the same loading conditions. Most importantly this behavior of partially saturated specimen occurred while r_u was kept lower and p´ was maintained, compared to fully saturated specimen. These would be attributed to the compressibility features of the occluded air bubbles which allowed for more deformable behavior.

- At the same r_u, partially saturated specimen accumulated more dissipated energy than fully saturated.

- Despite the undrained testing conditions, the behavior of the stress path (p′-q) of partially saturated sands showed a more drained-like stress path behaviour, compared to fully saturated specimens.

- Seismic wave measurements confirmed that Vp is highly sensitive to changes in Sr and can therefore provide a more reliable indication of saturation level than Skempton's B-value. This is because Vp is a compressional wave velocity and is strongly influenced by pore-fluid compressibility induced by the existing occluded air bubbles.

- At the same soil state (void ratio and mean confining pressure), shear wave velocity for the two different sands in the dry conditions should higher values and consequently slightly higher small strain stiffness than fully saturated. This behavior would be attributed to that the wetting-induced changes at grain contacts. In particular, weak layers formed on particle surfaces under saturated conditions reduce interparticle contact stiffness, leading to a small but systematic decrease in G_{max}.

6. Centrifuge modelling tests on Hostun sand: results and analyses

This chapter presents the detailed results and analysis of the performed dynamic centrifuge tests, focusing on how induced partial saturation IPS affects pore pressure build-up, surface settlement, seismic wave propagation, and the resulting shear stresses and strains at different soil depths. In addition, the chapter reports and interprets the seismic wave velocities P and S-waves measured during the testing phases.

6.1. Experimental Program details

Model setup

A rigid model container with one transparent acrylic side (internal dimensions: 500 mm × 250 mm × 350 mm) was used to simulate free-field conditions. Although rigid boxes can introduce boundary effects, but for centerline measurements in free-field configurations these influences are generally limited and were considered as negligible for interpretation. Three centrifuge models (M1, M2, M3) were performed to assess the influence of induced partial saturation IPS (via air injection) on the cyclic response of Hostun HN31 sand. All tests were conducted at 60 g and target relative density around Dr=45%. Relative densities and degrees of saturation in addition to the characteristics of the applied shakes are listed in Table 6-1 .

Loading protocol

Each centrifuge model followed a multi-stage loading sequence with successive shakes on the same specimen. In model 1 (M1), the first shake EQ1.1 was applied in the fully saturated state, followed by air injection to achieve partial saturation and a second shake EQ1.2 was then applied. A further air injection preceded a third shake EQ1.3, which was extended to 30 cycles (the first two comprised only 15 cycles) to study the response under prolonged excitation. In model 2 (M2), the specimen was prepared and spined up to 60 g, then partially saturated by injecting air bubbles before the first shake EQ2.1. A second air injection reduced saturation further prior to the second shake EQ2.2. In M3, air injection was performed at 1 g to induce partial saturation prior to spin-up. Two shakes followed EQ3.1, EQ3.2, then an additional air injection preceded a third shake EQ3.3 at a further reduced saturation. In M2 and M3, the sinusoidal input amplitude PGA was increased between stages to (i) approach Liquefaction ($r_{u,max}$=1) when feasible and (ii) compensate for small Dr(%) increases between consecutive shakes.

Seismic loading was simulated using a harmonic sinusoidal wave. The centrifuge tests were conducted at a centrifugal acceleration of 60g (N=60). Based on centrifuge dynamic scaling laws, dynamic time in the model scales as 1/N, while frequency scales as N. Therefore, to represent a prototype wave period of 1.0 s, the physical model was excited at a frequency of 60 Hz. The use of a viscous pore fluid, with viscosity approximately N times that of water, ensured compatibility between the seepage/consolidation time scale and the dynamic time scale.

Instrumentation

The models were instrumented with piezoelectric accelerometers (Acc; aligned parallel to the shaking direction), pore-pressure transducers (PPT; 11.4 mm length, 6.4 mm diameter) protected with sintered bronze porous tips to avoid direct soil contact, and linear variable displacement transducers, LVDT to monitor and report surface settlements. One central LVDT rested on a small Styrofoam float to track free surface water level variations linked to saturation changes and air injection. Accelerations, excess pore pressure at multiple depths, and vertical surface (soil and water) settlements were recorded continuously throughout all stages. The layout showing the instrumentation positioning for the three models M1, M2 and M3 are shown in Figure 6-1 , Figure 6-2, and Figure 6-3, respectively.

Specimen preparation

Hostun HN31 sand was used in the centrifuge testing program. Specimens were poured using air pluviation with controlled flow rate and automated moving fall height to achieve the targeted Dr% with the surface leveled under controlled vacuum. Instrumentation was installed at pre-planned depths during staged placement. Three pairs of bender elements BE (manufactured at LabGEO-FEUP) were embedded and fixed to an acrylic frame to measure shear and compressional wave velocities for small strain stiffness and saturation degree evaluation. A summary of the loading protocol, seismic excitation conditions, and specimen preparation conditions, including the relative density and degree of saturation before each stage, is presented in Table 6-1.

Table 6-1 Main parameters of the performed centrifuge models

Model	Shake	PGA (g)	N_o of Cycles	Sr(%)	Dr(%)
M1	**EQ1.1**	0.14	15	100	44.6
	EQ1.2	0.14	15	94	48.1
	EQ1.3	0.14	30	91.5	50.3
M2	**EQ2.1**	0.16	10	98.8	50.6
	EQ2.2	0.19	10	96	53.6
M3	**EQ3.1**	0.10	10	97	51.8
	EQ3.2	0.17	10	97	53.5
	EQ3.3	0.19	10	94	55.1

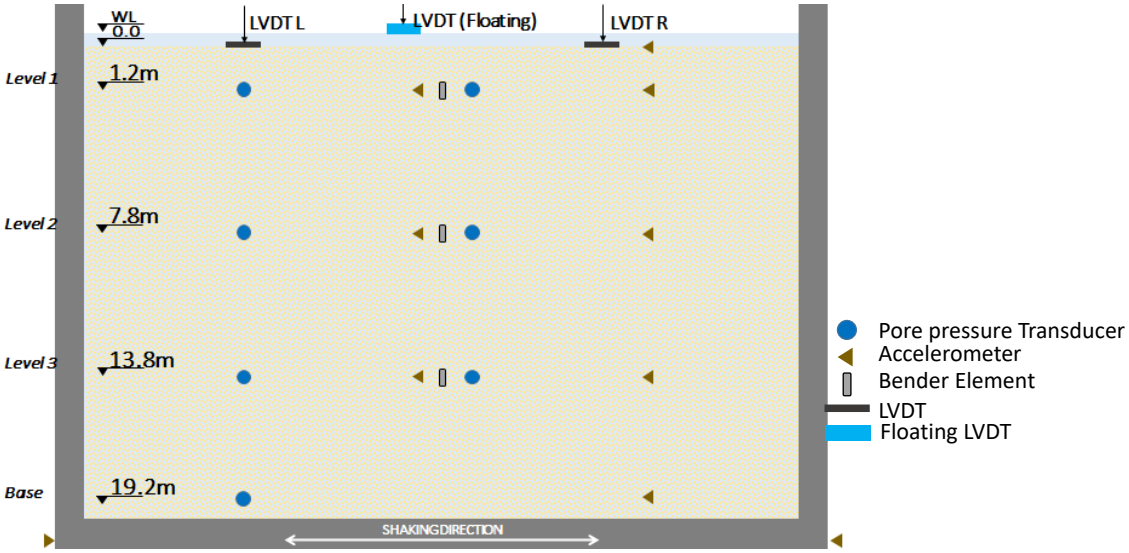

Figure 6-1 Centrifuge model layout for M1

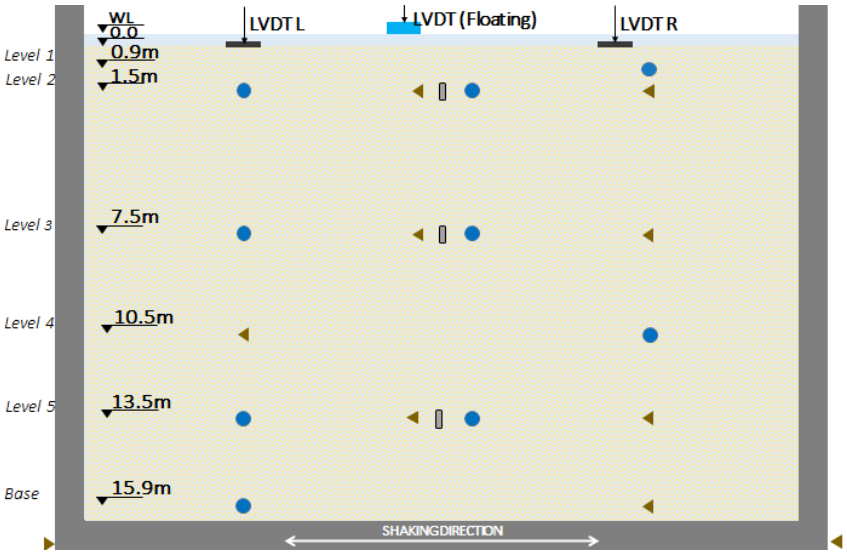

Figure 6-2 Centrifuge model layout for M2

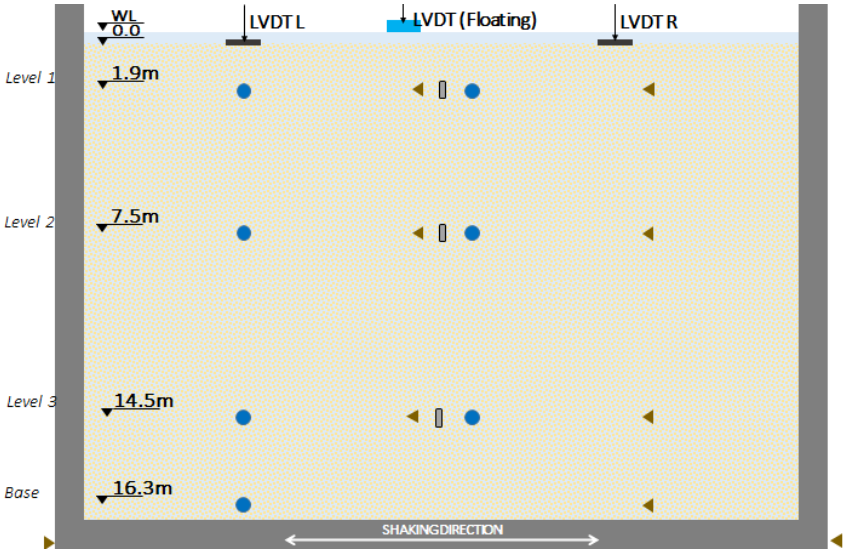

Figure 6-3 Centrifuge model layout for M3

6.2. Seismic wave measurement system

6.2.1. Bender Elements setup

In a novel experimental setup, three pairs of BE, were installed and fixed to an acrylic frame, and embedded within the soil model, as shown in Figure 6-4. These BE enabled the measurement of both compressional and shear wave velocities during the centrifuge testing phases, facilitating the assessment of key soil parameters, including small strain stiffness and confirming the full saturation. All details were already reported in chapter 3. A range of input signal frequencies, spanning from 1 kHz to 100 kHz, was applied to validate shear and compressional wave velocity measurements.

Wave velocities, Vp and Vs were determined from the direct and inclined wave travel times, which were determined using the first arrival method. These travel times were then evaluated with respect to the corresponding tip-to-tip propagation distances between the transmitting and receiving bender elements.

Figure 6-5 illustrates the geometric configuration of the BE array and the associated direct and inclined wave propagation paths. For all velocity calculations, the propagation distances Ld, Li1, and Li2 were measured from the tip of the transmitter to the tip of the corresponding receiver bender element, while td, ti1, and ti2 denote the respective first-arrival travel times along these paths.

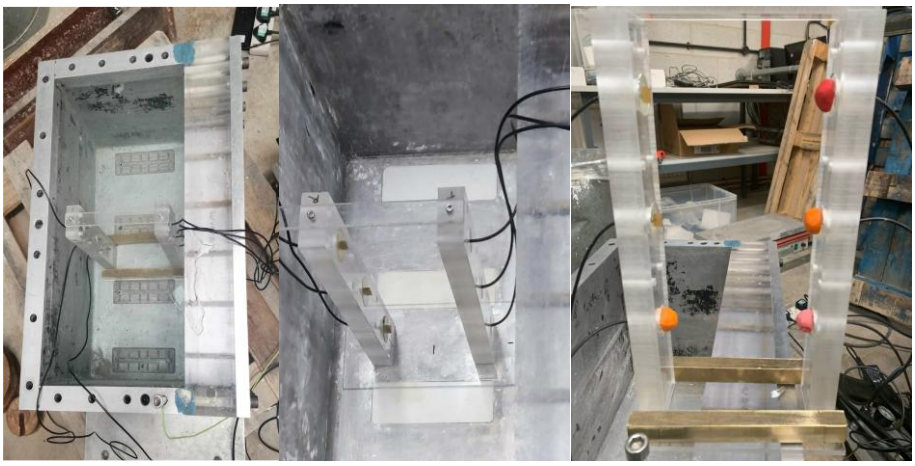

Figure 6-4 Idealization of the BE fixed to the frame within the model box

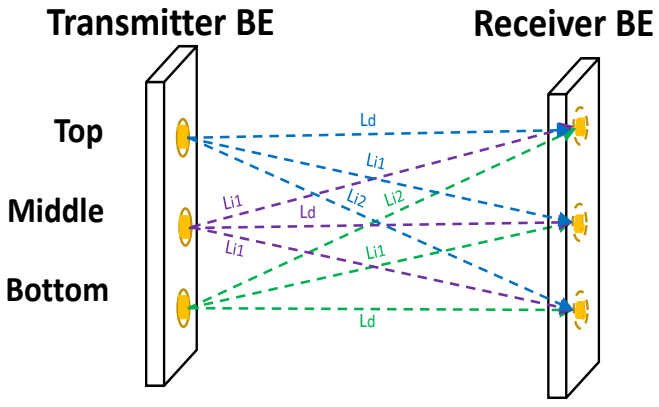

Figure 6-5 Configuration of the transmitted and received signals

6.2.2. Calibration of BE tests

In Model 1 (M1) Bender elements were installed at three different levels: (Bottom)13.8m, (Middle)7.8m, and (Top)1.2m, all in prototype scale. At 1.2 m received signals were found to be weaker and noise-affected, probably due to the low confinement.

Before centrifuge testing, the BE system was calibrated to verify the performance of the setup prior to its use in the centrifuge model box. The model box was filled with water and the bender element frame was positioned on the model box (before running the test). Figure 6-4 illustrates the configuration of the bender elements within the water-filled box during calibration, showing the adopted setup for subsequent experiments. Signals were transmitted from the three bender elements located on one side of the frame, with each transmitted signal received by the three bender elements positioned on the opposite frame side. Figure 6-6 shows the P-wave signals (propagating in the water) transmitted by the bottom BE and received by the three corresponding BEs at the three different levels. Compression wave velocity Vp in water was measured and found to be ranging from 1560 to 1585 m/s, as shown in Figure 6-6.

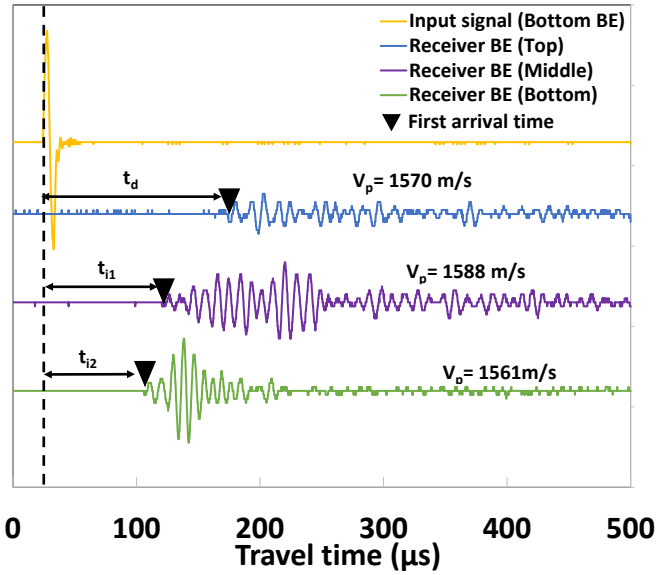

Figure 6-6 P-wave propagation time

The Vp values shown in Figure 6-6 were initially calculated using the direct and inclined propagation distances between the transmitting and receiving bender elements. These distances were obtained from tab-measured geometrical dimensions and basic trigonometric calculations, which may have introduced some measurement uncertainty and, consequently, possible errors in the calculated Vp values. The resulting velocities were slightly higher than the compressional wave velocity in water, commonly reported in the literature as approximately 1500 m/s. According to Santamarina et al. (2001), Vp values reaching or exceeding 1482 m/s (the velocity of sound in water) are strongly indicative of fully saturated conditions. Therefore, Vp was assumed to be approximately 1500 m/s, and the corresponding propagation distances were back-calculated from this value to obtain more accurate distance estimates.

Table 6-2 summarizes the propagation distances measured using the tab, the corresponding calculated Vp values, and the propagation distances derived from the back-analysis.

Table 6-2 Compressional wave velocity measured by the three levels of BE

	Based on manually measured distances between BE			Based on calibrated distances between BE, assuming Vp ≈1500m/s		
Measurement	**Propagation distance, L (mm)**	**First arrival time, t (μs)**	**Velocity Vp (m/s)**	**Propagation distance, L (mm)**	**First arrival time, t (μs)**	**Velocity Vp (m/s)**
Direct (d)	128	82	1561	123	82	1500
Indirect 1 (I1)	162	102	1588	153	102	1500
Indirect 2 (I2)	237	151	1570	227	151	1503

As shown in Table 6-2, the manually measured propagation distances were slightly different from those derived by assuming a fixed Vp value of approximately 1500 m/s. Therefore, the revised distances based on Vp≈1500 m/s were adopted in the calculation of Vp and Vs presented in the following sections.

6.2.3. BE testing results

This section presents the seismic wave velocity measurements obtained from the bender element BE array within centrifuge Model M1, where seismic wave signals were captured after the model M1 achieved the target centrifugal acceleration of 60g before applying the first shake, ensuring the soil deposit had reached its stable, in-flight effective stress state prior to shaking.

Figure 6-7 presents the P-wave propagation in the time domain captured across the soil profile. The testing sequence was conducted iteratively to capture a complete matrix of wave travel times: Figure 6-7a displays the signals generated by the top BE acting as the source and recorded by all BE receivers; Figure 6-7b shows the signals generated by the middle BE; Figure 6-7c presents the signals emitted by the bottom BE.

Similarly, Figure 6-8 illustrates the corresponding S-wave propagation results, following the exact same top, middle, and bottom source-excitation sequence, used for p-waves.

To enhance the accuracy of the arrival time determination, a range of input signal frequencies was utilized. Specifically, excitation frequencies ranging from 1 to 8 kHz were applied to assess Vs, while higher frequencies ranging from 50 to 100 kHz were employed to evaluate Vp.

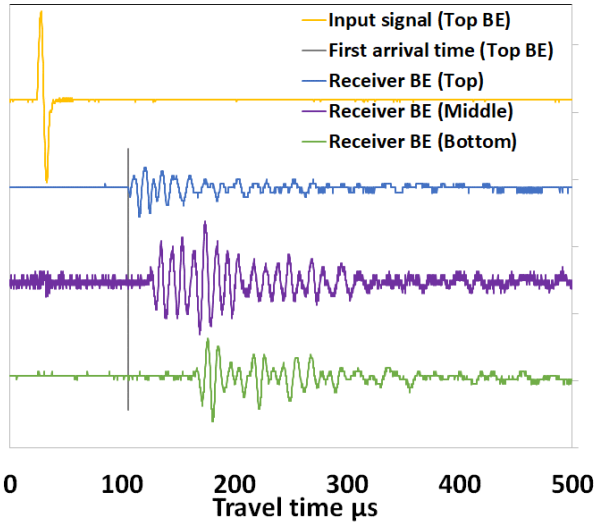

a)

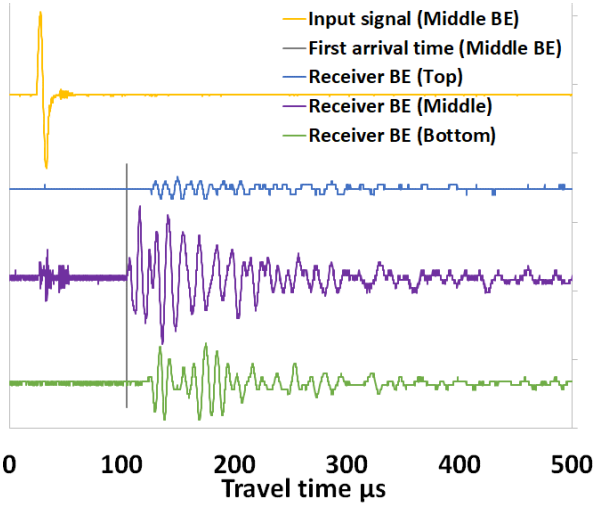

b)

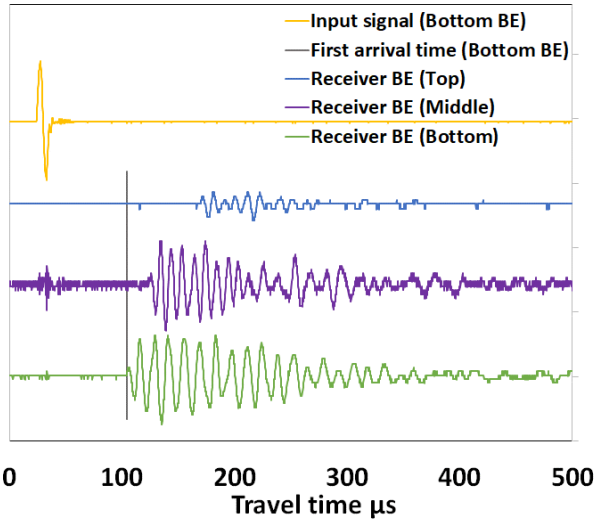

c)

Figure 6-7 Interpretation of P-wave in the time domain where signals were sent from: a) top; b) middle; c) bottom BE

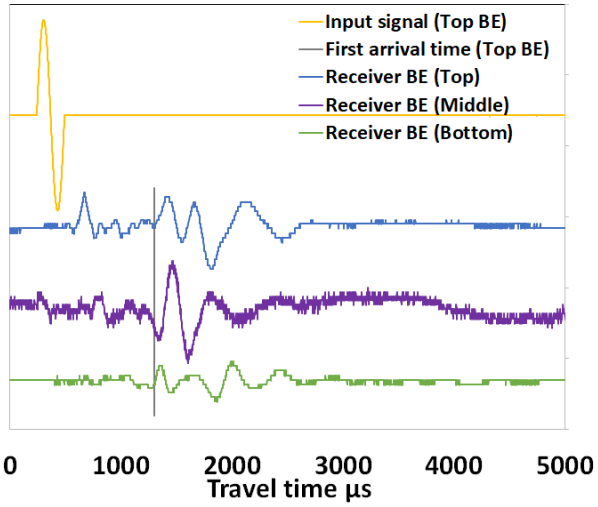

a)

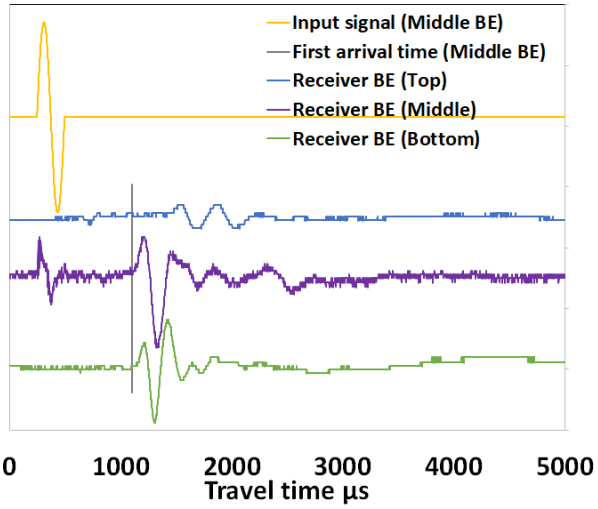

b)

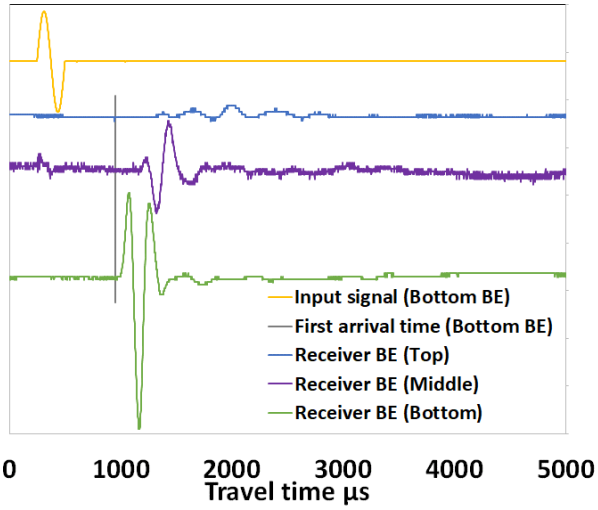

c)

Figure 6-8 Interpretation of S-wave in the time domain where signals were sent from: a) top; b) middle; c) bottom BE

During the P-wave measurements (Figure 6-7), waves were transmitted from the top bender element BE and recorded by the corresponding receiver BE on the opposite side of the acrylic frame. For the horizontal propagation path, the direct travel time t_d across the direct tip-to-tip distance l_d yielded calculated Vp ranging around 1500 m/s. These values are highly consistent with the propagation velocity of sound in water, confirming the fully saturated state of the soil model. When the same input signal was captured by the middle receiver BE, the inclined travel time t_{i1} increased due to the longer diagonal propagation path l_{i1} between the consecutive BE locations (i.e., top to middle). However, computing the velocity along this trajectory ($Vp = l_{i1}/t_{i1}$) yielded approximately the same P-wave velocity. Similarly, the signal recorded by the bottom receiver BE exhibited a further delayed inclined travel time t_{i2} corresponding to the longest diagonal path l_{i2} spanning across the non-consecutive sensor positions (i.e., top to bottom). Once again, the resulting velocity remained consistent. Notably, under these fully saturated conditions, variations in the mean effective stress across the depth of the soil profile did not alter the measured P-wave velocities, as the compressional wave propagation is mainly governed by the bulk stiffness of the pore fluid.

A comprehensive review of the S-wave propagation data across the three BE levels (Figure 6-8d, Figure 6-8e and Figure 6-8f), reveals two distinct, stress-dependent behaviours. For waves propagating upward through the soil profile (e.g., from the bottom transmitter to the middle or top receivers), the arrival times were significantly delayed. This occurred because the waves enter shallower soil depths, hence lower mean effective stress, p', which reduced the shear wave velocity Vs. This reduction in wave velocity, combined with the longer diagonal travel distance, adds up to significantly increase the overall travel time. Conversely, waves propagating downward (e.g., from the top transmitter to the middle or bottom receivers) plunge into deeper soil characterized by higher mean effective stress. The resulting stress-induced increase in Vs compensates for the longer diagonal travel distances, resulting in arrival times that are not very different from direct horizontal path travel times.

Figure 6-9 illustrates the first arrival travel time calculations of P-wave sent from the bottom BE to the three different receivers BE at varying depths for M1 at 60g, before applying the first shake. Vp was calculated by dividing the travel distance-either direct or inclined- as shown in Figure 6-5 by the corresponding travel time.

Table 6-3 summarizes the calculated Vp from direct and inclined propagation paths. The data confirms the consistency of the Vp values as measured at the three different receivers BE levels, highlighting the reliability of the measurements across different depths.

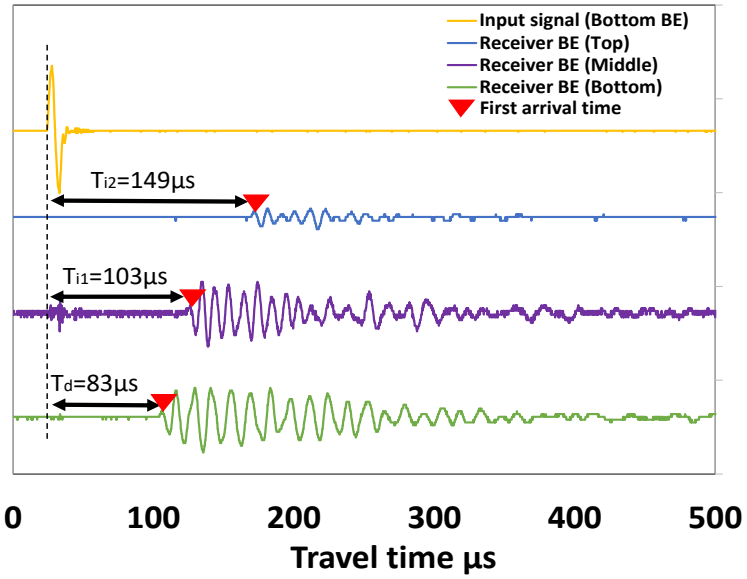

Figure 6-9 travel time calculation of Vp using first arrival method

Table 6-3 Compressional wave velocity measured by the three levels of BE for M1 after 60g centrifugal acceleration

Measurement	Propagation distance L (mm)	Propagation time t (µs)	Velocity Vp (m/s)
Direct	123	83	1482
Indirect 1 (I1)	153	103	1485
Indirect 2 (I2)	227	149	1524

Figure 6-10 and Figure 6-11 illustrate the measured travel times of P-waves and S-waves, respectively, transmitted from the bottom BE during different acceleration stages. Within each plot, the wave signals are grouped into three distinct clusters corresponding to the signals recorded at the top, middle, and bottom receiver BE. To evaluate the effect of increasing confining stress during the centrifuge swing-up (increasing p′), each specific centrifugal acceleration level is represented by a unique color.

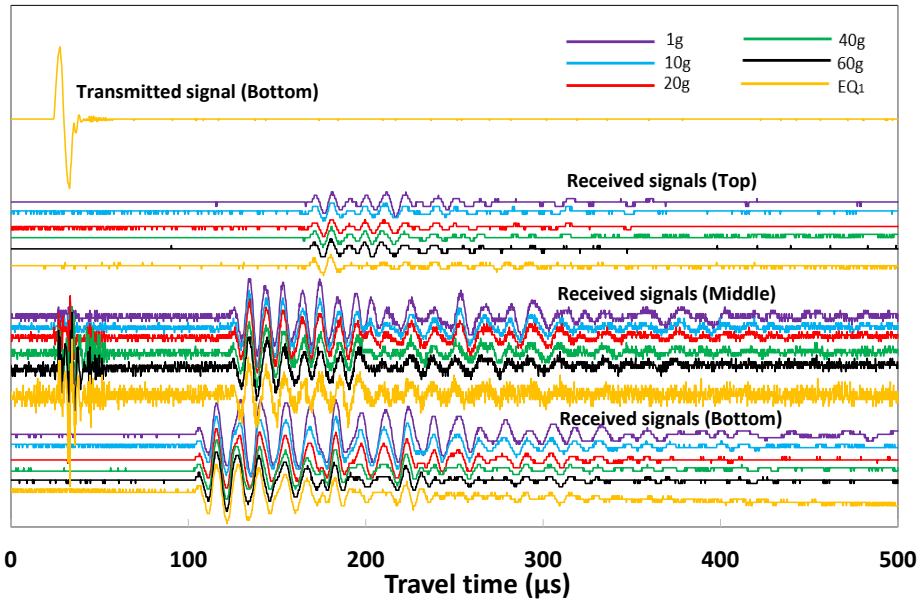

Figure 6-10 First arrival propagation time of Vp at different depths under various centrifuge accelerations

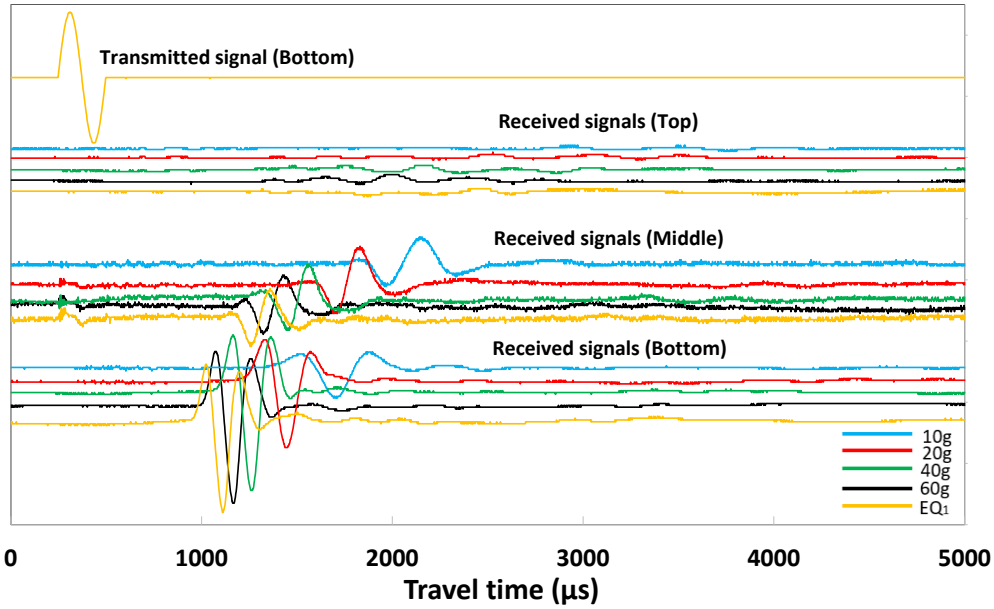

Figure 6-11 First arrival propagation time of Vs at different depths under various centrifuge accelerations

For example, looking at the signals recorded by the bottom receiver (BE is located at the same depth as the transmitter), a distinct contrast between the P-wave and S-wave behavior is visible. The P-wave travel times remained completely constant regardless of the increased centrifugal acceleration and the resulting higher mean effective stress, p'. Conversely, the S-wave travel times noticeably decreased as the acceleration and confining pressure increased. This direct comparison perfectly highlights the strong sensitivity of the soil's small strain stiffness to mean confining pressure.

A key observation is the consistency in wave velocity Vp and Vs, demonstrated by the proportional increase in travel time with increasing travel distance. This indicates accuracy of the novel setup, as the calculated velocities remain stable across different depths and acceleration levels. The clear and repeatable wave arrival times across different

acceleration stages suggest low experimental uncertainty, reinforcing the reliability of the recorded data for dynamic characterization of the tested soil.

Figure 6-12 and Figure 6-13 show the seismic wave stress dependency where the evolution of P and S wave velocities, respectively are illustrated as a function of varying confining stress p′, which is induced by the increased centrifugal acceleration during swing-up.

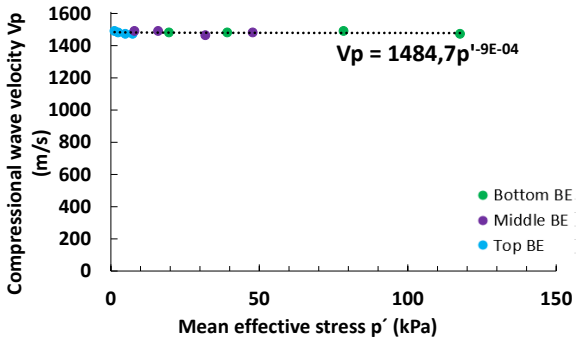

Figure 6-12 Evolution of Vp at different effective stress

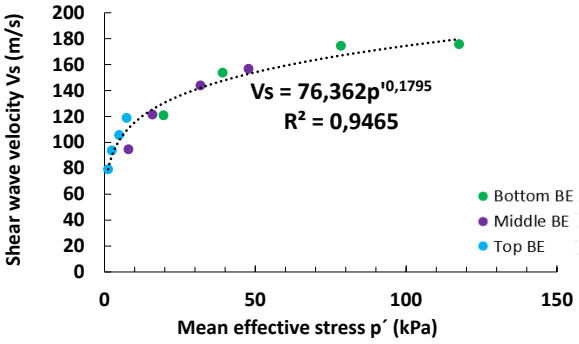

Figure 6-13 Evolution of Vs at different effective stress p′

For the S-wave data shown in Figure 6-13 the resulting stress-dependency exponent ß was calculated to be 0.18 under fully saturated conditions, which perfectly aligns well with typical values for natural sands.

The compressional wave velocity Vp serves as a highly reliable indicator of soil saturation. Throughout the centrifuge testing program, the Vp measurements obtained via the bender element array consistently met or exceeded this threshold in the saturated state.

In addition, the Vp values obtained at 60g centrifugal acceleration were consistent with those measured during the calibration tests conducted with the box filled with water. These results confirm that the soil model successfully achieved full saturation, validating the targeted saturation procedures conducted during the initial model preparation phase.

Once the soil reaches full saturation, Vp stabilizes at a nearly constant value (Figure 6-12), with an exponent ß of 0.0009, highlighting that p-waves is controlled by the bulk modulus of fluids as expected in fully saturated soils.

Post-Shaking S-Wave Measurements (Model M1)

Immediately following each of the three seismic shaking events EQ1.1, EQ1.2, and EQ1.3, shear wave velocities were measured across the soil profile. Figure 6-14 presents the S-wave time histories transmitted from the bottom BE and recorded by the receivers at the three corresponding depths.

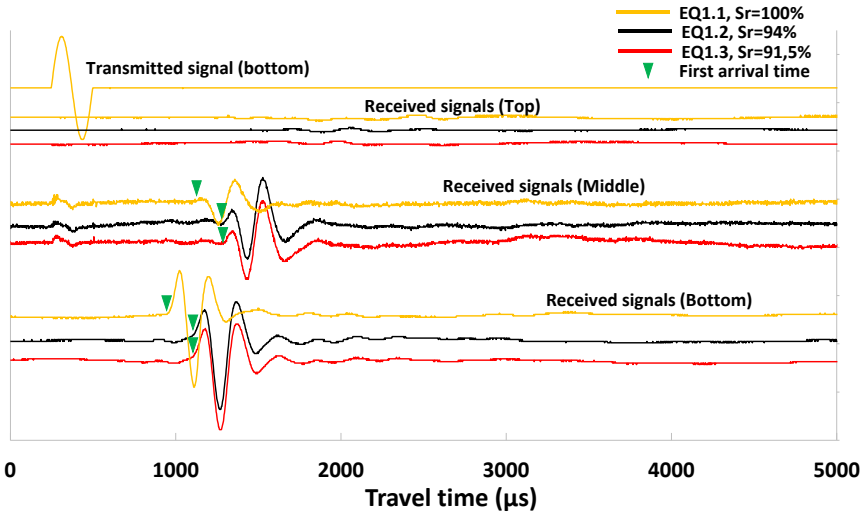

Figure 6-14 First arrival propagation time of Vs at different depths for the three shakes of M1

At the bottom receiver BE at 13.8 m depth, the first arrival times indicate that the soil was stiffest following the first shake EQ1.1 yielded the shortest travel time and a Vs of approximately 192.2 m/s. Following the subsequent shakes EQ1.2 and EQ1.3, the travel times delayed, resulting in a lower Vs of roughly 153.9 m/s. Because the maximum shear modulus is directly proportional to the square of the wave velocity ($G_{max} = \rho\ Vs^2$), this drop in Vs indicates a clear reduction in the small-strain stiffness of the soil after the first event. This same trend of initial stiffness followed by a reduction after further shaking was also observed at the middle receiver (7.8m depth). At the shallowest depth (1.2m depth), however, the signals were too attenuated to confidently identify a reliable first arrival. It is important to note that these bender element measurements apply exclusively to the very small-strain range. The calculated Vs and G_{max} values reflect the elastic stiffness of the soil post-shaking, and do not by themselves represent the large-strain degradation behavior that occurred during the actual centrifuge shaking events.

6.3. Experimental results

This section presents the main results of the dynamic centrifuge tests. Unless otherwise specified, all subsequent data and measurements are expressed in prototype scale. As earlier reported. All models were subjected to multiple shaking events under different degrees of saturation S_r%. The results are discussed in terms of accelerations, Arias intensity, excess pore pressure ratio, settlement, and stress–strain response to evaluate the influence of IPS on the soil's cyclic behavior.

6.3.1. Accelerations

The acceleration time histories recorded across the various depths are presented in Figure 6-15, Figure 6-16 and Figure 6-17 for the centrifuge models M1, M2, and M3, respectively. The data for each shaking event is consistently color-coded. For Model M1 (Figure 6-15), the three-event sequence progressed from a fully saturated baseline (EQ1.1, Sr=100%, blue) to increasingly partially saturated conditions (EQ1.2, Sr= 94%, orange; and EQ1.3, Sr =91.5%,

green). Figure 6-16 details the two successive events for Model M2: EQ2.1 (Sr=98.8%, blue) and EQ2.2 (Sr =96%, orange). Finally, Figure 6-17 illustrates the three-shake sequence applied to Model M3: EQ1.1 (Sr=97%, blue), EQ1.2 (Sr=97%, orange), and EQ1.3 (Sr=94%, green).

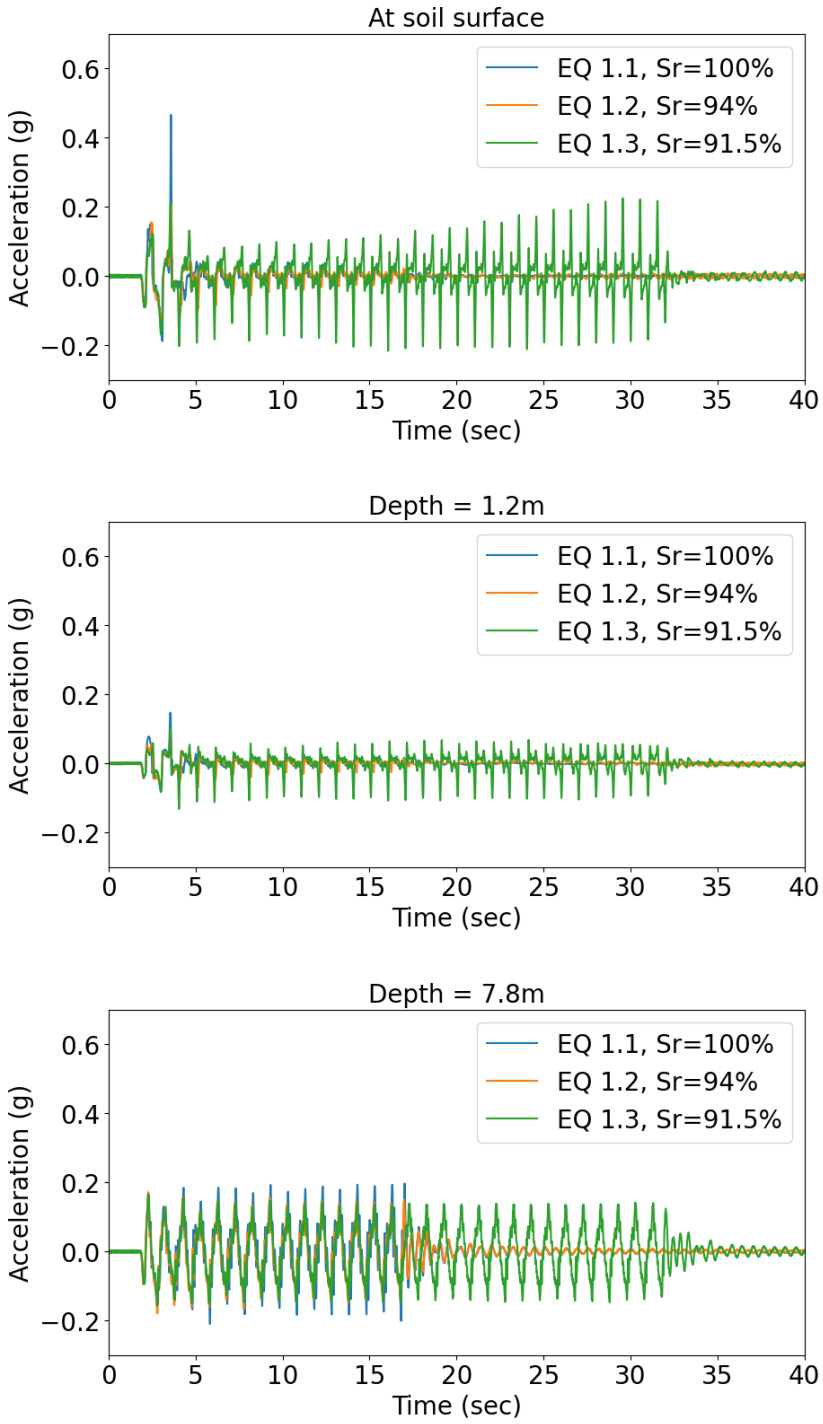

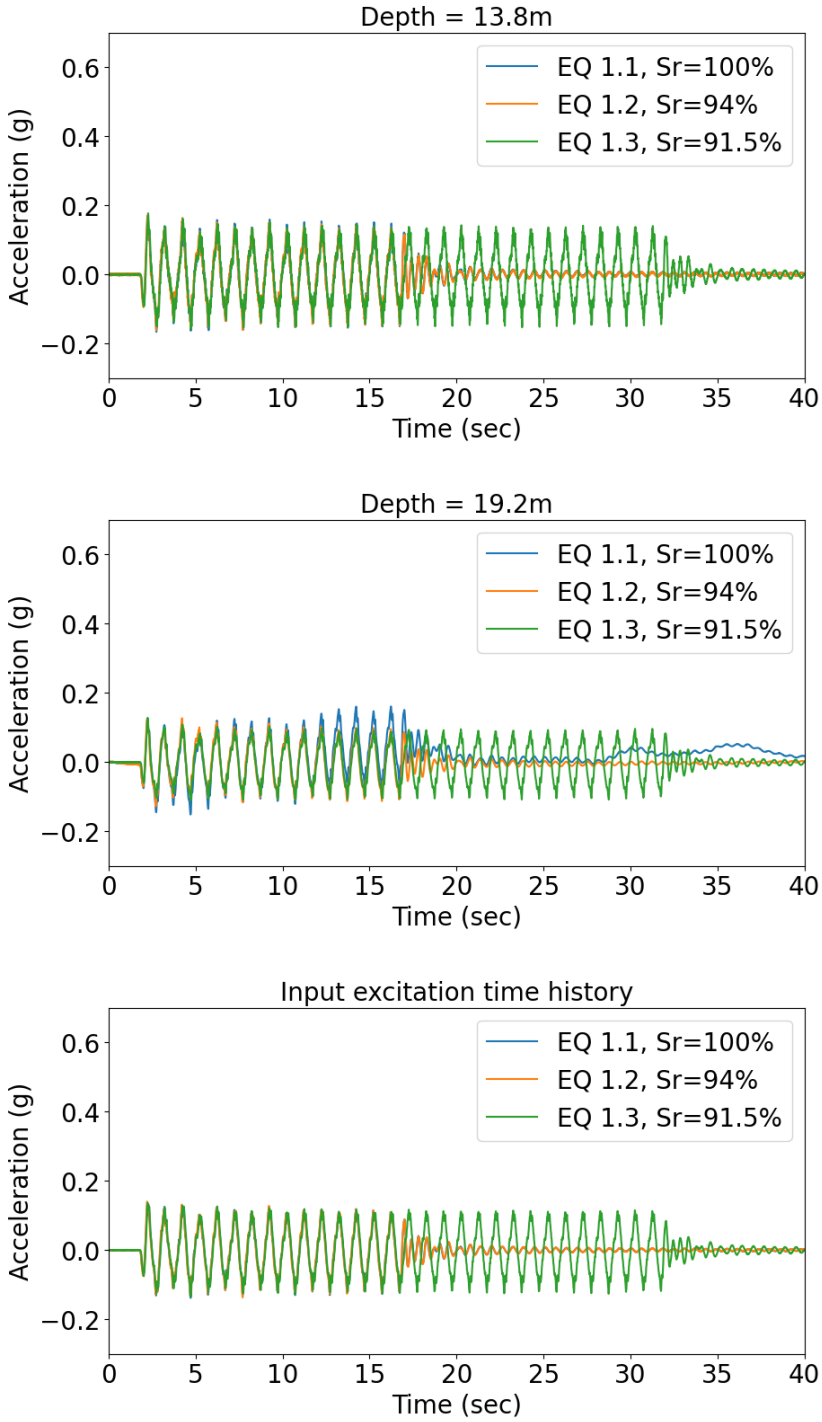

Figure 6-15 Acceleration time histories for M1 at various depths

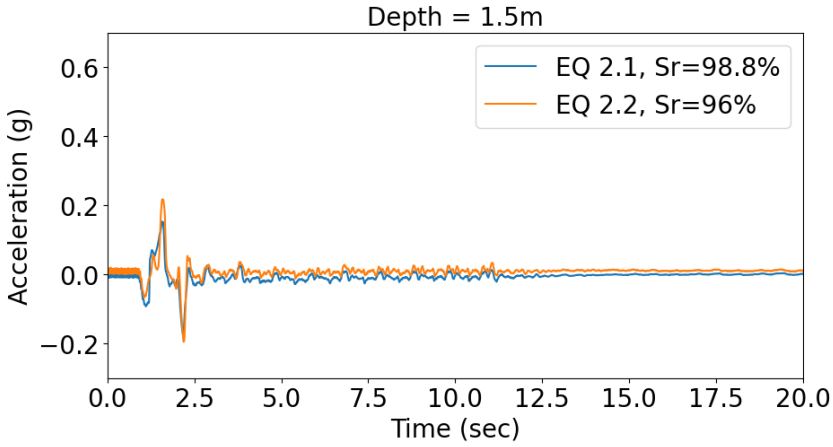
Depth = 1.5m
EQ 2.1, Sr=98.8%
EQ 2.2, Sr=96%
Acceleration (g)
0.6
0.4
0.2
0.0
−0.2
0.0
2.5
5.0
7.5
10.0
12.5
15.0
17.5
20.0
Time (sec)

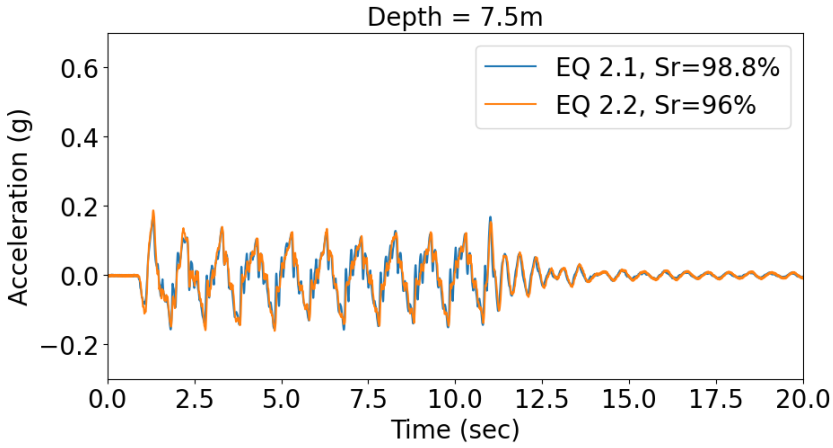
Depth = 7.5m
EQ 2.1, Sr=98.8%
EQ 2.2, Sr=96%
Acceleration (g)
0.6
0.4
0.2
0.0
−0.2
0.0
2.5
5.0
7.5
10.0
12.5
15.0
17.5
20.0
Time (sec)

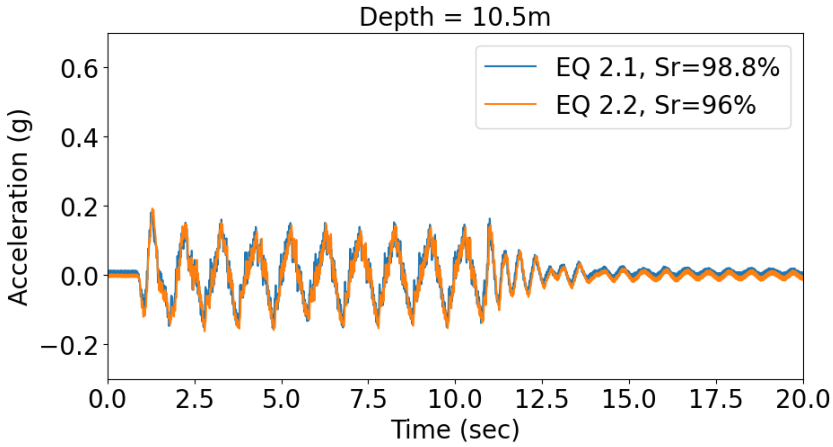
Depth = 10.5m
EQ 2.1, Sr=98.8%
EQ 2.2, Sr=96%
Acceleration (g)
0.6
0.4
0.2
0.0
−0.2
0.0
2.5
5.0
7.5
10.0
12.5
15.0
17.5
20.0
Time (sec)

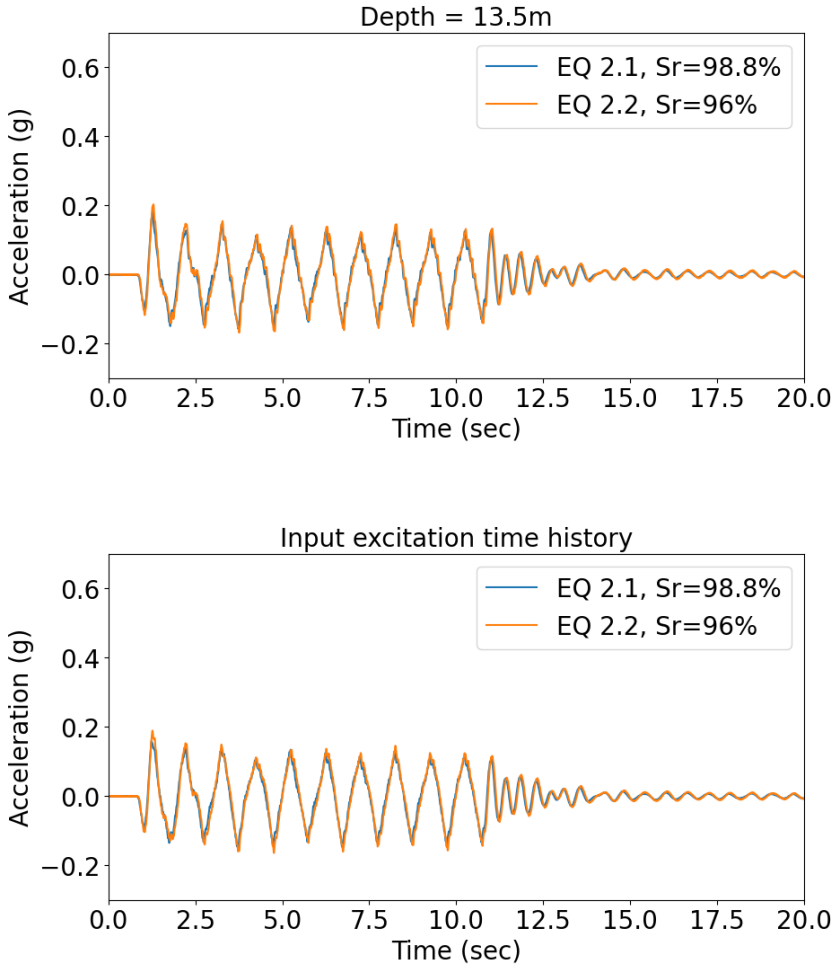

Figure 6-16 Acceleration time history-M2 at various depths (note that acceleration time history is not included in this plot at level 15.9m, due to malfunctioning accelerometer)

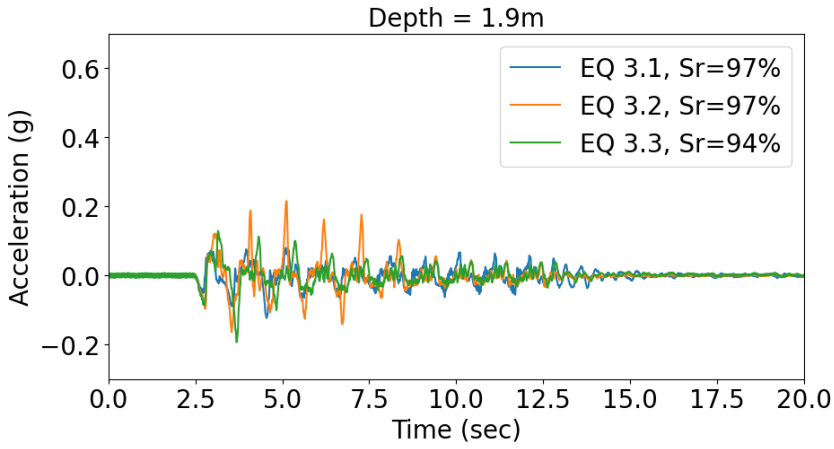

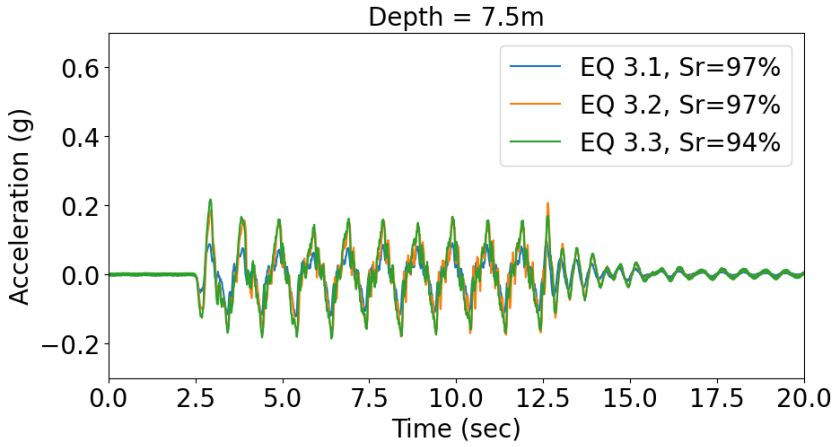
Depth = 7.5m
EQ 3.1, Sr=97%
EQ 3.2, Sr=97%
EQ 3.3, Sr=94%
Acceleration (g)
0.6
0.4
0.2
0.0
−0.2
0.0
2.5
5.0
7.5
10.0
12.5
15.0
17.5
20.0
Time (sec)

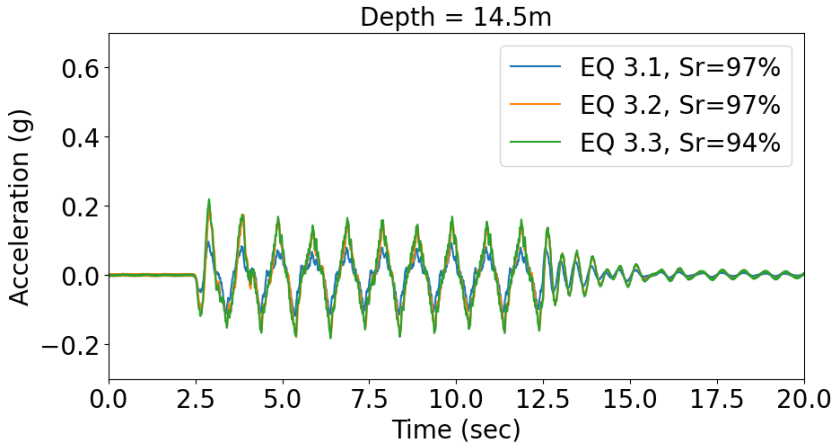
Depth = 14.5m
EQ 3.1, Sr=97%
EQ 3.2, Sr=97%
EQ 3.3, Sr=94%
Acceleration (g)
0.6
0.4
0.2
0.0
−0.2
0.0
2.5
5.0
7.5
10.0
12.5
15.0
17.5
20.0
Time (sec)

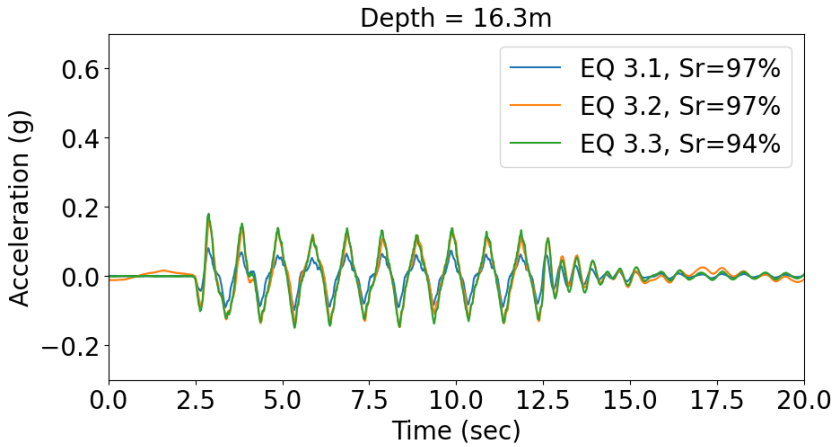
Depth = 16.3m
EQ 3.1, Sr=97%
EQ 3.2, Sr=97%
EQ 3.3, Sr=94%
Acceleration (g)
0.6
0.4
0.2
0.0
−0.2
0.0
2.5
5.0
7.5
10.0
12.5
15.0
17.5
20.0
Time (sec)

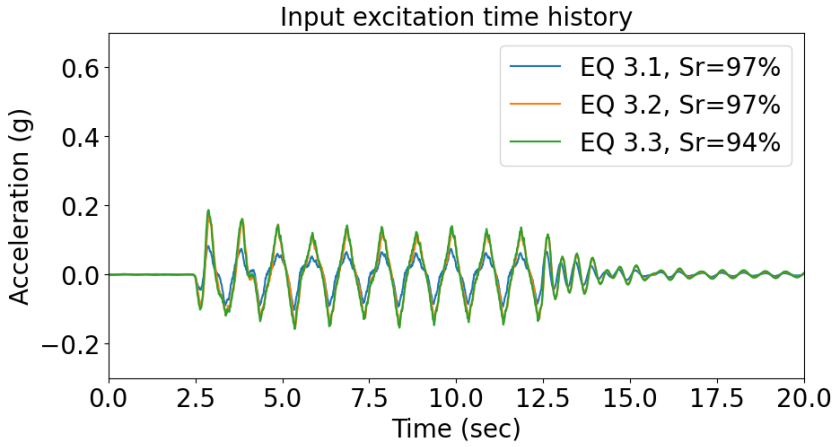

Figure 6-17 Acceleration time history-M3 at various depths

Across the three models, acceleration records generally amplified at mid-deep layers and attenuated toward the surface, with differences between fully and partially saturated conditions. Detailed explanations are presented in the following section using Arias intensities and resulting shear stresses and strains.

6.3.2. Arias Intensity

To evaluate seismic amplification and attenuation throughout the soil profile, Arias Intensity I_a was adopted as an energy-based ground-motion metric, defined as the time integral of squared acceleration scaled by π/2g as shown in Equation (6-1). It captures both amplitude and duration over the full record and is more informative than PGA for depth-dependent comparisons. For each depth, I_a was computed for the shaking duration and then normalized by the input shake I_a at the base; the resulting normalized $I_a(t)$ histories were plotted to evaluate the evolution of transmitted energy with time as it propagates upward through the soil column (Robert Kayen et al., 1997).

$$I_a = \frac{\pi}{2g}\int_0^t a_x(t)^2\,dt \tag{6-1}$$

where g is the gravitational acceleration and $a_x(t)$ is the horizontal acceleration recorded at a specific depth.

Conceptually, Arias intensity quantifies the total energy per unit weight absorbed by idealized oscillators during an earthquake, encompassing both the amplitude and duration of the shaking. Fundamentally, tracking this total energy metric as it propagates upward through the profile provides a direct measurement of how much seismic demand is attenuated by the soil's energy dissipation mechanisms.

Because these damping mechanisms consume the applied seismic energy, a highly damped soil layer will naturally absorb a larger fraction of the earthquake's demand. Consequently, less energy is permitted to propagate upward, resulting in a distinctly lower Arias intensity transmitted to the shallower depths.

Mathematically, the standard Arias intensity formula in equation (6-1) is derived by assuming that the damping ratio of the theoretical oscillators approaches zero. Because of this simplification, the equation does not contain an explicit damping variable; it simply integrates the squared acceleration over time to quantify the kinetic energy of the soil. However, the calculated I_a value inherently captures the physical damping of the soil profile. As the soil matrix dissipates seismic energy, the amplitude and duration of the upward-propagating wave are significantly reduced. This attenuated acceleration record naturally yields a much smaller integral, translating directly to a lower measured Arias intensity at the shallower depths. A low-pass filter was applied to the acceleration records before calculating Arias intensity to avoid overestimation of I_a caused by high-frequency noise.

A major advantage of adopting Arias intensity over the Peak Ground Acceleration (PGA)—which is the standard metric in traditional cyclic stress frameworks, is its comprehensive nature. While PGA represents a single, instantaneous spike that is often dominated by localized high-frequency motion, Arias intensity integrates the entire earthquake record. This allows to capture the true cumulative energy demand across the full frequency spectrum and duration of the shaking.

Figure 6-18 presents the Arias Intensity I_a time histories for Model M1 at multiple depths, normalized by the I_a of the input motion at the base. Curves correspond to EQ1.1 (Sr = 100 %, are in blue), EQ1.2 (Sr ≈ 94 %, orange), and EQ1.3 (Sr ≈ 91.5 %, green). Overall, the records show amplification in the mid-deep layers and progressive attenuation toward the surface.

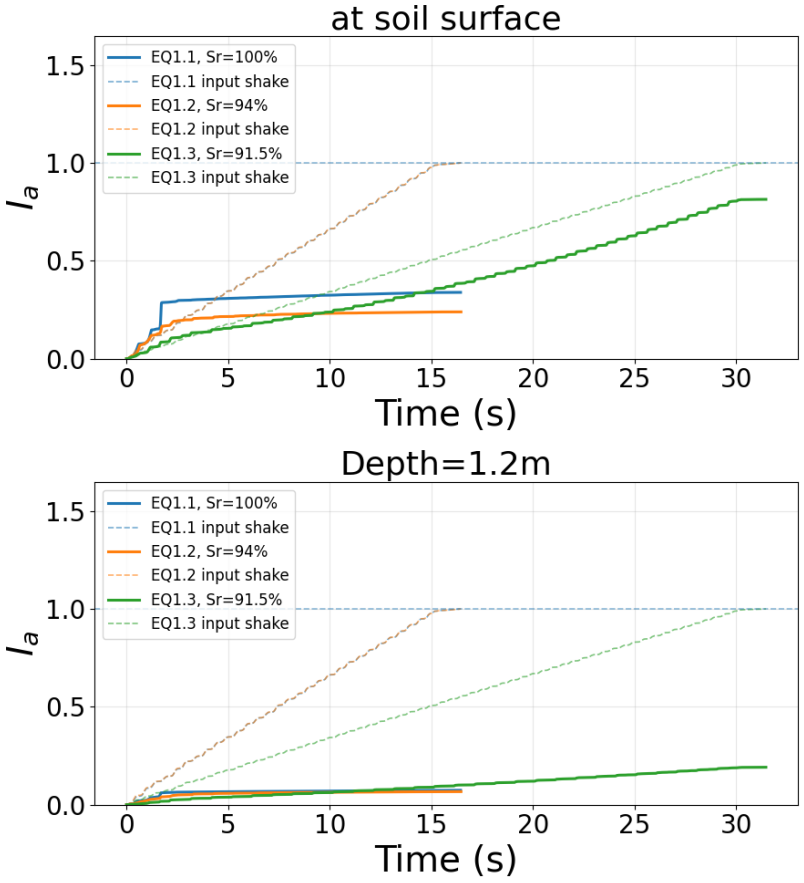

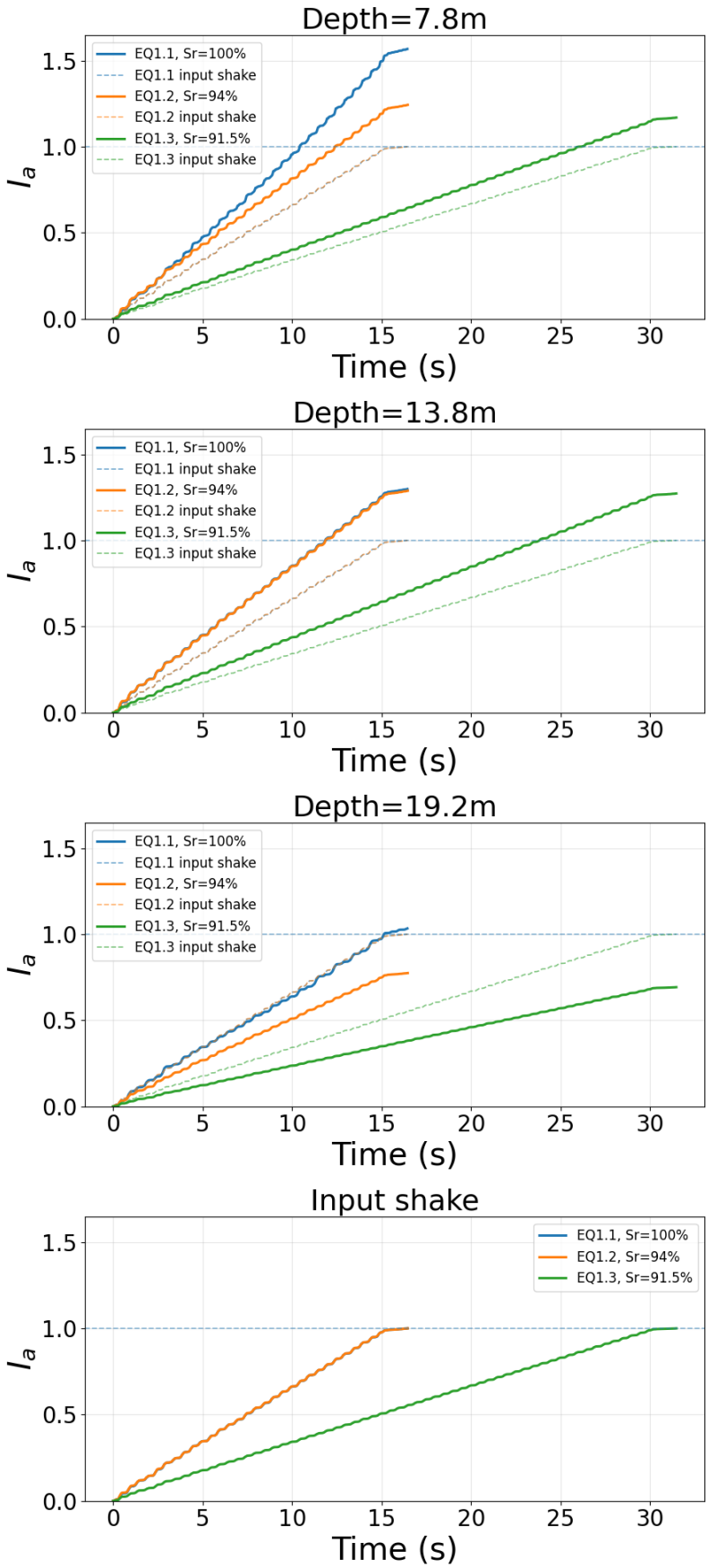

Figure 6-18 Normalized Arias Intensity Ia time history-M1 at various depths

In Figure 6-18, at the base (19.2 m), the I_a of the fully saturated case EQ1.1 was nearly equal to the input I_a (i.e., only very slight amplification), whereas the partially saturated cases EQ1.2, EQ1.3 showed lower normalized I_a, confirming greater attenuation as saturation decreased which could be attributed to the energy consumed by the cyclic compression of entrapped air bubbles.

At the intermediate depth of 13.8 m, the transmitted seismic energy remained largely unaffected by the induced partial saturation. Throughout this depth, all shaking events displayed similar acceleration amplification levels and yielded comparable final Arias Intensity I_a values. While a marginal reduction in transmitted energy was observed due to the introduction of air (where I_a, EQ1.1 > I_a, EQ1.2 > I_a, EQ1.3), these differences were exceptionally small.

At 7.8 m, the same attenuation pattern reappeared where I_a of EQ1.1 > EQ1.2 > EQ1.3, confirming the initial hypothesis that partial saturation leads to greater energy dissipation through pore-fluid compressibility.

Near the surface (1.2 m depth and at the soil surface), all saturation scenarios exhibited pronounced attenuation due to soil softening and probable liquefaction. In these two shallow depths, EQ1.1 and EQ1.2 showed early energy attenuation followed by stabilization, aligning with stiffness loss and the onset of liquefaction or severe softening. In contrast, EQ1.3 maintained higher stiffness and transmitted more energy upward.

To conclude, in partially saturated scenarios EQ1.2 and 1.3, the air-water mixture introduced added damping and energy-absorption pathways, where entrapped bubbles increased pore-fluid compressibility, so cyclic compression/expansion of bubbles dissipated part of the input energy, a mechanism absent in fully saturated soil. Consequently, less energy is transmitted upward. In contrast, in the fully saturated scenario, this additional fluid compressibility isn't present so, transmit seismic energy is more efficiently transmitted at depth (higher I_a).

Figure 6-19 details the Arias Intensity (I_a) time histories for Model M2 by depth, normalized to their input motion I_a, where, EQ1.1 (Sr = 98.8%, blue) and EQ1.2 (Sr ≈ 96%, orange).

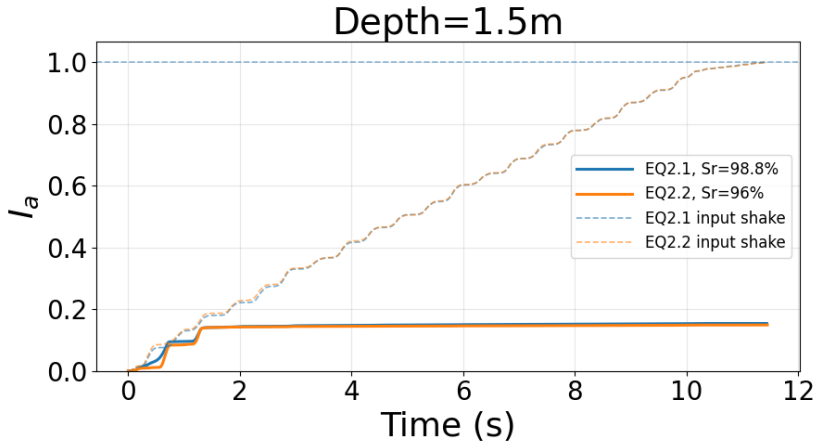

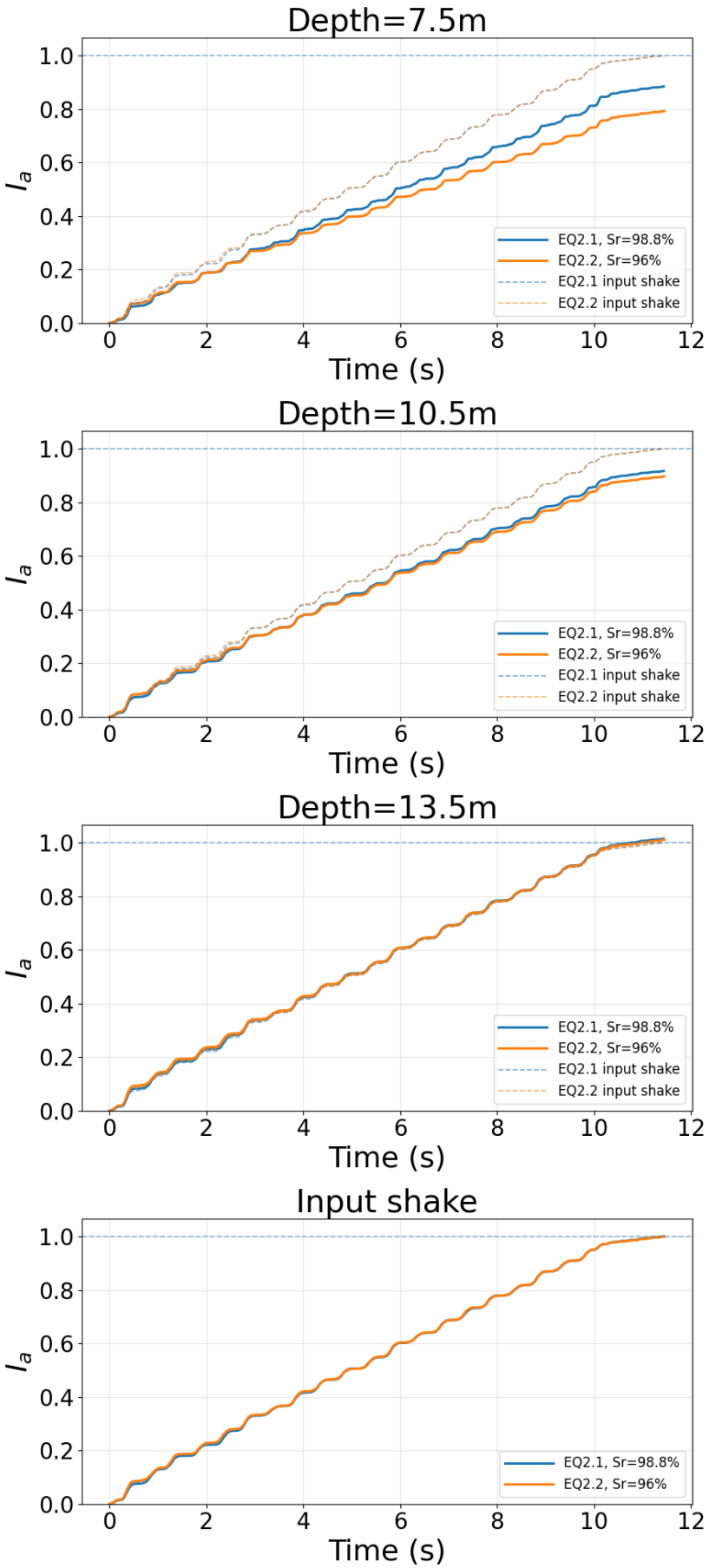

Figure 6-19 Normalized Arias Intensity I_a time history-M2 at various depths

From Figure 6-19 it can be concluded that, although EQ2.2 had a higher input PGA then EQ2.1, normalized cumulative Arias Intensity enabled a consistent comparison of energy transmission along the soil column. By definition, both shakes EQ2.1 and 2.2 ended at a normalized I_a of 1.0 at the input shake level. At the base level (13.5 m), both shakes showed slight amplification, indicating efficient coupling of the input motion into the soil. Above this level, attenuation became dominant, at 10.5 m both motions attenuated, with EQ2.2 exhibiting slightly greater attenuation than EQ2.1. At 7.5 m, attenuation increased further for both shakes, again with EQ2.2 showing the larger attenuation. At the shallow level (1.5 m), both records, displayed pronounced early attenuation followed by a plateau, a clear sign of stiffness loss and the onset of liquefaction/strong softening. In sum, despite its higher PGA, EQ2.2 transmits less energy upward than EQ2.1, reflecting the added damping from a partially saturated soil, most evident at mid depths, where confinement maintain air bubble stability and the zone is distant from both the input shake and the near-surface region where gas retention is less effective.

The normalized cumulative Arias intensity, $I_a(t)$, for the three shakes of Model M3 are presented in Figure 6-20.

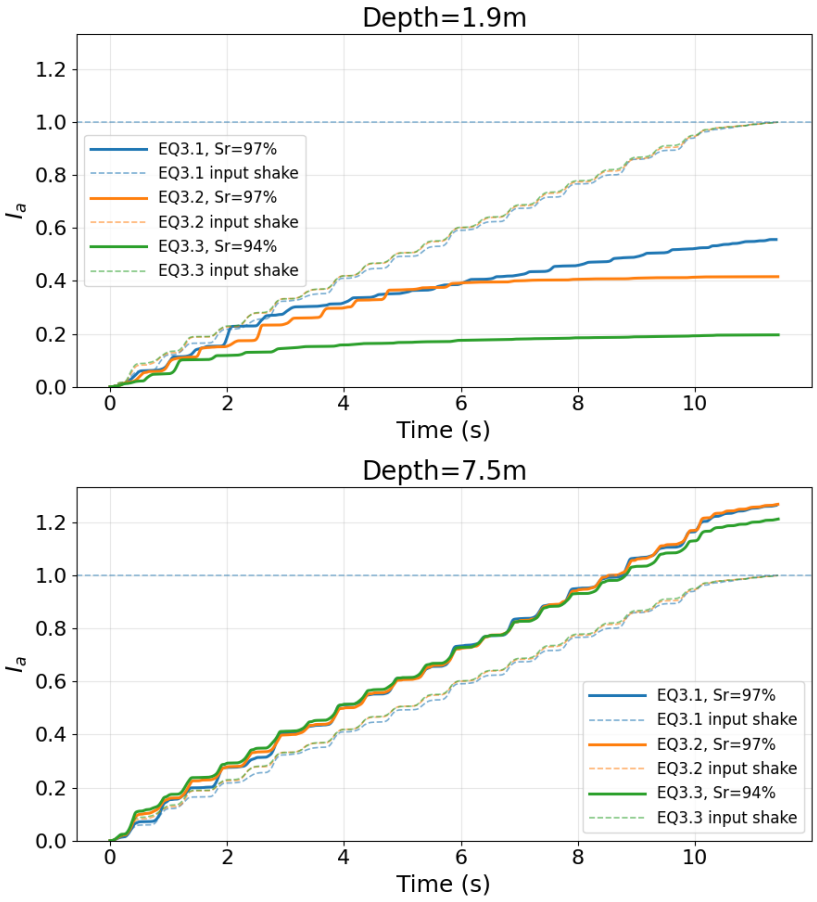

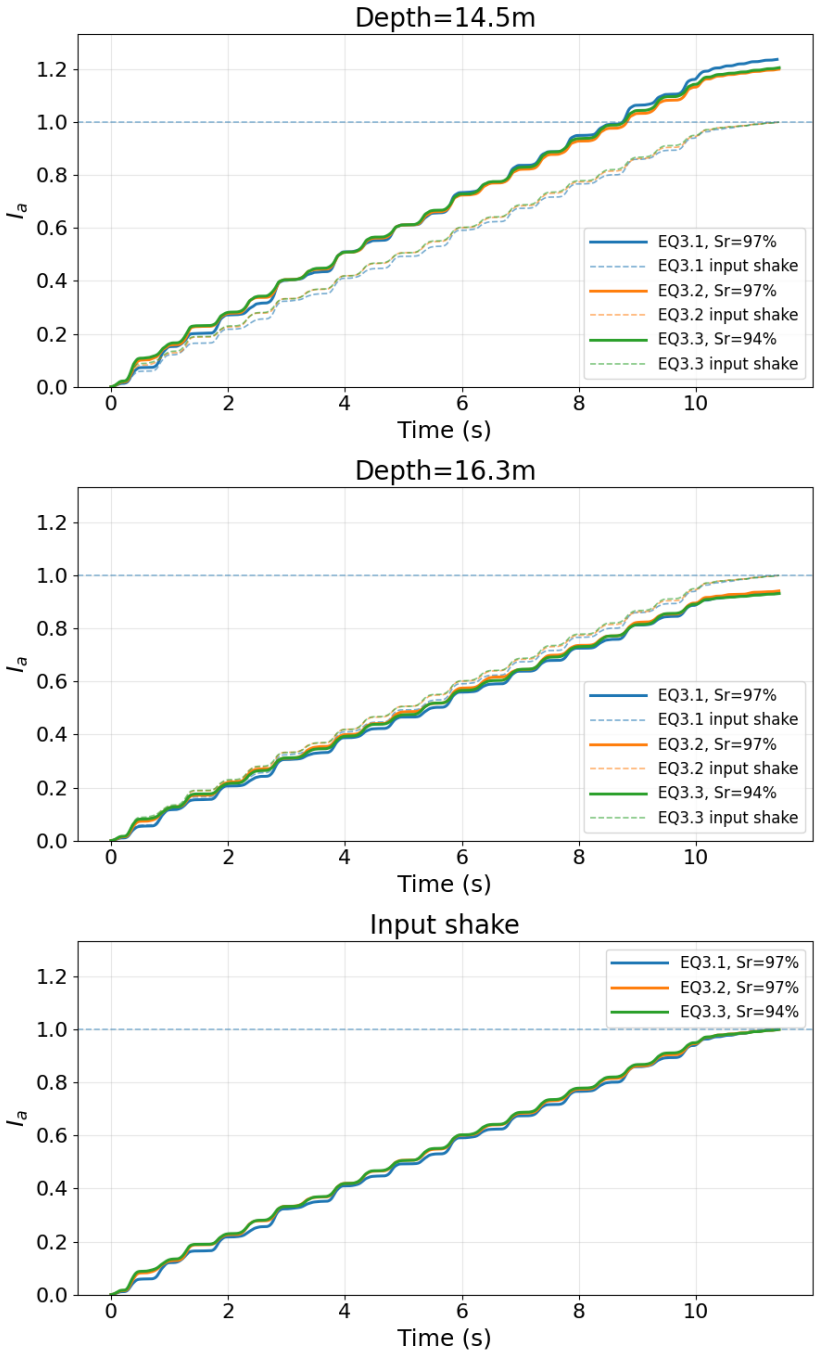

Figure 6-20 Normalized Arias Intensity I_a time history-M3 at various depths

The first two shakes were conducted at the same saturation levels, but different input shake amplitudes, while the third shake followed air injection to a lower saturation and a higher input amplitude as previously detailed in Table 6-1. Because Arias intensity reflects amplitude, frequency content, and duration, differences in PGA and duration can shift both the rate and final level of I_a. That is why the curves were interpreted using normalized plots (cumulative I_a vs. time).

The I_a of the three motions started at unity at the base input (by definition). At 16.3 m all three shakes showed slight attenuation (≈0.93), indicating efficient transmitting of the input with modest early loss.

Amplification was recorded at 14.5 m (I_a≈1.24 for EQ3.1; ≈1.20 for both EQ3.2 and EQ3.3), and again at 7.5 m (≈1.2 for EQ3.3; ≈1.27 for EQ3.1 and EQ3.2). The systematic reduction of mid-depth amplification as saturation decreases is aligned with added damping from occluded bubbles, which increases pore-fluid compressibility and diverts part of the input energy into cyclic bubble compression rather than wave transmission.

Near the surface (1.9 m) all shakes strongly deamplified (EQ3.1 ≈ 0.58, EQ3.2 ≈ 0.405, EQ3.3 ≈ 0.20); the pronounced drop with decreasing Sr shows that, despite the higher PGAs of EQ3.2 and EQ3.3, partial saturation governs the response by enhancing attenuation and limiting transmitted energy in the shallow zone. Overall, M3 reproduced the depth-dependent pattern seen in M1 and M2: modest losses at the base, peak transmission at mid-depths controlled by stiffness, and strong near-surface attenuation.

(Mirshekari & Ghayoomi, 2017) carried out centrifuge tests on dry, saturated and, unsaturated specimens with Sr ranging between (32 and 68%) and found that as Sr decrease the peak ground acceleration amplified towards the soil surface. Furthermore, they reported an increased cumulative intensity amplification in unsaturated soils compared to fully saturated ones. Also, reducing Sr decreased the lateral deformation and surface settlement.

But in this study, a different behavior was reported as Sr decreases, the peak ground acceleration attenuates towards the soil surface. This could be understood by distinguishing the difference between the dynamic behavior of Unsaturated Soils (where suction is induced and pronounced), and partially saturated soils (where only bubbles are entrapped within the continuous fluid path).

6.3.3. Excess pore pressure ratio r_u

Excess pore pressure data, Δu were recorded during and after each shake at the preset depths using pore pressure transducers PPT. Subsequently, excess pore pressure ratios r_u were calculated, $r_u = \Delta u/\sigma'_{v0}$ where σ'_{v0} is the initial vertical effective stress at each depth. Liquefaction onset is considered whenever r_u approach unity (zero of effective stress). This definition and criterion are standard in cyclic liquefaction studies and are adopted in the current study.

6.3.3.1. Model M1

Figure 6-21 presents the build-up and dissipation of excess pore pressure ratio r_u for Model M1 at depths of 1.2, 7.8, 13.8, and 19.2 m across the three shaking events; each panel shows the evolution of $r_u(t)$ during the shake and the subsequent post shake decay for the three shakes at a particular depth.

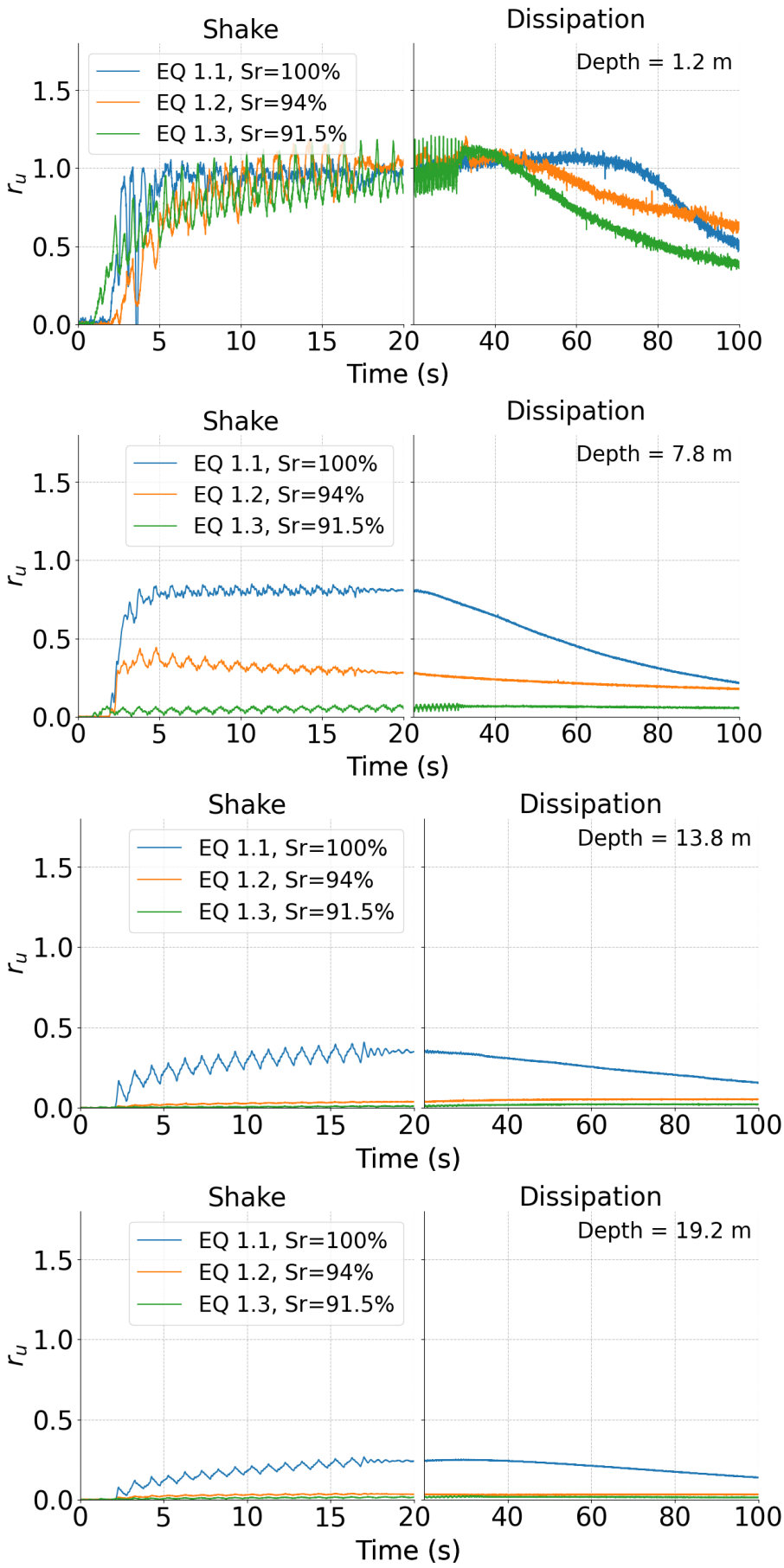

Figure 6-21 Excess pore pressure ratio r_u time history for the three shakes of M1 at various depths

The shake build-up (M1)

For M1, where PGA was kept the same for the three shakes, $r_u(t)$ increased upward through the profile with larger peaks toward the ground surface. Along the depth, the shallowest layer consistently exhibited the largest r_u while the deepest the smallest, reflecting the confining effect of overburden pressure, which raises cyclic resistance and limits pore-pressure generation at larger depths.

The plots in Figure 6-21 reveal the expected soil response, where (r_u (EQ1.1) > r_u (EQ1.2) > r_u (EQ1.3)) across all mid and deeper layers, where occluded air increased pore fluid compressibility and thereby suppressed excess pore pressure generation under cyclic loading. At higher depths (19.2 m and 13.8 m), the fully saturated case (EQ1.1) reached peak r_u values of approximately 0.25 and 0.40, respectively, whereas both partially saturated cases exhibited much smaller, almost negligible r_u.

At 7.8 m depth $r_{u,max}$ for EQ1.2 was almost half that of EQ1.1, while EQ1.3 remained very small.

On the other hand, at shallower depth (1.2m), all three shakes led to close $r_{u,max}$. values, with evidence of complete liquefaction, where $r_{u,max}$ approximately equal to unity. However, fully saturated conditions showed faster and higher r_u generation specially in the beginning of the shake, while partially saturated scenarios delayed the pore pressure build-up because part of the early cyclic loading was consumed in compressing the entrapped air bubbles within the pore fluid.

A plausible explanation to this limited enhancement at the very top layers compared to deeper depths could be due to the non-uniform distribution and upward migration/escape of injected gas, where air was injected from the model box base, and gas may partially rise and/or redistribute, leading to less persistent occluded gas near the surface (and hence a probable higher local Sr%), in addition to the lower confining pressure in the shallow layers.

Post-shake dissipation (M1)

Furthermore, Figure 6-21 shows that, across all depths, EQ1.1 produced the largest residual excess pore pressure ratios, whereas EQ1.2—and especially EQ1.3—led to very small residuals, resulting in shorter dissipation periods, which is a key effect of partial saturation: reduced pore-pressure build-up during shaking and faster re-establishment of effective stress. Apparent “lack of dissipation” in the partially saturated cases simply indicates that residual r_u was already minimal immediately after shaking. The influence of reduced saturation on post-shake dissipation remains depth-dependent, with stronger benefits at greater confinement (deeper layers).

6.3.3.2. Model M2

Figure 6-22 provides the results for Model M2 at 0.9, 7.5, 10.5, 13.5, and 15.9 m depths; data at 1.5 m are omitted due to evidence of PPT malfunction.

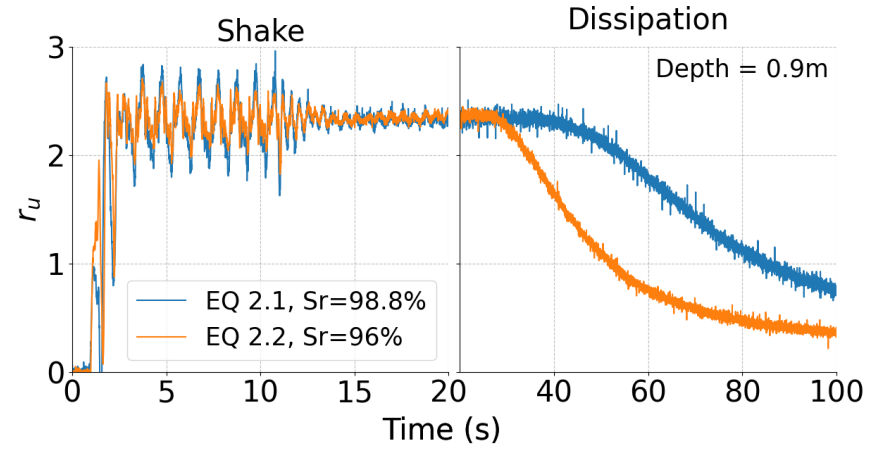
Shake
Dissipation
Depth = 0.9m
EQ 2.1, Sr=98.8%
EQ 2.2, Sr=96%
r_u
Time (s)

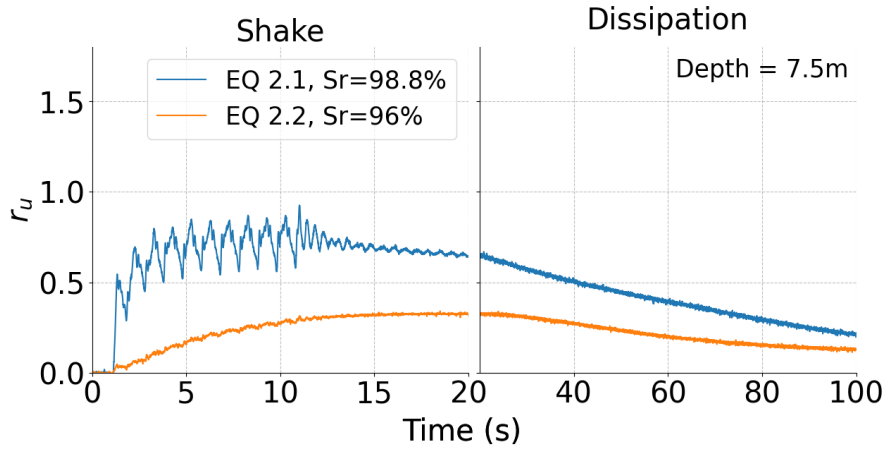
Shake
Dissipation
Depth = 7.5m
EQ 2.1, Sr=98.8%
EQ 2.2, Sr=96%
r_u
Time (s)

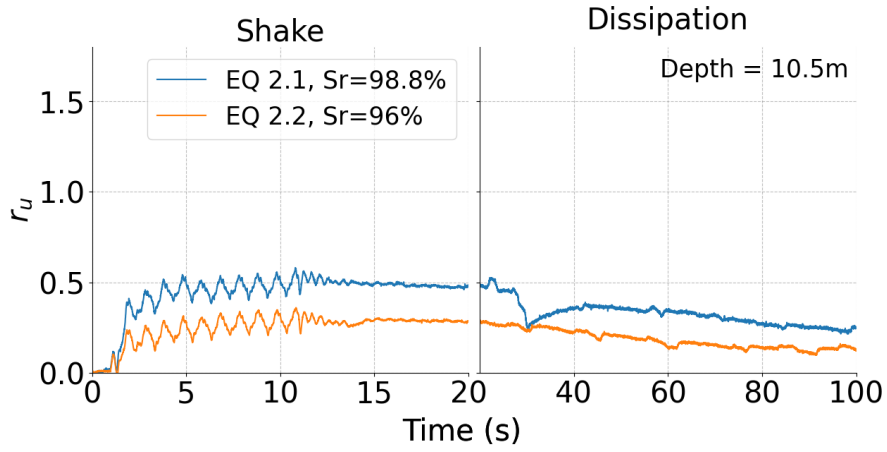
Shake
Dissipation
Depth = 10.5m
EQ 2.1, Sr=98.8%
EQ 2.2, Sr=96%
r_u
Time (s)

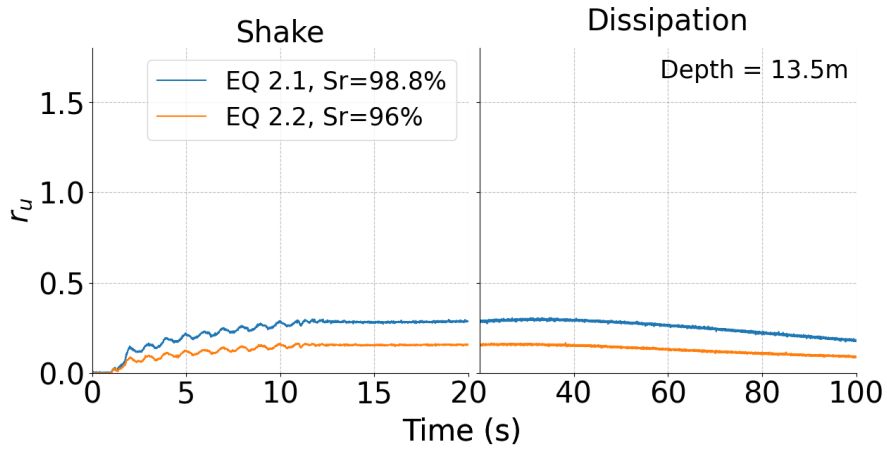
Shake
Dissipation
Depth = 13.5m
EQ 2.1, Sr=98.8%
EQ 2.2, Sr=96%
r_u
Time (s)

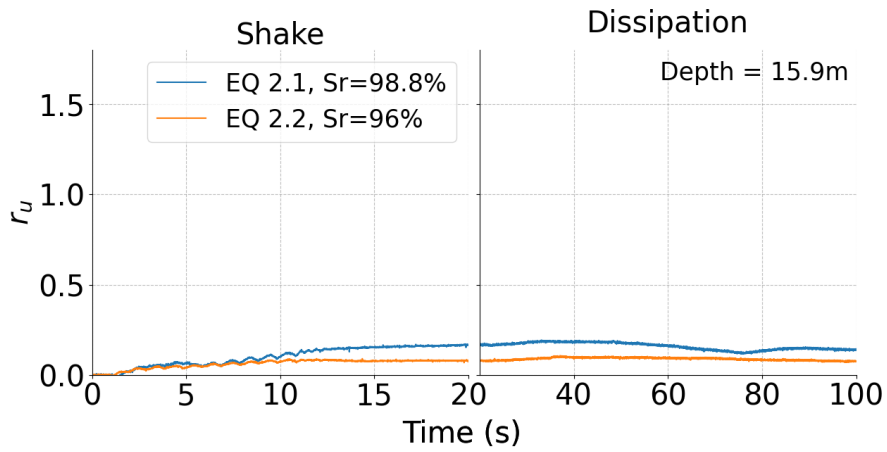

Figure 6-22 Excess pore pressure ratio r_u time history for the three shakes of M2 at various depths

The shake build-up (M2)

Model M2, exhibited an upward $r_u(t)$ increase throughout the profile in both shakes, with minimal values at the base and maximal values at the surface. Despite the higher input PGA of EQ2.2, r_u generally built up more slowly and with lower peaks than in EQ2.1, except at the shallowest level (0.9 m), where both motions reached $r_u>1$ (liquefaction onset). The minimum mitigation near the surface would be attributed to the reduced confinement and lower reliable gas retention close to the free surface, whereas mid-depths benefit from greater confinement and more stable occluded gas, as observed in M1 as well. Quantitatively, EQ2.2 achieved about 50% reduction in peak r_u relative to EQ2.1 at mid-depths, even with its higher PGA.

Post-shake dissipation (M2)

Across all instrumented depths (including the shallow layer), the residual excess pore-pressure ratio after dissipation for EQ2.2 was approximately one-half of that for EQ2.1.

6.3.3.3. Model M3

Figure 6-23 reports the build-up and dissipation of excess pore pressure ratio r_u for Model M3 results at 1.9, 7.5, 14.5, and 16.3 m.

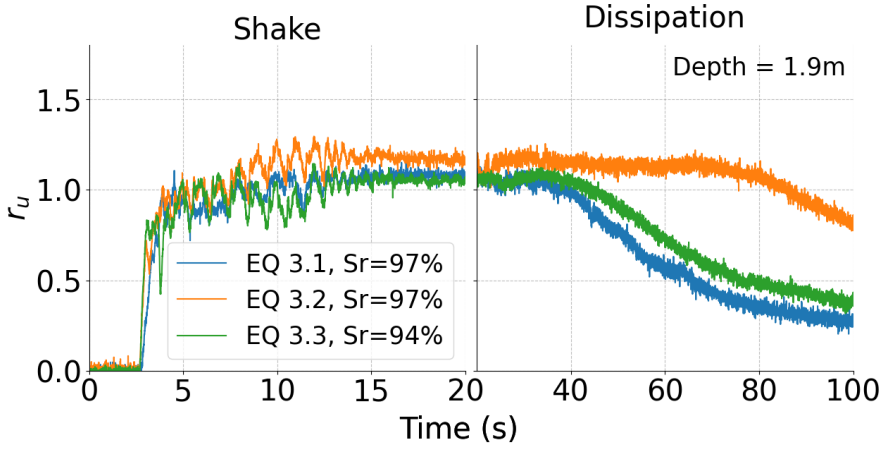

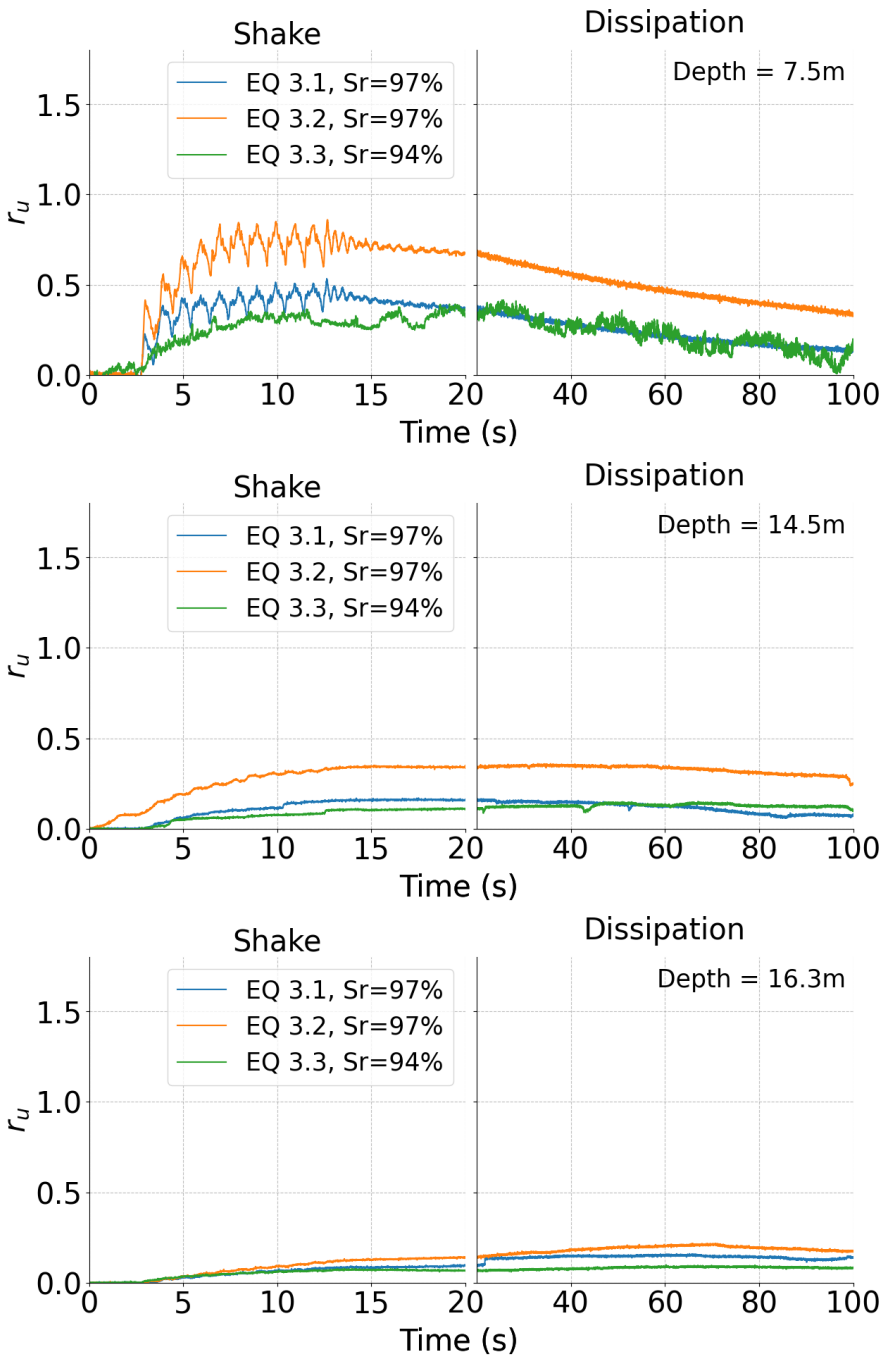

Figure 6-23 Excess pore pressure ratio ru time history for the three shakes of M3 at various depths

The shake build-up (M3)

The upward increase of r_u observed in Models 1 and 2, is reproduced in M3, with the shallowest layer reaching the largest peaks. In this model, the input PGA increased across shakes EQ3.1, EQ3.2, and EQ3.3 (≈0.10, 0.17, and 0.19 g) respectively, while the degree of saturation decreased (≈97 % for both EQ3.1and EQ3.2 while ≈94 % for EQ3.3). It is worth reminding that in Model M3, partial saturation was induced by air injection at 1g prior to centrifuge spin-up.

At the base (16.3 m), peak r_u values were ≈0.09 (EQ3.1), 0.14 (EQ3.2), and 0.06 (EQ3.3). At 14.5 m, r_u were ≈0.16, 0.34, and 0.10 while at 7.5 m these were ≈0.46, 0.75, and 0.35, respectively.

It can be concluded that the increase in PGA from 0.10 to 0.17 g between EQ3.1 and EQ3.2 led to a higher r_u in EQ3.2 at all depths than EQ3.1 because they have the same degree of saturation. By contrast, the further PGA increase to 0.19 g in EQ3.3 did not overcome the stronger desaturation effect in hindering excess pore pressure build-up, and r_u of EQ3.3 remained lower than EQ3.2 at every depth. At 1.9 m, r_u time history for all shakes reached $r_u>1$, indicating liquefaction under low confinement pressure.

Post-shake dissipation (M3)

Across all depths, EQ3.2 retained the largest residual r_u (least dissipation). The comparison between EQ3.1 and EQ3.3 is not straightforward: 16.3 m EQ3.1 exceeded EQ3.3, at 14.5 m the reverse held, at 7.5 m the two were similar, and at 1.9 m EQ3.3 again exceeded EQ3.1. This mixed pattern indicates depth-dependent compilation of two effects: (i) higher input shake amplitude (which tends to elevate residual r_u), and (ii) desaturation (which tends to suppress r_u). Near the surface, lower confinement and less reliable gas retention can further weaken the desaturation benefit, while at depth, greater confinement favors bubble stability and faster effective-stress recovery. Small inconsistencies between depths are acceptable in centrifuge data, given its sensitivity to local layering, hydraulic gradients and post-shake pore-pressure migration, and instrumentation noise or bias in individual PPT.

To summarize, across all three models, induced partial saturation (IPS) consistently mitigated excess pore-pressure generation under dynamic loading, even when input shaking was more intense, demonstrating robustness as a promising liquefaction countermeasure. The benefit is depth-dependent; reductions in r_u are most pronounced at mid and lower depths, where higher confinement stabilizes entrapped gas and limits air bubbles escape, whereas near the ground surface mitigation is weakest because gas can easily migrate or dissipate outward as the effective stress is low. Consequently, shallow layers frequently reach or exceed liquefaction thresholds ($r_u>1$) with only marginal differences among treatments, while mid–deep zones retain substantially lower r_u under IPS. These observations prove that IPS is most effective away from the free surface and support prioritizing injection/retention strategies that improve gas delivery and persistence in the upper layers (e.g., adjusted injection depth, staged treatment, or layering). Overall, the results point to IPS as a promising depth-targeted mitigation tool, capable of reducing transmitted energy and pore-pressure build-up at engineering-relevant depths while highlighting the need for enhanced near-surface gas retention to achieve uniform performance.

6.3.4. Excess pore pressure ratio, r_u (Isochrones)

Figure 6-24, Figure 6-25, and Figure 6-26 present time-based isochrone contours of excess pore pressure Δu and excess pore pressure ratio r_u for M1, M2 and M3 respectively, plotted at different time instants, for M1 at 5, 10, and 15 s. For Models M2 and M3, at 2, 5, and 7s, because those two models have shorter shaking durations relative to M1. The selected instants capture early, mid, and late stages of each record to illustrate the depth-wise evolution of excess pore pressure build-up and subsequent trends.

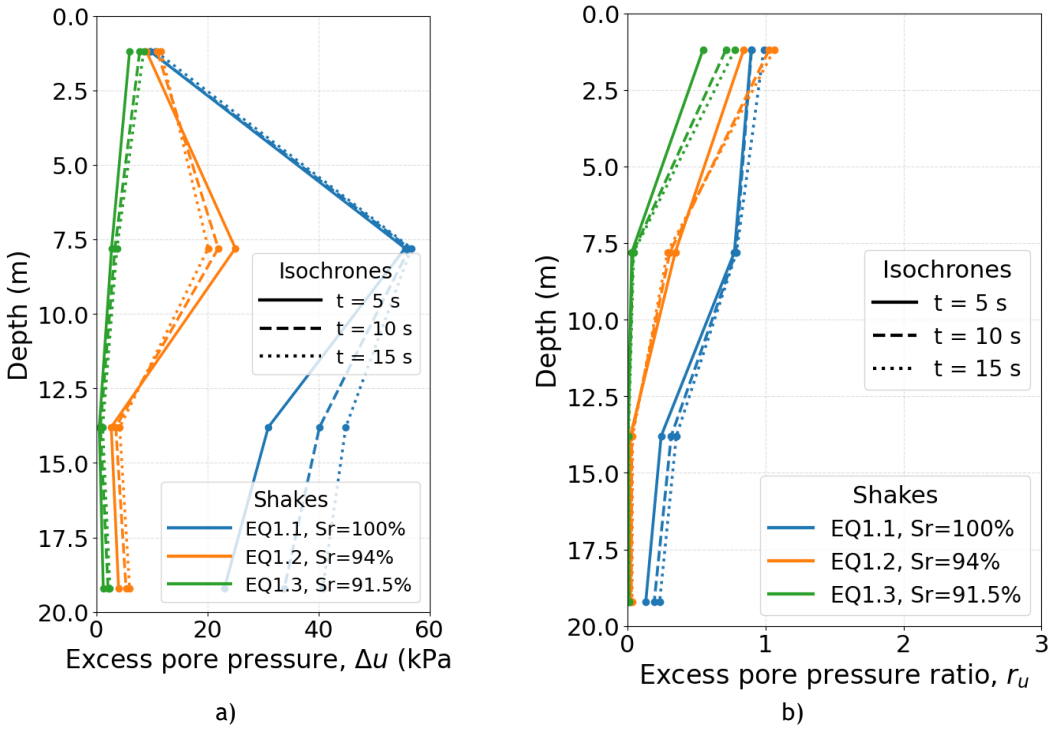

Figure 6-24 a) Excess pore pressure Du and; b) excess pore pressure ratio ru at various time instants (Isochrones) for the three shakes of M1

6.3.4.1. Model M1

At mid and deeper depths (below 7.8m), the partially saturated scenarios exhibited significantly lower pore pressure build-up than the fully saturated case across all time intervals. Furthermore, under full saturation, pore pressure increased rapidly within the first 5 seconds, showing a fast generation of excess pore pressure, and continued to rise progressively at 10 and 15 seconds. In contrast, the partially saturated shakes effectively suppressed pore pressure build-up during the early stages of shaking, and the subsequent increase with time remained minimal.

At shallower depths (above 7.8 m), the fully saturated shake consistently showed increasing r_u, whereas the partially saturated scenarios also began to exhibit gradual pore pressure development with time. Near the surface (1.2 m depth), the third shake EQ1.3 recorded the lowest r_u value at 5 and 10 seconds, followed by EQ1.2 and EQ1.1. However, by 15 seconds, the r_u values among the three cases converged, indicating that the mitigating effect of partial saturation diminished in the upper layers as shaking progressed.

These patterns confirm that partial saturation can delay and suppress excess pore pressure development especially in deeper strata, but its effectiveness diminishes with increasing time in near-surface zones.

In partially saturated scenarios, time did not play a major role in altering Δu along the deeper depths, as the values remained within a narrow range throughout shaking.

6.3.4.2. Model M2

Figure 6-25 shows that at the deepest instrumented level (15.9 m), excess pore pressure Δu during EQ2.2 (Sr≈96%) was consistently lower than in EQ2.1 (Sr≈98.8%) at 2, 5, and 7s.

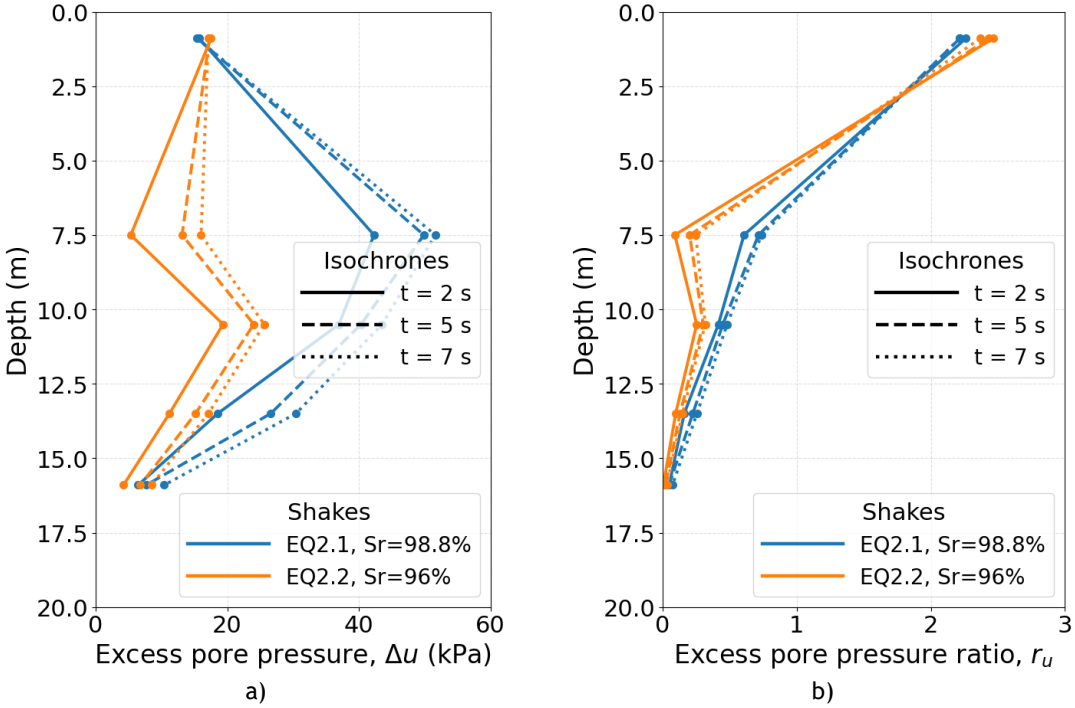

Figure 6-25 a) Excess pore pressure Δu and; b) excess pore pressure ratio r_u at various time instants (Isochrones) for the two shakes of M2

From 15.9 m up to 10.5 m, Δu increased for both motions, with a steeper rise in EQ2.1 than EQ2.2, the corresponding excess pore-pressure ratio r_u followed the same upward trend, and the difference between the motions widened toward 10.5 m.

Above 10.5 m, the contrast between records sharpened and peaked near 7.5 m. At 2s, EQ2.1 reached Δu≈42 kPa, while EQ2.2 was ≈5.4 kPa. Likewise, r_u at 7.5 m showed the largest divergence (≈0.60 in EQ2.1 versus ≈0.10 in EQ2.2 at 2 s).

This might have occurred because, at these mid-depths, confinement is still sufficient to retain occluded gas bubbles introduced by air injection, increasing pore-fluid compressibility and dampening pore-pressure build-up relative to the nearly saturated case.

Toward the shallow layer (0.9 m), the difference narrowed again as Δu in EQ2.1 falls and Δu in EQ2.2 rises, yielding similar values at 0.9 m. Near the free surface, the nearly saturated shake (EQ2.1) can dissipate excess pressures more readily via drainage, while the less saturated shake (EQ2.2) contains entrapped air that both increases fluid compressibility and can reduce hydraulic conductivity, slowing upward dissipation.

Consistent with these pore pressure trends, r_u above 7.5 m reconverged for the two motions, by 0.9 m these approached similar levels. At 2 s, EQ2.1 attained r_u=1 first at ≈5.9 m depth, while EQ2.2 reached r_u=1 only higher in the profile (≈4.9 m), indicating delayed liquefaction under partial saturation. This delay is in agreement with laboratory and centrifuge evidence that modest desaturation (gas bubbles/occluded air) substantially increases liquefaction resistance by increasing fluid compressibility and slowing pore-pressure generation.

6.3.4.3. Model M3

For M3, air was injected prior first shaking, then only between EQ3.2 and EQ3.3. The substantial increase in input motion (PGA from 0.10 g to 0.17 g) led EQ3.2 to develop high excess pore pressures (Δu) over the full depth than EQ3.1. Between EQ3.2 and EQ3.3, air was re-injected while the PGA increased only slightly (0.17 g to 0.19 g), Δu in EQ3.3 was therefore reduced at most depths as clear in Figure 6-26.

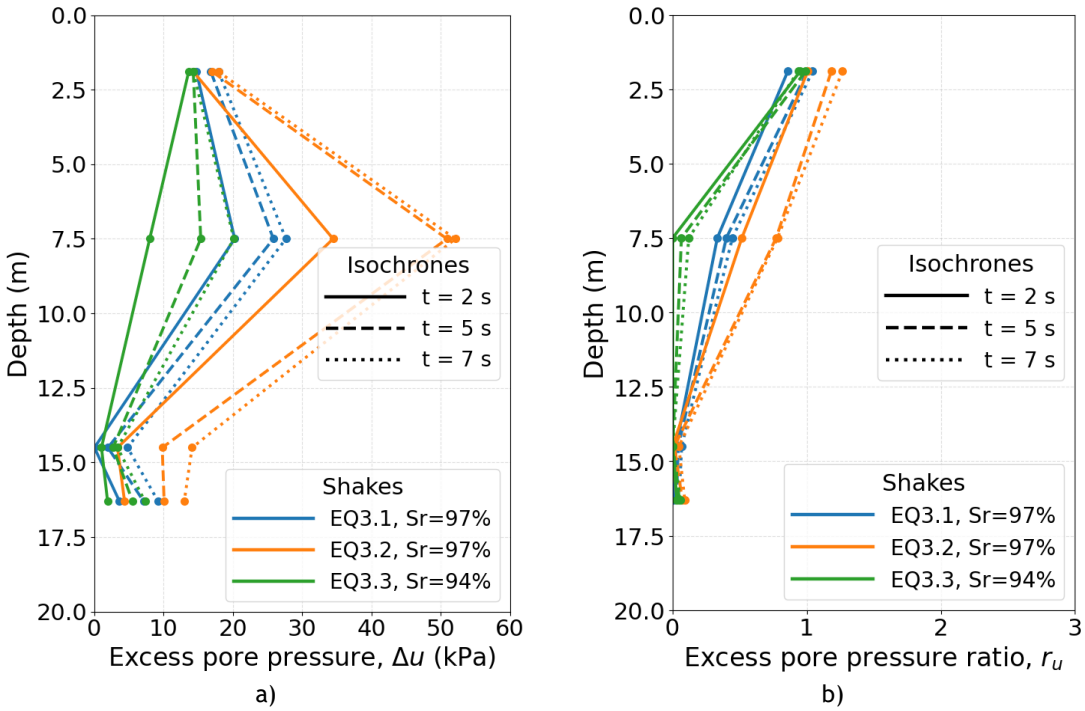

Figure 6-26 a) Excess pore pressure Δu and; b) excess pore pressure ratio r_u at various time instants (Isochrones) for the three shakes of M3

In a deep zone between 16.3 and 14.5 m, at 2 s and 5 s, Δu for EQ3.2 remained nearly constant, with a slight rise at 15 s. Both EQ3.1 and EQ3.3 exhibited reduced Δu, with EQ3.3 marginally smaller than EQ3.1 at all selected instants. The excess pore pressure ratio r_u followed the same pattern, with smaller variations because of the normalization by σ_v'.

At mid-depths from 14.5 to 7.5 m, Δu increased upward for all motions, with the largest separation at 7.5 m, i.e., at 2s, EQ3.2 ≈ 34.5 kPa, EQ3.1 ≈ 20.2 kPa, and EQ3.3 ≈ 8.14 kPa. The corresponding r_u profiles showed the same trend.

In the shallow zone (7.5 to 1.9 m), Δu in EQ3.2 decreased markedly at all time instants, in EQ3.1 it also decreased but more gradually. EQ3.3 decreased slightly at 10 s and 15 s, while at 5s, Δu continued to increase before the three motions converged near 1.9 m. The r_u profiles mirrored these trends and indicate liquefaction for the three motions, with higher r_u at 5–7 s for EQ3.2 than for the others. Liquefaction (r_u=1) first occurred after EQ3.2 at about 5 m depth at 5 s, whereas liquefaction was limited to the very shallow zone above 2 m for the other two shakes.

Across the three models, the r_u isochrones show that the principal soil improvement occurred at deep to mid layers, where mitigation is more effective than in the shallower zones. The likely reasons would be: (i) air injection from the base favors retention of occluded gas at high overburden stresses, so deep and mid layers maintain higher

compressibility of the pore fluid and reduced Δu accumulation; and (ii) near the surface, injected bubbles tend to migrate upward and accumulate at the surface, limiting sustained desaturation in the shallow layers. This is visually evidenced through the appearance of superficial bubbles, which were observed to escape towards the ground surface (Figure 6-27), captured at the end of air injection and similarly noted by the end of the other models.

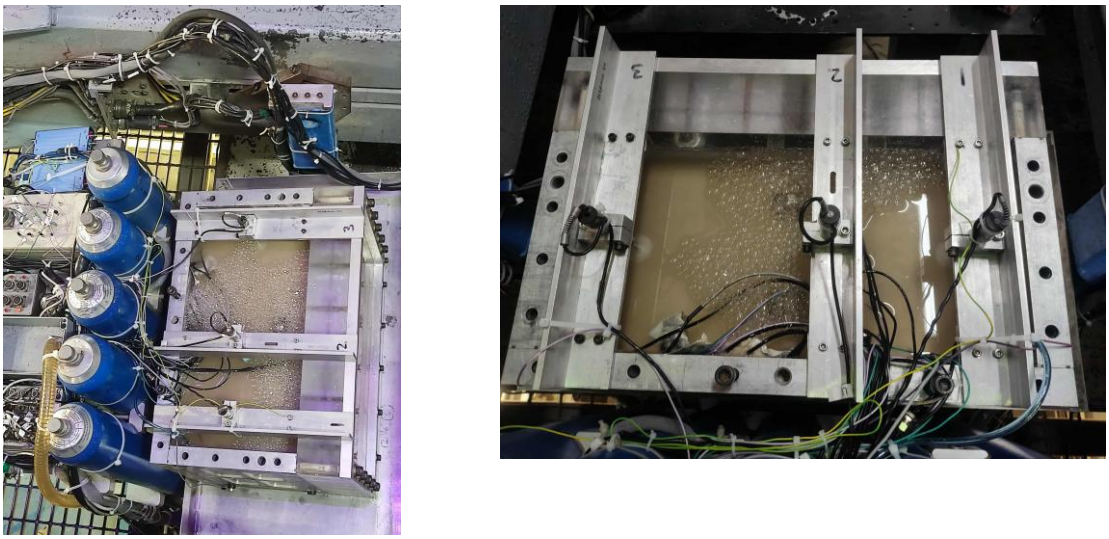

Figure 6-27 Escaped air bubbles shown at the model box surface after air injection for Model M3

6.3.5. Maximum excess pore pressure ratio r_u

Figure 6-28 presents the plots of maximum excess pore pressure ratio r_u along the soil profile. Figure 6-28a plots the peak r_u at each depth for the three shaking events of M1; Figure 6-28Figure 5-18b shows the two shakes of M2; while Figure 6-28c illustrates the three shakes of M3. These profiles confirmed that the mitigation achieved by induced partial saturation is most effective at mid and higher depths, and less effective near the surface, probably because the shallow layers were farther from the air injector located at the base of the box. In M1, the largest reduction in r_u occurs when transitioning from the fully saturated state to the first partially saturated state; further decreases in degree of saturation yield comparatively modest additional suppression of pore pressure generation. In M2 and M3, the gain appeared smaller than in M1 because both models start from a partially saturated state and subsequent stages combined incremental desaturation with elevated PGA, which partially offsets the benefit; nevertheless, reductions remain clearest at mid depths.

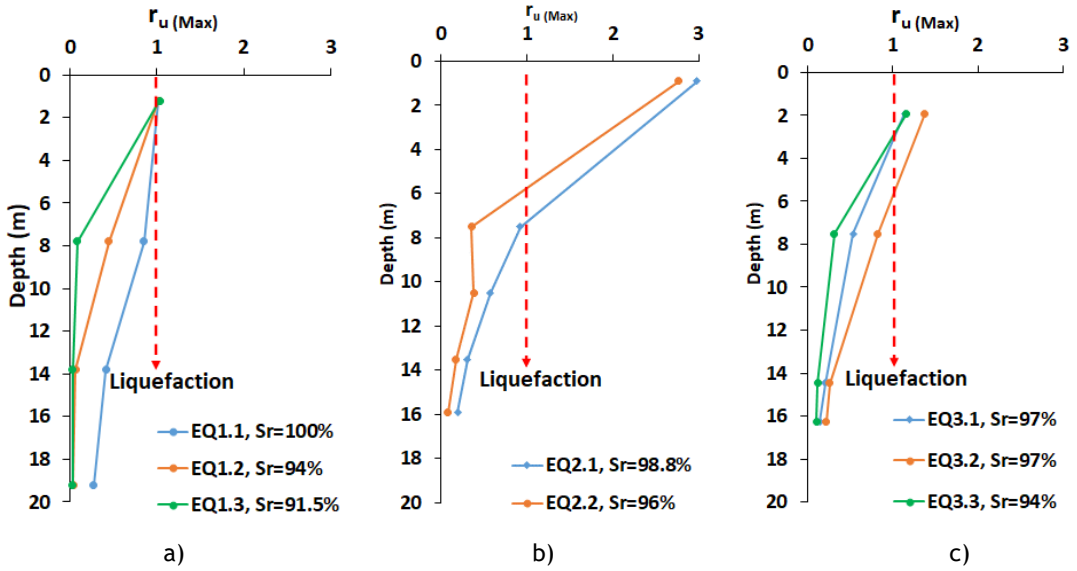

Figure 6-28 Maximum excess pore pressure ratio $r_{u,max}$ with depths for the three models; a) M1, b) M2, and c) M3

6.3.6. Soil surface settlement

Figure 6-29, Figure 6-30 and, Figure 6-31 display the time histories of the soil surface settlement measured by the LVDT placed on the soil surface during and after the three shaking events for the three Models M1, M2 and M3 respectively. Positive values represent downward settlement and vice-versa. As shown in Figure 6-29, to separate the soil settlement due to the air injection process for M1, dashed lines denote the settlement occurred during air Injection 1 (prior to EQ1.2) and air Injection 2 (prior to EQ1.3). Thus, settlement curves for EQ1.2 and EQ1.3 are offset, since EQ1.2 begins from the terminal point of the air Injection 1 settlement, and EQ1.3 accumulates on top of both prior air injection settlements. For Model M2 and M3, the same convention applies: dashed line denote settlement during each air-injection phase. However, in M3 settlement during air injection was minimal and was therefore considered negligible.

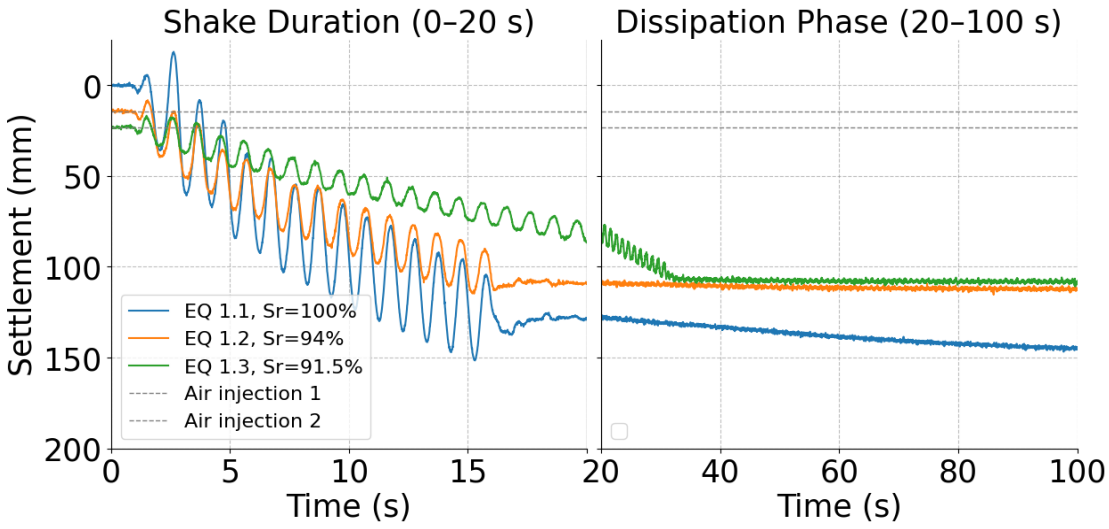

Figure 6-29 Time history soil surface settlement during shakes and air injections, followed by dissipation-M1

In M1, because the amplitude (PGA) was identical in all three shakes and the relative density remained not markedly different, observed differences in cumulative settlement are largely attributable to variations in the degree of saturation (Sr%). At roughly 15 loading cycles (a point at the end of EQ1.1 and EQ1.2, and mid-duration in EQ1.3), measured settlements were approximately 120 mm for EQ1.1, 99 mm for EQ1.2, and 66 mm for EQ1.3, these values correspond to settlement reductions of about 17.5 % in EQ1.2 and 45 % in EQ1.3, relative to EQ1.1. An important distinction emerges in residual settlement behavior following shaking: after EQ1.1 (fully saturated condition), a noticeable residual settlement is observed, indicating post-shake dissipation or consolidation. However, in the two partially-saturated scenarios (EQ1.2 and EQ1.3), no significant residual settlement was detected, implying that the partial desaturation inhibited subsequent deformation under the same loading and drainage conditions.

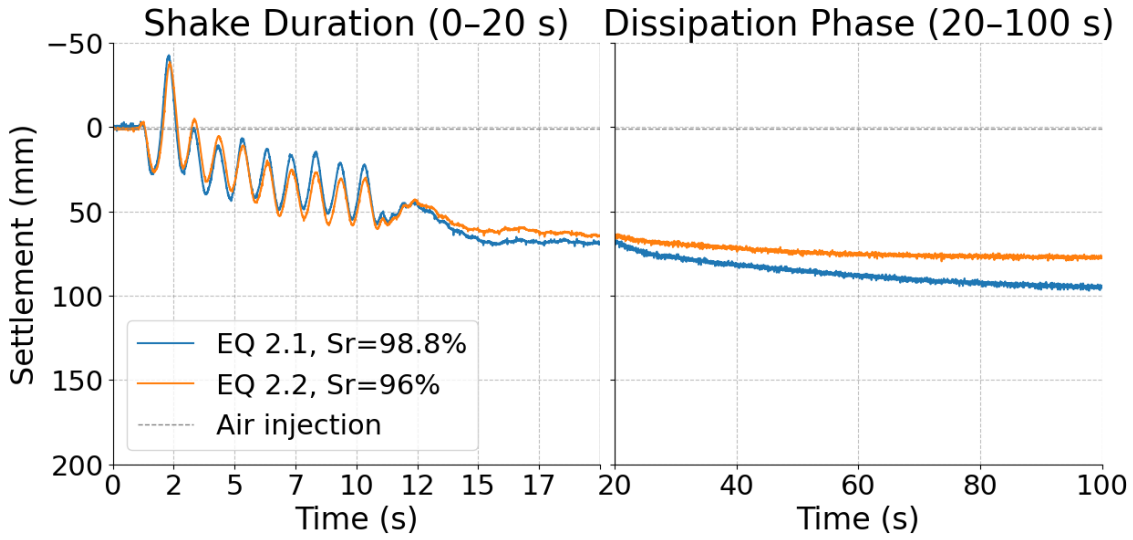

Figure 6-30 Time history of soil surface settlement during shakes and air injections, followed by dissipation-M2

Regarding Model M2, the settlement histories during and immediately after the two shakes were broadly similar, which is plausible given the elevated PGA of EQ2.2. However, during dissipation, EQ2.2 developed less additional settlement than EQ2.1. By t=80 s, the surface settlement for EQ2.2 was reduced by approximately 17% relative to EQ2.1.

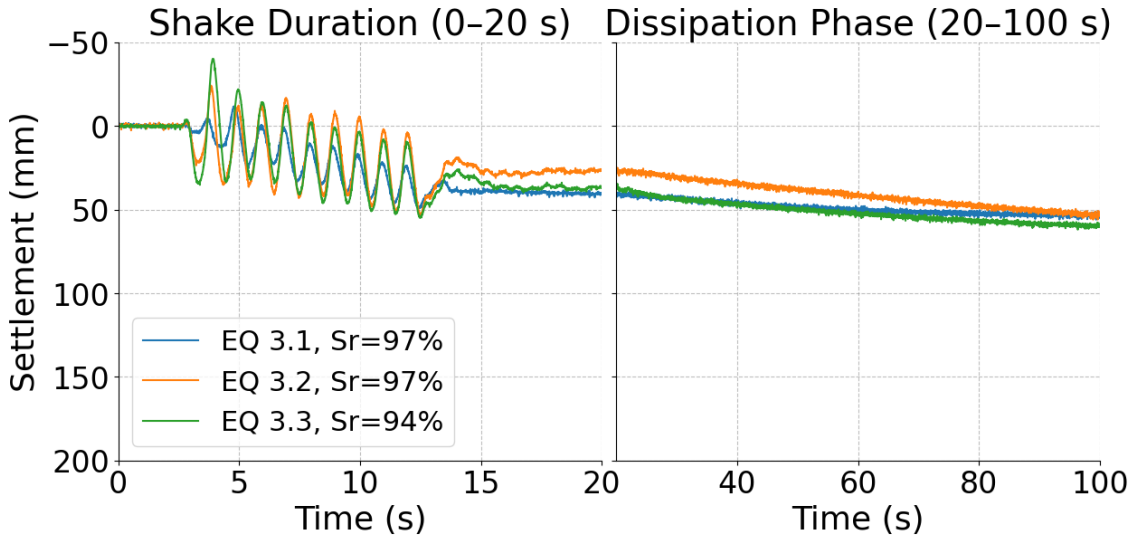

Figure 6-31 Time history soil surface settlement during shakes and air injections, followed by dissipation-M3

For Model M3, EQ3.1 and EQ3.2 have the same S_r% but different PGA (0.10 and 0.17 g), while EQ3.3 combines a lower Sr with a higher PGA (0.19 g). The three records exhibited very similar settlement time histories during shaking and reach nearly the same end-of-shake settlement (at t=10 s). Shortly into dissipation, EQ3.2 showed a slightly lower settlement than the other two, but the curves reconverged by about t=100 s.

These observations confirm that IPS can limit soil surface settlement under comparable or moderately increased input motions, whereas substantial PGA increases can reduce this gained enhancement. In other words, while decreasing the degree of saturation enhances liquefaction resistance by increasing pore-fluid compressibility, its capacity to limit deformation becomes less powerful under stronger seismic loading conditions.

On the other hand, Figure 6-32 illustrates the water level variation history recorded by the floating LVDT during the first air injection process of M1, which rested on the groundwater table (GWT) inside the model box, effectively tracking changes in the water level during testing. Over the shaking periods, the water level remained essentially constant, indicating negligible net exchange; however, during air injection phases, the water surface experienced an upward rise (i.e., negative "settlement"), attributable to the introduction and entrapment of air bubbles as occluded void. These entrapped air bubbles displaced water and raised the water level. From the magnitude of these water-level variations (after dissipation), the degree of saturation was re-calculated after each injection step for all models. As clearly shown in the same plot, the settlement of the soil during air injection was very small and added to the accumulated settlement for the accurate estimation of soil relative density, for all air injections in these models.

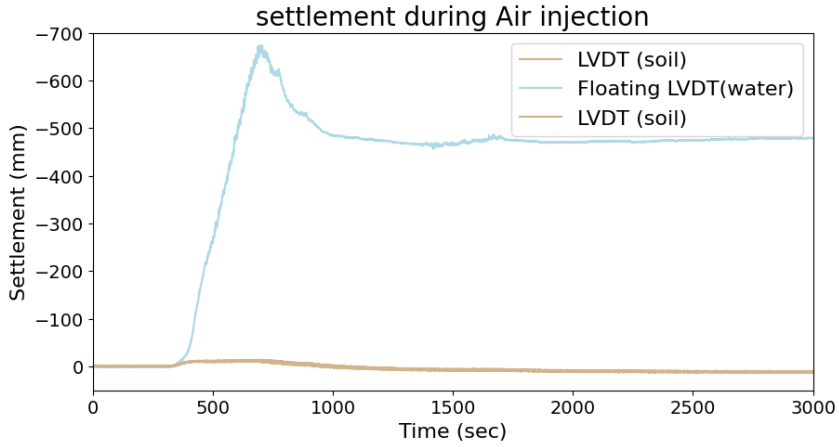

Figure 6-32 Time history of the water level and soil surface variations during the air injection process performed before applying EQ1.2 of M1

6.3.7. Air injection

Air injection was performed by introducing compressed air through a rubber air curtain hose placed diagonally at the center-bottom of the model container to reduce the degree of saturation. The diffuser, featuring 0.5 mm openings spaced at 5 mm intervals, was identified as optimal for this purpose, as previously used by Zeybek & Hall (2017). Preliminary tests in a Perspex box were conducted to determine the appropriate injection pressure and to prevent bubble coalescence and non-uniformity. The air pressure was regulated using a pressure controller. The air injection pressure was gradually increased until it exceeded the minimum injection pressure (P_{inj})min, equation (6-2), at which air bubbles began to flow

smoothly through the soil. At the same time, the pressure was kept below the maximum limit $(P_{inj})max$, shown in equation (6-3), (Okamura & Soga, 2006b).

$$(p_{inj})min = p_{hyd} + AEV \tag{6-2}$$

$$(p_{inj})max = p_{hyd} + 0.5\sigma'_c \tag{6-3}$$

Figure 6-33 shows the time history of air pressure injection performed before applying the second shake EQ1.2 of M1, indicating the maximum and minimum air injection pressures.

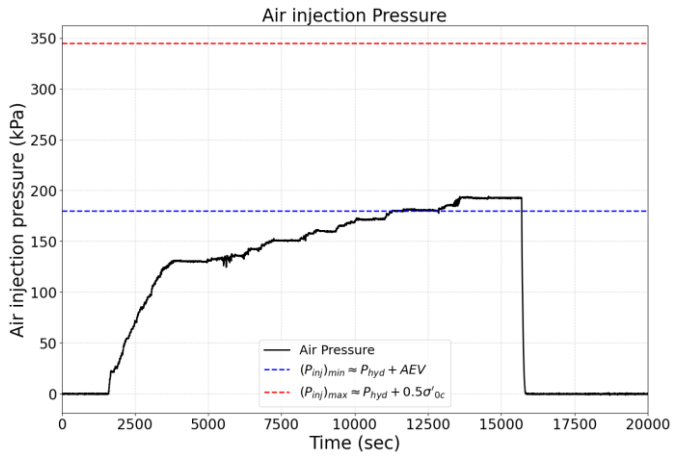

Figure 6-33 Air injection pressure time history applied before starting EQ1.2 of M1

6.4. Discussion on shear stresses and strains

Because the applied input motions of (EQ1.1, EQ1.2 and, EQ1.3) of Model M1 were identical and only the degree of saturation Sr varied, along with a slight change in relative density, it is appropriate to analyze the stress–strain response to investigate the effect of partial saturation on the soil dynamic response.

To extract these stress-strain histories from the accelerometer data, the soil profile was idealized as a one-dimensional shear beam. The vertically propagating shear waves within this framework are governed by the following equation of motion equation (6-4):

$$\partial\tau(z,t)/\partial z = \rho\, a(z,t) \tag{6-4}$$

Where, $\tau\,(z,\,t)$ is the shear stress on a horizontal plane at depth z, ρ is the bulk mass density of the soil, and $a\,(z,\,t)$ is absolute the horizontal acceleration.

By integrating equation (6-4) downward from the stress-free surface (z=0) downward, yields the continuous form of the shear stress profile equation (6-5).

$$\tau(z,t) = \int_0^z \rho\, a\,(z\,,t)\,dz \tag{6-5}$$

where z is the variable integration depth. In this analysis, the acceleration profile $a(z,t)$ was defined on a depth grid $z = z_i$ that included both sensor depths and midpoints between sensors (after interpolation). The integral was evaluated numerically using the trapezoidal rule between successive depths z_{i-1} and z_i, giving the form (6-6).

$$\tau_i(t) = \tau_{i-1}(t) + \rho \frac{a_{i-1}(t) + a_i(t)}{2} \triangle z_{i-1} \quad (6\text{-}6)$$

Where;

$\triangle z_{i-1} = z_i - z_{i-1}$

$\tau_0(t) = 0$

Shear stress time histories τ (t) were computed at each depth using equation (6-6).

To evaluate the corresponding deformation, velocity time histories were obtained by integrating the filtered acceleration data, followed by a second integration to compute displacement. To minimize baseline drift, zero-phase (forward–backward) bandpass filtering was applied to the displacement record.

Shear strain time histories were subsequently computed from the spatial gradient of the horizontal displacement. This was implemented numerically on the same depth grid (incorporating sensor depths and interpolated midpoints) using finite differences. The continuous 1D formulation for shear strain is presented in equation (6-7) where, u(z,t) represents the horizontal displacement at a given depth and time.

Using a centered finite-difference approximation at the interior grid points, the shear strain at depth z_i was estimated using equation (6-8).:

$$\gamma(z,t) = {\partial u(z,t)}/{\partial z} \quad (6\text{-}7)$$

$$\gamma_i(t) = \frac{u_{i+1}(t) - u_{i-1}(t)}{z_{i+1} - z_{i-1}} \quad (6\text{-}8)$$

These procedures follow standard 1D site-response mechanics (equation (6-4) and conventional numerical integration/zero-phase filtering practice for strong-motion processing and are consistent with the non-parametric system-identification approach for stress–strain reconstruction from vertical arrays, as reported by Zeghal and Elgamal (1994). Since τ and γ were both evaluated at the same depth, stress–strain pairs were available at sensor depths and midpoints between sensors, enabling construction of τ-γ hysteresis loops. It is important to acknowledge that the calculated shear stresses and observed dynamic responses in the deepest soil layers (deepest sensor) may be influenced by the basal boundary effects.

Figure 6-34a presents the shear stress time histories at multiple depths for the three shakes of M1 (EQ1.1, EQ1.2, EQ1.3), while Figure 6-34 b shows the corresponding shear strain time histories at various depths, and Figure 6-34c presents the respective stress strain hysteresis loops only during the shaking period between 7 and 15 seconds. In these plots, the blue, orange, and green curves correspond to shaking events EQ1.1, EQ1.2, and EQ1.3, respectively. The loops were used to compare cyclic response across the different Sr conditions for the three shakes, including stiffness degradation and energy dissipation inferred from loop shape and enclosed loop area.

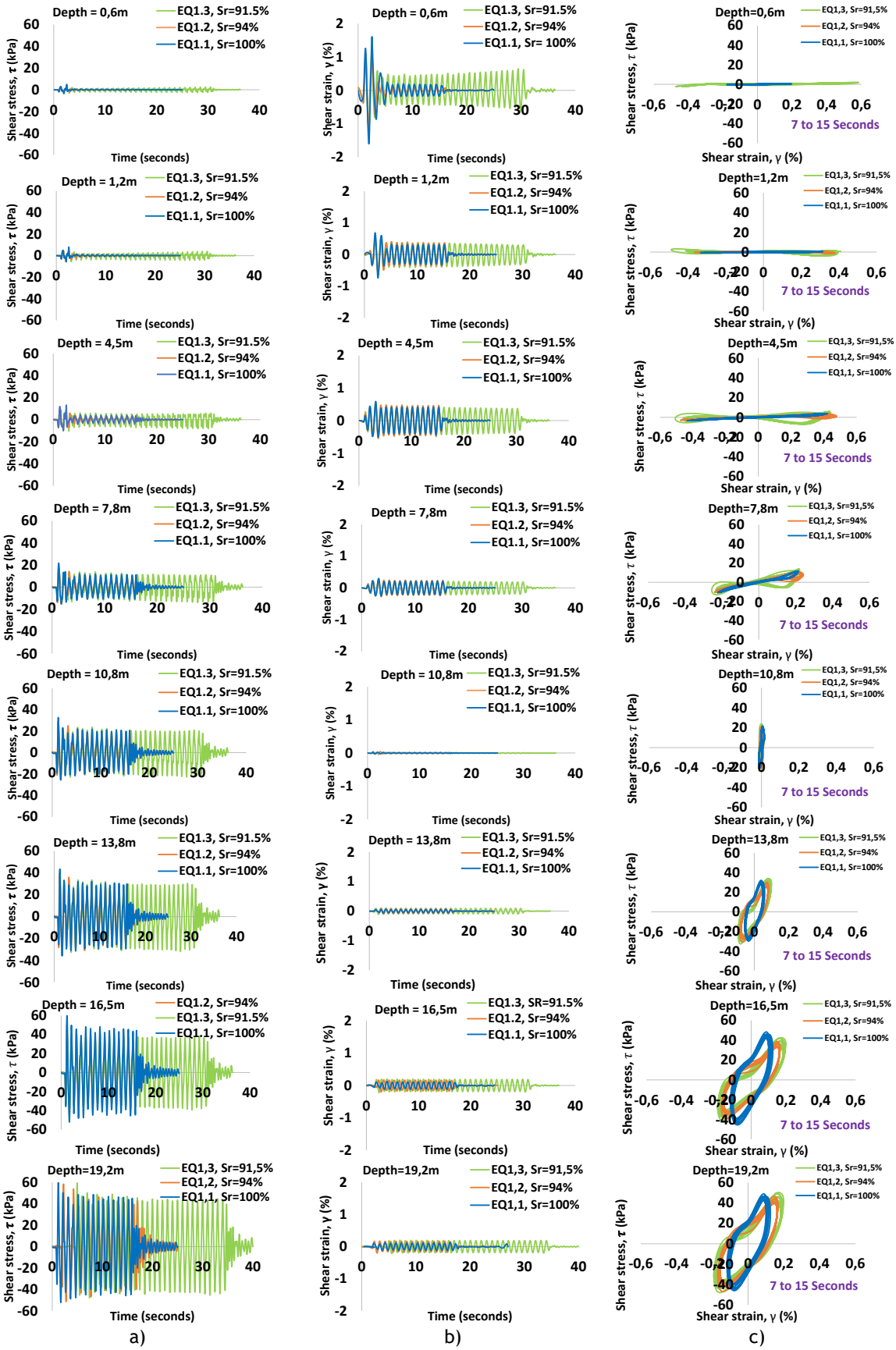

Figure 6-34 a) Shear stress time histories at various depths for the three shakes of M1 along the full shake durations; b) Shear strain time histories; and c) Stress-strain hysteresis loops from 7 to 15 seconds of the shake durations

In sum, Figure 6-34a and Figure 6-34b illustrates the depth-dependent distribution of the dynamic response. For all shaking events, the estimated cyclic shear stresses progressively attenuated as the input seismic motion propagated upward through the soil profile. Conversely, the corresponding cyclic shear strains exhibited a nonlinear profile in depth: strain amplitudes were moderate at the deepest layers, sharply diminished to a minimum at intermediate depths, and subsequently amplified toward the shallower layers.

Furthermore, Figure 6-34c depicts the corresponding stress strain hysteresis loops evaluated across the profile during the shakes, excluding the early cyclic loops. At deeper layers, the loops enclosed large areas, showing substantial dissipated energy (ΔW). As the depth decreased toward the mid-profile, the loops narrowed while the secant shear stiffness (G_{sec}) visibly increased (loops turned steeper). However, as the seismic waves approached the shallow subsurface, the hysteretic response transitioned significantly. The loops became highly elongated (due to high strains) and flattened, reflecting severe stiffness degradation, while the enclosed areas contracted, denoting a reduction in the hysteretic energy dissipation capacity as the confining stress decreased and the soil softened.

The deep soil layers (from 19.2 to 13.8m) efficiently absorbed the initial shock of the applied shake. Because they deformed heavily and dissipated a massive amount of energy (large loops / high ΔW), they acted like a natural shock absorber. The substantial energy dissipation observed in the deeper layers effectively attenuated the upward propagating seismic energy.

The mid-depth profile (10.8 m) experienced significantly high stiffness and drastically small cyclic loop areas. It is very important to note that this localized stiffness spike and the corresponding extremely low cyclic loops area at the 10.8 m “midpoint” demonstrate a numerical limitation of the 1D inverse analysis procedure. As noted by Hashash et al. (2010). the piece-wise linear interpolation used in the Zeghal and Elgamal (1994) method mathematically averages the soil behavior between sensor depths. Furthermore, Kamai & Boulanger (2010) demonstrated that, when severe localized stiffness degradation occurs as the soil approaches liquefaction (such as the massive softening observed at the 7.8 m depth), these inverse analyses fail to capture the sharp spatial variations, representing them only 'on average' and resulting in mathematical artifacts across the interpolation gap. In other words, the interpolation here combines the behavior of the soil at two different soil conditions, which led to this non-representative soil dynamic parameters.

As the attenuated wave reached the shallowest layers (7.8 m to 0.6 m), the drastic reduction in effective overburden pressure governed the response; this lack of confinement allowed even the weakened seismic waves to approach liquefaction. This analysis highlights the critical role of depth dependent confining stress on the soil dynamic resistance.

Note: Figure 6-34c exclusively shows the stress-strain hysteresis loops isolated within the 7 to 15 second time window. However, for the shallow strata (from the depth of 7.8m up to the shallower layers), the initial loading cycles preceding this window were of critical importance. Within these low-confinement layers, especially at 1.2 and 0.6m, the onset of mechanical instability occurred almost immediately. Consequently, the earliest cycles exhibit pronounced stress and strain spikes, forming distinctly broader hysteresis loops than those generated during the remainder of the shaking event. A comprehensive analysis of this early-cycle instability and the resulting massive strain accumulation is detailed in the subsequent section.

6.5. IPS influence on shear stiffness G_{sec} and dissipated energy ΔW

6.5.1. Concept

This analysis aims to evaluate the influence of IPS on shear stresses, strains, and, consequently, the secant stiffness and dissipated energy.

For the deeper layers extending up to the depth of 10.8 m (Model M1), the evaluation of secant shear stiffness G_{sec} and dissipated strain energy ΔW was limited to the stable dynamic response observed between t = 7.0 s and t = 15.0 s. This time period was selected because the soil within these deeper strata exhibited consistent cyclic shear stress and strain amplitudes throughout the shake time history. Conversely, for the shallower depths (above 7.8 m), the analytical focus shifts to the initial loading cycles (first 7 cycles). In these low-confinement near-surface layers, the earliest cycles generated substantially broader hysteresis loops that rapidly turned into highly narrower, flattened shapes. This reduction in loop area, coupled with severe cyclic stiffness degradation, serves as a clear indicator of mechanical instability and approaching liquefaction.

To accurately evaluate the dynamic soil properties, a rigorous cycle-by-cycle approach was revised. Simply extracting the absolute maximum stress and strain from the overall time history often yields erroneous stiffness values, as the largest positive and negative peaks frequently occur during completely different stages of the earthquake. Instead, individual hysteresis loops were systematically isolated using a zero-crossing methodology. Each full loading cycle was delimited by identifying sign changes within the shear strain time history $\gamma(t)$, with one complete loop spanning an interval of three consecutive zero-crossings. For every discrete cycle identified, the secant shear modulus G_{sec} was calculated based on its peak-to-peak amplitudes. Specifically, it was defined as the ratio of the peak-to-peak cyclic shear stress to the peak-to-peak cyclic shear strain $\Delta\tau$ /$\Delta\gamma$ within each isolated loop.

To calculate the dissipated strain energy per unit volume ΔW, a discrete numerical integration approach was utilized. Because the soil undergoes permanent deformation during seismic loading, the resulting stress-strain hysteresis loops frequently do not close perfectly. To account for this, the total dissipated energy for each cycle was calculated as the net cumulative plastic work along the unclosed strain path. This energy was computed via the trapezoidal rule by numerically integrating the product of the average shear stress and the incremental shear strain over the full duration of the isolated cycle, as expressed in equation (6-9).

$$\Delta W = A_{loop} = \int \tau \, d\gamma = \sum_i \frac{\tau_i + \tau_{i+1}}{2} (\gamma_{i+1} - \gamma_i) \tag{6-9}$$

Dissipated energy can be divided into two components. The first is associated with particle rearrangement and bond distortion, which lead to plastic strains. The second is stored or transformed as heat, kinetic energy, or surface energy of the particles, thereby increasing particle mobility. The accumulation of this energy over successive cycles is one of the main causes of dynamic instability in soils (Okur & Umu, 2013).

To accurately assess the influence of the degree of saturation Sr on the dissipated energy ΔW and secant shear stiffness G_{sec} across the three shaking events in Model M1, representative loading cycles were carefully extracted for analysis. For the deeper soil layers (19.2 m to 10.8 m), Cycle 10 was selected to evaluate both ΔW and G_{sec}, as it

effectively captured the stable, strong-motion phase of the shaking. In contrast, evaluating the shallower layers (7.8 m to 0.6 m) required a different approach due to the onset of softening. To evaluate the maximum energy dissipation, Cycle 2 was selected to calculate ΔW, as it produced the largest hysteresis loop and represented the critical early-stage response immediately preceding soil instability. However, extracting a reliable G_{sec} from Cycle 2 at these shallow depths proved mathematically challenging, due to the high irregularity of the stress-strain response. To maintain analytical consistency and reliability, G_{sec} for the shallow layers was instead calculated from Cycle 10, aligning with the methodology used for the deeper layers. This adjustment did not adversely affect the overall behavioral analysis; the shallow layers (particularly between 4.5 m and 0.6 m) had already experienced massive degradation by this stage, and the calculated secant shear modulus reflected this reduced stiffness.

6.5.2. Comparative analysis per depth

The subsequent analysis presents a comprehensive, depth-by-depth comparative analysis of the secant shear stiffness G_{sec} and dissipated energy ΔW across the three shaking events (EQ1.1, EQ1.2, and EQ1.3). To systematically evaluate the dynamic response at each specific depth, a standardized sequence of visualizations is established. First, the cyclic shear stress and corresponding shear strain time histories for all three earthquakes are plotted adjacently to facilitate a direct, side-by-side comparison of the whole time-domain records. These are subsequently accompanied by two distinct representations of the stress-strain behavior: the complete, unfiltered hysteresis loops encompassing the entire shaking duration, and the isolated filtered hysteresis loops, strictly representing the stable strong-motion phase (t = 7.0 s to t = 15.0 s). Furthermore, for the shallower depths (7.8 m to 0.6 m), the standard time history plots are supplemented by three additional figures. Each of these plots isolates the first seven hysteresis loops for a given shaking event, providing a clearer, zoomed-in view of the rapid strain accumulation that occurs right before the soil initiates instability phase.

For the depth of 19.2m, Figure 6-35a, b and c present the cyclic shear stress time histories for shaking events EQ1.1, EQ1.2, and EQ1.3, respectively. Similarly, Figure 6-36a, b and c display the corresponding shear strain time histories for the three shaking events.

In addition, Figure 6-37 a) and b) illustrate the superimposed stress-strain hysteresis loops for all three shakes, providing a direct comparison of both the complete, unfiltered shaking duration and the isolated strong-motion phase (t = 7.0 s to t = 15.0s), respectively.

Following this established sequence, the identical suite of plots, comprising cyclic shear stress, shear strain, and superimposed hysteresis loops is systematically presented for the other depths. These corresponding dynamic responses are detailed for prototype depths of 16.5 m, from Figure 6-38 to Figure 6-62.

The computed secant shear stiffness G_{sec} and dissipated strain energy DW extracted from Cycle 10 across the three shaking events are summarized individually for the deeper soil levels: 19.2m (Table 6-4), 16.5m (Table 6-5), 13.8m (Table 6-6), and 10.8m (Table 6-7).

For the shallower profile, the corresponding G_{sec} and ΔW values extracted from Cycle #10 and #2 respectively, are detailed at depths of 7.8 m (Table 6-8), 4.5m (Table 6-9), 1.2m (Table 6-10), and 0.6m (Table 6-11). Nevertheless, evaluating the secant shear stiffness G_{sec} at the shallower depths (from 4.5 m upward) during Cycle 10 involves a high degree of

analytical uncertainty, due to the highly irregular and distorted shapes of the stress-strain hysteresis loops. However, this mathematical uncertainty does not compromise the validity of the overall analysis. By Cycle 10, the shallow strata had already experienced massive structural degradation, and the physical stiffness had dropped to an extremely low, negligible magnitude. Therefore, extracting a precise numerical value for G_{sec} at this stage is secondary to the overarching physical observation: the layer had effectively lost its shear resistance and reached a state of near-zero stiffness.

Prototype depth:19.2m

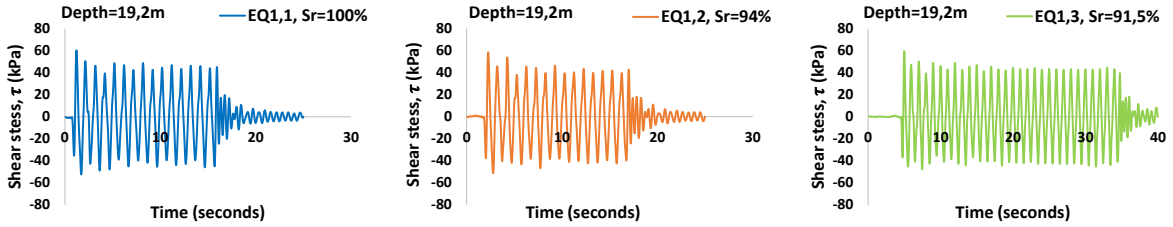

Figure 6-35 Shear stress time history at depth 19.2m: a) EQ1.1; b) EQ1.2 and; c) EQ1.3

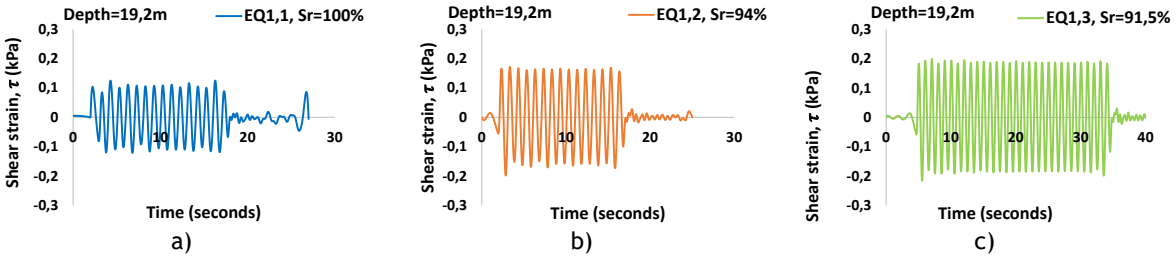

Figure 6-36 Shear strain time history at depth 19.2m: a) EQ1.1; b) EQ1.2 and; c) EQ1.3

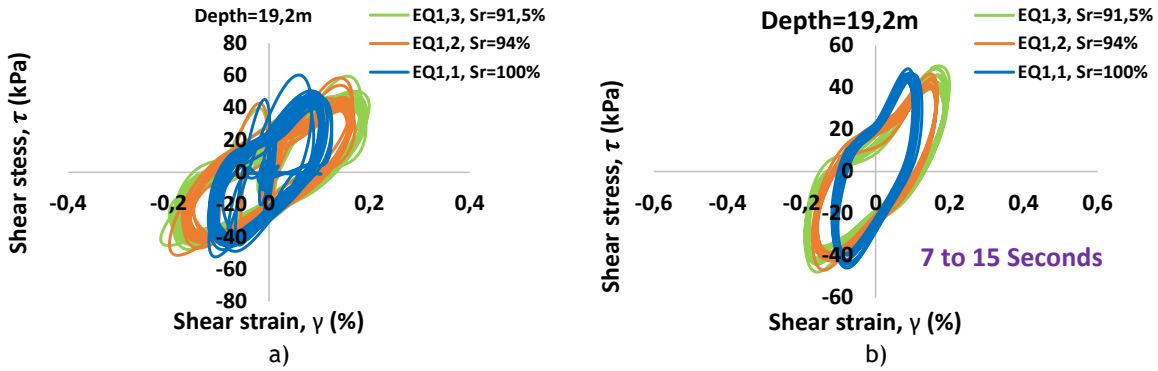

Figure 6-37 Stress-strain hysteresis loops for all three shakes at 19.2m: a) full data; b) representative loops from 7 to 15s

At the prototype depth of 19.2 m, the cyclic shear stresses exhibited negligible differences across the three shaking events. However, EQ1.1 showed slightly higher cyclic shear stresses than EQ1.2 and EQ1.3. Conversely, the corresponding shear strains demonstrated differences. The fully saturated baseline EQ1.1 recorded the lowest shear strain amplitudes. The strain magnitudes progressively increased in the subsequent shakes, with EQ1.2 exhibiting intermediate strains and EQ1.3 recording the highest peak shear strains among

the three events. These kinematic differences directly manifest in the geometric properties of the resulting stress-strain hysteresis loops. Because the induced shear stresses remained relatively uniform across the events while the shear strains amplified, the secant shear stiffness G_{sec} exhibited a clear, inverse trend. Specifically, the fully saturated soil in EQ1.1 maintained the highest relative stiffness. In contrast, EQ1.3 experienced the most significant stiffness degradation, resulting in broader, more elongated hysteresis loops that enclosed a larger area and indicated higher dissipated energy ΔW compared to both EQ1.2 and EQ1.1.

Table 6-4 Secant shear stiffness (G_{sec}) and dissipated energy (ΔW) calculated for Cyclic loop #10 across the three shaking events at a prototype depth of 19.2 m

Shake#	Sr (%)	Depth (m)	Dissipated energy, ΔW (KJ/m^3) Area of hysteresis loop	Secant stiffness G_{sec}(kPa)
EQ1.1	100 ↑	19.5	0.097 ↓	39640 ↑
EQ1.2	94	19.5	0.145	24600
EQ1.3	91.5	19.5	0.16	22400

Table 6-4 reveals that a 6% reduction in the degree of saturation between EQ1.1 and 1.2 increased the dissipated energy from 9.7 kJ/m^3 to 14.5 kJ/m^3. Further reducing the saturation to S_r = 91.5%, EQ1.3 yielded an additional increase, with the dissipated energy reaching 16.0 kJ/m^3. Conversely, the secant stiffness during this cycle exhibited an inverse trend, dropping from 396.4 kPa in EQ1.1 to 246.0 kPa and 224.0 kPa for EQ1.2 and EQ1.3, respectively.

Prototype depth: 16.5m

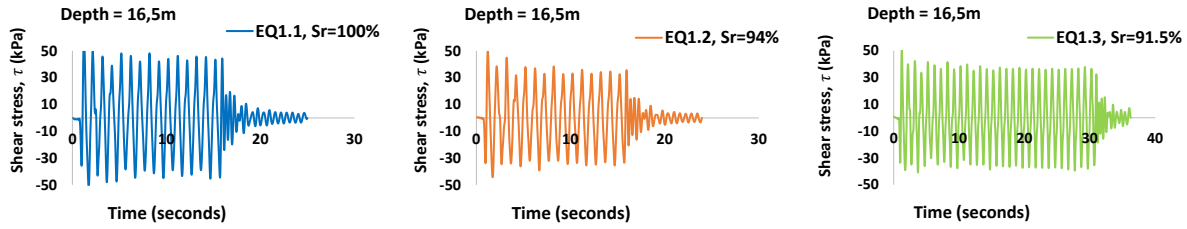

a) b) c)

Figure 6-38 Shear stress time history at depth 16.5m: a) EQ1.1; b) EQ1.2 and; c) EQ1.3

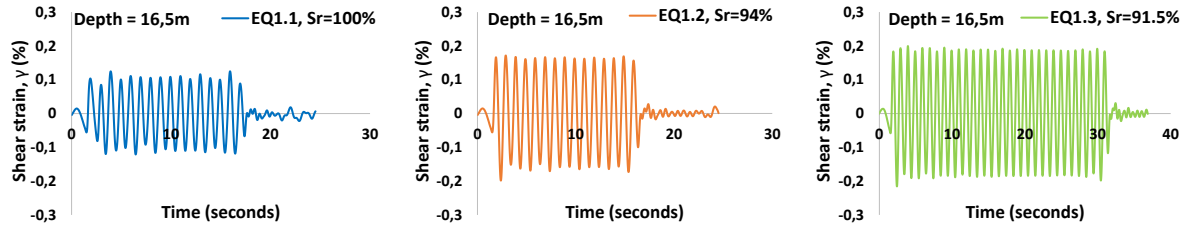

a) b) c)

Figure 6-39 Shear strain time history at depth 16.5m: a) EQ1.1; b) EQ1.2 and; c) EQ1.3

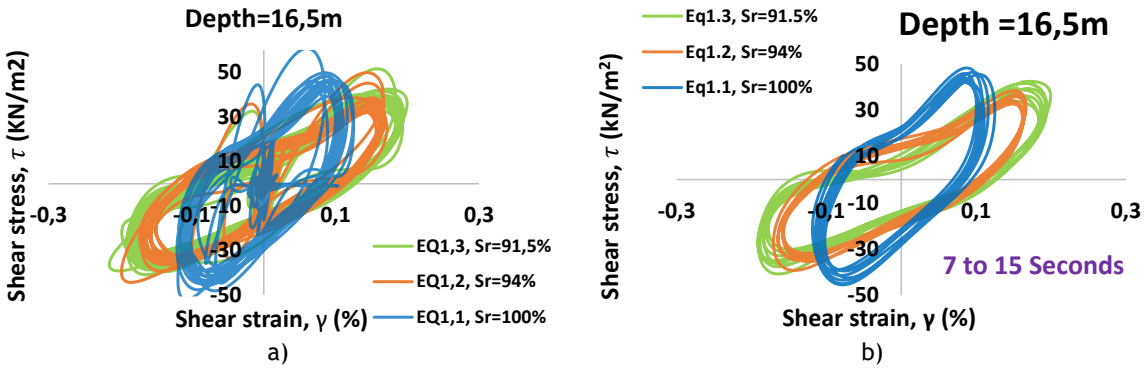

Figure 6-40 Stress-strain hysteresis loops for all three shakes at16.5m: a) full data; b) representative loops from 7 to 15s

Table 6-5 Secant shear stiffness (G_{sec}) and dissipated energy (ΔW) calculated for Cyclic loop #10 across the three shaking events at a prototype depth of 16.5 m

Shake#	Sr(%)	Depth (m)	Dissipated energy, ΔW (KJ/m^3) Area of hysteresis loop	Secant stiffness G_{sec}(kPa)
EQ1.1	100 ↑	16.5	0.095 ↓	39240 ↑
EQ1.2	94	16.5	0.118	20510
EQ1.3	91.5	16.5	0.127	19080

At the depth of 16.5 m, the comparative analysis of the G_{sec} and dissipated strain energy ΔW across the three shaking events revealed a dynamic response, highly consistent with the behavior observed at the 19.2 m depth.

Prototype depth: 13.8m

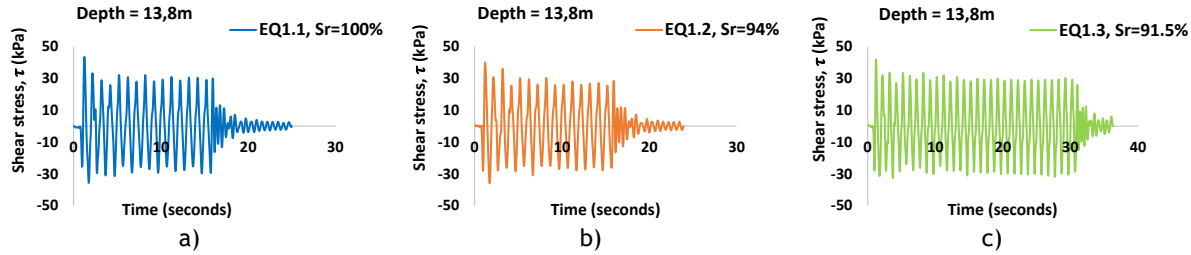

Figure 6-41 Shear stress time history at depth 13.8m: a) EQ1.1; b) EQ1.2 and; c) EQ1.3

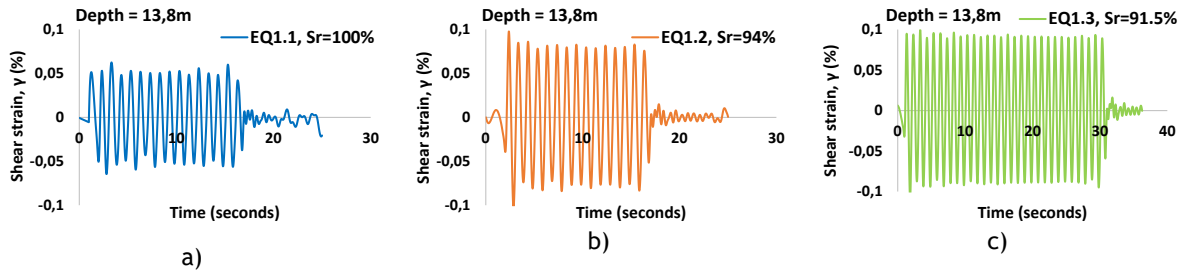

Figure 6-42 Shear strain time history at depth 13.8m: a) EQ1.1; b) EQ1.2 and; c) EQ1.3

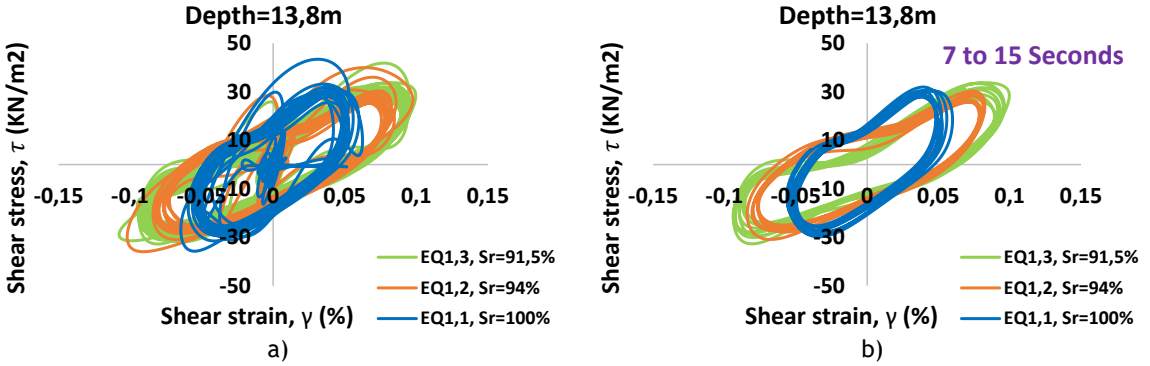

Figure 6-43 Stress-strain hysteresis loops for all three shakes at13.8m: a) full data; b) representative loops from 7 to 15s

Table 6-6 Secant shear stiffness (G_{sec}) and dissipated energy (ΔW) calculated for Cyclic loop #10 across the three shaking events at a prototype depth of 13.8 m

Shake#	Sr(%)	Depth (m)	Dissipated energy, ΔW (KJ/m^3) Area of hysteresis loop	Secant stiffness G_{sec}(kPa)
EQ1.1	100 ↑	13.8	0.032 ↓	54280 ↑
EQ1.2	94	13.8	0.046	32950
EQ1.3	91.5	13.8	0.05	31310

Upward to the profile depth of 13.8 m, the comparative dynamic response across the three shaking events continued to follow the previously established trends. However, a distinct shift in the magnitude of these parameters was observed. Across all three events (EQ1.1, EQ1.2, and EQ1.3), the enclosed areas of the stress-strain hysteresis loops decreased, which is a sign of a reduction in the dissipated strain energy ΔW relative to the deeper 16.5 m and 19.2 m depths. Concurrently, the soil at this 13.8 m depth exhibited an overall stiffening effect, with the computed secant shear stiffness G_{sec} noticeably increasing compared to the underlying strata.

Prototype depth: 10.8m

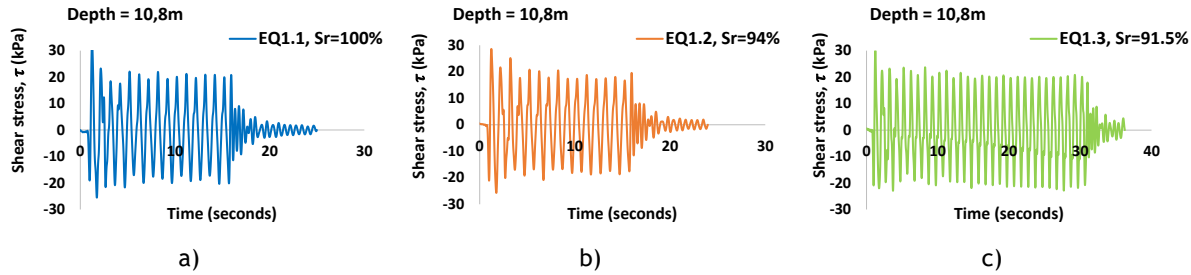

Figure 6-44 Shear stress time history at depth 10.8m: a) EQ1.1; b) EQ1.2 and; c) EQ1.3

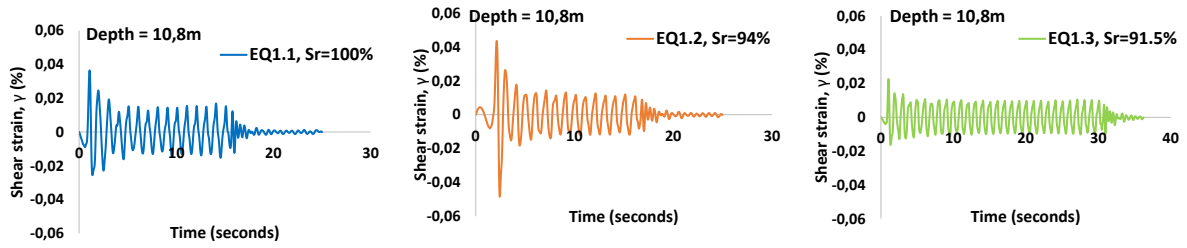

a) b) c)

Figure 6-45 Shear strain time history at depth 10.8m: a) EQ1.1; b) EQ1.2 and; c) EQ1.3

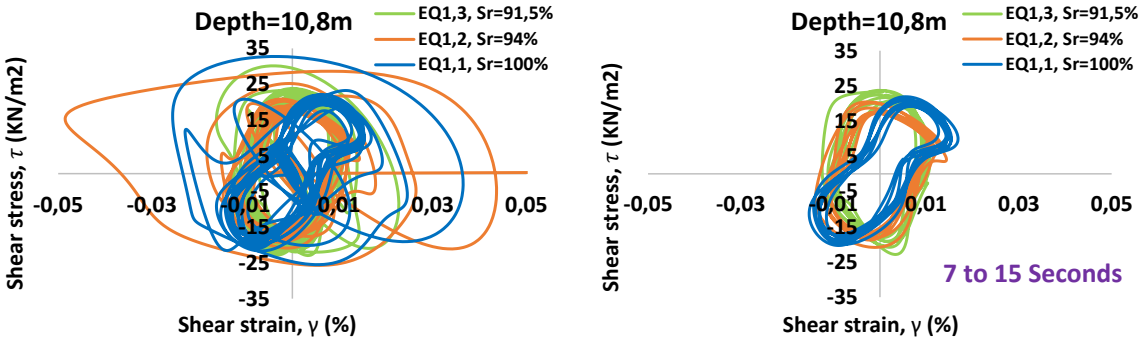

a) b)

Figure 6-46 Stress-strain hysteresis loops for all three shakes at 10.8m: a) full data; b) representative loops from 7 to 15s

Table 6-7 Secant shear stiffness (G_{sec}) and dissipated energy (ΔW) calculated for Cyclic loop #10 across the three shaking events at a prototype depth of 10.8 m

Shake#	Sr(%)	Depth (m)	Dissipated energy, ΔW (KJ/m^3) Area of hysteresis loop	Secant stiffness G_{sec}(kPa)
EQ1.1	100	10.8	0.0064	135530
EQ1.2	94	10.8	0.006	159200
EQ1.3	91.5	10.8	0.0059	215490

As previously reported, the marked increase in secant stiffness and decreased dissipated energy observed at the 10.8 m depth is a mathematical artifact inherent to the 1D shear beam interpolation technique. This is a a limitation to the Zeghal and Elgamal (1994) approach as it averages the dynamic soil response between recording nodes. Consequently, when the soil profile experienced severe softening—as seen at the 7.8 m array depth—this numerical averaging failed to resolve the sharp behavioral boundary.

Prototype depth: 7.8m

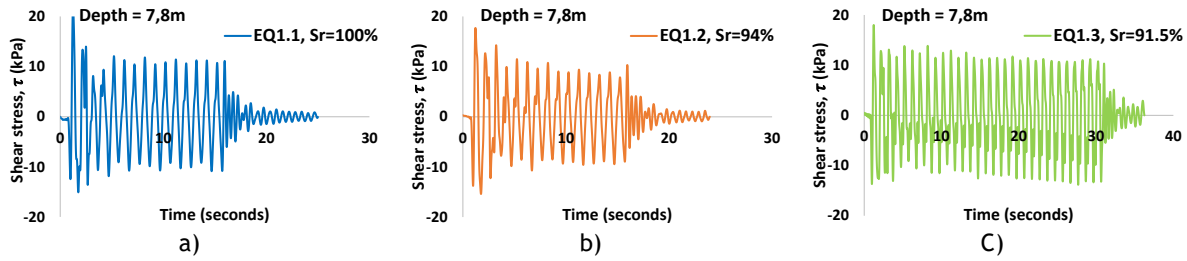

Figure 6-47 Shear stress time history at depth 7.8m: a) EQ1.1; b) EQ1.2 and; c) EQ1.3

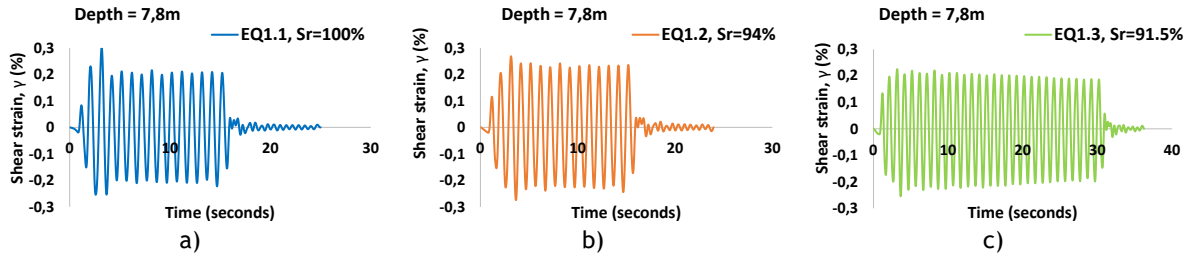

Figure 6-48 Shear strain time history at depth 7.8m: a) EQ1.1; b) EQ1.2 and; c) EQ1.3

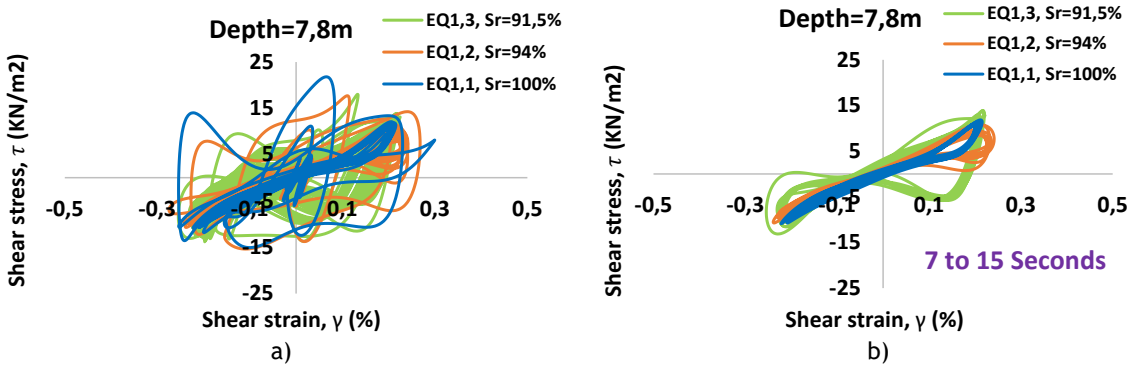

Figure 6-49 Stress-strain hysteresis loops for all three shakes at 7.8m: a) full data; b) representative loops from 7 to 15s

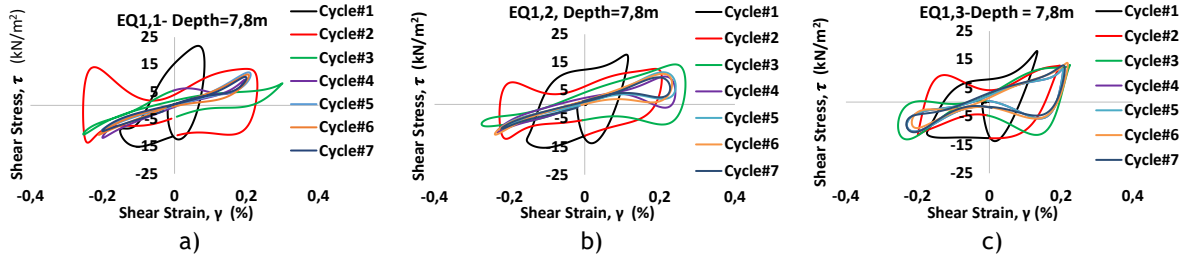

Figure 6-50 Stress-strain hysteresis loops for the first 7 cycles for the three shakes at 7.8m depth: a) EQ1.1; b) EQ1.2 and; c) EQ1.3

Table 6-8 Secant shear stiffness (G_{sec}) calculated for cyclic loop #10 and dissipated energy (ΔW) evaluated for Cyclic loop #2 across the three shaking events at a prototype depth of 7.8m.

Shake#	Sr(%)	Depth (m)	Dissipated energy, ΔW (KJ/m^3) : Cycle #2 Area of hysteresis loop	Secant stiffness G_{sec}(kPa) : Cycle #10
EQ1.1	100	7.8	0.081	4980
EQ1.2	94	7.8	0.064	4100
EQ1.3	91.5	7.8	0.054	5230

Prototype depth: 4.5m

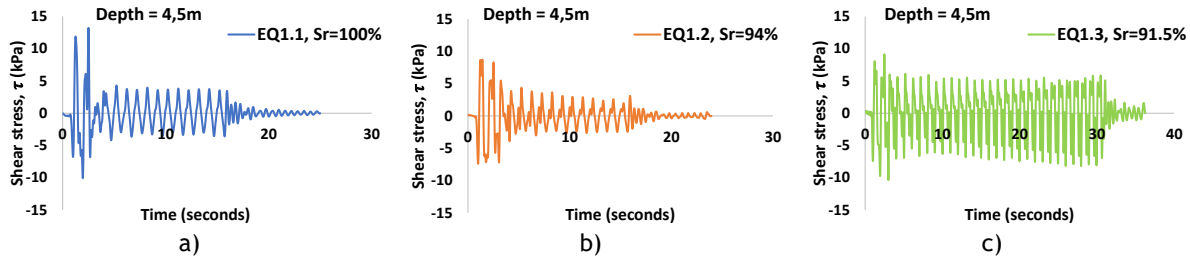

Figure 6-51 Shear stress time history at depth 4.5m: a) EQ1.1; b) EQ1.2 and; c) EQ1.3

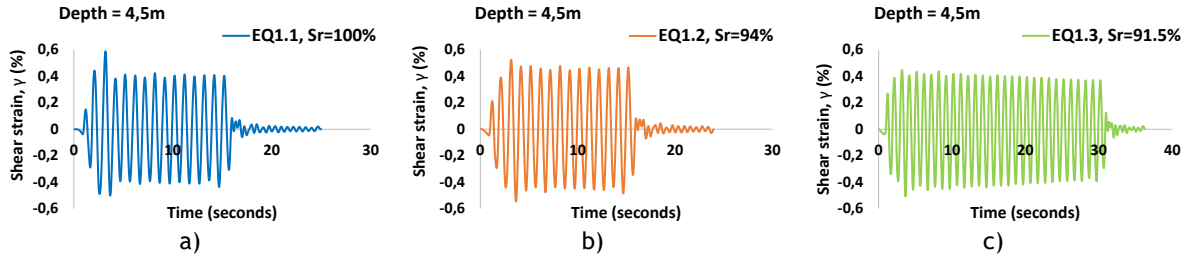

Figure 6-52 Shear strain time history at depth 4.5m: a) EQ1.1; b) EQ1.2 and; c) EQ1.3

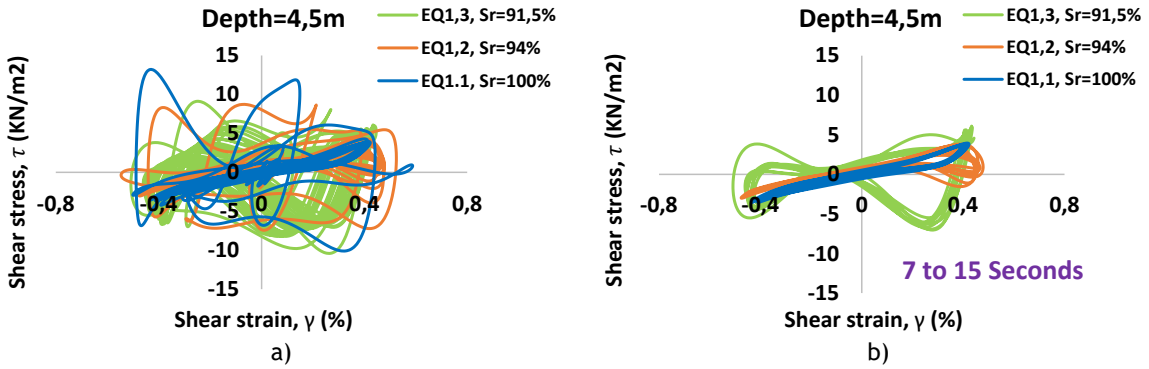

Figure 6-53 Stress-strain hysteresis loops for all three shakes at 4.5m: a) full data; b) representative loops from 7 to 15s

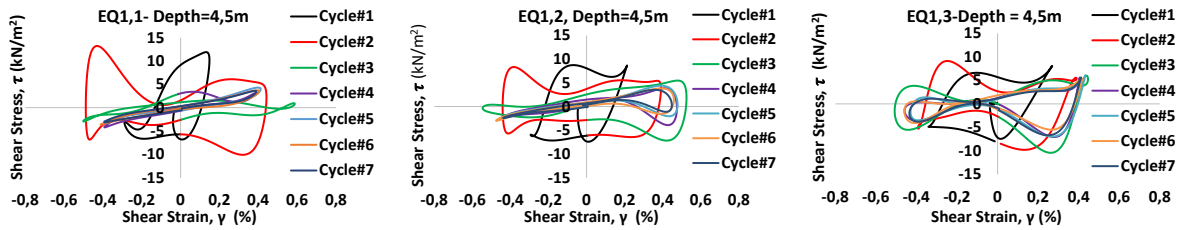

a) b) c)

Figure 6-54 Stress-strain hysteresis loops for the first 7 cycles for the three shakes at 4.5m: a) EQ1.1; b) EQ1.2 and; c) EQ1.3

Table 6-9 Secant shear stiffness (G_{sec}) calculated for cyclic loop #10 and dissipated energy (ΔW) calculated for Cyclic loop #2 across the three shaking events at a prototype depth of 4.5m

Shake#	Sr(%)	Depth (m)	Dissipated energy, ΔW (KJ/m^3): Cycle #2 Area of hysteresis loop	Secant stiffness G_{sec}(kPa): Cycle #10
EQ1.1	100	4.5	0.1	840
EQ1.2	94	4.5	0.077	640
EQ1.3	91.5	4.5	0.067	1410

Prototype depth: 1.2m

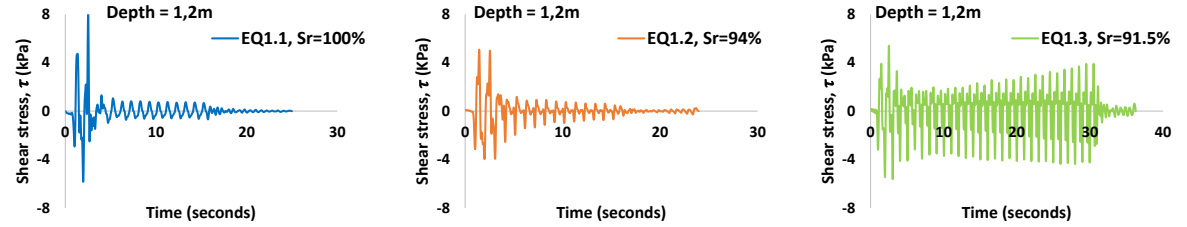

a) b) c)

Figure 6-55 Shear stress time history at depth 1.2m: a) EQ1.1; b) EQ1.2 and; c) EQ1.3

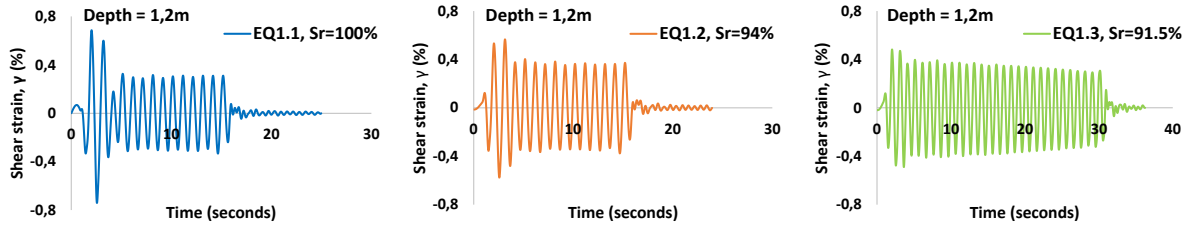

a) b) c)

Figure 6-56 Shear strain time history at depth 1.2m: a) EQ1.1; b) EQ1.2 and; c) EQ1.3

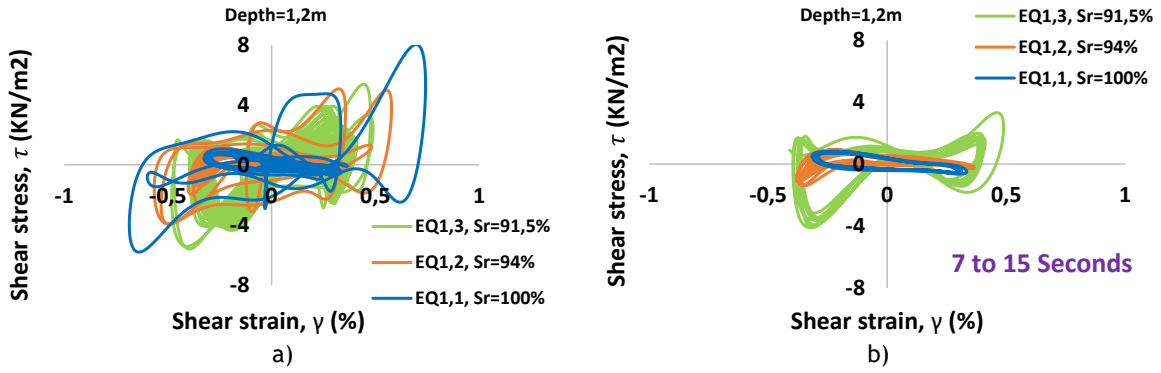

Figure 6-57 Stress-strain hysteresis loops for all three shakes at 1.2m: a) full data; b) representative loops from 7 to 15s

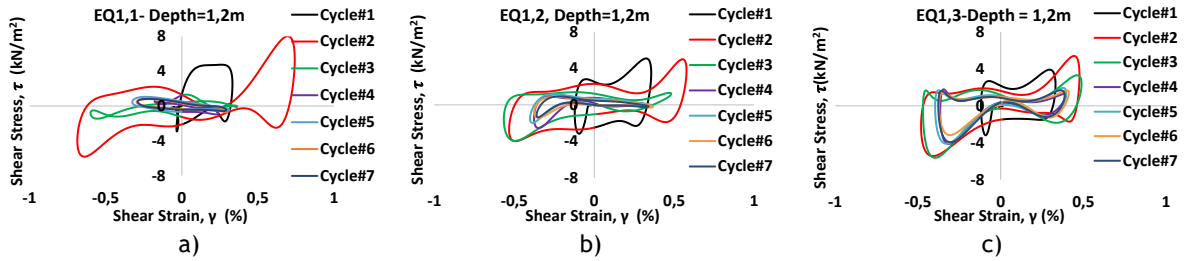

Figure 6-58 Stress-strain hysteresis loops for the first 7 cycles for the three shakes at 1.2m: a) EQ1.1; b) EQ1.2 and; c) EQ1.3

Table 6-10 Secant shear stiffness (G_{sec}) calculated for cyclic loop#10 and dissipated energy (ΔW) calculated for Cyclic loop #2 across the three shaking events at a prototype depth of 4.5m

Shake#	Sr(%)	Depth (m)	Dissipated energy, ΔW (KJ/m^3): Cycle #2 Area of hysteresis loop	Secant stiffness G_{sec}(kPa): Cycle #10
EQ1.1	100	1.2	0.06	210
EQ1.2	94	1.2	0.043	250
EQ1.3	91.5	1.2	0.04	710

Prototype depth: 0.6m

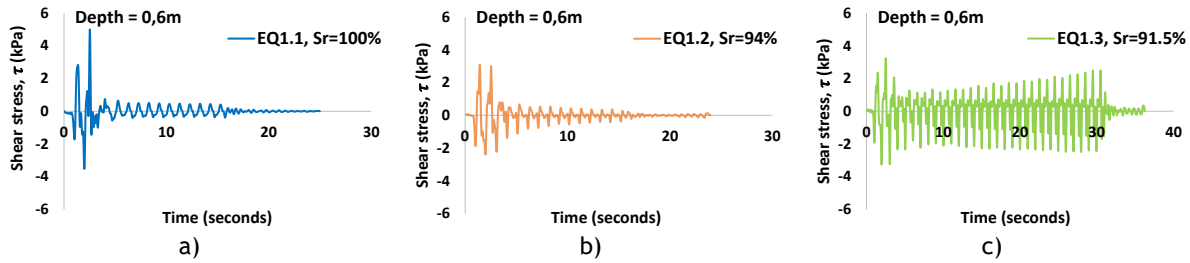

Figure 6-59 Shear stress time history at depth 0.6m: a) EQ1.1; b) EQ1.2 and; c) EQ1.3

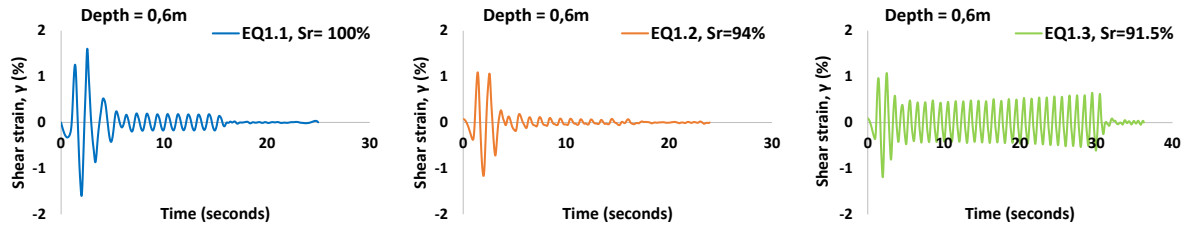

a) b) c)

Figure 6-60 Shear strain time history at depth 0.6m: a) EQ1.1; b) EQ1.2 and; c) EQ1.3

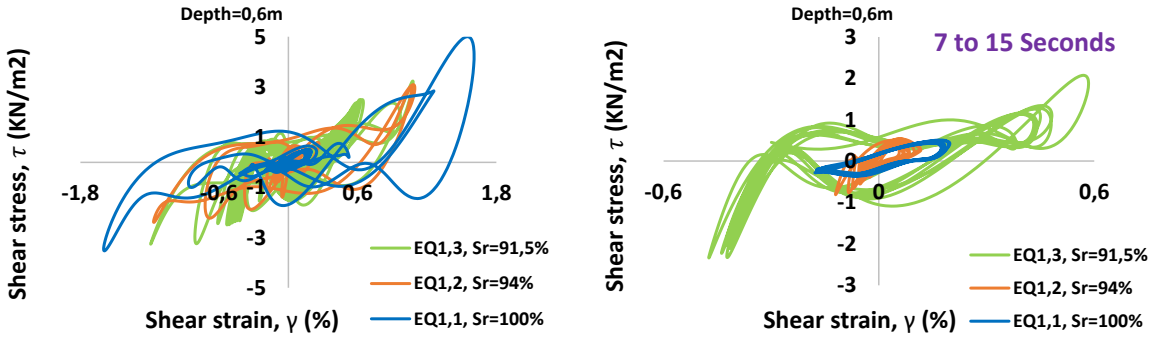

a) b)

Figure 6-61 Stress-strain hysteresis loops for all three shakes at 0.6m: a) EQ1.1; b) EQ1.2 and; c) EQ1.3: a) full data; b) representative loops from 7 to 15s

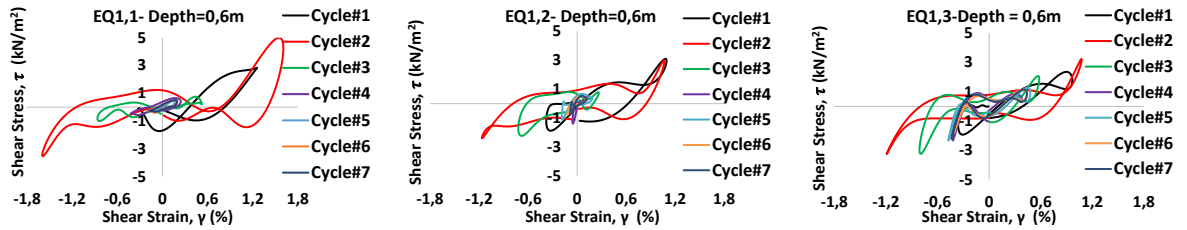

a) b) c)

Figure 6-62 Stress-strain hysteresis loops for the first 7 cycles for the three shakes at 0.6m: a) EQ1.1; b) EQ1.2 and; c) EQ1.3

Table 6-11 Secant shear stiffness (G_{sec}) calculated for cycle # 10 and dissipated energy (ΔW) calculated for Cyclic loop #2 across the three shaking events at a prototype depth of 0.6m

Shake#	Sr(%)	Depth (m)	Dissipated energy, ΔW (KJ/m^3): Cycle #2 Area of hysteresis loop	Secant stiffness G_{sec}(kPa): Cycle #10
EQ1.1	100 ▲	0.6	0.054 ▲	220
EQ1.2	94	0.6	0.032	720
EQ1.3	91.5	0.6	0.025	380

Moving up to the shallower layers (7.8 m to 0.6 m), the soil stress-strain response splits into two distinct phases. The initial cycles exhibited sudden spikes in both stresses and strains, resulting in relatively larger earlier hysteresis loops. This rapid, early-stage strain accumulation is a clear indicator of soil instability.

For the remainder of the shaking event, immediately following these initial spikes, the hysteresis loops became flatter, and narrower, as the soil underwent cyclic softening under this low confinement. Consequently, the shear stiffness remained low throughout the entire duration of the shakings.

Nevertheless, despite the overall deterioration of the hysteretic response within these low-confinement shallow depths, a distinct relative difference between the testing conditions persisted. Based on cycle 2, the partially saturated profiles (EQ1.2 and EQ1.3) exhibited smaller stress-strain hysteresis loops, thereby exhibiting less ΔW than the fully saturated baseline (EQ1.1).

6.5.3. Global analysis of the soil profile response

Figure 6-63 presents the depth profiles for secant shear stiffness G_{sec}, dissipated energy ΔW in addition to corresponding pre-calculated r_{umax} distribution across the three shaking events. These plots reflect the targeted cycle selection discussed earlier, showing data from cycle 10 for the deeper layers (19.2 m to 10.8 m) and cycle 2 for the shallower layers (7.8 m to 0.6 m). The data points are calculated directly at the exact accelerometer depths, directly using the accelerometer data for the stress and strain calculations.

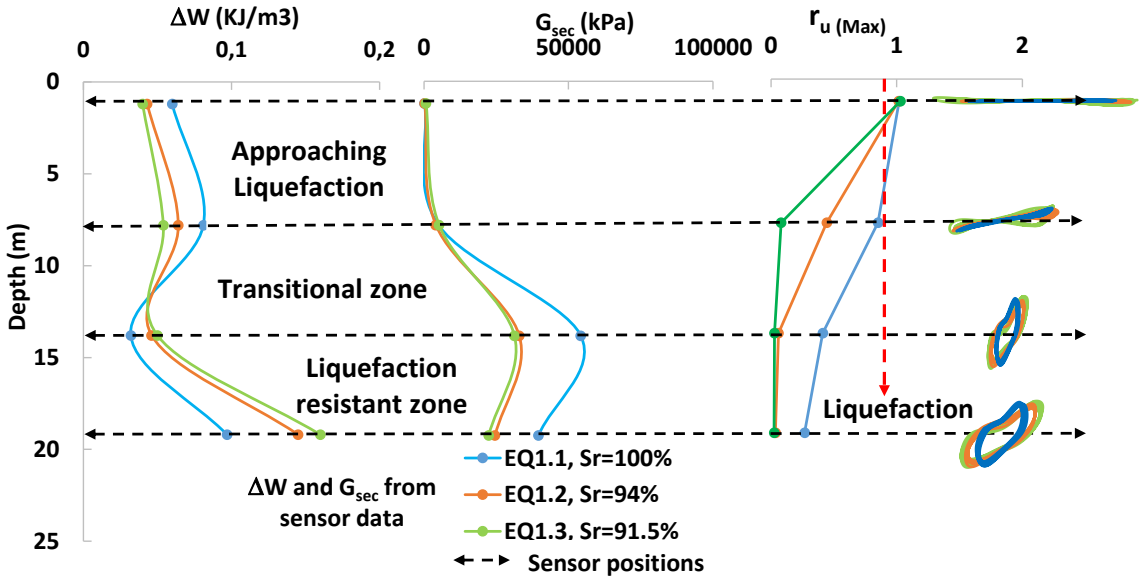

Figure 6-63 Secant shear stiffness (G_{sec}), dissipated energy (ΔW), evaluated during Cycle #10 for depths: (19.2 to 10.8m) and cycle#2 for depths: (7.8 to 0.6m) across the three shaking events (data are calculated at the sensors locations, based on the sensors records. The figure also presents the (r_{umax}) distribution and illustrative, unscaled shapes of the resulting hysteresis loops.

Figure 6-64a and b expand on these results; in addition to the known sensor locations, these plots incorporate intermediate values calculated at the midpoints between the accelerometers, utilizing the interpolation methodology established by Zeghal and Elgamal (1994).

As clear in Figure 6-46 and as noted previously, the pronounced increase in secant stiffness and the corresponding reduction in dissipated energy at a depth of 10.8 m result from a mathematical artifact introduced by the 1D shear-beam interpolation procedure. This limitation is associated with Zeghal and Elgamal (1994) method, which derives the dynamic soil response by averaging between adjacent recording levels. As a result, when pronounced

softening occurred within the soil profile, particularly at the 7.8 m array depth, the averaging procedure could not properly resolve the change in soil behavior.

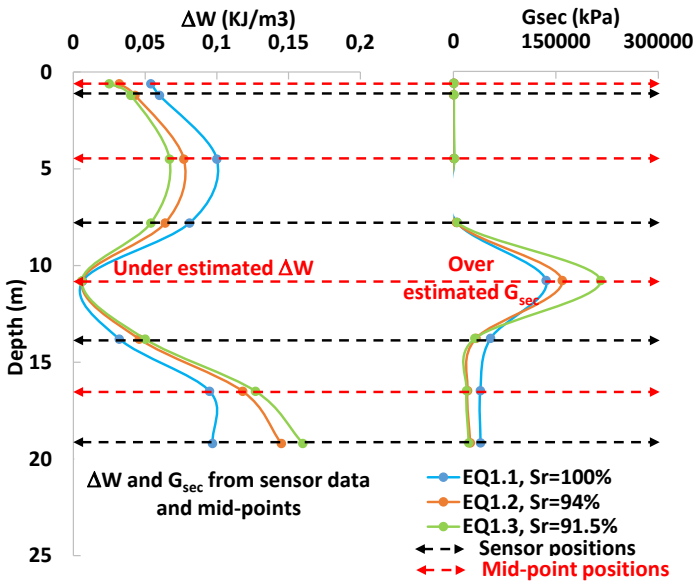

Figure 6-64 (a) Secant shear stiffness (G_{sec}) and (b) dissipated energy (ΔW) evaluated during Cycle #10 for depths: (19.2 to 10.8m) and cycle#2 for depths: (7.8 to 0.6m) across the three shaking events (data are calculated at the sensors locations and midpoints)

Moreover, the evolution of dynamic soil properties is presented in Figure 6-65: (a) dissipated energy ΔW and (b) secant shear stiffness G_{sec} as a function of maximum shear strain γ_{max} evaluated across the centrifuge model profile.

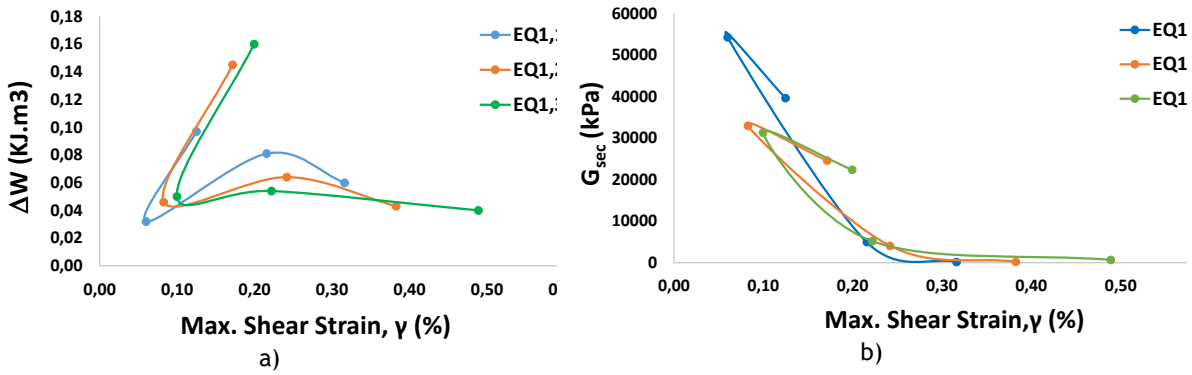

Figure 6-65 a) Variation of (a) secant shear stiffness (Gsec); and b) dissipated energy (DW) with maximum induced shear strain γmax.

From Figure 6-63, the depth profiles for the three shakes demonstrate the same general trend. From the base of the profile up to 13.8 m, the dissipated energy (ΔW) steadily decreased while the secant shear stiffness (G_{sec}) increased. Moving upward toward 7.8 m, this trend reversed: energy dissipation began to rise again as stiffness degraded. Finally, in

the shallowest layers (7.8 m to 1.2 m), the dissipated energy dropped, and the stiffness collapsed to lower values.

For isolating the impact of Induced Partial Saturation (IPS), the profiles for the subsequent shaking events (EQ1.2 and EQ1.3) demonstrate a clear redistribution of seismic energy throughout the soil column. In the deeper zones near the air injector, the partially saturated soil exhibited higher damping and lower stiffness compared to the fully saturated baseline shake (EQ1.1). The introduction of highly compressible air bubbles creates a highly dissipative soil matrix capable of absorbing seismic energy. However, as these shear waves propagated upward toward the shallowest depths (from 7.8 m upward), a distinct reversal in the dissipated energy (ΔW) trend occurred. In these shallow, low-confinement zones, the fully saturated baseline shake (EQ1.1) dissipated more energy than the partially saturated shakes. This reversal is a direct consequence of the seismic attenuation, also known as "base isolation" effect. Because the deeper desaturated layers attenuate a greater portion of the seismic energy, the shear waves that eventually reached the shallow layers during EQ1.2 and EQ1.3 were substantially weaker. Consequently, the shallow soil experienced lower shear strains and generated smaller hysteresis loops, leading to a lower overall ΔW compared to the less attenuated, fully saturated EQ1.1 shaking event.

This finding is fundamental because it captures the highly distinct nature of the soil profile. It clearly demonstrates how the dynamic response is controlled by a complex, compounding interaction between the effective confining pressure, the applied seismic stress, and the degree of saturation at any given depth.

6.6. Main findings

This chapter shows the results, its interpretation and analysis of the dynamic centrifuge tests, to examine the influence of induced partial saturation (IPS) on the earthquake-induced liquefaction mitigation. Pore-pressure build-up at different depths, arias intensity, soil settlement and stress strain loops were evaluated in fully and partially saturated states. Bender elements were able to capture seismic wave velocities, despite some limitations due to the noisy environment of the centrifuge.

One of the main findings evidenced by these tests is that the presence of occluded air fundamentally altered the energy dissipation mechanism of the soil. The highly compressible air-water mixture absorbs the volumetric contraction of the pores, drastically delaying the generation of excess pore pressure r_u. Consequently, the soil particles maintain their effective intergranular contact stresses over a greater number of loading cycles. This sustained confinement allows the soil skeleton to undergo more frictional sliding and particle rearrangement, manifesting as larger shear strains and broader hysteresis loops (ΔW), without experiencing catastrophic strength loss. This creates a highly defensible, albeit seemingly paradoxical, dynamic response: the partially saturated specimens exhibit a lower cycle-specific secant stiffness due to the larger accommodated shear strains, yet they simultaneously maintain a significantly higher overall effective strength and lower r_u than their fully saturated counterparts. Consequently, the IPS technique effectively transformed the soil matrix into a high-capacity energy sink. By sustaining larger shear strains without experiencing catastrophic strength loss, the partially saturated soil exhibited broader stress-strain hysteresis loops. Figure 6-66 presents an illustrative schematic comparing the evolution of dynamic soil behavior across fully saturated, partially saturated, and unsaturated states.

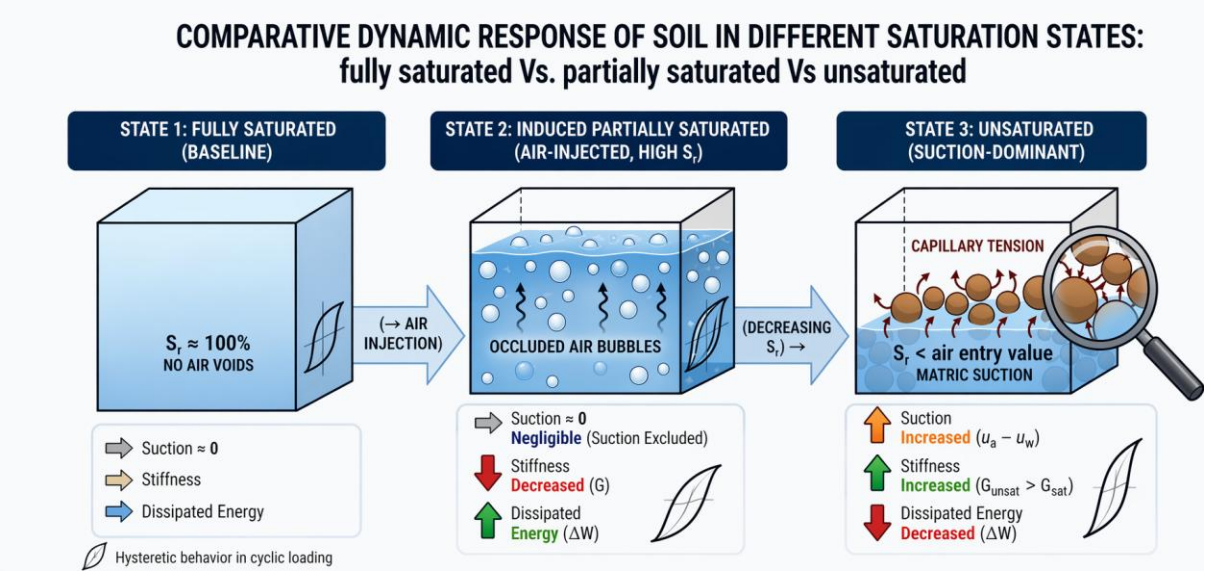

Figure 6-66 Illustrative figure showing the dynamic behavior evolution for fully, partially, and unsaturated soil states

The dynamic behavior of unsaturated sands has been extensively evaluated in geotechnical literature. For instance,Le & Ghayoomi (2017) customized a dynamic Direct Simple Shear (DSS) apparatus to control suction and evaluate the effect of the degree of saturation on dynamic properties of unsaturated soils including shear modulus and damping. The authors concluded that high matric suction increased soil stiffness (higher shear modulus) and decreased damping. On the other hand, the centrifuge test analysis conducted in this research on Induced Partially Saturated (IPS) sands exhibited the exact opposite trend. Because the induced degree of saturation remained high enough to prevent the formation of stiffness induced matric suction, the occluded air bubbles served primarily to increase pore fluid compressibility rather than increasing stiffness by suction (negative pore pressure). Consequently, the partially saturated shakes in this experimental model demonstrated a marked decrease in shear stiffness accompanied by an increase in dissipated energy compared to the fully saturated baseline scenario.

The main findings of this chapter can be summarized in the following highlights:

- Utilizing BE in centrifuge testing provided additional information, in terms of the degree of saturation, the compressional wave velocity (V_p) for the fully saturated model remained consistently around 1560 m/s, regardless of the depth at which the receiver bender element (BE) was positioned. This consistency highlights the strong reliability and compatibility of the measurement system.
- The evolution of shear wave velocity (V_s) with increasing confining pressures demonstrated excellent agreement, with an exponent" ß" which falls with the typical range of natural sands.
- Altering the input signal frequencies validated the system's capability to simultaneously measure both V_p and V_s with high precision.
- Moreover, the system proved to be fully functional under the extreme conditions of high spinning centrifuge accelerations, reinforcing its robustness and suitability for dynamic geotechnical testing. These results highlight the potential of the wave-based method as a promising approach for estimating the degree of saturation (Sr%)

and evaluating soil stiffness in sandy soils during dynamic centrifuge experiments. The method's ability to capture these key parameters with high accuracy presents a significant advancement in geotechnical testing and soil behavior analysis under dynamic loading conditions and particularly for liquefaction mitigation assessment.

- Arias intensity was found to be more representative than PGA alone for assessing attenuation and amplification of propagated waves along the soil profile, as it accounts for acceleration amplitude, frequency content, and shaking duration. The IA profiles showed clearer attenuation of the upward-propagating seismic motion in the partially saturated tests compared with the fully saturated condition.
- Even a small reduction in degree of saturation resulted in a significant decrease in excess pore pressure generation (smaller peak of r_u) and increased liquefaction resistance, even with elevated input motion PGA.
- IPS not only decreased the pore pressure build-up but also delayed it in terms of time due to the higher compressibility of the pore fluid when gas is present, in the form of occluded bubbles.
- IPS reduced soil surface settlement under comparable input motions. However, this benefit was reduced as the input amplitude increased, showing that settlement mitigation remains dependent on seismic demand. As these tests represented free-field conditions, the response may differ in the presence of a structure due to changes in stress state and soil–structure interaction.
- With air injection introduced from the base, the deep to mid-depth layers showed the most pronounced improvement compared with the near-surface zones. This enhancement can be attributed to being close to the air injection and also due to its high confining pressure.
- Arias intensity, and the the analysis of the hysteresis stress-strain loops were, to a large extent, mutually consistent.
- The hysteresis dissipated energy increased due to the induced partial saturation and shear stiffness decreased, particularly under high confining pressure (deeper zones).
- Finally, a broad comparison between fully saturated, partially saturated and unsaturated conditions has been presented in terms of the soil stiffness and dissipated energy.

7. Linking centrifuge modelling with cyclic triaxial testing

7.1. Introduction

This chapter presents a comparative analysis of the liquefaction resistance of Hostun HN31 sand, evaluating results derived from dynamic centrifuge modeling at varying degrees of saturation Sr against those obtained from cyclic triaxial (CTx) testing. This analysis assessment utilizes experimental data from centrifuge Model M1. This specific model was selected because it encompasses three distinct seismic events (EQ1.1, EQ1.2, and EQ1.3) conducted under different saturation conditions, all while being subjected to an identical peak ground acceleration (PGA).

It is worth mentioning that, for a valid comparison with the liquefaction resistance curve resulting from the CTx (Figure 5-54), this analysis was performed for Centrifuge M1 at the depth where liquefaction triggering was guaranteed for the three shakes (z =1.2 m prototype).

The comparative validation between the two testing methodologies is established by evaluating the Cyclic Stress Ratio CSR against the corresponding number of cycles required to trigger liquefaction N_L.

7.1.1. Cyclic stress ratio time history CSR(t)

Figure 7-1, Figure 7-2, and Figure 7-3 present the computed cyclic stress ratio time histories CSR(t), in addition to the r_u(t) for Model M1 at a prototype depth of 1.2 m for shaking events EQ1.1, EQ1.2, and EQ1.3, respectively.

As previously detailed, the cyclic shear stress time history, τ (t), was initially derived from centrifuge acceleration measurements using equation (6-5) and subsequently normalized by the initial vertical effective stress to determine CSR(t) using equation (7-1). To identify the onset of liquefaction, the corresponding pore pressure ratio, r_u(t), was plotted alongside each CSR(t) record. Finally, the pre-liquefaction triggering CSR peak amplitudes were evaluated, adopting $r_u > 0.95$ as the quantitative criterion for liquefaction onset.

$$CSR = \frac{\tau(t)}{\sigma'_{vo}} \tag{7-1}$$

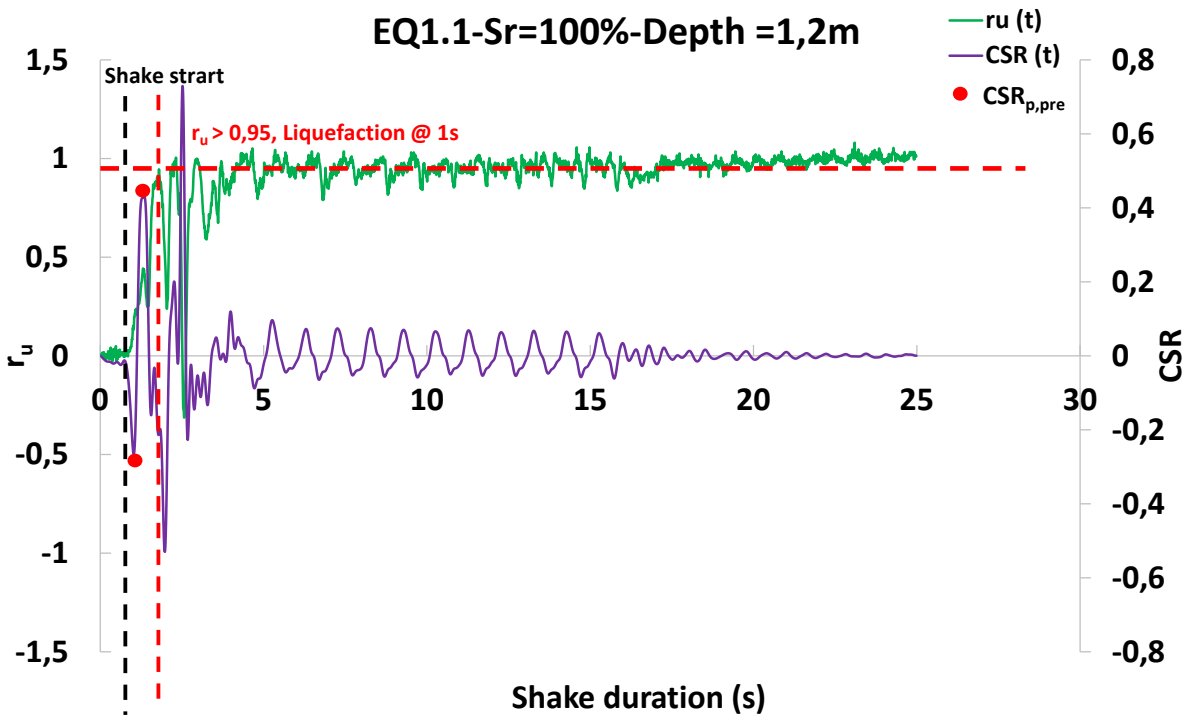

Figure 7-1 CSR(t) at depth 1.2m for shake EQ1.1-Centrifuge test M1

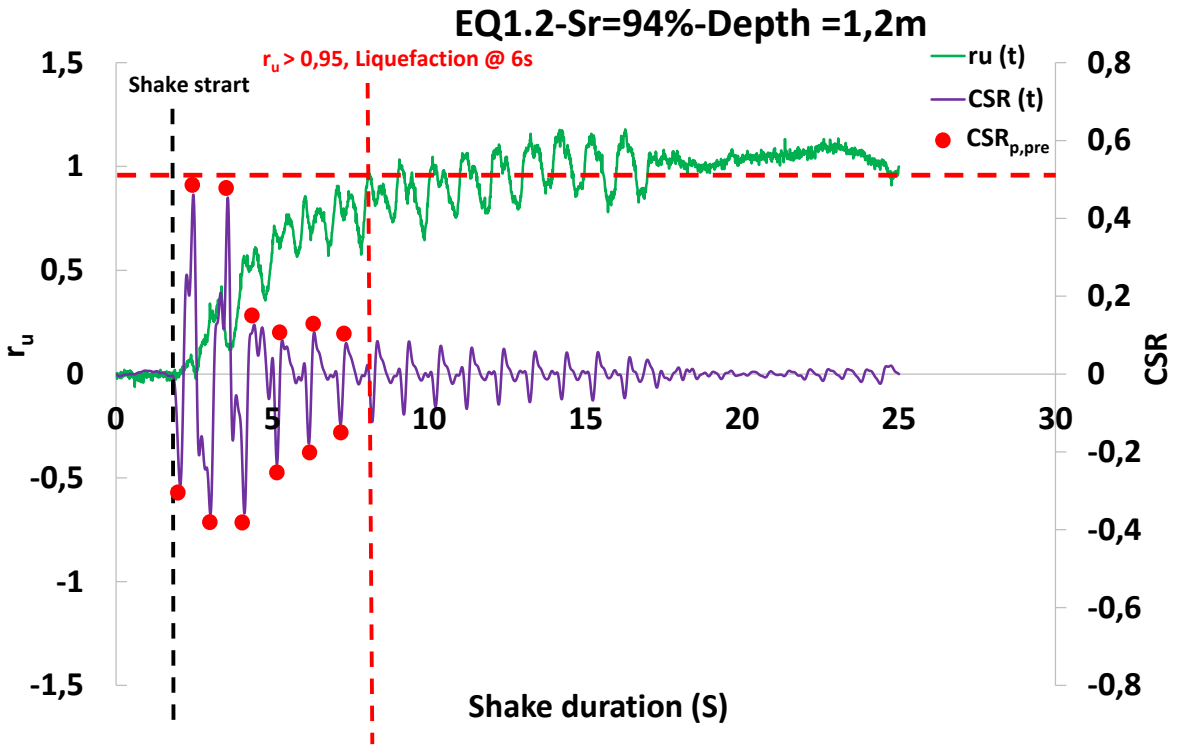

Figure 7-2 CSR(t) at depth 1.2m for shake EQ1.2-Centrifuge test M1

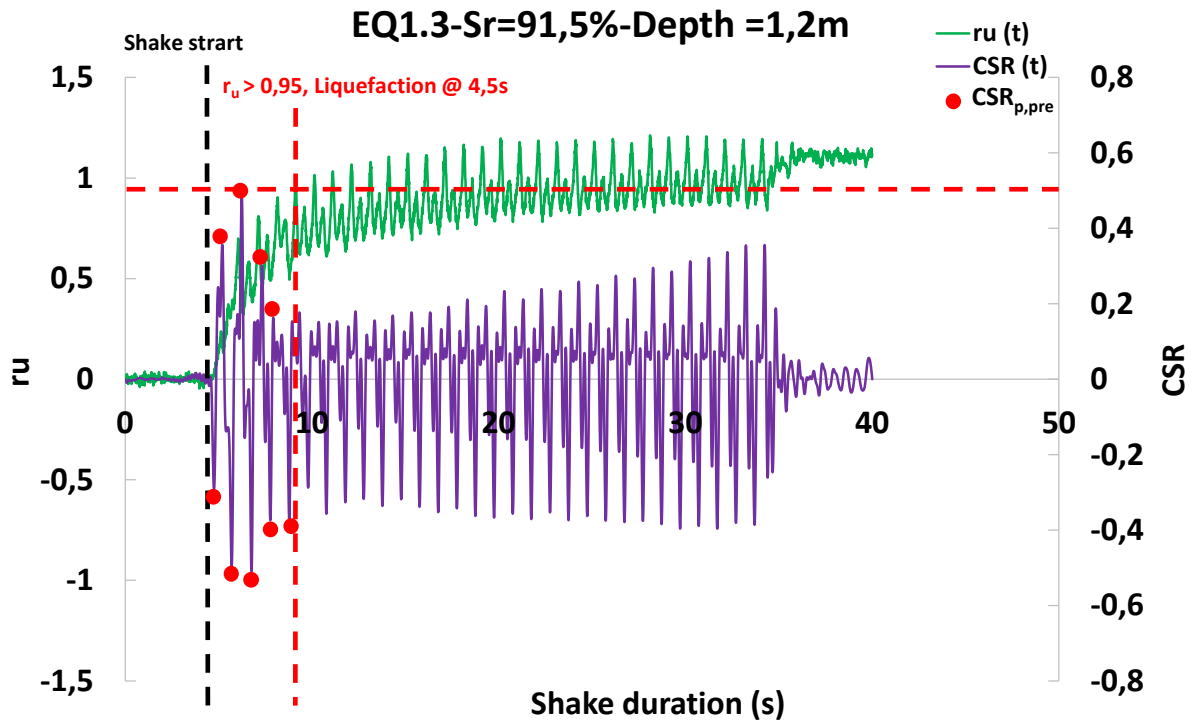

Figure 7-3 CSR(t) at depth 1.2m for shake EQ1.3-Centrifuge test M1

The CSR(t) record shown in Figure 7-1 exhibited a pronounced initial spike with a peak amplitude of approximately $CSR_{peak} \approx 0.42$. This high amplitude stress pulse was sufficient to trigger rapid liquefaction, as indicated by the pore pressure ratio exceeding the triggering criterion ($r_u > 0.95$) (Ishihara, 1993), within the first loading cycle at approximately t = 1.0 s. A second prominent cycle followed, after which the time history was dominated by lower amplitude cycles (CSR ≈ 0.05). Because these subsequent cycles occur under a liquefied state characterized by severely degraded effective stress, they do not represent the pre-liquefaction shear resistance of the soil and are therefore excluded from the derivation of the cyclic resistance.

On the other hand, Figure 7-2 demonstrates a distinct liquefaction response during EQ1.2 (Sr = 94%). The soil did not liquefy during the initial high amplitude CSR pulses; rather, it withstood the first three significant cycles with the pore pressure ratio r_u remaining below 0.5. The eventual failure was progressive: the initial high-stress spikes consumed a substantial portion of the soil's cyclic fatigue life, thereby enabling the subsequent lower-amplitude cycles to accumulate further pore pressure and drive the soil to initial liquefaction. As depicted by the CSR(t) time history, following the early spikes, the loading transitioned into a sequence of lower, variable amplitudes cycles, until liquefaction was triggered at t = 6.0 s. A similar behavioral pattern is evident in the CSR(t) record for EQ1.3 (Figure 7-3). The stress history exhibited early high amplitude spikes before settling into a prolonged phase of lower, variable CSR amplitudes, ultimately reached liquefaction triggering at t = 4.5s.

Although the input base motions for all three shaking events consisted of uniform harmonic sine waves, the resulting CSR(t) at 1.2m depth, time histories exhibited transient amplitude fluctuations. These variations arose primarily from the progressive softening of the soil as it approached liquefaction, compounded by the very low initial effective confining stress characteristic of this shallow zone.

To account for irregular seismic stresses, the variable-amplitude stress history must be systematically converted into an equivalently damaging sequence of uniform cycles N_{eq}.

7.1.2. The Palmgren-Miner Cumulative Damage Hypothesis

Dynamic loading in geotechnical testing is often idealized as regular (periodic, constant-amplitude) loading, typically sinusoidal cycles used in element tests or as irregular (transient, non-stationary, variable-amplitude) loading representative of real earthquake time histories.

To bridge the gap between these two domains, (Seed & Idriss, 1971) developed the "Simplified Procedure." This semi-empirical framework converts the chaotic, irregular peak acceleration a_{max} of an earthquake into an "equivalent" uniform cyclic stress ratio CSR_{eq} using the common classic formulation, Equation (7-2).

$$CSR = 0.65 \cdot \frac{a_{max}}{g} \cdot \frac{\sigma_{vo}}{\sigma'_{vo}} \, rd \, \frac{1}{MSF} \tag{7-2}$$

Where 0.65 is a weighting factor assuming that the "effective" average shear stress of an irregular earthquake record is approximately 65% of the absolute peak stress; σ_{vo} and σ'_{vo} are the total and effective stress at rest, respectively; r_d is a shear stress reduction factor; and MSF (Magnitude Scaling Factor) is a factor that normalizes the earthquake duration (number of cycles) to a reference magnitude (typically M_w = 7.5).

As previously reported, in the present study, the target input motion of the three shakes of M1 of the centrifuge tests was a uniform sinusoidal wave shake intended to mimic "regular" loading. However, the calculated shear stress and hence CSR time histories exhibited significant irregularities in the shallow depths. Because the calculated CSR(t) motion was neither "regular" (constant amplitude) nor a standard "earthquake" (transient), the use of the generic 0.65 weighting factor might be scientifically inappropriate. Applying a constant factor to a specific transient spike would either overestimate the damage (if based on the peak) or underestimate it (if based on the later steady phase). Here, the “steady phase” refers to the pre-liquefaction plateau, not post liquefaction behavior.

To rigorously account for the variable stress amplitudes recorded, the Palmgren-Miner Cumulative Damage Hypothesis (Milton Miner & Monica, 1945) was adopted.

This framework facilitates a standardized assessment of the soil's cyclic shear resistance. The calculated CSR(t) for each shaking event was derived exclusively from the time history prior to liquefaction triggering.

To validate the dynamic response of the centrifuge soil model M1, a direct comparison was established between the Cyclic Stress Ratio CSR and the number of cycles to liquefaction N_L observed in the three shakes of the centrifuge M1, and the Liquefaction Resistance Curve LRC derived from undrained Cyclic Triaxial CTx element tests of the same sand Hostun HN31.

The Cumulative Damage concept was introduced by Palmgren (1924) and later formalized by Milton Miner & Monica (1945) ; it is commonly expressed as a linear damage accumulation rule, in which the damage contribution of each stress amplitude level is summed over the record.

Milton Miner & Monica (1945) reported that the cumulative fatigue damage under repeated loading can be treated as a life consumption process, in which the fraction of "useful life" expended at a given stress level is the ratio of applied cycles to the cycles to failure at that same level. Failure is expected when the accumulated damage reaches 100% (i.e., when the summed life fractions reach unity (Damage, D=1), a concept the authors supported with experimental verification on aluminum alloys and presented as a simple, conservative basis for variable-amplitude loading assessment.

The basic form of the P–M cumulative damage hypothesis for uniform loading is expressed using equation (7-3), by Milton Miner & Monica (1945) and used by Green & Terri (2005):

$$\frac{\boldsymbol{\omega}_1}{W} = \frac{n_1}{N_1} \tag{7-3}$$

Where $\boldsymbol{\omega}_1$ is the work done at n_1 cycles; W is the work done to failure; n_1 is the number of stress cycles applied at S_1, where S_1 is the peak amplitude of an applied cyclic stress; and N_1 is the number of stress cycles to failure.

For an imposed cyclic stress history with variable peak amplitudes (i.e., non-uniform cyclic loading, rather than a constant-amplitude cycle), the Palmgren–Miner (P–M) cumulative damage hypothesis can be extended to the form shown in equations (7-4) and (7-5).

$$\frac{\boldsymbol{\omega}_1}{W} + \frac{\boldsymbol{\omega}_2}{W} + \frac{\boldsymbol{\omega}_3}{W} \dots\dots + \frac{\boldsymbol{\omega}_m}{W} = \frac{n_1}{N_1} + \frac{n_2}{N_2} + \frac{n_3}{N_3} \dots\dots + \frac{n_m}{N_m} \tag{7-4}$$

In other words:

$$\sum_{i=1}^{m} \frac{\boldsymbol{\omega}_i}{W} = \sum_{i=1}^{m} \frac{n_i}{N_i} \tag{7-5}$$

Where m represents the number of various peak stress amplitudes of the stress history (i.e., S_1, S_2, …..S_m); n_i is the number of cycles in the stress history having a given peak stress amplitude S_i; $\boldsymbol{\omega}_i$ is the absorbed work after n_i cycles ;and N_i is the number of stress cycles to failure at stress level S_i.

The cumulative damage D was then calculated by dividing the absorbed work $\boldsymbol{\omega}_i$ after number of cycles n_i by the work at failure W. The cumulative damage D can be defined by equation (7-6), (Milton Miner & Monica, 1945, Green & Terri, 2005, Kokusho, 2024).

$$D = \sum_{i=1}^{m} \frac{\boldsymbol{\omega}_i}{W} = \sum_{i=1}^{m} \frac{n_i}{N_i} = 1 \quad (\boldsymbol{at\ failure}) \tag{7-6}$$

Milton Miner & Monica (1945), had experimentally concluded that the cumulative damage concept holds true for Alclad 24S-T aluminum alloy and recommended that it should experimentally investigated for other materials to evaluate its range of usefulness.

Green & Terri (2005) calculated N_{eq} by replacing the variable-amplitude sequence with a uniform cyclic stress of amplitude S_{ref} which reaches failure after N_{ref} cycles such that the two load histories produce the same cumulative damage as clear in equation (7-7).

$$\frac{N_{eq}}{N_{ref}} = \sum_i \frac{n_i}{N_i} \rightarrow N_{eq} = \sum_i n_i \,.\, \frac{N_{ref}}{N_i} \tag{7-7}$$

Based on the Liquefaction resistance curve LRC regression equation for sands, Equation (7-8) was derived:

$$CSR = a.N_L{}^{-b}$$
$$\Downarrow \tag{7-8}$$
$$N = \left(\frac{CSR}{a}\right)^{-1/b} = a^{1/b}\,.\,CSR^{-1/b}$$

Substituting equation (7-8) into equation (7-7) yields the final formulation presented in equation in (7-9):

$$N_{eq} = \frac{N_{ref}}{N_i} = \left(\frac{CSR_{ref}}{CSR_i}\right)^{-1/b} = \left(\frac{CSR_i}{CSR_{ref}}\right)^{1/b}$$
$$\Downarrow \tag{7-9}$$
$$N_{eq} = \sum_{i=1}^{m} n_i \,.\, \frac{N_{ref}}{N_i} = \sum_{i=1}^{m} n_i \left(\frac{CSR_i}{CSR_{ref}}\right)^{1/b}$$

Where n_i is the number of full cycles applied at amplitude CSR_i prior to triggering; CSR_i is the cyclic stress ratio amplitude of the i^{th} counted cycle (pre-trigger); CSR_{ref} is the chosen reference CSR for the equivalent uniform series; and b is the exponent from the fitted LRC $CSR{=}aN^{-b}$.

This approach, was then widely validated for soil liquefaction by researchers, e.g., Annaki & Lee (1977), Green & Terri (2005), in which liquefaction is treated as a fatigue process where damage accumulates linearly from each individual loading cycle.

Green & Terri (2005) stated that liquefaction triggering assessments often require converting irregular earthquake stress histories into an equivalently damaging set of uniform cycles, an issue analogous to variable-amplitude fatigue in metals, where cumulative damage concepts were first developed. Building on Seed's adaptation of the Palmgren–Miner hypothesis for liquefaction, the authors proposed an energy-based implementation in which the equivalent number of cycles is obtained by equating the dissipated energy of the irregular and uniform motions, thereby directly incorporating the nonlinear stress–strain response of the soil.

In the current study, to facilitate a direct comparison with the cyclic triaxial CTx data, the irregular centrifuge time histories had to be converted into an equivalent number of uniform cycles N_{eq} at a standardized reference stress amplitude CSR_{ref}. Accordingly, the cumulative fatigue damage framework, expressed in equation (7-9) was employed to evaluate the equivalent cycles required to trigger liquefaction. Within this formulation, the pre-triggering CSR peak amplitudes extracted from the centrifuge records define the set of individual stress cycles CSR_i utilized in the variable-amplitude damage summation.

Rather than selecting a steady-state CSR amplitude from the CSR(t), CSR_{ref} was rigorously defined as the Cyclic Stress Ratio required to trigger liquefaction in 15 cycles (CSR_{15}), as determined directly from the performed Cyclic Triaxial CTx Liquefaction Resistance Curve for Hostun sand. The selection of N=15 is the established benchmark in geotechnical earthquake engineering, representing the equivalent cyclic demand of a baseline Mw = 7.5 earthquake (Idriss, 1999).

For each shaking event, N_{eq} was computed cycle by cycle for the pre-liquefaction triggering portion of the CSR(t) record by applying the cumulative-damage/equivalent-cycles formulation (7-9).

For a given cycle i, the cycle amplitude CSR_i was computed as the average peak to peak CSR for that cycle and substituted, together with the selected reference level CSR_{15}, to get the equivalent number of uniform cycles contributed by that cycle, $N_{eq,i}$. The total equivalent number of cycles for the shaking event was then obtained by summing the contributions over all pre-liquefaction cycles.

As such, CSR_{ref} (15) is the CSR at N_L=15 cycles from the LRC of the CTx after the conversion to DSS. Consequently, the specific weighting function used to compute N_{eq} was done using equation (7-10).

$$N_{eq} = \sum_{i=1}^{m} n_i \left(\frac{CSR_i}{CSR_{15}}\right)^{1/b} \tag{7-10}$$

To accurately extract the reference cyclic stress ratio at 15 cycles, CSR_{15} from the liquefaction resistance curve LRC derived from cyclic triaxial CTx tests on Hostun HN31 sand, and to ensure mechanical compatibility within the damage summation framework (CSR_i / CSR_{15}), both the numerator and denominator must represent identical stress states and loading paths. Consequently, the baseline cyclic stress ratio CSR_{15} obtained directly from the CTx testing cannot be utilized directly as the reference capacity CSR_{ref}. Instead, this value must be corrected to reflect equivalent centrifuge simple shear conditions at the specific prototype depth, applying the conversion detailed in equation (7-11).

$$CSR_{ref} = CSR_{15(CTx)} \cdot C_r \cdot K_{\sigma} \tag{7-11}$$

Where C_r is the established correction factor between simple shear and axisymmetric triaxial loading, and K_σ is the overburden correction factor to account for the difference in initial effective vertical stress between the CTx performed at 100 kPa initial mean effective stress and the shallow 1.2 m depth of the centrifuge model. Using this corrected CSR_{ref} ensures that the variable amplitude centrifuge CSR peaks are normalized against the true in-situ baseline resistance.

To address this, the laboratory LRC (CSR values) resulting from the undrained CTx tests were firstly converted to the equivalent direct simple shear cyclic resistance. A commonly adopted correction factor utilizes the lateral earth-pressure coefficient at rest (K_o), expressed in equations (7-12) and (7-13), (Castro, 1975).

$$C_r = \frac{2(1 + 2K_o)}{3\sqrt{3}} \tag{7-12}$$

$$K_o = 1 - sin\Phi'_{cv} \tag{7-13}$$

The resulting equivalent direct simple shear cyclic resistance correction factor was 0.73. The LRC trend was then corrected by the overburden correction factor K_σ. Boulanger & Idriss (2016) used a formula shown in equation (7-14) where, C_σ is given by equation (7-15):

$$K_\sigma = 1 - C_\sigma \, ln\left(\frac{\sigma'_v}{p_a}\right) \leq 1.1 \tag{7-14}$$

$$C_\sigma = \frac{1}{37.3 - 8.27\,(q_{c1Ncs})^{0.264}} \leq 0.3 \tag{7-15}$$

For the CTx interpretation in this study, a clean sand, overburden-normalized cone resistance of q_{c1Ncs}=95.5 was adopted. This value was back calculated to be consistent with the target relative density used in the CTx (Dr_{avg}= 53%), using the empirical Dr–q_{c1NCS} correlation, expressed as in equation (7-16).

$$D_r = 0.465\left(\frac{q_{c1Ncs}}{0.9}\right)^{0.264} - 1.063 \tag{7-16}$$

In addition, Youd & Idriss (2001) adopted an overburden correction factor K_σ to account for the nonlinear dependence of cyclic resistance on effective overburden stress, normalizing to an atmospheric pressure of p_a≈100kPa. The mathematical formula for this factor was previously introduced in equation (2-4). For the current analysis, the empirical exponent n was assigned a value of 0.75, which corresponds to a soil relative density Dr of 50%.

The final expressions for the fully converted cyclic stress ratio CSR are presented in Table 7-1. Specifically, $CSR_{DSS(1)}$ represents the equivalent direct simple shear DSS stress ratio derived from the cyclic triaxial CTx data, utilizing the Cr correction factor and the K_σ correction factor recommended by Youd & Idriss (2001). Alternatively, $CSR_{DSS(2)}$ represents the equivalent DSS stress ratio using the Cr in addition to the K_σ factor adopted from Boulanger & Idriss (2016).

Table 7-1 Correction factors (C_r and K_σ) for converting cyclic stress ratios from triaxial (CSR_{CTX}) to direct simple shear (CSR_{DSS}) conditions.

Cr	K_σ		Correction value	CSR_{DSS}
0.73	Youd & Idriss (2001)	1.736	1.27	$CSR_{DSS(1)}=CSR_{CTx}*1.27$
0.73	Boulanger & Idriss (2016)	1.23	0.9	$CSR_{DSS(2)}=CSR_{CTx}*0.9$

The formulation by Youd & Idriss (2001) was adopted for this analysis because the more recent Boulanger & Idriss (2016) formula would have introduced probable uncertainties into the analysis, due to the absence of direct CPT measurements in the current study.

Consequently, the reference CSR (CSR_{ref}) used to calculate N_{eq} is defined as the $CSR_{DSS(1)}$ value at 15 cycles. It is important to note that, within this context, the CSR required to trigger liquefaction is synonymous with the soil's cyclic resistance ratio CRR.

Table 7-2 summarizes the individual cyclic stress ratio CSR_i amplitudes recorded for each loading cycle prior to liquefaction triggering for the three shakes. Furthermore, it presents the computed equivalent number of uniform cycles N_{eq} required to trigger liquefaction at the specified reference stress level CSR_{ref}, derived from this variable amplitude sequence.

Table 7-2 CSRi, CSRref, and resulting ∑Neq for the three shakes EQ1.1, EQ1.2, and EQ1.3

Shake#	Cycle #	$CSR_{peak(+)}$	$CSR_{peak(-)}$	$CSR_i=CSR_{avg}$ (Peak to Peak)	$CSR_{ref(15)}$ from CTx, after correction	$N_{eq/cycle}$	ΣN_{eq}
EQ1.1	1	0.431	0.266	0.348	0.213	12.8	12.8
EQ1.2	1	0.461	0.286	0.374	0.213	18.4	49.3
	2	0.454	0.360	0.407		28.6	
	3	0.127	0.358	0.242		1.95	
	4	0.087	0.231	0.159		0.22	
	5	0.107	0.179	0.143		0.12	
	6	0.078	0.129	0.104		0.025	
EQ1.3	1	0.356	0.290	0.323	0.213	8.7	117.2
	2	0.491	0.495	0.493		77.2	
	3	0.301	0.509	0.405		27.97	
	4	0.163	0.374	0.268		3.3	

Figure 7-4 presents the liquefaction resistance curves LRC for fully saturated Hostun sand HN31 before and after the conversions. The black curve corresponds to the original CTx-LRC(without corrections), previously shown in Figure 5-54. The red curve $LRC_{DSS(1)}$ represents the adopted DSS-equivalent resistance corrected via Youd & Idriss (2001) while the grey curve $LRC_{DSS(2)}$ shows the alternative correction using Boulanger & Idriss (2016).

In addition, the plot includes the three discrete data points, which represent the computed seismic demand N_{eq} versus CSR_{ref} for the three centrifuge shaking events applied on Model M1 at varying degrees of saturation Sr.

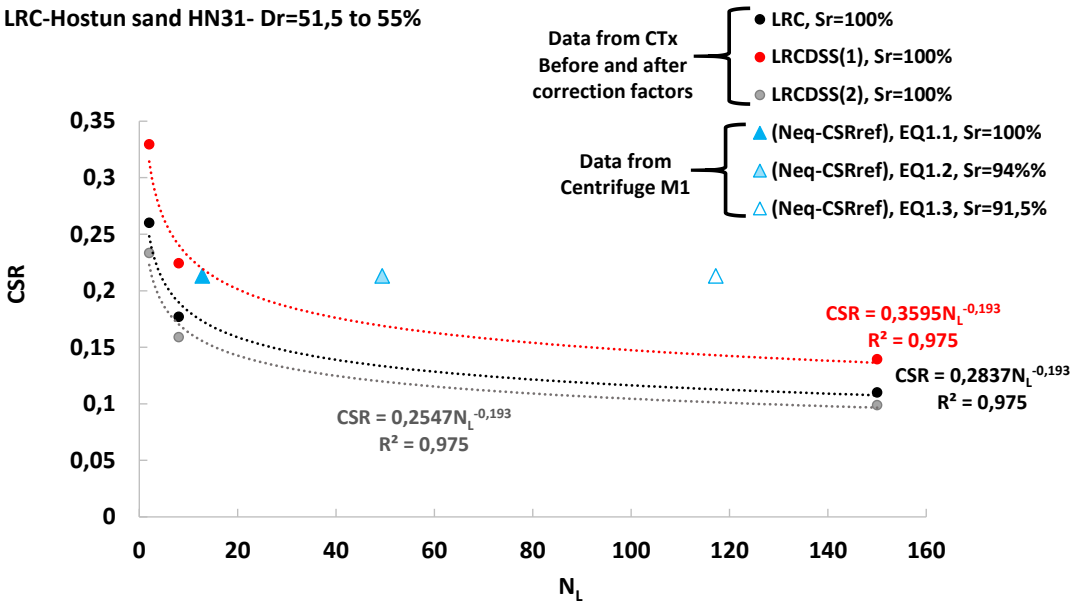

Figure 7-4 Liquefaction resistance curves (LRC) for fully saturated Hostun sand (HN31) before and after the loading type and overburden pressure correction in addition to N_{eq} at CSR_{ref} of the three points computed for the three centrifuge shaking events

Figure 7-4 presents a comparative validation of the soil liquefaction resistance for Hostun sand HN31, contrasting the dynamic centrifuge test results with the cyclic triaxial CTx data. As illustrated, applying the Cr along with the K_σ correction factors proposed by Boulanger & Idriss (2016) to the CTx data yielded a lower cyclic resistance than the original, uncorrected LRC. Conversely, applying the K_σ correction factors from Youd & Idriss (2001) produced a higher cyclic resistance than the original curve.

The liquefaction resistance from the centrifuge tests were projected onto this plot as discrete data points N_{eq} versus CSR_{ref}. As established, the reference CSR_{ref} was selected to be the 15th cycle capacity of the Youd & Idriss (2001) corrected curve $LRC_{DSS(1)}$. For the fully saturated baseline event (EQ1.1, plotted as a blue triangle), the computed demand N_{eq} was 12.8, demonstrated an excellent agreement with the $LRC_{DSS(1)}$ capacity curve.

Furthermore, the data clearly illustrates that introducing partial saturation significantly enhances the soil liquefaction resistance. Evaluated at the exact same CSR_{ref}, the slightly desaturated event EQ1.2, (Sr = 94%) resisted an equivalent N_{eq} = 49.3 cycles. Finally, the most desaturated event EQ1.3 (Sr = 91.5%) exhibited the highest overall resistance, enduring N_{eq} = 117.2 cycles before liquefaction.

Figure 7-5 presents the liquefaction resistance curve (LRC) for fully saturated Hostun sand after applying the loading-type and overburden-pressure corrections based on Youd & Idriss (2001). Superimposed on the LRC are three discrete data points representing the computed seismic demand, expressed as N_{eq} versus CSR_{ref}, for the three shaking events applied to centrifuge Model M1 at different degrees of saturation, Sr. Two estimated curves were also drawn through the points corresponding to Eq1.2 and Eq1.3, for visual approximation only. The comparison indicates reasonable agreement between the cyclic triaxial and centrifuge modelling approaches, supporting their combined use for liquefaction analysis.

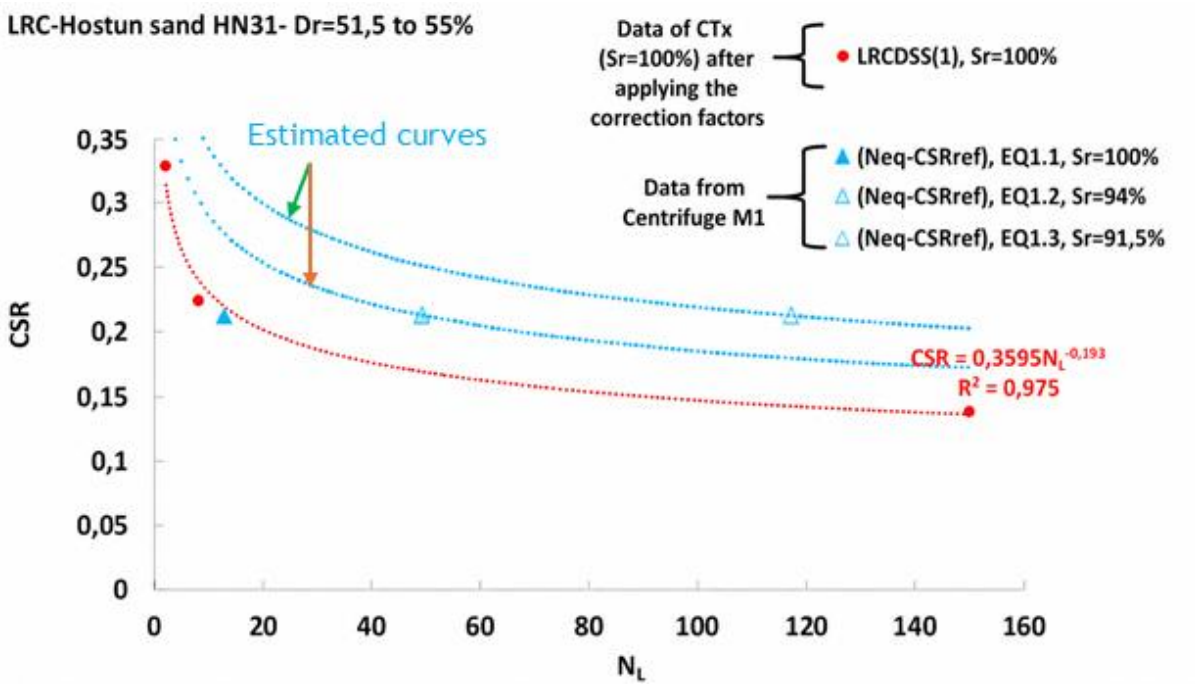

Figure 7-5 Liquefaction resistance curve (LRC) for fully saturated Hostun sand (HN31) after the loading type and overburden pressure correction in addition to N_{eq} at CSR_{ref} of the three points computed for the three centrifuge shaking events

This analysis demonstrates that the Youd & Idriss (2001) overburden pressure correction factor framework is highly appropriate for converting CTx data to DSS-equivalent conditions for this specific sand. Furthermore, the excellent agreement between the fully saturated centrifuge response EQ1.1 and the corrected laboratory curve serves as a robust validation of both the adopted correction factors and the accumulated fatigue damage procedure utilized to calculate N_{eq}.

8. Conclusions

8.1. Key findings

The conclusions derived from this research have been systematically presented at the end of each chapter.

The following highlights summarize and consolidate the main contributions of this document, demonstrating that the objectives of the research were achieved and that induced partial saturation (IPS) was critically assessed across different experimental approaches.

Selection and rationale of IPS

- Based on the reviewed body of literature on liquefaction mitigation, a comparative table of advantages and disadvantages was developed; this synthesis supported the selection of IPS as the most suitable technique among the reviewed options, given its capacity to enhance liquefaction resistance primarily through modification of the pore-fluid response while remaining a practical countermeasure in many applications.

Material and methods

- Two sands were employed: (i) NB sand, a Portuguese sand from the North Benavente area with historical evidence of liquefaction and high susceptibility; and (ii) Hostun sand HN31, a widely used reference sand to support benchmarking and broader comparability. The determination of key physical properties provided the basis for defining specimen state and calculating relative density and other essential parameters in the subsequent monotonic, cyclic, and centrifuge investigations.

- The experimental program procedures and used equipment and apparatus were reported, showing the level of accuracy, consistency, and repeatability across all campaigns, from physical characterization to advanced element testing and centrifuge modelling complemented with seismic wave testing.

Element testing findings

- Undrained monotonic behavior was evaluated under both fully and partially saturated conditions using (i) a conventional triaxial system and (ii) a double-wall (double-cell) apparatus, the latter adopted to reduce compliance effects and enable improved control and/or assessment of specimen volumetric change. From the monotonic tests, the critical state parameters of NB sand were determined and compared with published studies, and the sensitivity of computed critical state parameters to saturation condition was evaluated. In addition, the volumetric strain response, pore pressure build-up and confining effective stress evolution during compression loading was assessed across saturation levels.

- Undrained monotonic shearing in the unsaturated triaxial apparatus demonstrated that the partially saturated specimens developed volumetric strains due to the compressibility of occluded air bubbles, which limited excess pore-pressure build-up.

- The cyclic triaxial testing results of both sands showed that small decreases in Sr resulted in a marked improvement in cyclic resistance, expressed by slower excess pore-pressure accumulation, delayed the loss of effective stress, and hence an increase in the number of cycles required to trigger liquefaction at comparable CSR. The role of pore-fluid compressibility provides a direct mechanism for this behavior: part of the cyclic volumetric tendency is accommodated through gas compression rather than being converted entirely into excess pore-pressure build-up.

- Since void ratio has a strong influence on cyclic resistance, volumetric water content θ is an integrative parameter for the liquefaction assessment as it combines the effects of e and Sr.

- The wave-based observations supported the interpretation of saturation effects on small-strain stiffness: at comparable soil state and mean effective stress, dry conditions yielded higher S-wave velocities, resulting in slightly higher small-strain stiffness than under saturated conditions, indicating contact-level effects associated with wetting/saturation that can reduce interparticle contact stiffness. More importantly, P-wave velocity was strongly governed by the degree of saturation, as even small amounts of occluded air within the pore fluid increase the compressibility of the pore medium and produce a clear reduction in wave propagation velocity.

- Beyond delaying liquefaction, IPS altered the broader cyclic response, where the stress-path (p´-q response) under nominally undrained conditions shifted toward drained/partially drained-like characteristics due to the increased compressibility of the pore-fluid mixture.

- Based on the performed incremental stress-controlled undrained cyclic triaxial tests and evaluating the shear stress and strain behavior, partially saturated specimen developed larger shear strains than fully saturated specimen under the same loading steps and void ratios. This led to higher dissipated energy and higher maximum stored strain energy, and consequently to lower cycle-specific secant stiffness. Although the partially saturated specimen showed lower initial secant stiffness, its stiffness degradation was more gradual. In contrast, the fully saturated specimen started with higher stiffness but degraded more rapidly as liquefaction approached. Throughout the test, the fully saturated specimen generally maintained higher secant stiffness until it's liquefaction, but this was accompanied by faster pore pressure build-up and earlier loss of effective stress. The damping ratio of the partially saturated specimen was lower, despite the increase in dissipated energy, because the increase in maximum stored strain energy was proportionally larger than the increase in dissipated energy.

- Importantly, the larger shear strains and lower secant stiffness in the partially saturated specimen occurred while mean effective stress was better maintained and excess pore pressure ratio r_u, remained significantly lower than in the fully saturated specimen. This confirms that induced partial saturation modifies the cyclic response

mainly through increased pore fluid compressibility, allowing deformation to develop without rapid degradation of effective stress. This behaviour contrasts with suction-controlled unsaturated soils, where matric suction generally increases stiffness and reduces strain development under comparable loading conditions. In the present case, the specimen was partially saturated through the introduction of occluded air bubbles, with negligible suction effects; therefore, the dominant mechanism was the increased compressibility of the pore-fluid mixture rather than suction-induced stiffening.

Centrifuge modelling

- Dynamic centrifuge modelling extended the assessment of IPS to representative stress levels and boundary conditions, showing that even modest reductions in Sr led to lower peak excess pore-pressure ratios and improved liquefaction resistance at depth, including when input motion intensity was increased; IPS also delayed pore-pressure generation in time, reflecting the higher pore-fluid compressibility when gas is present.

- Arias intensity provided a more representative measure than PGA alone for assessing attenuation and amplification along the soil profile, because it accounts for the cumulative energy content of the input motion. The resulting profiles showed that induced partial saturation reduced the intensity of the upward-propagating acceleration intensity relative to the fully saturated case.

- Settlement response in centrifuge tests was reduced on average under IPS, while the benefit diminished as shaking amplitude increased.

- Bender element implementation in the centrifuge demonstrated strong potential for monitoring stiffness and saturation-related trends during dynamic testing: (i) measured V_p in fully saturated conditions remained near the expected saturated-water limit and showed limited sensitivity to receiver depth, supporting measurement reliability; (ii) the evolution of Vs with increasing confining stress followed typical power-law behavior for sands; and (iii) the system remained functional under high-g conditions.

- At the mid-depth and deeper layers, under comparable PGA levels, the partially saturated shakes showed larger shear-strain development and higher dissipated energy, which corresponded to a reduction in cycle-specific secant stiffness relative to the fully saturated condition.

- Arias intensity and shear stress–strain analyses provided complementary evidence of the effects of IPS under different saturation scenarios. The Arias intensity profiles showed that partially saturated conditions reduced the intensity of upward-propagating acceleration relative to the fully saturated case, while the shear stress strain loops highlighted the lower secant stiffness and greater deformability of the partially saturated soil.

- Collectively, the laboratory and centrifuge evidence showed that IPS modifies the liquefaction response through coupled pore-pressure, deformation, stiffness, energy-dissipation, and wave-propagation mechanisms. The main contribution of this

study is showing that IPS altered the liquefaction behavior by increasing the compressibility of the pore-fluid mixture, it reduces and delays excess pore-pressure build-up, limits the rapid loss of mean effective stress, and attenuates upward-propagating seismic motion, while allowing larger cyclic shear strains to develop. Consequently, the partially saturated soil exhibited a more deformable response, with lower cycle-specific secant stiffness and lower damping ratio, even though liquefaction was delayed compared with the fully saturated condition. Figure 8-1 provides a conceptual illustration summarizing the dynamic response of partially saturated sands under undrained conditions, based on the findings of the present study.

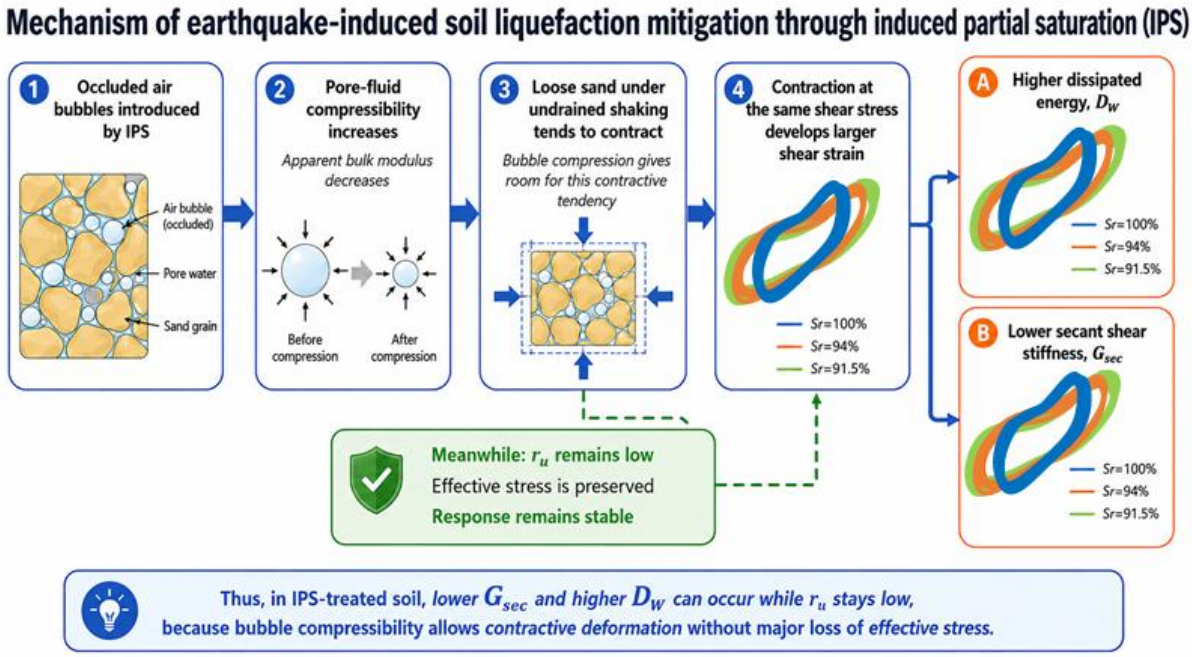

Figure 8-1 illustrative summary of the dynamic behaviour of partially saturated sands under undrained conditions as observed in the present study.

- These observations prove that IPS was more effective in the medium and deeper zones (closer to the air injector) and support prioritizing injection strategies that improve gas delivery and persistence in the upper layers (e.g., adjusted injection depths, staged treatment, or layering). Overall, the results point to IPS as a promising depth-targeted mitigation tool, capable of reducing transmitted energy and pore-pressure build-up at relevant depths while highlighting the need for enhanced near-surface gas retention to achieve uniform performance.

Linking cyclic triaxial testing and centrifuge modelling

- A methodology was proposed to integrate cyclic triaxial testing and centrifuge modelling for liquefaction analysis. The results showed good agreement between the two testing approaches, demonstrating that the cyclic triaxial data can be meaningfully linked to the centrifuge response for assessing liquefaction resistance.

8.2. Future work

After the detailed investigation undertaken in the current study, the following complementary research is proposed for future work, ranging from experimental to numerical to field implementation studies:

- Centrifuge modelling and field testing: conduct centrifuge tests and in-situ experiments to quantify the durability and time-dependent stability of occluded air bubbles (including dissipation, redistribution, and re-saturation mechanisms) under representative stress states and dynamic loading.
- Soil–structure interaction: future studies should repeat the investigation under soil–structure interaction conditions, rather than free-field conditions, to assess how the presence of a structure may influence the observed IPS-induced alterations in the dynamic properties of sands.
- Numerical assessment of stiffness and damping evolution: develop and validate numerical models to assess the evolution of damping and stiffness in partially saturated sands.
- Numerical analysis: future numerical studies on partially saturated soils should account for the IPS-induced alterations in the dynamic response of sandy soils, including changes in Arias intensity, damping ratio, and secant stiffness. The observed reduction in upward-propagating acceleration intensity under partially saturated conditions should also be considered in soil–structure interaction analyses, where structural loading may modify the local stress state and deformation response.
- Soil profile liquefaction resistance: produce formulas and relationships to account for the depth nonlinearity, considering partial saturation state (occluded air bubbles) in the estimate of liquefaction resistance.
- Empirical equations: generate empirical models to predict the liquefaction resistance of partially saturated granular soils with minimum number of required tests.
- Quantification of air-bubble distribution and homogeneity for in situ implementation: characterize the spatial distribution of occluded air to evaluate the uniformity of desaturation within the treated zone and identify preferential pathways or clustering.
- Optimization of injection configuration for in situ implementation: study the air-injection system (e.g., injection points, spacing, flow rate, pressure boundary conditions) to identify optimum injection location(s) that maximize desaturation efficiency and uniformity while minimizing disturbance.

References

A Hashash, Y. M., Phillips, C., Groholski, D. R., A, Y. M., & A Hashash Camilo Phillips, Y. M. (2010). *Mine Scholars' Mine International Conferences on Recent Advances in Geotechnical Earthquake Engineering and Soil Dynamics* (Vol. 8). https://scholarsmine.mst.edu/icrageesd/05icrageesd/session12/8

Akbas, M., Subasi, O., & Iyisan, R. (2023). The effect of RCA pavements on the liquefaction-induced settlement. *Scientific Reports*, *13*(1). https://doi.org/10.1038/s41598-023-34239-z

Altuhafi, F., O'Sullivan, C., & Cavarretta, I. (2013). Analysis of an image-based method to quantify the size and shape of sand particles. *Journal of Geotechnical and Geoenvironmental Engineering*, *139*(8), 1290–1307.

Amanta, A. S., & Dasaka, S. M. (2021). Air injection method as a liquefaction countermeasure for saturated granular soils. *Transportation Geotechnics*, *30*. https://doi.org/10.1016/j.trgeo.2021.100622

Amanta, A. S., & Dasaka, S. M. (2023). Particle Size Effect of Tire Derivative on the Dynamic Properties and Liquefaction Behavior of Sand Mixed with Tire Derivatives. *International Conference on Construction Resources for Environmentally Sustainable Technologies*, 85–93.

Annaki, M., & Lee, K. L. (1977). Equivalent uniform cycle concept for soil dynamics. *Journal of the Geotechnical Engineering Division*, *103*(6), 549–564.

Astuto, G., Molina-Gomez, F., Bilotta, E., Viana da Fonseca, A., & Flora, A. (2023). Some remarks on the assessment of P-wave velocity in laboratory tests for evaluating the degree of saturation. *Acta Geotechnica*, *18*(2), 777–790.

Atkinson, J. (2017). *The mechanics of soils and foundations*. CRC press.

Bahadori, H., & Manafi, S. (2015). Effect of tyre chips on dynamic properties of saturated sands. *International Journal of Physical Modelling in Geotechnics*, *15*(3), 116–128. https://doi.org/10.1680/jphmg.13.00014

Banerjee, A., Puppala, A. J., & Hoyos, L. R. (2022). Liquefaction assessment in unsaturated soils. *Journal of Geotechnical and Geoenvironmental Engineering*, *148*(9), 04022067.

Bao, X., Jin, Z., Cui, H., Chen, X., & Xie, X. (2019). Soil liquefaction mitigation in geotechnical engineering: An overview of recently developed methods. *Soil Dynamics and Earthquake Engineering*, *120*(February), 273–291. https://doi.org/10.1016/j.soildyn.2019.01.020

Bayat, E. E., Yegian, M. K., Alshawabkeh, A., & Gokyer, S. (2009). *A NEW mitigation technique for preventing liquefaction-induced building Damages during earthquakes*.

Baziar, M. H., Jafarian, Y., Shahnazari, H., Movahed, V., & Amin Tutunchian, M. (2011). Prediction of strain energy-based liquefaction resistance of sand-silt mixtures: An evolutionary approach. *Computers and Geosciences*, *37*(11), 1883–1893. https://doi.org/10.1016/j.cageo.2011.04.008

Bernal-Sanchez, J., McDougall, J., Barreto, D., Dimitriadi, V., Leak, J., & Anbazhagan, P. (2025). Influence of rubber content and particle morphology on the dynamic behaviour,

liquefaction susceptibility and internal stability of shredded rubber-sand mixtures. *Geosynthetics International*, 1–21.

Berrill,] B, & Davrs, R. 0. (1985). ENERGY DISSIPATION AND SEISMIC LIQUEFACTION OF SANDS: REVISED MODEL. In *SOILS AND FOUNDATIONS* (Vol. 25, Number 2).

Berrill, J. B., & Davis, R. O. (1985). Energy Dissipation and Seismic Liquefaction of Sands: Revised Model. *Soils and Foundations*, *25*(2), 106–118. https://doi.org/10.3208/sandf1972.25.2_106

Bicalho, K. V., Correia, A. G., Ferreira, S., Fleureau, J.-M., & Marinho, F. (2007). Filter paper method of soil suction measurement. *Proceedings of 13th Panamerican Conference on Soil Mechanics and Geotechnical Engineering, Isla Margarita, Venezuela*, 215–219.

Biglari, M., Jafari, M. K., Shafiee, A., Mancuso, C., & d'Onofrio, A. (2011). Shear modulus and damping ratio of unsaturated kaolin measured by new suction-controlled cyclic triaxial device. *Geotechnical Testing Journal*, *34*(5), 525–536.

Biot, M. A. (1956). Theory of propagation of elastic waves in a fluid-saturated porous solid. II. Higher frequency range. *The Journal of the Acoustical Society of America*, *28*(2), 179–191.

Bishop, A. W. (1959). The principal of effective stress. *Teknisk Ukeblad*, *39*, 859–863.

Bolton Seed, H., Tokimatsu, K., Harder, L. F., & Chung, R. M. (1985). Influence of SPT procedures in soil liquefaction resistance evaluations. *Journal of Geotechnical Engineering*, *111*(12), 1425–1445.

Boulanger, R. W., & Idriss, I. M. (2016). CPT-based liquefaction triggering procedure. *Journal of Geotechnical and Geoenvironmental Engineering*, *142*(2), 04015065.

Cappellaro, C. (2019). *The influence of fines content, fabric and layered structure on the undrained cyclic behaviour of Christchurch sandy soils*.

Casagrande, A. (1936). Characteristics of cohesionless soils affecting the stability of slopes and earth fills. *J. Boston Society of Civil Engineers*, *23*(1), 13–32.

Castro, G. (1975). Liquefaction and cyclic mobility of saturated sands. *Journal of the Geotechnical Engineering Division*, *101*(6), 551–569.

Chandler, R. J., Crilly, M. S., SMITH, M., Smith, M. G., & E, B. R. (1992). A low-cost method of assessing clay desiccation for low-rise buildings. *Proceedings of the Institution of Civil Engineers-Civil Engineering*, *92*(2), 82–89.

Chandler, R. J., & Gutierrez, C. I. (1986). The filter-paper method of suction measurement. *Géotechnique*, *36*(2), 265–268.

Chavan, D., Sitharam, T. G., & Anbazhagan, P. (2022). Liquefaction resistance and cyclic response of air injected-desaturated sandy soil. *Geotechnical and Geological Engineering*, *40*(4), 1851–1872.

Chen, R., Chen, Y., Liu, H., Zhang, K., Zhou, Y., Xu, S., & Wu, K. (2021). In situ desaturation tests by electrolysis for liquefaction mitigation. *Canadian Geotechnical Journal*, *58*(11), 1744–1756. https://doi.org/10.1139/cgj-2020-0580

Cho, G.-C., Dodds, J., & Santamarina, J. C. (2007). Closure to “particle shape effects on packing density, stiffness, and strength: natural and crushed sands” by Gye-Chun Cho, Jake Dodds, and J. Carlos Santamarina. *Journal of Geotechnical and Geoenvironmental Engineering*, *133*(11), 1474.

Chowdepalli, B., Rathore, A. S., & Watanabe, K. (2025). Cyclic behavior of unsaturated sandy soil: effects of compaction, saturation, and suction under traffic-like loading. *Geotechnical and Geological Engineering*, *43*(8), 423.

Chu, J. (2013). Innovation in disaster mitigation technologies. In *Geotechnical Predictions and Practice in Dealing with Geohazards* (pp. 375–384). Springer.

Chung, R. M., Yokel, F. Y., & Drnevich, V. P. (1984). Evaluation of dynamic properties of sands by resonant column testing. *Geotechnical Testing Journal*, *7*(2), 60–69.

Conlee, C. T., Gallagher, P. M., Boulanger, R. W., & Kamai, R. (2012). Centrifuge Modeling for Liquefaction Mitigation Using Colloidal Silica Stabilizer. *Journal of Geotechnical and Geoenvironmental Engineering*, *138*(11), 1334–1345. https://doi.org/10.1061/(asce)gt.1943-5606.0000703

Contreras-Ferreyra, D. U., Chávez-Negrete, C., & Martínez-Rojas, A. (2026). Assessment of Seismic Wave Velocities in Unsaturated Granular Soils Using Low-Cost Piezoelectric Sensors. *Geotechnical and Geological Engineering*, *44*(1), 15.

Costa, C. F. G. da. (2009). *Desenvolvimento de um sistema de monitorização e controlo para ensaios triaxiais de solos*.

DeJong, J. T., Fritzges, M. B., & Nüsslein, K. (2006). Microbially Induced Cementation to Control Sand Response to Undrained Shear. *Journal of Geotechnical and Geoenvironmental Engineering*, *132*(11), 1381–1392. https://doi.org/10.1061/(asce)1090-0241(2006)132:11(1381)

Dobry, R., & Ladd, R. S. (1980). Discussion of “Soil Liquefaction and Cyclic Mobility Evaluation for Level Ground during Earthquakes and Liquefaction Potential: Science Versus Practice.” *Journal of the Geotechnical Engineering Division*, *106*(6), 720–724.

Dobry, R., Ladd, R. S., Yokel, F. Y., Chung, R. M., & Powell, D. (1982). *Prediction of pore water pressure build-up and liquefaction of sands during earthquakes by the cyclic strain method* (Vol. 138). National Bureau of Standards Gaithersburg, MD.

El Mohtar, C. S., Bobet, A., Drnevich, V. P., Johnston, C. T., & Santagata, M. C. (2014). Pore pressure generation in sand with bentonite: From small strains to liquefaction. *Geotechnique*, *64*(2), 108–117. https://doi.org/10.1680/geot.12.P.169

El Mohtar, C. S., Bobet, A., Santagata, M. C., Drnevich, V. P., & Johnston, C. T. (2013). Liquefaction Mitigation Using Bentonite Suspensions. *Journal of Geotechnical and Geoenvironmental Engineering*, *139*(8), 1369–1380. https://doi.org/10.1061/(asce)gt.1943-5606.0000865

Emerson, M., & Foray, P. (2006). Laboratory P-wave measurements in dry and saturated sand. *Acta Geotechnica*, *1*(3), 167–177.

Eseller-Bayat, E., Yegian, M. K., Alshawabkeh, A., & Gokyer, S. (2013). Liquefaction Response of Partially Saturated Sands. I: Experimental Results. *Journal of Geotechnical and Geoenvironmental Engineering*, *139*(6), 863–871. https://doi.org/10.1061/(asce)gt.1943-5606.0000815

Eyo, E. U., Ng'ambi, S., & Abbey, S. J. (2022). An overview of soil–water characteristic curves of stabilised soils and their influential factors. *Journal of King Saud University-Engineering Sciences*, *34*(1), 31–45.

Ferreira, C., Díaz-Durán, F., Viana da Fonseca, A., & Cascante, G. (2021). New approach to concurrent Vs and Vp measurements using bender elements. *Geotechnical Testing Journal*, *44*(6), 1801–1820.

Flavigny, E., Desrues, J., & Palayer, B. (1990). Note technique: le sable d'Hostun «RF». *Revue Française de Géotechnique*, (53), 67–70.

Flora, A., Bilotta, E., Chiaradonna, A., Lirer, S., Mele, L., & Pingue, L. (2021a). A field trial to test the efficiency of induced partial saturation and horizontal drains to mitigate the susceptibility of soils to liquefaction. *Bulletin of Earthquake Engineering*, *19*(10), 3835–3864. https://doi.org/10.1007/s10518-020-00914-z

Flora, A., Bilotta, E., Chiaradonna, A., Lirer, S., Mele, L., & Pingue, L. (2021b). A field trial to test the efficiency of induced partial saturation and horizontal drains to mitigate the susceptibility of soils to liquefaction. *Bulletin of Earthquake Engineering*, *19*, 3835–3864.

Flora Alessandro, Bilotta Emilio, Lirer Stefania, Mele Lucia, & Modoni Giuseppe. (2023). Liquefaction mechanisms and mitigation techniques. *Rivista Italiana Di Geotecnica*, 33–88.

Foti, S., Lai, C. G., & Lancellotta, R. (2002). Porosity of fluid-saturated porous media from measured seismic wave velocities. *Géotechnique*, *52*(5), 359–373.

Fredlund, D. G., & Xing, A. (1994). Equations for the soil-water characteristic curve. *Canadian Geotechnical Journal*, *31*(4), 521–532.

Gallagher, P. M., & Lin, Y. (2005). Column testing to determine colloidal silica transport mechanisms. In *Innovations in grouting and soil improvement* (pp. 1–10).

Gallagher, P. M., Pamuk, A., & Abdoun, T. (2007). Stabilization of liquefiable soils using colloidal silica grout. *Journal of Materials in Civil Engineering*, *19*(1), 33–40.

Gomes, A. M. T. (2008). *Poços elípticos pelo método de escavação sequencial na vertical: o caso do Metro do Porto*.

Gómez, F. A. M. (2023). *Liquefaction resistance assessment of the TP-Lisbon sand in partially saturated conditions: experimental evidence and physical modelling validation*.

Green, R. A. (2001). Energy-based evaluation and remediation of liquefiable soils [Ph. D. thesis]: Blackburg. *Virginia, Virginia Tech*.

Green, R. A., & Terri, G. A. (2005). Number of equivalent cycles concept for liquefaction evaluations—Revisited. *Journal of Geotechnical and Geoenvironmental Engineering*, *131*(4), 477–488.

Grozic, J. L., Robertson, P. K., & Morgenstern, N. R. (1999). The behavior of loose gassy sand. *Canadian Geotechnical Journal*, *36*(3), 482–492.

Gu, X., Yang, J., Huang, M., & Gao, G. (2015). Bender element tests in dry and saturated sand: Signal interpretation and result comparison. *Soils and Foundations*, *55*(5), 951–962.

Hamderi, M., & Gallagher, P. M. (2015). Pilot-scale modeling of colloidal silica delivery to liquefiable sands. *Soils and Foundations*, *55*(1), 143–153. https://doi.org/10.1016/j.sandf.2014.12.011

Hardin, B. O. (1978). The nature of stress-strain behavior for soils. *From Volume I of Earthquake Engineering and Soil Dynamics--Proceedings of the ASCE Geotechnical Engineering Division Specialty Conference, June 19-21, 1978, Pasadena, California. Sponsored by Geotechnical Engineering Division of ASCE in Cooperation With:*, (Proceeding).

Hardin, B. O., & Richart Jr, F. E. (1963). Elastic wave velocities in granular soils. *Journal of the Soil Mechanics and Foundations Division*, *89*(1), 33–65.

Hazarika, H., Hyodo, M., & Yasuhara, K. (2010). *Investigation of Tire Chips-Sand Mixtures As Preventive Measure against Liquefaction*. 338–345. https://doi.org/10.1061/41108(381)44

Hazarika, H., Yasuhara, K., Kikuchi, Y., Karmokar, A. K., & Mitarai, Y. (2010). Multifaceted potentials of tire-derived three dimensional geosynthetics in geotechnical applications and their evaluation. *Geotextiles and Geomembranes*, *28*(3), 303–315. https://doi.org/10.1016/j.geotexmem.2009.10.011

He, J. (2013). *Mitigation of liquefaction of sand using microbial methods*. 879–887.

He, J., & Chu, J. (2014). Undrained Responses of Microbially Desaturated Sand under Monotonic Loading. *Journal of Geotechnical and Geoenvironmental Engineering*, *140*(5), 04014003. https://doi.org/10.1061/(asce)gt.1943-5606.0001082

He, J., Chu, J., & Liu, H. (2014). Undrained shear strength of desaturated loose sand under monotonic shearing. *Soils and Foundations*, *54*(4), 910–916. https://doi.org/10.1016/j.sandf.2014.06.020

He, J., Chu, J., Wu, S. fan, & Peng, J. (2016). Mitigation of soil liquefaction using microbially induced desaturation. *Journal of Zhejiang University: Science A*, *17*(7), 577–588. https://doi.org/10.1631/jzus.A1600241

Houston, S. L., Houston, W. N., & Wagner, A.-M. (1994). Laboratory filter paper suction measurements. *Geotechnical Testing Journal*, *17*(2), 185–194.

Huang, Y., & Wang, L. (2016). Laboratory investigation of liquefaction mitigation in silty sand using nanoparticles. *Engineering Geology*, *204*, 23–32. https://doi.org/10.1016/j.enggeo.2016.01.015

Huang, Y., & Wen, Z. (2015). Recent developments of soil improvement methods for seismic liquefaction mitigation. *Natural Hazards*, *76*(3), 1927–1938. https://doi.org/10.1007/s11069-014-1558-9

Idriss, I. M. (1999). An update to the Seed-Idriss simplified procedure for evaluating liquefaction potential. *Proc., TRB Worshop on New Approaches to Liquefaction, Pubbl. n. FHWA-RD-99-165, Federal Highway Administation*.

Imamura, S., Hirano, T., Yoshino, O., Hagiwara, T., Takemura, J., & Fujii, N. (2022). Chemical grouting as a countermeasure against soil liquefaction of sand with existing oil tanks. In *Physical Modelling in Geotechnics* (pp. 575–580). Routledge. https://doi.org/10.1201/9780203743362-104

Ishihara, K. (1993). Liquefaction and flow failure during earthquakes. *Geotechnique*, *43*(3), 351–451.

Iwasaki, T., Tatsuoka, F., & Takagi, Y. (1978). Shear moduli of sands under cyclic torsional shear loading. *Soils and Foundations*, *18*(1), 39–56.

Jafarzadeh, F., Ahmadinezhad, A., & Sadeghi, H. (2021). Effects of initial suction and degree of saturation on dynamic properties of sand at large strain. *Scientia Iranica*, *28*(1), 156–174.

Jafarzadeh, F., & Sadeghi, H. (2009). Effect of water content on dynamic properties of sand in cyclic simple shear tests. *Proceedings of the International Conference on Performance-Based Design in Earthquake Geotechnical Engineering*, 1–8.

Jafarzadeh, F., & Sadeghi, H. (2012). Experimental study on dynamic properties of sand with emphasis on the degree of saturation. *Soil Dynamics and Earthquake Engineering*, *32*(1), 26–41.

Jamiolkowski, M., Lancellotta, R., & Presti, D. C. F. Lo. (1995). Remarks on the stiffness at small strains of six Italian clays. In *Developments in deep foundations and ground improvement schemes* (pp. 197–216). CRC Press.

Jovcic, V. (2015). *The measurement and interpretation of small strain stiffness of soils*.

Kamai, R., & Boulanger, R. W. (2010). Characterizing localization processes during liquefaction using inverse analyses of instrumentation arrays. *Meso-Scale Shear Physics in Earthquake and Landslide Mechanics*, 219–238.

Kaneko, T., Orense, R. P., Hyodo, M., & Yoshimoto, N. (2013). Seismic Response Characteristics of Saturated Sand Deposits Mixed with Tire Chips. *Journal of Geotechnical and Geoenvironmental Engineering*, *139*(4), 633–643. https://doi.org/10.1061/(asce)gt.1943-5606.0000752

Khalili, N., & Khabbaz, M. H. (2002). A unique relationship for chi for the determination of the shear strength of unsaturated soils. *Geotechnique*, *52*(1), 76–77.

Khan, K. A., Das, S., & Maheshwari, B. K. (2021). Effect of Degree of Saturation on Dynamic Properties of Solani Sand in Small Strain. *Proceedings of the Indian Geotechnical Conference 2019: IGC-2019 Volume IV*, 223–231.

Kim, H., Prezzi, M., & Salgado, R. (2016). Calibration of Whatman Grade 42 filter paper for soil suction measurement. *Canadian Journal of Soil Science*, *97*(2), 93–98.

Kim, J., Won, J., & Park, J. (2021). Effects of water saturation and distribution on small-strain stiffness. *Journal of Applied Geophysics*, *186*, 104278.

Knittel, L., & Lieske, W. (2025). On liquefaction behaviour of partially saturated sand. *Geotechnik*, *48*(1), 26–36.

Kocaman, K., Mele, L., Özocak, A., & Flora, A. (2025). Effect of Matric Suction on Monotonic and Cyclic Behaviour of a Low-Plastic Silty Soil from Sakarya Region. *E3S Web of Conferences*, *642*, 03005.

Kokusho, T. (2024). State of the practice on energy-based liquefaction evaluation and research significance. *AIMS Geosciences*, *10*(4), 792–863.

Krahn, J., & Fredlund, D. G. (1972). On total, matric and osmotic suction. *Soil Science*, *114*(5), 339–348.

Kramer, S. L. (1996a). *Geotechnical earthquake engineering*. Pearson Education India.

Kramer, S. L. (1996b). *Geotechnical earthquake engineering*. Pearson Education India.

Kumar, J., & Madhusudhan, B. N. (2010). Effect of relative density and confining pressure on Poisson ratio from bender and extender elements tests. *Géotechnique*, *60*(7), 561–567.

Le, K., & Ghayoomi, M. (2016). Suction-controlled dynamic simple shear apparatus for measurement of dynamic properties of unsaturated soils. *E3S Web of Conferences*, *9*, 09001.

Le, K. N., & Ghayoomi, M. (2017a). Cyclic direct simple shear test to measure strain-dependent dynamic properties of unsaturated sand. *Geotechnical Testing Journal*, *40*(3), 381–395.

Le, K. N., & Ghayoomi, M. (2017b). Cyclic direct simple shear test to measure strain-dependent dynamic properties of unsaturated sand. *Geotechnical Testing Journal*, *40*(3), 381–395.

Leong, E.-C., Kizza, R., & Rahardjo, H. (2016). *Measurement of soil suction using moist filter paper*.

Lins, Y., Schanz, T., & Fredlund, D. G. (2009). Modified pressure plate apparatus and column testing device for measuring SWCC of sand. *Geotechnical Testing Journal*, *32*(5), 450–464.

Madabhushi, G. (2017). *Centrifuge modelling for civil engineers*. CRC press.

MADABHUSHI, S. P. G., Schofield, A. N., & Lesley, S. (1998). A new stored angular momentum (SAM) based earthquake actuator. *Centrifuge 98*, 111–116.

Madhusudhan, B. N., & Kumar, J. (2013). Damping of sands for varying saturation. *Journal of Geotechnical and Geoenvironmental Engineering*, *139*(9), 1625–1630.

Maher, M. H., Ro, K. S., & Welsh, J. P. (1994). High strain dynamic modulus and damping of chemically grouted sand. *Soil Dynamics and Earthquake Engineering*, *13*(2), 131–138. https://doi.org/10.1016/0267-7261(94)90005-1

Marasini, N. P., & Okamura, M. (2015). Numerical simulation of centrifuge tests to evaluate the performance of desaturation by air injection on liquefiable foundation soil of light structures. *Soils and Foundations*, *55*(6), 1388–1399. https://doi.org/10.1016/j.sandf.2015.10.005

Mele, L., & Flora, A. (2019). On the prediction of liquefaction resistance of unsaturated sands. *Soil Dynamics and Earthquake Engineering*, *125*, 105689.

Mele, L., Lirer, S., & Flora, A. (2022). An energetic interpretation of liquefaction laboratory tests on partially saturated soils. *Journal of Geotechnical and Geoenvironmental Engineering*, *148*(10), 04022082.

Millen, M. D. L., Rios, S., Quintero, J., & da Fonseca, A. V. (2020). Prediction of time of liquefaction using kinetic and strain energy. *Soil Dynamics and Earthquake Engineering*, *128*, 105898.

Milton Miner, B. A., & Monica, S. (1945). *Cumulative Damage in Fatigue*. https://www.tarjomano.com

Mirshekari, M., & Ghayoomi, M. (2017). Centrifuge tests to assess seismic site response of partially saturated sand layers. *Soil Dynamics and Earthquake Engineering*, *94*, 254–265.

Molina-Gómez, F., da Fonseca, A. V., Ferreira, C., & Caicedo, B. (2024). Insights into the assessment and interpretation of earthquake-induced liquefaction in sands under different degrees of saturation. *Earth-Science Reviews*, *258*, 104925.

Molina-Gómez, F., da Fonseca, A. V., & Galindo-Aires, R. (2025). On the undrained cyclic resistance of a partially saturated sand. *E3S Web of Conferences*, *642*, 03021.

Moug, D. M., Sorenson, K. R., Khosravifar, A., Preciado, M., Stallings Young, E., van Paassen, L., Kavazanjian, E., Zhang, B., Stokoe, K. H., Menq, F. M., & Wang, Y. (2022). Field Trials of Microbially Induced Desaturation in Low-Plasticity Silt. *Journal of Geotechnical and Geoenvironmental Engineering*, *148*(11). https://doi.org/10.1061/(asce)gt.1943-5606.0002890

NAGAO, K. (2007). A micro-bubble injection method for a countermeasure against liquefaction. *4th International Conference on Earthquake Geotechnical Engineering, 2007*, *392*.

Nemat-Nasser, S., & Shokooh, A. (1979). A unified approach to densification and liquefaction of cohesionless sand in cyclic shearing. *Canadian Geotechnical Journal*, *16*(4), 659–678.

Nikitas, G., & Bhattacharya, S. (2023). Experimental study on sand-tire chip mixture foundations acting as a soil liquefaction countermeasure. *Bulletin of Earthquake Engineering*, *21*(8), 4037–4063. https://doi.org/10.1007/s10518-023-01667-1

Ochoa-Cornejo, F., Bobet, A., Johnston, C., Santagata, M., & Sinfield, J. V. (2014). Liquefaction 50 years after Anchorage 1964; how nanoparticles could prevent it. *Tenth US National Conference on Earthquake Engineering Frontiers of Earthquake Engineering. Anchorage, Alaska*, 21–25.

Ochoa-Cornejo, F., Bobet, A., Johnston, C. T., Santagata, M., & Sinfield, J. V. (2016). Cyclic behavior and pore pressure generation in sands with laponite, a super-plastic nanoparticle. *Soil Dynamics and Earthquake Engineering*, *88*, 265–279. https://doi.org/10.1016/j.soildyn.2016.06.008

Okamura, M., & Soga, Y. (2006a). Effects of pore fluid compressibility on liquefaction resistance of partially saturated sand. *Soils and Foundations*, *46*(5), 695–700.

Okamura, M., & Soga, Y. (2006b). Effects of Pore Fluid Compressibility on Liquefaction Resistance of Partially Saturated Sand. *Soils and Foundations*, *46*(5), 695–700. https://doi.org/https://doi.org/10.3208/sandf.46.695

Okamura, M., Takebayashi, M., Nishida, K., Fujii, N., Jinguji, M., Imasato, T., Yasuhara, H., & Nakagawa, E. (2011). In-Situ Desaturation Test by Air Injection and Its Evaluation through Field Monitoring and Multiphase Flow Simulation. *Journal of Geotechnical and Geoenvironmental Engineering*, *137*(7), 643–652. https://doi.org/10.1061/(asce)gt.1943-5606.0000483

Okur, V., & Umu, S. U. (2013). Energy approach to unsaturated cyclic strength of sand. *Bulletin of Earthquake Engineering*, *11*(2), 503–519.

Otsubo, M., Towhata, I., Hayashida, T., Liu, B., & Goto, S. (2016). Shaking table tests on liquefaction mitigation of embedded lifelines by backfilling with recycled materials. *Soils and Foundations*, *56*(3), 365–378. https://doi.org/10.1016/j.sandf.2016.04.004

Palmgren, A. (1924). Die Lev/bensdauer von kugellagern. *VDI. Z.*, *68*, 339–341.

Patricia, G. G., & James, M. M. (2002). Influence of colloidal silica grout on liquefaction potential and cyclic undrained behavior of loose sand. *Soil Dynamics and Earthquake Engineering*, *22*(9–12), 1017–1026. https://doi.org/10.1016/s0267-7261(02)00126-4

Peng, E., & Zhang, D. (2017). Prevention of liquefaction of saturated sand using biogas produced by Pseudomonas stutzeri. *International Conference on Transportation Infrastructure and Materials, Qingdao, China*.

Persoff, B. P., Apps, J., Moridis, G., & Whang, J. M. (1999). EFFECT OF DILUTION AND CONTAMINANTS ON SAND GROUTED WITH COLLOIDAL SILICA. *Manager*, *125*(June), 461–469.

Porcino, D., Marcianò, V., & Granata, R. (2015). Cyclic liquefaction behaviour of a moderately cemented grouted sand under repeated loading. *Soil Dynamics and Earthquake Engineering*, *79*, 36–46. https://doi.org/10.1016/j.soildyn.2015.08.006

Poulos, S. J., Castro, G., & France, J. W. (1985). Liquefaction evaluation procedure. *Journal of Geotechnical Engineering*, *111*(6), 772–792.

Ramos, C. P. F. C. (2021). *Cyclic liquefaction susceptibility of soils from field and laboratory tests. Methodologies and critical analyses*.

Rebata-Landa, V., & Santamarina, J. C. (2012). Mechanical effects of biogenic nitrogen gas bubbles in soils. *Journal of Geotechnical and Geoenvironmental Engineering*, *138*(2), 128–137.

Rio, J. F. M. E. (2006). *Advances in laboratory geophysics using bender elements*. University of London, University College London (United Kingdom).

Robert Kayen, B. E., Mitchell, J. K., & Member, H. (1997). *ASSESSMENT OF LIQUEFACTION POTENTIAL DURING EARTHQUAKES BY ARIAS INTENSITY*.

Roscoe, K. H., Schofield, A. N., & Wroth, C. P. (2015). On The Yielding of Soils. *Https://Doi.Org/10.1680/Geot.1958.8.1.22*, *8*(1), 22–53. https://doi.org/10.1680/GEOT.1958.8.1.22

Rugg, D. A., Yoon, J., Hwang, H., & El Mohtar, C. S. (2011). Undrained shearing properties of sand permeated with a bentonite suspension for static liquefaction mitigation. In *Geo-Frontiers 2011: Advances in Geotechnical Engineering* (pp. 677–686).

Rupam, S. (2014). A Review on Soil Improvement Techniques to Mitigate Liquefaction. *North East Students Geo-Congress on Advances in Geotechnical Engineering-2014*, *2014*(March), 1–6.

Sadiq, A. B. A. and T. S. Ali. (2023). Improvement of liquefaction potential in saturated sandy soil by CKD and bentonite. *Pollack Periodica*.

Saito, J., Watanabe, Y., Yamada, T., & Lee, J. (2012). Verification of long-term durability of chemical grout employed as countermeasure against liquefaction. In *Grouting and Deep Mixing 2012* (pp. 2024–2033).

Salvatore, E., Modoni, G., Mascolo, M. C., Grassi, D., & Spagnoli, G. (2020). Experimental Evidence of the Effectiveness and Applicability of Colloidal Nanosilica Grouting for Liquefaction Mitigation. *Journal of Geotechnical and Geoenvironmental Engineering*, *146*(10). https://doi.org/10.1061/(asce)gt.1943-5606.0002346

Santamarina, J. C., & Fam, M. A. (1997). Discussion: Interpretation of bender element tests. *Géotechnique*, *47*(4), 873–877.

Santamarina, J. C., Klein, K. A., & Fam, M. A. (2001). Soils and Waves, ; ohn Wiley & Sons. *Ltd.: Chichester, UK*.

Seed, H. B., Idriss, I. M., & Arango, I. (1983). Evaluation of liquefaction potential using field performance data. *Journal of Geotechnical Engineering*, *109*(3), 458–482.

Seed, H. B., Martin, G. R., & Finn, W. D. L. (1975). Fundamentals of liquefaction under cyclic loading. *Journal of the Geotechnical Engineering Division*, *101*(5), 423–438.

SEED HB, & IDRISS IM. (1971). Simplified Procedure for Evaluating Soil Liquefaction Potential. *Journal of the Soil Mechanics and Foundations Division*, *97*(9), 1249–1273. https://doi.org/10.1061/JSFEAQ.0001662

Shi, C., Huang, Z., Zhou, Y., He, J., Yang, F., & Hang, L. (2019). Soil Desaturation Methods for the Improvement of Liquefiable Ground. *IOP Conference Series: Materials Science and Engineering*, *562*(1). https://doi.org/10.1088/1757-899X/562/1/012015

Siddique, S. N., Deng, J., & Mohamedelhassan, E. (2023a). Improving the Strength Properties of Sand Using Laponite, a Promising Nanoparticle. *International Journal of Civil Engineering*, *21*(4), 679–693. https://doi.org/10.1007/s40999-022-00791-4

Siddique, S. N., Deng, J., & Mohamedelhassan, E. (2023b). Review on the Application of Nanoparticles to Mitigate Liquefaction Risks. *Soil Mechanics and Foundation Engineering*. https://doi.org/10.1007/s11204-023-09888-x

Simatupang, M., & Okamura, M. (2017). Liquefaction resistance of sand remediated with carbonate precipitation at different degrees of saturation during curing. *Soils and Foundations*, *57*(4), 619–631. https://doi.org/10.1016/j.sandf.2017.04.003

Skempton, A. W. (1954). The pore-pressure coefficients A and B. *Geotechnique*, *4*(4), 143–147.

Stewart, D. P., Chen, Y.-R., & Kutter, B. L. (1998). Experience with the use of methylcellulose as a viscous pore fluid in centrifuge models. *Geotechnical Testing Journal*, *21*(4), 365–369.

Tamura, S., Tokimatsu, K., Abe, A., & Sato, M. (2002). Effects of air bubbles on B-value and P-wave velocity of a partly saturated sand. *Soils and Foundations*, *42*(1), 121–129.

Teves-Costa, P., & Batlló, J. (2011). The 23 April 1909 Benavente earthquake (Portugal): macroseismic field revision. *Journal of Seismology*, *15*, 59–70.

Tsuchida, H. (1970). Prediction and countermeasure against the liquefaction in sand deposits. *Abstract of the Seminar in the Port and Harbor Research Institute*, 31–333.

Tsukamoto, Y., Ishihara, K., Nakazawa, H., Kamada, K., & Huang, Y. (2002). Resistance of partly saturated sand to liquefaction with reference to longitudinal and shear wave velocities. *Soils and Foundations*, *42*(6), 93–104.

Tsukamoto, Y., Kawabe, S., Matsumoto, J., & Hagiwara, S. (2014). Cyclic resistance of two unsaturated silty sands against soil liquefaction. *Soils and Foundations*, *54*(6), 1094–1103. https://doi.org/10.1016/j.sandf.2014.11.005

Vanapalli, S. K., Fredlund, D. G., Pufahl, D. E., & Clifton, A. W. (1996). Model for the prediction of shear strength with respect to soil suction. *Canadian Geotechnical Journal*, *33*(3), 379–392.

Viana da Fonseca, A., Cordeiro, D., & Molina, F. (2021). *Recommended Procedures to Assess Critical State Locus from Triaxial Tests in Cohesionless Remoulded Samples. Geotechnics 2021, 1, 1–34.* s Note: MDPI stays neu-tral with regard to jurisdictional claims in ….

Viana da Fonseca, A., Ferreira, C., & Fahey, M. (2009). A framework interpreting bender element tests, combining time-domain and frequency-domain methods. *Geotechnical Testing Journal*, *32*(2), 91–107.

Viana da Fonseca, A., Millen, M., Quintero, J., Sargin, S., Rios, S., Romão, X., Pereira, N., Panico, F., Oztoprak, S., & Kelesoglu, M. K. (2023). Macromechanism Approach for Vulnerability Assessment of Buildings on Shallow Foundations in Liquefied Soils. *Journal of Geotechnical and Geoenvironmental Engineering*, *149*(3). https://doi.org/10.1061/jggefk.gteng-10881

Viggiani, G., & Atkinson, J. H. (1995). Interpretation of bender element tests. *Geotechnique*, *45*(1), 149–154.

White, D. J. (2002). *The measurement of particle size distribution using the Single Particle Optical Sizing (SPOS) method*. University of Cambridge, Department of Engineering.

White, N. F., Duke, H. R., Sunada, D. K., & Corey, A. T. (1970). Physics of desaturation in porous materials. *Journal of the Irrigation and Drainage Division*, *96*(2), 165–191.

Woessner, W. W., & Poeter, E. P. (2020). *Hydrogeologic properties of earth materials and principles of groundwater flow*. Groundwater Project.

Xiao, P., Liu, H., Xiao, Y., Stuedlein, A. W., & Evans, T. M. (2018). Liquefaction resistance of bio-cemented calcareous sand. *Soil Dynamics and Earthquake Engineering*, *107*(September 2017), 9–19. https://doi.org/10.1016/j.soildyn.2018.01.008

Xu, B., He, N., & Li, D. (2019). Study on the treatments and countermeasures for liquefiable foundation. *MATEC Web of Conferences*, *272*, 01012. https://doi.org/10.1051/matecconf/201927201012

Yang, J., Savidis, S., & Roemer, M. (2004). Evaluating liquefaction strength of partially saturated sand. *Journal of Geotechnical and Geoenvironmental Engineering*, *130*(9), 975–979.

Yasuhara, H., Okamura, M., & Kochi, Y. (2008). Experiments and predictions of soil desaturation by air-injection technique and the implications mediated by multiphase flow simulation. *Soils and Foundations*, *48*(6), 791–804. https://doi.org/10.3208/sandf.48.791

Yegian, M. K., Eseller-Bayat, E., Alshawabkeh, A., & Ali, S. (2007). Induced-Partial Saturation for Liquefaction Mitigation: Experimental Investigation. *Journal of Geotechnical and Geoenvironmental Engineering*, *133*(4), 372–380. https://doi.org/10.1061/(asce)1090-0241(2007)133:4(372)

Yang, J. (2002). Liquefaction resistance of sand in relation to P-wave velocity. *Geotechnique*, *52*(4), 295–298.

Yoshimi, Y., Tanaka, K., & Tokimatsu, K. (1989). Liquefaction resistance of a partially saturated sand. *Soils and Foundations*, *29*(3), 157–162.

Youd, T. L., & Idriss, I. M. (2001). Liquefaction resistance of soils: summary report from the 1996 NCEER and 1998 NCEER/NSF workshops on evaluation of liquefaction resistance of soils. *Journal of Geotechnical and Geoenvironmental Engineering*, *127*(4), 297–313.

Zachariah, J. P., & Jakka, R. S. (2025). Cyclic behavior and liquefaction resistance of sand with partial bagasse replacement. *Soil Dynamics and Earthquake Engineering*, *191*, 109237.

Zamani, A., Xiao, P., Baumer, T., Carey, T. J., Sawyer, B., DeJong, J. T., & Boulanger, R. W. (2021). Mitigation of Liquefaction Triggering and Foundation Settlement by MICP Treatment. *Journal of Geotechnical and Geoenvironmental Engineering*, *147*(10). https://doi.org/10.1061/(asce)gt.1943-5606.0002596

Zeghal and Elgamal. (1994). *ANALYSIS OF SITE LIQUEFACTION USING EARTHQUAKE RECORDS*.

Zeghal, M., & El Shamy, U. (2008). Liquefaction of saturated loose and cemented granular soils. *Powder Technology*, *184*(2), 254–265. https://doi.org/10.1016/j.powtec.2007.11.032

Zeybek, A. (2022). Experimental and empirical studies to evaluate liquefaction resistance of partially saturated sands. *Applied Sciences*, *13*(1), 81.

Zeybek, A., & Hall, C. (2017). *Air Injection Technique to Mitigate Liquefaction beneath Shallow Foundations*.

Zeybek, A. & Madabhushi, G. S. P. (2017a). Durability of partial saturation to counteract liquefaction. *Proceedings of the Institution of Civil Engineers: Ground Improvement*, *170*(2), 102–111. https://doi.org/10.1680/jgrim.16.00025

Zeybek, A. & Madabhushi, S. P. G. (2017b). Centrifuge testing to evaluate the liquefaction response of air-injected partially saturated soils beneath shallow foundations. *Bulletin of Earthquake Engineering*, *15*(1), 339–356. https://doi.org/10.1007/s10518-016-9968-6

Zeybek, A., & Madabhushi, S. P. G. (2017c). Influence of air injection on the liquefaction-induced deformation mechanisms beneath shallow foundations. *Soil Dynamics and*

Earthquake Engineering, *97*(October 2015), 266–276. https://doi.org/10.1016/j.soildyn.2017.03.018